NUMERICAL MODELLING OF TIDAL FLOWS AROUND HEADLANDS AND ISLANDS

Scott John Couch MEng

This thesis is submitted in fulfilment of the requirements for the degree of Doctor of Philosophy in the Department of Civil Engineering, University of Strathclyde, Glasgow

October 2001

ACKNOWLEDGEMENTS

I am indebted to my supervisor Dr. Graham Copeland, Senior Lecturer, University of Strathclyde for his support, guidance and the benefit of his experience, all provided unfailingly throughout this research. It may have taken a little longer than originally envisaged, but we got there in the end. The assistance of various members of staff within the Department of Civil Engineering both past and present is also gratefully acknowledged. The support and friendship of the many colleagues who have passed through the 4.05 office during my time has only enriched the Ph.D experience.

Most importantly I would like to acknowledge the support (both moral and financial) provided by my parents. In particular, I must thank them for their forbearance and the steadfast encouragement provided throughout the emotional roller coaster that I have experienced while undertaking this research. My parents have provided me with the means and opportunity to choose my own path throughout the 26 years of my life. I just hope that they have, and will continue to be proud of the person that I have become.

Funding for the research presented in this thesis was provided by an EPSRC studentship (award reference number 96304556).

ABSTRACT

This thesis presents a study of tidal flow interaction with headland and island features. Wake development in the lee of topographic features can generate complex two- and three-dimensional flow structures. The primary objectives of the research are to (i) determine the suitability of traditional numerical modelling techniques for application in the coastal environment, (ii) elucidate the development of wake features in the coastal environment, and (iii) illustrate the impact of wake features on tidal mixing and dispersion processes.

A numerical finite-difference model has been developed using standard methods to solve the two-dimensional Shallow Water Equations. The model has undergone an extensive validation and verification exercise. Comparisons of model output with field data and output from other numerical simulations presented in the literature confirms the suitability of the numerical model for investigating wake and eddy development in the coastal environment.

The sequence of events necessary for a wake eddy to develop from flow separation through to eddy shedding has been elucidated using idealised numerical modelling cases. Simulation and interpretation of test cases obtained from the literature has confirmed these findings. Important differences between eddy shedding events in headland and island wakes have been identified. Symmetry of the governing equations has been confirmed as the source of numerical models' failure to reproduce eddy shedding around symmetrical islands.

Mixing and dispersion around a headland in a deterministic tidal flow field is simulated. Lagrangian analysis techniques are required to properly interpret transport processes. The significant impact of transient eddy features generated by the headland is indicated by the mixing and dispersion diagrams presented. A defined front between the well mixed and unmixed regions of flow is apparent. This indicates the extent of the mixing zone. Dispersion of individual patches around the headland is described using a three stage process.

CONTENTS

LIST OF FIGURES

Chapter 7: UNSTEADY WAKE PHENOMENA

Chapter 8: RATTRAY ISLAND CASE STUDY

LIST OF SYMBOLS

c = wave celerity.
C = conservative tracer (of concentration C).
C_{CFL} = Courant-Friedrichs-Lewey condition.
C_D = depth-averaged drag coefficient.
C_r = Courant number.
C_v = phase velocity.
C_w = air-water resistance coefficient.
d = depth (measured from mean water level to the sea-bed $\cong$ mean depth).
D = global diffusion coefficient.
D_{12} = depth-averaged dispersion-diffusion coefficient. Subscripts 1 and 2 refer to the plane and direction of action.
e = volume dilation.
E = Young's modulus of elasticity.
f = Coriolis parameter.
F = force.
Fr = Froude number.
g = gravitational acceleration.
G = shear modulus.
h = total depth ($= d + \eta$).
H.O.T. = higher order terms.
HW = high water (peak tidal elevation).
$\mathbf{i}, \mathbf{j}, \mathbf{k}$ = unit vectors.
$\hat{k}$ = the vertical unit vector.
K = dispersion coefficient.
K_C = Keulegan-Carpenter number.
K_z = vertical eddy diffusion coefficient.
l_m = Prandtl's mixing length.
L = characteristic length scale.
LW = low water.
M = mass.
n = Manning's friction coefficient.
P = island wake parameter.
P_a = atmospheric pressure.
P_h = hydrodynamic (or hydrostatic) pressure.
q = modelled convective momentum coefficient (user-variable).
qu, qv = discharge per unit width in the x- and y- direction respectively.
r = Poisson's ratio.
r^2 = (statistical) correlation coefficient.
R = hydraulic radius.
RAN= randomly generated number between 0 and 1.
Re = (horizontal) Reynolds number ($= Re_h$).
Re_f = 'equivalent' Reynolds number.
Ro = Rossby number.
S = wake stability parameter.
S_e = rate of energy loss per unit length.
St = Strouhal number.

St_c = critical Strouhal number.
S_{12} = displacement. Subscripts 1 and 2 refer to the plane and direction of action.
t = time.
T = total elapsed time.
u_*, v_* = friction velocity in the x- and y- directions respectively.
u, v, w = velocity components in the x-, y- and z- directions respectively.
U, V, W = depth-averaged velocity components in the x-, y- and z- directions respectively.
$\hat{V}$ = mean fluctuating velocity.
V_T = vector velocity = $\mathbf{i}u+\mathbf{j}v+\mathbf{k}w$; in horizontal plane = $\mathbf{i}u+\mathbf{j}v$.
W_{10} = wind speed measured at 10 metres above the surface level.
$x, y, z,$ = Cartesian co-ordinates in the x-, y- and z- planes respectively.
X, Y, Z = body force per unit mass in the x-, y- and z- directions.
z_* = boundary roughness length.

β = correction parameter for the vertical variation of the velocity profile.
Δa = a finite change in the property 'a'.
ε_{12} = strain. Subscripts 1 and 2 refer to the plane and direction of action.
ε'_{12} = strain per unit time. Subscripts 1 and 2 refer to the plane and direction of action.
ε_v = volumetric strain.
Φ = variance.
γ_{12} = angular strain. Subscripts 1 and 2 refer to the plane and direction of action.
γ'_{12} = angular strain per unit time. Subscripts 1 and 2 refer to the plane and direction of action.
η = elevation (describes the fluctuating component of the total depth in relation to the mean water level).
κ = von Karman's constant.
μ = absolute molecular (or dynamic) viscosity.
ν = kinematic molecular viscosity = (μ/ρ).
ν_t = horizontal eddy (or turbulent) viscosity.
ρ = fluid density.
ρ_a = air density.
σ_{12} = normal stress. Subscripts 1 and 2 refer to the plane and direction of action.
$\overline{\sigma}$ = mean of the three normal stress components.
σ'_{12} = deviatoric (Reynolds) normal stress. Subscripts 1 and 2 refer to the plane and direction of action.
σ_d = standard deviation.
σ_d^2 = variance.
σ_t = wave frequency (in Radians).
τ_{12} = shear stress. Subscripts 1 and 2 refer to the plane and direction of action.
τ = boundary shear stress.
τ_b = bottom friction term.
τ_w = wind stress term.
ω = frequency of eddy shedding (time taken for 2 alternate eddies to shed).
Ω = angular velocity.

ζ = the vertical component of vorticity relative to the rotating frame.

∞ = infinity.

$\bar{a}$ = mean component of variable 'a'.

$a`$ = fluctuating component of variable 'a'.

$|a|$ = modulus of the variable 'a'.

$\tilde{a}$ = value of variable 'a' at the free surface.

$\underline{a}$ = value of variable 'a' at the sea-bed.

$\frac{\partial a}{\partial b}$ = partial differentiation of property 'a' with respect to property 'b'.

$\frac{\partial^2 a}{\partial b^2} = \frac{\partial}{\partial b}\left(\frac{\partial a}{\partial b}\right)$.

$\frac{D}{Dt}$ = the total derivative $= \frac{D}{Dt} = \frac{\partial}{\partial t} + u\frac{\partial}{\partial x} + v\frac{\partial}{\partial y} + w\frac{\partial}{\partial z}$.

$a \bullet b$ = the scalar (or dot) product of the two vectors 'a' and 'b'.

$a \times b$ = the vector (or cross) product of the two vectors 'a' and 'b'.

∇ = del, or grad, the vector operator.

Σ = summation.

$\int_b^c da$ = integrate with respect to variable 'a' between the limits 'b' and 'c'.

$\ln(x) = \log_e(x)$.

1. INTRODUCTION

1.1 Background

Interest in understanding oceanic processes has developed in tandem with the needs of society. Man's first real interest in the sea was as a vehicle for transportation. As society developed and trade became an important part of life and people's livelihood, scholars directed their interest to understanding problems relevant to the time. Questions such as why the sea would appear to rise and fall, why this process varied from place to place, discovering the best sea-routes and developing navigational aids would inspire the intellectual community. As solutions to these problems have been proposed, rejected and synthesised over time, society has continued to develop and pose further questions for following generations to ponder. As the knowledge base has continually expanded, it has become necessary to specialise in a particular narrow area in order to become well-versed in the subject area. Dependent upon the particular application, oceanographers, meteorologists, marine biologists, chemists, geologists, geographers and civil engineers can be involved in projects relating to the oceanic environment. The work being presented herein concentrates on flow development in the nearshore coastal zone. Understanding this aspect of the oceanic environment is of direct relevance in addressing contentious problems facing society today relating to offshore waste disposal, ecosystem dynamics, coastal erosion and sediment transport.

In an idealised coastal environment exhibiting a steady flow regime with uniform topographic and bathymetric conditions, the flow development is well understood, and can be easily predicted using simple numerical or physical modelling techniques, or by analogy with open channel hydraulics. Relating such simple idealised cases to the real coastal environment is however of little or no direct benefit, as the interaction of an unsteady (tidal) turbulent flow with complex topographic and bathymetric conditions produces a totally different result. The most complicated flows occur when topographic and bathymetric variation reach extremes. Coastal features such as headlands, islands and sea-mounts are examples which consistently exhibit complex flow interactions.

1.2 Objectives

The aim of the research described in this thesis is to enhance understanding of nearshore coastal flow processes, specifically the results of tidal interaction with coastal features. Particular attention will be focussed on the occurrence and development of transient eddies. The major research tool will be a numerical model developed specifically for the project. Separating out numerically generated errors from the real flow development is of fundamental importance to both the continued development of modelling techniques, and the proper interpretation of the real phenomena. The following key objectives form the core of the research:

(i) To develop a robust grid based numerical model able to simulate nearshore coastal flow processes and use it to assist in meeting the following objectives.

(ii) To identify factors influencing the occurrence of transient eddies.

(iii) To understand the continued development of transient eddy features.

(iv) To illustrate the impact of transient eddy features on tidal mixing and dispersion characteristics.

(v) To compare and contrast between results obtained from laboratory experiments and full scale shallow water flows in the nearshore coastal environment.

(vi) To enhance understanding of the impact grid based numerical modelling techniques have on the accuracy of the model solution.

1.3 Synopsis

This thesis is arranged in 10 chapters, a bibliography and 2 appendices, which document the progress of the research. Chapter 2 presents a review of the existing literature relating to coastal flow processes and outlines areas that require further examination. Chapter 3 introduces the mathematical framework used to describe and analyse coastal flow processes. Chapter 4 describes the discretisation of the model equations, and development of the numerical model applied throughout this research. Chapter 5 details the validation and verification of the numerical model using a variety of analytical, text-book and real world cases. In chapter 6, the principle eddy

generating mechanisms are identified and illustrated. Common numerical modelling problems associated with the study of transient eddy features are also discussed. Chapter 7 compares and contrasts unsteady eddy regimes occurring in the laboratory and coastal environment. Important limitations of popular numerical modelling techniques are identified and addressed. Chapter 8 disputes perceived failings presented in the literature associated with fixed-grid based numerical modelling techniques using a real case study. Chapter 9 discusses the impact of transient eddy features on localised tidal mixing and dispersion characteristics. Conclusions and suggestions for further work are given in chapter 10. A full list of references from the thesis is contained in the bibliography. Details of the mathematical techniques and identities referred to in the main body of the thesis are presented in Appendix A. A complete listing of the grid-based numerical model code developed during the project is provided in Appendix B.

2. TIDAL FLOW DEVELOPMENT IN THE NEARSHORE COASTAL ENVIRONMENT

Non-linear interaction of tidal flow with topographic (surface) and bathymetric (submerged) features can generate complex two- and three-dimensional flow structures. Mixing and diffusion processes in the near-shore coastal environment are therefore quite different from those observed in the open sea. The impact these processes have on wastewater and spillage distribution, sediment transportation and ecosystem dynamics generates significant interest in the academic community. This interest is driven by the concerns of the wider general public, and reflected by recent political enactment of stringent legislation (e.g. the EC Urban Waste Water Treatment Directive, the EC Bathing Waters Directive and the EC Shellfish Directive).

Coastal flow processes are in general dominated by tidal forcing. Other driving mechanisms that can contribute towards coastal flow development are storm surges, salinity intrusions and short-wave induced currents (Falconer, 1994). This research will be focussed on flow processes derived from tidal forcing. Chapter 3 will introduce the mathematical descriptions predominantly used to study coastal flow processes, namely the two- and three- dimensional equations of motion. These equations provide the foundation upon which the majority of academic understanding of coastal flows is based. However, direct application of these equations in all but the simplest of idealised cases is a hopeless task. The traditional method for evaluating complicated fluid dynamics problems (other than direct observation) has been to construct a physical model. The (comparatively) recent development of the computer, and subsequent rapid development of computational power, coupled with the development of advanced numerical techniques has offered an alternative numerical modelling approach. The reality of the situation however is that both physical and numerical modelling techniques are subject to errors and reduction in accuracy when applied to anything other than the simplest idealised cases. Consequently, although physical and numerical modelling techniques provide important research tools, neither presents an accurate and complete description of fluid flow. Continued research is therefore necessary to increase knowledge and understanding of fluid flow processes. Tidal flow development is the focus of this work, although some of the findings may well be of relevance to other branches of

fluid mechanics. The purpose of this chapter is to introduce and discuss the existing literature relating to the study of tidal flow development in the coastal environment. It is assumed that the reader has a basic understanding of fluid dynamics.

2.1 Flow Classification

The simplest classification of any flow is whether it is laminar (smooth) or turbulent (chaotic). Flow in the coastal zone is considered to be turbulent although a narrow band of laminar flow must exist adjacent to solid boundaries. From direct observation it is also possible to state that coastal flows are three-dimensional, time-dependent and primarily driven by tidal processes. Coastal flows can be further classified when they interact with bluff body features into two distinct groups, attached and separated flow (Batchelor, 1967). The simpler of the two cases is attached flow, where the flow (streamlines) remain parallel to the feature as the flow progresses around the obstacle. This phenomenon has also been referred to as a potential or irrotational flow (Milne-Thompson, 1968). In the coastal environment, flow separation can be described as having taken place when streamlines break away from the rigid parallel structure observed in an attached flow. Batchelor (1967) and van Dyke (1982) present numerous photographic comparisons and examples of attached and separated flow regimes.

In reality, a fully potential or irrotational flow solution is unobtainable, as the condition of exactly parallel streamlines can only be achieved when considering a theoretically inviscid fluid (i.e. a fluid which cannot support shear). In the case of all real fluids (i.e. those that possess viscosity), the flow streamlines remain only approximately parallel to the bluff body (The Open University, 1984). The attached and separated flow phenomena are still distinctly different however, as can be confirmed by considering boundary layer theory.

2.1.1 Boundary layer theory and flow separation

Having established that fluid flowing around a bluff body either remains attached to, or separates from the boundary, it is necessary to understand the mechanism for change from one regime to the other. Such flow situations are not just restricted to the coastal environment, and the prevalence of such phenomena has attracted the interest of a number of eminent scientists (e.g. Prandtl, von Karman,

Schlichting). From basic observation, it can generally be stated that the flow will remain attached to the bluff body boundary under conditions where the velocity is low, and the boundary remains either parallel or near parallel to the flow direction (Mitsuyasu & Hiraki, 1969). The simplest method of describing why flow separation occurs is to introduce the concept of the boundary layer. Boundary layer theory was originally developed as an analysis tool applicable to laboratory flows, but the philosophy is equally appropriate when considering the coastal environment. Numerical relationships developed for laboratory type flows which are often tied into the concept of boundary layer theory however are not necessarily directly relevant in the coastal zone (see section 2.2).

As the viscosity of water is relatively small, inviscid flow theory is often applied (i.e. where the effect of viscosity is neglected, and the fluid is therefore considered to be unable to support any shear), and the fluid is considered to flow uninterrupted over solid surfaces in order to simplify analysis (Batchelor, 1967). The assumptions inherent in this theory are no longer valid when the flow over a boundary is of significance, as in reality there will be no movement immediately adjacent to the solid surface (referred to as a no-slip condition), and therefore a shear layer must be established. In 1904, Prandtl proposed the key concept of boundary layer theory (Liggett, 1994) as a more generally applicable expansion of inviscid flow theory. This theory again considers the majority of the flow to be inviscid, but significantly, also incorporates a thin layer of fluid adjacent to the boundary (the boundary layer) whose forward motion is impeded by drag exerted by the solid surface. The general characteristics of a boundary layer are (i) that it encompasses the distance normal to the boundary where the velocity increases from zero to that of the free-stream flow, (ii) the pressure intensity throughout the boundary layer is governed by the surrounding (inviscid) flow, and (iii) as long as the free-stream velocity is either constant or steadily increasing at the outer border of the boundary layer, growth in the thickness of the boundary layer will be retarded (Rouse, 1938; Vallentine, 1969; Vardy, 1990). The second point provides a major analytical simplification, as the pressure intensity or pressure gradient (which describes the effect of gravity on the fluid motion in free surface flow) is easily derived from the characteristics of the free-stream velocity. The importance of the pressure gradient is that it is normally the major forcing factor acting on the fluid (particularly in the tidally dominated environment of the coastal zone). If the free-stream velocity is

increasing, this is indicative of a *favouring* pressure gradient. Under conditions of a favouring pressure gradient, there is a resultant pressure force in the direction of the flow which transfers kinetic energy from the free-stream into the boundary layer. The kinetic energy gained in the boundary layer under these conditions aids in overcoming the retarding action of the no-slip condition, and restricts expansion of the boundary layer. If on the other hand the free-stream velocity were decreasing, that would be indicative of an *adverse* pressure gradient. The resultant pressure force is opposed to the direction of flow in the case of an adverse pressure gradient. The occurrence of an adverse pressure gradient removes kinetic energy from both the free-stream and boundary layer flows. As the flow velocity immediately adjacent to the boundary is very small due to the no-slip solid boundary interface, there is no significant momentum available in this region to overcome the opposing pressure gradient. If the opposing pressure gradient persists, the result is expansion of the boundary layer width, as the flow velocity across the existing boundary is eroded, and a return flow becomes established. As soon as a return flow occurs in the boundary layer, the flow is considered to have separated from the boundary, and proceeds along the edge of the region of discontinuity that encompasses the reversed flow. A consequence of the flow separation is that the boundary layer flow immediately upstream of the point of separation is carried along the separation streamline into the interior of the flow. After separation has occurred, the flow downstream of the separation point can develop in a number of ways. If the separated boundary layer re-attaches downstream, thereby enclosing the region of discontinuity, the feature is referred to as a *wake bubble* (Ingram & Chu, 1987; Lloyd & Stansby, 1997(a)). A steadily re-circulating eddy in the lee of a headland is a commonly occurring example of a wake bubble feature observed in the coastal zone. If on the other hand, the boundary layer becomes caught up in the interior of the flow and does not re-attach, flow features such as detached eddies, eddy shedding, turbulent wakes, vortex street wakes, and jets have all been observed in the coastal environment (Pingree, 1978; Awaji, 1982; Wolanski et al., 1984; Hearn et al. 1985; Pattiaratchi et al. 1986; Ingram & Chu, 1987; Geyer & Signell, 1990; Davies & Mofor, 1990; Wang, et al., 1998).

The important point that has arisen, and is necessary for boundary layer flow separation to develop, is the occurrence of an adverse pressure gradient. As previously identified, if the boundary is near parallel to the flow direction, the flow remains attached to the boundary layer. This is because in this case, no significant

adverse pressure gradient would be established. In order for a critical adverse pressure gradient to occur, it would therefore appear that a significant divergence between the free-stream flow direction and boundary alignment is a prerequisite condition. Considering the case of a headland, the effect of the pressure gradient on the flow upstream of the headland tip in the local area would be a strong increase in the flow velocity. Downstream of the headland tip as the flow region expands, the localised flow velocity would be decreasing, this being the necessary condition to satisfy continuity. This phenomenon is referred to as tidal streaming (Pingree, 1978). Examining the effect of tidal streaming on the surface elevation profile around the headland, a low point is observed at the headland tip (Imasato, 1983). This elevation (and pressure) low point can be explained by consideration of the Bernoulli equation. The Bernoulli equation states that peak velocity and low pressure coincide. The low pressure region is indicative of a strong favouring pressure gradient on the upstream face of the headland and a strong adverse pressure gradient on the downstream face (Signell & Geyer, 1991). The consequence of this, as has now been established, is that if there is not enough momentum in the boundary layer, flow separation occurs.

2.1.2 Vorticity

Vorticity is the characteristic of a fluid that expresses the tendency for portions of the fluid to rotate (Pond & Pickard, 1993). Vorticity is created by differences in the flow speed laterally across the direction of flow (Faber, 1993). Dependent upon the frame of reference, vorticity can be described as either relative or planetary. Vorticity is normally measured relative to the earth in order to avoid complications, and is therefore referred to as the relative vorticity. The relative vorticity ζ (the vertical component of vorticity relative to the rotating frame (Gill, 1982)) can be expressed as:

$$\zeta = \frac{\partial v}{\partial x} - \frac{\partial u}{\partial y} \qquad (2.1)$$

The majority of studies of flow in the coastal environment are still restricted to the depth-averaged representation of the equations of motion (the Shallow Water Equations to be introduced in chapter 3). Consequently, the generation and transportation of vorticity is generally considered using a similar depth-averaged format (e.g. Pingree & Maddock, 1979; Zimmerman; 1978; Robinson 1981; Signell

& Geyer, 1991), which is derived by taking the curl of the momentum equation. This produces a vector equation. Equation 2.2 presents a typical representation of the depth-averaged vorticity equation (equation 2.2):

$$\underbrace{\frac{\partial \zeta}{\partial t}}_{(a)} + \underbrace{U \bullet \nabla \zeta}_{(b)} = \underbrace{\frac{\zeta + f}{h}\left[\frac{\partial \eta}{\partial t} + U \bullet \nabla h\right]}_{(c)} - \underbrace{\frac{C_D |U|}{h^2}[U \times \nabla h] \bullet \hat{k}}_{(d)} + \underbrace{\frac{C_D (U \times \nabla |U|) \bullet \hat{k}}{h}}_{(e)} - \underbrace{\frac{C_D |U| \zeta}{h}}_{(f)} + \underbrace{\overline{\nu}_t \nabla^2 \zeta}_{(g)},$$

where a×b is the vector, or cross product of the two vectors a and b, a•b is the scalar, or dot product of the two vectors a and b, and ∇ is the vector operator (called del, or grad). Robinson (1981) has presented a simple description of the effect of the various terms ((a) - (g)) in equation (2.2)) in terms of the generation, transportation and dissipation of vorticity. Figure 2.1 indicates the three vorticity generating mechanisms (term (c), 'squashing or stretching' of the water column, term (d), 'slope torque', and term (e), 'speed torque').

Analysing the vorticity generating mechanisms, it is clear that all three mechanisms would be acting in the vicinity of headland or island feature in the coastal environment (Signell & Geyer, 1991). The theoretical boundary layer previously introduced would particularly exhibit high levels of vorticity generation and concentration because of the action of 'speed torque'. When a flow separation event takes place, an avenue for transporting concentrated vorticity away from the boundary layer and into the interior of the flow is established. Although the theory behind this process is relatively well understood, there is limited physical or numerical modelling output which adequately demonstrates vorticity generation, or in

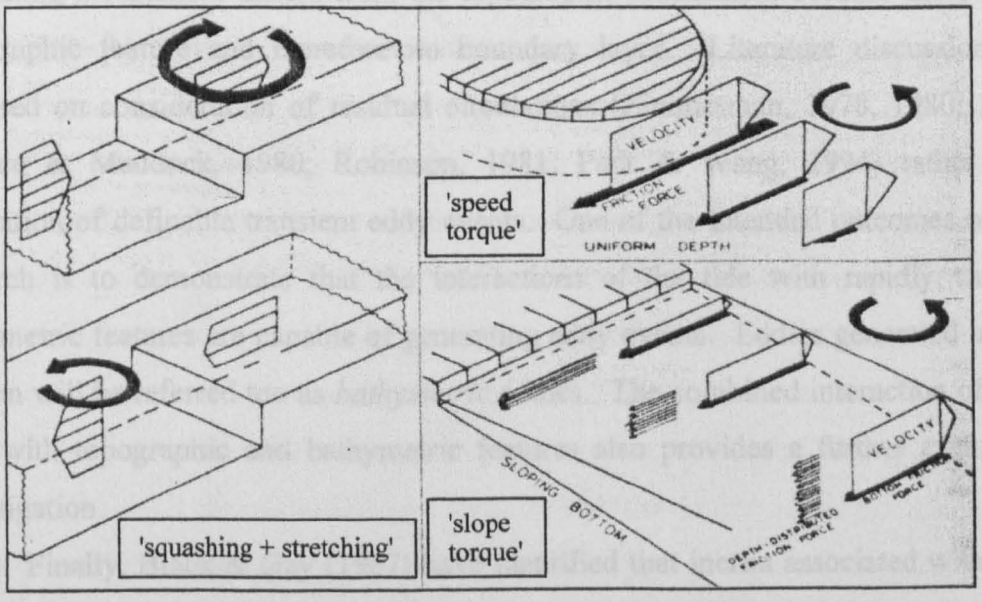

Figure 2.1 - Schematic illustration of the three distinct vorticity generating mechanisms (from Robinson, 1981).

particular subsequent vorticity transportation. This provides an avenue for investigation as part of this research.

2.1.3 Eddy generating mechanisms in tidal flow regimes

The process of boundary layer flow separation and subsequent vorticity roll-up is the principal eddy generating mechanism considered by the majority of fluid mechanics literature. Transfer of this knowledge to application in the coastal environment introduced in the previous two sections has been the subject of much academic interest. Additional factors specific to the coastal zone such as the influence of bottom friction and unsteady tidal flow condition have required further analysis to reconcile with the traditional laboratory based understanding of the eddy generating process (Maddock & Pingree, 1978; Pattriatchi et al. 1986; Davies et al. 1995; Wolanski et al. 1996). These factors will be expanded on in chapter 6. Eddies generated by a flow separation event have been referred to in the literature using a variety of different terminology. The one flow feature that is key to establishing an eddy in this case is the ability to support a boundary layer. A topographic feature is necessary in order to support a boundary layer. Eddies generated in this fashion will therefore be referred to as *topographic* eddies throughout this document.

Careful examination of the literature identifies a further possible eddy generating mechanism. The interaction of flow with a bathymetric feature also appears to provide conditions suitable for generating re-circulating flows. The eddy generating mechanism differs from the topographic mechanism because there is no topographic feature and therefore no boundary layer. Literature discussion has focussed on consideration of residual circulations (Zimmerman, 1978, 1980, 1986; Pingree & Maddock, 1980; Robinson, 1981; Park & Wang, 1994) rather than generation of definable transient eddy events. One of the intended outcomes of this research is to demonstrate that the interactions of the tide with rapidly varying bathymetric features are capable of generating eddy events. Eddies generated in this fashion will be referred too as *bathymetric* eddies. The combined interaction of tidal flow with topographic and bathymetric features also provides a further avenue of investigation.

Finally, Black & Gay (1987) have identified that inertia associated with tidal periodicity is an important force responsible for eddy formation. They also described

how this mechanism can develop pseudo-eddy features referred to as '*phase*' eddies in situations where large phase differences develop between the free-stream current and the current in the lee of an obstruction or in an area of relatively high friction. Characterising these features as eddies appears to have created subsequent confusion in the interpretation of Black & Gay's analysis, and its importance often appears to be undervalued when interpreting observed or modelled eddy development. In support of the proposed theory, Hyder and Elliott (1995) have suggested that the phase effect proposed by Black & Gay is responsible for the increasing eddy strength and extent demonstrated by a topographically generated eddy in the Menai Straits observed during flood tide slacks. Furthermore, Signell & Geyer (1991) and Denniss & Middleton (1994) have also acknowledged the important influence of flow inertia on flow and eddy development in unsteady tidal flow regimes.

2.1.4 Eddy shedding

Eddy shedding can occur in general fluid dynamics for a number of reasons. In the wake of a symmetric flow obstacle, eddy shedding can occur if the flow is subject to sufficient turbulent fluctuations in the free-stream (as described by the Reynolds number in the laboratory flow situation). Eddy shedding can also occur in the case of an asymmetric flow obstacle through interaction of the asymmetric eddy pair in the lee of the obstacle. Yet eddy shedding in the nearshore coastal environment in the form of a shedding wake regime is a relatively rare occurrence in comparison with other branches of fluid dynamics. There are a number of contributory factors to this state of affairs. The energy required to overcome friction experienced by a flow in shallow water regime is one factor that reduces the likelihood of eddy shedding occurring. Another factor is the periodicity of the tidal flow regime. In many headland and island cases, if a steady flow were to be maintained, repeated eddy shedding would eventually occur. However, the unsteady flow of the tidal period restricts the amount of time available for the wake flow to develop. The flow reversal of the tide can however be considered to force the shedding of an individual topographic eddy generated during the previous tidal period. This eddy becomes detached from its vorticity source as the tide turns, and is then transported into the flow interior by the prevailing tidal condition. The important point to be addressed regarding repeated eddy shedding phenomena is to

understand the transition from a stable wake, originally exhibiting either one (headland) or two (island) closed circulations (eddies), to the periodic shedding of eddies observed in a von Karman street wake. There are in reality a number of different transitions that the flow is required to undergo. Initially, consider the transition observed behind a bluff body generating two eddies. The first transition takes place when instability becomes apparent in the wake. A slow oscillation of the far wake is observed. This is initially only apparent far downstream of the re-circulating region. If steady state has been reached, the oscillation becomes regular in both space and time. On the other hand, if the free-stream velocity continues to increase, the instability propagates upstream. Once the unstable region has propagated far enough upstream to interact with the previously steadily rotating closed circulation, the eddies also begin to oscillate. At this stage, some of the rotating fluid in each of the eddies is alternately shed into the downstream wake during the oscillation of the wake. Downstream, a regular array of patches of rotating fluid is observed, each new patch encompassing the fluid shed during the previous oscillation of the re-circulating region. The regular downstream pattern of the fluid patches is referred to as a *vortex street wake*. If the flow develops further, in which case alternate eddies are completely shed from the downstream face of the bluff body, a special vortex street wake is observed which is referred to as a *von Karman street wake*. The rotating patches of fluid in the street wake travel downstream at a velocity less than that of the free-stream. Whichever level of instability is observed, if the input flow has reached steady state, the unsteady downstream wake maintains a regular periodic oscillation. Gerrard (1966) has described the important role of entrainment of near potential flow from outside the re-circulating eddy region into the eddy in generating an eddy shedding wake in the lee of a bluff body:

> "The growing vortex continues to be fed by circulation from the shear layer until the vortex becomes strong enough to draw the other shear layer across the wake. The approach of oppositely signed vorticity in sufficient concentration cuts off further supply of circulation to the vortex, which then ceases to increase in strength. We may speak of the vortex as being shed from the body at this stage."

The author is in agreement with this statement. However, acceptance of Gerrard's description of the shedding phenomenon indicates that eddy shedding in the wake of

a headland type feature must undergo a different shedding mechanism (as there is no obvious source of oppositely signed vorticity or opposing second eddy). Verron et al. (1991) have demonstrated using a numerical modelling approach that eddy shedding around a headland feature requires the presence of two re-circulating regions of opposite vorticity. The second eddy is generated through the interaction of the attached eddy generated at the headland tip with the closed boundary describing the downstream region of the headland. When the main eddy is shed from the headland, the associated oppositely signed secondary eddy also becomes detached from the boundary, and is wrapped up around the primary eddy. The eddy pair is then transported downstream. The frequency of eddy shedding once a regular periodic oscillation has been established can be quantified using the Strouhal number, $S_t = \frac{\omega L}{U}$, where ω is the frequency of eddy shedding (the time taken for two alternate eddies to shed). The Strouhal number is reported to be approximately 0.2 over a wide range of Reynolds numbers for flow around a cylindrical shaped flow obstacle (Liggett, 1994). Whether the Strouhal number would be appropriate for application to the shallow water environment is unclear. The variation of island shape and influence of turbulence and friction on the flow may all have some effect on the value of the Strouhal number. When vortex shedding regimes are encountered during this research, the Strouhal number will be calculated. This will enable analysis of whether the Strouhal number is suitable for application in the nearshore coastal environment. An important consideration when analysing eddy shedding regimes is that in order to generate a true von Karman street wake, a two-dimensional bluff body must be considered. In the case of a three-dimensional body, an irregular pattern of shedding is observed in the wake (Batchelor, 1967).

2.1.5 Eddy longevity in tidal flow regimes

Eddies generated by the topographic mechanism during the flood or ebb tide which are not subject to eddy shedding in the form of a vortex street wake remain attached to the headland as the tidal period progresses. While the separated flow region remains attached to the headland, vorticity generated in the boundary layer is continuously wrapped up around the centre of the re-circulating eddy. This continues to strengthen the circulation, and the pressure difference between the separation point

and the centre of the eddy continues to increase until the tide peaks. After the eddy has been detached from the headland as the tide turns, there is no longer a constant source of vorticity to help strengthen the circulation. At this stage the eddy begins to spin-down as vorticity is dissipated by viscous action and frictional resistance. Once the opposing tide has become established, the effect of the prevailing tide advects the eddy feature away from the original vorticity source. The influence of the circulation maintained by the eddy at this stage on the flow is minimal, although vorticity contour plots indicate that the background circulation is maintained. However, throughout the tidal period the eddy feature is subject to vorticity dissipation. Without a continuous replenishing source of vorticity, transient eddy features are generally fully spun-down by the time of the following tidal slack water in a shallow tidal regime. Little interest is therefore shown in the literature regarding the life span of transient eddy features in the coastal environment. Signell & Geyer (1991) have demonstrated using numerical model output that an order of magnitude reduction of the strength of frictional resistance produces a marked difference in the flow development. In the case of a headland flow, the topographic eddy generated during one tidal period that is subsequently shed as the tide reverses becomes paired with the start-up eddy generated by the new tidal stream direction. The mutual interaction of the two eddies causes the new eddy to shed before the tide slacks. The two eddies are then carried downstream by the tide. During tidal slacks, both re-circulating regions are well defined. The presence of the well-defined eddy regions is maintained throughout a number of the following tidal cycles until viscous dissipation of vorticity finally dampens the energy contained in the eddy system. The overall effect of reducing the friction coefficient by an order of magnitude is similar to increasing the depth by an order of magnitude. This work demonstrates that bed friction is of more importance in dictating the life span of a transient eddy feature in the coastal environment than viscous action. However, Imasato (1983) has also demonstrated through numerical model analysis that variation of the value of eddy viscosity within the model can have a significant effect on the life-span of the eddy.

2.2 Physical Modelling and Non-dimensional Parameters

A physical model of a system attempts to replicate the physical processes inherent in the system at a reduced scale. In order to accurately replicate the original

system at a different scale, it is important to ensure that the ratios of forces acting on the system are maintained. The correct ratio of forces can be derived using dimensionless expressions through a process referred to as dimensional analysis. Dimensional analysis is a simple procedure covered in most basic fluid mechanics texts (e.g. Featherstone & Nalluri, 1991; Liggett, 1994). For a more detailed analysis, books specifically addressing the subject of physical modelling can be consulted (e.g. Yalin, 1971; Sharp, 1981). Non-dimensional parameters can also be useful for categorising flow regimes or characteristic flow types. In the case of a coastal or estuarial physical model, the three major forces that need to be considered are gravity, viscous action and inertia (Price & Thorn, 1994). The dimensionless expressions relating the scale of these forces are the Froude Number $\left(Fr = \frac{V_T}{\sqrt{gL}}\right)$, and Reynolds Number $\left(Re = \frac{V_T L}{\nu}\right)$. Yalin (1971) has highlighted the difficulty of obtaining similitude between the prototype and model systems using these two scaling parameters because of the difficulty of altering the force of gravity, and difficulty in varying the kinematic viscosity. The success of the modelling exercise is consequently reliant on the experience and knowledge of the modeller, and their ability to achieve suitable compromises in the set-up of the model (Price & Thorn, 1994). Other dimensionless parameters can be considered as suitable scaling parameters dependent upon the conditions imposed on the model set-up, and the scale of the problem. A wide range of dimensionless parameters are presented in the literature (e.g. Vardy (1990) and Liggett (1994)).

Physical modelling of coastal and estuarial regions presents additional problems for the modeller. The first major difficulty is that the typical horizontal and vertical length scales in these regions are indicative of a shallow flow. Applying a uniform geometric scale in the horizontal and vertical planes generally produces an excessively shallow flow. With such a thin fluid layer, it is often difficult to generate a realistic turbulent flow regime. Furthermore, the influence of surface tension on the model results can become exaggerated. From a practical point of view, measuring velocities and elevation gradients is often not viable if an appropriate horizontal scale is also applied in the vertical direction. The engineering response to this problem is

to build a distorted model, with the scale in the vertical direction exaggerated. This procedure can only be considered practical in studies where the flow in the vertical direction is not significant. As discussed in chapter 3, this is a simplification that is generally acceptable when considering flow in the coastal zone. However, it is important not to excessively exaggerate the vertical scale, as fluid gradients in the model are similarly exaggerated. This can lead to the generation of unrealistic flow separation events (Breusers & van Os, 1981). A second major difference faced when modelling shallow water flows in the laboratory environment is the enhanced influence of bottom friction and bed generated turbulence (Boyer & Davies, 2000). This problem is magnified when an exaggerated vertical scale is applied. A further problem encountered when modelling a shallow water flow (particularly coastal flows) is in being able to generate a realistic turbulent regime in the laboratory. Finally, modelling of nearshore coastal flow regimes requires appropriate scaling of the temporal variation associated with the tidal cycle. Although in some cases a steady flow model will produce results that meet the requirements of the modeller, in most cases it is necessary to incorporate the tidal oscillation. Scaling of the temporal variation requires a further dimensionless expression. Dependent on the extent of the modelled domain, and the significance of Coriolis acceleration different parameters are required. When considering non-rotating small scale features (< 5 km), the Keulegan-Carpenter number $\left(K_c = \frac{V_T}{\sigma_t L}\right)$ provides an appropriate balance of forces which can be applied as a suitable dimensionless parameter.

The listed key differences specific to a shallow water flow ensure that much of the existing physical modelling literature and derived theory is not directly transferable to coastal application. For instance, the classical studies of an unbounded uniform flow past an obstacle (typically a flat plate or cylinder) relate the transition of the downstream flow regime to a specific range of Reynolds numbers (work generally attributed to Prandtl and von Karman in the early part of the 20th Century). Examples of the type of output obtained are presented in Batchelor (1967) and van Dyke (1982). While these results and the associated theory (for instance Prandtl's boundary layer theory) have become cornerstones of fluid mechanics, their application to coastal flow regimes has been misinterpreted. An example of this is

the direct application of the classic Reynolds number (now sometimes referred to as the horizontal Reynolds number, Re_h) to coastal flow situations. It is only relatively recently that the importance of the differences between coastal and laboratory flow regimes previously discussed has been fully understood. Analysing these differences indicates that the horizontal Reynolds number is not relevant in shallow water situations. This is because the controlling flow mechanisms in shallow water are frictional forces associated with the surface and bottom boundary layers rather than those associated with lateral boundaries in the classical unbounded flow situation (Wolanski et al. 1984, Coutis & Middleton, 1999). Opinions in the literature regarding the correct dimensionless expression to apply in shallow water situations have since become very confused. Commonly quoted (but often conflicting) expressions include the 'equivalent' Reynolds number $\left(Re_f = \frac{h}{C_D L}\right)$ advocated by Pingree & Maddock (1980) and Signell & Geyer (1991), the wake stability parameter, $\left(S = \frac{c_f L}{h}\right)$ advocated by Chen & Jirka (1997) and Lloyd & Stansby (1997a, b), and the island wake parameter $\left(P = \frac{V_T h^2}{K_z L}\right)$ advocated by Wolanski et al. (1984), Pattiaratchi et al. (1987) and cited by Boyer & Davies (2000). Furthermore, although the wake stability parameter is little more than the reciprocal of the equivalent Reynolds number, the values indicated in the literature related to specific flow phenomena (such as the characteristics of a bluff body wake) do not fit the same mathematical relationships (i.e. one parameter may indicate an attached flow regime, whereas the other predicts a steadily re-circulating eddy pair). The preferred parameters appear to be the 'equivalent' Reynolds number and island wake parameter following the analysis of Pattiaratchi et al. (1987). However, the island wake parameter is difficult to apply, particularly in a laboratory situation, because of the difficulty of measuring or specifying the vertical eddy viscosity (K_z). During this research, the predictive abilities of the 'equivalent' Reynolds number will be evaluated.

This discussion indicates the immense difficulties facing the prospective physical modeller. As yet there has been no mention of incorporating the tidal

oscillation characteristic of the coastal environment which further complicates both the scaling and construction of the physical model. In reality, this takes the problem too far. The majority of laboratory based projects have only considered a steady flow situation. The laboratory based analyses that have been produced in recent years can be categorised in two separate branches. The first branch (a) has focussed on processes related to mesoscale (10 - 100 km) or global scale (100+ km) flow processes (Boyer & Tao, 1987; Boyer et al. 1987(a); Boyer et al. 1987(b); Narimousa & Maxworthy, 1989; Davies et al. 1991; Boyer & Davies, 2000). The second branch (b) has addressed generalised studies of flow processes (e.g. only laminar flows modelled, or only applying traditional laboratory scaling relationships) (Mitsuyasu & Hiraki, 1969; Despard & Miller, 1971; Yanagi, 1976; Jiang & Falconer, 1983; MacDonald & Jirka, 1997), the results of which are then considered to be analogous to shallow water flow (either by the original or subsequent investigators). Studies falling into group (a) are of limited relevance at the scale of coastal shallow water processes being considered in this research. This is because (i) the results presented in these studies are specifically applicable to oceanic scale flows because of the relative importance of Coriolis compared with at nearshore coastal scales, and (ii) the balance of the dominant driving forces would be different, therefore different flow processes are being investigated (e.g. wind driven currents). Studies falling into group (b) are also limited in their application to coastal flow processes because the scaling applied bears little resemblance to coastal scales. For instance, two-dimensional return flow velocities in the lee of bluff bodies have been observed to be less than 1% of the free stream velocity in the laboratory (Keller & Niewstadt, 1973), whereas in the coastal environment, flow velocities in the re-circulating region are of the same magnitude as in the free-stream (Wolanski et al., 1984). Consequently only the broadest conclusions can be drawn from this type of output, as the balance of forces investigated are not directly comparable between model and prototype. Falconer & Guoping (1991) serves as a good example of a study that can be characterised as a group (b) type experiment. During an investigation of tidal currents and exchange processes in an idealised laboratory harbour, the authors were able to illustrate the significant divergence between modelled and prototype processes. Having applied the standard Froude law scaling relationship to ensure dynamic similarity, further analysis demonstrated that the laboratory system

underestimated frictional dissipation by an order of magnitude, and over-estimated the rate of transfer of bed-generated turbulence and dispersion processes by a similar order of magnitude. Taking into account the serious discrepancies between the modelled and prototype systems, the results could only be presented in the most generalised terms. For example, "... results showed that the tidal exchange coefficient reduced strongly with increasing depth ...".

The above discussion has demonstrated the limited role that laboratory based physical modelling can play when investigating microscale (< 10 km) coastal flow processes. Combined with the expense involved in obtaining reliable in-situ data, this provides a good indication why there is a significant on-going academic interest in coastal (and deep-ocean) flow processes, as our understanding of these systems is still relatively limited. It is only in the last 20 - 30 years that the necessary tools (e.g. computational power, numerical modelling techniques, satellites and remote-sensing technology) have been developed to aid in enhancing knowledge and understanding of these processes. In a sense, these developments have brought about a renaissance in the use of physical modelling and study of archived laboratory output in a new role - producing reliable data under controlled conditions for use in validation and verification of the newer technologies (Pattiaratchi, 1986; Falconer & Guoping, 1991; Verron et al. 1991; Wolanski et al. 1996; Lloyd & Stansby 1997(a), (b)). For instance, one key feature that comparison of laboratory data and numerical modelling output has highlighted is the widespread inability of fixed-grid numerical models to predict or replicate eddy shedding features observed both at prototype and model scales (Davies et al. 1995; Furukawa & Wolanski, 1998). Specialised numerical techniques have consequently been developed to address problems relating to the modelling of circulation and eddy features (e.g. discrete vortex models) which produce results more in line with observed data (Borthwick et al. 1988; Borthwick & Barber, 1992; Furukawa & Wolanski, 1998).

2.3 Tidal Mixing and Dispersion Processes

Tidal flow processes determine the transportation of pollutants, organisms and other suspended or dissolve material in shallow coastal regions (Signell & Geyer, 1990). Close to the source of the tracer element, the phenomenon may have a three-dimensional character (e.g. a buoyant plume discharging from a submerged sewage

outfall) (Koutitas, 1988). In the far-field however, the phenomenon will generally become two-dimensional, as horizontal motion is at least an order of magnitude larger than in the vertical plane. It is therefore assumed that the original tracer source will quickly become vertically well mixed. Consequently, the transport, mixing and dispersion of the tracer element can be considered using a one- or two-dimensional framework.

Mixing in the shallow water environment results from a combination of the variation of the advective mean velocity and small-scale turbulent diffusion (Fischer et al. 1979). Turbulence is generated by the action of the sea-bed on the tidal flow (friction). In the coastal environment, the tidal current contributes to mixing and dispersion in a variety of guises. Shear effects in the tidal flow make an obvious contribution to dispersion through the differential velocity of the receiving fluid. Residual circulation observed when the tidal periodicity is averaged across the domain of interest provides another mechanism for dispersion of tracer elements in the fluid. Residual circulation can be instigated by the earth's rotation, interaction of the tidal flow with irregular topography (Tee, 1976, 1988), bathymetry (Zimmerman, 1978), or tidal interaction with both features (Nihoul & Ronday, 1975; Pingree & Maddock, 1980). A further tidally induced mixing and dispersion mechanism is the 'trapping' of parcels of fluid in embayments and channels (Fischer et al. 1979). The theory behind the 'trapping' mechanism appears to be very similar to Black & Gay's 'phase' eddy theory, being related to differential momentum between the free-stream region and sheltered or shallow regions which ensures that flow reversal across the domain is not a uniform occurrence. In the case of a plume of a tracer element caught up in a small side embayment, the spatial variation of the reversal of the tide ensures that the tracer plume is detached from the original tracer plume after the reversing tide has become fully established. An in-depth discussion and description of mixing and dispersion processes is beyond the scope of this document. For a more rigorous discussion, the reader is referred to Fischer et al. (1979), Dyer (1988), List et al. (1990), and Bedford (1994).

2.4 Numerical Modelling of Nearshore Coastal Processes

A plethora of numerical modelling techniques, models and applications are presented in the literature. This indicates that there is still room for improvement and

development in numerical modelling techniques as no one model has become pre-eminent. Commenting on ongoing modelling practice, Aubrey (1990) has called for an improved balance between site-specific local studies and more generally applicable process-oriented studies of the basic physics. This would enable a more concentrated development of knowledge relating to both the physical processes and modelling techniques. The interests of individual engineering projects and related local concerns maintain the existing fragmented situation.

Numerical models and techniques have been developed to address every conceivable area of interest to the practising coastal engineer or oceanographer. An excellent review of numerical modelling of the nearshore coastal environment is presented by Abbott & Price (1994), which includes contributions from a wide cross-section of modelling experts. Of fundamental importance to understanding any nearshore coastal process is a realistic simulation of the local shallow water tidal currents (Clarke and Elliott, 1998). Analysis of the forces acting on a body of water is generally referred to as *hydroynamics*.

2.4.1 Hydrodynamics

Depending upon the scale of interest, hydrodynamic analysis can be focussed on wind-driven currents (Pingree & Griffiths, 1980; Wu & Tsanis, 1995), wave-driven currents (Rahman, 1988; Davies, 1992), or tidally driven currents (Falconer, 1984; Wang et al. 1998). In the nearshore coastal environment, tidally driven currents are generally the dominant hydrodynamic process. The three-dimensional equations of motion introduced in chapter 3 form the basis of numerical modelling analysis. Early work was restricted by computational expense to two-dimensions. This is achieved by simplification of the governing equations. Vertical integration of the equations, which produces the Shallow Water Equations is a popular method of simplification. Various numerical techniques were developed to solve the modelled equations. Some examples of these techniques are provided by Pingree & Maddock (1977), Falconer, (1980), Davis (1984), and Smith (1985), (finite-differencing), Navon (1988), and Peyret & Taylor (1983), (finite-element analysis), and Abbott & Basco (1989), (the method of characteristics). For further discussion and comparison of the available modelling techniques, the reader is referred to Liu & Leendertse (1978), and Abbott & Basco (1989). More recently, hydrodynamic model developers

have attempted to incorporate the fully three-dimensional governing equations (Heaps, 1987; Casulli & Cheng, 1992; Deleersnjider et al. (1992)). This step forward has been aided by the experienced gained developing two-dimensional models, and by development of increasingly more powerful computers. Three-dimensional modelling has been applied across a wide range of scales (Davies & Gerritsen, 1994; Casulli & Stelling, 1996). The number of calculation nodes required to generate a three-dimensional solution is still better suited to analysis of large scale coastal flow processes such as coastal shelf upwelling and down-welling (Allen et al. 1995, 1996) in the opinion of the author. At smaller scales, two-dimensional models still have difficulty in incorporating sufficient nodes to capture fine scale features important to the flow development (e.g. Galloway et al. 1996; Furukawa & Wolanski, 1998). The ability of three-dimensional models to simulate these features is further reduced by the larger horizontal cell sizes required in order to ensure a manageable level of computational expense. Three-dimensional models would therefore appear to be more suited to modelling of gross flow features until the expansion of computational power enables a further order of magnitude increase in model resolution.

2.4.2 Modelling of transport processes

The ultimate aim in developing an understanding of nearshore coastal flow processes is to be able to accurately predict the transportation of fluid properties (e.g. temperature, salinity and other solutes (particularly pollutants)), and particulate matter (e.g. sediment, fish larvae, coral eggs, etc.). A variety of factors influencing the rate of fluid transport were outlined in chapter 2.3. For the purposes of modelling fluid transport, two distinct processes are introduced. *Advection* describes the transport of entrained particulate matter and fluid properties by the ambient flow. *Diffusion* describes transport associated with unresolved flow processes. The effect of diffusion is the continuous spreading of the tracer element under consideration. The modelling of transport processes can be approached from two different perspectives. Using an Eulerian framework, a similar approach to the modelling of the overall fluid transportation described in chapter 3 is adopted. This technique is referred to as an *advection-diffusion* model. Assuming a conservative tracer (of concentration C), the two-dimensional advection-diffusion equation can be expressed as (Falconer & Liu, 1988),

$$\frac{\partial Ch}{\partial t}+\frac{\partial CUh}{\partial x}+\frac{\partial CVh}{\partial y}=\frac{\partial}{\partial x}\left(hD_{xx}\frac{\partial C}{\partial x}+hD_{xy}\frac{\partial C}{\partial y}\right)+\frac{\partial}{\partial y}\left(hD_{xy}\frac{\partial C}{\partial x}+hD_{yy}\frac{\partial C}{\partial y}\right) \quad (2.3)$$

The advection-diffusion equation is solved simultaneously with the calculation of the hydrodynamic properties of the fluid. This approach enables the transport and distribution of the tracer element to feedback on the hydrodynamic development. This is only an important consideration when modelling the transport of fluid properties such as temperature and salinity (e.g. James, 1987; Heaps, 1987; Garrett et al. 1993). Obtaining an accurate representation of the transport and distribution is however highly dependent upon correct specification of the dispersion-diffusion coefficients. The alternative approach which is generally better suited to describing the transport of particulate matter is to use a *particle tracking* model. This uses a Lagrangian analysis technique. The advection stage of the transport process is modelled by directly tracking particles using the fluid velocity output from a hydrodynamic model. Using small tracking time-steps and interpolating the velocity for each individual particle (e.g. using predictor-corrector algorithms) ensures accurate representation of the advective transportation of the tracer element. The diffusion stage of the transport process is described using a randomly varying velocity component for each individual particle at each time-step. The variance (Φ) of the spreading of the particles derived from the standard deviation of the turbulent velocity is normally described as (Awaji, 1982; Signell & Geyer, 1990; Hunter et al. 1993; Hathhorn, 1997),

$$\Phi = 2Dt \quad (2.4).$$

In this manner, each individual particle follows its own 'tidal random-walk' as outlined by Zimmeman (1986). To produce a realistic representation of the Lagrangian distribution of a tracer element, a large number of particles are generally considered, with each particle representing a defined mass. The distribution of the particles is then presented by summing the particles in a representative cell. The cell distribution selected can be as for the hydrodynamic output or finer if preferred, as little computational effort is incurred. Recent advances in grid based analysis techniques such as quadtree meshing have also been applied to provide a smoother representation of the particle (and consequently mass) distribution (e.g. Copeland et al. 1999, Borthwick et al. 2000). The major advantages offered by the particle

tracking approach are: (i) more accurate predictions of the advective transport (Hunter et al. 1993), which in turn reduces numerical diffusion (Cooper, 1994), (ii) as the calculation procedure is post-processed from stored hydrodynamic data, the particle tracking exercise can be repeated with varying conditions at little computational expense, and (iii) a wind effect can be simply applied to each particle.

A further consideration when modelling transport of particulate matter is possible physical, chemical or biological processes that the matter undergoes. Typical processes that need to be considered are environmental chemical reactions (e.g. degradation and oxidation), biological increase or decrease of bacteria, and settlement or re-suspension of sedimentary material. A material which is subject to any of these processes which all can create a variation of the mass of the tracer element is referred to as a *non-conservative* substance. A material which is not influenced by these processes, and therefore does not alter in mass is referred to as a *conservative* substance. Ng et al. (1996) describes an application involving the transport of non-conservative substances using the Eulerian advective-diffusion model approach. Similar analysis using a particle tracking model can prove to be a very complex operation. In the simplest case where the substance is degrading instead of combining with other substances encountered, the decay can be described by either decreasing the mass of the quantity represented by each individual particle, or by the random removal of particles from the simulation (Hunter et al., 1993). Copeland (1997) provides an example of the application of particle tracking theory which incorporates decay, and is subsequently used to evaluate a sewage outfall positioning study. This is a common approach advocated by the engineering community. More advanced discussion of transport modelling is out-with the scope of this discussion. Fischer et al. (1979) provides a more detailed account of the majority of the concepts, ideas and techniques introduced in this section.

3. DERIVATION OF THE GOVERNING EQUATIONS

Fluid flow in an estuary or coastal environment is three-dimensional, time-dependent, and turbulent. Tides are generally the most important and consistent driving force in the coastal zone. Tidal phenomena have been one of the most thoroughly studied areas in physical oceanography (Liu *et al.*, 1978), drawing the attention of eminent scientists such as Newton, Airy, Lamb, Lorentz and Proudman. Tide generating forces originate from the sun and moon, however the tidal motions in an estuary or in coastal areas are generally caused by the ocean tide entering through an opening or shelf sea. Extensive study in this area has led to the development of a basic set of governing equations which model a combination of hydrodynamic, transport and turbulent processes.

The derivation of the governing equations for long period (tidal) wave propagation is based on the conservation laws of mass and momentum. The law of mass conservation states that the mass of an object, such as a fluid particle, remains permanently unchanged, despite any outside influences on it. The law of conservation of momentum (incorporating Newton's 2nd law of motion) states that the rate of change of (linear) momentum of a body is proportional to the resultant force acting upon it, and is in the direction of that force. Application of these two principles, in conjunction with the assumption that a continuous fluid can be subdivided repeatedly without losing its properties (Neumann and Pierson, 1966), enables the mathematical description of fluid flow that follows. Throughout the derivation, the x, y, z spatial co-ordinate system described in Figure 3.1, and the respective velocity component layout will be used.

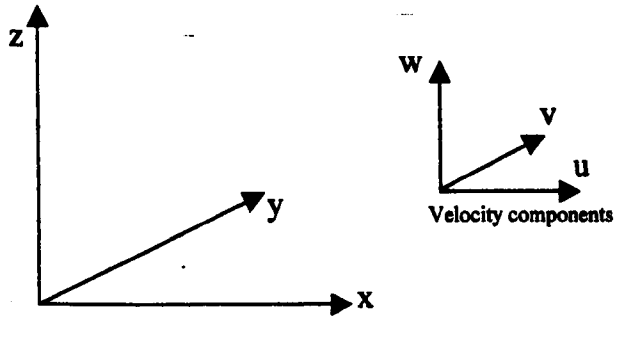

Figure 3.1 – Spatial and velocity component co-ordinate systems.

3.1 The Continuity Equation

The continuity equation is derived from the principle that matter may not be created or destroyed in the flow through an infinitesimal control volume (Raudkivi and Callander, 1975). This theory follows from the concept of mass conservation. The expressions derived can be further simplified by assuming that the density of sea-water is constant. The effect of this is to reduce the theory of mass conservation to the concept of conservation of fluid volume. The derivation below roughly follows that of Eagleson and Dean (1966).

Consider a small stationary cubic volume with sides of length Δx, Δy, Δz, as shown in Figure 3.2. Conservation of mass requires that the net mass of fluid flowing across the boundaries into the element in a certain time Δt be equal to the amount by which the mass of the element has changed in the same time Δt. Let the velocity components in the x, y, and z directions be given by u, v, and w respectively (where $V_T = (iu+jv+kw)$, and **i**, **j**, **k** are unit vectors).

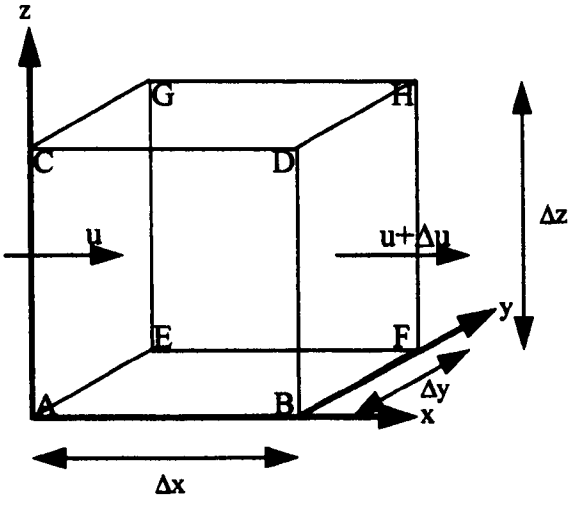

Figure 3.2 - A small cubic fluid element.

The volume inflow of mass across face AEGC in time Δt is

$$\rho u \Delta y \Delta z \Delta t. \qquad (3.1.1)$$

The volume outflow of mass across face BFHD in time Δt is

$$(\rho + \Delta\rho)(u + \Delta u)\Delta y \Delta z \Delta t.$$

Applying Taylor's Theorem (Appendix A2), to the terms $\Delta\rho$ and Δu in the outflow, neglecting higher-order terms, and multiplying out the brackets produces

$$\left(\rho u + \rho\frac{\partial u}{\partial x}\Delta x + u\frac{\partial \rho}{\partial x}\Delta x + \frac{\partial \rho}{\partial x}\frac{\partial u}{\partial x}\Delta x \Delta x\right)\Delta y \Delta z \Delta t.$$

The final term in the brackets becomes negligible in comparison with the other terms if Δx is sufficiently small. Application of the chain rule (Appendix A1) to the second and third terms simplifies the description of the outflow of mass across BFHD in time Δt to

$$\left(\rho u + \frac{\partial(\rho u)}{\partial x}\Delta x\right)\Delta y \Delta z \Delta t . \qquad (3.1.2)$$

Summating the effect of equations (3.1.1) and (3.1.2) yields the net inflow of mass to the cubic volume in the x direction during Δt,

$$-\frac{\partial(\rho u)}{\partial x}\Delta x \Delta y \Delta z \Delta t .$$

In a similar manner, it can be shown that the net inflow of mass during Δt in the y and z directions are respectively,

$$-\frac{\partial(\rho v)}{\partial y}\Delta x \Delta y \Delta z \Delta t ,$$

$$-\frac{\partial(\rho w)}{\partial z}\Delta x \Delta y \Delta z \Delta t .$$

The net inflow of mass into the volume element during Δt is the sum of the contributions of the three co-ordinate directions, i.e.,

$$\left[-\frac{\partial(\rho u)}{\partial x} - \frac{\partial(\rho v)}{\partial y} - \frac{\partial(\rho w)}{\partial z}\right]\Delta x \Delta y \Delta z \Delta t . \qquad (3.1.3)$$

If the mass present in the fluid element (figure 3.2) at time t is $\rho \Delta x \Delta y \Delta z$, then at time $t+\Delta t$, by applying Taylor's theorem and neglecting higher-order terms, the mass present will be equal to,

$$\rho \Delta x \Delta y \Delta z + \frac{\partial(\rho \Delta x \Delta y \Delta z)}{\partial t}\Delta t .$$

Therefore, the net increase of mass within the cubic volume in time Δt is,

$$\frac{\partial \rho}{\partial t}\Delta x \Delta y \Delta z \Delta t . \qquad (3.1.4)$$

If there is no creation or destruction of mass within the volume element, term (3.1.3) must be equal to term (3.1.4) i.e., the net inflow of mass equals the net increase in mass,

$$\frac{\partial \rho}{\partial t} = -\left[\frac{\partial(\rho u)}{\partial x} + \frac{\partial(\rho v)}{\partial y} + \frac{\partial(\rho w)}{\partial z}\right].$$

Using the chain rule (Appendix A1), the right-hand side of the equation can be expanded out to produce,

$$\frac{\partial \rho}{\partial t} + u\frac{\partial \rho}{\partial x} + v\frac{\partial \rho}{\partial y} + w\frac{\partial \rho}{\partial z} + \rho\left(\frac{\partial u}{\partial x} + \frac{\partial v}{\partial y} + \frac{\partial w}{\partial z}\right) = 0. \qquad (3.1.5)$$

The first four terms in equation (3.1.5) are in the form of the total derivative (see Appendix A3). Equation (3.1.5) can consequently be simplified to,

$$\frac{D\rho}{Dt} + \rho\left(\frac{\partial u}{\partial x} + \frac{\partial v}{\partial y} + \frac{\partial w}{\partial z}\right) = 0. \qquad (3.1.6)$$

This form of the principle of conservation of mass is referred to as the 'continuity equation' for a compressible fluid. In the case of an incompressible fluid, by definition, the mass density must be constant over time (i.e., $D\rho/Dt = 0$). Application of this to equation (3.1.6) produces the continuity equation for an incompressible fluid,

$$\frac{\partial u}{\partial x} + \frac{\partial v}{\partial y} + \frac{\partial w}{\partial z} = 0. \qquad (3.1.7)$$

As sea-water can generally be considered to be an incompressible fluid (Pond & Pickard, 1983), equation (3.1.7) will be applied as the governing continuity equation.

3.2 The Momentum Equations

Derivation of the momentum equations is based upon the concept of momentum conservation as described by Newton 2nd law of motion. Mathematically this can be stated as,

$$\sum F = \frac{D(mV_T)}{Dt} = m\frac{DV_T}{Dt} + V_T\frac{Dm}{Dt}.$$

(where ΣF is the sum of all forces acting on mass m). Mass conservation states that $\frac{Dm}{Dt} = 0$, giving

$$\sum F = m\frac{DV_T}{Dt} \qquad (3.2.1)$$

The derivation that follows draws from a number of sources, including Timoshenko & Goodier (1970), Raudkivi & Callander (1975), Knight (1986), Vardy (1990), Falconer (1994), and Bayne (1996).

3.2.1 Derivation of the Navier-Stokes equation

The forces acting on a small cubic control volume with sides of length Δx, Δy, Δz, are shown in Figure (3.3). The symbols σ and τ refer to normal and shear stresses respectively. Normal stresses are a description of the compressive (pressure) forces acting on the element from the surrounding elements. This force acts perpendicular to the surface of the fluid element. Shear stresses result from momentum transfer between fluid elements due to the effects of turbulence and

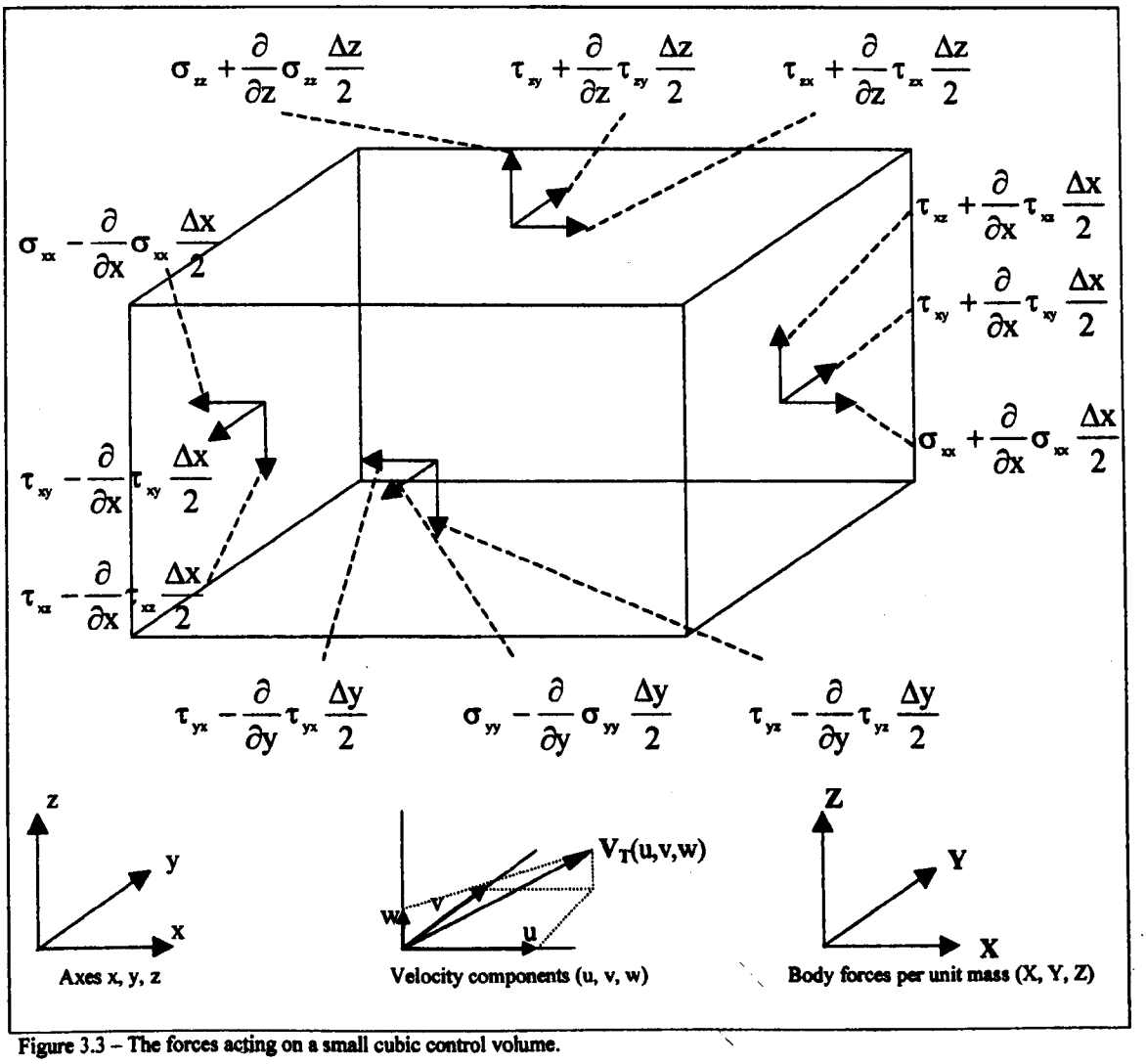

Figure 3.3 – The forces acting on a small cubic control volume.

because of viscous drag between surfaces in contact with each other. Stresses are normally annotated using two subscripts, the first identifies the plane normal to the stress action, the second the direction of the action. To describe the stresses acing on the six sides of the element three symbols, σ_{xx}, σ_{yy}, σ_{zz}, are necessary for normal

stresses, and six symbols, τ_{xy}, τ_{yx}, τ_{xz}, τ_{zx}, τ_{yz}, τ_{zy}, for shearing stresses. The nine stress components are normally presented using an array, as shown,

$$\begin{matrix} \sigma_{xx} & \tau_{xy} & \tau_{xz} \\ \tau_{yx} & \sigma_{yy} & \tau_{yz} \\ \tau_{zx} & \tau_{zy} & \sigma_{zz} \end{matrix} . \qquad (3.2.2)$$

The sum of the forces acting in the x-direction on the fluid control volume shown in Figure 3.3 include the body force per unit mass, X, the normal stress component σ_{xx}, and the shear stress components τ_{yx} and τ_{zx}. Invoking Newton' s 2nd law of motion (equation 3.2.1), for the x-directed components,

$$\rho X\Delta x\Delta y\Delta z+\frac{\partial\sigma_{xx}}{\partial x}\Delta x\Delta y\Delta z+\frac{\partial\tau_{yx}}{\partial y}\Delta x\Delta y\Delta z+\frac{\partial\tau_{zx}}{\partial z}\Delta x\Delta y\Delta z=\rho\Delta x\Delta y\Delta z\frac{Du}{Dt}$$

Dividing through by the mass of the element, $\rho\Delta x\Delta y\Delta z$, and rearranging the equation so that it is in terms of the acceleration,

$$\frac{Du}{Dt}=X+\frac{1}{\rho}\left[\frac{\partial\sigma_{xx}}{\partial x}+\frac{\partial\tau_{yx}}{\partial y}+\frac{\partial\tau_{zx}}{\partial z}\right].$$

The term on the left hand side of the equation describing the acceleration of the fluid is in the form of the total derivative, and can therefore be expanded out (see Appendix A3) to provide,

$$\frac{\partial u}{\partial t}+u\frac{\partial u}{\partial x}+v\frac{\partial u}{\partial y}+w\frac{\partial u}{\partial z}=X+\frac{1}{\rho}\left[\frac{\partial\sigma_{xx}}{\partial x}+\frac{\partial\tau_{yx}}{\partial y}+\frac{\partial\tau_{zx}}{\partial z}\right]$$

Similar equations can be derived for the y- and z-directions,

$$\frac{\partial v}{\partial t}+u\frac{\partial v}{\partial x}+v\frac{\partial v}{\partial y}+w\frac{\partial v}{\partial z}=Y+\frac{1}{\rho}\left[\frac{\partial\tau_{xy}}{\partial x}+\frac{\partial\sigma_{yy}}{\partial y}+\frac{\partial\tau_{zy}}{\partial z}\right], \qquad (3.2.3)$$

$$\frac{\partial w}{\partial t}+u\frac{\partial w}{\partial x}+v\frac{\partial w}{\partial y}+w\frac{\partial w}{\partial z}=Z+\frac{1}{\rho}\left[\frac{\partial\tau_{xz}}{\partial x}+\frac{\partial\tau_{yz}}{\partial y}+\frac{\partial\sigma_{zz}}{\partial z}\right].$$

The set of equations (3.2.3) are in general valid for all incompressible fluid flows. However, they cannot be solved unless additional relationships are available in order to describe the stress terms (Vardy, 1990). In order to provide relationships to describe the stress terms, a common approach is to evaluate the equations for stress and strain in an elastic solid, and then through an analogy between the behaviour of the solid, and that of a viscous fluid, determine similar relationships for the fluid behaviour (Raudkivi & Callander, 1975).

3.2.1.1 *Stress & strain*

Figure 3.3 introduced the components of stress acting on a small cubic element (applicable both to a fluid and an elastic solid),

$$\begin{bmatrix} \sigma_{xx} & \tau_{xy} & \tau_{xz} \\ \tau_{yx} & \sigma_{yy} & \tau_{yz} \\ \tau_{zx} & \tau_{zy} & \sigma_{zz} \end{bmatrix}.$$

The nine stress components describe the *surface forces* which are distributed over the surface of the element, such as the pressure of one body on another or hydrostatic pressure (Timoshenko & Goodier, 1970). Of these nine components, there are only six independent stresses, as,

$$\tau_{xy} = \tau_{yx}, \qquad \tau_{xz} = \tau_{zx}, \qquad \tau_{yz} = \tau_{zy}.$$

This implies that for two perpendicular sides of a cubic element, the components of shearing stress perpendicular to the line of intersection of these sides are equal, as can be shown by taking moments of force about the centre of the element. The six quantities σ_{xx}, σ_{yy}, σ_{zz}, τ_{xy}, τ_{xz}, τ_{yz} are all that are required to describe the stresses acting on the elemental object.

3.2.1.2 *Deformation of an elastic body*

Normal strains

Consider an element Δx, Δy, Δz of an elastic body (Figure 3.4). If the body

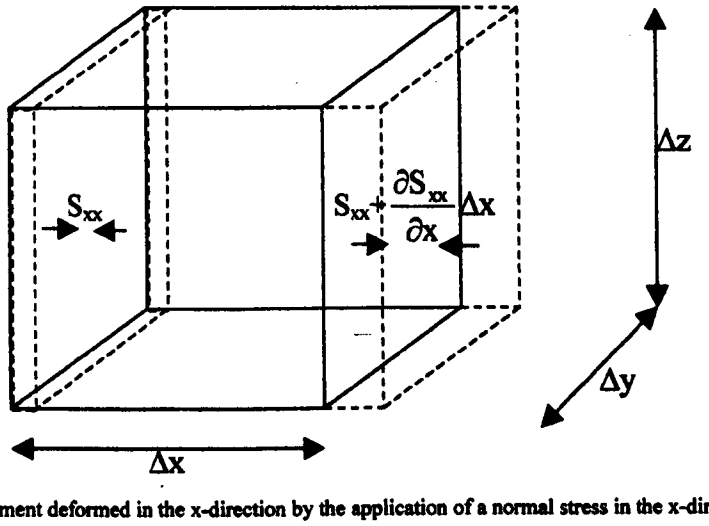

Figure 3.4 – An elastic element deformed in the x-direction by the application of a normal stress in the x-direction.

undergoes a linear deformation in the x-direction, such that the left-hand side of the element is displaced by S_{xx}, the deformation of the right-hand side of the element (applying Taylor's theorem to the first order), is,

$$S_{xx} + \frac{\partial S_{xx}}{\partial x}\Delta x,$$

due to the change, $\frac{\partial S_{xx}}{\partial x}\Delta x$ in the displacement with change of the co-ordinate x.

The change in length across the element due to deformation is therefore, $\frac{\partial S_{xx}}{\partial x}\Delta x$.

The *unit elongation*, which describes the component of strain (annotated ε), in the x-direction is consequently,

$$\varepsilon_{xx} = \frac{\partial S_{xx}}{\partial x}.$$

Following similar derivation in the y- and z-direction, (3.2.4)

$$\varepsilon_{yy} = \frac{\partial S_{yy}}{\partial y},$$

$$\varepsilon_{zz} = \frac{\partial S_{zz}}{\partial y}.$$

Shearing strains

Figure 3.5 describes the two-dimensional distortion of the angle between the elements OA and OB. If S_{xx} and S_{zz} are the displacements of the point O in the x- and z- directions, the displacement of point A in the z-direction is $S_{zz}+(\partial S_{zz}/\partial x)\Delta x$, and the displacement of point B in the x-direction is, $S_{xx}+(\partial S_{xx}/\partial z)\Delta z$.

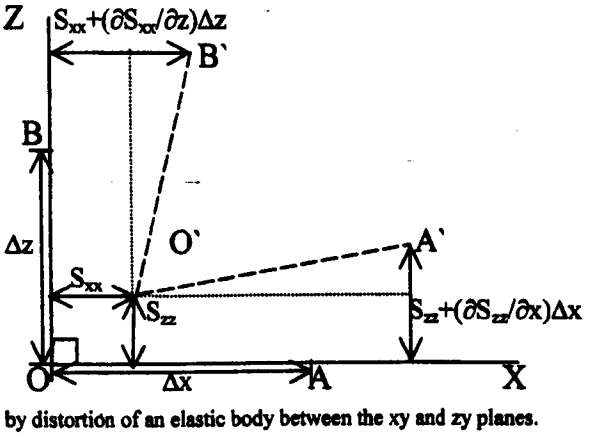

Figure 3.5 – Shearing strain caused by distortion of an elastic body between the xy and zy planes.

In figure 3.5, the angle BOA forms a right angle. However, the differential displacement between O-O` in comparison with the displacements of A-A` and B-B` means that the new angle B`O`A` has been altered from that of a right angle. The

difference in displacement between OA and O`A` is equal to $(\partial S_{zz}/\partial x)\Delta x$, and between OB and O`B` is $(\partial S_{xx}/\partial z)\Delta z$. The original right angle can be seen to have been diminished by the angle $(\partial S_{zz}/\partial x) + (\partial S_{xx}/\partial z)$. This formulation describes the *shearing*, or *angular strain* between the planes xy and zy, as opposed to the linear strain deformation introduced previously. The shearing strains between the planes xz and yz, and the planes xy and xz can be obtained in a similar manner. The unit shearing strains (annotated γ), on the elastic body can therefore be summarised as,

$$\left.\begin{aligned} \gamma_{xy}(=\gamma_{yx}) &= \left(\frac{\partial S_{xx}}{\partial y}+\frac{\partial S_{yy}}{\partial x}\right), \\ \gamma_{xz}(=\gamma_{zx}) &= \left(\frac{\partial S_{xx}}{\partial z}+\frac{\partial S_{zz}}{\partial x}\right), \\ \gamma_{yz}(=\gamma_{yz}) &= \left(\frac{\partial S_{yy}}{\partial z}+\frac{\partial S_{zz}}{\partial y}\right). \end{aligned}\right\} \quad (3.2.5)$$

3.2.1.3 *Stress-Strain relationships applicable to an elastic body*

The components of stress and strain have been introduced to describe the force acting on the elemental elastic body, and the deformation of the body respectively. The two effects must obviously be related, as in order for deformation to take place, a stress (force) must be applied. As an example, consider the effect of applying a normal stress σ_{xx} uniformly distributed at each end of an elastic body, as in the commonly observed 'tensile test' (see figure 3.6). The result of applying the stress in this manner is to cause a deformation of the body in the x-direction. For an

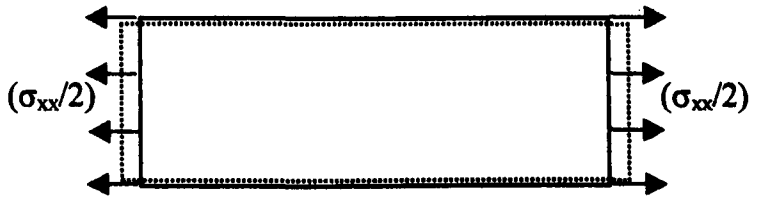

Figure 3.6 – Two-dimensional representation of the tensile test (common to undergraduate engineering courses).

elastic material, the amount of deformation caused by the application of a particular normal stress can be described using the *modulus of elasticity* (annotated E), of the material in question (up to the plastic limit), such that,

$$\varepsilon_{xx} = \frac{\sigma_{xx}}{E}. \quad (3.2.6)$$

The modulus of elasticity of a given material is derived experimentally. Linear relationships between the components of stress and strain, such as in equation (3.2.6) are known generally as Hooke's law. As indicated in figure 3.6, the extension of the element in the x-direction, caused by the application of the stress σ_{xx}, is accompanied by lateral strain components (contractions) in the other direction(s), in this case they would be,

$$\varepsilon_{yy} = -r\frac{\sigma_{xx}}{E}, \qquad \varepsilon_{zz} = -r\frac{\sigma_{xx}}{E}, \tag{3.2.7}$$

where r is a constant referred to as Poisson's ratio (Hulse & Cain, 1991), and is dependent upon the material under consideration (0.25 is a commonly observed value for Poisson's ratio). If the original stress applied had been compressive instead of in tension, equations (3.2.6) and (3.2.7) would still hold true. When the elastic solid is subject to all three normal stress components, σ_{xx}, σ_{yy}, σ_{zz} simultaneously, assuming that the effects discussed above can be superposed upon each other, the corresponding components of strain become,

$$\varepsilon_{xx} = \frac{1}{E}\left(\sigma_{xx} - r(\sigma_{yy} + \sigma_{zz})\right), \quad (a)$$

$$\varepsilon_{yy} = \frac{1}{E}\left(\sigma_{yy} - r(\sigma_{xx} + \sigma_{zz})\right), \quad (b) \qquad (3.2.8)$$

$$\varepsilon_{zz} = \frac{1}{E}\left(\sigma_{zz} - r(\sigma_{xx} + \sigma_{yy})\right). \quad (c)$$

Equation (3.2.8) has been experimentally verified, thereby validating the superposition technique used in deriving the equations.

A similar linear relationship to that of the normal stresses and strains (equations (3.2.6) and (3.2.7) can be derived to describe the relationship between a shearing stress τ_{xy} and an equivalent shearing strain γ_{xy}. In order to do so, the modulus of elasticity (E) is replaced by the *shear modulus* (G), (where the general theory of elasticity states $G = \frac{E}{2(1+r)}$), such that (Timoshenko & Goodier, 1970),

$$\gamma_{xy} = \frac{\tau_{xy}}{G}, \qquad \gamma_{xz} = \frac{\tau_{xz}}{G}, \qquad \gamma_{yz} = \frac{\tau_{yz}}{G}. \tag{3.2.9}$$

Summating the effects of the three normal stress components in equation (3.2.8) across the elastic body, the *volumetric strain* (annotated ε_v) is derived,

$$\varepsilon_v = \varepsilon_{xx} + \varepsilon_{yy} + \varepsilon_{zz} = \frac{(1-2r)}{E}(\sigma_{xx} + \sigma_{yy} + \sigma_{zz}), \qquad (3.2.10)$$

which can be re-arranged to produce,

$$\sigma_{xx} + \sigma_{yy} + \sigma_{zz} = \frac{E\varepsilon_v}{(1-2r)} = 3\bar{\sigma}, \qquad (3.2.11)$$

where $\bar{\sigma}$ is the mean of the three normal stress components. Further re-arrangement of equation (3.2.10) produces,

$$\sigma_{yy} + \sigma_{zz} = \left[\frac{E\varepsilon_v}{(1-2r)}\right] - \sigma_{xx}. \qquad (3.2.12)$$

Substituting equation (3.2.12) into equation (3.2.8(a)) gives,

$$\varepsilon_{xx} = \frac{1}{E}\left(\sigma_{xx} - r\left(\left[\frac{E\varepsilon_v}{(1-2r)}\right] - \sigma_{xx}\right)\right). \qquad (3.2.13)$$

Recalling the shear modulus representation, and re-arranging in terms of the modulus of elasticity, E = 2G(1+r). Equation (3.2.13) can therefore be presented as,

$$\varepsilon_{xx} = \frac{1}{2G(1+r)}\left(\sigma_{xx} - r\left(\left[\frac{2G(1+r)\varepsilon_v}{(1-2r)}\right] - \sigma_{xx}\right)\right).$$

Multiplying-out the brackets,

$$\varepsilon_{xx} = \frac{\sigma_{xx}}{2G} - \left(\frac{r}{(1-2r)}\right)\varepsilon_v.$$

Hence,

$$\sigma_{xx} = 2G\varepsilon_{xx} + 2G\frac{r}{(1-2r)}\varepsilon_v. \qquad (3.2.14)$$

Similarly, replacing for E and rearranging in equation (3.2.11),

$$\bar{\sigma} = \frac{\sigma_{xx} + \sigma_{yy} + \sigma_{zz}}{3} = \frac{2}{3}G\frac{(1+r)}{(1-2r)}\varepsilon_v. \qquad (3.2.15)$$

As equations (3.2.14) and (3.2.15) are not equal, normal stresses can be considered to be composed of a mean normal stress component, $\bar{\sigma}$, and a *deviatoric stress* component (annotated, σ'_{12}). The deviatoric stress in the x-direction can be derived using equations (3.2.14) and (3.2.15),

$$\sigma'_{xx} = \sigma_{xx} - \bar{\sigma} = 2G\varepsilon_{xx} + 2G\frac{r}{(1-2r)}\varepsilon_v - \frac{2}{3}G\frac{(1+r)}{(1-2r)}\varepsilon_v$$

$$= 2G\varepsilon_{xx} - \frac{2}{3}G\varepsilon_v, \qquad (3.2.16)$$

with similar representations applicable in the y- and z-directions. Summating the mean and deviatoric stress components from equations (3.2.15) and (3.2.16), a final representation of the normal stresses in an elastic body can be constructed which requires only one numerical constant (G),

$$\left.\begin{aligned}
\sigma_{xx} &= \bar{\sigma} + \sigma'_{xx} = \frac{\sigma_{xx}+\sigma_{yy}+\sigma_{zz}}{3} + 2G\varepsilon_{xx} - \frac{2}{3}G\varepsilon_v \quad (a)\\
\sigma_{yy} &= \bar{\sigma} + \sigma'_{yy} = \frac{\sigma_{xx}+\sigma_{yy}+\sigma_{zz}}{3} + 2G\varepsilon_{yy} - \frac{2}{3}G\varepsilon_v \quad (b)\\
\sigma_{zz} &= \bar{\sigma} + \sigma'_{zz} = \frac{\sigma_{xx}+\sigma_{yy}+\sigma_{zz}}{3} + 2G\varepsilon_{zz} - \frac{2}{3}G\varepsilon_v \quad (c)
\end{aligned}\right\} \quad (3.2.17)$$

3.2.1.4 *Stress-strain relationships applicable to a fluid element*

So far, the derivation of stress-strain relationships has been exclusively in terms of an elastic body. Now consider the effects of stress and strain on a fluid element. Linear strain, or deformation of a fluid element, is due to a normal stress caused by stream-wise velocity gradients. When considering fluids, it is the rate of strain that is of interest rather than the magnitude of strain as was the case when considering an elastic body. The different approach is necessary, as applying a constant stress to a fluid element will cause it to deform at a continuous, constant rate, and the element will maintain the final deformed shape if the stress is later removed and no other force is applied. Apply a constant stress to an elastic body however, and it will deform by a finite amount that will be independent of the length of time the stress acts for, and will return to its original shape when the stress is released[1]. The strain per unit time (annotated ε'_{12}) is defined as the elongation of the fluid element per unit time divided by the original length of the element (with reference to Figure 3.7). Assuming that the flow is incompressible, applying Taylor's theorem and neglecting higher-order terms, then,

[1] As long as the plastic limit is not exceeded, at which point, the action of the material is governed by a different set of laws. This point has little bearing upon the current discussion, and therefore will not be expanded upon.

$$\varepsilon^t_{xx} = \left(\frac{\partial u}{\partial x}\Delta x\Delta t\right)/\Delta x\Delta t = \frac{\partial u}{\partial x}.$$

Similar analysis in the y- and z-directions produces, (3.2.18)

$$\varepsilon^t_{yy} = \frac{\partial v}{\partial y},$$

$$\varepsilon^t_{zz} = \frac{\partial w}{\partial z}.$$

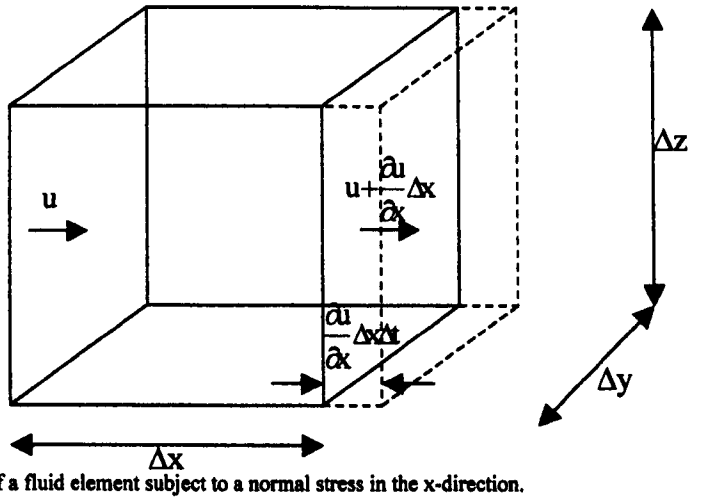

Figure 3.7 – Description of a fluid element subject to a normal stress in the x-direction.

With reference to equation (3.1.7), which describes the continuity of volume it can be seen that,

$$\varepsilon^t_{xx} + \varepsilon^t_{yy} + \varepsilon^t_z = \frac{\partial u}{\partial x} + \frac{\partial v}{\partial y} + \frac{\partial w}{\partial z} = 0, \qquad (3.2.19)$$

in the case of an incompressible flow. If the fluid is compressible however, the equation above is unlikely to sum to zero. The value that is determined for a compressible fluid is referred to as the *volume dilation*, normally annotated 'e'.

Shear strains (annotated γ_{12}, and also referred to as angular strains), are due to shear stresses acting on the fluid element (Figure 3.8). The rate of angular strain (annotated γ^t_{12}) quantifies the rate of deformation of the right angle ($d\theta_1$+$d\theta_2$). This

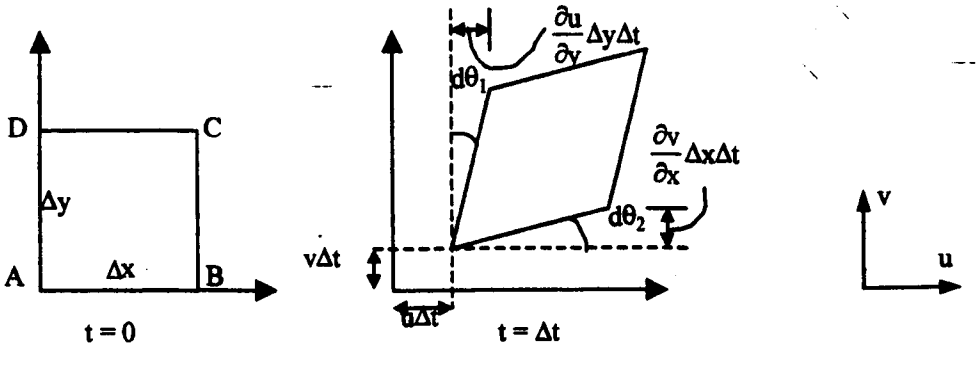

Figure 3.8 – 2-D description of a fluid element subject to a shear stress in the x-directed plane acting in the y-direction (ignoring the effects of rotation and extension).

is analogous to the shearing strain caused by deformation of an elastic body shown in figure 3.5.

After time Δt, as shown in figure (3.8), the velocity of the fluid particles initially at points A and B move in the y-direction by $v\Delta t$ and $\left(v+\frac{\partial v}{\partial x}\cdot\Delta x\right)\Delta t$ respectively. The difference in distance travelled in the y-direction in time Δt by the two points is therefore $\left(\frac{\partial v}{\partial x}\cdot\Delta x\right)$, and the deformation of the angle $d\theta_2 = \left(\frac{\partial v}{\partial x}\right)$. Similarly, the difference in distance travelled in the x-direction in time Δt by the two points A and D is $\left(\frac{\partial u}{\partial y}\cdot\Delta y\right)$, and the deformation of the angle $d\theta_1 = \left(\frac{\partial u}{\partial y}\right)$. The overall angular strain rate in the x-y plane in time Δt is consequently,

$$\gamma^t_{xy} = \left(\frac{\partial u}{\partial y}+\frac{\partial v}{\partial x}\right).$$

Similar expressions can be derived for the other axes, such that,

$$\gamma^t_{xz} = \left(\frac{\partial u}{\partial z}+\frac{\partial w}{\partial x}\right), \qquad \gamma^t_{yz} = \left(\frac{\partial v}{\partial z}+\frac{\partial w}{\partial y}\right). \tag{3.2.20}$$

For Newtonian fluids (such as air and water), experimental analysis has shown that for laminar flows, the shear stress is directly proportional to the rate of shear strain (Vardy, 1990). The proportionality constant (annotated μ) is referred to as the *dynamic viscosity*, such that,

$$\tau_{xy} = \mu\gamma^t_{xy}, \qquad \tau_{xz} = \mu\gamma^t_{xz}, \text{ and,} \qquad \tau_{yz} = \mu\gamma^t_{yz}. \tag{3.2.21}$$

3.2.1.5 *Analogy between elastic solid and fluid behaviour*

The derivation in terms of an elastic solid has been necessary in order to introduce a simple analogy between the action of solids and fluids under stress. In the case of an elastic solid, deformation is proportional to the strain as described in section 3.2.1.2. In the case of a Newtonian fluid, deformation is proportional to the rate of strain as outlined in section 3.2.1.4. Comparing equations (3.2.9) and (3.2.21),

$$\tau_{xy} = G\gamma_{xy}, \text{ and, } \tau_{xy} = \mu\gamma'_{xy}, \qquad (3.2.22)$$

has led to the analogy that suggests that the shear modulus, G, can be replaced by the dynamic viscosity, μ. This enables the application of the derivation of the stress components acting on an elastic body in terms of strain to similar situations experienced by a fluid element. In order to do so, it is also necessary to assume that displacement strains can be replaced by velocity strains, such that when comparing equations (3.2.7) and (3.2.14) they can be considered to be describing the same phenomena,

$$\varepsilon_{xx} = \frac{\partial S_{xx}}{\partial x} \Rightarrow \cong \varepsilon'_{xx} = \frac{\partial u}{\partial x}, \qquad (3.2.23)$$

or with respect to shearing strains, (comparing equations (3.2.5) and (32.20)),

$$\gamma_{xy} = \left(\frac{\partial S_{xx}}{\partial y} + \frac{\partial S_{yy}}{\partial x}\right) \Rightarrow \cong \gamma'_{xy} = \left(\frac{\partial u}{\partial y} + \frac{\partial v}{\partial x}\right) \qquad (3.2.24)$$

The analogy is completed by defining the hydrodynamic pressure, P_h, as the average value of the three components of normal stress, such that,

$$-P_h = \frac{\sigma_{xx} + \sigma_{yy} + \sigma_{zz}}{3}, \qquad (3.2.25)$$

which can be seen to be equivalent to the mean normal stress $\bar{\sigma}$ introduced in the elastic body derivation (see equations (3.2.11) and (3.2.17)).

This now allows the assumption that the behaviour of a fluid element under stress can be described in the same manner as the behaviour of an elastic solid by replacing the shear modulus with the fluid viscosity (equation (3.2.22)), and displacement strains by velocity strains (equations (3.2.23) and (3.2.24)) (Raudkivi & Callander, 1975). Considering the three normal stress components, the equivalent elastic body stress–strain relationships were presented in equation (3.2.17). The three fluid normal stresses are related to the rates of strain via equations (3.2.22), (3.2.23), and (3.2.25) such that,

$$\begin{aligned}
\sigma_{xx} &= \bar{\sigma} + \sigma'_{xx} = -P_h + 2\mu\frac{\partial u}{\partial x} - \frac{2\mu}{3}\left(\frac{\partial u}{\partial x} + \frac{\partial v}{\partial y} + \frac{\partial w}{\partial z}\right), \quad \text{(a)} \\
\sigma_{yy} &= \bar{\sigma} + \sigma'_{yy} = -P_h + 2\mu\frac{\partial v}{\partial y} - \frac{2\mu}{3}\left(\frac{\partial u}{\partial x} + \frac{\partial v}{\partial y} + \frac{\partial w}{\partial z}\right), \quad \text{(b)} \\
\sigma_{zz} &= \bar{\sigma} + \sigma'_{zz} = -P_h + 2\mu\frac{\partial w}{\partial z} - \frac{2\mu}{3}\left(\frac{\partial u}{\partial x} + \frac{\partial v}{\partial y} + \frac{\partial w}{\partial z}\right), \quad \text{(c)}
\end{aligned} \qquad (3.2.26)$$

Similarly, the three independent shear stress components applicable to a fluid element can be derived by analogy with the behaviour of an elastic body via equations (3.2.22) and (3.2.24), such that,

$$\left.\begin{aligned} \tau_{xy}\left(=\tau_{yx}\right)&=\mu\gamma^{t}_{xy}=\mu\left(\frac{\partial u}{\partial y}+\frac{\partial v}{\partial x}\right), && \text{(a)}\\ \tau_{xz}\left(=\tau_{zx}\right)&=\mu\gamma^{t}_{xz}=\mu\left(\frac{\partial u}{\partial z}+\frac{\partial w}{\partial x}\right), && \text{(b)}\\ \tau_{yz}\left(=\tau_{zy}\right)&=\mu\gamma^{t}_{yz}=\mu\left(\frac{\partial v}{\partial z}+\frac{\partial w}{\partial y}\right). && \text{(c)} \end{aligned}\right\} \quad (3.2.27)$$

Returning to equation set (3.2.3), and inserting the relevant components from equations (3.2.26) and (3.2.27), gives the equations of motion for viscous flow. Considering the x-direction provides,

$$\frac{Du}{Dt}=X+\frac{1}{\rho}\left[\frac{\partial\sigma_{xx}}{\partial x}+\frac{\partial\tau_{yx}}{\partial y}+\frac{\partial\tau_{zx}}{\partial z}\right]=$$

$$X+\frac{1}{\rho}\frac{\partial}{\partial x}\left[-P_h+2\mu\frac{\partial u}{\partial x}-\frac{2\mu}{3}\left(\frac{\partial u}{\partial x}+\frac{\partial v}{\partial y}+\frac{\partial w}{\partial z}\right)\right]+\frac{1}{\rho}\frac{\partial}{\partial y}\left[\mu\left(\frac{\partial u}{\partial y}+\frac{\partial v}{\partial x}\right)\right]+\frac{1}{\rho}\frac{\partial}{\partial z}\left[\mu\left(\frac{\partial u}{\partial z}+\frac{\partial w}{\partial x}\right)\right].$$

This can be simplified by multiplying out some of the terms, and using the fact that for incompressible fluids, the term in rounded brackets is the continuity equation, which is equal to zero (equation 3.1.7). At this stage, it is also assumed that the viscosity of the fluid is constant (i.e. there is no spatial gradient), such that,

$$\frac{Du}{Dt}=X-\frac{1}{\rho}\frac{\partial P_h}{\partial x}+2\frac{\mu}{\rho}\left(\frac{\partial^2 u}{\partial x^2}\right)-0+\frac{\mu}{\rho}\left(\frac{\partial^2 u}{\partial y^2}+\frac{\partial v}{\partial xy}\right)+\frac{\mu}{\rho}\left(\frac{\partial^2 u}{\partial z^2}+\frac{\partial w}{\partial xz}\right),$$

Collecting together similar terms, further simplification is possible,

$$\frac{Du}{Dt}=X-\frac{1}{\rho}\frac{\partial P_h}{\partial x}+\frac{\mu}{\rho}\left[\frac{\partial^2 u}{\partial x^2}+\frac{\partial^2 u}{\partial y^2}+\frac{\partial^2 u}{\partial z^2}\right]+\frac{\mu}{\rho}\frac{\partial}{\partial x}\left(\frac{\partial u}{\partial x}+\frac{\partial v}{\partial y}+\frac{\partial w}{\partial z}\right).$$

Once more, the term in the rounded brackets is equal to zero, and can therefore be discarded. The final manipulation is to expand the total derivative (see Appendix A3), to produce,

$$\frac{\partial u}{\partial t}+u\frac{\partial u}{\partial x}+v\frac{\partial u}{\partial y}+w\frac{\partial u}{\partial z}=X-\frac{1}{\rho}\frac{\partial P_h}{\partial x}+\frac{\mu}{\rho}\left[\frac{\partial^2 u}{\partial x^2}+\frac{\partial^2 u}{\partial y^2}+\frac{\partial^2 u}{\partial z^2}\right]. \quad (3.2.28(a))$$

Similarly, in the y- and z-directions,

$$\frac{\partial v}{\partial t}+u\frac{\partial v}{\partial x}+v\frac{\partial v}{\partial y}+w\frac{\partial v}{\partial z}=X-\frac{1}{\rho}\frac{\partial P_h}{\partial y}+\frac{\mu}{\rho}\left[\frac{\partial^2 v}{\partial x^2}+\frac{\partial^2 v}{\partial y^2}+\frac{\partial^2 v}{\partial z^2}\right], \qquad (3.2.28(b))$$

$$\frac{\partial w}{\partial t}+u\frac{\partial w}{\partial x}+v\frac{\partial w}{\partial y}+w\frac{\partial w}{\partial z}=X-\frac{1}{\rho}\frac{\partial P_h}{\partial z}+\frac{\mu}{\rho}\left[\frac{\partial^2 w}{\partial x^2}+\frac{\partial^2 w}{\partial y^2}+\frac{\partial^2 w}{\partial z^2}\right]. \qquad (3.2.28(c))$$

Equations (3.2.28(a-c)), and the continuity equation, equation (3.1.7), form four equations describing four unknown values (u, v, w, P_h). This equation set is referred to as the Navier-Stokes equations for incompressible fluids. These equations can be considered to be generally applicable to all incompressible flow situations.

3.2.2 Equations to describe turbulent flows

Fluid flow may be broadly divided into two categories depending upon the behaviour of the fluid as it flows. If the fluid has a smooth appearance with a tendency to flow in layers, then it is referred to as a laminar flow. If however the fluid flows in an apparently chaotic and random structure, with significant mixing throughout the fluid, then it is referred to as a turbulent flow. Flow in the coastal environment is turbulent. The most important property of a turbulent flow is that there is a continuously fluctuating velocity component to the flow. However, if the velocity components are analysed over a long time period, it is apparent that the velocity is composed of a mean ($\bar{u}$) and fluctuating (u`) velocity component, such that in the x-direction,

$$u(t)=\bar{u}+u`, \qquad (3.2.29)$$

where $$\bar{u}=\frac{1}{T}\int_{t}^{t+T} u\,dt \text{ as } T\to\infty,$$

and $$u`=\frac{1}{T}\int_{t}^{t+T} u`\,dt=\bar{u}`=0.$$

Similar expressions apply for the other flow variables, v, w and P.

The random nature of a turbulent flow provides great difficulty in mathematically describing the flow development. It is standard practice to describe the flow in terms of the mean values of the flow properties, and incorporate the fluctuating velocity components using statistical representations. Including a description of the turbulent fluctuations is of fundamental importance in obtaining an accurate representation of flow development because of:

(i) the wide range of rotational flow structures (turbulent eddies) encapsulated in a turbulent flow,

(ii) the enhanced mixing observed in turbulent regimes as a result of the eddying motion of the flow, and,

(iii) the three-dimensional spatial character of turbulence (even in flow situations which can be generally characterised by properties in only one- or two-dimensions).

Consequently, the Navier-Stokes equations need to be further expanded when considering a turbulent flow in order to include the effect of the turbulent velocity fluctuations. This is made possible by incorporating the mean and fluctuating components into the Navier-Stokes equations as laid out below. Before beginning the derivation, it is necessary to note that the average of the derivative of any dependent variable is equal to the derivative of the average of that variable (Knight, 1986),

$$\overline{\frac{\partial a}{\partial b}} = \frac{\partial \overline{a}}{\partial b}.$$

Beginning with the continuity equation (3.1.7), and considering the effect of a turbulent flow over a long time period (with reference to equation (3.2.29)),

$$\overline{\frac{\partial(\overline{u}+u`)}{\partial x}}+\overline{\frac{\partial(\overline{v}+v`)}{\partial y}}+\overline{\frac{\partial(\overline{w}+w`)}{\partial z}}=\frac{\partial \overline{u}}{\partial x}+\frac{\partial \overline{v}}{\partial y}+\frac{\partial \overline{w}}{\partial z}=0, \qquad (3.2.30)$$

as by definition $\overline{u`},\overline{v`},\overline{w`}=0$. Also,

$$\frac{\partial u`}{\partial x}+\frac{\partial v`}{\partial y}+\frac{\partial w`}{\partial z}=0. \qquad (3.2.31)$$

Equations (3.2.30) and (3.2.31) state that both the mean and fluctuating components of the turbulent velocity satisfy the continuity equation.

Now considering the x-directed momentum equation (3.2.28(a)), it is first necessary to multiply the continuity equation by u,

$$u\frac{\partial u}{\partial x}+u\frac{\partial v}{\partial y}+u\frac{\partial w}{\partial z}=0.$$

Adding this into equation (3.2.28(a)) using the chain rule (Appendix A1) gives,

$$\frac{\partial u}{\partial t}+\frac{\partial u^2}{\partial x}+\frac{\partial uv}{\partial y}+\frac{\partial uw}{\partial z}=X-\frac{1}{\rho}\frac{\partial P_h}{\partial x}+\frac{\mu}{\rho}\left[\frac{\partial^2 u}{\partial x^2}+\frac{\partial^2 u}{\partial y^2}+\frac{\partial^2 u}{\partial z^2}\right]. \qquad (3.2.32)$$

Substituting the turbulent velocity representations into equation (3.2.32) produces,

$$\frac{\partial}{\partial t}(\bar{u}+u`)+\frac{\partial}{\partial x}(\bar{u}+u`)^2+\frac{\partial}{\partial y}(\bar{u}+u`)(\bar{v}+v`)+\frac{\partial}{\partial z}(\bar{u}+u`)(\bar{w}+w`)=$$
$$(\bar{X}+X`)-\frac{1}{\rho}\frac{\partial}{\partial x}(\bar{P}_h+P_h`)+\frac{\mu}{\rho}\left[\frac{\partial^2}{\partial x^2}(\bar{u}+u`)+\frac{\partial^2}{\partial y^2}(\bar{u}+u`)+\frac{\partial^2}{\partial z^2}(\bar{u}+u`)\right]. \quad (3.2.33)$$

In coastal waters, the main concern is in obtaining the pattern of the mean flow. Therefore, interest lies only in the effect of the turbulent terms over an extended time period. This enables the continuation of the derivation by time-averaging equation (3.2.33). The equation will also be expanded where relevant during this step,

$$\frac{\partial}{\partial t}\overline{(\bar{u}+u`)}+\frac{\partial}{\partial x}\overline{(\bar{u}\bar{u}+2u`\bar{u}+u`u`)}+\frac{\partial}{\partial y}\overline{(\bar{u}\bar{v}+\bar{u}v`+u`\bar{v}+u`v`)}+\frac{\partial}{\partial z}\overline{(\bar{u}\bar{w}+\bar{u}w`+u`\bar{w}+u`w`)}$$
$$=\overline{(\bar{X}+X`)}-\frac{1}{\rho}\frac{\partial}{\partial x}\overline{(\bar{P}_h+P_h`)}+\frac{\mu}{\rho}\left[\frac{\partial^2}{\partial x^2}\overline{(\bar{u}+u`)}+\frac{\partial^2}{\partial y^2}\overline{(\bar{u}+u`)}+\frac{\partial^2}{\partial z^2}\overline{(\bar{u}+u`)}\right]. \quad (3.2.34)$$

Recalling the relationships defined by equation (3.2.29), equation (3.2.34) can be simplified to,

$$\frac{\partial\bar{u}}{\partial t}+\frac{\partial\bar{u}\bar{u}}{\partial x}+\frac{\partial\overline{u`u`}}{\partial x}+\frac{\partial\bar{u}\bar{v}}{\partial y}+\frac{\partial\overline{u`v`}}{\partial y}+\frac{\partial\bar{u}\bar{w}}{\partial z}+\frac{\partial\overline{u`w`}}{\partial z}=\bar{X}-\frac{1}{\rho}\frac{\partial\bar{P}_h}{\partial x}+\frac{\mu}{\rho}\left[\frac{\partial^2\bar{u}}{\partial x^2}+\frac{\partial^2\bar{u}}{\partial y^2}+\frac{\partial^2\bar{u}}{\partial z^2}\right]. \quad (3.2.35)$$

Multiplying the time-averaged continuity equation (3.2.30) (which is equal to zero), by $\bar{u}$, and subtracting from equation (3.2.35) using the chain rule (the reverse of the step leading to equation (3.2.32)), and rearranging such that the equation has the form of the original Navier-Stokes equation gives,

$$\frac{\partial\bar{u}}{\partial t}+\bar{u}\frac{\partial\bar{u}}{\partial x}+\bar{v}\frac{\partial\bar{u}}{\partial y}+w\frac{\partial\bar{u}}{\partial z}=\bar{X}-\frac{1}{\rho}\frac{d\bar{P}_h}{dx}+\frac{1}{\rho}\frac{\partial}{\partial x}\left[\mu\frac{\partial\bar{u}}{\partial x}-\rho\overline{u`u`}\right]+$$
$$\frac{1}{\rho}\frac{\partial}{\partial y}\left[\mu\frac{\partial\bar{u}}{\partial y}-\rho\overline{u`v`}\right]+\frac{1}{\rho}\frac{\partial}{\partial z}\left[\mu\frac{\partial u}{\partial z}-\rho\overline{u`w`}\right]. \quad (3.2.36)$$

Similar equations can be derived for the y- and z-directions. Comparison of equation (3.2.33) with the original Navier-Stokes equation (3.2.25) in the x-direction, shows that the instantaneous values of velocity and pressure have been replaced by temporally averaged values and that three additional terms have appeared in the equation,

$$-\frac{1}{\rho}\frac{\partial}{\partial x}\rho\overline{u`u`}, \qquad -\frac{1}{\rho}\frac{\partial}{\partial x}\rho\overline{u`v`}, \qquad -\frac{1}{\rho}\frac{\partial}{\partial x}\rho\overline{u`w`}.$$

The terms $-\rho\overline{u`u`}$, $-\rho\overline{u`v`}$, and $-\rho\overline{u`w`}$ are known as the Reynolds or turbulent stresses and are a consequence of the presence of turbulence. In the case of a laminar flow, the Reynolds stresses are equal to zero. However, when the Reynolds stress terms are non-zero, it is impossible to solve the equations, as there are more unknowns than equations in the set. This is referred to as the *closure problem.*

Boussinesq's eddy viscosity concept (1877, see Rodi, 1984), assumes that, by analogy to the viscous stresses in laminar flows (i.e. the theory used to derive the Navier-Stokes equations), that turbulent stresses are proportional to the mean-velocity gradients, as experiment has shown that the turbulent stresses increase as the mean strain rate increases. The benefit of this analogy is that it simplifies the equation set by reducing the number of unknown variables. For instance, the Reynolds terms in the x-direction become,

$$\left.\begin{aligned} -\rho\overline{u`u`} &= \rho\nu_t\left[\frac{\partial\bar{u}}{\partial x}+\frac{\partial\bar{u}}{\partial x}\right]\left(\equiv\sigma_{xx}\right)\\ -\rho\overline{u`v`} &= \rho\nu_t\left[\frac{\partial\bar{u}}{\partial y}+\frac{\partial\bar{v}}{\partial x}\right]\left(\equiv\tau_{xy}\right),\\ -\rho\overline{u`w`} &= \rho\nu_t\left[\frac{\partial\bar{u}}{\partial z}+\frac{\partial\bar{w}}{\partial x}\right]\left(\equiv\tau_{xz}\right) \end{aligned}\right\} \quad (3.2.37)$$

where ν_t is the turbulent or eddy viscosity. The eddy viscosity coefficient quantifies the ability of turbulent fluctuations to support shear stresses. The similarity between equations (3.2.37) and (3.2.26 and 3.2.27) highlights the similarity between the theories being applied. Although the underlying theory behind Boussinesq's assumption has since been called into question regarding its physical reality, the concept has been found to work well in practice, is in wide spread use, and is computationally simple to deal with (Rodi, 1984). Derivation of the value of eddy viscosity 'ν_t' will be dealt with later, using Prandtl's mixing length hypothesis, the derivation of which makes use of relationships that have yet to be introduced (see section 3.3.2.2). Summating the effects of the Reynolds stresses as described by equation (3.2.37), substituting into equation (3.2.36), and averaging over a time period such that $\bar{u}\cong u$, produces in the x-direction,

$$\frac{\partial u}{\partial t}+u\frac{\partial u}{\partial x}u+v\frac{\partial u}{\partial y}+w\frac{\partial u}{\partial z}=X-\frac{1}{\rho}\frac{dP_h}{dx}+\frac{1}{\rho}\frac{\partial}{\partial x}\left[\mu\frac{\partial u}{\partial x}+\rho\nu_t\left(\frac{\partial u}{\partial x}+\frac{\partial u}{\partial x}\right)\right]+$$
$$\frac{1}{\rho}\frac{\partial}{\partial y}\left[\mu\frac{\partial u}{\partial y}+\rho\nu_t\left(\frac{\partial u}{\partial y}+\frac{\partial v}{\partial x}\right)\right]+\frac{1}{\rho}\frac{\partial}{\partial z}\left[\mu\frac{\partial u}{\partial z}+\rho\nu_t\left(\frac{\partial u}{\partial z}+\frac{\partial w}{\partial x}\right)\right] \quad (3.2.38)$$

In most flow regions at coastal scales, the turbulent stresses are much larger than their laminar counterparts, and therefore the effect of terms involving the fluid viscosity are normally neglected (Wang & Falconer, 1998). In order to simplify the derivation of the shallow water equations which follows, the Reynolds stress terms will be represented using σ_{xx}, τ_{xy} and τ_{xz} respectively. This alters the definition of these symbols from this point forward, as they no longer represent the overall normal and shear stresses, only the normal and shear stress components due to Reynolds stress. Consequently, equation (3.2.38) becomes,

$$\frac{\partial u}{\partial t}+u\frac{\partial u}{\partial x}u+v\frac{\partial u}{\partial y}+w\frac{\partial u}{\partial z}=X-\frac{1}{\rho}\frac{dP_h}{dx}+\frac{1}{\rho}\left[\frac{\partial \sigma_{xx}}{\partial x}+\frac{\partial \tau_{xy}}{\partial y}+\frac{\partial \tau_{xz}}{\partial z}\right] \quad (3.2.39)$$

Similar equations can be derived for the y- and z-directions.

3.2.3 Body forces and Coriolis acceleration

The only term as yet unaccounted for acting on the control volume is the effect due to gravity, previously referred to as the body force per unit mass, X. Gravity acts in the vertical direction, imposing a force per unit mass acting downwards, which is equal to the gravitational acceleration. In the horizontal plane, there are no other forces to be considered. It is at this stage however that it is necessary to consider that the derivation so far undertaken has been restricted to a fixed set of axes as originally depicted in Figure 3.1. As the axes are considered to be fixed to a point in the sea, moving particles must be subject to additional accelerations as a consequence of the earth's rotation when viewed by an observer also subject to the earth's rotation. The additional accelerating effect is known as the Coriolis acceleration. The effect of the Coriolis acceleration in the vertical direction is negligible when compared with the effect of gravitational acceleration, and is therefore ignored (Knight, 1986). The components of Coriolis acceleration considered with respect to the fixed axes in the x- and y-directions are $2v\Omega \sin\theta$ and $-2u\Omega \sin\theta$ respectively (Dronkers, 1964). The term Ω refers to the angular velocity

of the earth (7.3×10^{-5} s^{-1}). Examining the x- and y- components, it appears that the Coriolis acceleration acts perpendicularly to the velocity vector, the direction of action of the acceleration is always to the right, and is proportional to the size of the velocity vector. The repeated term $2\Omega \sin\theta$ in the Coriolis acceleration is referred to as the Coriolis frequency, which is represented by 'f'. Considering the effect of the Coriolis and gravitational acceleration together, the components of the body force per unit mass X, Y, and Z can be expressed as,

$$X = fv \qquad Y = -fu \qquad Z = -g.$$

3.3 The Shallow Water Equations

The three dimensional equations of motion so far derived are notoriously difficult to solve except in the simplest of cases (Ponce, 1981). Therefore, for practical engineering applications, simplifications are necessary. The most common simplifications of the equations applied in the coastal zone which still retain the relevant physics produce the Shallow Water Equations (S.W.E.). The S.W.E. are based on the premise that the horizontal scale is much larger than the vertical scale and that the flow is nearly horizontal. The major simplification is therefore to reduce the system from three-dimensions to two-dimensions by neglecting vertical motion and depth-averaging (Appendix A4) the horizontal equations (Dronkers, 1964). Information about variations in the vertical is lost, but the resulting equations are much easier to solve. However, application of the equations must therefore be restricted to areas where the assumptions hold. The first criterion generally accepted in engineering practice is that the S.W.E. are only applicable in cases where the depth is less than twenty times the wavelength (Eagleson & Dean, 1966). Permissible situations for application of the S.W.E. include regions where the flow is unstratified or only weakly stratified, in harbours, bays and coastal seas, and where the effect of wind shear is relatively small (Falconer, 1994). Unusual features such as tidal fronts may also limit the applicability of the S.W.E. From the above discussion, it is clear that the decision regarding the appropriate equation set to apply must be made on a case by case basis and requires careful consideration by an experienced user.

3.3.1 The Shallow Water Equations – Continuity

The major simplification is the assumption that the vertical component of velocity, w, is small in comparison with the horizontal components, u and v, which permits the use of depth-averaged values to describe the flow. This process involves the vertical integration from the sea bed ($z = -d(x,y)$) to the free surface ($z = \eta(x,y,t)$, where $z = 0$ is the mean water level) so that the three-dimensional equations are reduced to two-dimensions. However, this is not a simple process and relies upon making several necessary assumptions in order to allow the derivation to proceed. The first of these assumptions is to assume that the density is constant throughout the fluid depth.

The continuity equation (3.1.7) is to be depth integrated between the sea-bed and the free surface,

$$\int_{-d}^{\eta}\left(\frac{\partial u}{\partial x}+\frac{\partial v}{\partial y}+\frac{\partial w}{\partial z}\right)dz=0. \qquad (3.3.1)$$

Leibnitz's theorem (see Appendix A5), is used to integrate the terms in the continuity equation, such that the first term in equation (3.3.1) becomes,

$$\int_{-d}^{\eta}\frac{\partial}{\partial x}u\,dz=\frac{\partial}{\partial x}\int_{-d}^{\eta}u\,dz-\tilde{u}\frac{\partial \eta}{\partial x}+\underline{u}\frac{\partial(-d)}{\partial x}, \qquad (3.3.2)$$

where the over-symbol ~ is used to denote the value of a variable at the free surface (at $z = \eta$), and the under-bar is used to denote the value at the sea-bed (at $z = -d$). Following the same procedure for the other two terms in equation (3.3.1) produces,

$$\int_{-d}^{\eta}\frac{\partial}{\partial y}v\,dz=\frac{\partial}{\partial y}\int_{-d}^{\eta}v\,dz-\tilde{v}\frac{\partial \eta}{\partial y}+\underline{v}\frac{\partial(-d)}{\partial y}, \qquad (3.3.3)$$

and,

$$\int_{-d}^{\eta}\frac{\partial}{\partial z}w\,dz=\tilde{w}-\underline{w}. \qquad (3.3.4)$$

Combining the terms from (3.3.2 - 3.3.4), a complete description of the depth-integration of the continuity equation is obtained,

$$\frac{\partial}{\partial x}\int_{-d}^{\eta}u\,dz-\tilde{u}\frac{\partial \eta}{\partial x}+\underline{u}\frac{\partial(-d)}{\partial x}+\frac{\partial}{\partial y}\int_{-d}^{\eta}v\,dz-\tilde{v}\frac{\partial \eta}{\partial y}+\underline{v}\frac{\partial(-d)}{\partial y}+\tilde{w}-\underline{w}=0. \qquad (3.3.5)$$

In order to continue the derivation, the problem has to be specialised somewhat. The assumption is made that the flow is constrained between a solid sea-bed and a free surface. The free surface is considered as a moving impermeable boundary. If the equation of a boundary surface is S(x,y,z,t)=0, then the movement of the free surface $z=\eta(x,y,t)$ must be described by (Dronkers, 1964),

$$\frac{D\eta}{Dt} = \tilde{w} \Rightarrow = \frac{\partial \eta}{\partial t} + \tilde{u}\frac{\partial \eta}{\partial x} + \tilde{v}\frac{\partial \eta}{\partial y} - \tilde{w} = 0. \qquad (3.3.6)$$

Similarly, at the sea-bed, z=(-d)(x,y), as the sea-bed is considered to be solid, and therefore is not time dependent. Consequently,

$$\frac{D(-d)}{Dt} = \underline{w} \Rightarrow \underline{u}\frac{\partial(-d)}{\partial x} + \underline{v}\frac{\partial(-d)}{\partial y} - \underline{w} = 0. \qquad (3.3.7)$$

Adding the effect of the surface boundary condition (equation 3.3.6) and subtracting the effect of the sea-bed boundary condition (equation 3.3.7) from the depth-integrated continuity equation (3.3.5), reduces the expression to,

$$\frac{\partial \eta}{\partial t} + \frac{\partial}{\partial x}\int_{-d}^{\eta} u dz + \frac{\partial}{\partial y}\int_{-d}^{\eta} v dz = 0. \qquad (3.3.8)$$

The depth-averaged values of u and v are (where total depth $h = (\eta+d)$),

$$U = \frac{1}{h}\int_{-d}^{\eta} u dz, \qquad V = \frac{1}{h}\int_{-d}^{\eta} v dz. \qquad (3.3.9)$$

Therefore, equation (3.3.8) can be written in depth-averaged form as,

$$\frac{\partial \eta}{\partial t} + \frac{\partial (Uh)}{\partial x} + \frac{\partial (Vh)}{\partial y} = 0, \qquad (3.3.10)$$

3.3.2 The Shallow Water Equations - Momentum

As the depth-integration of the momentum equation into shallow water equations changes the expression from three-dimensions to two dimensions, the velocity in one of the directions must be neglected. Fortunately the vertical velocity can be assumed to be very small because accelerations due to hydrodynamic processes are generally regarded as being small in comparison with gravitational effects. The equation of motion in the z-direction can therefore be simplified by neglecting the terms incorporating the vertical velocity, w, which leaves the hydrostatic equation:

$$0 = -\frac{1}{\rho}\frac{\partial P_h}{\partial z} - g \Rightarrow \frac{\partial P_h}{\partial z} = -\rho g. \qquad (3.3.11)$$

Assuming that the pressure at the free surface is equal to atmospheric pressure, Pa, the pressure distribution at depth (z) would be,

$$Pa - P_h(z) = -\int_z^\eta (\rho g)dz$$

$$\therefore P_h(z) = Pa + \int_z^\eta (\rho g)dz$$

In a uniform density flow, ρ is constant everywhere,

$$\therefore P_h(z) = Pa + \rho g(\eta - z), \qquad (3.3.12)$$

and in the x-direction, the effect of a pressure gradient would be

$$\frac{\partial P_h}{\partial x} = \frac{\partial Pa}{\partial x} + \rho g \frac{\partial \eta}{\partial x.} \qquad (3.3.13)$$

This relationship, and a similar relationship in the y-direction can be used to substitute for the negative pressure gradients in equation (3.2.36). The scale appropriate to studies in the coastal zone is normally too small for changes in atmospheric pressure across the domain of interest to be of any relevance, and therefore the atmospheric pressure term in equation (3.3.13) is normally neglected.

From earlier derivation, the momentum equations can be represented as shown in equation (3.3.14) by adding the body forces (see section 3.2.3) to the momentum equations described by equation (3.2.39)

$$\frac{\partial u}{\partial t} + u\frac{\partial u}{\partial x} + v\frac{\partial u}{\partial y} + w\frac{\partial u}{\partial z} = fv - g\frac{\partial \eta}{\partial x} + \frac{1}{\rho}\left[\frac{\partial \sigma_{xx}}{\partial x} + \frac{\partial \tau_{xy}}{\partial y} + \frac{\partial \tau_{xz}}{\partial z}\right], \quad (a)$$

$$\frac{\partial v}{\partial t} + u\frac{\partial v}{\partial x} + v\frac{\partial v}{\partial y} + w\frac{\partial v}{\partial z} = -fu - g\frac{\partial \eta}{\partial y} + \frac{1}{\rho}\left[\frac{\partial \tau_{yx}}{\partial x} + \frac{\partial \sigma_{yy}}{\partial y} + \frac{\partial \tau_{yz}}{\partial z}\right], \quad (b) \qquad (3.3.14)$$

$$-\frac{1}{\rho}\frac{\partial P_h}{\partial z} - g = 0, \text{ which after re-arranging becomes, } \frac{\partial P_h}{\partial z} = -\rho g. \quad (c)$$

The next step involves the integration of the momentum equations (3.3.14) over the depth. As for the calculations involving the continuity equation, Leibnitz's Theorem is used, and the same boundary conditions are applied at the free surface and the solid bed.

Begin by considering the z-direction. As shown in equation (3.3.12), integrating over the depth in the z-direction produces the pressure distribution,

$$P_h(z) = Pa + \rho g(\eta - z).$$

Now considering the x-directed momentum equation (3.3.14(a)), the vertical integration required is laid out below (equation (3.3.15)),

$$\underset{(1)}{\int_{-d}^{\eta}\frac{\partial u}{\partial t}dz} + \underset{(2)}{\int_{-d}^{\eta}\left(u\frac{\partial u}{\partial x}+v\frac{\partial u}{\partial y}+w\frac{\partial u}{\partial z}\right)dz} = \underset{(3)}{\int_{-d}^{\eta}(fv)dz} - \underset{(4)}{\int_{-d}^{\eta}\left(g\frac{\partial \eta}{\partial x}\right)dz} + \frac{1}{\rho}\int_{-d}^{\eta}\left[\underset{(5)}{\frac{\partial \sigma_{xx}}{\partial x}}+\underset{(6)}{\frac{\partial \tau_{xy}}{\partial y}}+\underset{(7)}{\frac{\partial \tau_{xz}}{\partial z}}\right]dz$$

Applying Leibnitz's theorem to each of the terms in equation (3.3.15) individually allows the derivation to proceed without the equations under consideration containing an overwhelming number of terms. Using Leibnitz's Theorem and applying the depth-averaged identity to term (1) produces

$$\int_{-d}^{\eta}\frac{\partial u}{\partial t}dz = \frac{\partial}{\partial t}\int_{-d}^{\eta}udz - \tilde{u}\frac{\partial \eta}{\partial t} + \underline{u}\frac{\partial(-d)}{\partial t} = \frac{\partial(Uh)}{\partial t} - \tilde{u}\frac{\partial \eta}{\partial t} + \underline{u}\frac{\partial(-d)}{\partial t}.$$

Dealing with term (2) is simpler if it is written in a slightly different form, using the chain rule (Appendix A1) produces. The change also ensures that the equation remains mass conservative when finite differencing occurs (see chapter 4.2). Where upon,

$$\left(u\frac{\partial u}{\partial x}+v\frac{\partial u}{\partial y}+w\frac{\partial u}{\partial z}\right)+u\left(\frac{\partial u}{\partial x}+\frac{\partial v}{\partial y}+\frac{\partial w}{\partial z}\right) = \frac{\partial uu}{\partial x}+\frac{\partial uv}{\partial y}+\frac{\partial uw}{\partial z}.$$

This is possible because the additional term sums to zero as described by the continuity equation (3.1.7). Integrating this new representation of (2) term by term produces,

$$\int_{-d}^{\eta}\frac{\partial uu}{\partial x}dz = \frac{\partial}{\partial x}\int_{-d}^{\eta}(uu)dz - \tilde{u}\tilde{u}\frac{\partial \eta}{\partial x} + \underline{uu}\frac{\partial(-d)}{\partial x} = \beta\frac{\partial(UUh)}{\partial x} - \tilde{u}\tilde{u}\frac{\partial \eta}{\partial x} + \underline{uu}\frac{\partial(-d)}{\partial x},$$

$$\int_{-d}^{\eta}\frac{\partial uv}{\partial y}dz = \frac{\partial}{\partial y}\int_{-d}^{\eta}(uv)dz - \tilde{u}\tilde{v}\frac{\partial \eta}{\partial y} + \underline{uv}\frac{\partial(-d)}{\partial y} = \beta\frac{\partial(UVh)}{\partial y} - \tilde{u}\tilde{v}\frac{\partial \eta}{\partial y} + \underline{uv}\frac{\partial(-d)}{\partial y},$$

$$\int_{-d}^{\eta}\frac{\partial uw}{\partial z}dz = \tilde{u}\tilde{w} - \underline{uw},$$

where β accounts for the vertical variation of the velocity profile. The value of β is generally at or close to unity (being dependent on the velocity profile selected). β is therefore assumed to be 1 throughout the derivation and in the model code. Summating the results obtained for terms (1) and (2),

$$\frac{\partial(Uh)}{\partial t} - \tilde{u}\frac{\partial \eta}{\partial t} + \underline{u}\frac{\partial(-d)}{\partial t} + \frac{\partial(UUh)}{\partial x} - \tilde{u}\tilde{u}\frac{\partial \eta}{\partial x} + \underline{uu}\frac{\partial(-d)}{\partial x} + \frac{\partial(UVh)}{\partial y} - \tilde{u}\tilde{v}\frac{\partial \eta}{\partial y} + \underline{uv}\frac{\partial(-d)}{\partial y} + \tilde{u}\tilde{w} - \underline{uw}$$

which can be simplified by adding the effects of the surface boundary condition, and

subtracting the sea-bed boundary conditions (equations 3.3.6 and 3.3.7) after multiplying by $\tilde{u}$ and $\underline{u}$ respectively too finally produce,

$$\frac{\partial(Uh)}{\partial t}+\frac{\partial(UUh)}{\partial x}+\frac{\partial(UVh)}{\partial y}.$$

Similar application of Leibnitz's theorem and manipulation of the depth-averaged identity leads to, term (3),

$$\int_{-d}^{\eta}(fv)dz = fVh.$$

Analysing term (4),

$$-\int_{-d}^{\eta}\left(g\frac{\partial\eta}{\partial x}\right)dz = -gh\frac{\partial\eta}{\partial x}.$$

Analysing term (5) produces,

$$\frac{1}{\rho}\int_{-d}^{\eta}\frac{\partial\sigma_{xx}}{\partial x}dz=\frac{1}{\rho}\left(\frac{\partial}{\partial x}\int_{-d}^{\eta}\sigma_{xx}dz-\tilde{\sigma}_{xx}\frac{\partial\eta}{\partial x}+\underline{\sigma_{xx}}\frac{\partial(-d)}{\partial x}\right)=\frac{1}{\rho}\left(\frac{\partial\left(\overline{\sigma_{xx}}h\right)}{\partial x}-\tilde{\sigma}_{xx}\frac{\partial\eta}{\partial x}+\underline{\sigma_{xx}}\frac{\partial(-d)}{\partial x}\right).$$

Term (6) produces,

$$\frac{1}{\rho}\int_{-d}^{\eta}\frac{\partial\tau_{xy}}{\partial y}dz=\frac{1}{\rho}\left(\frac{\partial}{\partial y}\int_{-d}^{\eta}\tau_{xy}dz-\tilde{\tau}_{xy}\frac{\partial\eta}{\partial y}+\underline{\tau_{xy}}\frac{\partial(-d)}{\partial y}\right)=\frac{1}{\rho}\left(\frac{\partial\left(\overline{\tau_{xy}}h\right)}{\partial y}-\tilde{\tau}_{xy}\frac{\partial\eta}{\partial y}+\underline{\tau_{xy}}\frac{\partial(-d)}{\partial y}\right).$$

Finally term (7) produces,

$$\frac{1}{\rho}\int_{-d}^{\eta}\frac{\partial\tau_{xz}}{\partial z}dz=\frac{1}{\rho}\left(\frac{\partial}{\partial z}\int_{d_o}^{\eta}\tau_{xz}dz-\tilde{\tau}_{xz}\frac{\partial\eta}{\partial z}+\underline{\tau_{xz}}\frac{\partial(-d)}{\partial z}\right)=\frac{1}{\rho}\left(0-\tilde{\tau}_{xz}+\underline{\tau_{xz}}\right).$$

Summating the integrated terms 1-7, produces,

$$\frac{\partial(Uh)}{\partial t}+\frac{\partial(UUh)}{\partial x}+\frac{\partial(UVh)}{\partial y}=fVh-gh\frac{\partial\eta}{\partial x}+\frac{1}{\rho}\left[\begin{array}{l}\dfrac{\partial\left(\overline{\sigma_{xx}}h\right)}{\partial x}+\dfrac{\partial\left(\overline{\tau_{xy}}h\right)}{\partial y}-\left(\tilde{\sigma}_{xx}\dfrac{\partial\eta}{\partial x}+\tilde{\tau}_{xy}\dfrac{\partial\eta}{\partial y}+\tilde{\tau}_{xz}\right)\\ +\left(\underline{\sigma_{xx}}\dfrac{\partial(-d)}{\partial x}+\underline{\tau_{xy}}\dfrac{\partial(-d)}{\partial y}+\underline{\tau_{xz}}\right)\end{array}\right]$$

(3.3.16).

In the momentum equation, (3.3.16), the term

$$\left(\underline{\sigma_{xx}}\frac{\partial(-d)}{\partial x}+\underline{\tau_{xy}}\frac{\partial(-d)}{\partial y}+\underline{\tau_{xz}}\right), \qquad (3.3.17)$$

represents processes occurring at the interface between the water column and the sea-bed. The overall effect of these terms will be combined, and described using the bottom friction term, τ_b, described below. Similarly, the term,

$$-\left(\tilde{\sigma}_{xx}\frac{\partial \eta}{\partial x}+\tilde{\tau}_{xy}\frac{\partial \eta}{\partial y}+\tilde{\tau}_{xz}\right), \qquad (3.3.18)$$

in equation (3.3.16) represents processes occurring at the interface between the water column and the atmosphere. The overall effect of these terms will be combined, and described using the wind stress term, τ_w, also described below.

3.3.2.1 *Bed friction & wind stress*

Examination of the literature shows that bed friction, or resistance models applied to unsteady flows in the coastal environment are exactly the same as resistance models used to evaluate steady flows in uniform channels. As yet, no improved bed shear stress representations are available (Falconer, 1984). However, what little experimental work that has been carried out into the application of steady flow bed friction models in unsteady situations has tended to show good agreement between the systems (Liggett, 1994).

The effect of bed friction on the velocity profile is relatively easy to understand, the fluid immediately adjacent to the boundary must be stationary, and the velocity will increase with distance from the sea-bed. This fundamental interaction will be described using a mathematical model of the effect of the frictional resistance on the depth-averaged velocity. The mathematical model not only describes energy losses due to shear stresses at the sea-bed, but also losses incurred by non-resolved flow processes in the vertical due to the two-dimensional depth-averaged flow representation (Vieira, 1994). This is possible because the frictional models are themselves derived from observations of real flows.

For uniform steady flow in an open channel, the boundary shear stress, τ is (Abbott & Basco, 1989),

$$\tau = \rho g R S_e. \qquad (3.3.19)$$

Equation (3.3.19) in its present form offers no assistance in creating a closed set of equations for describing the equations of motion, as it introduces more unknowns into the system, namely the hydraulic radius (R) and rate of energy loss

per unit length (S_e). Empirical relationships relating the depth-averaged fluid velocity to the unknown variables have been proposed by numerous investigators who have attempted to fit the output obtained from experimental results into a mathematical form. Three of these empirical relationships have found widespread acceptance, the Darcy-Weisbach equation, which is normally applied in the study of pipe flows, the Chezy equation and Manning's equation. In the field of coastal and estuarial modelling, Manning's representation has found favour and has been successfully applied in numerous studies. Manning's equation, states that,

$$V_T = \frac{1}{n} R^{\frac{2}{3}} S_e^{\frac{1}{2}} = \frac{1}{n} R^{\frac{1}{6}} \sqrt{RS_e} \Rightarrow RS_e = \frac{n^2 V_T^2}{R^{\frac{1}{3}}}. \qquad (3.3.20)$$

Equating equations (3.3.19) and (3.3.20), it is possible to derive a relationship to describe the boundary shear stress in terms of known values with the appropriate value of 'n', (referred to as the Manning number) being obtained from tables,

$$\tau = \rho g RS = \rho g \frac{n^2 V_T^2}{R^{\frac{1}{3}}}. \qquad (3.3.21)$$

In the coastal environment, as the width of a cross-section is normally at least an order of magnitude larger than the depth, the hydraulic radius $R \rightarrow h$. Replacing the hydraulic radius with depth is therefore a reasonable assumption that also simplifies the computation. It is also assumed that the depths of water under consideration are sufficiently shallow so that the influence of the Ekman spiral can be neglected following Cheng et al (1993). Thus, the direction of bottom shear stress is assumed to be directly opposed to the depth-averaged velocity. In order to ensure that the boundary shear always opposes the flow direction, the V_T^2 term is written as $V_T|V_T|$. The final representation of the boundary shear stress (referred to in this case as the depth-averaged bed friction, τ_b) is,

$$\tau_b = \rho g n^2 \frac{V|V|}{h^{\frac{1}{3}}}. \qquad (3.3.22)$$

Manning's representation of the bed friction varies according to the composition of the bed material. Typical values range from 0.01 to 0.05. Table 3.2 illustrates some values derived from experimental data. Typical values applied in the coastal zone fall in the range $0.022 - 0.035\ sm^{-1/3}$.

Bed material	Value of 'n'
Perspex	0.01
Planed Wood	0.01
Smoothed Cement	0.01
Earth	0.022
Sand	0.025
Gravel	0.030
Rock	0.035-0.040

Table 3.2 – Typical values of Manning's number.

In a similar manner to the variation of fluid velocity with depth, wind velocities are retarded at the surface of the earth, whether it be over land or at sea. At the boundary between the atmosphere and the sea (as is the case under consideration), at the molecular level, the velocities of the atmosphere and the fluid must be equal. As the height above the ocean increases, the wind velocity increases. The interaction between the atmosphere and ocean is therefore similar to that described between the ocean and the sea-bed. Observation of the action of wind on the fluid velocity has shown that the boundary shear stress is proportional to the square of the wind velocity (Open University, 1989),

$$\tau = \rho_a C_w W_{10}^2 . \qquad (3.3.23)$$

where ρ_a is the air density (varies significantly with temperature), C_w is an air-water resistance coefficient which attempts to describe the amount of slip between the two (commonly quoted values in the literature range from 0.002 – 0.003), and W_{10} is the wind speed measured at 10 metres above the surface.

Incorporating the boundary shear stress representations at the sea-bed (equation 3.3.22) and surface (equation 3.3.23), the depth-integrated x-directed momentum equation (3.3.16) becomes,

$$\frac{\partial(Uh)}{\partial t} + \frac{\partial(UUh)}{\partial x} + \frac{\partial(UVh)}{\partial y} = fVh - gh\frac{\partial \eta}{\partial x} - gn^2 \frac{U\sqrt{U^2+V^2}}{h^{\frac{1}{3}}} + \frac{\rho_a C_w W_x \sqrt{W_x^2 + W_y^2}}{\rho} + \frac{1}{\rho}\left[\left(\frac{\partial(\overline{\sigma_{xx}}h)}{\partial x} + \frac{\partial(\overline{\tau_{xy}}h)}{\partial y}\right)\right] \qquad (3.3.24)$$

Using the full representation of the expanded Reynolds stress terms (equation 3.2.37), equation (3.3.24) becomes,

$$\frac{\partial(Uh)}{\partial t}+\frac{\partial(UUh)}{\partial x}+\frac{\partial(UVh)}{\partial y}=fVh-gh\frac{\partial\eta}{\partial x}-gn^2\frac{U\sqrt{U^2+V^2}}{h^{\frac{1}{3}}}+$$
$$\frac{\rho_a C_w W_x\sqrt{W_x^{\,2}+W_y^{\,2}}}{\rho}+\frac{1}{\rho}\left[2\frac{\partial}{\partial x}\left(\rho\overline{\nu_t}h\frac{\partial U}{\partial x}\right)+\frac{\partial}{\partial y}\left(\rho\overline{\nu_t}h\left[\frac{\partial U}{\partial y}+\frac{\partial V}{\partial x}\right]\right)\right] \quad (3.3.25)$$

Similarly, in the y-direction,

$$\frac{\partial(Vh)}{\partial t}+\frac{\partial(UVh)}{\partial x}+\frac{\partial(VVh)}{\partial y}=-fUh-gh\frac{\partial\eta}{\partial y}-gn^2\frac{V\sqrt{U^2+V^2}}{h^{\frac{1}{3}}}+$$
$$\frac{\rho_a C_w W_y\sqrt{W_x^{\,2}+W_y^{\,2}}}{\rho}+\frac{1}{\rho}\left[\frac{\partial}{\partial x}\left(\rho\overline{\nu_t}h\left[\frac{\partial U}{\partial y}+\frac{\partial V}{\partial x}\right]\right)+2\frac{\partial}{\partial y}\left(\rho\overline{\nu_t}h\frac{\partial V}{\partial y}\right)\right] \quad (3.3.26)$$

Equations (3.3.25) and (3.3.26) represent the x and y components of the fully depth-averaged momentum equations applicable to coastal situations. The use of depth-averaged equations of motion has been widespread over the past twenty years in numerical modelling applications, with the aims of developing theory (Signell & Geyer, 1991; Davies, et al., 1995), investigating water quality issues in case study situations (Hyder & Elliott, 1995; Cheng, et al., 1998), and creating multi-use numerical modelling tools (Bayne, 1996). The theory and applicability of the equations is therefore widely accepted.

Combining the depth-integrated momentum equations, (3.3.25) and (3.3.26), with the depth-integrated continuity equation (3.3.10) provides a set of three equations. However, there are five unknown variables, η, u, v, ν_t and ρ in the three equations. It has been assumed previously in the derivation that the fluid is of uniform density. Applying this criterion again, the influence on the flow development of density variation in the normal and shear stress terms would be neglected. In the case of the wind stress term, the fluid and air density terms can be determined according to typical values available in published tables. This removes one of the unknown variables, ρ, from the equation set. Prandtl's mixing length hypothesis provides a methodology for determining the value of eddy viscosity, ν_t, with respect to known values (physical constants), and the three remaining variables in the equation set. This therefore provides a closed set of equations (i.e., one in which the number of unknown values is equal to the number of equations), the

solution of which can be obtained using numerical techniques such as finite differencing (see chapter 4).

3.3.2.2 *Closure of the Equations of Motion using eddy viscosity concepts*

In section 3.2.2, Boussinesq's eddy viscosity concept was introduced in order to relate turbulent flow processes to known parameters (velocity gradients), such that the turbulent component of the normal and shear stresses in the x-direction become,

$$\sigma_{xx} = \rho\nu_t\left[\frac{\partial\bar{u}}{\partial x}+\frac{\partial\bar{u}}{\partial x}\right], \quad \tau_{xy} = \rho\nu_t\left[\frac{\partial\bar{u}}{\partial y}+\frac{\partial\bar{v}}{\partial x}\right], \text{ and, } \tau_{xz} = \rho\nu_t\left[\frac{\partial\bar{u}}{\partial z}+\frac{\partial\bar{w}}{\partial x}\right]. \quad (3.3.27)$$

In order to provide a closed set of equations, it is necessary to determine the value of the eddy viscosity coefficient, ν_t. As the expressions in equation (3.3.27) are being used to represent turbulent processes, the derivation of an appropriate expression for ν_t must be based on considerations of turbulent behaviour.

In the coastal environment, bed generated turbulence will be the dominant turbulence mechanism in the majority of the domain. The exception will be areas close to boundaries, where free shear layer turbulence will also be of significance. The effect of free shear layer turbulence will be neglected in this derivation. Therefore, as turbulence is only considered to be generated at the sea-bed, the significant turbulent shear stresses will be τ_{xz} and τ_{yz}, as these are the stresses that propagate the effect of flow processes occurring at the bed through the depth. From Bousinessq's eddy viscosity concept,

$$\tau_{xz}+\tau_{yz} = \rho\nu_t\left[\left(\frac{\partial u}{\partial z}+\frac{\partial w}{\partial x}\right)+\left(\frac{\partial v}{\partial z}+\frac{\partial w}{\partial y}\right)\right] = \tau_z. \quad (3.3.28)$$

As a depth-averaged flow is under consideration, the vertical velocity, w, is assumed to be negligible. As the effect of bed generated turbulence will vary across the depth, it is necessary to assume the profile of the shear stress and velocity distribution over depth using empirical formulations. Assuming that the velocity profile follows a logarithmic distribution and that the shear stress varies linearly (Knight, 1986; Abbott & Basco, 1989) produces,

$$u = \frac{u_*}{\kappa}\ln\left(\frac{d+z}{z_*}\right) \quad \text{and} \quad \tau_z = \tau_b\left(1-\frac{d+z}{h}\right). \quad (3.3.29)$$

Integrating the x- and y-directed velocities across depth,

$$\frac{\partial u}{\partial z} = \frac{u_*}{\kappa(d+z)} \qquad \text{and} \qquad \frac{\partial v}{\partial z} = \frac{v_*}{\kappa(d+z)}. \tag{3.3.30}$$

In equations (3.3.29) and (3.3.30), the friction velocities, $u_* = \sqrt{\frac{\tau_{bx}}{\rho}}$ and $v_* = \sqrt{\frac{\tau_{by}}{\rho}}$, the integration constant, z_*, is the boundary roughness length, and κ is von Karman's 'constant' (normally taken as being equal to 0.4). Recalling Manning's bottom friction representation (3.3.22),

$$\frac{\tau_b}{\rho} = gn^2 \frac{(U^2+V^2)}{h^{\frac{1}{3}}} = \frac{\tau_{bx}+\tau_{by}}{\rho} = u_*^2 + v_*^2. \tag{3.3.31}$$

Substituting this representation into the linear shear stress profile (equation (3.3.29)) produces,

$$\tau_z = \rho g n^2 \frac{(U^2+V^2)}{h^{\frac{1}{3}}}\left(1-\frac{d+z}{h}\right) \tag{3.3.32}$$

Prandtl's mixing length hypothesis assumes that the eddy viscosity, ν_t, is proportional to the mean fluctuating velocity, $\hat{V}$, and a "mixing length", l_m. Prandtl then postulated that $\hat{V}$ is equal to the mean velocity gradient times the mixing length, l_m. Applying the mixing length hypothesis with respect to a depth-averaged flow situation, where bed generated turbulence is dominant,

$$\nu_t = l_m^2\left(\left|\frac{\partial u}{\partial z}\right| + \left|\frac{\partial v}{\partial z}\right|\right). \tag{3.3.33}$$

Using this identity, equation (3.3.28) can be re-stated (ignoring cross-terms) as,

$$\tau_z = \rho\nu_t\left(\frac{\partial u}{\partial z}+\frac{\partial v}{\partial z}\right) = \rho l_m^2\left(\frac{\partial u}{\partial z}^2 + \frac{\partial v}{\partial z}^2\right). \tag{3.3.34}$$

Equating equations (3.3.30), (3.3.32), and (3.3.34), produces (equation (3.3.35)),

$$\tau_z = \rho l_m^2\left(\frac{\partial u}{\partial z}^2 + \frac{\partial v}{\partial z}^2\right) = \rho l_m^2\left(\frac{u_*^2}{\kappa^2(d+z)^2} + \frac{v_*^2}{\kappa^2(d+z)^2}\right) = \rho g n^2 \frac{(U^2+V^2)}{h^{\frac{1}{3}}}\left(1-\frac{d+z}{h}\right).$$

From this expression it is possible to derive a representation of the mixing length, l_m, with respect to known variables, and the three remaining parameters, η, U, and V, by cancelling the ρ terms, multiplying through by $\kappa^2(d+z)^2$, and recalling equation (3.3.31) such that,

$$l_m^2 = \kappa^2(d+z)^2\left(1-\frac{(d+z)}{h}\right). \qquad (3.3.36)$$

This provides an appropriate representation for the mixing length which can now be applied in order to derive a representation of the eddy viscosity term. Recalling equations (3.3.30), (3.3.32), and (3.3.33), the eddy viscosity coefficient, ν_t, can be expressed in a manner appropriate for describing the effect of bed generated turbulence,

$$\begin{aligned}
\nu_t &= l_m^2\left(\left|\frac{\partial u}{\partial z}\right|+\left|\frac{\partial v}{\partial z}\right|\right)= \\
&\kappa^2(d+z)^2\left(1-\frac{(d+z)}{h}\right)\sqrt{\left(\frac{u_*^2+v_*^2}{\kappa^2(d+z)^2}\right)}= \\
&\kappa^2(d+z)^2\left(1-\frac{(d+z)}{h}\right)\sqrt{\left(\frac{gn^2(U^2+V^2)}{\kappa^2(d+z)^2h^{\frac{1}{3}}}\right)}= \qquad (3.3.37)\\
&\kappa^2(d+z)^2\left(1-\frac{(d+z)}{h}\right)\left(\frac{\sqrt{g}n\sqrt{U^2+V^2}}{\kappa(d+z)h^{\frac{1}{6}}}\right)= \\
&\frac{\kappa\sqrt{g}n\sqrt{U^2+V^2}}{h^{\frac{1}{6}}}(d+z)\left(1-\frac{(d+z)}{h}\right)=\nu_t.
\end{aligned}$$

The final step is to determine the depth-integrated form of the eddy viscosity,

$$\overline{\nu}_t=\frac{1}{h}\int_{-d}^{\eta}\frac{\kappa\sqrt{g}n\sqrt{U^2+V^2}}{h^{\frac{1}{6}}}\left[\left((d+z)-\frac{(d+z)^2}{h}\right)\right]dz=\frac{1}{h}\frac{\kappa\sqrt{g}n\sqrt{U^2+V^2}}{h^{\frac{1}{6}}}\left[\frac{(d+z)^2}{2}-\frac{(d+z)^3}{3h}\right]_{-d}^{\eta}$$

As (d+z) = 0 when z = -d, and (d+z) = h when z = η,

$$\overline{\nu}_t=\frac{\kappa\sqrt{g}n\sqrt{U^2+V^2}}{h^{\frac{7}{6}}}\left[\frac{h^2}{2}-\frac{h^3}{3h}\right]=\frac{\kappa\sqrt{g}n\sqrt{U^2+V^2}}{h^{\frac{7}{6}}}\frac{h^2}{6}=\frac{\kappa\sqrt{g}n\sqrt{U^2+V^2}h^{\frac{5}{6}}}{6}. \qquad (3.3.38)$$

This zero equation (empiricaly based) turbulence model is similar to that originally proposed by Elder (1959). See chapters (4.2 and 5.2.4) for further discussion of turbulence model selection and application.

3.4 Conclusion

The initial problem of determining the governing equations of fluid flow has been discussed from first principles through a rigorous analysis to obtain a complete

description of the fluid flow (equation 3.2.38). Difficulties in solving the full set of equations due to the number of unknowns in the system has led to various simplifications being applied in order to present a description of the fluid flow which is relevant for practical engineering application. The major simplification commonly applied at scales appropriate for the coastal zone is to reduce the problem to two-dimensions. This reduces the complexity of the situation, and by making use of various assumptions of how the fluid behaves under particular conditions, a system of 3 equations with 3 unknowns has been achieved. The three equations are the depth-integrated continuity, x-directed and y-directed momentum equations, which can be used to derive the three unknowns, the depth-averaged x-directed velocity (U), the depth-averaged y-directed velocity (V), and the surface elevation (η). The final equations are:

$$\frac{\partial \eta}{\partial t}+\frac{\partial (Uh)}{\partial x}+\frac{\partial (Vh)}{\partial y}=0. \qquad (3.4.1)$$

$$\frac{\partial (Uh)}{\partial t}+\frac{\partial (UUh)}{\partial x}+\frac{\partial (UVh)}{\partial y}=fVh-gh\frac{\partial \eta}{\partial x}-gn^2\frac{U\sqrt{U^2+V^2}}{h^{\frac{1}{3}}}+$$
$$\frac{\rho_a C_w W_x\sqrt{W_x^{\,2}+W_y^{\,2}}}{\rho}+\left(\frac{\kappa\sqrt{g}n\sqrt{U^2+V^2}h^{\frac{5}{6}}}{6}\right)\left[2\frac{\partial^2 Uh}{\partial x^2}+\frac{\partial^2 Uh}{\partial y^2}+\frac{\partial^2 Vh}{\partial x\partial y}\right]. \qquad (3.4.2)$$

$$\frac{\partial (Vh)}{\partial t}+\frac{\partial (UVh)}{\partial x}+\frac{\partial (VVh)}{\partial y}=-fUh-gh\frac{\partial \eta}{\partial y}-gn^2\frac{V\sqrt{U^2+V^2}}{h^{\frac{1}{3}}}+$$
$$\frac{\rho_a C_w W_y\sqrt{W_x^{\,2}+W_y^{\,2}}}{\rho}+\left(\frac{\kappa\sqrt{g}n\sqrt{U^2+V^2}h^{\frac{5}{6}}}{6}\right)\left[2\frac{\partial^2 Vh}{\partial y^2}+\frac{\partial^2 Vh}{\partial y^2}+\frac{\partial^2 Uh}{\partial x\partial y}\right]. \qquad (3.4.3)$$

The final assumption in the momentum equations has been to neglect the gradient of the eddy viscosity and take the second gradient rather than the first gradient of the depth in the eddy viscosity terms (Falconer & Owens, 1984). This is necessary in order to make the equations more manageable when it comes to constructing a finite-difference representation of the governing equations (a subject covered in chapter 4).

4 NUMERICAL MODELLING

Chapter 3 introduced the equations of motion, and determined a suitable format for application in the coastal zone (equations 3.4.1 - 3.4.3). Obtaining analytical solutions to these equations is difficult, as the solution is dependent upon integration of the equations through time. Mathematically, such problems are classified as being of the *initial value* type, meaning that initial values representing the solution at the initial time in the integration process must be known in order to obtain a solution. It is also necessary to specify boundary conditions at each time-step in order to fully specify the problem. Together the initial values, boundary conditions and model equations describe the propagation of the solution through the domain of interest. As the solution propagates forward in time at a finite numerical propagation speed, $(\Delta x/\Delta t)$, it is necessary to guard against introducing excessive numerical instability into the solution by judicious selection of the step lengths, Δx and Δt. Various numerical techniques have been developed which present a framework for obtaining a solution of initial value type problems. The three most widely accepted and applied techniques are,

1. The method of characteristics,
2. The finite element method, and
3. The finite difference method.

Of these three methods, the solution of problems involving fluid dynamics has been dominated by the use of finite-difference approximations (Peyret & Taylor, 1983). It has also been suggested (Falconer, 1986) that finite-difference methods have more advantages than disadvantages in comparison with the other two methods when applied to free surface, time-dependent flows. Consequently, the finite difference method has been applied during this project in order to obtain solutions of the governing equations.

Application of finite-difference techniques, the number of calculations necessary to maintain stability criteria, and the extent of the domain of interest encourage automation of the calculation procedure using a computer. A computer programme was developed during this project to handle the numerical modelling requirements.

4.1 The Finite Difference Method

Obtaining solutions of partial differential equations using finite differencing is based upon the assumption that partial derivatives of the form $\frac{\partial \phi}{\partial x}$ can be approximated using the divided difference expression $\frac{\Delta \phi}{\Delta x} \Rightarrow \frac{\phi_2 - \phi_1}{x_2 - x_1}$, provided that Δx is sufficiently small. The dependent variable 'ϕ' and the independent variable 'x' are thought of as existing at regular points on a grid. Therefore, $\Delta \phi$ represents the change in the dependent variable 'ϕ' across one grid cell, where Δx is a measure of the displacement represented by the grid cell. The grid cell displacement in space or time determines the spatial or temporal resolution of the solution.

The differential equations can be converted into differenced equations using divided differences. The differenced equations can be constructed in a number of different ways, leading to different solution schemes with distinct properties. Solution methods utilising either explicit or implicit difference schemes are available. *Explicit difference* schemes express unknown variables in terms of known variables at every step enabling a direct calculation of the unknown variable. *Implicit difference* schemes require the solution of implicit equations, which describe the unknown variables in combination. Iterative techniques are required to solve the large set of simultaneous equations produced. Solution methods applied to solve implicit equation sets include double sweep methods, Newton iteration, successive-over-relaxation and Gaussian elimination. The major difference between applying an explicit and implicit difference scheme is that the explicit scheme is only conditionally stable, whereas implicit schemes are (at least theoretically) unconditionally stable. The stability condition imposed upon explicit finite difference schemes is called the Courant-Friedrichs-Lewey (CFL) condition. A stable solution is only achieved when this condition is satisfied (Abbott & Basco, 1989):

$$C_{CFL} = \frac{\text{celerity of propagation in the analytical solution}}{\text{celerity of propagation in the numerical solution}} \leq 1. \quad (4.1.1)$$

Further stability problems can arise in both explicit and implicit difference schemes as a consequence of non-linearity in the governing equations. Instability derived from non-linear processes is manifested in the form of transfer of energy from large

to small scales. In the numerical representation of this process, energy cannot be transferred to scales smaller than twice the grid size. Consequently, there can be a build-up of energy of wavelength $2\Delta x$ which can invalidate the solution. Early investigators avoided these problems by introducing artificial dissipative processes into the model, or by imposing an artificially high level of viscosity across the solution (artificial diffusion). While these methods could be 'tuned' to smooth out the instabilities, the level of the artificial dissipative effect often severely damped the entire solution obtained. Subsequently, methods have been developed to compute numerically stable solutions to non-linear equations by damping the difference scheme itself. The original scheme used first-order upstream differencing, which has since been found to be excessively diffusive. Extensive research has produced more refined techniques which incorporate higher-order differencing (Borris & Book, 1973; Leonard, 1978, 1979, 1981, 1983, 1988; Gaskell & Lau, 1988; Falconer, 1991; Leonard & Drummond, 1995). Solution techniques are now generally available for most finite-differencing applications which offer results free of excessive instability without unduly compromising the accuracy of the calculations (for example, flux-corrected transport, QUICK, third-order upwinding and SMART).

A characteristic common to both explicit and implicit finite-difference methods is that the solution is only defined at the grid points in the domain. To obtain information between the grid points, interpolation is necessary.

In this work, an explicit finite difference scheme has been developed for the numerical model. An explicit scheme was selected for the following reasons:

- The purpose of the project is not to develop new numerical modelling methods, rather, the numerical model will be used as a tool to aid in the development of the research into flow around islands and headlands. Consequently, the model will be based upon established theory and well founded methods whenever possible.
- Explicit schemes are described more thoroughly in the available literature, particularly regarding the pitfalls to be avoided.
- An explicit scheme requires simpler algorithms than an implicit scheme and is therefore cheaper in terms of the time necessary for development.

- The numerical model will be applied to simulate flows around islands and headlands. It is expected that non-linear interaction will be important to the flow development in these regions. Energy transfer by non-linear processes will provide a serious test of the stability of the code. The simplest method of increasing the stability of a particular simulation is to use a smaller spatial and temporal step in the numerical model. The major advantage of applying implicit finite difference schemes is their (theoretical) insensitivity to the Courant condition, which allows the selection of a large time-step in the calculation, and consequently reduces the simulation run-time. For this type of application, the need to restrict the time-step because of energy transfer concerns would limit the benefit of developing an implicit scheme.
- When using an explicit finite difference scheme, all the calculations are derived directly from existing data. This is beneficial in certain situations that are relevant to this work. For instance, simulating an idealised case with a symmetrical domain should (from a numerical modelling standpoint) produce a symmetrical result. An example of the application of this type of situation would be when testing for the correct application of boundary conditions. Using an implicit finite difference scheme, it is very difficult to ensure that there is no residual error generated during the iterative solution of the simultaneous equation matrix. Implicit schemes operate by specifying an acceptable residual error across the simultaneous equation matrix, at which point the iterative procedure stops, and the simulation moves on a time-step. The smaller the residual error value specified, the more iteration steps are necessary to achieve the desired accuracy. Special relaxation methods and other numerical techniques such as Chebyshev acceleration have been developed to reduce the number of iteration cycles required at each time-step (Patankar, 1980; Press et al., 1997: Griebel et al., 1998). Even utilising these specialised techniques, it would be optimistic to expect to match the level of accuracy achieved using a reliable explicit difference scheme when considering an extended and complex domain without compromising the major advantage (reduced computational expense due to quicker run-times) of applying an implicit difference scheme.

4.1.1 Finite differencing

The previous section introduced the concept of representing a partial derivative $\frac{\partial\phi}{\partial x}$ by $\frac{\Delta\phi}{\Delta x}$. Taylor's theorem (Appendix A2) is now applied in order to calculate the value of the dependent variable 'ϕ' as it propagates over the distance 'x'. Forward difference approximations are obtained by truncating an equation of the form (Appendix A, A.2.3) after the second term (i.e. assuming that second and higher order powers are insignificant). For the case under consideration, where the variable 'ϕ' is a function of the independent variable 'x', this produces,

$$\frac{\partial\phi}{\partial x} = \frac{[\phi(x+\Delta x)-\phi(x)]}{\Delta x}. \qquad (4.1.2)$$

Similarly, the backward difference approximation can be derived by truncation of (Appendix A, A.2.4),

$$\frac{\partial\phi}{\partial x} = \frac{[\phi(x)-\phi(x-\Delta x)]}{\Delta x}. \qquad (4.1.3)$$

The truncation of equations (4.1.2) and (4.1.3) produces an approximation, or truncation error, the leading (and numerically dominant) part of which is the largest truncated term, $(\pm)\frac{\Delta x}{2}\frac{\partial^2\phi}{\partial x^2}$. This term tends towards zero as Δx tends towards zero. The error of approximation is therefore said to be of first order, written as $O(\Delta x)$. This term means that the approximation error decreases linearly with Δx.

If instead an equation of the form (Appendix A, A.2.3) is added to a similar representation of equation (Appendix A, A.2.4), then,

$$\frac{\partial\phi}{\partial x} = \frac{[\phi(x+\Delta x)-\phi(x-\Delta x)]}{2\Delta x} - \frac{\Delta x^2}{6}\frac{\partial^3\phi}{\partial x^3} + \text{H.O.T.} \qquad (4.1.4)$$

Truncating the higher-order terms, the central difference approximation is obtained,

$$\frac{\partial\phi}{\partial x} = \frac{[\phi(x+\Delta x)-\phi(x-\Delta x)]}{2\Delta x}. \qquad (4.1.5)$$

The leading part of the truncation error for this central difference approximation is $\frac{\Delta x^2}{6}\frac{\partial^3\phi}{\partial x^3}$. This implies that the error tends towards zero as Δx^2 tends towards zero, and the truncation error is of second order accuracy $O(\Delta x^2)$. In this case the error decreases directly by the square of the ratio of decrease in Δx.

The central difference approximation scheme provides the most accurate of the three representations of the original partial derivative, as the truncation error is the smallest. The three approximation schemes are represented graphically in Figure 4.1 below, where it is obvious that the gradient of the line AC, representing the central difference approximation, best represents the gradient of the curve at B.

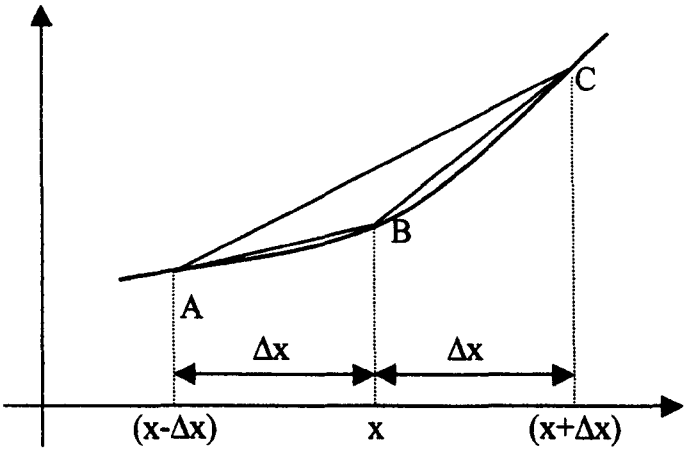

Figure 4.1 – Diagrammatic representation of the three basic finite-difference approximations. The forward, backward and central difference approximations are represented by the gradient of lines BC, AB and AC respectively.

From the discussion above, and consideration of figure 4.1, the logical conclusion would be to always apply the centred difference approximation, as the forward and backward difference schemes are subject to excessive numerical error. In general applications this conclusion holds true. However, when applying these mathematical techniques to the field of computational fluid dynamics (CFD), numerous examples showing a lack of stability, and in some cases serious non-convergence occur in the literature (Leonard, 1979; Fletcher, 1991(a, b)). The classic example of this is the occurrence of unnatural grid scale oscillations that were common to output from early CFD modelling in the 1960's – 1980's. It has since become well understood that centred difference techniques are well-suited to modelling physical processes involving even-ordered spatial derivatives, such as diffusion, wave motion and elastic failure (Leonard, 1981). The key difference in CFD applications to most other branches of computational physics is the importance of the convection term which is a first (odd-) ordered spatial derivative (Leonard, 1983). When applying a symmetrically centred central difference operator (of any order) to an odd-ordered derivative, the result is insensitive to fluctuations in the value of the central node, and is described as having neutral sensitivity. Considered

from a physical viewpoint, the action of the convective term is to transport fluid properties from upstream to downstream. It is therefore necessary for the mathematical description to mirror these properties (Gaskell & Lau, 1988). Returning to the centred difference approximation with its inherently neutral sensitivity, the mathematical operation may well be dominated by fluctuations occurring either up or downstream. It is now clear that central differencing methods are inappropriate for modelling the convective terms.

4.1.2 Higher-order finite difference techniques

Modelling the convective terms in the governing equations of fluid dynamics using central difference methods of any order is inappropriate. The alternative offered by first-order forward or backward differencing is unacceptable due to the poor numerical accuracy of such techniques. The only option available is to move to a higher-order scheme.

Already, the discussion has cast doubt on the application of first-order and all even-ordered finite difference techniques. The options left available are upwind biased odd-ordered schemes of third-order and higher. Higher-order finite difference techniques operate by modelling directly what would otherwise be the truncation terms in the Taylor series expansion of the convective terms. The obvious effect of incorporating higher-order schemes is to increase both the numerical complexity and computational expense. Arguments against the use of increasingly higher-order accuracy schemes have been led by the opinion that (Leonard, 1983),

> "... above fourth-order, algorithmic complexity begins to escalate, and soon outstrips the normal powers of human comprehension and debugging skills."

Nonetheless, accuracy schemes as high as fifth- and sixth-order have been discussed in the literature for a range of applications (Falconer, 1992), and found to have increased accuracy over lower-order schemes (although these tests were restricted to one-dimension due to the computational complexity of extending to two-dimensions). Fortunately, finite-difference schemes based upon third-order upwinding have been found to offer good accuracy, inherent numerical stability and (relative) computational simplicity (Leonard, 1979, 1981, 1984, 1988; Falconer and Liu, 1988;

Falconer, 1992; Lin and Falconer, 1997). The success of third-order upwinding techniques has led to the proposal of numerous different schemes, such as QUICK, QUICKEST, SHARP and SMART, all intended to improve a particular aspect or application of the basic third-order upwinding scheme.

The Tidal Flow Development (TFD) model developed during this research incorporates an algorithm presented by Fletcher (1991) to model the effects of convective transport,

$$\frac{\partial\phi}{\partial x}=\frac{\phi(x+\Delta x)-\phi(x-\Delta x)}{2\Delta x}+\frac{q\left(\phi(x-2\Delta x)-3\phi(x-\Delta x)+3\phi(x)-\phi(x+\Delta x)\right)}{3\Delta x} \quad (4.1.6)$$

Equation (4.1.6) is applicable in situations where the dependent variable, $\phi(x)$ is positive. If $\phi(x)$ is negative, the equation becomes,

$$\frac{\partial\phi}{\partial x}=\frac{\phi(x+\Delta x)-\phi(x-\Delta x)}{2\Delta x}+\frac{q\left(\phi(x-\Delta x)-3\phi(x)+3\phi(x+\Delta x)-\phi(x+2\Delta x)\right)}{3\Delta x} \quad (4.1.7)$$

in order to maintain the upstream directed bias of the algorithm.

Both equations contain two distinct parts. The first term in the equations is the simple centred difference representation (equation 4.1.5). The second term provides a mechanism to modify the results obtained by selection of an appropriate value of the coefficient q. Considering the second part of equation (4.1.6), a Taylor series expansion about the central node produces (Fletcher, 1991),

$$\phi(x-2\Delta x)-3\phi(x-\Delta x)+3\phi(x)-\phi(x+\Delta x)\equiv\left[-\Delta x^3\frac{\partial^3\phi}{\partial x^3}+0.5\Delta x^4\frac{\partial^4\phi}{\partial x^4}+\text{H.O.T.}\right].$$

This enables the user to counteract specific terms in the Taylor series expansion of the original equation. With reference to the central difference representation in equation (4.1.4), where the leading truncation error term is $-\frac{\Delta x^2}{6}\frac{\partial^3\phi}{\partial x^3}$, it should be clear that appropriate selection of the value of the coefficient q (0.5 in this case), can be used to entirely eliminate the leading truncation error term, reducing the inherent error in the calculation to third order $O(\Delta x^3)$. The advantage of using this particular algorithmic representation is the flexibility available to the user – by varying the value of the coefficient q, the algorithm can be tuned to provide a second-order central difference scheme (q = 0), or coincide with Leonard's control-volume QUICK representation (q = 0.375), or a fully third-order upwind scheme as shown (q = 0.5). Further increasing

the value of the coefficient q above 0.5 produces a smoother but more diffuse solution as the weighting of the upwind biased term is increased, eventually producing a solution more akin to that of a simple two-point upwind scheme. Comparison of output using a variety of values of q has shown that there is little difference between the results obtained using the QUICK and fully third-order scheme (q = 0.375 and q = 0.5 respectively), but that these modifications provide a considerably improved simulation than results obtained using significantly higher or lower values of q (see chapter 5.2.3). Hu & Kot (1997) have indicated that the QUICK scheme reduces numerically generated dispersion by a factor of eight compared with the central differencing scheme.

4.2 Discretising the Governing Equations

To assist in the discretisation of the governing equations, a simple regular grid system is implemented. This provides both a system for referencing the different variables, as explained below, and a framework for viewing the results obtained from the model. For each simulation it is necessary to select an appropriate uniform length for the spatial and temporal grid cells, where Δx and Δy represent uniform displacements in the x- and y- component directions, and Δt represents uniform displacement in time. The grid position of the state variables is represented by indices i-1, i, i+1, ... i+n, in the x component direction, by j-1, j, j+1, ... j+n, in the y component direction, and by k-1, k, k+1, ... k+n, in the temporal direction. This enables a particular variable to be easily positioned and referenced to in space and time. For instance, using this convention, the dependent variable ϕ positioned at (i, j, k) can now easily be referred to, $\phi^k_{i,j}$, be represented visually (Figure 4.2) and reduced to an array variable, $\phi(i, j, k)$, for implementation in a computer program.

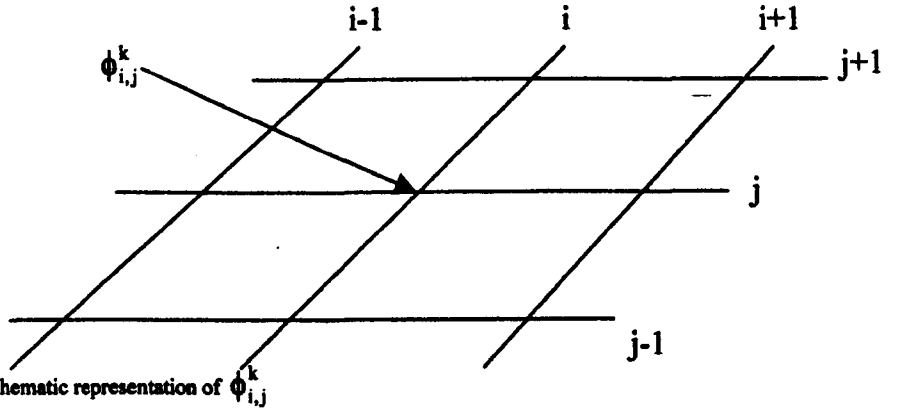

Figure 4.2 - Schematic representation of $\phi^k_{i,j}$

In this work, an explicit three-dimensional central difference space and time staggered scheme was used to approximate the governing equations. The scheme can be represented pictorially in three-dimensions as

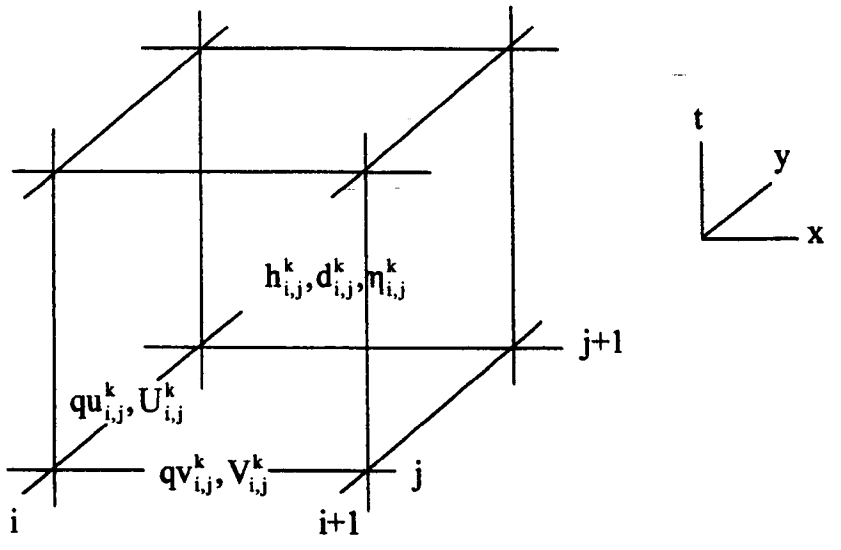

Figure 4.3 – Arrangement of variables on the staggered grid.

The x-directed flow components, $qu^k_{i,j}$ and $U^k_{i,j}$, are positioned at the centre of the bottom left edge of the cell at (i, $j+\frac{1}{2}$, k), the y-directed flow components $qv^k_{i,j}$ and $V^k_{i,j}$, are positioned at the centre of the front bottom edge of the cell at ($i+\frac{1}{2}$, j, k) and the depth related variables, $h^k_{i,j}, d^k_{i,j}$ and $\eta^k_{i,j}$, are positioned at the centre of the cell at ($i+\frac{1}{2}$, $j+\frac{1}{2}$,$k+\frac{1}{2}$).

The $\frac{1}{2}$ step discrepancies between the variable names and their positions are accounted for by the staggering of the grid. A staggered grid has been selected for a number of reasons. The primary reason is that by staggering the grid in the manner shown in Figure 4.3, it is possible to time-centre the finite-difference calculations even although they are being derived explicitly. This would not be possible without using a staggered grid with an explicit formulation. The benefits of this are an increase in numerical accuracy and stability as it allows second order accuracy in time even although only a simple forward difference procedure is being applied. A further benefit of using the staggered representation is that it lends itself to a satisfying yet simple means of discretising the equations using a control volume approach. This manipulation of the variable positions and finite difference techniques is referred to as the staggered leap-frog approach (Falconer, 1986).

Considering an individual grid cell in the domain, the continuity equation states that the total flow in minus the total flow out equals the change in storage (or elevation in this case) as outlined in chapter 3.1. The total flow into the cell is equal to the area of the cell face multiplied by the depth-averaged velocity. In the two-dimensional case, the total flow can be considered in terms of the total flow per metre length, which is equal to the depth of water multiplied by the depth-averaged velocity. This quantity is referred to as the discharge per unit width, and is assigned the variable names qu for x-directed discharge and qv for y-directed discharge. Therefore,

$$qu = Uh, \text{ and, } qv = Vh. \tag{4.2.1}$$

It is important to note that the unit discharge variables remain centred at $U^k_{i,j}$ and $V^k_{i,j}$ respectively. Explicitly stating the derivation of qu and qv using the staggered grid,

$$\begin{aligned} qu^k_{i,j} &= U^k_{i,j}\left(\frac{h^{k-1}_{i,j} + h^{k-1}_{i-1,j} + h^k_{i,j} + h^k_{i-1.j}}{4}\right) \\ qv^k_{i,j} &= V^k_{i,j}\left(\frac{h^{k-1}_{i,j} + h^{k-1}_{i,j-1} + h^k_{i,j} + h^k_{i,j-1}}{4}\right) \end{aligned} \tag{4.2.2}$$

The subtle differences between the centring of these two terms, and the remaining terms to be discussed is absolutely vital in maintaining stability and in ensuring that the equations are properly representative of the physical processes that are being approximated. The benefit of using the discharge per unit width will become apparent during the discretisation of the governing equations.

The arrangement of variables using the staggered grid provides a framework for discretisation of the governing equations to be used in the model. As there are three unknowns and three equations, a system must be established for calculating the unknowns 'future' variable based upon known values. The staggered leap-frog approach referred to earlier will be applied to each of the model terms unless otherwise indicated.

The governing continuity equation and x-directed momentum equation as derived in two-dimensional depth-averaged form (see chapter 3.4), with the relevant substitution for discharge per unit width (as outline in equation (4.2.1)) become,

$$\frac{\partial \eta}{\partial t} + \frac{\partial qu}{\partial x} + \frac{\partial qv}{\partial y} = 0, \tag{4.2.3}$$

$$\frac{\partial qu}{\partial t}+\frac{\partial(quU)}{\partial x}+\frac{\partial(quV)}{\partial y}=fqv-gh\frac{\partial \eta}{\partial x}-gn^2\frac{U\sqrt{U^2+V^2}}{h^{\frac{1}{3}}}+$$
$$\frac{\rho_a C_w W_x\sqrt{W_x^{\,2}+W_y^{\,2}}}{\rho}+\left(\frac{\kappa\sqrt{g}n\sqrt{qu^2+qv^2}}{6h^{\frac{1}{6}}}\right)\left[2\frac{\partial^2 qu}{\partial x^2}+\frac{\partial^2 qu}{\partial y^2}+\frac{\partial^2 qv}{\partial x\partial y}\right]. \qquad (4.2.4)$$

Examining the system of equations and the staggered grid, it is easily understood that the purpose of discretising the continuity equation will be to derive the change in the value of η with respect to time, and the discretisation of the respective momentum equations to derive the change in the x- and y- directed velocities (discharges) with respect to time. Initially considering the continuity equation (4.2.3), discretisation of the equation should allow the future time-step value of η to be determined from known values of qu, qv and η from the current time-step,

$$\frac{\eta_{i,j}^{k}-\eta_{i,j}^{k-1}}{\Delta t}+\frac{qu_{i+1,j}^{k}-qu_{i,j}^{k}}{\Delta x}+\frac{qv_{i,j+1}^{k}-qv_{i,j}^{k}}{\Delta y}=0. \qquad (4.2.5)$$

This equation can then be rearranged to produce an equation that expresses the value of the unknown variables in terms of the known variables

$$\eta_{i,j}^{k}=\eta_{i,j}^{k-1}-\Delta t\times\left(\frac{qu_{i+1,j}^{k}-qu_{i,j}^{k}}{\Delta x}+\frac{qv_{i,j+1}^{k}-qv_{i,j}^{k}}{\Delta y}\right) \qquad (4.2.6)$$

This representation follows the process of the staggered leap-frog approach in order to determine the future value of η from known variables which are arranged in such a fashion as to remain fully centred in both time and space. This procedure is commonly applied when deriving a finite difference representation of the continuity equation as it provides for easy centring, and reduces the necessary programming effort (Black & Gay, 1987). Deriving similar expressions for the x- and y-momentum equations enables the calculation of the future values of qu and qv respectively, and the 'marching' finite-difference scheme is established.

Considering the x-directed momentum equation (4.2.4) term by term, the discretisation followed in the TFD numerical model is,

$$\frac{\partial(qu)}{\partial t}=\frac{qu_{i,j}^{k+1}-qu_{i,j}^{k}}{\Delta t}. \qquad (4.2.7)$$

This representation of the temporal term leads to the discretisation of the complete momentum equations being of the FTCS (Forward-in-Time, Centred-in-Space) type.

The advantage of this system in collaboration with the staggered grid over the leap frog approach is that it reduces the amount of variables necessary to be stored to carry out the calculation by almost half, with a similar reduction in computational time. However as implied in the name, the formulation is of the forward difference type in time, rather than centred difference. This suggests a loss in precision in the formulation from the earlier discussion of accuracy. However, the staggering of the variables ensures that the system remains stable. The consequences of the loss of accuracy brought about by the forward difference in time are minimal, as the change of the discharge per unit width variable is calculated over very small time-steps (i.e. as Δt tends towards zero in comparison with the tidal time-scale, the error also tends towards zero). Application of the Courant condition (see the discussion in the following section) ensures that the time-step, Δt, in simulations at coastal scales is restricted to very low levels (typically $\Delta t \leq 10$ seconds).

For the stream-wise convective momentum term, equation 4.1.6 (or 4.1.7 if appropriate) has been applied as described in chapter 4.1.2, rather than using central differencing,

$$\frac{\partial(quU)}{\partial x} = \left\{ \begin{array}{l} \dfrac{(qu^k_{i+1,j} \times U^k_{i+1,j}) - (qu^k_{i-1,j} \times U^k_{i-1,j})}{2\Delta x} + \\ \dfrac{q}{3 \times \Delta x} \left[\begin{array}{l} (qu^k_{i-2,j} \times U^k_{i-2,j}) - 3 \times (qu^k_{i-1,j} \times U^k_{i-1,j}) + \\ 3 \times (qu^k_{i,j} \times U^k_{i,j}) - (qu^k_{i+1,j} \times U^k_{i+1,j}) \end{array} \right] \end{array} \right\}. \qquad (4.2.8)$$

In normal application, the coefficient q is set to equal 0.5 to coincide with a fully third-order representation of this term. Similarly, the cross-stream convective momentum term also applies the Fletcher algorithm, with the value of the coefficient q always being set to the same value as applied to the stream-wise term,

$$\frac{\partial(quV)}{\partial y} = \left\{ \begin{array}{l} \dfrac{\left[\begin{array}{l} \left[(qu^k_{i,j+1} \times ((V^k_{i,j+1} + V^k_{i,j+2} + V^k_{i-1,j+1} + V^k_{i-1,j+2})/4) \right] - \\ \left[(qu^k_{i,j-1} \times ((V^k_{i,j-1} + V^k_{i,j} + V^k_{i-1,j-1} + V^k_{i-1,j})/4) \right] \end{array} \right]}{2\Delta x} + \\ \dfrac{q}{3 \times \Delta x} \left[\begin{array}{l} \left[(qu^k_{i,j-2} \times ((V^k_{i,j-2} + V^k_{i,j-1} + V^k_{i-1,j-2} + V^k_{i-1,j-1})/4) \right] - \\ \left[3 \times (qu^k_{i,j-1} \times ((V^k_{i,j-1} + V^k_{i,j} + V^k_{i-1,j-1} + V^k_{i-1,j})/4) \right] + \\ \left[3 \times (qu^k_{i,j} \times ((V^k_{i,j} + V^k_{i,j+1} + V^k_{i-1,j} + V^k_{i-1,j+1})/4) \right] - \\ \left[(qu^k_{i,j+1} \times ((V^k_{i,j+1} + V^k_{i,j+2} + V^k_{i-1,j+1} + V^k_{i-1,j+2})/4) \right] \end{array} \right] \end{array} \right\}. \qquad (4.2.9)$$

The cross-stream convective term is slightly more complicated than the stream-wise term. This is necessary to obtain exact centring of the terms in the equation.

The pressure gradient term is very simply discretised as,

$$gh\frac{\partial \eta}{\partial x} = g \times \frac{(h^{k}_{i,j} + h^{k}_{i-1,j})}{2} \times \left(\frac{\eta^{k}_{i,j} - \eta^{k}_{i-1,j}}{\Delta x}\right). \qquad (4.2.10)$$

The bottom friction representation uses depth-averaged velocity variables rather than the discharge per unit width representation, even although it is very simple to alternate between the two representations. There are a number of reasons for this. First of all, having derived the bottom friction term with respect to depth-averaged velocity components, the physical reality of the situation becomes clouded if it were to now be represented using the discharge per unit width variable. Secondly, the necessity of centring the y-directed velocity term around the x-directed velocity term occurs on numerous occasions throughout the model. Therefore the overall calculation time can be reduced by evaluating and storing these values prior to the calculation steps in the numerical model. A further point to note is that it is necessary to use variables obtained for the previous time-step in order to discretise the bottom friction term, so the friction term is lagged by $\Delta t/2$.

$$gn^2 \frac{U\sqrt{U^2+V^2}}{h^{1/3}} = \left\{ \frac{g \times \left[\frac{(n_{i,j} + n_{i-1,j})}{2}\right]^2 \times U^{k}_{i,j} \times \sqrt{\left(U^{k}_{i,j}\right)^2 + \left(\left(V^{k}_{i,j} + V^{k}_{i-1,j} + V^{k}_{i,j+1} + V^{k}_{i-1,j+1}\right)/4\right)^2}}{\left((h^{k}_{i,j} + h^{k}_{i-1,j} + h^{k-1}_{i,j} + h^{k-1}_{i-1.j})/4\right)^{1/3}} \right\}. \qquad (4.2.11)$$

The Coriolis term is simply represented, as it does not require any finite differencing, it is just a direct discretisation to establish the correct centring,

$$fqv = f \times \left(\left(qv^{k}_{i,j} + qv^{k}_{i-1,j} + qv^{k}_{i,j+1} + qv^{k}_{i-1,j+1}\right)/4\right) \qquad (4.2.12)$$

Similarly, the wind stress term is also a direct discretisation requiring no differencing. The components of wind stress used are from the future time-step, as this information would normally be available from either determining prevailing wind conditions, or a direct record of the conditions from a particular day,

$$\frac{\rho_a C_w W_x \sqrt{W_x^{\,2} + W_y^{\,2}}}{\rho} = \frac{\rho_a \times C_w \times W^{k+1}_{xi,j} \times \sqrt{\left(W^{k+1}_{xi,j}\right)^2 + \left(W^{k+1}_{y_{i,j}}\right)^2}}{\rho}. \qquad (4.2.13)$$

The ratio of the air to water density is approximately 1:800 although temperature variation can alter this relationship.

The discretisation of the direct and turbulent shear terms, and eddy viscosity formulation is relatively complicated to ensure that everything is fully centred. Although only a zero–level turbulence model has been applied as described in chapter 3, all the direct and turbulent shear terms have been maintained, avoiding the tendency of many models to ignore the direct stresses, and/or the cross-momentum term in the turbulent shear stress representation. The direct and lateral stresses have been finite differenced using a second-order central difference representation, and the eddy viscosity value is derived directly from known values.

$$\left(\frac{\kappa\sqrt{g}n\sqrt{qu^2+qv^2}}{6h_{i,j}^{k\,\frac{1}{6}}}\right)\left[2\frac{\partial^2 qu}{\partial x^2}+\frac{\partial^2 qu}{\partial y^2}+\frac{\partial^2 qv}{\partial x\partial y}\right]=$$

$$\left\{\left(\frac{\kappa\sqrt{g}\left(\frac{n_{i,j}-n_{i-1,j}}{2}\right)\sqrt{\left(qu_{i,j}^{k}\right)^2+\left(\frac{qv_{i,j}^{k}+qv_{i,j+1}^{k}+qv_{i-1,j}^{k}+qv_{i-1,j+1}^{k}}{4}\right)}}{6\left(\frac{h_{i,j}^{k}+h_{i-1,j}^{k}+h_{i,j}^{k-1}+h_{i-1,j}^{k-1}}{4}\right)^{\frac{1}{6}}}\right)\times\right.$$

$$\left.\left[2\left(\frac{qu_{i+1,j}^{k}-2qu_{i,j}^{k}+qu_{i-1,j}^{k}}{\Delta x^2}\right)+\left(\frac{qu_{i,j+1}^{k}-2qu_{i,j}^{k}+qu_{i,j-1}^{k}}{\Delta y^2}\right)+\frac{\left(\frac{qv_{i,j+1}^{k}-qv_{i,j}^{k}}{\Delta y}\right)-\left(\frac{qv_{i-1,j+1}^{k}-qv_{i-1,j}^{k}}{\Delta y}\right)}{\Delta x}\right]\right\}. \qquad (4.2.14)$$

Combining equations (4.2.7) through equation (4.2.14), and rearranging so that the one unknown 'future' value, the term describing $qu_{i,j}^{k+1}$, is described in terms of all the known values, the x-directed momentum equation becomes (see equation 4.2.15 overleaf). A similar equation for the y-directed momentum has also been derived with the calculation centred around the $qv_{i,j}$ variable. The major advantage of having used discharge per unit width in the discretisation is that the left-hand side of equation (4.2.15) contains only one unknown 'future' value, whereas if the representation had remained as the depth-averaged velocity multiplied by the overall depth, there would have been two unknown 'future' values in the calculation.

$$qu_{i,j}^{k+1} = qu_{i,j}^{k} - \Delta t \left[\begin{array}{l} \left\{ \begin{array}{l} \dfrac{(qu_{i+1,j}^{k} \times U_{i+1,j}^{k}) - (qu_{i-1,j}^{k} \times U_{i-1,j}^{k})}{2\Delta x} + \\ \dfrac{q}{3\times\Delta x}\left[\begin{array}{l} (qu_{i-2,j}^{k} \times U_{i-2,j}^{k}) - 3\times(qu_{i-1,j}^{k} \times U_{i-1,j}^{k}) + \\ 3\times(qu_{i,j}^{k} \times U_{i,j}^{k}) - (qu_{i+1,j}^{k} \times U_{i+1,j}^{k}) \end{array} \right] \end{array} \right\} + \\ \left\{ \begin{array}{l} \dfrac{\left[\begin{array}{l} \left[(qu_{i,j+1}^{k} \times ((V_{i,j+1}^{k} + V_{i,j+2}^{k} + V_{i-1,j+1}^{k} + V_{i-1,j+2}^{k})/4) \right] - \\ \left[(qu_{i,j-1}^{k} \times ((V_{i,j-1}^{k} + V_{i,j}^{k} + V_{i-1,j-1}^{k} + V_{i-1,j}^{k})/4) \right] \end{array} \right]}{2\times\Delta x} + \\ \dfrac{q}{3\times\Delta x}\left[\begin{array}{l} \left[(qu_{i,j-2}^{k} \times ((V_{i,j-2}^{k} + V_{i,j-1}^{k} + V_{i-1,j-2}^{k} + V_{i-1,j-1}^{k})/4) \right] - \\ \left[3\times(qu_{i,j-1}^{k} \times ((V_{i,j-1}^{k} + V_{i,j}^{k} + V_{i-1,j-1}^{k} + V_{i-1,j}^{k})/4) \right] + \\ \left[3\times(qu_{i,j}^{k} \times ((V_{i,j}^{k} + V_{i,j+1}^{k} + V_{i-1,j}^{k} + V_{i-1,j+1}^{k})/4) \right] - \\ \left[(qu_{i,j+1}^{k} \times ((V_{i,j+1}^{k} + V_{i,j+2}^{k} + V_{i-1,j+1}^{k} + V_{i-1,j+2}^{k})/4) \right] \end{array} \right] \end{array} \right\} + \\ \left\{ g\times(h_{i,j}^{k} - h_{i-1,j}^{k}) \times \left(\dfrac{\eta_{i,j}^{k} - \eta_{i-1,j}^{k}}{\Delta x} \right) \right\} - \left\{ f_c \times \left(\dfrac{(qv_{i,j}^{k} + qv_{i-1,j}^{k} + qv_{i,j+1}^{k} + qv_{i-1,j+1}^{k})}{4} \right) \right\} + \\ \left\{ \begin{array}{l} g\times\left(\dfrac{n_{i,j} + n_{i-1,j}}{2} \right)^2 \times \\ \dfrac{U_{i,j}^{k} \times \sqrt{(U_{i,j}^{k})^2 + \left(\dfrac{(V_{i,j}^{k} + V_{i-1,j}^{k} + V_{i,j+1}^{k} + V_{i-1,j+1}^{k})}{4} \right)^2}}{((h_{i,j}^{k} + h_{i-1,j}^{k} + h_{i,j}^{k-1} + h_{i-1,j}^{k-1})/4)^{1/3}} \end{array} \right\} - \\ \left\{ \dfrac{\rho_a \times C_w \times W_{xi,j}^{k+1} \times \sqrt{(W_{xi,j}^{k+1})^2 + (W_{yi,j}^{k+1})^2}}{\rho} \right\} - \\ \left\{ \begin{array}{l} \left(\dfrac{\kappa\sqrt{g}\left(\dfrac{n_{i,j} - n_{i-1,j}}{2} \right)\sqrt{(qu_{i,j}^{k})^2 + \left(\dfrac{qv_{i,j}^{k} + qv_{i,j+1}^{k} + qv_{i-1,j}^{k} + qv_{i-1,j+1}^{k}}{4} \right)}}{6\left(\dfrac{h_{i,j}^{k} + h_{i-1,j}^{k} + h_{i,j}^{k-1} + h_{i-1,j}^{k-1}}{4} \right)^{\frac{1}{6}}} \right) \times \\ \left[\begin{array}{l} 2\left(\dfrac{qu_{i+1,j}^{k} - 2qu_{i,j}^{k} + qu_{i-1,j}^{k}}{\Delta x^2} \right) + \left(\dfrac{qu_{i,j+1}^{k} - 2qu_{i,j}^{k} + qu_{i,j-1}^{k}}{\Delta y^2} \right) + \\ \dfrac{\left(\dfrac{qv_{i,j+1}^{k} - qv_{i,j}^{k}}{\Delta y} \right) - \left(\dfrac{qv_{i-1,j+1}^{k} - qv_{i-1,j}^{k}}{\Delta y} \right)}{\Delta x} \end{array} \right] \end{array} \right\} \end{array} \right] \qquad (4.2.15)$$

Examining the discretised equations, it is apparent that it is only necessary to store information from three time-steps, the 'future' step being derived ($t = t^{k+1}$), and the two previous 'known' steps ($t = t^{k}$, and $t = t^{k-1}$). As a simulation of 2 – 3 tides often requires in the region of 20,000 time-steps, storage of the complete output from a simulation is excessive, not viable from a hardware view-point and unnecessary. By pre-selecting the desired output interval (for instance every half hour of simulated time), it is possible to operate the model by storing information only from the three current time-steps, and outputting the desired data as the simulation reaches the appropriate time-step. As each calculation loop is completed, the 'future' values have all been derived, and the known values from the lowest time level become defunct. The storage arrays are therefore manipulated so that the defunct data is discarded, the information from the two remaining time levels is each moved back a time-step (and storage level), which leaves a blank storage level which can then used to store the future time-step variables during the next calculation loop. This over-writing procedure is maintained throughout the simulation in order to avoid problems of data storage.

4.3 User Selected Modelling Conditions

The discretised governing equations represented in section 4.2 cannot be implemented without providing appropriate initial, input and boundary conditions, as well as specifying the details of the grid domain, bathymetry and topography. One of the key features of the TFD model is the flexibility in selection and specification of boundary conditions that it allows. A significant amount of the code contained in the program is involved in either prescribing the available input and boundary conditions or fitting the solution algorithms to the selected conditions. In particular, great care has been taken to ensure that the solution is symmetrical when a symmetrical domain and boundary conditions are prescribed. The great care given to the centring of the equations and specific fixes at boundaries for the different combinations of boundary conditions and possible alignments has been vindicated by the accuracy of the solutions obtained. The level of detailed work done in this area ensures that for a properly specified symmetrical problem, the output obtained is symmetrical to 16 decimal places (the level of accuracy available using the DOUBLE PRECISION

FORTRAN 77 compiler), no matter how complicated the domain selected. In the following discussion, where necessary, boundaries are referred to using compass point references, such that the 'top' of the domain (or view screen) is known as the northern boundary, and so on.

4.3.1 Initial conditions and grid selection

The TFD model has been specifically written to simulate estuaries and coastal areas where the tide is the dominant driving force. As this implies that a varying input condition will be applied, specification of a realistic initial condition across the entire domain for a particular simulation is not feasible. In order to get around this problem, simulations are generally set up using a uniform initial condition, where elevations throughout the domain are specified as being equal to the mean water level, and the velocities in the domain are set to zero. This is equivalent to specifying that slack tide is occurring without considering any non-linear effects. In order to ensure that the final simulation is not adversely affected by this simplification, simulations are normally allowed to 'spin-up' for a minimum of one tidal cycle before making use of the output produced. This allows for any non-linear effects brought about by the interaction of the equations and the domain to become properly established.

Selection of the grid size and cell size is theoretically unrestricted. However, the Courant-Friedrichs-Lewey condition applied to tidal situations ensures that other factors must be considered when selecting the relevant sizes. Recalling the CFL condition, equation (4.1.1),

$$C_{CFL} = \frac{\text{celerity of propagation in the analytical solution}}{\text{celerity of propagation in the numerical solution}} \leq 1.$$

Applied to a tidal situation, the celerity of propagation in the analytical solution is the celerity of the tidal wave,

$$c_a = \sqrt{gh}, \tag{4.3.1}$$

and in the numerical solution, the celerity of propagation is determined by the ratio of the cell size to the time-step,

$$c_n = \frac{\Delta x}{\Delta t}. \tag{4.3.2}$$

Combining equations (4.3.1) and (4.3.2) with the CFL condition, the Courant condition is arrived at,

$$\frac{\Delta x}{\Delta t} > \sqrt{gh}\,. \qquad (4.3.3)$$

A physical interpretation of this statement is that the celerity of propagation of the solution in the numerical simulation must be greater than or equal to the celerity of propagation of the real case. In practice, the Courant condition forces the user to trade off selection of time-step, cell size and grid extent in order to provide a balance between computational expense and the level of detail produced by the simulation. The experienced user becomes adept at selecting appropriate values suitable for the particular application in hand.

Extensive use of the TFD model has shown that an even more stringent Courant condition is necessary in order to avoid stability problems. If a Courant number of around 0.5 or higher is imposed, instabilities occur at boundaries, which quickly swamp the entire domain. This is because certain combinations of boundary conditions (particularly radiating boundaries) require a forward or backward difference calculation, which spans across two cells. This explains why the more restrictive Courant condition of $C_r \leq 0.5$ provides stable solutions, as the effect of the boundary calculation is to propagate across $2\times\Delta x$ rather than Δx in time Δt (see equation 4.3.3). The TFD program code checks that the Courant condition is being satisfied before the calculation procedure is initiated by predicting the maximum Courant number using the deepest cell in the domain (i.e. predicting the greatest wave celerity $(gh)^{1/2}$). If the Courant condition is not satisfied, the calculation automatically stops, outputs the relevant variables to screen, and alerts the user of the maximum acceptable time-step in order to satisfy the Courant condition using the current domain. If the Courant condition is satisfied, the model outputs the predicted maximum Courant number and proceeds with the simulation.

4.3.2 Boundary conditions

Model boundaries can either be described as being 'open' or 'closed'. An *open* boundary is used to allow the flow parameters to propagate into or out of the model domain. Driving and radiating boundaries are the possible open boundary

conditions. A *closed* boundary is used to define and describe the interface between wet or inter-tidal cells, and dry cells (or more simplistically, between the ocean and the land). Each of the four external boundaries in the modelling domain must be prescribed as one particular boundary type for each application. Internal boundaries use the closed boundary condition in the same manner as for external boundaries.

4.3.2.1 *Driving boundaries*

Driving boundaries allow the user to specify a driving or input condition at the edge of the domain. It is possible to specify one, more or all of the available boundaries as driving boundaries, but the TFD model is normally applied using one driving boundary in conjunction with other boundary types. The model is configured to enable the user to select either an elevation or velocity driving condition. Furthermore, the relevant data can be read in from a separate file if a time series is available, or an idealised (sinusoidal) M2 tidal condition can be simulated by stipulating the amplitude, phase and period of the tide. If a velocity input condition is specified, the model automatically converts this into a discharge per unit width representation in order to allow the calculation to proceed. The model is also able to apply an appropriate Coriolis slope to the input data in relation to the hemisphere and latitude data provided in the parameter file. Experience has shown that using an elevation driving condition is normally preferable, as the solution obtained close to the boundary is able to interact with the local bathymetry and topography. Using a velocity driving condition does not provide the same flexibility, as a uniform inflow/outflow is maintained across the width of the boundary independent of local factors. Use of a steady input condition simulation is modelled by ramping-up from the conditions at slack tide to the desired input or velocity condition (as for the first quarter of a tidal simulation), which is then held constant. This provides a better solution than initialising the whole domain as being equal to the input condition, as any significant expansion or contraction of the domain cross-section would invalidate the solution. The ramping-up of the input condition is necessary in order to avoid introducing spurious waves into the solution both at the front of the input wave, and from reflection at other boundaries.

4.3.2.2 *Radiating boundaries*

The difficulty in hydrodynamic modelling at coastal scales is that the majority of situations of interest are not self-contained. This presents problems for any modelling analysis whether it be physical or numerically based, as conditions both inside and outside the domain of interest are unknown. This presents a problem in determining effective boundary conditions in situations where no true physical boundary condition exists (Raymond & Kuo, 1984). Orlanski (1976) has indicated that what is required in situations where advection or wave motions are the dominant physical mechanisms is an open boundary condition. In the case of a radiating boundary, the fundamental property of the radiating mechanism is that any disturbance should be allowed to propagate out of the domain with the minimum of reflection of the radiating property. Orlanski (1976), Raymond & Kuo (1984) and Blumberg & Kantha (1985) advocate the use of the Sommerfeld radiation condition in such cases:

$$\frac{\partial \phi}{\partial t} + C_v \frac{\partial \phi}{\partial x} = 0, \qquad (4.3.4)$$

where ϕ is the propagating variable, and C_V the phase velocity.

In the TFD numerical model, the discharge per unit width is the desired propagating variable, and the phase velocity refers to the propagation of the surface tidal wave. Therefore the local wave celerity ($c = \sqrt{gh}$), is the appropriate variable such that the radiation condition (equation (4.3.4)) appropriate for the modelled situation is,

$$\frac{\partial qu}{\partial t} + \sqrt{gh}\frac{\partial qu}{\partial x} = 0. \qquad (4.3.5)$$

The discretised form of equation (4.3.5) applied is,

$$qu_{i,j}^{k+1} = qu_{i\pm1,j}^{k} - \frac{\Delta x}{\sqrt{g \times h_{i\pm1,j}^{k}}}\left(\frac{qu_{i\pm1,j}^{k} - qu_{i\pm1,j}^{k-1}}{\Delta t}\right). \qquad (4.3.6)$$

The time centring used for the radiation condition is not exact. This is necessary in order to maintain exact agreement regarding symmetry between solutions using multiple radiating boundaries. Otherwise it is impossible to use variables from a standardised time-step due to the sequence of the program calculation (the sweeping process across the domain) in cases where opposite boundaries are both radiating.

The time-scale discrepancy of one time-step that this necessitates compared with the tidal period once more ensures that the effect on the solution is minimal.

Application of a radiating boundary condition is of particular benefit when analysing idealised cases or in real cases where there is a lack of field data, as the flow is allowed to develop in the domain without the boundary condition artificially constraining the solution. Use of a radiating condition is however limited to situations where a generalised running wave is the appropriate tidal regime, as the only means of offsetting the phase in the solution is through bathymetric or internal boundary interaction with the flow. In a situation where features such as a standing wave or quarter-diurnal effects are apparent, if the topographic feature that creates the phenomenon is not contained within the domain, it is necessary to explicitly derive and input both a velocity and elevation boundary condition in order to ensure that the correct phase is achieved. Radiating boundaries should also generally be applied with care as formally the solution is under-specified.

4.3.2.3 *Closed boundaries*

A closed boundary condition can be applied at any desired combination of external and internal boundaries. A closed boundary is normally applied to describe the boundary between a dry, land cell, and either an inter-tidal, or fully wet cell (i.e. a no flow boundary). The major feature of a closed boundary cell is that it remains dry at all times, and that all the velocity components in the cell and inland of the cell are always set equal to zero. Examining figure 4.3 which described the layout of the staggered grid, the previous statement ensures that the shared velocity (discharge) component between the dry, land cell and adjacent wet cell is equal to zero. In the literature, this condition is described as the velocity component normal to the boundary being set to zero. Closed boundaries all share the previously described properties, however, there are a variety of other properties that can be simulated, most importantly the amount of slip occurring at the boundary. The most commonly applied closed boundary conditions are the no-slip and free-slip conditions. The no-slip condition assumes that the tangential velocity immediately at the boundary must be equal to zero, which is theoretically correct according to boundary layer theory. Application of a free-slip condition assumes that there is no boundary layer, and that

the tangential velocity is not retarded by the presence of the closed boundary. The effect on the development of a simulation of selecting either a no-slip or free-slip boundary condition is discussed further in chapter 6. In the TFD model, the user is able to select either a no-slip or free-slip closed boundary condition. It is also possible to apply the two conditions in combination, but this requires alteration of the program code on a case by case basis, and will not be discussed here. Selection of either closed boundary condition is simply achieved via the model parameter file.

4.4 TFD Model Procedure

The flowchart overleaf (figure 4.4) describes the procedure followed by the main TFD model program. Where input is required, the relevant data is provided by the user via a parameter file. The parameter file allows the user to specify information such as the bathymetry file to be read in from, description of the input conditions, description of the boundary conditions, define model parameters such as the hemisphere, latitude and wind conditions, select output conditions, and more. A sample parameter file is included in Appendix B. The only topics that remain to be discussed are how to deal with inter-tidal regions, the available output formats, and compatibility of the TFD model with other programs.

Modelling inter-tidal regions requires a special procedure, usually referred to as the flooding and drying algorithm. Flooding and drying procedures are reasonably well documented in the literature (Falconer & Owens, 1987; Cheng, Casulli & Gartner, 1993). The features incorporated in the TFD model are as recommended in the literature. The most important point to raise is that although an inter-tidal cell may be considered to be dry at a particular time, serious problems have been documented in the literature if the water level in the cell is actually allowed to reduce to zero. Therefore an arbitrary limit can be set via the parameter file (normally 0.25m), below which, the cell is considered to be dry. In the nominally dry cell, the staggered velocity (and discharge) values are set to zero, although the arbitrary depth is maintained. A dry cell becomes flooded and is returned to the normal calculation procedure when the depth in an adjacent wet cell exceeds the arbitrary depth limit plus 25%. The depth in the previously dry cell is then set equal to the adjacent wet cell depth. The extra 25% is included in the calculation to ensure that the cell does

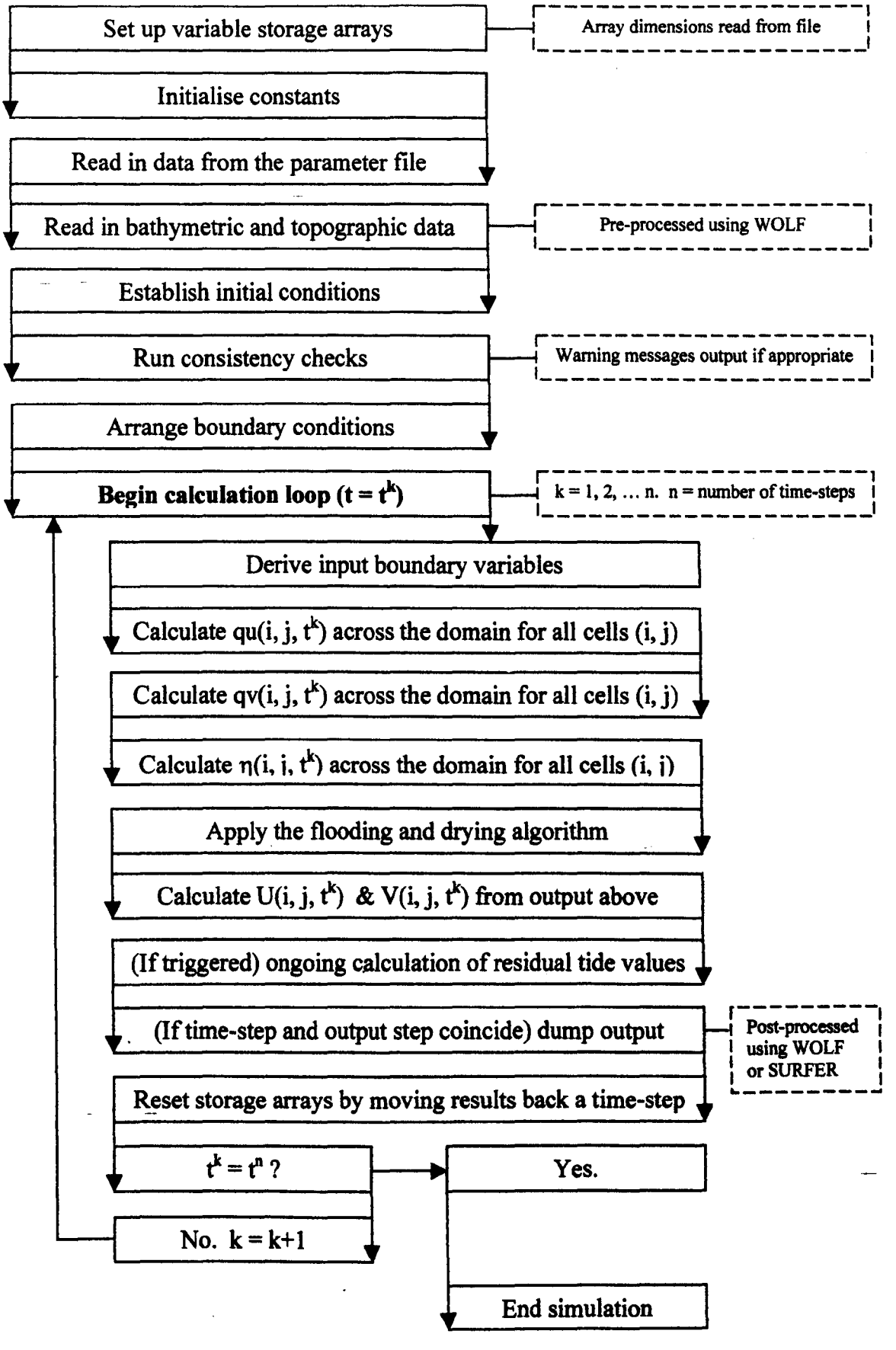

Figure 4.4 – TFD model procedure flowchart.

not go through a cycle of wetting and drying due to spurious instabilities propagating across the domain when in fact it should remain dry. A further advantage of applying this method is that it ensures that there is never a cell with a depth small enough that supercritical flow occurs, avoiding the attendant instability problems that this could generate.

The output from the model is post-processed using a Windows based graphical front-end originally developed within the civil engineering department at the University of Strathclyde for use with the WOLF numerical model. This program enables the numerical output files from the model to be displayed graphically, interrogated on-screen via the mouse, and provides an animation facility for analysis of time-series data. The data output from WOLF can also be easily adapted to create .avi streaming animations for presentation purposes. The output format necessary to interact with the WOLF numerical model is also consistent with that of Golden Software's SURFER surface mapping program which provides an alternative presentation format. The WOLF interface is also used to pre-process the relevant bathymetric and topographic data to provide a uniform grid that can be stored and interfaces with the TFD model

The output obtained from the model provides hydrodynamic data of value and interest to investigators studying other tidal phenomena. Within the University, the model is being operated by other researchers who have tailored their own models to accept output from the TFD program (Copeland et al. 1999; Neill et al. 2000(a), 2000(b)). These independent programs therefore add additional applications which interface with the TFD model, that although not applied in this work, are of general benefit. They offer features such as modelling of pollutant dispersion and derivation of velocity data across vertical cross-sections. Finally, during the research, a simple post-processing particle-tracking program has been produced to provide a further means of analysing the hydrodynamic data produced by the TFD model. The particle-tracking program uses a direct tracking procedure, with no allowance for turbulent transportation, as the intention is not to model dispersion, but visualise tracks and streamlines from the TFD model hydrodynamic output.

4.5 Summary

This chapter has detailed how the governing shallow water equations previously derived in chapter 3 have been mathematically modelled using the TFD program. More than just providing a discretised form of the equations, the TFD model code provides an interface to allow the user to apply different boundary condition combinations, and deliver the desired output for post-processing. The flexibility of the model allows the user to not only produce a realistic and accurate simulation of a particular case, but analyse the reasons behind why the flow developed in a particular manner by altering different parameters, boundary conditions, or by disabling and activating the individual terms in the equations. Therein lies the reasoning behind the need to have developed the model as part of the research work. The use of a commercially available hydrodynamic program would not have been viable due to the lack of flexibility of such products. A particular problem would have been the inability to access the numerical code to determine how the program was operating, alter the code for special applications or adjust the output format. In the next chapter, the TFD numerical model code is subjected to a thorough validation and verification exercise to ensure its robustness and provide examples of the features referred to and outlined in this chapter.

5. NUMERICAL MODEL TESTING

A full theoretical description of a numerical model applicable to simulating tidal flows in the coastal zone has been provided in the preceding chapters. Before the model can be applied as a research tool, it is necessary to determine the robustness and accuracy of the model through a rigorous testing procedure. Fischer and Rhodes (1994) advocate the following three-step approach to model testing. *Verification*, a procedure to ensure that the program solves the modelled equations correctly. This is the responsibility of the code developer. *Validation*, a procedure to validate numerical models to complex flows, i.e., testing of the models predictive capabilities against detailed test data. Validation is the responsibility of the code developer and end user jointly. Finally, *calibration* is a procedure to calibrate code from a particular model in its ability to predict global quantities for realistic geometries of design interest. Calibration is a project specific exercise, and is therefore the responsibility of the end user. In this case, as the code developer and end user are one and the same, all three steps must be carried out. No universally accepted standard test-cases are provided in the literature for model testing, and therefore, each developer is required to create or provide their own test-cases (Cheng *et al.*, 1993). Following the framework outlined by Fischer and Rhodes, and in a similar manner to Monteiro (1995) and Bayne (1996), the model testing follows.

5.1 Verification of the TFD Numerical Model (Equations)

Developing a complete test to check the exact solution produced by the equations is not possible. It is possible however to develop simple tests involving the individual terms in the model equations. Model results can then be compared with analytical solutions of the simplified governing equations. This is possible because, having access to the model code enables the user to toggle the individual terms of the discretised governing equations on or off, effectively disabling terms in the equations when they are not required. If this facility were not available, the complexity of including all the governing equation terms in both the modelled and analytical solution would defeat any attempt to focus on the influence of an individual term in the model. Table 5.1 summarises the test-cases that will be used to verify that the code solves the equations correctly in the model. It should be noted that there is no

individual test for the local acceleration term, or continuity equation. These terms are therefore verified via their use throughout the test procedure. Each test will be described in more detail as the results are presented.

Test	Term	Name	Effect illustrated
1-8	$\frac{\partial qu}{\partial t}$	Local acceleration	Unsteady tidal effect
1-8	$\frac{\partial \eta}{\partial t}+\frac{\partial qu}{\partial x}+\frac{\partial qv}{\partial y}$	Continuity equation	Maintenance of continuity / mass
1,7,8	$g(d+\eta)\frac{\partial \eta}{\partial x}$	Pressure term	Free surface elevation, and elevation input conditions
2,7,8	$gn^2\frac{U\sqrt{U^2+V^2}}{(d+\eta)^{4/3}}$	Bottom friction term	Dissipative effect, and velocity input conditions
3	fqu	Coriolis acceleration	Propagation of the Coriolis slope across the domain.
4,7,8	$\frac{\partial quU}{\partial x}+\frac{\partial quV}{\partial y}$	Convective acceleration	Acceleration through convergent or divergent section
5,7	$C_w W_x\sqrt{W_x+W_y}$	Wind term	Wind stress
6-8	$\bar{\varepsilon}\left[\frac{2\partial^2 qu}{\partial x^2}+\frac{\partial^2 qu}{\partial y^2}+\frac{\partial^2 qv}{\partial x\partial y}\right]$	Eddy viscosity	Turbulent mixing
7	Finite-difference centring	Centring	Solution symmetry
8	Input boundary conditions	Directionality	Repeatability of result

Table 5.1 - Summary of the test-cases used to verify the TFD numerical model.

Throughout the verification tests, the model parameters and domain were selected to coincide with conditions appropriate for the coastal zone. The model domain was represented by a grid of 50 x 25 cells, with the following model parameters selected unless otherwise indicated in the text:

- Sinusoidal input wave: period = 12.4 hours = 44640 seconds
- water depth = 20 m
- gravitational constant = 9.81 ms^{-2}
- wavelength = 44640 x $\sqrt{gh}$ = 625278.78 m
- Manning number, n = 0.025 $sm^{-1/3}$
- internal boundaries = no-slip

Other model parameters will be introduced to the tests where applicable, and will be described in the text.

5.1.1 Verification Test 1 - Pressure Term

In order to obtain a unique solution, an equation must contain a minimum of two terms. Similarly, in order to obtain a solution of the finite difference representations of the Shallow Water Equations (SWE), it is necessary to have a set of related equations in order to determine the variation of the variables through time using the staggered leap-frog approach. A simplified representation of the equations that can be solved analytically omits all the terms in the momentum equation except for the local acceleration and pressure term. Examining a quasi-one-dimensional case also simplifies the operation. The simplified 1D unsteady equations of continuity and momentum respectively therefore become

$$\frac{\partial \eta}{\partial t} + \frac{\partial qu}{\partial x} = 0 \qquad (5.1)$$

$$\frac{\partial qu}{\partial t} + g(d+\eta)\frac{\partial \eta}{\partial x} = 0. \qquad (5.2)$$

The model was applied for unsteady horizontal flow conditions using a sinusoidal elevation input condition, of amplitude 0.5m. The model domain was a quasi-one-dimensional channel of extent 625 x 312.5 km, using a cell size of 12.5 km, of uniform depth 20m. The channel dimensions were selected in order to produce an output that included one complete wavelength. This enables comparison of the results in terms of the expected theoretical wave propagation through space. The elevation output obtained from the model after 1.5 tides, and from the equivalent theoretical analysis is shown in Figure 5.1. A similar comparison is also obtained by comparing elevation data obtained at a fixed point through time at the centre of the domain (Figure 5.2) with the expected sinusoidal variation. Although there is a slight discrepancy in both cases between the two curves, this can be explained by the non-linearity in the modelled situation, which is not represented in the comparative sinusoidal plots. Non-linearity is imparted in both equations (5.1) and (5.2) by the discharge per unit width term (as $qu = u(d+\eta)$), and in equation (5.2) by the pressure term. In both terms, the source of the non-linearity is the elevation term η. However, as $\eta << d$, the influence of the non-linearity on the overall solution is trivial. This simple test has confirmed that the selected input wave is propagating correctly through the domain. This indicates that the equations and boundary conditions used must therefore be operating correctly.

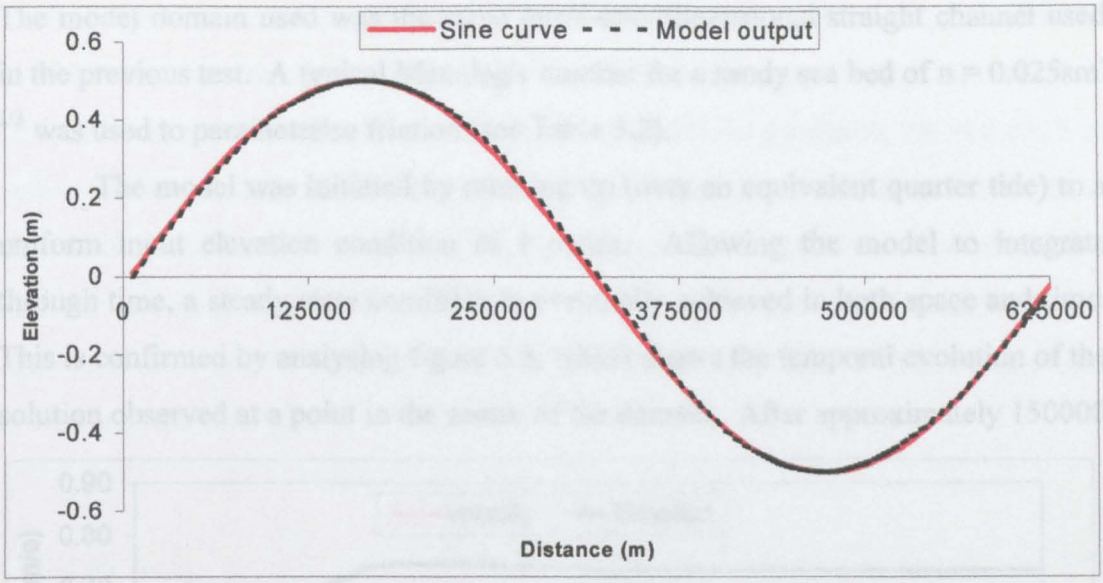

Figure 5.1 - Comparison of theoretical and model derived wave propagation through the domain after 1.5 tides.

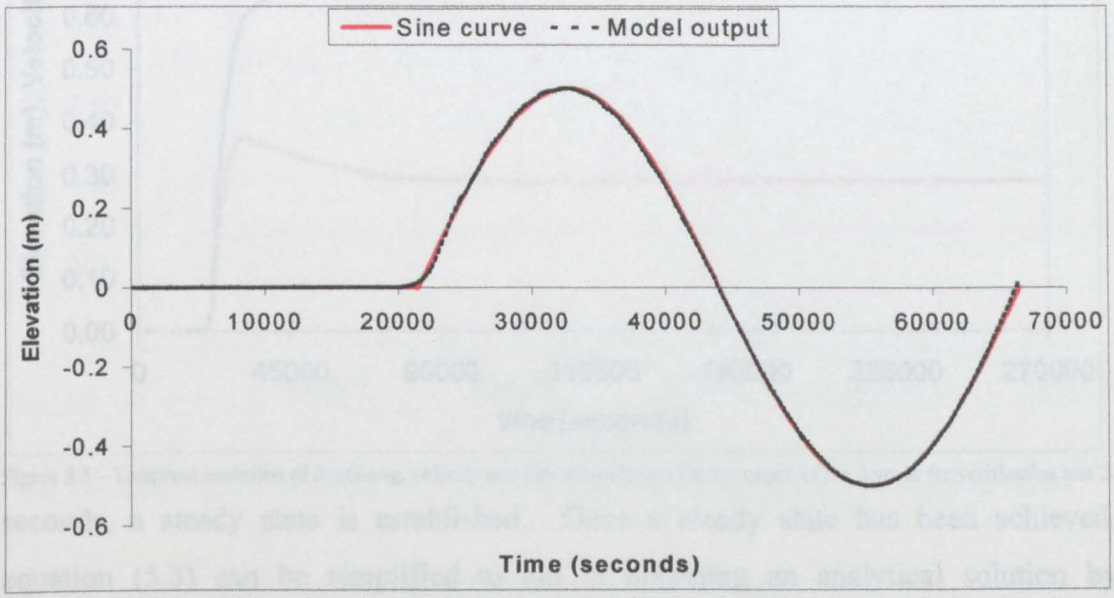

Figure 5.2 - Comparison of theoretical and model derived wave propagation through time 312.5 km from the input boundary.

5.1.2 Verification Test 2 - Bottom Friction Term

The bottom friction term is tested to confirm that the expected dissipative effect on the flow variables is being produced. The bottom friction term will be verified once the flow has achieved a steady state to enable a simple comparison with an analytical solution. The momentum equation used to verify the bottom friction effect was obtained by adding the bottom friction term to the simplified 1D unsteady x-component momentum equation (5.2), to obtain

$$\frac{\partial qu}{\partial t} + g(d+\eta)\frac{\partial \eta}{\partial x} + gn^2 \frac{U\sqrt{U^2+V^2}}{(d+\eta)^{1/3}} = 0 . \qquad (5.3)$$

The model domain used was the same quasi-one-dimensional straight channel used in the previous test. A typical Manning's number for a sandy sea bed of $n = 0.025 sm^{-1/3}$ was used to parameterise friction (see Table 3.2).

The model was initiated by ramping up (over an equivalent quarter tide) to a uniform input elevation condition of 1 metre. Allowing the model to integrate through time, a steady state condition is eventually achieved in both space and time. This is confirmed by analysing figure 5.3, which shows the temporal evolution of the solution observed at a point in the centre of the domain. After approximately 150000

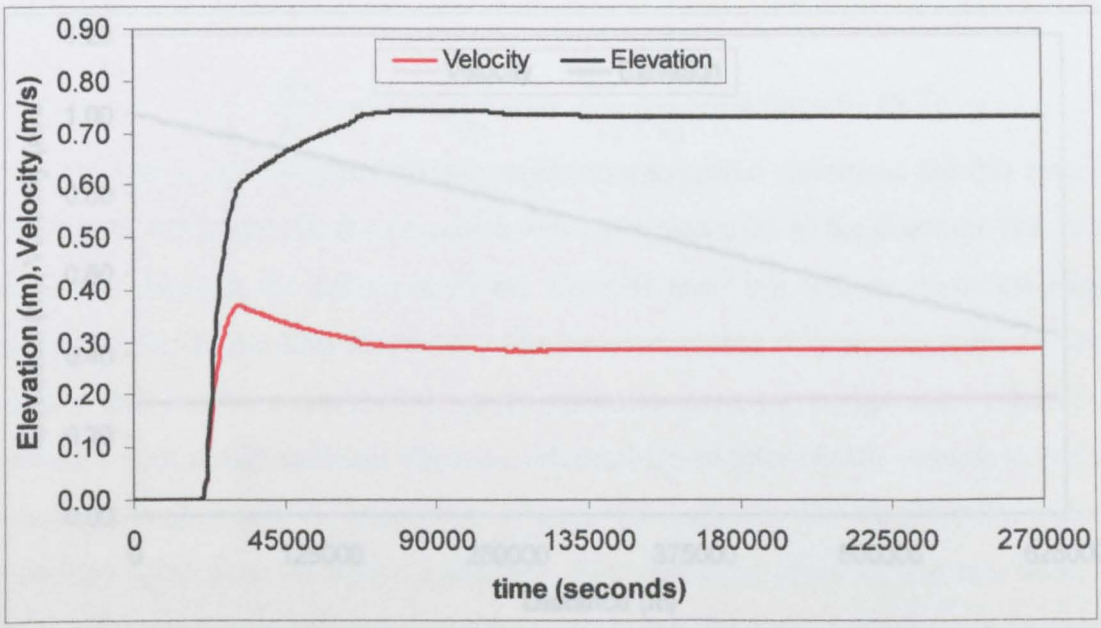

Figure 5.3 – Temporal evolution of depth-avg. velocity and elevation obtained at the centre of the domain for verification test 2.

seconds, a steady state is established. Once a steady state has been achieved, equation (5.3) can be simplified to aid in obtaining an analytical solution by removing the temporal term. Therefore,

$$g(d+\eta)\frac{\partial \eta}{\partial x} + gn^2 \frac{U\sqrt{U^2+V^2}}{(d+\eta)^{1/3}} = 0 \quad \Rightarrow \tag{5.4}$$

$$g(d+\eta)\frac{\partial \eta}{\partial x} = -gn^2 \frac{U\sqrt{U^2+V^2}}{(d+\eta)^{1/3}}, \tag{5.5}$$

which can be simplified to,

$$\frac{\partial \eta}{\partial x} = -n^2 \frac{U\sqrt{U^2+V^2}}{(d+\eta)^{4/3}}. \tag{5.6}$$

Equation (5.6) states that the pressure term will balance frictional dissipation at steady state. Figure 5.4 shows the elevation slope obtained from the numerical

model output after 270000 seconds (steady state depth-averaged velocity = 0.285 ms^{-1}). Inserting the relevant variables obtained from the program output into equation (5.6) (d = 20 m, average η = 0.733 m, Δx = 618750 m) produces, $\Delta\eta$ = 0.5515 m across the domain length. Examining the model output, the elevation at the left hand side of the domain is 1 m, and on the right hand side is 0.448 m. The model has therefore predicted that $\Delta\eta$ = (1 – 0448) = 0.552 m across the domain. The excellent agreement between the model and analytical solutions indicates that the friction term is working effectively.

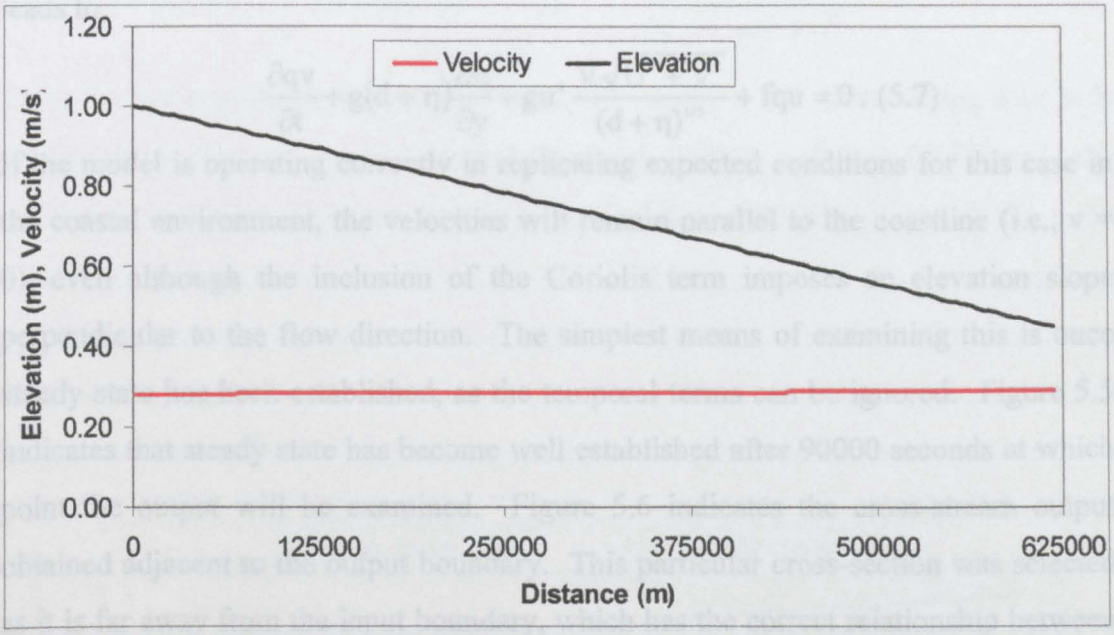

Figure 5.4 – Spatial evolution of depth-avg. velocity and elevation across the domain length obtained after 270000 seconds.

5.1.3 Verification Test 3 - Coriolis Acceleration Term

As described in chapter 3.2.3, the effect of Coriolis acceleration on a moving body acts perpendicularly to the velocity vector, the direction of action of the acceleration is always to the right, and is proportional to the size of the vector. This is as a consequence of the Earth's rotation, and is therefore a necessary consideration when examining case study situations. This indicates that the plane of interest for this particular test-case will be perpendicular to the flow direction. The model domain applied is made up of 50 × 25 square cells of extent Δx = 1 km each. The overall extent has been selected in order to ensure that the domain of interest is large enough to require the incorporation of the Coriolis acceleration term, yet small enough so that the Coriolis acceleration can be treated as a constant (Cheng et al.,

1993). The model domain represents a two-dimensional coastal area of uniform depth 20m, with a long straight coastline (closed boundary on one side) and open boundaries on the three remaining spatial boundaries. The input boundary condition will be ramped up to an elevation amplitude of 1 metre over an equivalent quarter tidal period. The coding of the TFD model is constructed to apply the relevant Coriolis slope across the input boundary. The momentum equation applied incorporates equation (5.3) from the previous test with the added inclusion of the Coriolis term. Considering in the y-direction, as the relevant plane of action, this leads to,

$$\frac{\partial qv}{\partial t} + g(d+\eta)\frac{\partial \eta}{\partial y} + gn^2 \frac{V\sqrt{U^2+V^2}}{(d+\eta)^{1/3}} + fqu = 0 \,. \quad (5.7)$$

If the model is operating correctly in replicating expected conditions for this case in the coastal environment, the velocities will remain parallel to the coastline (i.e., v = 0), even although the inclusion of the Coriolis term imposes an elevation slope perpendicular to the flow direction. The simplest means of examining this is once steady state has been established, as the temporal terms can be ignored. Figure 5.5 indicates that steady state has become well established after 90000 seconds at which point the output will be examined. Figure 5.6 indicates the cross-stream output obtained adjacent to the output boundary. This particular cross-section was selected as it is far away from the input boundary, which has the correct relationship between elevation and velocity components imposed on it by the boundary conditions applied.

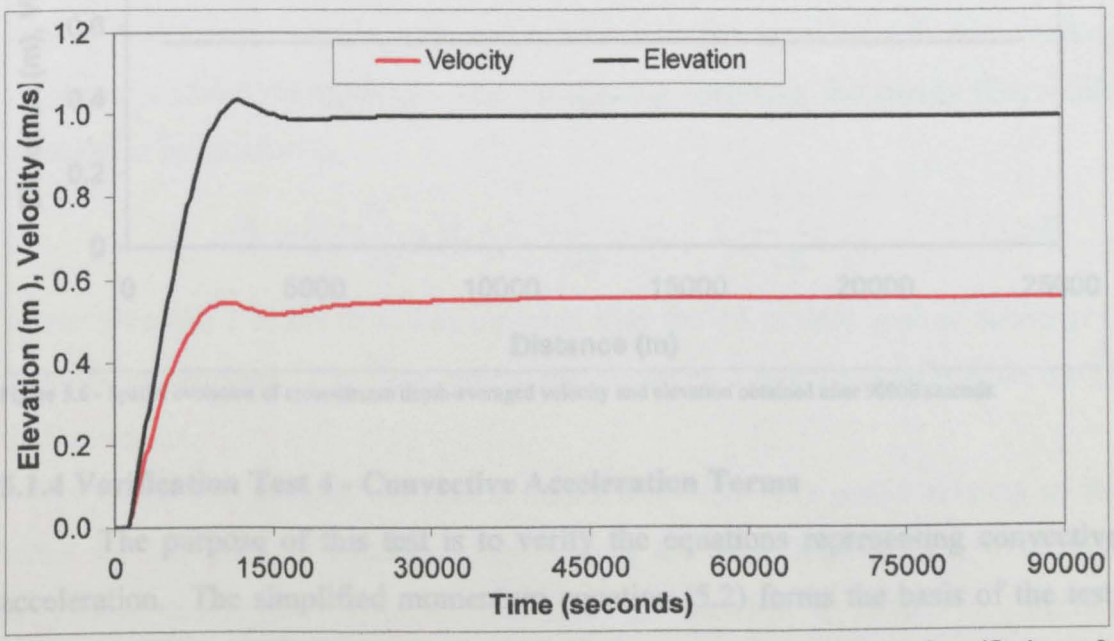

Figure 5.5 - Temporal evolution of depth-avg. velocity and elevation obtained at the centre of the domain for verification test 3.

Figure 5.6 indicates that at this point, the U and V velocity components equal 0.557 ms^{-1} and 0.000 ms^{-1} respectively across the domain width. The elevation value varies uniformly across the domain with a gradient of ((1.00135-0.843396)/23) 0.006867 m/km. Returning to equation (5.7), manipulation of the terms in this case will produce a simple analytical expression for deriving the expected elevation gradient across the domain,

$$\frac{\partial qv}{\partial t} + g(d+\eta)\frac{\partial \eta}{\partial y} + gn^2 \frac{V\sqrt{U^2+V^2}}{(d+\eta)^{1/3}} + fqu = 0$$

$$0 + g(d+\eta)\frac{\partial \eta}{\partial y} + 0 + fqu = 0 \quad \Rightarrow \quad \frac{\partial \eta}{\partial y} = -\frac{fqu}{g(d+\eta)} = -\frac{fu}{g} \qquad (5.8)$$

From the test conditions, and model output, $f = -1.209 \times 10^{-4}$ (considering a latitude applicable to the area around central Scotland, 56°N), and $u = 0.557$ ms^{-1}, the predicted analytical elevation gradient of $\partial\eta/\partial y = 0.006865$ m/km is in good agreement with the model predictions. This indicates that both the input boundary conditions, and momentum equation applied are operating correctly under conditions incorporating the effect of Coriolis acceleration, as errors in either would have been propagated across the domain, and therefore been apparent in the results presented.

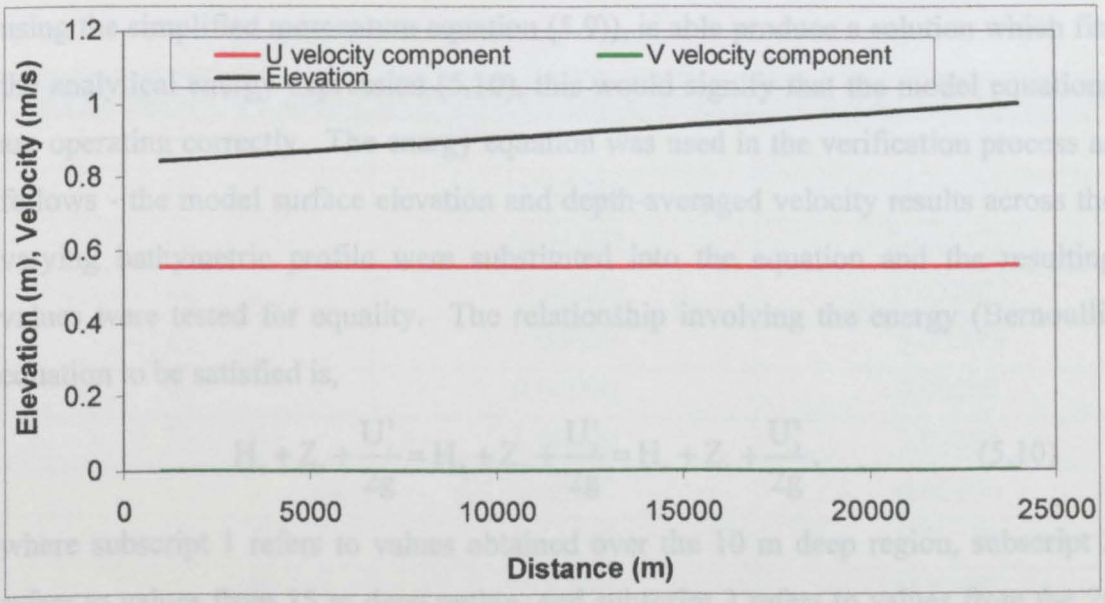

Figure 5.6 - Spatial evolution of cross-stream depth-averaged velocity and elevation obtained after 90000 seconds.

5.1.4 Verification Test 4 - Convective Acceleration Terms

The purpose of this test is to verify the equations representing convective acceleration. The simplified momentum equation (5.2) forms the basis of the test, with the addition of the convective acceleration terms

$$\frac{\partial qu}{\partial t} + g(d+\eta)\frac{\partial \eta}{\partial x} + \frac{\partial quU}{\partial x} + \frac{\partial quV}{\partial y} = 0. \qquad (5.9)$$

The model domain used for this test-case is a straight channel with three 'steps' in the bathymetry (of 10 m, 15 m and 20 m respectively), occurring at the third points in the x-direction. A steady depth-averaged flow velocity of 1.0 ms^{-1} was achieved at the input boundary by ramping up from a cold start over an equivalent quarter tidal period. A cell size of Δx = 1 km was selected throughout the domain. The model domain was selected because convective (or spatial) accelerations occur where the flow interacts with bathymetric change.

The most convenient method of examining the effect of the depth change on the solution is by evaluating the energy equation (5.10). If the simplified momentum equation (5.9) is considered in terms of a streamline, then the energy equation can be derived by integrating along the streamline (Batchelor, 1967; Duncan et al. 1970). The energy and momentum equations can therefore be directly related. The model solution to the convective term can subsequently be validated in terms of the energy equation. Theoretically, there should be no loss of energy across the depth change because friction effects are small over such a small distance. If the model (which is using the simplified momentum equation (5.9)), is able produce a solution which fits the analytical energy expression (5.10), this would signify that the model equations are operating correctly. The energy equation was used in the verification process as follows - the model surface elevation and depth-averaged velocity results across the varying bathymetric profile were substituted into the equation and the resulting values were tested for equality. The relationship involving the energy (Bernoulli) equation to be satisfied is,

$$H_1 + Z_1 + \frac{U_1^2}{2g} = H_2 + Z_2 + \frac{U_2^2}{2g} = H_3 + Z_3 + \frac{U_3^2}{2g}, \qquad (5.10)$$

where subscript 1 refers to values obtained over the 10 m deep region, subscript 2 refers to values from 15 m deep region, and subscript 3 refers to values from the 20 m deep region.

Table 5.2 presents the results output from the TFD model relating to the terms in, and sum of equation (5.10), using the fully third-order and QUICK convective momentum calculation schemes, as described in chapter 4. Similar

results were also achieved using the centred-difference representation of the convective terms. However, the centred-difference results were subject to instability in both the velocity and elevation results over each bathymetric plateau in the form of oscillating output. Although the instability is small (the oscillation being restricted to the third-decimal place), the numerically induced error that this indicates invalidates the centred-difference results. This instability was not unexpected, as numerous cases in the literature have indicated that models using centred difference methods to discretise the convective momentum terms are unstable unless artificially high values of diffusion are imposed on the solution (Hyder & Elliott, 1995; Galloway et al., 1996). As no diffusion term has been included in the simplified momentum equation applied (equation 5.9), instability is to be expected in the results produced.

The close agreement between the results obtained (see table 5.2) confirms that the convective acceleration terms must be functioning correctly in the model code. The minimal deviation between the two numerical schemes presented indicates that there is little to choose between the two. Later tests will attempt to determine a preferred scheme for general application with the TFD model based on overall accuracy and stability of the procedures.

Term	3rd-order scheme	QUICK scheme
H_1	10.77902	10.77885
H_2	15.80581	15.80576
H_3	20.81572	20.81571
Z_1	10.00000	10.00000
Z_2	5.00000	5.00000
Z_3	0.00000	0.00000
U_1	1.00000	1.00000
U_2	0.68197	0.68196
U_3	0.51783	0.51782
$\Sigma_1 = H_1 + Z_1 + \frac{U_1^2}{2g}$	**20.82998**	**20.82982**
$\Sigma_2 = H_2 + Z_2 + \frac{U_2^2}{2g}$	**20.82951**	**20.82947**
$\Sigma_3 = H_3 + Z_3 + \frac{U_3^2}{2g}$	**20.82939**	**20.82938**

Table 5.2 – Model output obtained after 90000 seconds for verification test 4, and comparison of output derived via equation (5.10).

5.1.5 Verification Test 5 - Wind Stress Term

The wind stress will be tested in a similar manner to the bottom friction term in section 5.1.2. This is because of the similarity in the derivation of the terms, both of which are being used to describe the action of a boundary stress on the water column. The simplified momentum equation (5.2) is again applied, this time with the addition of the wind stress term

$$\frac{\partial qu}{\partial t} + g(d+\eta)\frac{\partial \eta}{\partial x} - \frac{\rho_{air} C_w W \sqrt{W_x^2 + W_y^2}}{\rho_{water}} = 0. \qquad (5.11)$$

Two simple cases will be considered. The first case examined is a west - east channel of uniform depth 20m, and Δx = 1 km. The model is initiated from a cold start with an arbitrary uniform wind condition of 10 ms^{-1} acting at 90° (straight up the channel from west to east). A steady state condition is quickly arrived at with a depth-averaged velocity of 0.027 ms^{-1} maintained across the domain. Manipulation of the terms in equation (5.11) produces an analytical expression for deriving the expected wind-induced set-up at steady state, as shown,

$$\begin{aligned} & 0 + g(d+\eta)\frac{\partial \eta}{\partial x} - \frac{\rho_{air} C_w W \sqrt{W_x^2 + W_y^2}}{\rho_{water}} = 0 \\ \Rightarrow \quad & \Delta\eta = \Delta x \frac{\rho_{air} C_w W \sqrt{W_x^2 + W_y^2}}{\rho_{water} g(d+\eta)}. \end{aligned} \qquad (5.12)$$

Inserting the appropriate values for the first test-case (Δx = 49000 m, W = 10 ms^{-1}, d = 20 m, η = 0 m), and using representative values for the properties of the fluids, C_w = 0.0026, $\frac{\rho_{air}}{\rho_{water}} = 0.00125$, the analytical solution indicates $\Delta\eta$ = 0.08117 m across the domain length. Figure 5.7 indicates the elevation profile in the x-direction obtained after steady state has become established. From this output, the model results indicate a variation of $\Delta\eta$ = 0.08117 m across the domain. The model and analytical results coincide exactly. Figure 5.7 also indicates further satisfying features which agree well with the expected theoretical results. For instance, the water elevations rise linearly from –0.0406 m at the upwind west boundary to 0.0406 m at the downwind east boundary. Furthermore, mass conservation is confirmed across the domain by the equal volumes of water gain and loss regions observed.

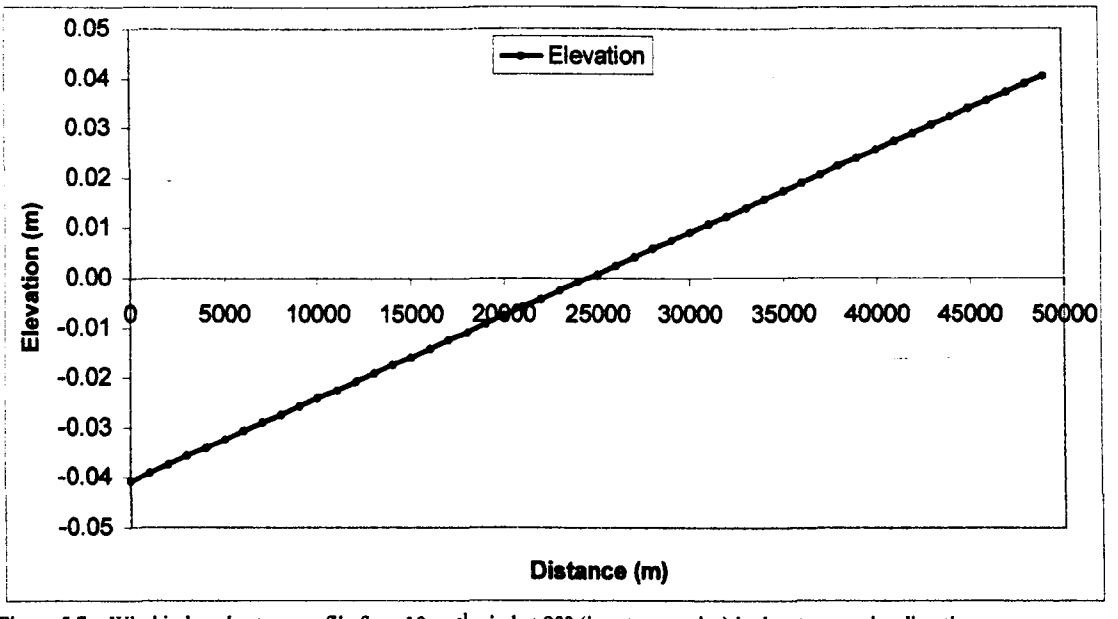

Figure 5.7 – Wind induced set-up profile for a 10 ms^{-1} wind at 90° (i.e. stream-wise) in the stream-wise direction.

The second case to be considered uses a similar domain to the first test, except the channel walls are removed to create a completely open domain. The wind condition imposed is a uniform velocity of 14.142 ms^{-1} acting at 45° (nominally from the south-west of the domain). Otherwise the test conditions are exactly as for the initial test. Using the analytical relationship (equation 5.12), an elevation gradient of $\Delta\eta = 0.002342$ m per km in the x- and y- directions is predicted. The model shows a good agreement by predicting an elevation gradient of $\Delta\eta = 0.002345$ m per km in the x- and y-directions (see figure 5.8). The slight difference between the analytical and model derived results in the second test was not apparent in the first. The added complexity in the second case of all the boundaries being open is believed to be the

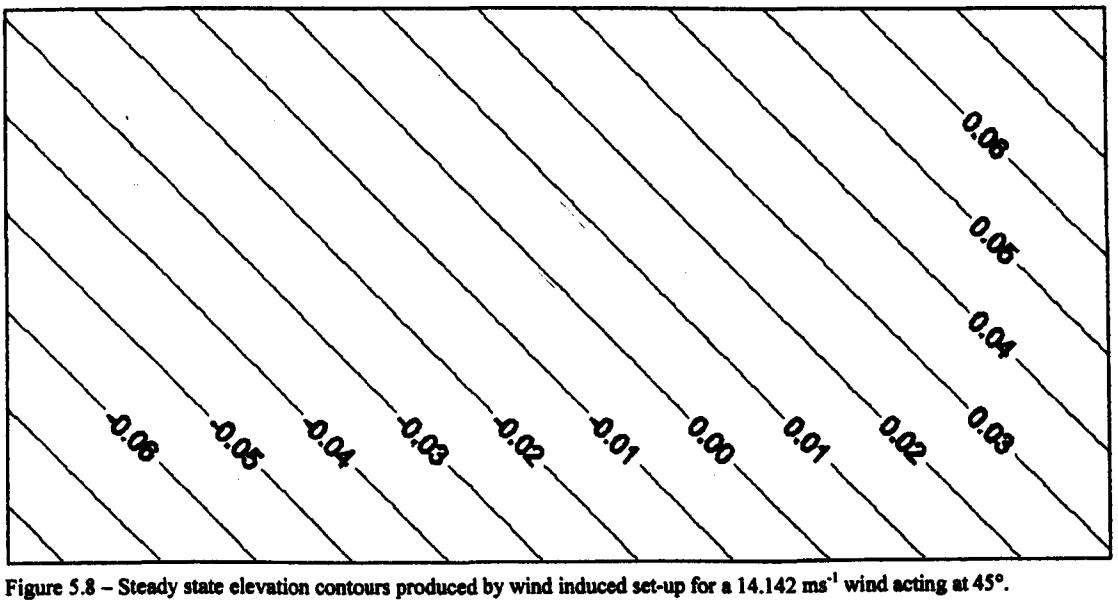

Figure 5.8 – Steady state elevation contours produced by wind induced set-up for a 14.142 ms^{-1} wind acting at 45°.

source of the slight error. Mass conservation is once more confirmed by the equal volume of water level gain versus loss. Further confirmation of the correct model operation is proved in figure 5.8, as the surface elevation contours remain parallel and at right angles to the wind direction.

5.1.6 Verification Test 6 - Eddy Viscosity Term

The only simplification to the full x- and y-directed momentum equations necessary for this test is to ignore the Coriolis acceleration and wind stress terms. This leaves the continuity equation (5.13) and momentum equations as related (x-directed momentum only presented),

$$\frac{\partial \eta}{\partial t}+\frac{\partial qu}{\partial x}+\frac{\partial qv}{\partial y}=0, \tag{5.13}$$

$$\frac{\partial qu}{\partial t}+g(d+\eta)\frac{\partial \eta}{\partial x}+\frac{\partial quU}{\partial x}+\frac{\partial quV}{\partial y}+gn^2\frac{U\sqrt{U^2+V^2}}{(d+\eta)^{1/3}}+\bar{\nu}_t\left[2\frac{\partial^2 qu}{\partial x^2}+\frac{\partial^2 qu}{\partial y^2}+\frac{\partial^2 qv}{\partial x\partial y}\right]=0. \tag{5.14}$$

The domain to be considered is of uniform depth 20 m, Δx = 2 m (a small Δx variable is necessary for this test in order to generate a measurable boundary layer, see chapter 6.4.3 for further discussion), and the input boundary is ramped up to and maintained at an elevation of 1 m. The southern boundary in the domain is closed with the other boundaries open. If a free slip boundary condition were imposed on this test, the cross-sectional depth-averaged velocity output would be uniform. However, if a no-slip condition is enforced, the effect of the eddy viscosity term is to establish a boundary layer in the direction normal to the flow.

The side-wall boundary layer established in the model instigated by the no-slip condition will be compared with an analytical relationship commonly used to describe the velocity profile near a boundary (Duncan, et al., 1970; Tennekes & Lumley, 1972; Abbott & Basco, 1989),

$$V(y)=\frac{V_*}{\kappa}\ln(y)+\text{constant}. \tag{5.15}$$

Equation (5.15) is normally referred to as the law of the wall. The integration constant is dependent upon the boundary roughness, and is often ignored (as in this case). The friction velocity,

$$V_* = \sqrt{\frac{\tau_{wall}}{\rho}} = \sqrt{gRS} \approx \frac{\sqrt{g} n_{wall} U}{(d+\eta)^{1/6}} \quad (5.16)$$

(from consideration of, and extrapolation from chapters 3.3.2.1 + 3.3.2.2). However, the law of the wall obviously fails as $y \rightarrow 0$. This is because the expression is derived from consideration of turbulent flow conditions and subsequently analysis of the Reynolds shear stresses. Equation (5.15) therefore takes no account of the laminar sub-layer immediately adjacent to the boundary. Figure 5.9 shows a comparison between the model stream-wise velocity profile in the cross-stream direction generated by the no-slip condition, and the analytically derived distribution predicted by the law of the wall formulation (equation 5.15). The two different analytical predictions made using the law of the wall formulation arise from the selection of different friction velocities. In the first case, a constant friction velocity curve was generated by selecting a friction velocity that provided the best-fit with the modelling output ($u_* = 0.05$ m/s). This is not a particularly satisfactory means of comparison for a verification exercise. Therefore the analytical expression relating the friction velocity to the local stream velocity suggested by equation (5.16) was also applied. This representation also requires some calibration, as the wall friction, n_{wall}, is an unknown value. Once more fitting the unknown variable was predicted by selecting the value that presented the best-fit to the model results ($n_{wall} = 0.05$ $sm^{-1/3}$). The model output profile is qualitatively very similar to the log profiles predicted by the

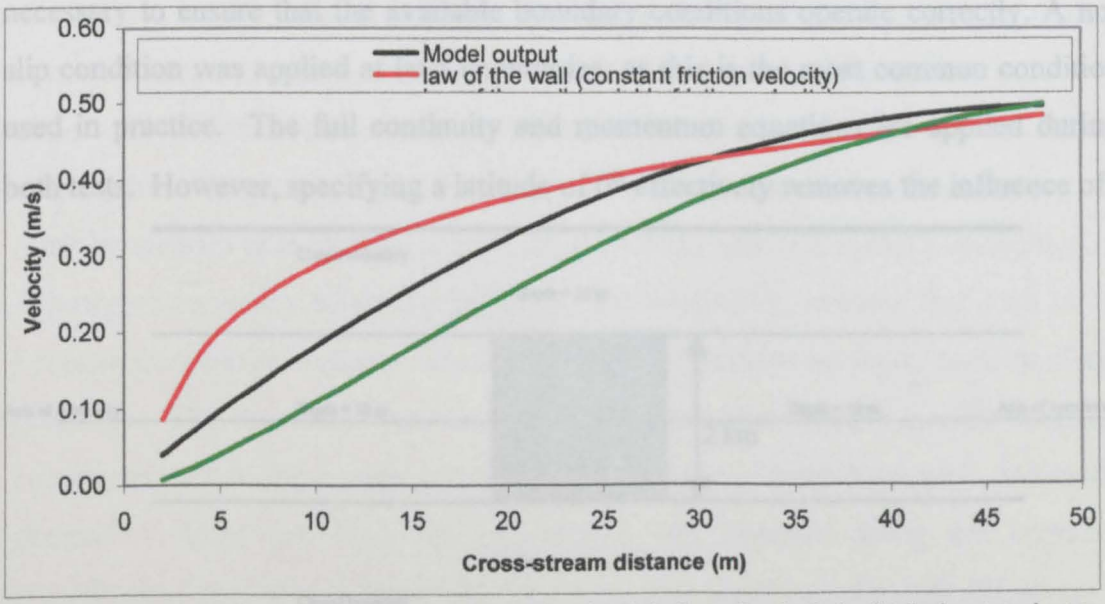

Figure 5.9 – Comparison of model generated (no-slip condition) and analytically predicted velocity distribution at steady state.

law of the wall expressions. This is taken as indicating that the combination of the no-slip boundary condition and eddy viscosity terms in the TFD model are acting in accordance with the expected theoretical boundary layer development.

5.1.7 Verification Test 7 - Finite Difference Centring

The previous six tests have verified that the individual terms in the governing equations are producing the theoretically expected solution through comparison with analytical results. However, as the tests have been predominantly quasi-one-dimensional, the important aspect of centring of the equations determined by the discretisation (chapter 4.2) has not been verified for all the terms. The simplest means of verifying the centring of the equations is to examine a fully two-dimensional problem in a complex domain, with the limitation that the domain is symmetrical about the centre of the y-axis. If the centring of the equations has been properly executed, the solution generated by the model will also be symmetrical (it is necessary to omit the Coriolis term to reach this conclusion). The input condition used for this test is a sinusoidally varying elevation input of amplitude 1.0 m propagating into the model from the west boundary. The domain used for this test is illustrated in Figure 5.10. The same test conditions were also applied in a second test, where the only difference was in applying a radiating rather than closed boundary condition along the north and south of the domain. Both tests are necessary to ensure that the available boundary conditions operate correctly. A no-slip condition was applied at land boundaries, as this is the most common condition used in practice. The full continuity and momentum equations are applied during both tests. However, specifying a latitude of 0° effectively removes the influence of

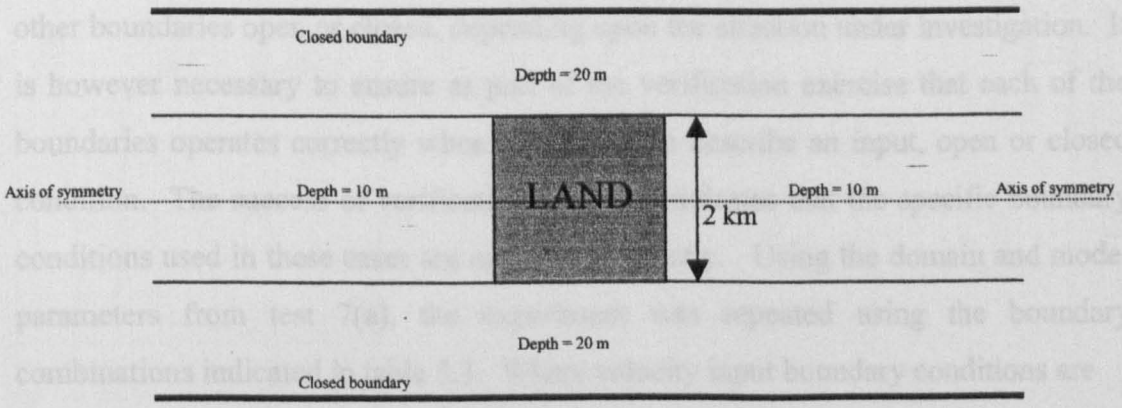

Figure 5.10 - Symmetrical domain used in verification test 7 to verify the correct centring of the model equations.

Coriolis acceleration from the simulation. Similarly, the wind stress is omitted by setting the wind velocity to 0 ms^{-1} across the domain, as the centring of this term is trivial. The simulations were run for two complete tides before examining the solution in order to allow any non-linear interaction occurring in the domain to become established. The solution obtained is found to be fully symmetric in all the available model output formats (depth-averaged velocity, elevation, vorticity and depth-averaged residual velocity). Figures 5.11 (closed lateral boundary) and 5.12 (radiating lateral boundary) present depth-averaged velocity profiles obtained from the model as the flood tide peaks for both the model domains. The cross-stream velocity component (V) is presented in the form of an absolute value to simplify the comparison of symmetry (otherwise the sign of this velocity component would change across the line of symmetry). The exact symmetry of the results confirm that the centring of the finite-differenced representation of the model equations have been both correctly derived, and then applied in the TFD model code.

5.1.8 Verification Test 8 - Boundary Condition Repeatability

An important and fundamental feature incorporated into the TFD model is the ability to select any of the four boundaries as the input boundary, as well as the option to prescribe any of the other boundaries as either 'open' (radiating), or 'closed' (land) in any combination desired (see chapter 4.3.2). In the course of this discussion, the four available boundaries will be distinguished by referring to their relative position as points of the compass, either north, south, east or west.

All the tests carried out so far during verification have made use of the western boundary as the input boundary, with the eastern boundary open, and the other boundaries open or closed, depending upon the situation under investigation. It is however necessary to ensure as part of the verification exercise that each of the boundaries operates correctly when being used to describe an input, open or closed condition. The success of verification tests 1-7 indicates that the specific boundary conditions used in these cases are operating correctly. Using the domain and model parameters from test 7(a), the experiment was repeated using the boundary combinations indicated in table 5.3. Where velocity input boundary conditions are

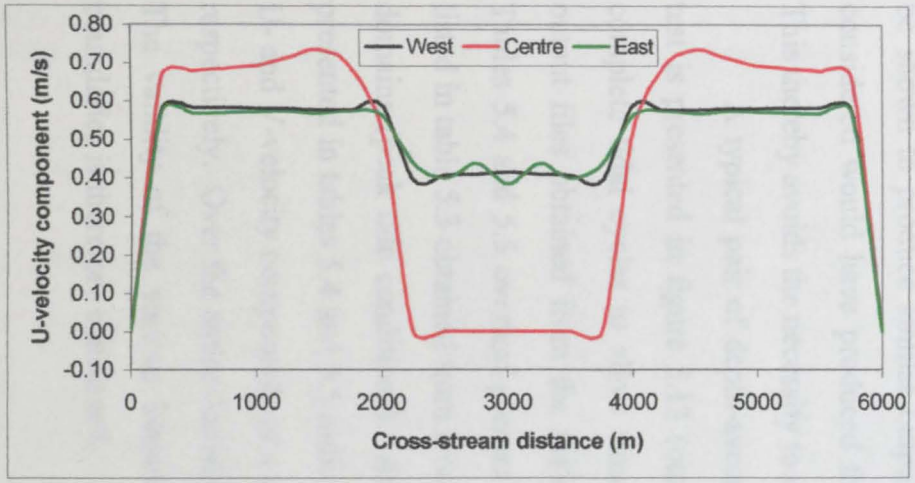

Figure 5.11(a) – U-velocity profile at three points across the domain at peak tide conditions.

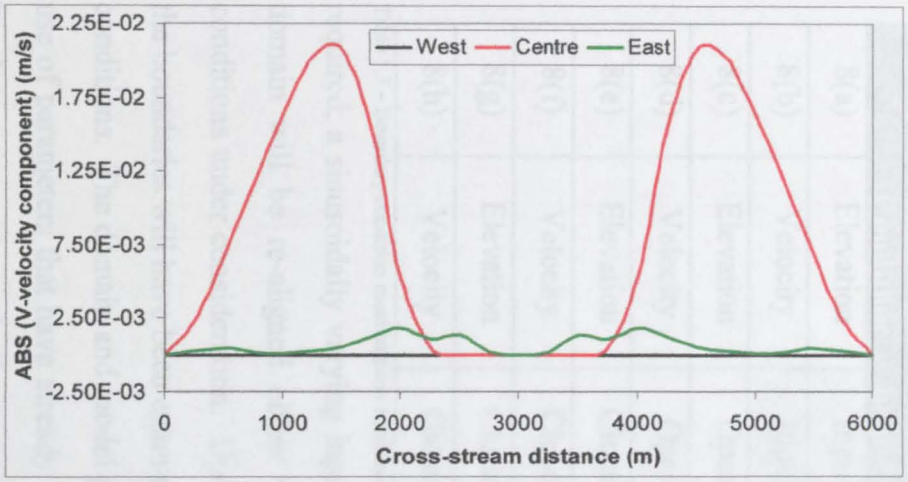

Figure 5.11(b) – V-velocity profile at three points across the domain at peak tide conditions.

Figure 5.11 - Evidence of symmetrical output from the domain (closed lateral boundary conditions).

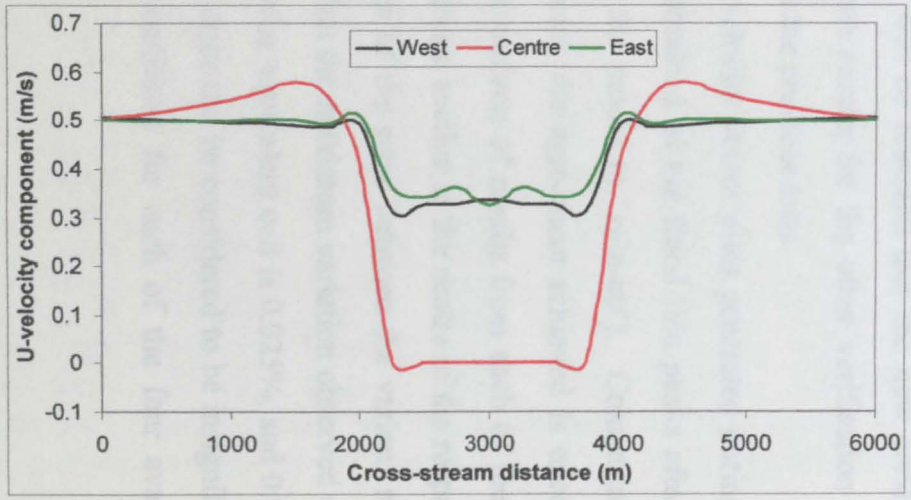

Figure 5.12(a) - U-velocity profile at three points across the domain at peak tide conditions.

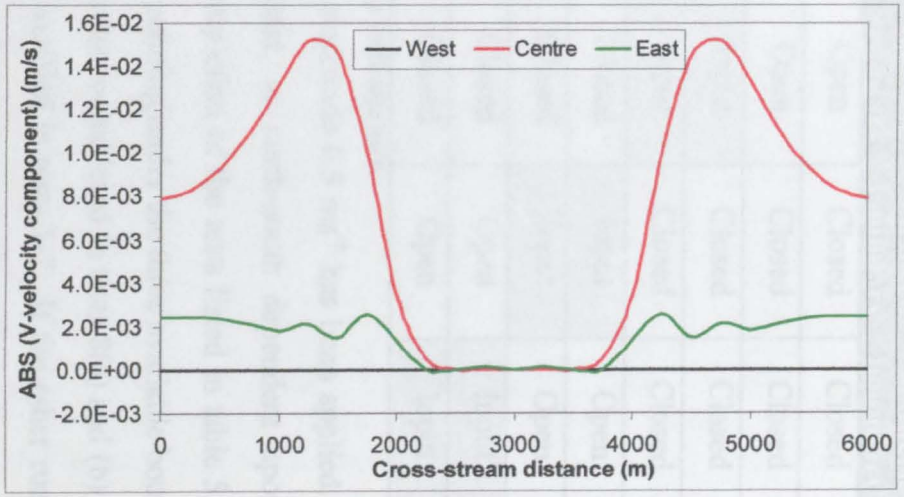

Figure 5.12(b) – V-velocity profile at three points across the domain at peak tide conditions.

Figure 5.12 - Evidence of symmetrical output from the domain (radiating lateral boundary conditions).

Test	Driving Condition	Western boundary	Eastern boundary	Northern boundary	Southern boundary
8(a)	Elevation	Input	Open	Closed	Closed
8(b)	Velocity	Input	Open	Closed	Closed
8(c)	Elevation	Open	Input	Closed	Closed
8(d)	Velocity	Open	Input	Closed	Closed
8(e)	Elevation	Closed	Closed	Input	Open
8(f)	Velocity	Closed	Closed	Input	Open
8(g)	Elevation	Closed	Closed	Open	Input
8(h)	Velocity	Closed	Closed	Open	Input

Table 5.3 – Boundary condition combinations considered during verification test 8.

required, a sinusoidally varying input of amplitude 0.5 ms^{-1} has been applied. The domain will be re-aligned either west-east, or north-south dependent upon the conditions under consideration. Upon completion of the tests listed in table 5.3, all the boundaries will have been examined operating under the three available boundary conditions. The domain and model parameters considered in tests 8(a) and (b) make use of parameters that have already been verified in tests 1-7. If the other runs can be shown to produce similar outputs, it will be assumed that the new conditions considered would have produced the same results for the other verification tests. This thereby avoids the necessity to repeat the previous tests.

A typical pair of depth-averaged velocity vector plots generated during this test is presented in figure 5.13 (output obtained as the flood tide peaks after two complete tidal cycles to allow time for the model to 'spin-up'). Comparing the output files obtained from the various tests, the agreement achieved is excellent. Tables 5.4 and 5.5 overleaf present a comparison of results from each of the tests listed in table 5.3 obtained from a cross-stream section at the centre of the respective domains (peak tide conditions). Analysis of the error between the various results presented in tables 5.4 and 5.5 indicates that the maximum variation observed of the U- and V-velocity components in a particular equivalent cell is 0.025%, and 0.934% respectively. Over the entire domain, the error can be considered to be insignificant. The validity of the various boundary conditions for each of the four available boundaries is therefore confirmed.

Validation test 8(a) - Elevation driving condition propagating west-east.				Validation test 8(c) - Elevation driving condition propagating east-west.				Validation test 8(e) - Elevation driving condition propagating north-south.				Validation test 8(g) - Elevation driving condition propagating south-north.			
x	y	u	v	x	y	u	v	x	y	u	v	x	y	u	v
6000	0	0.0000	0.0000	6000	0	0.0000	0.0000	0	6000	0.0000	0.0000	0	6000	0.0000	0.0000
6000	250	0.5182	-0.0015	6000	250	-0.5182	-0.0015	250	6000	-0.0015	-0.5182	250	6000	-0.0015	0.5182
6000	500	0.5285	-0.0046	6000	500	-0.5285	-0.0046	500	6000	-0.0046	-0.5285	500	6000	-0.0046	0.5285
6000	750	0.5318	-0.0078	6000	750	-0.5317	-0.0077	750	6000	-0.0077	-0.5317	750	6000	-0.0078	0.5318
6000	1000	0.5375	-0.0107	6000	1000	-0.5376	-0.0106	1000	6000	-0.0106	-0.5376	1000	6000	-0.0107	0.5375
6000	1250	0.5479	-0.0128	6000	1250	-0.5480	-0.0127	1250	6000	-0.0127	-0.5480	1250	6000	-0.0128	0.5479
6000	1500	0.5516	-0.0129	6000	1500	-0.5517	-0.0128	1500	6000	-0.0128	-0.5517	1500	6000	-0.0129	0.5516
6000	1750	0.5010	-0.0096	6000	1750	-0.5009	-0.0095	1750	6000	-0.0095	-0.5009	1750	6000	-0.0096	0.5010
6000	2000	0.3538	-0.0035	6000	2000	-0.3536	-0.0034	2000	6000	-0.0034	-0.3536	2000	6000	-0.0035	0.3538
6000	2250	0.0000	0.0000	6000	2250	0.0000	0.0000	2250	6000	0.0000	0.0000	2250	6000	0.0000	0.0000
6000	2500	0.0000	0.0000	6000	2500	0.0000	0.0000	2500	6000	0.0000	0.0000	2500	6000	0.0000	0.0000
6000	2750	0.0000	0.0000	6000	2750	0.0000	0.0000	2750	6000	0.0000	0.0000	2750	6000	0.0000	0.0000
6000	3000	0.0000	0.0000	6000	3000	0.0000	0.0000	3000	6000	0.0000	0.0000	3000	6000	0.0000	0.0000
6000	3250	0.0000	0.0000	6000	3250	0.0000	0.0000	3250	6000	0.0000	0.0000	3250	6000	0.0000	0.0000
6000	3500	0.0000	0.0000	6000	3500	0.0000	0.0000	3500	6000	0.0000	0.0000	3500	6000	0.0000	0.0000
6000	3750	0.0000	0.0000	6000	3750	0.0000	0.0000	3750	6000	0.0000	0.0000	3750	6000	0.0000	0.0000
6000	4000	0.3538	0.0035	6000	4000	-0.3536	0.0034	4000	6000	0.0034	-0.3536	4000	6000	0.0035	0.3538
6000	4250	0.5010	0.0096	6000	4250	-0.5009	0.0095	4250	6000	0.0095	-0.5009	4250	6000	0.0096	0.5010
6000	4500	0.5516	0.0129	6000	4500	-0.5517	0.0128	4500	6000	0.0128	-0.5517	4500	6000	0.0129	0.5516
6000	4750	0.5479	0.0128	6000	4750	-0.5480	0.0127	4750	6000	0.0127	-0.5480	4750	6000	0.0128	0.5479
6000	5000	0.5375	0.0107	6000	5000	-0.5376	0.0106	5000	6000	0.0106	-0.5376	5000	6000	0.0107	0.5375
6000	5250	0.5318	0.0078	6000	5250	-0.5317	0.0077	5250	6000	0.0077	-0.5317	5250	6000	0.0078	0.5318
6000	5500	0.5285	0.0046	6000	5500	-0.5285	0.0046	5500	6000	0.0046	-0.5285	5500	6000	0.0046	0.5285
6000	5750	0.5182	0.0015	6000	5750	-0.5182	0.0015	5750	6000	0.0015	-0.5182	5750	6000	0.0015	0.5182
6000	6000	0.0000	0.0000	6000	6000	0.0000	0.0000	6000	6000	0.0000	0.0000	6000	6000	0.0000	0.0000

Table 5.4 - Comparison of velocity components output by the TFD numerical model. Results in each case are obtained from a cross-stream section 6km downstream of the input boundary (i.e.at the centre of the domain) (**Elevation driving conditions**).

Validation test 8(b) - Velocity driving condition propagating west-east.				Validation test 8(d) - Velocity driving condition propagating east-west.				Validation test 8(f) - Velocity driving condition propagating north-south				Validation test 8(h) - Velocity driving condition propagating south-north.			
x	y	u	v	x	y	u	v	x	y	u	v	x	y	u	v
6000	0	0.0000	0.0000	6000	0	0.0000	0.0000	0	6000	0.0000	0.0000	0	6000	0.0000	0.0000
6000	250	0.4813	-0.0011	6000	250	-0.4813	-0.0011	250	6000	-0.0011	-0.4813	250	6000	-0.0011	0.4813
6000	500	0.4902	-0.0034	6000	500	-0.4902	-0.0034	500	6000	-0.0034	-0.4902	500	6000	-0.0034	0.4902
6000	750	0.4920	-0.0055	6000	750	-0.4920	-0.0054	750	6000	-0.0054	-0.4920	750	6000	-0.0055	0.4920
6000	1000	0.4970	-0.0069	6000	1000	-0.4970	-0.0068	1000	6000	-0.0068	-0.4970	1000	6000	-0.0069	0.4970
6000	1250	0.5086	-0.0072	6000	1250	-0.5087	-0.0071	1250	6000	-0.0071	-0.5087	1250	6000	-0.0072	0.5086
6000	1500	0.5159	-0.0061	6000	1500	-0.5160	-0.0060	1500	6000	-0.0060	-0.5160	1500	6000	-0.0061	0.5159
6000	1750	0.4661	-0.0037	6000	1750	-0.4661	-0.0036	1750	6000	-0.0036	-0.4661	1750	6000	-0.0037	0.4661
6000	2000	0.3063	-0.0011	6000	2000	-0.3063	-0.0011	2000	6000	-0.0011	-0.3063	2000	6000	-0.0011	0.3063
6000	2250	0.0000	0.0000	6000	2250	0.0000	0.0000	2250	6000	0.0000	0.0000	2250	6000	0.0000	0.0000
6000	2500	0.0000	0.0000	6000	2500	0.0000	0.0000	2500	6000	0.0000	0.0000	2500	6000	0.0000	0.0000
6000	2750	0.0000	0.0000	6000	2750	0.0000	0.0000	2750	6000	0.0000	0.0000	2750	6000	0.0000	0.0000
6000	3000	0.0000	0.0000	6000	3000	0.0000	0.0000	3000	6000	0.0000	0.0000	3000	6000	0.0000	0.0000
6000	3250	0.0000	0.0000	6000	3250	0.0000	0.0000	3250	6000	0.0000	0.0000	3250	6000	0.0000	0.0000
6000	3500	0.0000	0.0000	6000	3500	0.0000	0.0000	3500	6000	0.0000	0.0000	3500	6000	0.0000	0.0000
6000	3750	0.0000	0.0000	6000	3750	0.0000	0.0000	3750	6000	0.0000	0.0000	3750	6000	0.0000	0.0000
6000	4000	0.3063	0.0011	6000	4000	-0.3063	0.0011	4000	6000	0.0011	-0.3063	4000	6000	0.0011	0.3063
6000	4250	0.4661	0.0037	6000	4250	-0.4661	0.0036	4250	6000	0.0036	-0.4661	4250	6000	0.0037	0.4661
6000	4500	0.5159	0.0061	6000	4500	-0.5160	0.0060	4500	6000	0.0060	-0.5160	4500	6000	0.0061	0.5159
6000	4750	0.5086	0.0072	6000	4750	-0.5087	0.0071	4750	6000	0.0071	-0.5087	4750	6000	0.0072	0.5086
6000	5000	0.4970	0.0069	6000	5000	-0.4970	0.0068	5000	6000	0.0068	-0.4970	5000	6000	0.0069	0.4970
6000	5250	0.4920	0.0055	6000	5250	-0.4920	0.0054	5250	6000	0.0054	-0.4920	5250	6000	0.0055	0.4920
6000	5500	0.4902	0.0034	6000	5500	-0.4902	0.0034	5500	6000	0.0034	-0.4902	5500	6000	0.0034	0.4902
6000	5750	0.4813	0.0011	6000	5750	-0.4813	0.0011	5750	6000	0.0011	-0.4813	5750	6000	0.0011	0.4813
6000	6000	0.0000	0.0000	6000	6000	0.0000	0.0000	6000	6000	0.0000	0.0000	6000	6000	0.0000	0.0000

Table 5.5 - Comparison of velocity components output by the TFD numerical model. Results in each case are obtained from a cross-stream section 6 km downstream of the input boundary (i.e. at the centre of the domain) (**Velocity driving conditions**).

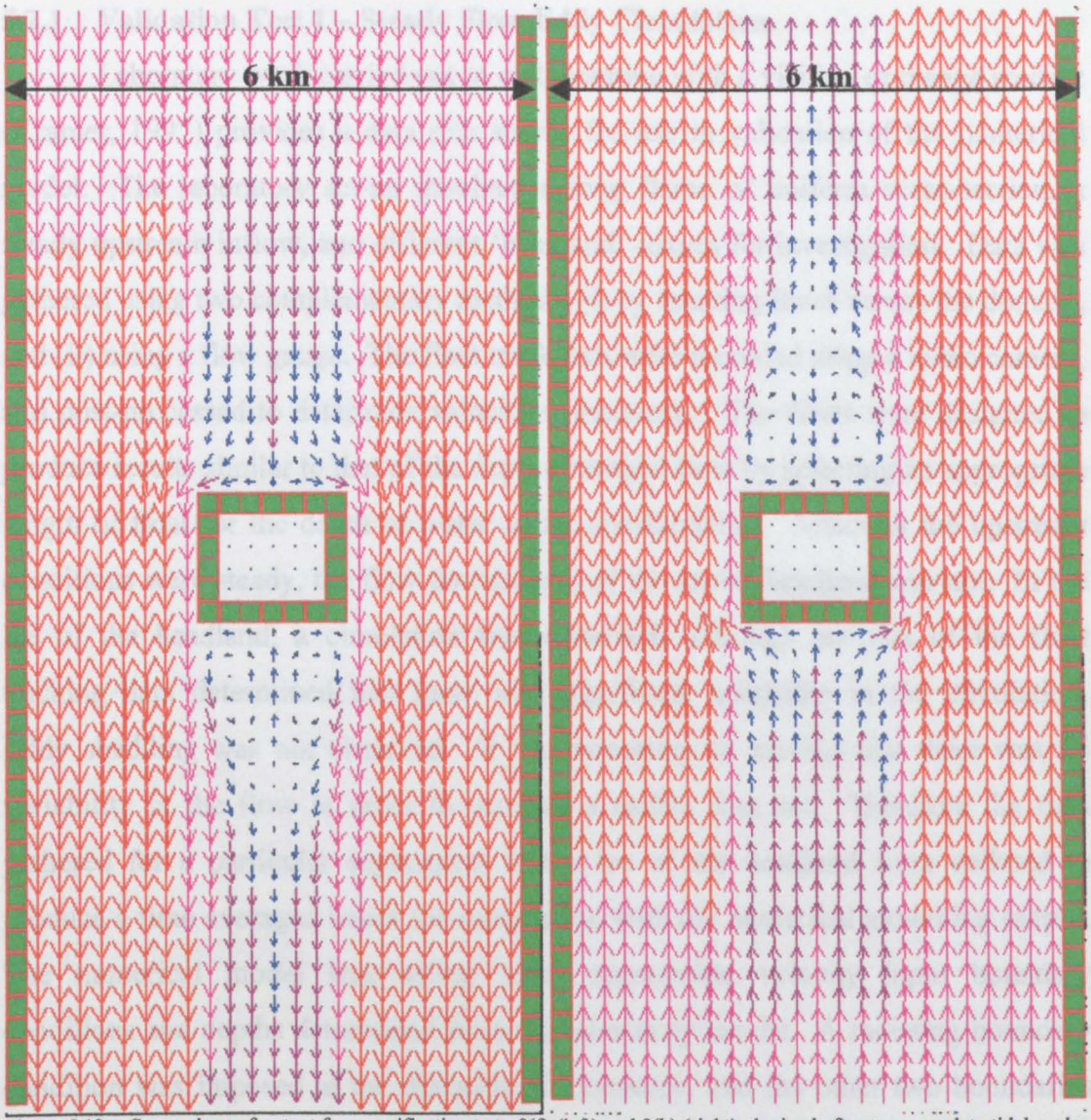

Figure 5.13 – Comparison of output from verification tests 8(f) (left) and 8(h) (right) obtained after two complete tidal cycles, just after the flood tide has peaked. Ignoring the effect of domain orientation, the results can be seen to be visually identical.

5.2 Validation of the TFD Numerical Model

The verification exercise has identified that the model equations, finite-differencing derivation and program code are all acting correctly using simple analytical test cases. However, the combined action of the equations and the model's ability to simulate realistic coastal and estuarine processes must also be validated. Although the TFD model can theoretically be applied to any hydrodynamic problem, it has been specifically developed with the aim of simulating circulation, or 'eddies' created as a consequence of flow separation. It is therefore good practice to validate the overall performance of the model using test cases that correspond with the intended final application of the model. Four validation tests will be described.

5.2.1 Validation Test 1 – Steady Flow Eddy Circulation.

Laboratory work carried out in collaboration with a visiting exchange student (Kramer, 1997) provides a data rich source for use in validation of the numerical model. The laboratory set-up involved a long flume of uniform cross-section, a steady upstream inflow, and different 'headland' shapes for investigation. Data was gathered using two complementary methods, (i) by tracking floats across the domain, and (ii) using a flow gauge. The float track data were recorded using a video camera, and post-processed to determine velocity components. The floats were designed to produce results similar to that of the depth-averaged flow by selecting an appropriate length of float for the depth of water under consideration. Although the upstream conditions were steady, the flow downstream of the model headland was not. In the lee of the headland, a circulation was observed, although analysis of the float tracking data determined that there was significant instability in the circulation. Eddy shedding was not observed. It was necessary to assume that there was no variability in the flow in order to produce a usable data set. Therefore the data gathered for a particular experiment in the lee of the headland were collated to produce a time averaged result for comparison with the numerical modelling output. The numerical model was set-up using appropriate velocity input boundary conditions and depths determined from the laboratory results. A radiating boundary condition was imposed at the downstream boundary, and the other two boundaries formed the channel walls (Figure 5.9). A cell size of 0.02 m x 0.02 m was selected to represent the domain, and the extent was enlarged from that recorded by the video apparatus to 3 m x 0.9 m to limit the effect of the boundaries on the solution obtained (see figure 5.14). The simplest method of comparing the available data with the

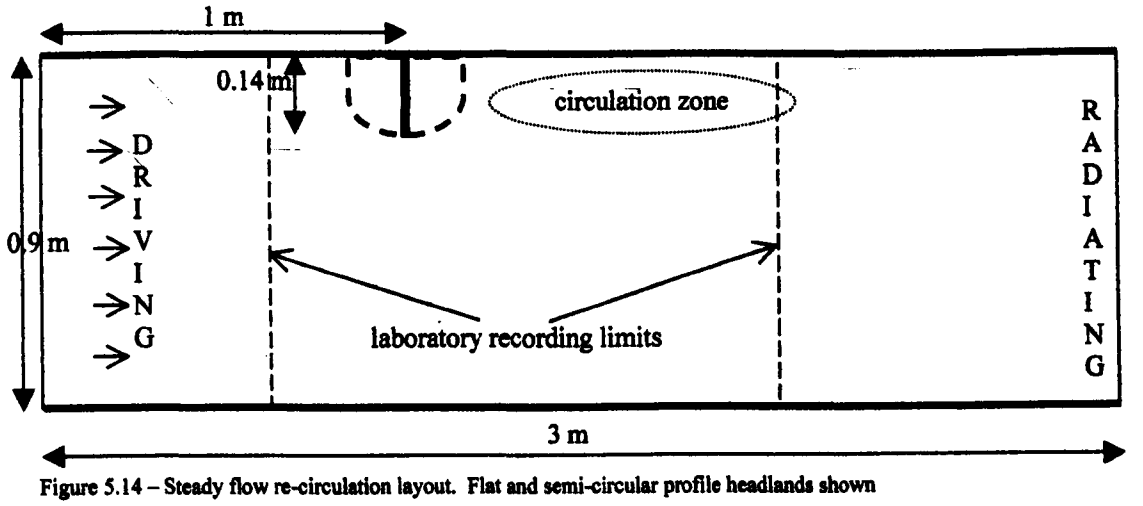

Figure 5.14 – Steady flow re-circulation layout. Flat and semi-circular profile headlands shown

output from the model is to compare cross-sectional data. Cross-sections were selected approximately 0.25m apart which coincides with the interval between the majority of the laboratory data. Results obtained using a headland of length 0.14 m with a thin (flat plate) and semi-circular profile are presented in figures 5.15 and 5.16 respectively. The laboratory data at a cross-section have been averaged from results obtained within a 3 centimetre band either side of the section. The density of data obtained in the circulation zone allows the averaging of the data at intervals of 2 centimetres (chosen to agree with the numerical modelling cell size) which provides a suitable method for removing the variability in the data, and providing an appropriate 'steady-state' solution for comparison. Several difficulties arose in the numerical modelling of this test-case. The major problem is that the numerical model never reaches a steady state solution due to instability in the wake region. This is believed to be a consequence of feedback from the radiating downstream

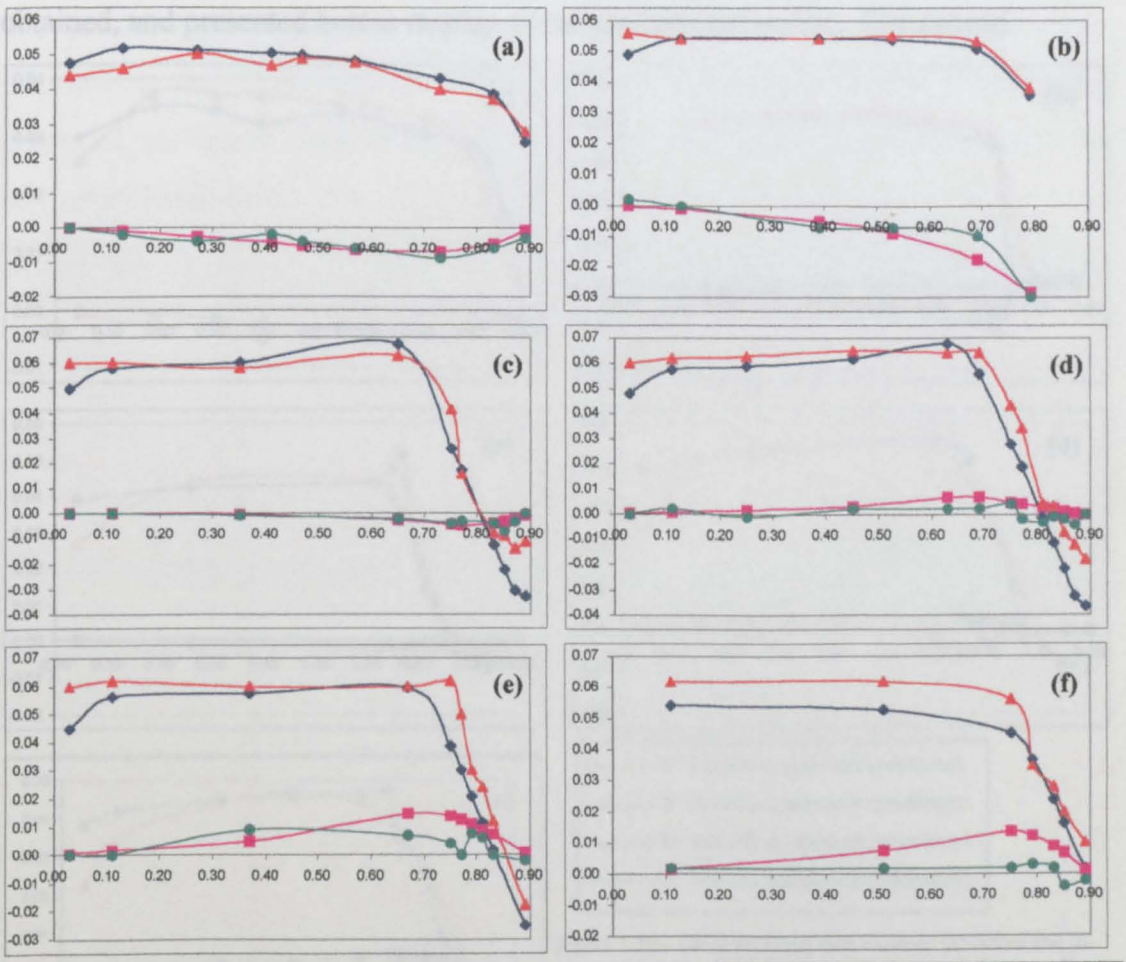

Figure 5.15 – Cross-sectional data obtained (a) before (b) at and (c-f) progressively downstream of the headland feature. The headland in this test is a flat plate, input velocity = 0.047 ms^{-1}, Manning's n = 0.012 $sm^{-1/3}$, no-slip boundary applied at channel walls.

boundary condition. When studying unsteady flow situations the level of feedback is so insignificant as to be of no concern. However, when trying to maintain a steady state situation, the feedback (reflection) from the radiating boundary generates instability in the domain. In this case, the problem is compounded because of the necessary application of a velocity input boundary condition. This is because a velocity input condition does not react to downstream changes in the domain propagating back upstream in the same way as an elevation boundary condition. Therefore, if this simulation is permitted to run indefinitely, the instability eventually grows to an extent that swamps the solution. The results presented were obtained by averaging the output obtained during the 50000 time-steps (25 seconds of real-time simulation) immediately after the steady state input velocity has propagated throughout the domain (see figures 5.17(a and b)). The intention was to obtain results before the instability had a major influence on the solution. The results obtained, and presented herein display no measurable instability. The second

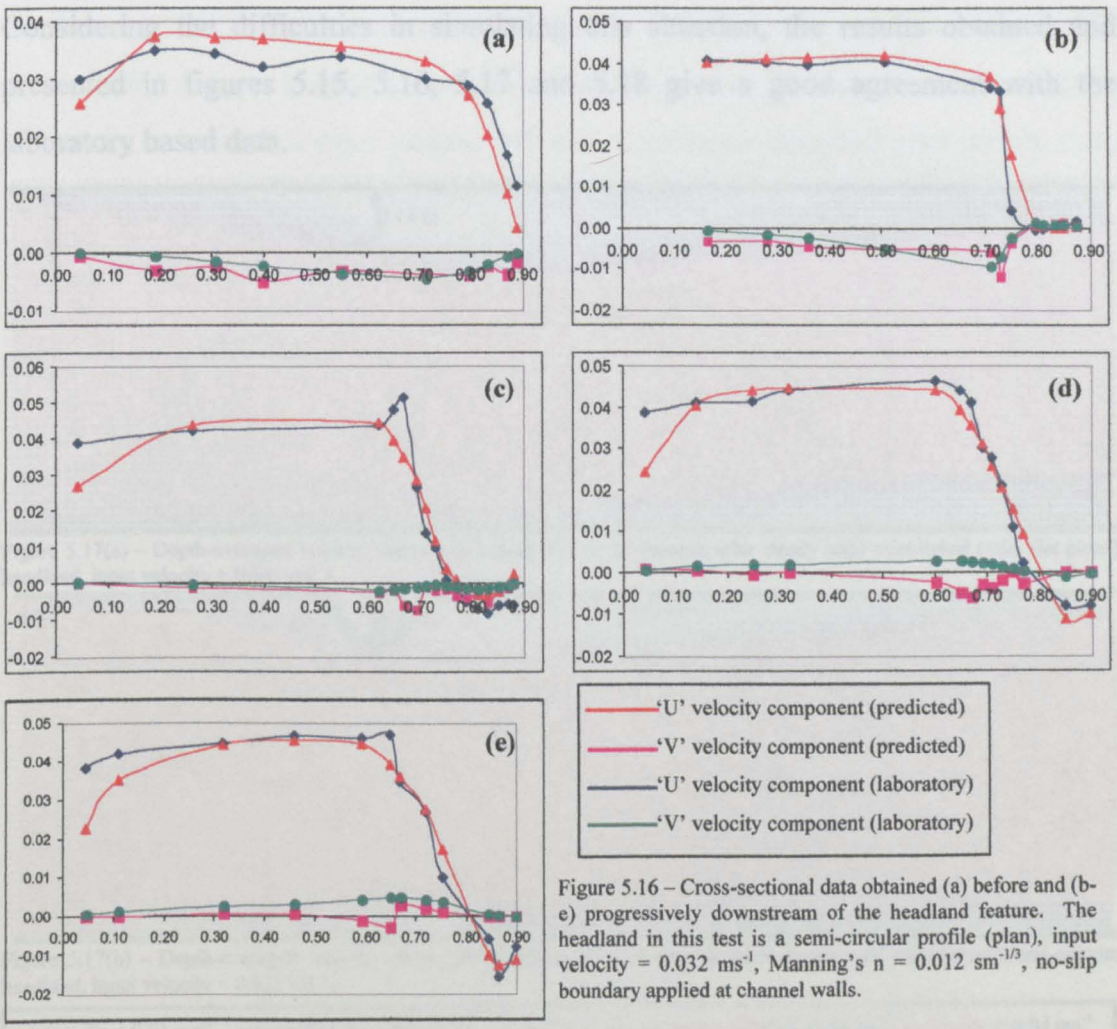

Figure 5.16 – Cross-sectional data obtained (a) before and (b-e) progressively downstream of the headland feature. The headland in this test is a semi-circular profile (plan), input velocity = 0.032 ms^{-1}, Manning's n = 0.012 $sm^{-1/3}$, no-slip boundary applied at channel walls.

difficulty in the modelling exercise was to correctly prescribe the eddy viscosity in the domain. The eddy viscosity model normally applied using the TFD program is based upon considerations of turbulence at coastal scales. Application of the same formula at laboratory scales provides a significant underestimation of the eddy viscosity value, which is further complicated by the inability to obtain the level of bed friction in the laboratory suggested by scaling analysis. An appropriate value of eddy viscosity was therefore arrived at through a calibration process. This involved comparing the cross-stream width of the eddy region, and the width of the shear layer created between the eddy and the free-stream region obtained in the laboratory with the numerical model results. In the end, the eddy viscosity formulation (equation 3.3.41) was multiplied by a factor of 6 in order to obtain the best-fit solution.

This case has provided a severe test of the limits of the numerical model due to the excessively small time-step (0.005 s), cell size (0.02 m) and water depth (0.08 m), with the consequent values of $\Delta\eta$, Δu and Δv occurring throughout the domain. Considering the difficulties in simulating this situation, the results obtained and presented in figures 5.15, 5.16, 5.17 and 5.18 give a good agreement with the laboratory based data.

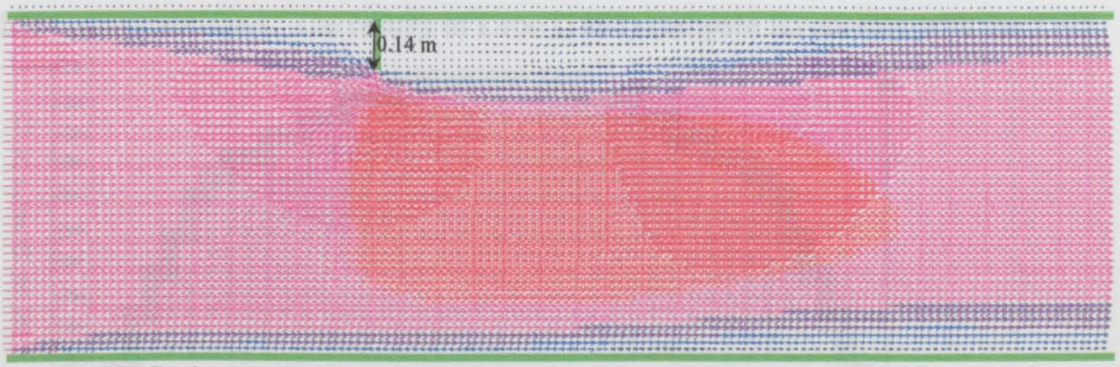

Figure 5.17(a) – Depth-averaged velocity vector plot averaged over 25 seconds after steady state established (thin 'flat plate') headland, input velocity = 0.047 ms^{-1}).

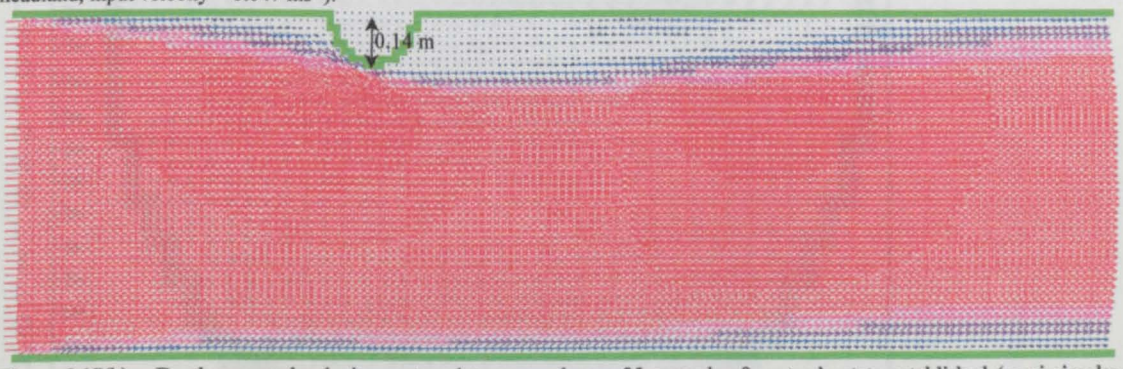

Figure 5.17(b) – Depth-averaged velocity vector plot averaged over 25 seconds after steady state established (semi-circular headland, input velocity = 0.032 ms^{-1}).

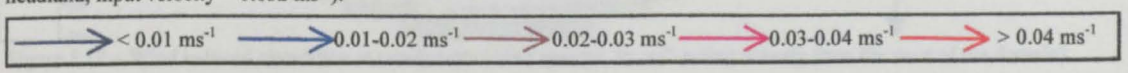

5.2.2 Validation Test 2 – Wind Induced Circulation in a Circular Basin

In a circular bowl-shaped basin, the expected flow reaction to a uniform wind condition is the formation of two symmetrical counter-rotating eddies, with the return flow through the centre of the domain being opposed to the wind direction (Fischer, et al. 1979). Examining the TFD model response to wind-induced set-up in a circular bowl-shaped basin will provide a stringent test of the governing equations (3.4.1-3). The model domain and parameters are selected to enable comparison between the results obtained from the TFD model with the quadtree grid based model of Leon (1997). It is not possible to create a perfectly circular domain using a square grid-based numerical scheme (Δx = 10 m). A best-fit representation is therefore applied. The bathymetry is set-up to vary uniformly from 0.5 m at the edges of the domain to 0.9m at the centre. The wind speed is set at 10 ms^{-1} from a westerly direction acting uniformly across the domain. The other model parameters are set as follows: C_W = 0.002, n = 0.025, and no Coriolis term. The resulting output contains all the expected features outlined previously. The depth-averaged velocity in the centre of the domain is approximately 0.1 ms^{-1} once a steady state flow has evolved. Figure 5.18 shows a depth-averaged velocity vector plot obtained after steady state has been established. The results of Leon (1997) compare favourably with the TFD

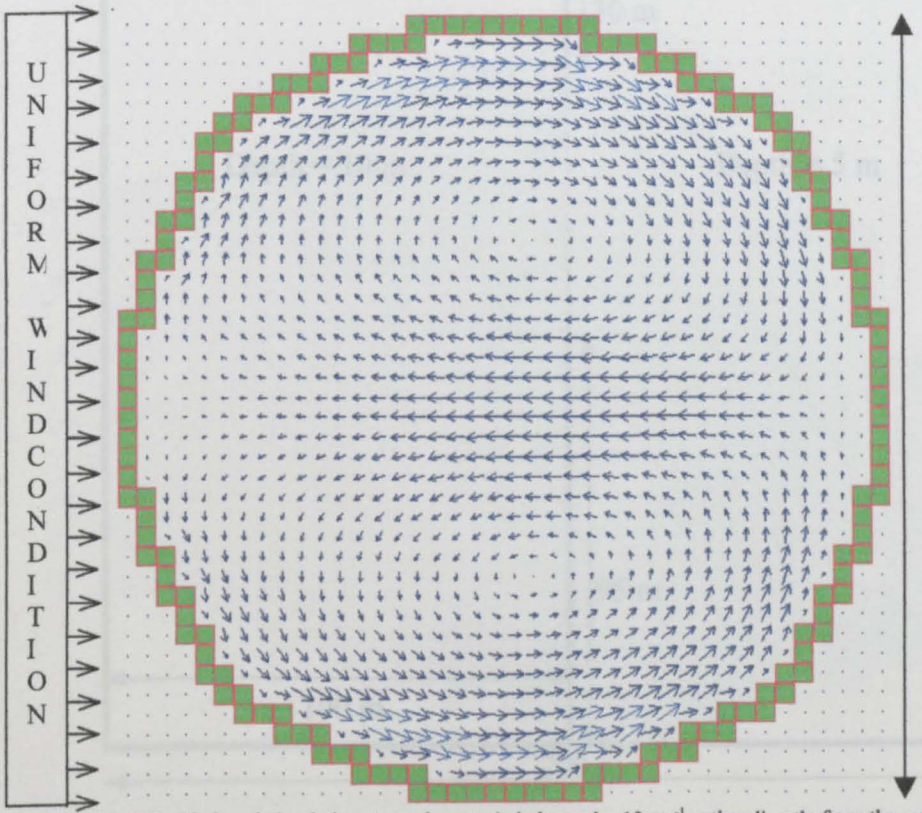

Figure 5.18 – Wind induced circulation at steady state (wind speed = 10 ms^{-1} acting directly from the west of the domain).

model output. The one significant difference is that Leon's results suggest that the down-wind position of the eddy centres would be slightly more off-centre (by 1 or 2 cells). The ability of Leon's adaptive grid to more closely represent a circular domain is perhaps the reason for this slight discrepancy between the results. Kranenburg (1992) has also presented similar results. Kranenburg's results however showed that the eddy pair should be positioned on a line at the centre of the basin perpendicular to the wind direction. Leon (1997) has suggested that this result is a consequence of simplifications in the equations applied in Kranenburg's model. Nonetheless the TFD model is able to predict the key features of the flow regime, and in this case provides a satisfactory agreement with two independent modelling exercises.

5.2.3 Validation Test 3 – Two-dimensional Partial Dam-break Study

A numerical experiment commonly applied for the purposes of validating Computational Fluid Dynamic (CFD) models is the two-dimensional partial dam-break test (Fennema and Chaudry, 1990). The model domain considered is described by figure 5.19. Dam-break is assumed to occur instantaneously with a consequent

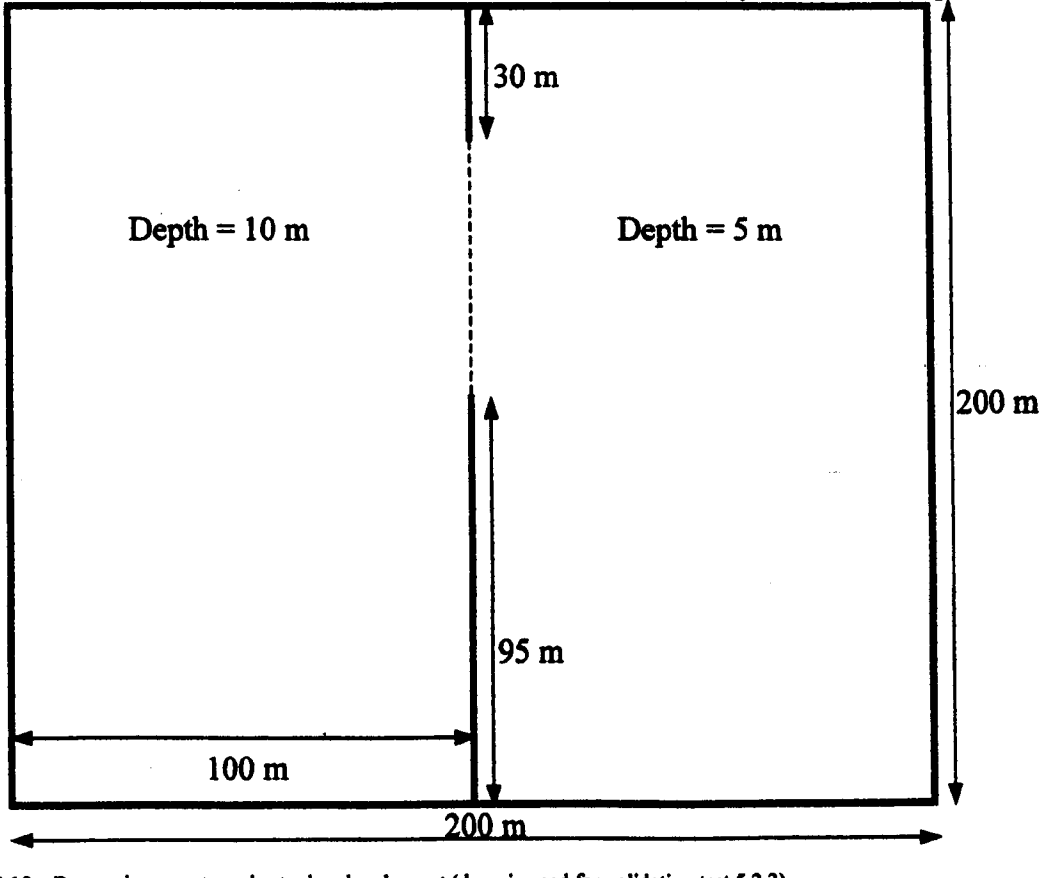

Figure 5.19 – Reservoir geometry prior to dam-break event (domain used for validation test 5.2.3).

downstream wave propagation and simultaneous lateral spread. The dam-break case presents a rigorous test of the governing equations (3.4.1-3), and the modelling of the convective momentum term in particular. Following the standard procedure advocated by Fennema and Chaudray (1990), and subsequently adhered to by Alcrudo and Garcia-Navarro (1993), Glaister (1991), Anatasiou and Chan (1997), Leon (1997) and Zoppou and Roberts (2000), the test assumes a frictionless environment (n = 0), and Coriolis effects are ignored. The only alteration from the normal operation of the TFD model was the requirement to specify an eddy viscosity coefficient as the expression normally applied is dependent upon Manning's friction coefficient, n, which has been set to zero as noted above. Therefore a uniform eddy viscosity coefficient of 0.5 m^2s^{-1} is applied across the domain (in fact the model provided a satisfactory result with the eddy viscosity coefficient set to zero, but the smoothing effect of the eddy viscosity term removes some spurious oscillations from the wave propagation). The model is allowed to run for 7.2 seconds after failure of the reservoir 'bank' at which point the results are output. Figure 5.20 shows an isometric plot of the water surface at the end of the simulation. A two-dimensional plot of the depth-averaged velocity vectors is presented in figure 5.21. The corresponding surface elevation contours are presented in figure 5.22(a). The

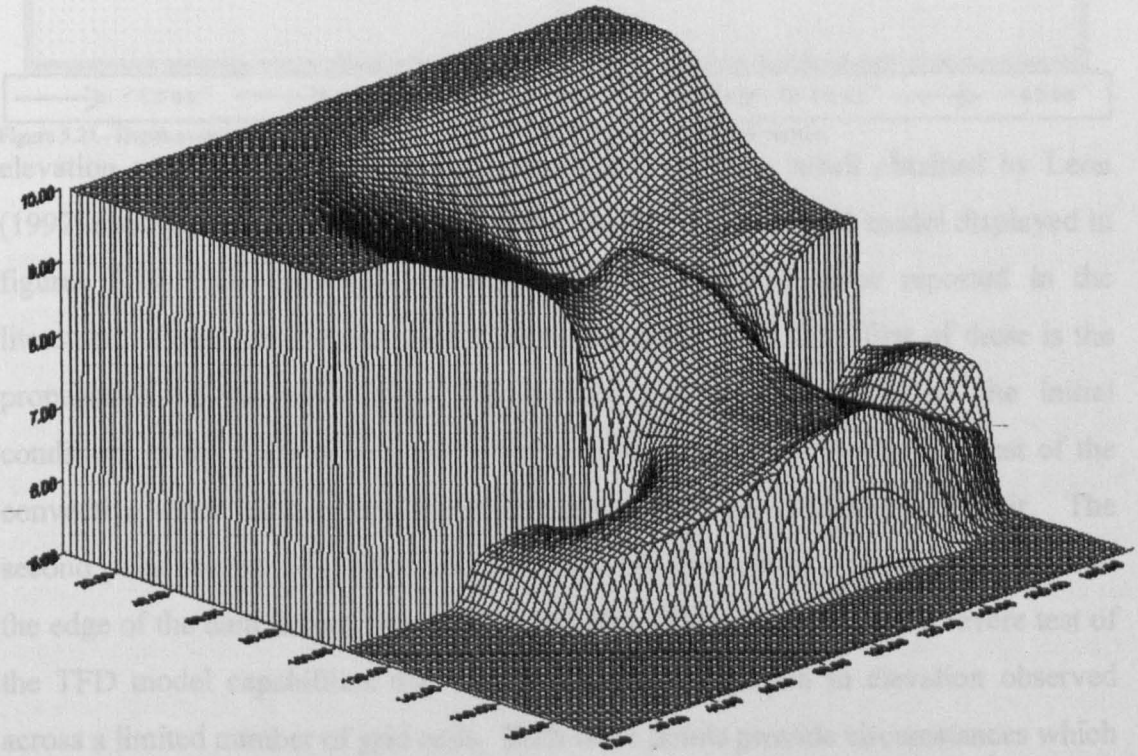

Figure 5.20 - Water surface plot 7.2 seconds after dam-break.

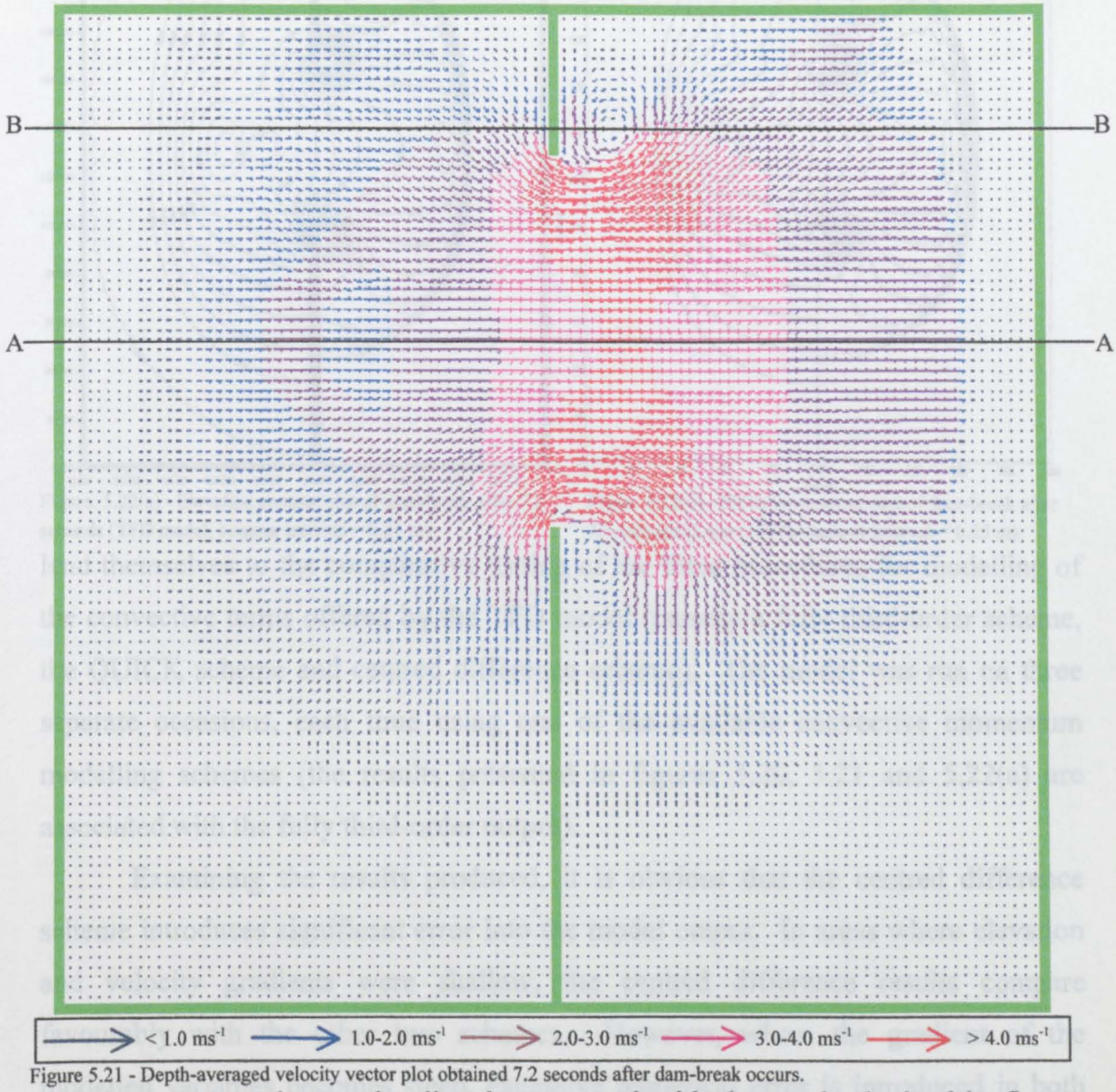

Figure 5.21 - Depth-averaged velocity vector plot obtained 7.2 seconds after dam-break occurs.

elevation contour plot can be directly compared with the result obtained by Leon (1997) shown in figure 5.22(b). The results produced by the TFD model displayed in figures 5.20, 5.21 and 5.22(a) compare favourably with those reported in the literature. Two points in the results are of particular note. The first of these is the propagation of the wave front. The severe gradient introduced by the initial conditions at the point of the dam break presents a particularly rigorous test of the convective terms as the wave front propagates into the shallower reservoir. The second point worthy of further discussion are the two vortices apparent adjacent to the edge of the dam failure line (see figure 5.21). They also provides a severe test of the TFD model capabilities due to the significant variation in elevation observed across a limited number of grid cells. Both these points provide circumstances which

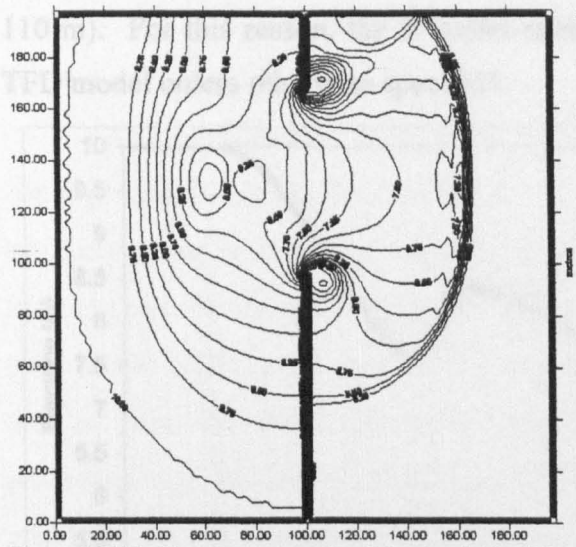

Figure. 5.22(a) - Elevation contour plot of dam-break after 7.2 seconds (TFD model, contour interval = 0.25 m).

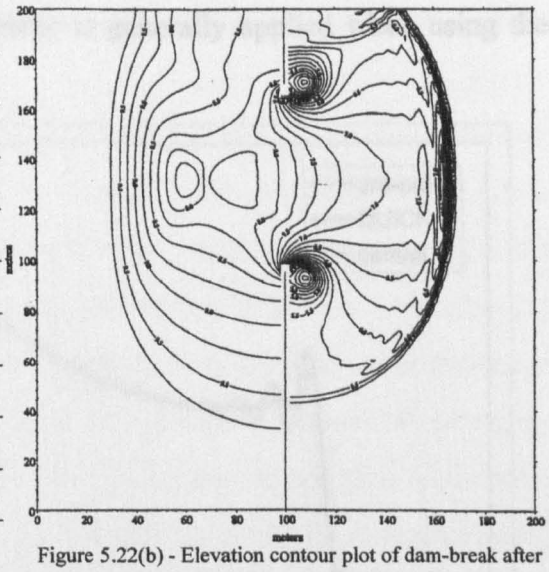

Figure 5.22(b) - Elevation contour plot of dam-break after 7.2 seconds (Leon (1997), contour interval = 0.25 m).

lend themselves to the comparative testing of the three procedures for modelling of the convective terms offered by the TFD model (namely a fully third-order scheme, the QUICK scheme and centred difference scheme). The model was run on three separate occasions, each time using one of the available convective momentum modelling schemes (the results presented in figures 5.20, 5.21 and 5.22(a) are associated with the fully third-order output).

Examining the results produced, it is obvious that the centred difference scheme introduces significant error into the model output. In areas where elevation and velocity gradients were shallow, the centred difference results compare favourably with the other two schemes. However, where the gradient of the modelled variables becomes steep, excessive numerical error is introduced in both the upstream and downstream directions in the form of significant oscillations. The centred difference scheme is also unable to accurately represent the full extent of the gradient of the modelled variables in the centre of the vortices depicted in figure 5.21 on either side of the failure region. Figure 5.23 compares the elevation profile derived from the three numerical schemes as a section taken through the centre of the dam-break region (cross-section A-A, figure 5.22). Figure 5.24 presents a similar comparison taken as a section through the centre of the northern vortex (cross-section B-B, figure 5.22). Examining the QUICK and 3rd-order results, there is no significant difference between them. Of the two, the third-order output can perhaps be considered to be less prone to numerical error (mainly because of the greater numerically induced oscillation observed in the QUICK plot in figure 5.24 at around

110 m). For this reason, the 3rd-order scheme is generally applied when using the TFD model unless otherwise specified.

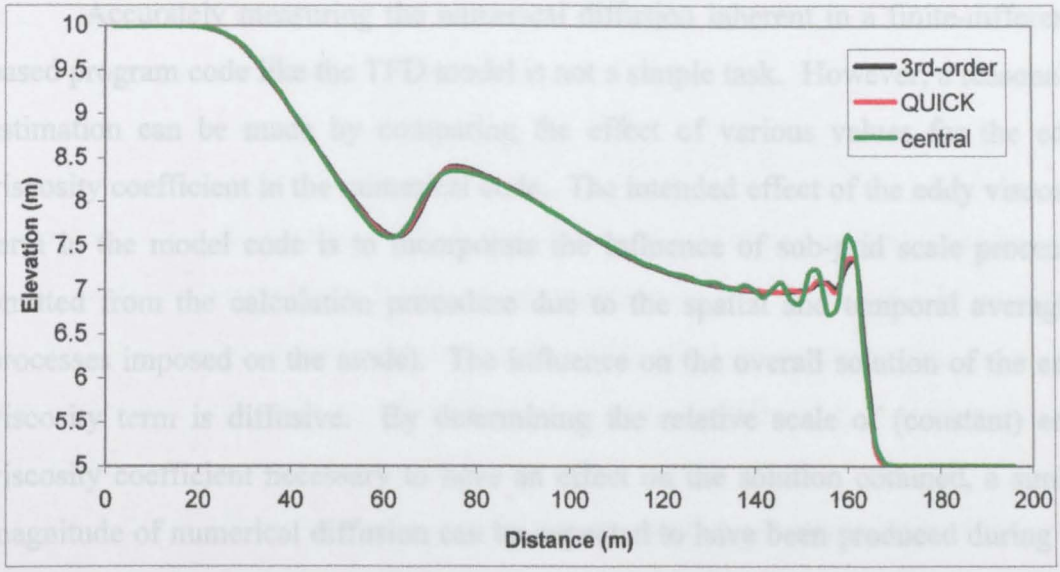

Figure 5.23 - Elevation profile across section y = 134 m (through cross-section A-A (see figure 5.21)).

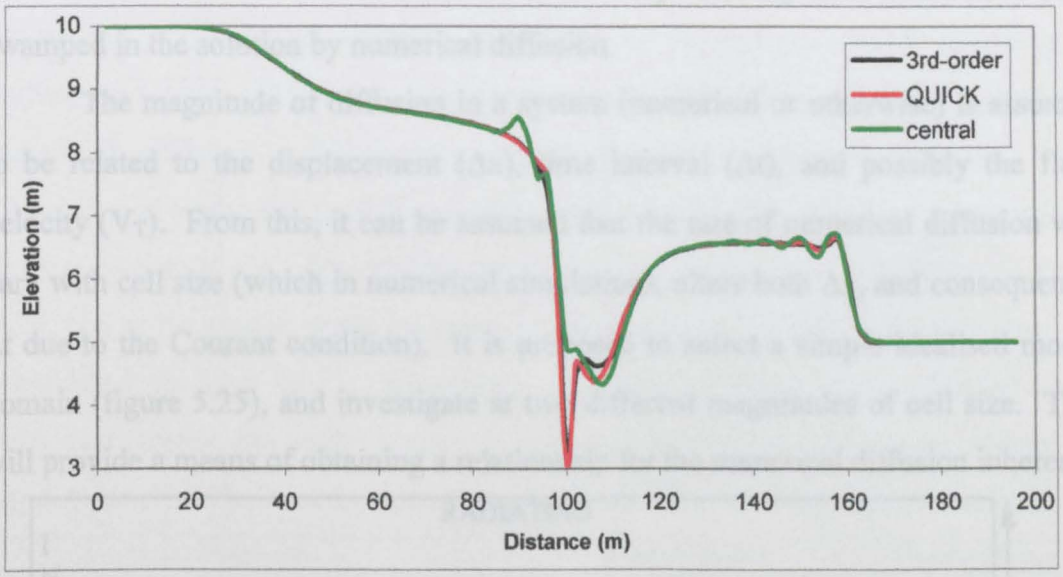

Figure 5.24 - Elevation profile across section y = 168 m (through cross-section B-B (see figure 5.21)),

5.2.4 Validation Test 4 – Estimation of the Numerical Diffusion Inherent to the TFD Numerical Model

In chapter 4, significant attention was focussed on achieving an accurate representation of the convective terms in the numerical modelling code. This was deemed necessary to avoid excessive numerical diffusion. However, it is unrealistic to expect that there will be no numerical diffusion in the solutions produced by the numerical model. Having a basic understanding of the level of numerical diffusion inherent in the model will enable a more precise interpretation of the results produced. Furthermore, understanding the amount of numerical diffusion will aid in

selection of the various calibration coefficients introduced by the discretisation of the equations (chapter 3).

Accurately measuring the numerical diffusion inherent in a finite-difference based program code like the TFD model is not a simple task. However, a reasonable estimation can be made by comparing the effect of various values for the eddy viscosity coefficient in the numerical code. The intended effect of the eddy viscosity term in the model code is to incorporate the influence of sub-grid scale processes omitted from the calculation procedure due to the spatial and temporal averaging processes imposed on the model. The influence on the overall solution of the eddy viscosity term is diffusive. By determining the relative scale of (constant) eddy viscosity coefficient necessary to have an effect on the solution obtained, a similar magnitude of numerical diffusion can be expected to have been produced during the simulation. Otherwise the diffusion due to the eddy viscosity term would have been swamped in the solution by numerical diffusion.

The magnitude of diffusion in a system (numerical or otherwise) is assumed to be related to the displacement (Δx), time interval (Δt), and possibly the fluid velocity (V_T). From this, it can be assumed that the rate of numerical diffusion will vary with cell size (which in numerical simulations, alters both Δx, and consequently Δt due to the Courant condition). It is proposed to select a simple idealised model domain (figure 5.25), and investigate at two different magnitudes of cell size. This will provide a means of obtaining a relationship for the numerical diffusion inherent

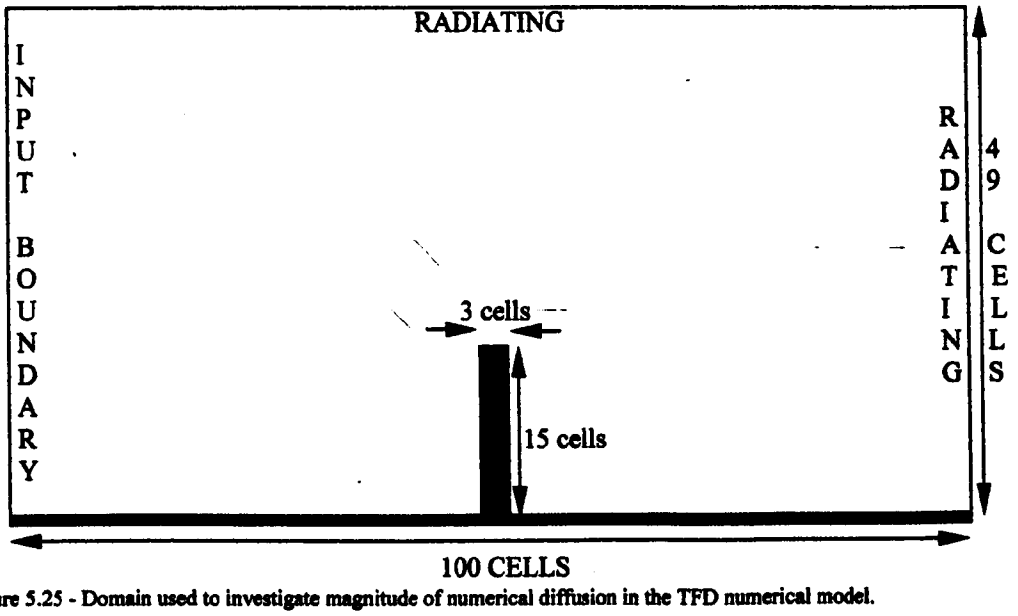

Figure 5.25 - Domain used to investigate magnitude of numerical diffusion in the TFD numerical model.

in the model. In order to compare the two simulations, it will be necessary to scale the relevant variables in order to avoid introducing experimental error. Vieira (1994) has suggested a number of possible relationships which could be considered to control the rate of diffusion. These include,

$$K_1 \frac{\Delta x^2}{\Delta t}, \qquad K_2 U \Delta x, \quad \text{and,} \quad K_3 U^2 \Delta t. \tag{5.17}$$

where K is the dispersion coefficient. The results obtained will be considered in terms of these relationships. Table 5.6 summarises the two cases under investigation. As the TFD model is normally run using a fully third-order convective momentum representation (although the QUICK and a centred difference algorithm are also available), this will be the set-up considered.

A range of constant eddy viscosity coefficients were applied across the model at both scales. In both cases, a datum situation was established by running the simulation with the eddy viscosity coefficient set to zero (effectively disabling the turbulence model). Diffusion in the datum results is therefore limited to numerically generated diffusion. Subsequent simulations were compared with the datum simulation at equivalent peak tide conditions (3.5 hours after initiating the simulation from a cold start-up). The results obtained at the larger scale are shown in figure 5.26, and at the smaller scale in figure 5.27 (overleaf). The eddy viscosity term was considered to have had a measurable influence on the results obtained when velocities across the eddy region in the lee of the headland were altered by approximately 10% from the datum output. In the large cell size case, an effective

Property	Large cell size	Small cell size
Cell size (Δx), metres	100	10
Time-step (Δt), seconds	2.5	1
Depth (H), metres	10	1
headland extent (L), metres	1500	150
Input velocity amplitude (U), ms^{-1}	1	0.1
Manning's friction coefficient (n), $ms^{-1/3}$	0.025	0.017
Vorticity generating scale, $\Delta U/\Delta x$	0.01	0.01
'equivalent' Reynolds no. ($Re_f = H^{4/3}/(gn^2L)$).	2.342	2.351
Equivalent eddy viscosity coefficient, ($\overline{\nu}_t$).	**1**	**0.01**
1st diffusion coefficient (K_1), $K_1(\Delta x^2/\Delta t) \approx \overline{\nu}_t$	0.00025	0.0001
2nd diffusion coefficient (K_2), $K_2 U \Delta x \approx \overline{\nu}_t$	0.01	0.01
3rd diffusion coefficient (K_3), $K_3 U^2 \Delta t \approx \overline{\nu}_t$	0.4	1

Table 5.6 - Summary of variables used, results obtained and analysis of diffusion coefficients to determine the magnitude of numerical diffusion generated in the TFD numerical model code.

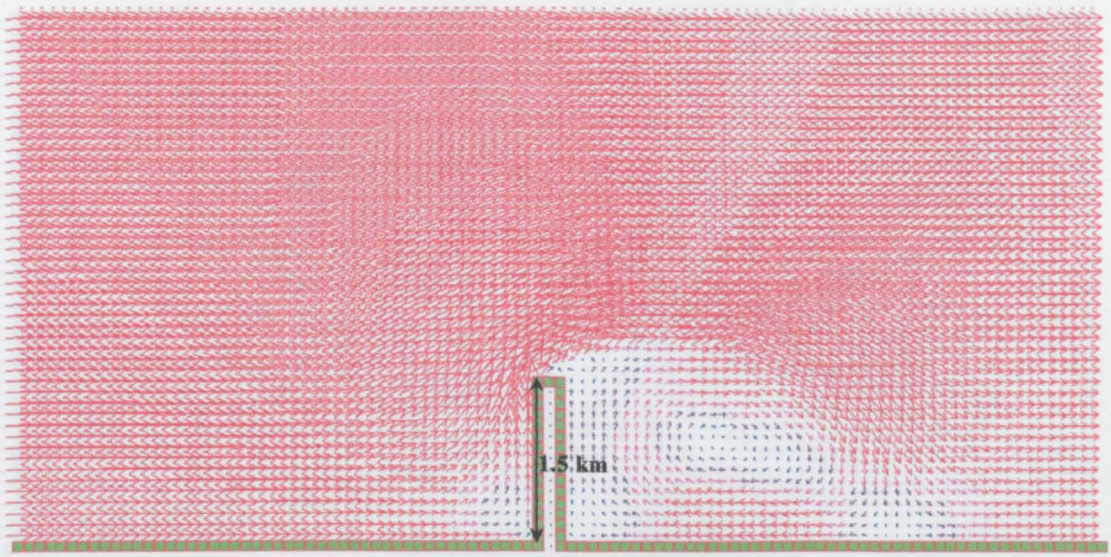

Figure 5.26(a) – Flow development at equivalent peak tide conditions (no eddy viscosity simulation ⇒ diffusion limited to numerical diffusion only).

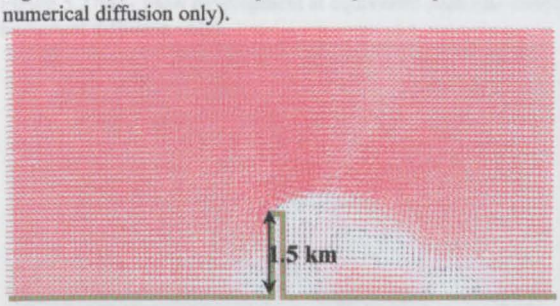

Figure 5.26(b) - Flow development simulated using constant eddy diffusivity coefficient of 0.1 m^2s^{-1}.

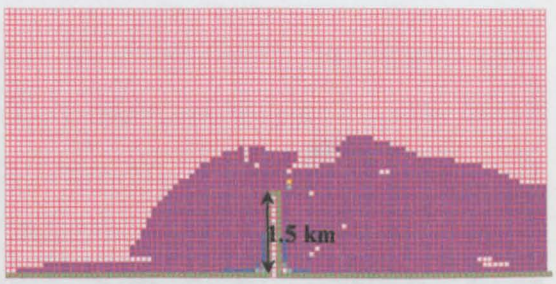

Figure 5.26(c) - Percentage variation per cell between total velocity measured in simulations (b) and (a).

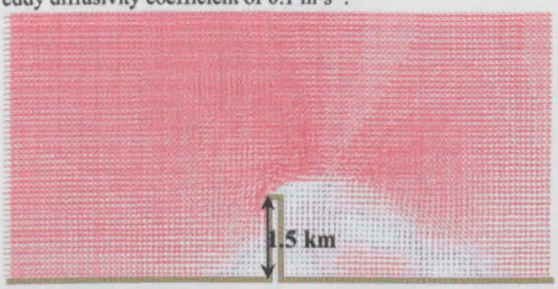

Figure 5.26(d) - Flow development simulated using constant eddy diffusivity coefficient of 1.0 m^2s^{-1}.

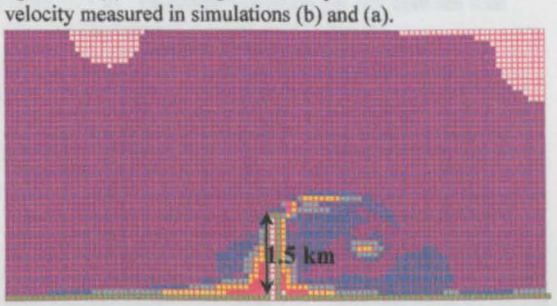

Figure 5.26(e) - Percentage variation per cell between total velocity measured in simulations (d) and (a).

Figure 5.26(f) - Flow development simulated using constant eddy diffusivity coefficient of 10.0 m^2s^{-1}.

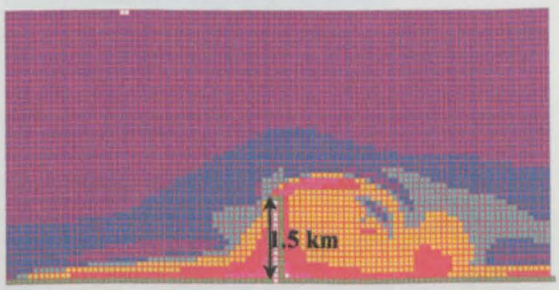

Figure 5.26(g) - Percentage variation per cell between total velocity measured in simulations (f) and (a).

Colour								
% difference	land	< 0.1	0.1 - 5.0	5.0 - 10.0	10.0-20.0	20.0-50.0	50.0-90.0	> 90.0

< 0.1 ms^{-1} → 0.1-0.2 ms^{-1} → 0.2-0.3 ms^{-1} → 0.3-0.4 ms^{-1} → > 0.4ms^{-1}

Figure 5.26-Estimation of numerical diffusion inherent to the TFD code (large cell size).

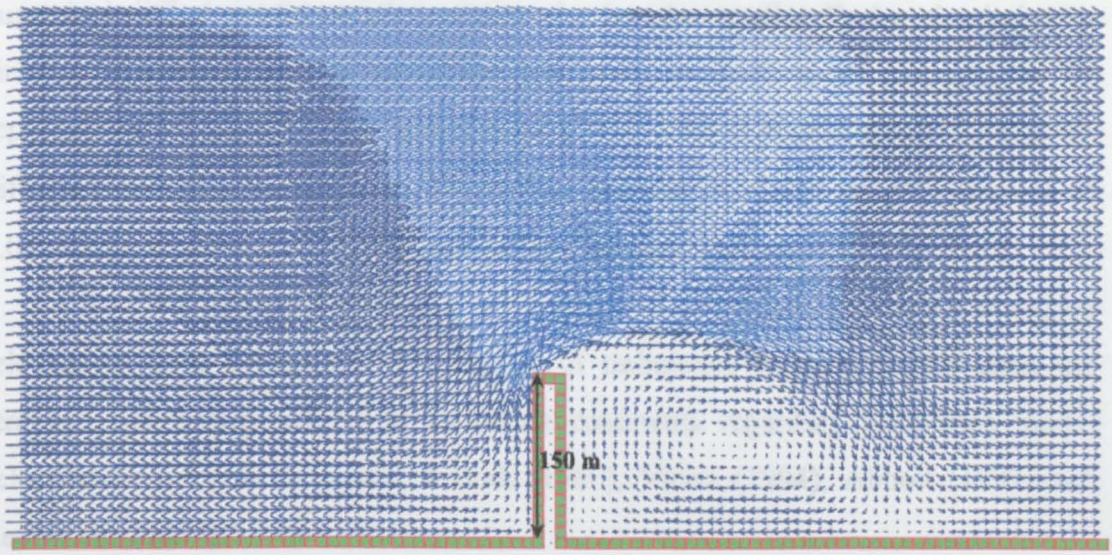

Figure 5.27(a) - Flow development at equivalent peak tide conditions (no eddy viscosity simulation ⇒ diffusion limited to numerical diffusion only).

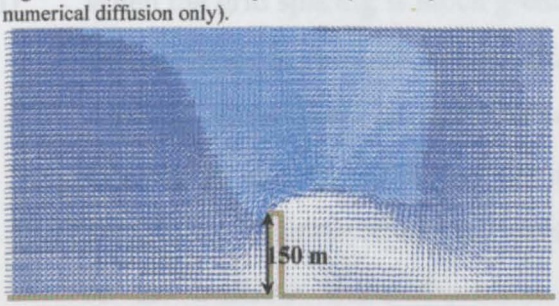

Figure 5.27(b) - Flow development simulated using constant eddy diffusivity coefficient of 0.001 m^2s^{-1}.

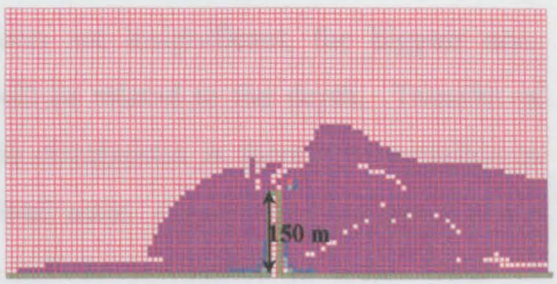

Figure 5.27(c) - Percentage variation per cell between total velocity measured in simulations (b) and (a).

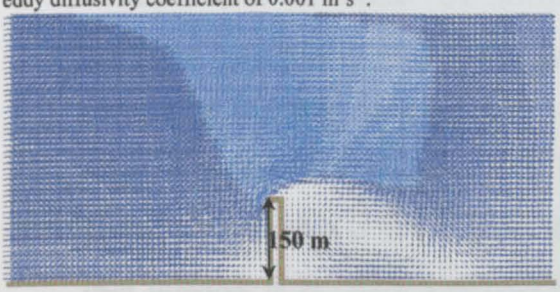

Figure 5.27(d) - Flow development simulated using constant eddy diffusivity coefficient of 0.01 m^2s^{-1}.

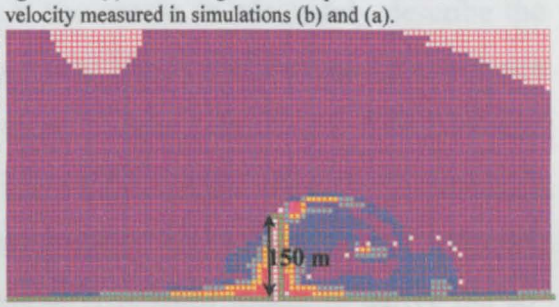

Figure 5.27(e) - Percentage variation per cell between total velocity measured in simulations (d) and (a).

Figure 5.27(f) - Flow development simulated using constant eddy diffusivity coefficient of 0.1 m^2s^{-1}.

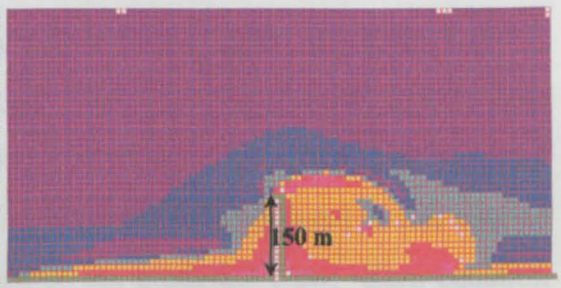

Figure 5.27(g) - Percentage variation per cell between total velocity measured in simulations (f) and (a).

Colour								
% difference	land	< 0.1	0.1 - 5.0	5.0 - 10.0	10.0-20.0	20.0-50.0	50.0-90.0	> 90.0

< 0.1 ms^{-1} → 0.1-0.2 ms^{-1} → 0.2-0.3 ms^{-1} → 0.3-0.4 ms^{-1} → > 0.4ms^{-1}

Figure 5.27-Estimation of numerical diffusion inherent to the TFD code (small cell size).

numerical diffusion of 1 m^2s^{-1} is observed. For the small cell size simulation, a similar estimation of the numerical diffusion of 0.01 m^2s^{-1} appears to be representative. Analysing the three diffusion relationships quoted earlier for the two different cases indicates that $K_2U\Delta x$ provides the best fit. From table 5.6, a value of 0.01 provides a conservative estimate of the diffusion coefficient K_2.

Rodi (1980) has reviewed a wide range of turbulence modelling strategies relevant to fluid dynamics. The choice of turbulence model depends upon the resolved scales required. The following comments regarding turbulence model selection draw upon the work of Rodi (1980), Vieira (1994), Abbott (1997) and Leon-Cruz (1997):

(a) When the grid spacing is much greater than the depth, the bathymetry is fairly regular, and three-dimensional effects are insignificant, the biggest non-resolved circulations (turbulence) will be related to the depth. Transfer of momentum due to the non-resolved circulations is therefore negligible in comparison with the minimum resolved scale. Consequently, a model based on the Shallow Water Equations will be insensitive to local values of turbulence, as the model resolution is too coarse to adequately describe the turbulent behaviour. This would appear to justify the absence of turbulence modelling in early hydrodynamic codes (Flather & Heaps, 1974; Weare, 1976; Prandle, 1978; Runchal, 1978). However, as the effect of the Reynolds stresses in this case is to act as an energy absorber, the generally agreed upon best practice is to apply a zero-equation turbulence model to derive the so-called eddy viscosity coefficient.

(b) When the grid spacing is much greater than the depth, the bathymetry is highly irregular, and three-dimensional effects are therefore of significance, the scale of non-resolved circulations (turbulence) are of the same order of magnitude as Δx. The non-resolved circulation is considered in this case to be of importance to the development of the modelled flow. Zero-equation turbulence models are once more advocated as the preferred modelling approach. A common derivation of the eddy viscosity coefficient in this case is,

$$\overline{\nu}_t = K\frac{\Delta x^2}{\Delta t}, \text{ with, } 0.01 < K < 0.06. \qquad (5.17)$$

(c) When the grid spacing is of a similar order of magnitude to the depth, the biggest non-resolved flow property is the vertical velocity profile. The effective stress term is fundamental to ensure a reasonable representation of the flow development. A zero-equation turbulence model is once more considered the appropriate turbulence modelling tool, but the eddy viscosity coefficient derivation should be directly related to the vertical velocity profile. A standard application is the Elder formula (Elder, 1959) derived assuming a logarithmic vertical velocity profile,

$$\overline{\nu}_t = \frac{\kappa}{6} h \sqrt{C_f (U^2 + V^2)}. \qquad (5.18)$$

From the above description, it is obvious that complex turbulence models are only necessary outwith the scope of coastal hydrodynamic interest.

The general application of the TFD numerical model is targeted at coastal and estuarial hydrodynamic use. At appropriate modelling scales, the application generally falls into group (a) with respect to turbulence modelling. This indicates that a simple zero-equation turbulence model is suitable to quantify the influence of unresolved scales. Consequently a simple zero-equation model of the form of the Elder equation is applied in the TFD model (derivation detailed in chapter 3.3.2.2),

$$\overline{\nu}_t = \frac{\kappa \sqrt{g} n \sqrt{U^2 + V^2} h^{\frac{5}{6}}}{6}. \qquad (5.19)$$

The numerical diffusion inherent in the code at these scales is perhaps an order of magnitude larger than suggested by the eddy viscosity coefficient formulation (equation 5.19). However, the discussion above indicates that the effect this has on the model solution is still insignificant in comparison with non-resolved circulations associated with the depth.

At times during the life of this project, it has also been necessary to apply the TFD model at laboratory scales, which generally fall into group (c) with regards to turbulence model selection. The simple zero-equation model applied is therefore appropriate in these circumstances. Numerical diffusion in this situation is generally of a similar order of magnitude as the diffusion generated by the turbulence modelling. In general, the combined system of measured numerical diffusion and turbulence model specification can be considered to provide an adequate representation of unresolved circulations (turbulence) in the form of energy transfer across the domain.

5.3 Calibration Exercise – Flamborough Head Case-study.

Sections 5.1 and 5.2 have detailed the extensive verification and validation procedure applied to the TFD numerical model. This has followed the procedure advocated by Fischer & Rhodes (1994), of verifying the modelled equations, and validating the models ability to simulate complex flows. If the model had been developed for commercial purposes, testing of the model would now be complete. The responsibility for calibrating the model for a specific application would then lie with the end-user. However, the TFD model has been developed specifically for use in the research presented in this document. Consequently, calibration of the model in this situation is also the responsibility of the model developer.

Once the TFD numerical model had been fully developed, verified and validated, application to a specific case study was eagerly awaited. As the research interest is primarily focussed on eddy generation and development in the coastal zone, investigating an area that incorporated such features was desirable. Selection of a suitable region is not a simple task, as identifying coastal features and local tidal conditions which combine to generate eddy features can involve laborious investigation of various sites with no guarantee of success. Further model specific problems such as generating a realistic representation of the local bathymetry and topography and having access to data for use as boundary complications further limits the site selection process. Fortunately, the UK Environment Agency provided access to their record of coastal aerial photography gathered quarterly during 1995 around England and Wales. Examining the photographic records (provided in the form of CASI (Compact Airborne Spectrographic Imager) true colour composite images), a number of sites were identified which exhibited characteristics which indicated the presence of eddy features during the tidal cycle. Of these, the region around Flamborough Head in the north-east of England (54°07'N, 00°04'W) was selected as providing the most suitable site for calibrating the TFD numerical model. Evidence of potential eddy generation in the vicinity is presented in figure 5.28, as indicated by the apparent uptake and downstream transportation of turbidity from the shoreline. The turbid water appears to be being rolled-up in the lee of the headland in the form of a re-circulation, or eddy. Successfully simulating the flow around Flamborough Head would produce a strong test of the TFD model's ability to

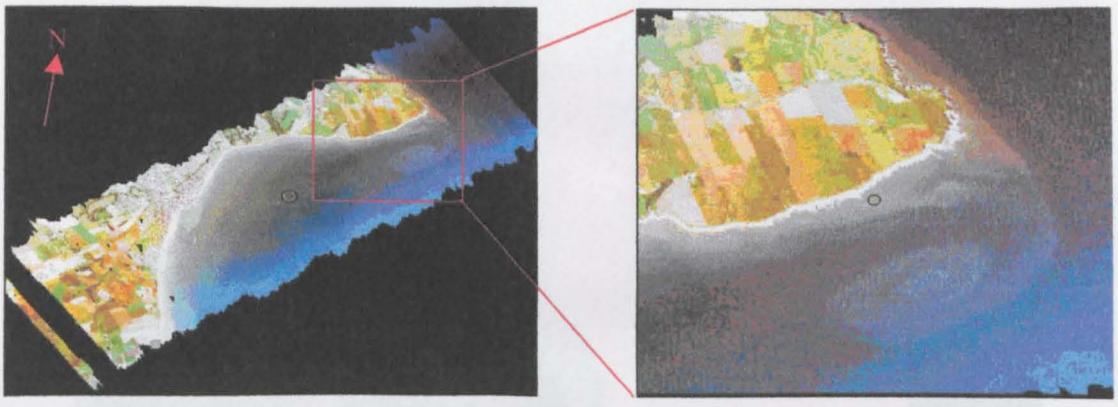

Figure 5.28 – CASI true-colour composite aerial image of Flamborough Head taken on 26 July 1995 at 14:39 indicating eddy generation at the tip of the headland during the flood tide (*provided by the Environment Agency).

correctly predict the occurrence of flow separation, and the consequent roll-up of vorticity into an eddy feature, as observed in the aerial image. The aerial photograph was obtained on the 26 July 1995 at 14:39. Topographic and bathymetric data for the simulation was obtained from Admiralty Chart numbers 121, 129 and 1882. Data from tidal diamonds on the Charts provided basic flow data with which to quantitatively compare the output from the simulation and generate input boundary conditions. The physical extent of Flamborough Head, and the need to include a downstream tidal diamond site in the modelled area for calibration purposes required a domain size of 35.5km by 38.25 km. The need to balance computational expense and storage against numerical accuracy led to the selection of a 450m cell size, necessitating a grid of 79x85 cells, with the grid rotated through 325° in order to minimise the number of redundant cells. The simulation was driven from the northern boundary with the east and south boundaries radiating. The western boundary is completely enclosed by land (see Figure 5.29). The elevation driving boundary conditions were derived for Filey Bay (54°13'N, 00°16'W) using the Simplified Harmonic Method of Tidal Prediction with input data taken from Admiralty Tide Tables (Hydrographer of the Navy, 1994). Although the domain does not extend as far north as the Filey Bay tidal diamond (falling short by approximately 4 kilometres), it does provide the nearest independent and reliable source of tidal elevation information for use as a driving condition. A uniform Manning's number of $0.025 sm^{-1/3}$ and a Coriolis frequency equivalent to a latitude of 54°N was applied across the domain throughout the simulation. The model was run for four complete tides, in order to allow the model to fully 'spin-up', with the fourth tide coinciding with that observed in the aerial photograph (figure 5.28).

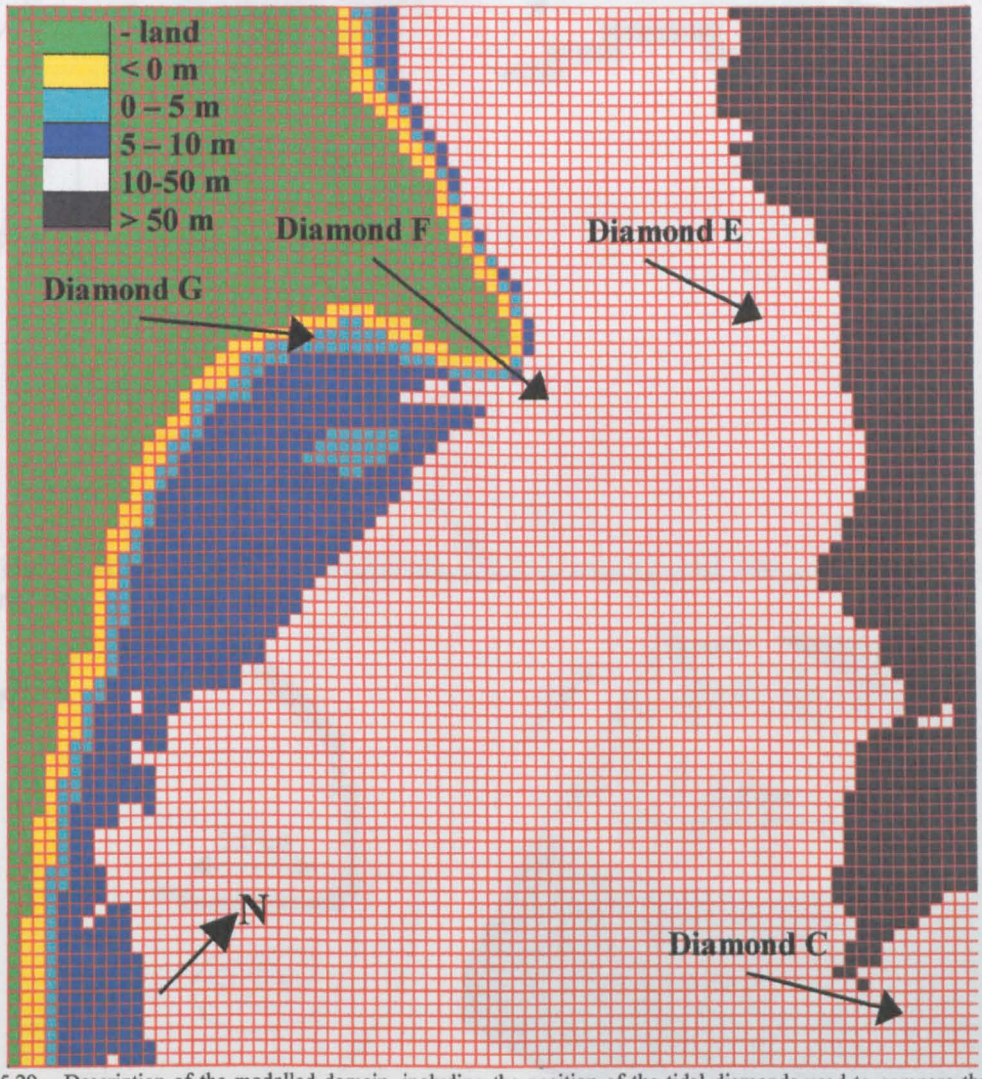

Figure 5.29 – Description of the modelled domain, including the position of the tidal diamonds used to compare the model output with in-situ data (see figures 5.31 and 5.32)

A snapshot result obtained from the model output at 14:45 is shown in figure 5.30(a), with a close-up of the eddy region presented in figure 5.30(b). A particle-tracking plot obtained from a continuous source, output at 30 second intervals, is shown in figure 5.31. The particle-tracking plot elucidates the roll-up of high vorticity flow from the shoreline boundary at the headland into an eddy feature as the flow separates around the headland. The significance of tracking particles introduced from a continuous source point is discussed further in chapter 6.4.2. Comparing the results in figures 5.30 and 5.31 with the original aerial photograph (taken at 14:39) demonstrates the success achieved in simulating the flow development around Flamborough Head using the TFD numerical model. Especially gratifying is that the position and extent of the eddy appears to heave been particularly well replicated in the simulation.

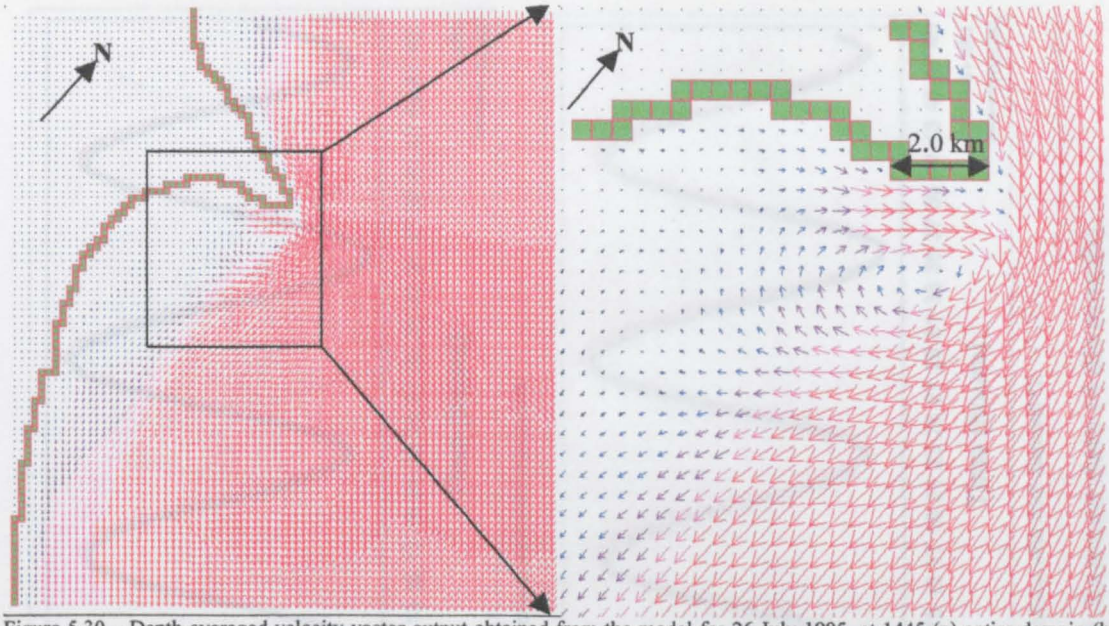

Figure 5.30 – Depth-averaged velocity vector output obtained from the model for 26 July 1995, at 1445 (a) entire domain (b) close-up of eddy.

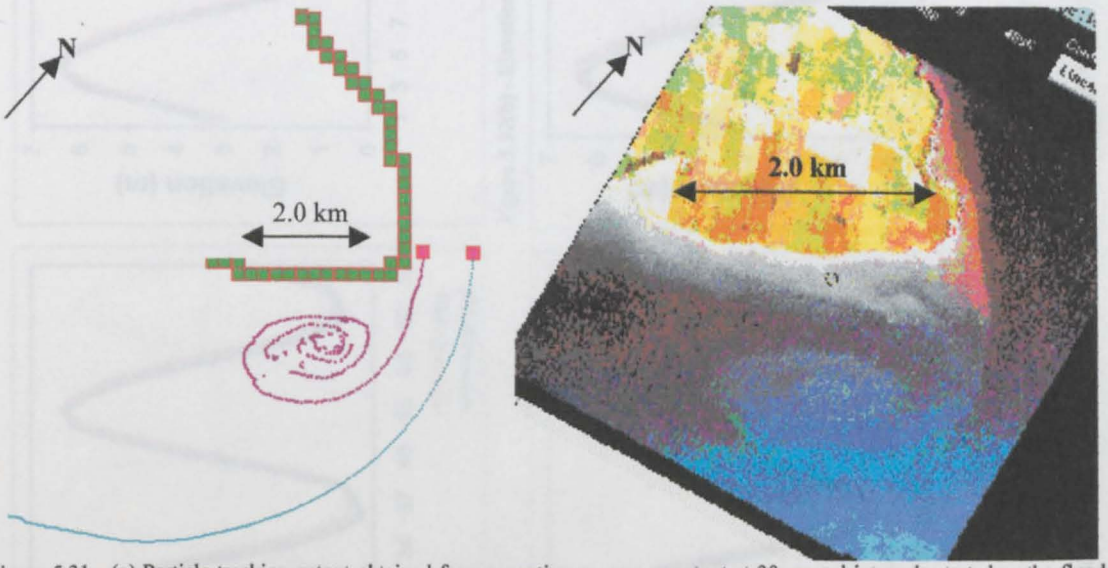

Figure 5.31 - (a) Particle tracking output obtained from a continuous source output at 30 second intervals started as the flood tide becomes established, (b) Original CASI true-colour composite image which instigated the modelling exercise (rotated).

As a quantitative comparison of the output from the simulation, elevation and velocity data obtained from tidal diamond information was compared with that output from the model. The easiest method of interpreting the results is to plot the data in a time-series, as shown in figures 5.32 and 5.33. The elevation data comparison in figure 5.32 demonstrates good agreement in both phase and magnitude at all four sites. The two offshore diamonds (C (Chart No. 121) and E (Chart No.129), shown in figures 5.33(a) and (b)) display good agreement between the U and V velocity components, both in phase and magnitude. This confirms that the driving conditions derived for Filey Bay, and applied at the northern boundary

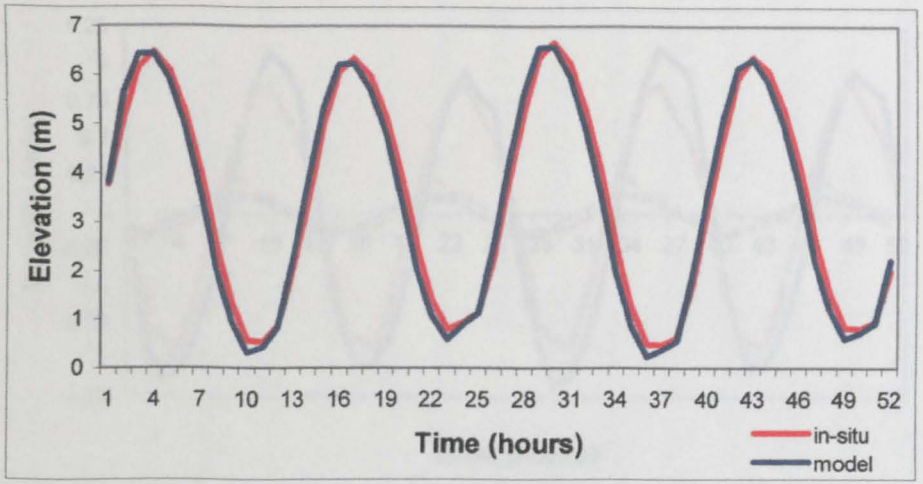

Figure 5.32(a) - Elevation comparison with tidal diamond C.

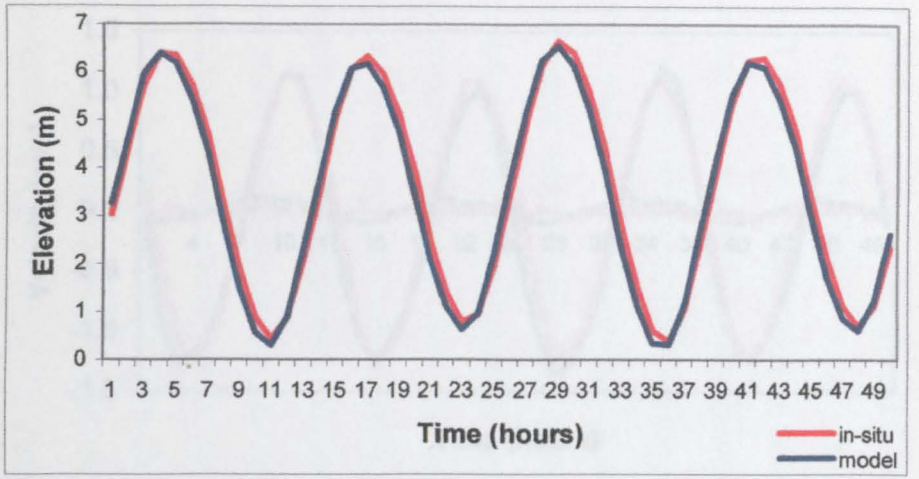

Figure 5.32(b) - Elevation comparison with tidal diamond E.

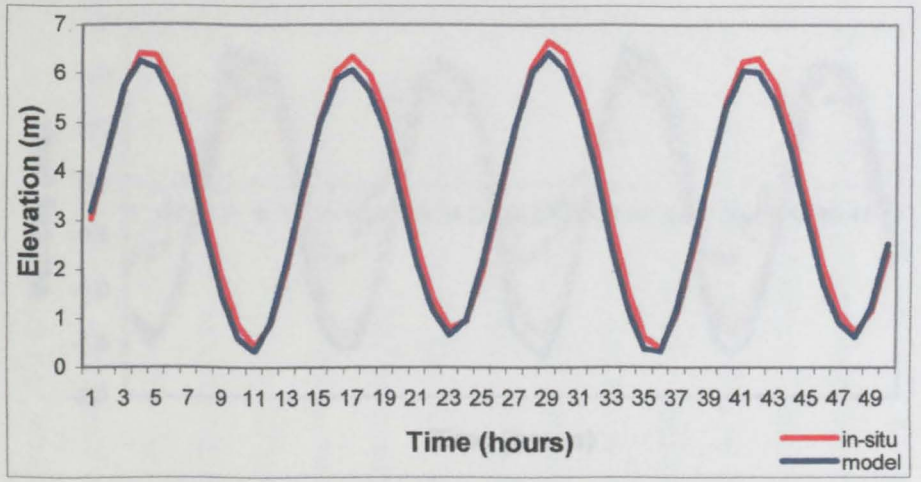

Figure 5.32(c) - Elevation comparison with tidal diamond F.

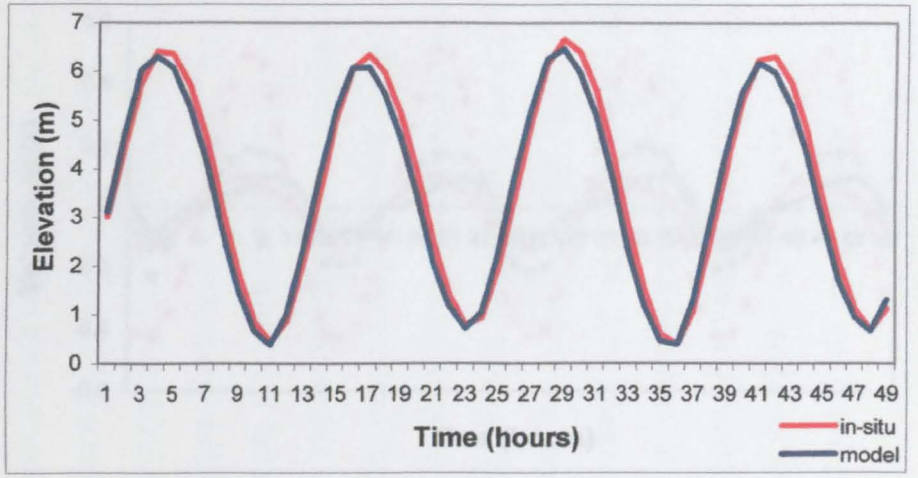

Figure 5.32(d) - Elevation comparison with tidal diamond G.

Figure 5.32 - Comparison of TFD model elevation simulation with tidal diamond data (4 diamonds).

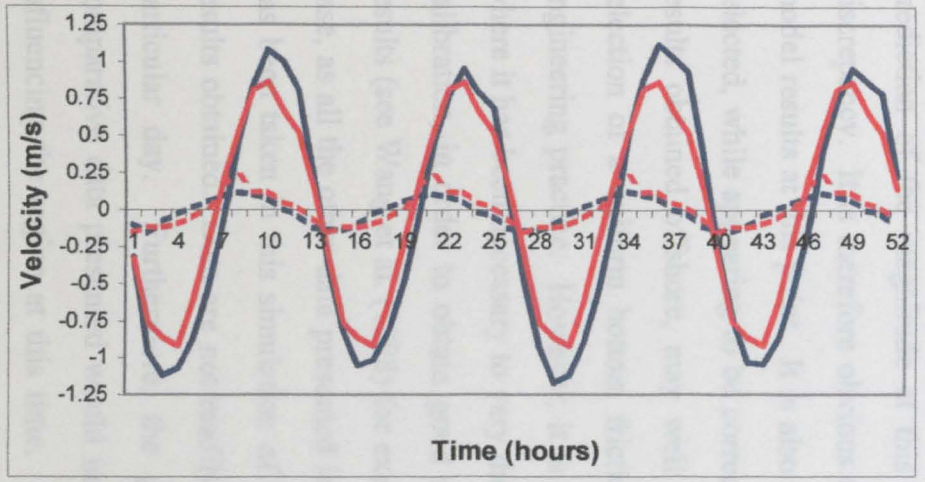

Figure 5.33(a) - Velocity component comparison with tidal diamond C.

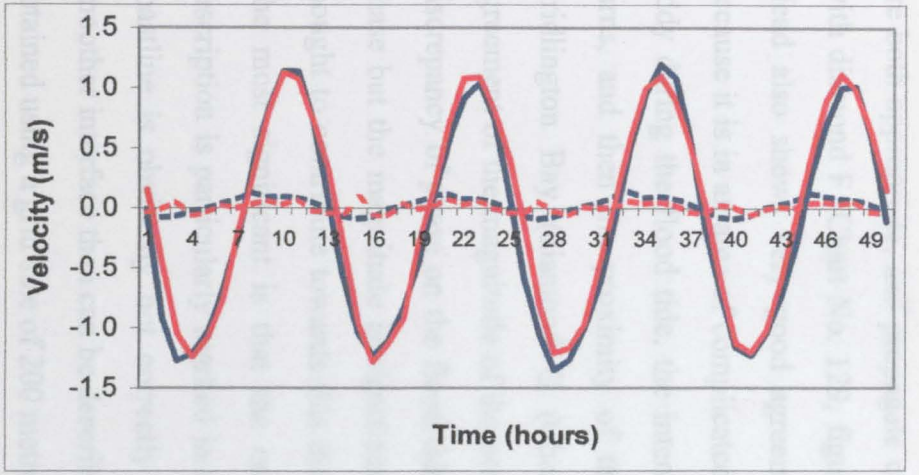

Figure 5.33(b) - Velocity component comparison with tidal diamond E.

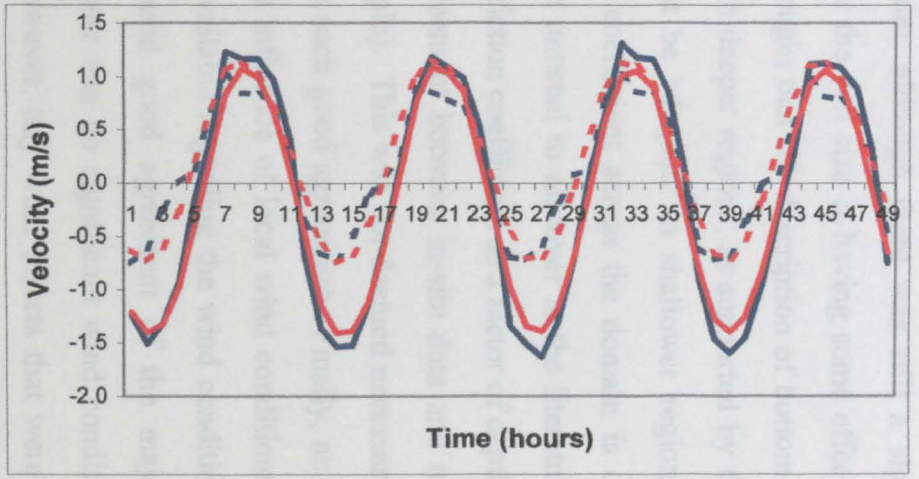

Figure 5.33(c) - Velocity component comparison with tidal diamond F.

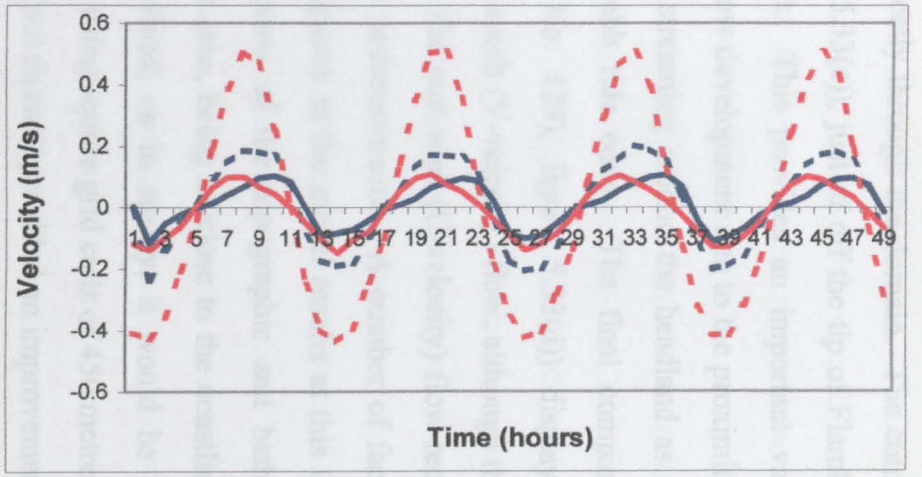

Figure 5.33(d) - Velocity component comparison with tidal diamond G.

U velocity component (model) — V velocity component (model)
U velocity component (data) — V velocity component (data).

Figure 5.33 - Comparison of TFD model velocity component simulation with tidal diamond data (4 diamonds).

are both appropriate, and propagate correctly through the domain. The comparison with diamond F (Chart No. 129, figure 5.33(c)), just of off the tip of Flamborough Head also shows very good agreement. This provides an important validation because it is in an area of complicated flow development due to the proximity of the eddy during the flood tide, the intense streaming around the headland as the tide turns, and then the proximity of the ebb tide eddy. The final comparison in Bridlington Bay (diamond G (Chart No. 129), figure 5.33(d)) displays good agreement of the magnitude of the north-south (V-velocity) flow, although there is a discrepancy of phase on the flood tide. The east-west (U-velocity) flow remains in phase but the magnitude is significantly underestimated. A number of factors are thought to contribute towards this discrepancy in the model results at this location. The most significant is that the crudeness of the topographic and bathymetric description is particularly marked in this area, being so close to the coastline. The coastline is obviously not correctly defined, as in reality, it would be a much smoother interface than can be described using square grid cells of 450 metres. Runs obtained using a grid size of 200 metres (not shown) provided an improvement in the prediction of the magnitude at this point, although there was still a significant discrepancy. It is therefore obvious that the cell size is having some effect on the model results at this point. It is also thought that the description of bottom friction selected, while appearing to be correct in deeper regions, as supported by the good results obtained offshore, may well not be adequate in shallower regions. The selection of a uniform bottom friction coefficient across the domain is common engineering practice. However, it is not unusual to discover in the literature cases where it has been necessary to vary the friction coefficient as a factor of depth during calibration, in order to obtain good agreement between in-situ data and modelled results (see Wang et al. (1998) for example). This was not deemed necessary in this case, as all the other data presented is in such good agreement. Finally, no account has been taken in this simulation of the influence of local wind conditions on the results obtained. Data are not readily available regarding the wind conditions on a particular day. Furthermore, the general good agreement of the majority of comparative data presented would indicate that no significant wind condition was influencing the region at this time. However, any wind effects that were present

during the period of investigation would have a more significant influence on the depth-averaged velocity profile in shallow regions. This therefore presents a further possible contributory factor that could be construed as the cause of the lack of agreement observed in the velocity components at tidal diamond G.

Without access to extensive (and expensive) survey data, it is not possible to correctly apportion the cause of the disagreement between the data and simulated output at tidal diamond G. Nevertheless, the TFD model has been able to provide a generally good agreement with the available data. This has been achieved without recourse to numerous re-runs of the model to obtain a best-fit solution. Considering the data available to construct the modelled problem (one relevant aerial image, three admiralty charts and the relevant admiralty tide tables), it is perhaps surprising that the simulated results produced bare any resemblance to the in-situ data. The ability of the TFD model to operate effectively in this situation combined with the success of the verification and validation exercises presented previously instils confidence in the model's capabilities and flexibility in application.

6. EDDY GENERATING MECHANISMS

Eddies in coastal flows are caused by three distinct physical mechanisms; (i) interaction with topographic features, (ii) interaction with bathymetric features and (iii) by phase effects associated with tidal periodicity. The occurrence of an eddy is normally further complicated by the combined action of the three mechanisms, which can often all be contributing to the flow development to a greater or lesser extent throughout the tidal cycle. Although much of the theory describing eddy generating mechanisms is readily available in the existing literature, when it comes to practical application, there is a lack of consideration of the individual mechanisms and in particular, their interaction. This confusion ensures that interpretation of physical data is either lacking important detail, or in the worst instances incorrect. The ability of numerical models to simulate the gross features of flow development further compounds the lack of understanding as the user is not required to independently interpret the flow development. Repeated unsuccessful attempts to model flow development and eddy generation in the lee of Rattray Island provide a salient warning of our increasing over-reliance on numerical modelling output (Falconer et al. 1986; Wolanski, 1988; Deleersnijder et al 1992; Galloway et al. 1996; Wolanski et al. 1996). These attempts were each originally reported by the authors as being successful, but the interpretation of the corroborating survey data applied has subsequently been shown to be flawed (see Furukawa & Wolanski (1998) for further discussion). Before entering into further discussion of the Rattray Island case, it is necessary to consider the eddy generating mechanisms at a more fundamental level. Rattray Island will be discussed at length in chapter 8.

Each of the eddy generating mechanisms under discussion exhibit individual distinguishing properties that set them apart, as well as sharing many characteristics. A rigorous description of the characteristics of each mechanism will be presented. Using the TFD numerical model described in chapter 4 and 5, the mechanisms will then be compared directly to highlight the differences between them. Direct comparisons of the three eddy generating mechanisms are absent so far from the literature. This may be because of the lack of understanding of the differences between the mechanisms, or because one particular mechanism (topographic) dominates the existing literature. Whatever the reasons, it is useful to demonstrate the individual characteristics.

6.1 Topographic Eddy Generation

Eddies generated by tidal interaction with topographic features have been studied at length by various authors. The consensus opinion expressed is that flow separation is necessary in order to instigate conditions suitable for establishing an eddy. Flow development as a consequence of separation is not however limited to eddy generation, as turbulent wakes (Ingram & Chu, 1987), jets (Hearn, et al., 1985; Mardapitta-Hadjipandeli & Falconer, 1990), and plumes (Oey & Mellor, 1993) are other flow features that are associated with separation events. Therefore, in order to understand topographic eddy generation, it is first necessary to understand the conditions that induce flow separation. It is necessary to initially consider a sheer-sided topographic feature in order to isolate the individual eddy generating mechanism.

Topographic eddies develop by the injection of vorticity from the boundary layer into the flow interior facilitated by flow separation. Flow separation at coastal scales occurs in a similar manner as in viscous flow around bluff bodies, and can therefore be described using boundary layer theory (chapter 2.1.1). Flow in the boundary layer is maintained upstream of the bluff body because the favouring pressure gradient (associated with decreasing pressure in the direction of flow) helps balance the loss of momentum in the boundary layer. Downstream of the bluff body, momentum is extracted from the flow by an adverse pressure gradient. The adverse pressure gradient occurs as a consequence of the low pressure region around the tip(s) of the bluff body, which is associated with the maximum velocities observed at the tip(s) (this is the Bernoulli effect, but is often referred to as 'tidal streaming'). If there is not enough momentum in the boundary layer to overcome the adverse pressure gradient, the flow will reverse. Upstream of the flow reversal, the boundary layer flow is forced offshore. This injection of boundary layer flow into the interior free-stream flow provides a source of vorticity. Vorticity in the boundary layer of the shear sided topographic feature is generated by the 'speed torque' mechanism introduced in chapter 2.1.2. The strong shear encountered in the boundary layer ensures that the vorticity produced by the 'speed torque' mechanism is both intense and highly concentrated.

Boundary layer theory therefore adequately describes the flow separation process. The question still remains as to how an eddy feature is generated after the

flow separation occurs. The importance of the low pressure region at the tip of the bluff body in instigating flow separation has been described. The importance of the topographic feature in providing conditions suitable for supporting the existence of a strong pressure gradient is also now apparent. After separation occurs, the low pressure region is transported away from the topographic feature as part of the separated flow. The low pressure region is transported by the surrounding flow, but the presence of the low pressure also feeds back on the flow development, providing a favouring pressure gradient that acts towards the centre of the depression. An interesting balance of forces acts on fluid particles within the low pressure region. Frictional resistance can be assumed to be directly opposed to the flow direction in a shallow water flow regime (Cheng et al. 1993). In the Northern Hemisphere, the Coriolis force would oppose the pressure gradient in an anti-clockwise rotating eddy, and act in the same (favouring) direction in a clockwise rotating eddy. In the Southern Hemisphere the action of the Coriolis force would be reversed. From general observation of data available in the literature of shallow water flow around bluff bodies (Pingree, 1978; Wolanski et al., 1984; Ingram & Chu, 1987; Geyer & Signell, 1990; Davies & Mofor, 1990; Couch & Copeland, 1999), it appears that a low pressure region intense enough to instigate flow separation always provides a favouring pressure gradient strong enough to balance the opposing forces while the favouring upstream pressure gradient is maintained. Localised flow is therefore entrained around the low pressure region. The circulation established is referred to as an eddy. The centre of the eddy and the position of the low pressure region are coincident. As the localised fluid is transporting high levels of vorticity originating from the boundary layer, vorticity is intensely concentrated in the low pressure region. The process of vorticity transport around the low pressure depression is referred to as vorticity roll-up. An idealised simulation of the flow separation and eddy generating processes is presented in figure 6.1. The simulation was produced using the TFD model. The modelling conditions used are outlined in chapter 6.5. The Flamborough Head study discussed in the previous numerical model testing chapter (5.3), presents a good example of flow development around a headland that is dominated by the topographic eddy generating mechanism.

6.1.1 Secondary circulation generated by eddy features

A secondary effect observed to occur because of the presence of the eddy is the accumulation of sedimentary material at the sea-bed directly beneath the eddy. Pingree (1978) was the first to link the formation of sand banks commonly found in the vicinity of headland and islands to the occurrence of topographically generated eddies, features which had previously been generally accepted to be two-dimensional. In the depth-averaged situation described above, the effects of the pressure gradient, Coriolis force, flow momentum and bottom friction in the low pressure region are assumed to be in dynamic balance in order to ensure a closed circulation. Pingree suggested that as the flow velocity is reduced by the frictional effect approaching the sea-bed, the effect of the Coriolis force (assuming a clockwise rotating eddy in the Northern Hemisphere) would be similarly diminished. However, the influence of the pressure gradient would be maintained throughout the fluid depth. Accepting this supposition, the fluid nearer the sea-bed would converge towards the centre of the low pressure/eddy region due to the dominant influence of the pressure gradient brought about by the imbalance of forces. As the eddy is assumed to be in balance in two-dimensions, this must indicate that the effect of the pressure gradient is reduced nearer the sea surface creating flow divergence because of the consequent dominant influence of the remaining forces (summarised in diagram 6.1). In order to maintain continuity, upwelling must occur at the centre of the eddy. Pingree referred to this phenomenon as 'tidal stirring'. The hypothesis is supported by Ferentinos & Collins (1980), Wolanski et al. (1984, 1988) and Couch & Copeland (1999) who variously

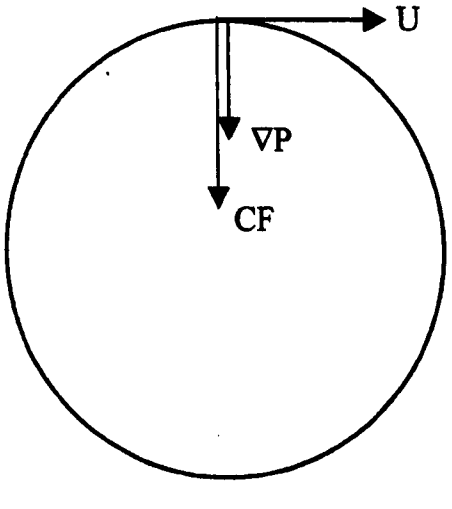

If ∇P = CF, circulation maintained.

If ∇P > CF, resultant velocity tends to spiral inwards.

If ∇P < CF, resultant velocity tends to spiral outwards.

∇P = Pressure gradient.
CF = Centripetal force.

Diagram 6.1 - Consequences of different force interactions on a fluid element in a re-circulating low pressure region.

used the tidal stirring concept to explain the accumulation of turbid water, waterborne eggs, larvae, plankton, and sedimentary material observed in the vicinity of bluff body features which exhibited topographic eddy generation. Tidal stirring would also appear to explain sea-surface temperature irregularities (patches of cooler water observed during the tidal cycle) reported in Nan Wan Bay, Taiwan (22°N, 120° 30'E) by Lee et al. (1999). Numerical modelling output and in-situ data presented by Lee et al. indicates that the cold water patches and topographically generated eddies in the region are coincident. Upwelling of cooler water from the sea-bed towards the sea surface caused by the tidal stirring effect would aid in explaining the regular occurrence of cold water patches in the bay. A final point to be raised regarding 3-dimensional effects associated with topographically generated eddies is that the theory should be equally applicable to any eddy, the method of generation should have no apparent influence on the occurrence of this phenomenon.

6.2 Bathymetric Eddy Generation

Bathymetric eddy generation is a topic generally ignored in the literature (Boyer & Davies, 2000). The only relevant studies that the author is aware of focus entirely on bathymetric vorticity generation mechanisms (Zimmerman, 1978, 1980; Pingree and Maddock, 1979, 1980; Robinson, 1981; Falconer et al., 1986) as outlined in chapter 2.1.2. Although vorticity is an important feature necessary to generate a bathymetric eddy, vorticity generation and transport are only two stages of the complete process. Topographic and bathymetric eddy generation follow a similar pattern of events, although the absence of a topographic feature alters the process and order of these events. In order to directly compare this mechanism with the previous topographic eddy generating mechanism, a sheer-sided bathymetric feature will be considered (e.g. a reef).

Having analysed the output from a number of numerical model runs, including the case outlined in section 6.5.3, the series of events that appear necessary to instigate a bathymetric eddy over a shoal are (with reference to figures 6.2 and 6.3):

1. Upstream of and over the upstream face of the shoal, pressure builds up because of the obstacle to flow discharge that the shoal presents. This creates a high pressure

region immediately upstream of the shoal which causes the upstream flow to diverge around it.

2. Over the top of the shoal, a low pressure region is formed as the flow velocity increases over the top of the shoal (this is the Bernoulli effect).
3. The majority of the upstream flow is forced to diverge around the shoal. With increasing flow velocity, momentum around the edges of the shoal increases, and the tendency of the divergent flow is to continue along its existing trajectory. Flow in the immediate lee of the shoal is restricted by the relatively small upstream discharge over the top of the shoal.
4. Two adjacent low pressure regions are created in the downstream lee of the shoal because of the velocity gradient between the flow sheltered by the shoal, and the flow diverted around the shoal. In the specialised case of a submerged headland, only one low pressure region would be observed.
5. As the two low pressure regions become established, the upstream flow divergence can be considered to be similar to the flow separation event described in the topographic case. Downstream of the twin low pressure regions, a high pressure region is established where the free-stream flow re-attaches (see figure 6.3).
6. Further downstream of the shoal the flow eventually returns to a rectilinear flow regime, as the flow is systematically re-distributed across the domain (i.e. the pressure gradient of the input wave is re-established as the dominant driving force as opposed to the locally derived pressure gradient created around the shoal region).
7. Positive vorticity is generated over the southern half of the shoal, and negative vorticity is generated over the northern half of the shoal (neglecting coriolis). The vorticity generating mechanisms observed in the case of a sheer-sided bathymetric feature are 'squashing and stretching' of the water column, and 'speed torque'. If a sloping shoal feature was considered, the third vorticity generating mechanism ('slope torque') would also be observed.
8. The vorticity generated over the shoal region rolls-up into the centre of the low pressure region in the lee of the shoal in a similar manner as described in the topographic generation section.

9. The combination of high vorticity and the balance of forces in the low pressure regions causes the flow to rotate around the centre of the pressure depressions. The rotating regions are restricted in extent by (i) higher pressure regions up- and downstream, (ii) by the free-stream flow around the low pressure regions created by the presence of the upstream high pressure region, and (iii) by the presence of the mirror low pressure region around the x-axis centreline (in this particular case).

The major differences between topographic and bathymetric eddy generation can therefore be summarised as:

- In the case of a sheer-sided topographic feature, vorticity is generated by the 'speed torque' mechanism, and is restricted to the boundary layer until flow separation takes place – this is the mechanism that instigates the conditions necessary for eddy generation.
- In the case of a sheer-sided bathymetric feature, vorticity is generated by the combined action of 'squashing and stretching' of the water column and 'speed torque' and is transported freely around the domain, as the vorticity is not restricted in any way by a boundary layer. Although there is strong flow divergence around the shoal and downstream circulation region, upstream flow still feeds into the two eddies, therefore no flow separation is observed.

The bathymetric eddy generation examined in section 6.5.2 displays two small, weakly rotating eddies. The height of the sheer-sided shoal required to generate this eddy pair is of a similar order of magnitude to the far-field depth. Analysis of a variety of different shoal heights (not shown) indicates that a significant shoal feature is necessary to independently generate eddies. Simply expressed, the height of the shoal is proportional to the strength of local pressure gradient, and the amount of vorticity produced.

Modelling a bathymetric depression to the extent of an order of magnitude deeper than the far-field depth does not produce an eddy feature. As bathymetric features exhibiting characteristics of this scale or larger are rarely encountered on the continental shelf, it is not expected that bathymetric vorticity generation by hollow depressions will generate eddies in the coastal zone. The work of Park & Wang (1994) suggests that tidal residual eddies can be observed in the region of

both shoal and hollow features, which is not surprising, as vorticity is still produced whenever flow encounters bathymetric change. However, unless the bathymetric variation is extreme, bathymetric eddy generation will not take place, as the influence of the bathymetry on the pressure gradients encountered in such regions is not significant enough to overcome the driving force of the tide.

6.3 Phase Eddies and Phase Lag Effects

Phase eddies are most commonly found in estuaries. In unsteady conditions, the high velocity and greater depth in the central part of the estuary allows the flow to maintain its existing trajectory against opposing pressure gradients. In shallower regions of the estuary, less momentum has been built up, and the flow is unable to overcome the opposing pressure gradient for as long a period as the flow in deeper regions. The observer therefore views this as two adjacent, oppositely directed currents at certain stages of the tidal cycle, which appears to indicate a large scale eddy, although what is really being observed is a strong shearing effect (Black & Gay, 1987). This phenomenon is nonetheless referred to in the literature as a phase eddy (even although there is no closed circulation). The phase difference observed during the tidal cycle should be locked in sync with the tidal period - this phenomenon is referred to as 'phase lock'. Black & Gay (1987) also highlighted the point that phase effects can be instigated not only by variation in depth but by any non-linearity in the flow domain. The interaction of tidal flow with bluff bodies presents a number of mechanisms that impart non-linearity to the flow. The importance of phase effects in determining the flow development around bluff bodies in the tidal environment would appear to be undervalued or ignored by the majority of investigators in the literature. Whether this ambivalence is due to lack of understanding of the arguments of Black & Gay (1987) or because of the complexity involved in separating out phase induced flow processes from other physical mechanisms is unclear.

One of the major objectives of this chapter is to highlight the importance of phase effects on flow development in the coastal zone. In particular, the analysis will be focussed on the influence of phase effects on the continued development of eddy systems previously generated by topographic or bathymetric features. As previously

outlined, direct comparison of the eddy generating mechanisms and the consequences of their combined interaction will be discussed in section 6.5 using output from the TFD numerical model.

Simple conclusions regarding the differences between this mechanism and the two previous mechanisms can be derived from consideration of the description of flow influenced by phase effects and from numerical modelling experience. The impact of both topographic and bathymetric eddy generation is most significant at tidal peaks, as this coincides with the strongest far-field flow velocity. Consequently the strongest vorticity generation and pressure differences between the far-field and eddy region occur as the tide peaks. Phase effects are maintained throughout the tidal cycle, as the phase is locked to the tidal period across the domain. However, the impact of phase effects on flow development will be most significant as the tide slacks, as the influence of the other mechanisms is minimised at this time. Topographic and bathymetric eddy generation can both be considered to generate 'true' eddies because they have a closed circulation, whereas although phase eddies observed from an Eulerian snapshot may exhibit recirculatory features, no closed circulation is apparent. This point will be further discussed in section 6.5 using a Lagrangian analysis technique (particle tracking) to analyse the nature of the circulation. Finally, phase effects and flow features referred to as phase eddies occur independently of vorticity generation or transportation. Vorticity generation and subsequent transportation is a key feature necessary for either a topographic or bathymetric eddy to develop.

As phase effects are one of the major mechanisms which disrupt rectilinear flow (through non-linear interaction), incorporating these effects must be given proper consideration in application of numerical and physical models. This is one of the major reasons why it is necessary when considering tidal analysis to 'warm-up' the modelling system for one or more tidal periods in order to ensure that phase effects and other non-linear processes are present in the simulation. This is also why the use of uni-directional analysis techniques (i.e. steady state flow) is of limited application when considering tidal situations, as many aspects of the flow are lost from the analysis. Accurate boundary specification is also of paramount importance in ensuring that the correct phase is established in the domain.

From the points raised in this and the previous section of the discussion, the three mechanisms outlined can be considered to be separate events, even although their occurrence can be very involved, as each of the three mechanisms regularly contribute to the flow development in the coastal environment. The interaction of the individual eddy generating mechanisms will be considered in section 6.5.

6.4 Numerical modelling issues relating to the simulation of eddies

Numerical models have a proven track record as analysis tools applied to coastal flow problems and across the wider fluid mechanics field. At times however, the engineering community has become over-reliant on numerical model output. A number of modelling derived problems or flawed analysis techniques continue to crop up in the literature even although earlier literature has at least identified the cause of the problem. The purpose of this section is therefore to identify these common problems. This discussion is necessary before beginning an in-depth analysis of numerical model results or output in order to ensure that the author does not succumb to the same mistakes or bad practice.

6.4.1 Eulerian and Lagrangian analysis techniques

The solution of the shallow water equations using the TFD model follows the standard modelling practice of using finite-difference techniques on a uniform grid. This is an Eulerian method of analysis, as the information is calculated and stored at a set of fixed points, or nodes across the domain. This is a perfectly acceptable and mathematically sound method of analysis. However, there is a tendency in the literature to extend this Eulerian view-point further, and average the model output at each node across a tidal cycle,

$$[U(x,y),V(x,y)]=\frac{1}{T}\int_{t_0}^{t_0+T}[h(x,y)+\eta(x,y,t)]\times[u(x,y,t),v(x,y,t)]dt. \quad (6.4.1)$$

The output from this equation is referred to as the Eulerian transport velocity which describes the time averaged volumetric flux per unit width (Cheng et al., 1993). A similar, but more commonly applied representation is the Eulerian residual transport velocity which is equivalent to equation (6.4.1) divided by the mean water depth (used by Tee, 1976; Pingree & Maddock, 1977; Prandle, 1978; Postma et al. 1989;

Falconer & Owens, 1990; Ridderinkhof & Zimmerman 1990(a)). While there is nothing wrong in theory with the visualisations produced using these procedures, the authors listed then went on to interpret the transportation of wastewater products and sedimentary material over the short and long term using these Eulerian residual velocity fields. This is an incorrect application of these physical properties as they are Lagrangian phenomena, and must therefore be studied in a Lagrangian manner (Awaji, 1982). The important concept ignored by this Eulerian viewpoint is the time dependence of any non-linear processes occurring in the domain. This has been generally understood since the analysis of Imasato (1983), who stated that "The Eulerian residual current is only a mathematical representation of the tide-induced transient eddy or the result of the averaging process of transient phenomena, and has no physical basis". Nevertheless, Eulerian residual results are still repeatedly presented and manipulated in the literature. In order to demonstrate the problems encountered when using Eulerian residual velocity results to determine long-term transport rates, a short numerical experiment will be considered. The flow development around a (roughly) circular island surrounded by a uniform depth of 20 metres, with Manning's n value of 0.025 $sm^{-1/3}$, no Coriolis force, and sinusoidally varying input wave of amplitude 1 metre and tidal period 12.4 hours will be examined ($Re_f \approx 3.94$). The simulation was run for two complete tidal periods, and the Eulerian residual transport velocity was calculated over the second tidal cycle (figure 6.4(a)). The four residual eddies are mathematical representations of the transient eddy pairs generated in the lee of the island during the flood and ebb tides. A simple Lagrangian particle-tracking model was then applied to the results in two stages (no random step is included in the computation, the direct results from the TFD model simulation alone are used). Initially a set of particles was tracked for an equivalent tidal period (12.4 hours) using the Eulerian transport velocity as advocated by the authors listed previously (figure 6.4(b)). The results of the final position of each of the particles varies significantly when compared to the results obtained when the same particle-tracking analysis was applied across the tidally varying velocity fields output during the second tidal cycle (figure 6.4(c)). The contrasting finishing position of each of the particle tracks indicate that using the Eulerian residual velocity field in this manner is a fundamentally flawed procedure.

6.4.2 Vorticity roll-up demonstration

In section 6.1 the transportation of high levels of vorticity originating from the boundary layer into the low pressure region shed from the headland tip during flow separation was referred to as 'vorticity roll-up'. Although this theory is accepted in the literature (Imasato, 1983; Signell & Geyer, 1991), practical visualisations of the process are lacking. The following case is presented as an example of vorticity roll-up. Selecting a simple situation, consider the flow separation arising around a coastal scale backward step feature where the flow is ramped up to steady state and maintained at that level for the duration of a tidal period. Using a cell size of 250 metres on a uniform grid of 70 × 43 cells, uniform bathymetry of 20 metres, step extent of 20 cells (5 kilometres), Manning's n value of 0.025 $sm^{-1/3}$, and input wave amplitude of 1 metre (free-stream velocity = 0.5 ms^{-1}, Re_f = 1.77), the flow develops as presented in figure 6.5(a-d). Using the same Lagrangian particle tracking technique as in section 6.4.1, the transportation of four individual parcels of water in the flow (particles) can be visualised (no random step is included in the computation, the direct results from the TFD model simulation alone are used) (Figure 6.6(a)). The results indicate that particles released close to shore upstream of the headland tip interact with the eddy region generated around the backward step, and can be repeatedly caught up in and released from the eddy core. Particles released further offshore are carried downstream in the free-stream region without interacting with the eddy feature. While this representation is of general interest in indicating the interaction of the flow features and individual parcels of water, there is no indication of vorticity roll-up. In order to visualise the vorticity roll-up phenomenon it is necessary to alter the particle tracking model to release a continuous stream of particles at a set interval (30 seconds in this case). The output (figure 6.6(b)), demonstrates the systematic roll-up of the particle streams (in this case representative of a continuous stream of water parcels, considered to exhibit high levels of vorticity). Figure 6.6(c) presents the vorticity contour plot associated with the timing of the output in figure 6.6(b). Peak vorticity values are coincident with the centre of the eddy and particle track, indicating that the transportation of vorticity is mirrored by the particle transport presented. This short case study indicates the importance of

correctly interpreting the numerical procedures being applied and their relevance to the real physical environment.

6.4.3 Numerical generation and transportation of vorticity - a question of scale.

Having indicated in the previous section how vorticity is systematically rolled-up around the low pressure region shed from the headland tip during flow separation, it is necessary to discuss the generation and subsequent transport of vorticity by numerical models. The difficulty of modelling flow processes using large cell sizes when the boundary layer is of importance is a constant topic of concern and discussion in the numerical modelling community. The inability to properly represent the boundary layer because of the disparity between cell size and boundary layer width has dominated much of the subsequent modelling development. Various branches have become established in the numerical modelling community, each advocating different methods of tackling the boundary layer – cell size problem. A common technique applied is the use of variable grid sizes in order to concentrate the numerical effort in areas where there are strong velocity gradients (in particular the boundary layer region). These techniques include grid nesting (Verboom et al. 1984; van Pagee, 1989), curvilinear co-ordinates (Signell & Geyer, 1991; Rodenhuis, 1994), telescoping grids (Rodenhuis, 1994) and quadtree-meshing (Leon, 1997; Copeland et al., 1999). The TFD model used throughout this project is a standard numerical model operating on a fixed uniform grid. The TFD model has been developed to allow the specification of either a no-slip boundary condition (i.e. attempting to generate a boundary layer at the sea-land interface), or free-slip boundary condition (i.e. no attempt to model the boundary layer). Interest in numerical modelling of vorticity generation and transportation arose from the intention to accurately model processes potentially important in determining subsequent flow development. Special attention was therefore paid to properly specifying the convective momentum and eddy viscosity terms in the shallow water equations as discussed in chapter 3. However, during tests of flow separation around a backward facing step (Δx = 250 m, uniform depth = 20m, free-stream velocity = 0.5 m), the importance (or lack of) of boundary type specification became apparent (see the comparison in figure 6.7). The difference in the lee of the headland for both the

vorticity contour and velocity vector plots (comparing no-slip and free-slip results) throughout the simulation was negligible. This raised obvious concerns that something was wrong with the modelling code. After some thought, it was re-called that laboratory scale flows modelled previously using the TFD model generated apparently sensible boundary layers, and consequent vorticity fields. It was therefore deemed necessary to investigate how the numerical model operated at laboratory scale. A similar case to the backward-step examined in figure 6.7 (coastal scale), will be examined at laboratory scale using appropriate non-dimensional numbers for scaling purposes (Fr = 0.00127, Re_f = 1.771, K_c = 4.464, with a vertical exaggeration of 1:100). The scaling produces model conditions of free-stream velocity = 0.5 ms^{-1}, Δx = 0.025 m, uniform depth = 0.02 m (i.e. vertical exaggeration of 1:100). The numerical simulations with no-slip and free-slip boundary conditions were both ramped up to steady state over an equivalent quarter tidal period derived using the Keulegan-Carpenter parameter (results presented in figure 6.8). Although differences are noticeable between the coastal and laboratory scale results if the simulation is maintained at steady state for a prolonged period of time, the laboratory scale results obtained at equivalent peak tide display excellent agreement with the larger scale analysis. What is learned from the simulations is that the no-slip and free-slip boundary conditions are operating correctly, as indicated by the model scale results. The difference between the two cases is that at prototype scale the cell size precludes the set-up of an effective boundary layer, whereas at model scales, no such problem arises. However, in both the prototype and model scale results, the difference in the extent and strength of the eddy region is largely unaffected by the boundary slip condition selected. This is an interesting, if not unexpected result at prototype scale, as the transfer of energy between the theoretical boundary layer and free-stream is determined by the turbulent shear stresses described in the model using the eddy viscosity term (chapter 3.3.2.2). As the spacing of variables is determined by the cell size, and the eddy viscosity term calculation is based upon the gradient of velocity, the value of the eddy viscosity term is very small in comparison with the other terms in the shallow water equations. In the model scale analysis however, the cell size is such that a boundary layer is established in the no-slip case over an area 5–6 cells wide, and vorticity is therefore effectively transported downstream and away from the

boundary layer. As the laboratory scale cell size is more appropriate for describing the boundary shear layer, the same velocity difference observed at prototype scale over 250 metres occurs over a distance of 0.1 - 0.2 metres at model scales. The velocity gradient produced at laboratory scale is consequently 3 orders of magnitude larger than at prototype scale. The impact this has on the flow is demonstrated by the existence of the boundary layer in the laboratory scale analysis where the no-slip condition is imposed (figure 6.8(a) and (b)). Surprisingly, the impact on the downstream eddy region simulated is still negligible, in both the vorticity, and velocity plots, when comparing the output of the no-slip and free-slip simulations. This conclusion is of great significance, as it suggests that the generation and transport of boundary layer vorticity has a limited influence on downstream flow development *when considered from the numerical modelling view-point.* When the numerical model is unable to properly generate a boundary layer (as is obviously the case in both the prototype and model scale free-slip boundary simulations), this points to another source of vorticity which occurs at the flow discontinuity established at the headland tip. Comparing the results obtained from the model scale results around the headland tip after separation, the no-slip case indicates that the difference between the separated boundary layer flow velocity and the flow velocity in the sheltered area in the immediate lee of the headland region is approximately half the size of the difference observed in the free-slip case. At this point, the discontinuity between the separated flow and sheltered flow provides a strong vorticity generating potential because of the strong shear between the two regions. As the shear is demonstrably stronger in the free-slip case, more vorticity would be generated. The difference in overall vorticity consequently transported into the downstream flow interior by the flow separation between the free-slip and no-slip cases appears to be minimal as is indicated by consideration of the cross-sections of the depth-averaged vertical component of vorticity (ϖ) in figure 6.9. These results indicate that the model is able to generate a realistic downstream eddy region at coastal scales even although no upstream boundary layer was established in the free-slip model analysis. This is a very important point to understand, as the TFD model, and models reliant upon similar discretising techniques (e.g. Pingree & Maddock, 1977; Falconer 1984) are all subject to this false numerical procedure which proxies for the effect of the boundary

layer in generating vorticity in the model domain when the flow separates. At coastal numerical modelling scales, where the cell size is so restricted by computational expense that it is unrealistic to expect to properly model the boundary layer, boundary condition specification can be considered to have a limited influence on the flow development. The need for a complex eddy viscosity model at such scales is also questionable (Rodi, 1980), as the associated direct and lateral shear stresses are deemed necessary in the modelling exercise for two main reasons. These are (i) to support the boundary layer by transferring energy between the boundary flow and free-stream, and (ii) to transfer energy across streamlines (theoretically necessary to maintain a closed circulation (Flokstra, 1977; Ponce, 1981). As a boundary layer is not properly established at coastal scales, one of the major arguments supporting the need for complex eddy viscosity models is invalidated (although acknowledging that at different scales such models are appropriate). Furthermore, the level of energy transfer across streamlines required to overcome friction is relatively small in the slowly rotating eddies observed in the coastal environment. In some numerical models it is therefore possible to run with very small eddy viscosity coefficients (or even no eddy viscosity), and still maintain a closed circulation. This apparent divergence from theoretical understanding is credible, because it is impossible to avoid introducing at least some numerical diffusion into the calculation when using the finite-difference approach. The effect of numerical diffusion on the solution is to transfer energy in an analogous manner to the action of numerically modelled turbulent diffusion. In the TFD model, numerical diffusion has been limited by providing higher-order schemes in the calculation of the convective momentum terms, as outlined in chapter 4.1.2, and demonstrated in chapter 5.2.3. The ability to run the model with very low levels of eddy viscosity demonstrates the stability of the TFD code, as many similar models (e.g. Hyder & Elliott, 1995; Galloway et al. 1996) require the specification of what can be considered to be excessively high values of eddy viscosity (1 - 10 m^2/s) in order to overcome instabilities. The need for such an excessive amount of damping in order to produce an acceptable solution suggests deficiencies in these program codes.

In conclusion, this discussion has highlighted the important effect of scale on the manner of vorticity generation in numerical models. When the boundary layer is

adequately described across a number of cells in the simulation, boundary slip prescription and energy transfer by eddy viscosity have a significant effect on the flow development. If however interest is focussed at coastal scales where it is unlikely that the boundary layer can be adequately replicated, these processes become irrelevant. Although this causes grave concern regarding the ability of numerical models to produce an accurate simulation, the generation and transport of vorticity in the boundary layer would only be of significance on the overall flow development if the flow were to separate. As has been demonstrated, when flow separation does occur, the act of separation itself in the numerical model produces a similar pattern of vorticity generation and vorticity at the point of separation as would be expected from the combined action of the boundary layer and flow separation observed in the real world. Consequently, the development downstream of the flow separation is comparable in both the prototype numerical simulation and in the real world, even although the upstream vorticity generating processes in the two cases can not be directly compared.

6.4.4 Comparison of headland and symmetrical island flows

Interest in flow development in the coastal environment pays particular attention to headland and island features, in both the existing literature and this document itself. It is often implicitly suggested that the flow observed around an idealised symmetrical island can be considered equivalent to the flow around a headland of equivalent half-width (due to the symmetry of the results expected around the island). An important constraint on this approach is that the effect of Coriolis must have a limited influence on the solution (i.e. a small Rossby radius condition). This criterion is often met in the literature by removing the Coriolis effect completely from the numerical procedure (or in laboratory studies the scale of analysis makes the Coriolis effect negligible). Such idealisation of the physics increases the general applicability of the research output, as the relative strength of the Coriolis force would be related to the specific locality being investigated. Accepting this simplification (no Coriolis applied), an idealised numerical experiment investigating the level of agreement obtained using equivalent island and headland cases was set-up. Using appropriate domains (a sheer-sided island ($Re_f = 3.54$) or headland ($Re_f = 7.08$) surrounded by a uniform depth of 20 metres), and applying the

same driving conditions and specification of characteristic values to each, the results presented in figure 6.10(a, b) were obtained. Direct comparison of these results is aided by figure 6.10(c), which shows the residual velocity values obtained by subtracting the results from the headland case from those obtained using the island domain. These results give a clear indication that in the correct circumstances, island and headland results can be directly compared. This would not however be the case in a realistic case study based situation, as a perfectly symmetrical domain is not a natural occurrence - any conclusion drawn from comparison of the two systems must remain as a theoretical supposition. This restriction is brought home in cases where eddy shedding is observed in an island domain simulation. Eddy shedding can often be instigated by interaction of the two separated regions established at the island tips. In the headland situation the same interaction would not take place (only one separation event), and eddy shedding would not necessarily be expected (see chapter 7 for further discussion on eddy shedding). This is highlighted by the flow development around Rattray Island to be discussed in chapter 8, where only one eddy region is observed, even although experience of headland flows would suggest that each island tip would produce an individual re-circulation (Furukawa & Wolanski, 1998).

6.4.5 Influence of lateral boundary specification on numerical model output

While replicating the numerical modelling work of fellow researchers reported in the literature, to better understand their hypotheses, and test out the flexibility and reliability of the TFD numerical model, the importance of lateral domain extent and boundary specification on the results obtained became apparent. A series of simple numerical modelling experiments will be presented to demonstrate the importance of these aspects of the numerical simulation, and their impact on the solution obtained. The domains used were of length 120 cells and width varying between 20 – 60 cells. The cell size is 50 metres of uniform depth 20 metres, which necessitates a calculation time-step of 1 second to comply with the Courant condition (Cr = 0.281). A symmetrical island feature of extent 10 × 3 cells is included (see figure 6.11(a)) to provide a representative 'barrier' to the flow which will generate a flow interaction with the lateral boundary (Re_f = 17.71). The input flow condition is

ramped up to steady state from cold conditions over the duration of a quarter tidal period, and maintained until steady state has been achieved across the domain (adjudged to have been reached after 7.5 hours simulation time). Comparison of the results obtained at this time are presented in figure 6.11(b, c), with reference to the cross-section just upstream of the island as indicated in figure 6.11(a). The results for all the cases examined show good agreement close to the centre of the domain where the flow is forced to diverge by the presence of the island feature. As the results are analysed adjacent to the island tips out to the lateral boundary, the influence of the selected criteria presents a damning indication of the significant effect the lateral boundary width has on the results obtained. What is occurring in each of the simulations using free-slip boundary conditions is that, as the flow perpendicular to the boundary is set to zero (see chapter 4.3.2), what is being modelled is essentially a channel configuration. Between the channel walls and the sheer-sided island, the upstream flow converges. The channel width therefore dictates the increase in discharge (and consequently velocity) between the island tips and sidewalls. As the channel width increases, the ratio of the amount of flow diverted by the island feature to the flow in the free-stream reduces linearly. The downstream effect of this (not shown) is that the narrower the channel the longer the extent and greater the strength of re-circulating eddy region produced. This is because the higher flow velocity observed at the island tips as the flow develops produces a larger adverse pressure gradient due to the Bernoulli effect, and higher levels of vorticity are generated around the island. Similar results would have been produced if a headland configuration had been examined. As the real intention is to model a small segment of the oceanic environment, the channel wall constraint is adversely influencing the accuracy and representative nature of the numerical simulation. Using a radiating lateral boundary condition produces the smallest currents around the island tips as shown in the comparative results in figure 6.11(b, c). This is because the flow is able to develop more naturally, with the upstream flow divergence being accompanied by flow divergence at the lateral boundaries, and similarly downstream flow convergence is observed both within the domain and at the lateral boundaries. Use of the basic gravity wave radiating condition at the lateral boundaries would from the results of this simple test present a more realistic simulation than using a free-slip

condition as is normally the case in the majority of the existing literature. Although such an apparently simplistic radiating condition may not present a completely realistic simulation, it presents a significant improvement in both realism and accuracy over using the free-slip boundary condition as indicated by the results presented.

6.5 Comparison of Eddy Generating Mechanisms

A series of tests have been carried out using the TFD numerical model to demonstrate the existence and individual features of each of the three eddy generating mechanisms. From the descriptions presented earlier in the chapter, individual characteristics can be attributed to each mechanism. In the case of topographic eddy generation, the key feature is the occurrence of flow separation instigated by a low pressure region downstream of the headland tip(s), and the consequent flow discontinuity encountered. In order to ensure the occurrence of these features, the domain must incorporate a significant topographic feature. Bathymetric eddy generation relies on a similar low pressure region creating a region of high vorticity which instigates an eddy. The occurrence of the eddy in the flow domain forces upstream flow separation, as the flow is forced to diverge around the discontinuity (eddy). The source of vorticity in the domain in this case is from interaction with non-uniform bathymetry. The variation in bathymetry must be either large or occur in rapid succession in order to generate significant amounts of vorticity, and overcome diffusion and dissipation processes. Phase eddies occur in regions where there is a feature or features (topographic and/or bathymetric) that cause a phase lag to occur, and only occur in oscillatory (tidal) flows. The important difference when considering phase eddies is that their occurrence is independent of vorticity transportation. Another key difference is that phase eddy effects are most significant as the tide slacks, whereas for the other two mechanisms, tidal peaks coincide with their strongest effect.

A symmetrical domain of uniform depth 20 metres will be applied throughout the test procedure, with topographic and bathymetric features incorporated when required. The domain incorporates a regular grid of extent 70 cells × 43 cells. An odd number of cells in the y-direction are necessary to ensure a completely symmetrical domain because of the layout of the variables across the cells (this is

only true when radiating boundary conditions are being applied. For a 'channel' domain, an even number of cells would also have been acceptable). The cell size is set at 250 metres, providing a domain of 17.5 km × 10.5 km. A time-step of 5 seconds was selected to satisfy the Courant condition (Courant number = 0.28 when depth = 20 metres), with Manning's friction coefficient set at 0.025 $sm^{-1/3}$. Elevation input conditions will be applied, with the tidal amplitude fixed at 1 metre for each simulation. The free-stream velocity at peak tide in each of the simulations is around 0.5 ms^{-1} (although there is some variation depending upon the exact set-up of the domain in each case). The 'equivalent' Reynolds number, $Re_f = 3.22$ in each of these cases. The 'equivalent' Reynolds number was derived using Mannings representation of the friction coefficient $\left(C_D = \frac{gn^2}{H^{\frac{1}{3}}} \right)$, so that $Re_f = \frac{H^{\frac{4}{3}}}{gn^2L}$. The input condition will either be applied as an unsteady sinusoidal varying tidal wave (period = 12.4 hours), or ramped up to steady state conditions over an equivalent quarter tide (both cases operating from a 'cold' start). All the steady test cases are allowed to run for 45000 seconds (equivalent to a complete tidal cycle). It is acknowledged that steady state conditions are not relevant when considering a tidal situation. However, the continued development of the flow introduces interesting points for discussion regarding time and length scale considerations. For the unsteady test cases, the flow is allowed to develop for a complete tidal cycle before examining the output produced in order to allow non-linear processes to become fully established in the domain.

During the test procedure situations will be introduced that bear little resemblance to reality. This is necessary to properly construct an argument outlining the different eddy generating mechanisms. In order to demonstrate each mechanism in isolation, it is necessary to investigate such hypothetical situations. The value of developing a numerical model is underlined by the ability to pose such hypothetical questions and still obtain a representative solution based upon the equations and boundary conditions applied. Application of the traditional methods of observation, analogy and physical modelling would not be possible in this situation, as it is not such an easy proposition to disable aspects of the laws of physics in the real world.

6.5.1 Standard case simulation (topographic eddy generation)

The first case to be considered demonstrates topographic eddy generating effects in isolation. It is therefore necessary to completely remove the influence of the other two generating mechanisms from the simulation. To avoid phase effects, the model is ramped up from a 'cold' start condition, and then maintained at steady state (equivalent to peak flood tide conditions). This eliminates the influence of tidal periodicity from the results. The influence of bathymetric variation is removed by using a uniform depth across the domain. Topographic variation is imposed on the simulation using a sheer-sided symmetrical island positioned in the centre of the domain as shown in diagram 6.2 (as for the domain width, the topography must span across an odd number of cells to ensure computational symmetry in combination with the specified boundary conditions). The input condition is imposed uniformly across

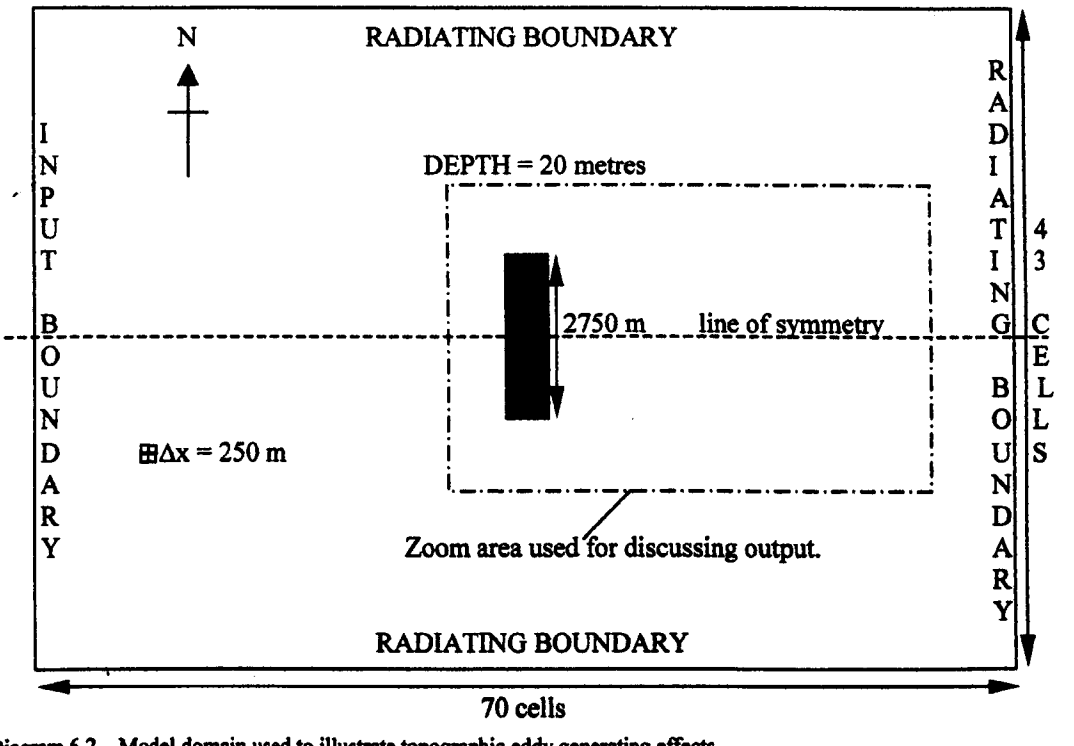

Diagram 6.2 – Model domain used to illustrate topographic eddy generating effects.

the western boundary (i.e. no Coriolis force is considered), with the other three boundaries radiating. These model parameters should provide an exactly symmetrical set of results along the x-axis centreline. The model is set-up in this manner to avoid the numerical modelling problems described in the previous section, and also to avoid the possibility of eddy shedding (discussed in chapter 7). The results presented in figure 6.1 highlight the flow development through the stages of attached flow, flow separation and vorticity roll-up as would be expected from the original description of

the consequences of flow interaction with topography. This initial simulation will be considered a standard case against which subsequent simulations will be compared and contrasted.

As a simple exercise to demonstrate the likelihood of flow separation around a topographic feature of similar lateral extent to the original island. A number of simulations were run using the same modelling conditions while systematically altering the island shape. The refined solution presents a more streamlined obstacle to the flow in an attempt to maintain an attached flow regime. The resultant island shape and flow development is presented in figure 6.12. This demonstrates that a highly streamlined shape is necessary to avoid flow separation under these conditions. This demonstrates that in any reasonably energetic coastal environment, flow around the majority of islands of extent 2 – 3 kilometres would exhibit flow separation.

6.5.2 Bathymetric Eddy Generation Simulation

In order to isolate the effect of bathymetric eddy generation, it is necessary to maintain the steady state analysis as for the previous case, and to remove the topographic feature from the domain. The sheer-sided topographic feature will be replaced by a sheer-sided sea-mount of crest depth 2 metres, while maintaining the uniform depth of 20 metres across the rest of the domain. Although this bathymetric set-up is uncommon, the idealised domain simplifies the analysis of the results obtained, and could be considered to be representative of a reef. Otherwise, the test conditions are as for the previous simulation. The depth-averaged results presented in figure 6.2 are obtained at the same stage of the simulation as for the previous topographic case, enabling direct comparison. Although both simulations display many similarities, there are two features which differentiate the mechanisms. The first of these can be observed directly in the vorticity contour diagrams – in the topographic eddy generation case, vorticity is only generated in the boundary layer, whereas in the bathymetric case vorticity is generated in the flow region over the shoal. The vorticity generating mechanism in the topographic case would be by 'speed torque' alone. In the bathymetric case, two of the three vorticity generating mechanisms would be acting ('speed torque', and 'squashing and stretching' of the water column). The simple conclusion from this would be to expect higher levels of

vorticity in the bathymetric case, as the input velocity conditions are the same in both cases. This however, is not reflected in the results. This is because the topographic feature generates large amounts of speed torque because of (i) the no-slip topographic boundary condition, (ii) the stronger tidal streaming effect around the feature, and (iii) the discontinuity in the flow created by the separation events. Furthermore, in the sea-mount case, some of the vorticity generated on the upstream face would be negated by the creation of vorticity of the opposite sense as the flow traverses the downstream face of the shoal. Overall the difference in the levels of vorticity in the two cases is reflected by the stronger re-circulation observed in the topographically generated eddies, and the slightly larger width and downstream extent of the eddy pair. The other significant difference is of course the total flow separation at the downstream island tips observed in the topographic case prior to the eddies being generated, whereas the flow in the bathymetric case cannot be considered to have undergone separation. The strong flow divergence around the shoal and flow discontinuity created by the eddy regions and the associated pressure gradients is not indicative of a flow separation event.

Comparison of the topographic and bathymetric cases has demonstrated that although the velocity plots generated in both cases may be similar, the underlying physical processes are substantially different. The highly idealised domains examined have proved to be necessary in order to separate out the combined action of the two processes which would have occurred if a real domain had been analysed. An extension of these two cases combining the action of the two mechanisms is discussed in section 6.5.4

6.5.3 Phase Eddy Simulation

Unfortunately it is almost impossible to construct even an idealised situation where phase effects can be observed in isolation. One of the major differences between phase effects and the other generating mechanisms is that this mechanism is independent of vorticity transportation. If vorticity were to be transported through the domain, then the other two mechanisms would be observed to some extent. In order to disable the transportation of vorticity, it is necessary to remove the convective terms from the momentum equations. As tidal periodicity is of key importance in

generating phase effects, the tidal wave input condition (period = 12.4 hours) is specified at the input boundary. The same domain is used as for the datum case (diagram 6.2), with the refinement of a 5 metre shelf region added in the lee of the topographic feature, extending from the island to the eastern edge of the domain. If the shelf region is not included in the simulation, a near potential flow solution, as would be expected for a very low Reynolds number laboratory flow is achieved (for example see Batchelor, 1967, or Schlichting, 1979). The initial results (see figure 6.13) are extracted from the first tidal cycle to draw direct comparison with the previous cases (i.e. the non-linear effect has not become fully established as the simulation is started from a uniform state). As the influence of the phase lag is best observed as the tide slacks, the results are concentrated around this stage of the tide. Figure 6.13(a) obtained as the flood tide peaks can be directly compared with the topographic and bathymetric simulations in figures 6.1(c) and 6.2(c). In figure 6.13(a) the flow has remained attached to the topography, no eddy feature is apparent, and the vorticity plots demonstrate that although vorticity is being produced in the domain, there is no subsequent vorticity transport (i.e. the vorticity contours are solely indicative of shear in the flow). This is because vorticity transportation requires the convective momentum terms. A comparison of the elevation contours across the domain between the topographic and phase simulations as the flood tide builds is presented in figure 6.14. The elevation low occurring at the headland tip in the topographic case, contrasts with the near-potential flow solution obtained from the phase dominated simulation due to the absence of the convective momentum terms. In both cases, the spacing of the elevation contours can be seen to be indicative of increasing flow velocity upstream of the headland tip, and decreasing velocity downstream. This is due to the pressure gradient reacting to the presence of the flow obstacle in the middle of the domain (tidal streaming). In the topographic case, this effect is observed to be markedly stronger, with peak velocities occurring at the headland tips throughout the majority of the simulation. Consideration of the Bernoulli equation would suggest that an area of low pressure would be associated with the peak flow velocity, and this is reflected in the topographic case. The low pressure region was not observed in the phase dominated simulation, as removing the convective momentum terms from the momentum equations has invalidated the

physical basis of the equations – that the total energy along a flow streamline is considered to remain constant. The existence of the low pressure region at the headland tip accounts directly for the adverse pressure gradient set-up downstream of the headland in the topographic case. Once the low pressure region and adverse pressure gradient become established, flow momentum is eroded in order to overcome the opposing pressure gradient (kinetic energy is converted to potential energy). Initially, this did not pose a particular problem, as the strength of the opposing pressure gradient is dependent upon the velocity at the headland tip, which creates the low pressure region. The question therefore arises as to why under certain circumstances, the flow is unable to overcome the adverse pressure gradient. Signell & Geyer (1991) demonstrated analytically that frictional losses incurred by the flow as it traverses the low pressure region ensure that in the shallow coastal environment, it is almost impossible for flow to remain attached once an adverse pressure gradient has become established. As the removal of the convective terms from the shallow water momentum equations is the only difference between the two simulations, the importance of the pressure gradient around the topographic feature (as described by the Bernoulli effect) is highlighted by the contrast in the subsequent flow development demonstrated and discussed.

Returning to the phase dominated simulation (figure 6.13), as the tide begins to slack (HW+2), the phase lock associated with the two flow regions, delineated by the depth change and sheltering of the shallow region by the topographic feature, becomes apparent. The situation in figure 6.13(a) at high water demonstrates the peak flow velocities achieved over the two regions. After the flood tide peaks, the comparative lack of flow momentum over the shallower region is overcome by the combined action of the opposing pressure gradient, and stronger influence of bottom friction within two hours (figure 6.13(b)). In contrast, in the adjacent deeper unsheltered region, the flooding currents are maintained until HW+3 hours. During the period between HW+2 hours and HW+3 hours, when the flow directions are opposed over the two flow regions, an Eulerian view of the overall flow suggests that an eddy may have been created across the region of bathymetric change. Lagrangian analysis throughout the tidal cycle using a direct particle tracking technique demonstrates that there is no circulation (figure 6.15(a)), all that is being observed in

the Eulerian view is a strong shearing effect across the bathymetric gradient, which is manifested in the elliptic tidal pattern obtained. In comparison, the same analysis applied to the combined topographic and phase case to be discussed in section 6.5.4 highlights the existence of the re-circulatory region in this case (figure 6.15(b)). In both cases, the exact symmetry of the results around the x-axis centreline presents supplementary evidence of the accuracy of both the boundary conditions in operation, and the centring of the finite-difference equations.

6.5.4 Effects of combining eddy generating mechanisms

In the preceding sections, the three possible eddy generating mechanisms have been presented and discussed using idealised situations. In the real world, the mechanisms can be expected to combine and interact to influence the flow development. Figures 6.16 - 6.19 demonstrate the combined effect of the mechanisms, initially in pairs, and finally all three acting together. Based upon the previous analysis, the influence of the mechanisms upon each other are reasonably self-explanatory from the figures presented, therefore the discussion will be kept to a minimum. The same domain and modelling conditions are applied as for the previous examples. Beginning with the combined topographic and phase (tidal) effect, the results presented (figure 6.16) are obtained during the second tidal cycle in order to allow phase (and other non-linear) effects to become established. Results from before and after high water are necessary in order to highlight the importance of phase effects as the tide reverses. The results obtained differ significantly from the results of the steady topographic case (figure 6.1). As peak flood tide approaches, the separated flow region becomes very lethargic, and a 'dead zone' of virtually no-flow occurs. After high water, the significant difference in flow momentum in the dead zone and free-stream region, combined with the high levels of vorticity trapped in the no-flow region produces conditions where a far stronger eddy region is observed as the tide slacks than at peak tide conditions. This is a direct consequence of the phase influence on the solution, and is maintained until the ebb tide becomes established. The circulation generated during the flood tide is still in existence throughout the following ebb tide, as can be ascertained from the vorticity patch in the vorticity plots (as an example, the ebb tide eddy vorticity can be tracked through the flood tide

presented in figure 6.16). However, the relative magnitude of the flow generated is insignificant in comparison with the flow generated by the input wave pressure gradient, and is therefore masked by the main flow. For further discussion of the longevity or life-span of eddies see chapter 7. Overall this case provides a good example of the interaction of topographic and phase effects.

Figure 6.17 outlines the interaction of bathymetric and phase effects. Apart from the differences between the original topographic and bathymetric eddy generation, this case is very similar to the previous case in figure 6.16, and most of the same arguments can be applied to describe the flow development as influenced by the two mechanisms.

Topographic and bathymetric effects are combined by including a 4 cell slope of uniform gradient (5 metres per 250 metres), around the original island presented in diagram 6.2. Phase effects are removed from the simulation by ramping up to, and then maintaining a steady state input condition. The results obtained (figure 6.18) can be directly compared with the original topographic and bathymetric cases (figures 6.1 and 6.2 respectively). The most obvious differences are that the circulation obtained is stronger than in either of the cases using the mechanisms individually, and that the flow separates from the topographic feature at the upstream tips of the island rather than at the downstream tips (compare figures 6.1(c) and 6.18(c)). The increased circulation is because the overall level of vorticity generated around the feature in the domain is increased by the combination of the mechanisms. The bathymetric feature contributes slope torque, speed torque and the stretching and squashing vorticity generating mechanisms. The topographic feature contributes a further speed torque effect due to the action of the no-slip boundary condition. The increased width of the re-circulation region is also a consequence of the larger separation area dictated by the earlier (in a spatial sense) separation, because of the presence of the bathymetric slope around the island.

Finally, when all three mechanisms are combined by running the previous case using a tidal varying input condition, a more representative flow development as would be expected in the coastal zone is produced (figure 6.19). The results presented are obtained from the second tidal cycle. Comparing with the steady state simulation, the onset of flow separation is delayed by more than 2 hours by non-linear

effects in the flow generated by influences from the previous tide. The non-linear interaction is dominated by the influence of the tidal phase (figure 6.19(b) as opposed to figure 6.18(a)). At high water, the eddy pair generated by topographic and bathymetric effects has been retarded by phase effects of the tide as can be seen by direct comparison with the steady state case. However, the result obtained at HW+3 hours demonstrate that phase effects instigated by the existence of the small eddy pair provide ideal conditions for strengthening and expanding the re-circulating region as the tide slacks. The high levels of vorticity introduced to the flow by the combined effects of the topographic and bathymetric mechanisms while flow separation was taking place ensures that the re-circulation is maintained throughout the flood tide slacks, and into the ebb tide.

In all the cases presented of flow around a symmetrical island, the eddy generating mechanisms combine in a positive manner to create stronger eddy features. In the correct circumstances however it is possible that the mechanisms can counteract each other, for instance in certain situations the mechanisms may contribute vorticity of the opposite sense to the flow, thereby cancelling each other out at least to some extent. An example of this flow interaction is presented is now presented. Diagram 6.3 describes the domain to be considered. A uniform elevation input condition (i.e. no Coriolis force) is applied across the western boundary

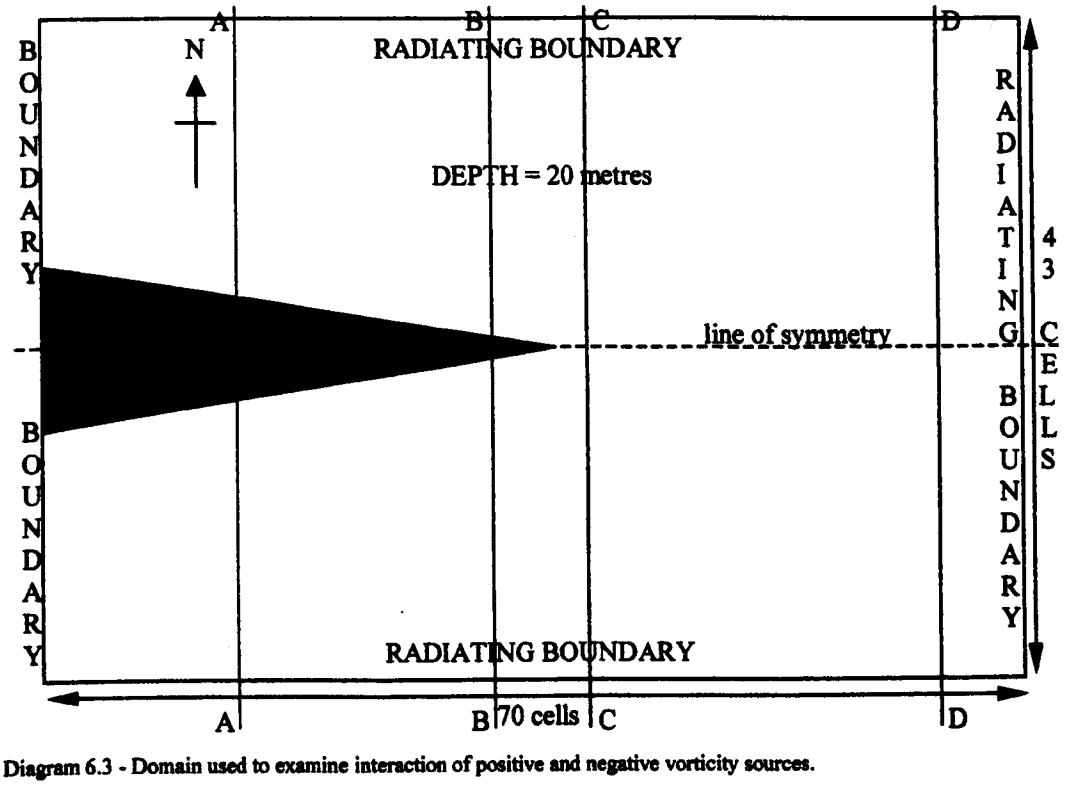

Diagram 6.3 - Domain used to examine interaction of positive and negative vorticity sources.

ramping up to a steady state (1 metre) condition over an equivalent quarter tidal period (free-stream velocity ≈ 0.5 ms^{-1}). Steady state is then maintained for 20000 seconds of modelled time. Other model parameters are specified uniformly across the model domain using typical coastal values. In the northern half of the domain, negative vorticity is generated by the no-slip condition along the closed boundary. Similarly, in the southern half of the domain, positive vorticity is generated along the boundary. At the tip of the coastal feature, positive and negative vorticity being transported through the domain from the north and south cancel (vorticity values at cross-section A-A through D-D are shown in figure 6.20(a)). In this case, as the domain and modelling conditions are symmetrical, the positive and negative values of vorticity cancel exactly. No eddy or wake feature is apparent in the domain (see figure 6.20(b)).

6.6 Conclusion

Three distinct eddy generating mechanisms have been introduced. The mechanisms have been compared and contrasted theoretically, and using numerical model output. Inappropriate numerical analysis and modelling techniques commonly occurring in the literature have been illustrated and discussed. Alternative techniques have been presented with examples of their application. The difficulty of accurately numerically modelling flow separation and eddy generation associated with fixed-grid based techniques has been discussed. Insight into the operation of the numerical model code has demonstrated the differences between the real physics and model application. This discussion continues in the following chapter, which focuses on eddy shedding and the life-span of transient eddy features.

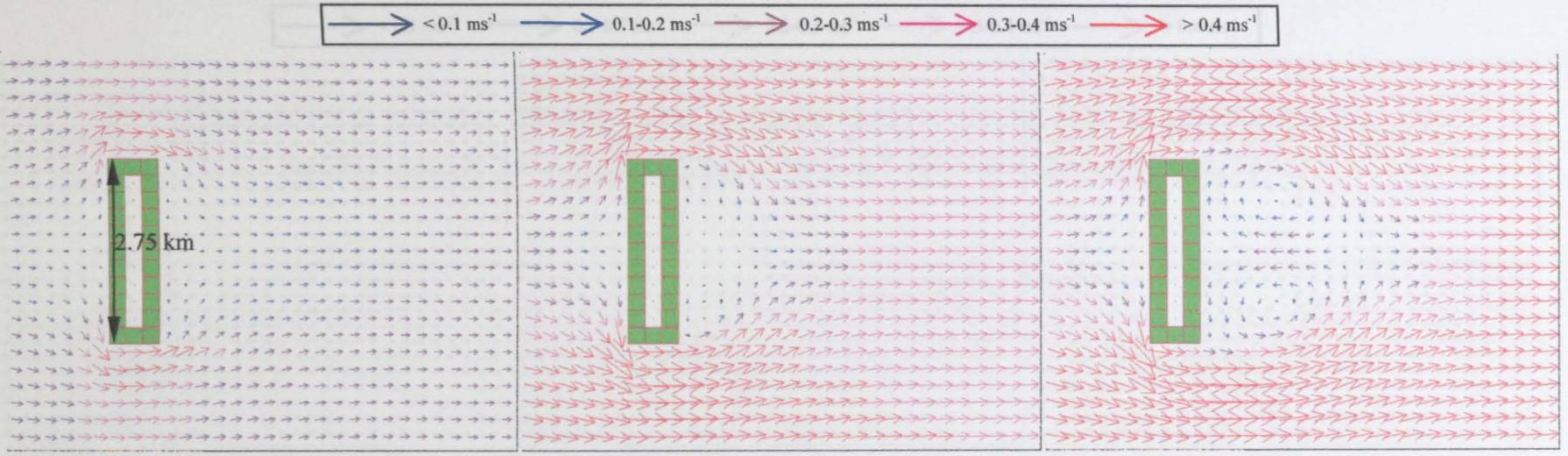

Figure 6.1 (a) - Flow remains attached to the island (1 hour after simulation initiated).

Figure 6.1 (b) Flow has just separated from the island, and an eddy pair has been established (2 hours after simulation initiated).

Figure 6.1 (c) Flow separation is maintained and eddy regions have expanded and strengthened (equivalent peak tide conditions).

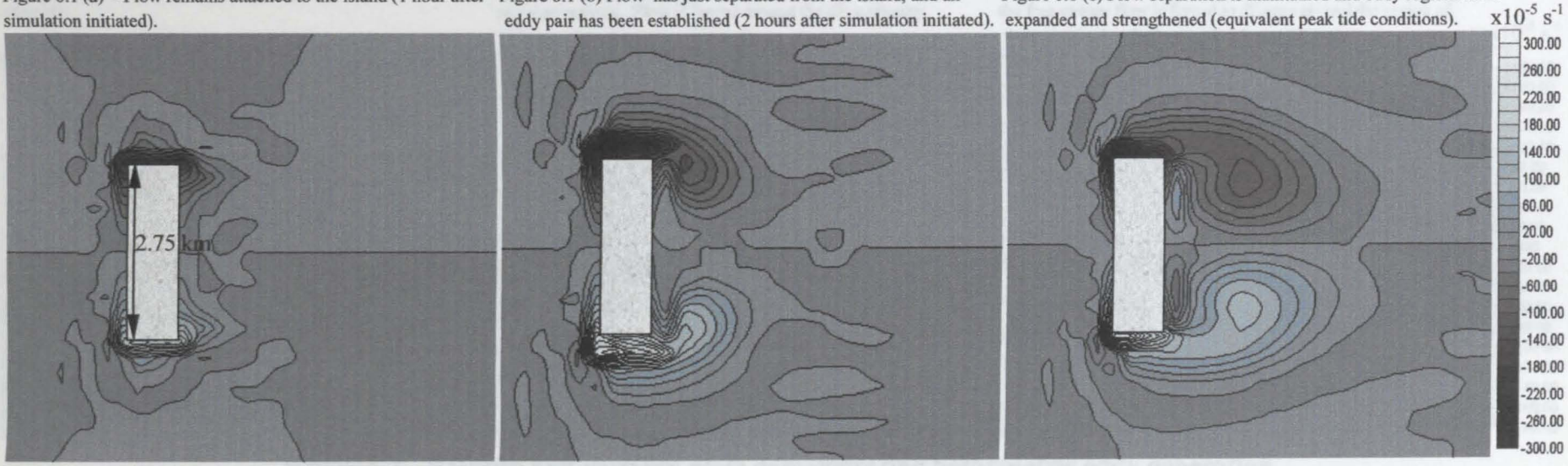

Figure 6.1 - Velocity and vorticity plots demonstrating topographic eddy generation around a 2750 m wide island.

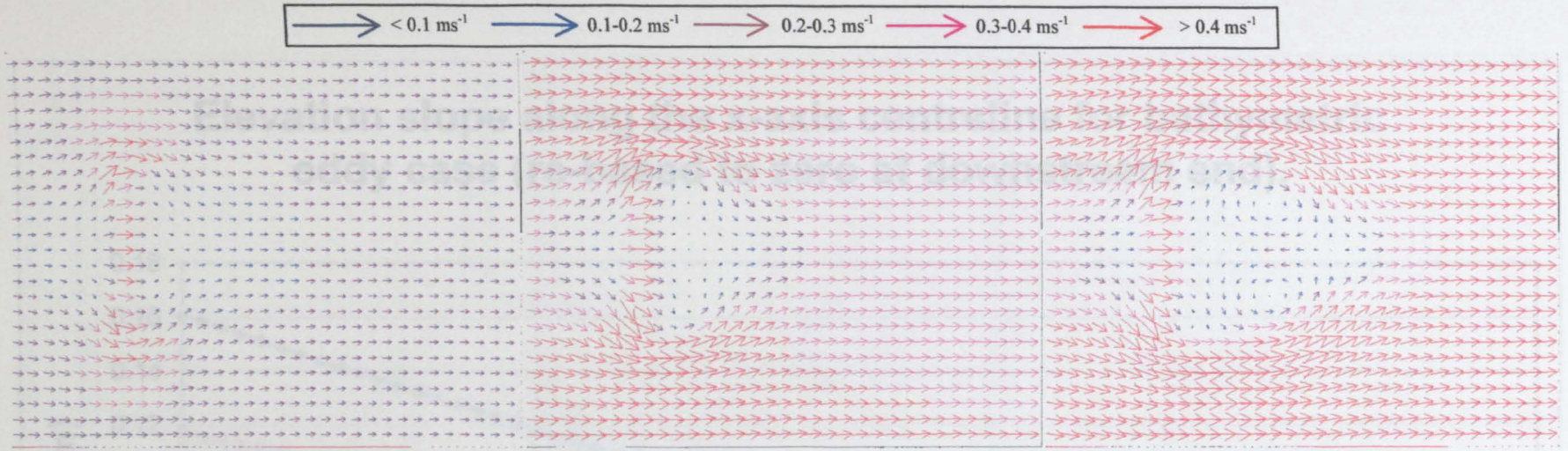

Figure 6.2 (a) - Flow remains attached (1 hour after simulation initiated).

Figure 6.2 (b) An eddy pair has been established in the low-pressure regions. Flow is forced around the discontinuity. (2 hours after simulation initiated).

Figure 6.2 (c) The rwin eddies have expanded and strengthened as the free-stream flow is forced to diverge around the region of discontinuity (equivalent peak tide conditions).

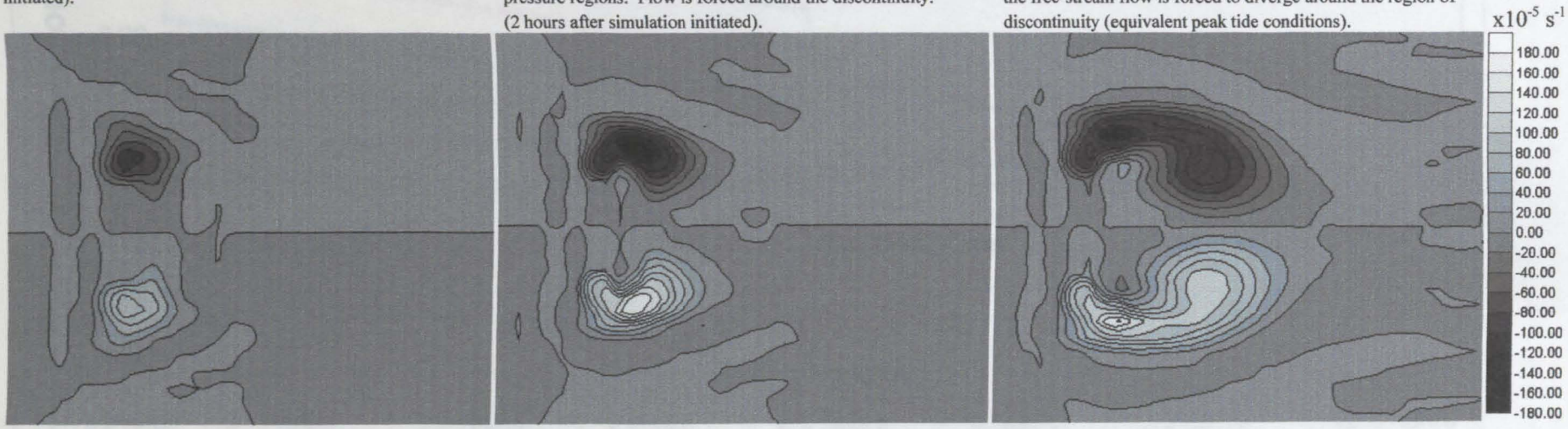

Figure 6.2 - Velocity and vorticity plots demonstrating bathymetric eddy generation.

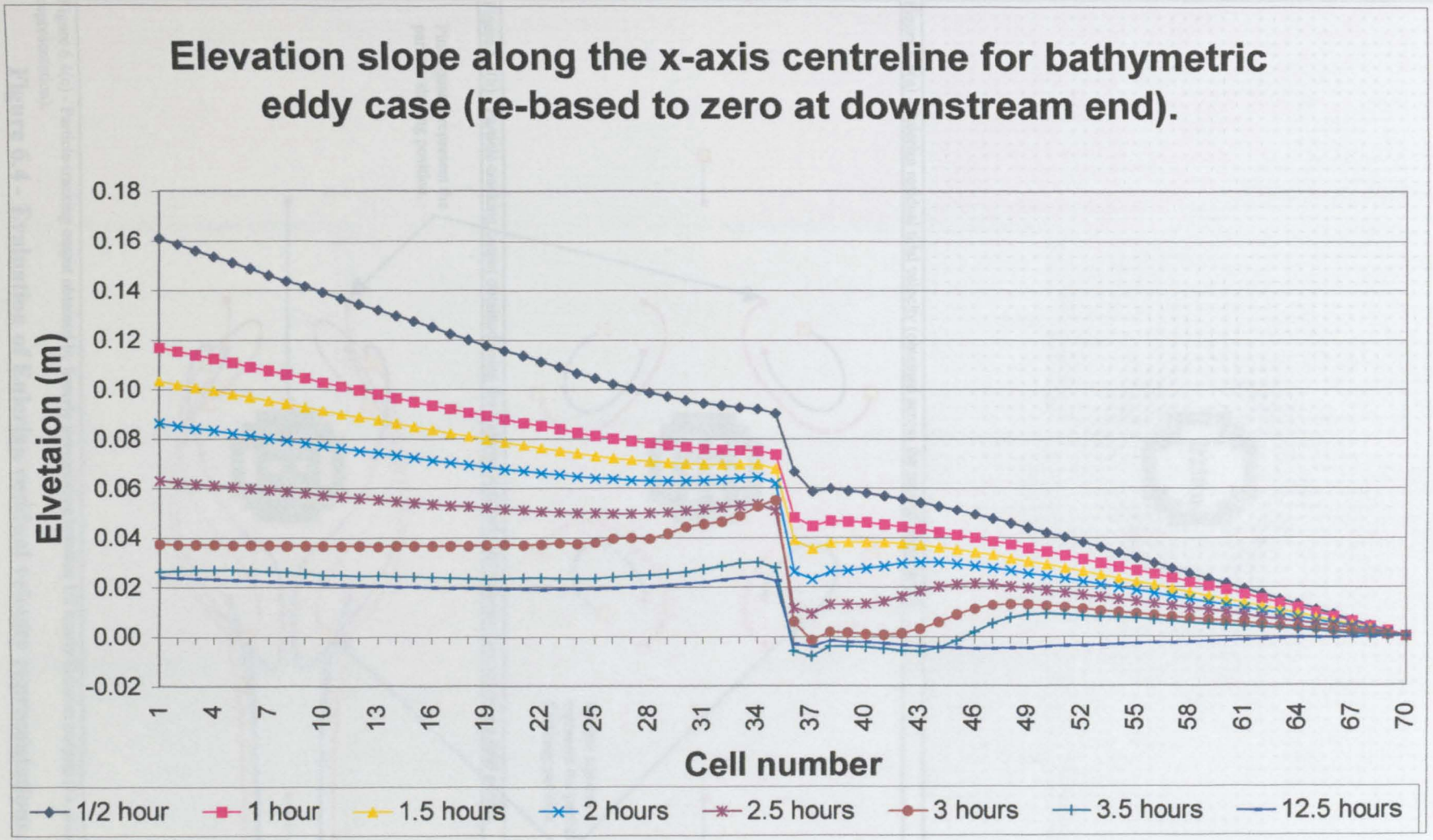

Figure 6.3 – Elevation slopes along the x-axis centreline for a bathymetrically induced eddy situation (results re-based to zero at downstream boundary for comparative purposes).

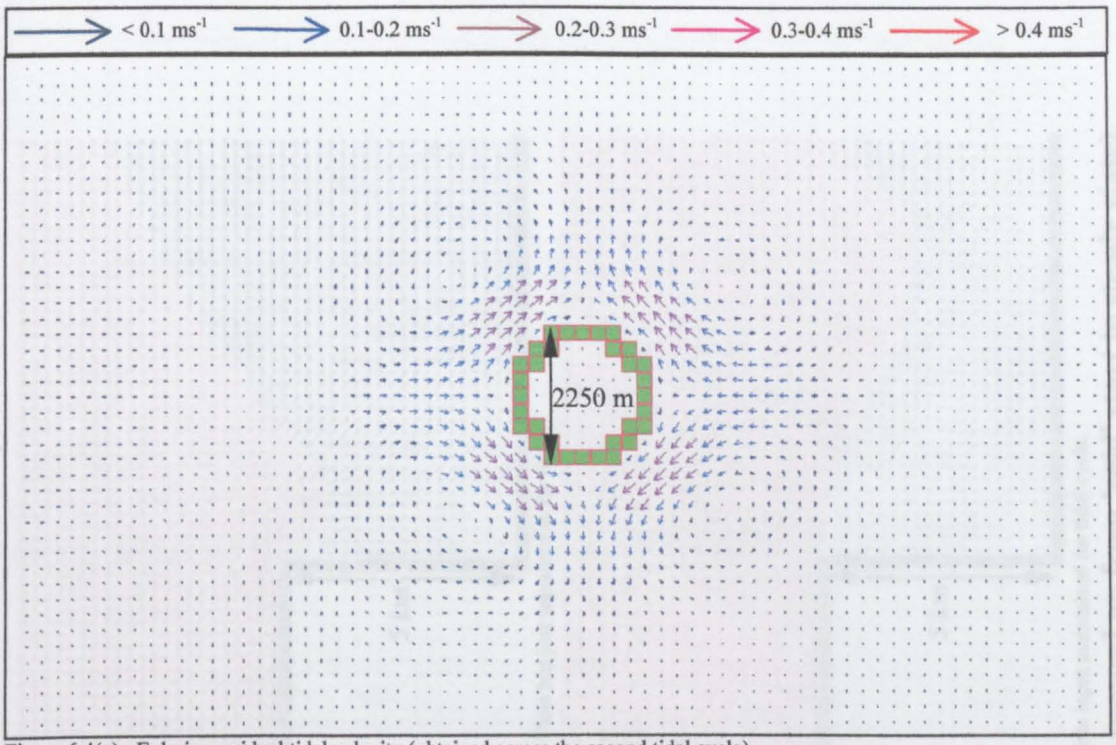

Figure 6.4(a) - Eulerian residual tidal velocity (obtained across the second tidal cycle).

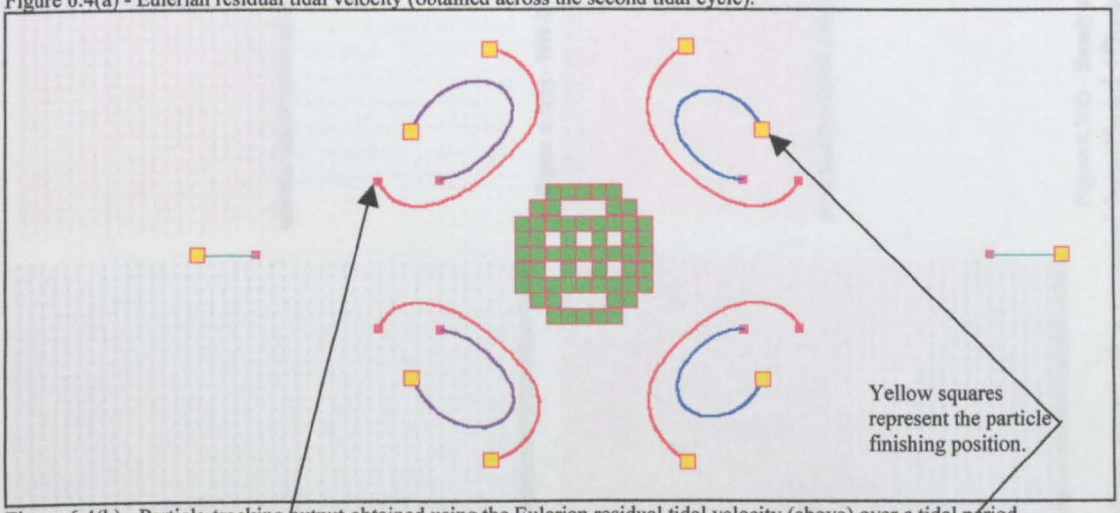

Figure 6.4(b) - Particle-tracking output obtained using the Eulerian residual tidal velocity (above) over a tidal period.

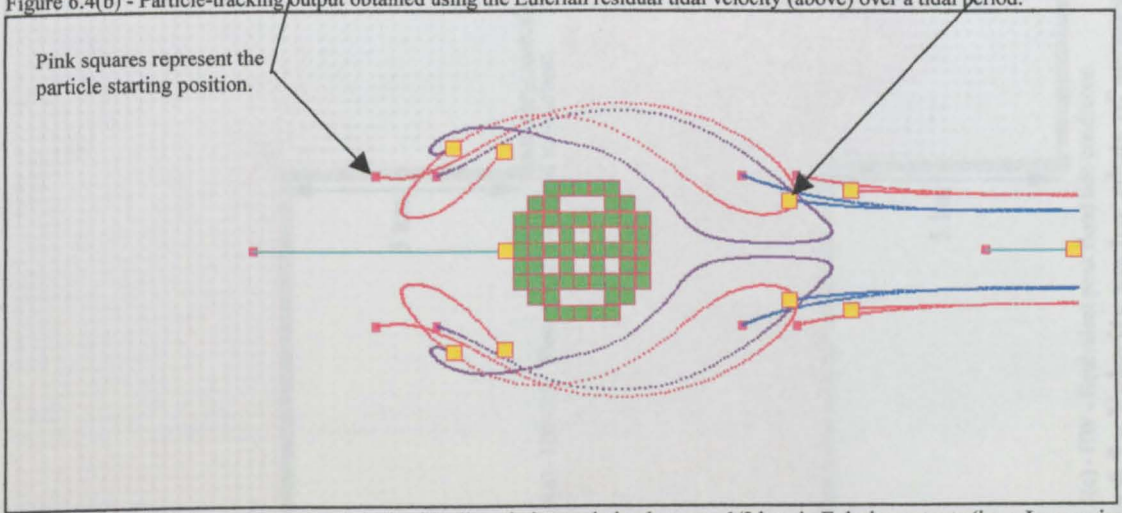

Figure 6.4(c) - Particle-tracking output obtained by linearly interpolating between 1/2 hourly Eulerian outputs (i.e. a Lagrangian representation).

Figure 6.4 - Evaluation of Eulerian residual velocity representations.

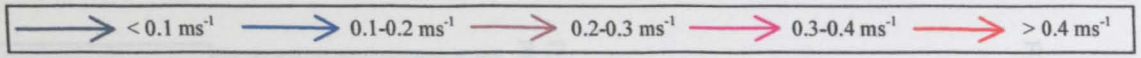

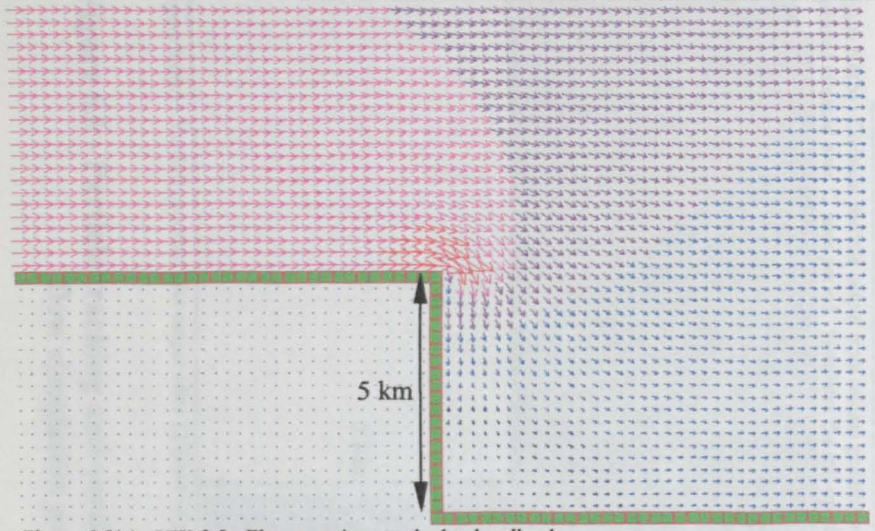

Figure 6.5(a) - HW-2.5 - Flow remains attached to headland.

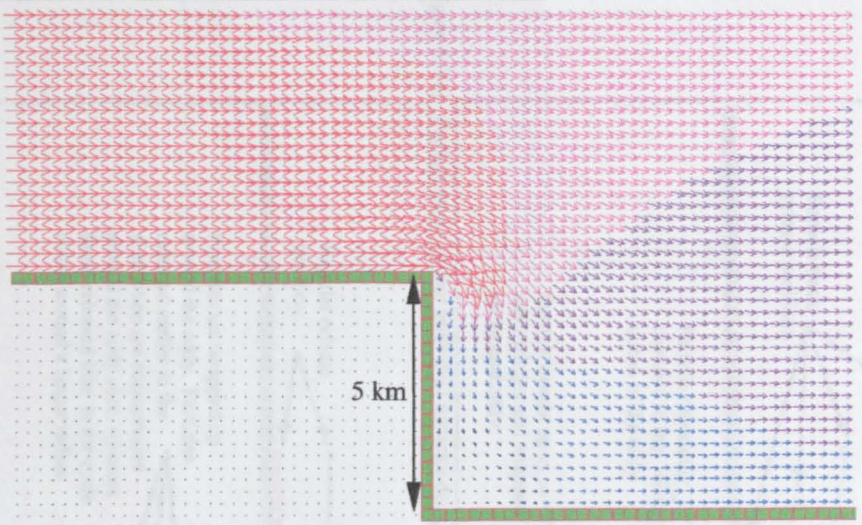

Figure 6.5(b) - HW-2 - Flow has just separated at the tip.

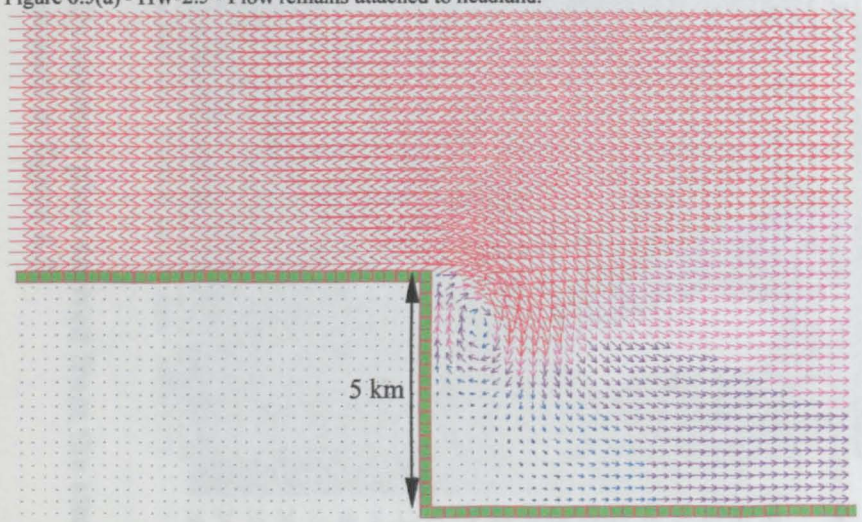

Figure 6.5(c) - HW - Equivalent peak flood tide conditions.

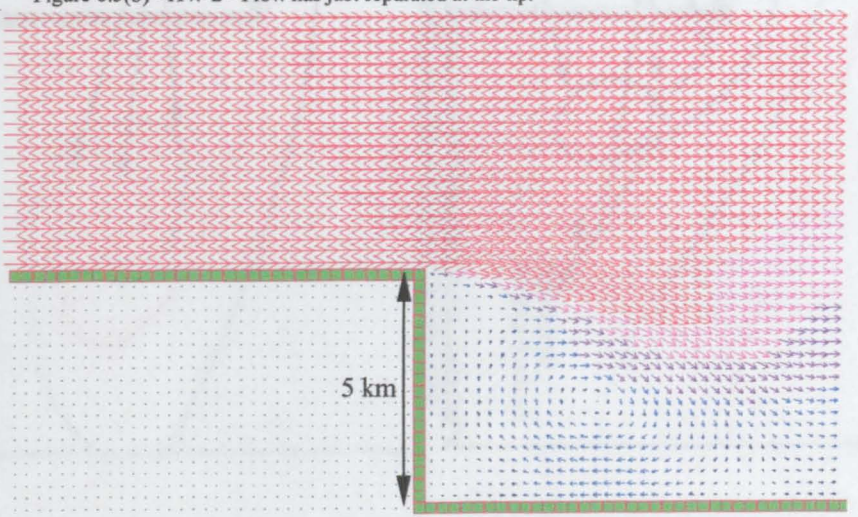

Figure 6.5(d) - Steady state input maintained for tidal cycle.

Figure 6.5 - Velocity vector plots of separation around a coastal headland (flow ramped up from 'cold' start to steady state).

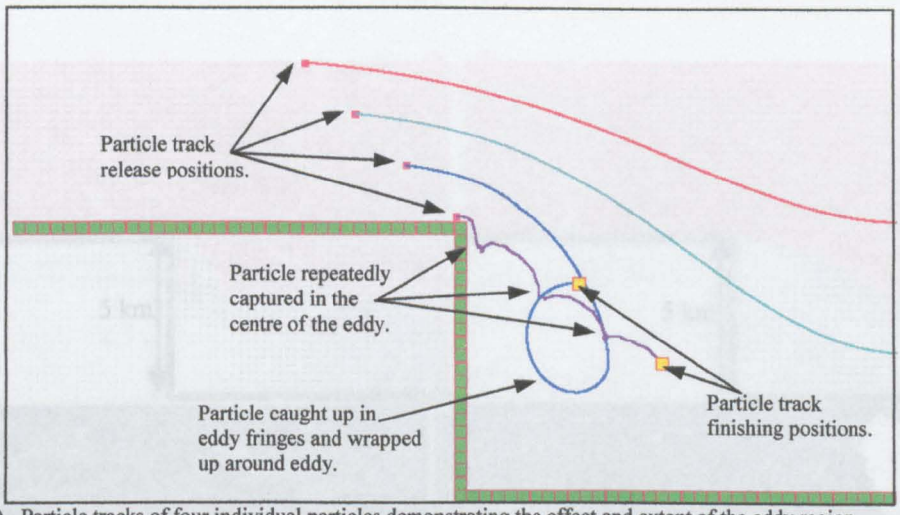

Figure 6.6(a) - Particle tracks of four individual particles demonstrating the effect and extent of the eddy region.

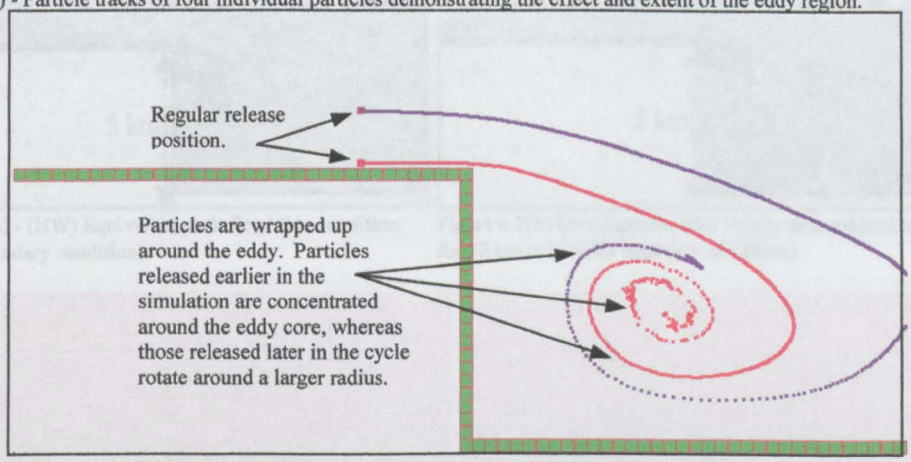

Figure 6.6(b) - Constant particle output from release position at 30 second interval. Visualisation is of the final position of all the particles released over 12 hour period. Simulates the roll-up of vorticity around the eddy core as the eddy develops.

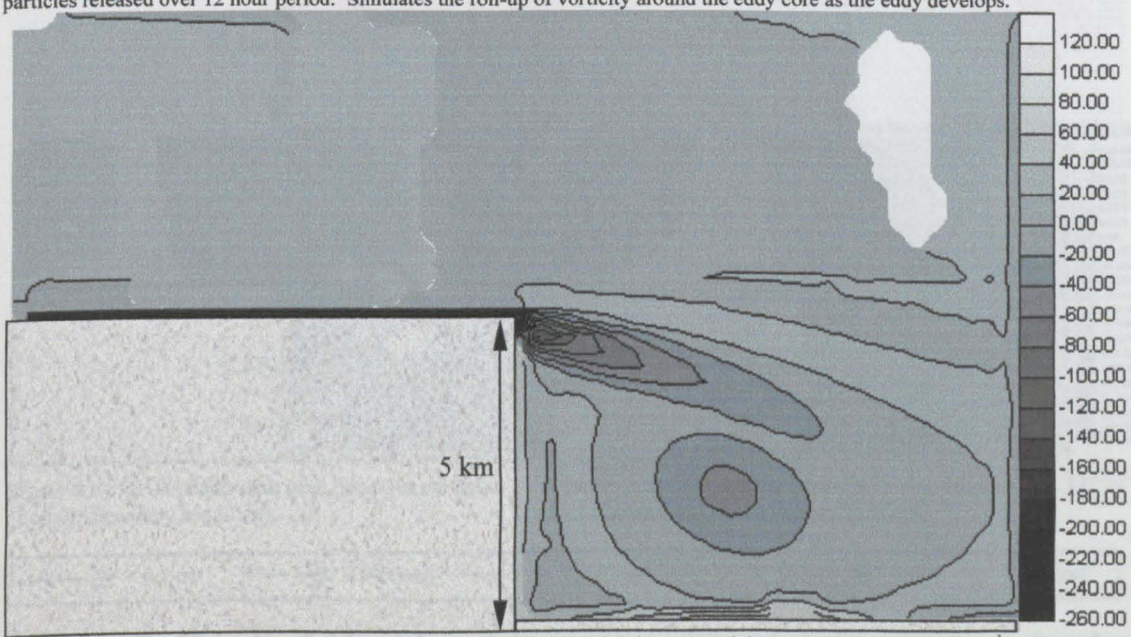

Figure 6.6(c) - Vorticity contour plot output after 12 hours of simulated time. (Vorticity contour scale = x10E-5 s^{-1}).

Figure 6.6 - Particle tracking and vorticity contour plots derived from the steady flow simulation presented in figure 6.5.

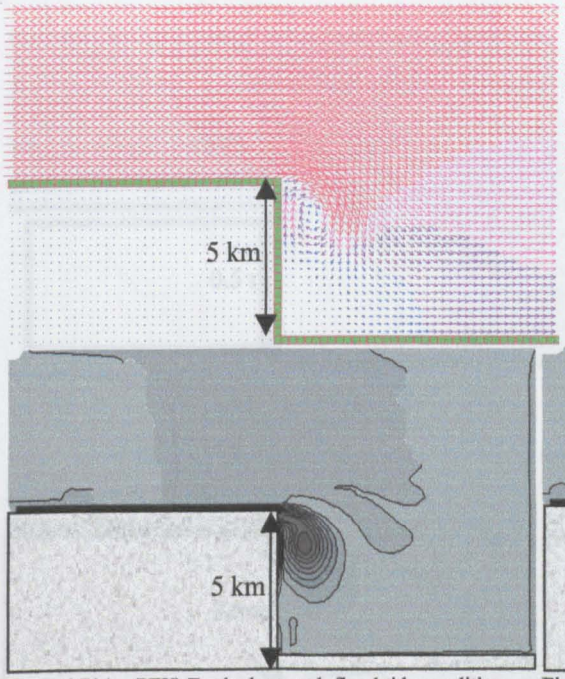

Figure 6.7(a) - (HW) Equivalent peak flood tide condition (no-slip boundary condition).

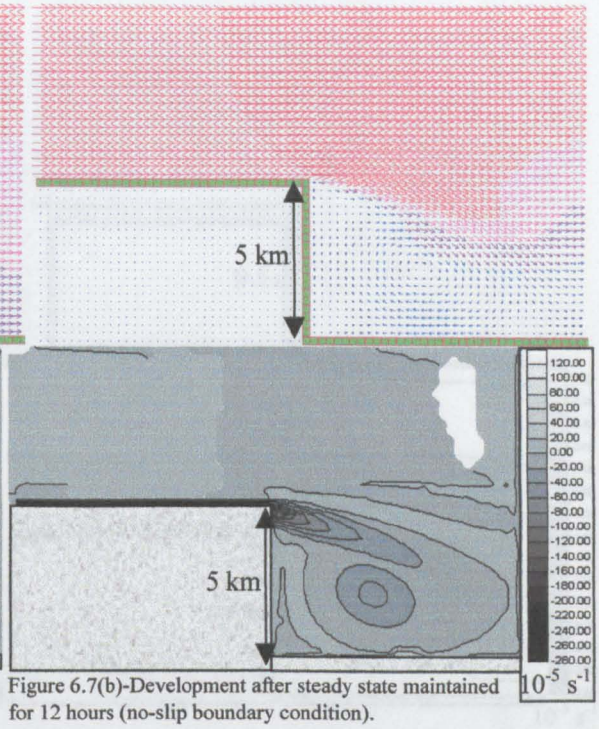

Figure 6.7(b)-Development after steady state maintained for 12 hours (no-slip boundary condition).

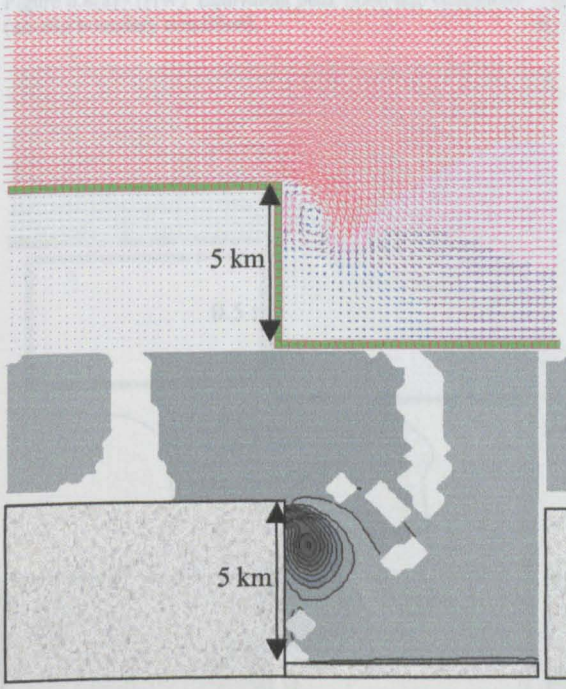

Figure 6.7(c)-(HW) Equivalent peak flood tide condition. (free-slip boundary condition).

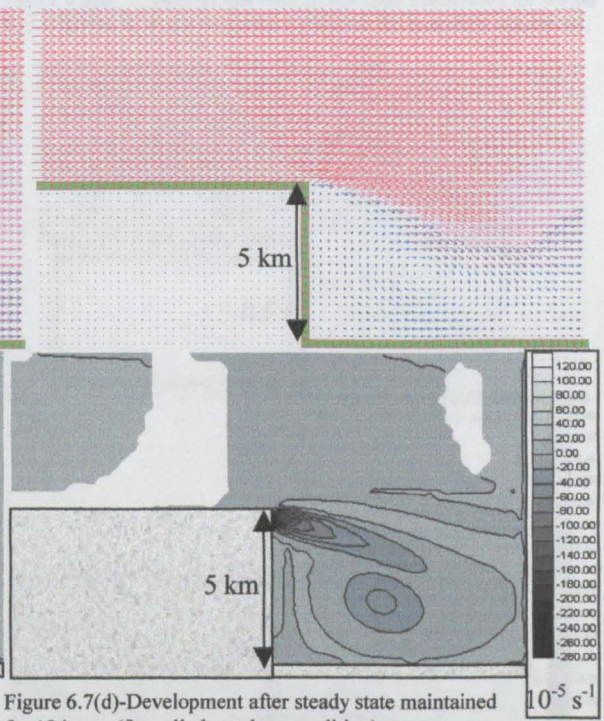

Figure 6.7(d)-Development after steady state maintained for 12 hours (free-slip boundary condition)..

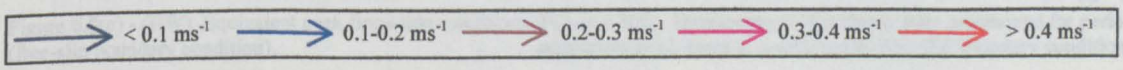

Figure 6.7 - Velocity fields and vorticity contours generated at prototype scale using no-slip and free-slip conditions (negligible difference observed in the two cases).

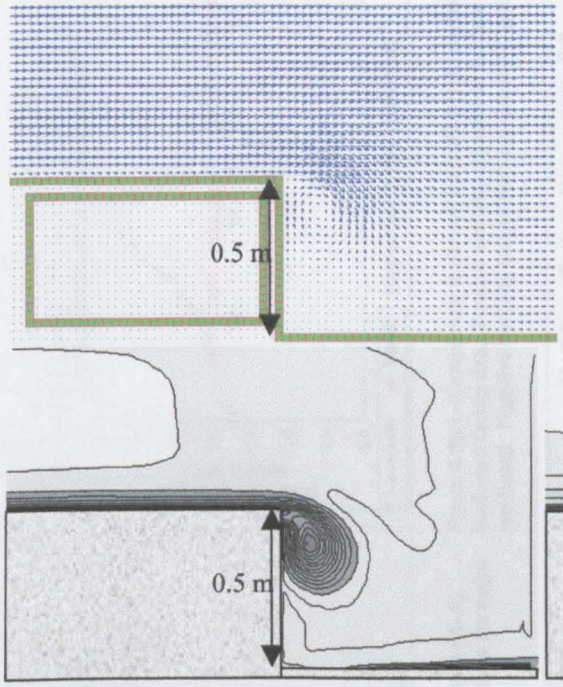

Figure 6.8(a) - (HW) Equivalent peak flood tide conditions (no-slip boundary condition).

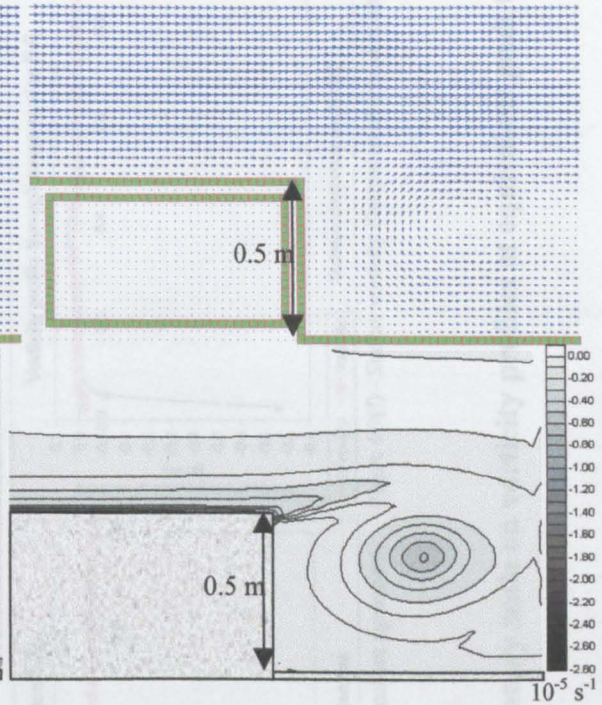

Figure 6.8(b) - Development after steady state maintained for period equivalent to 12 hours at coastal scale (no-slip boundary condition).

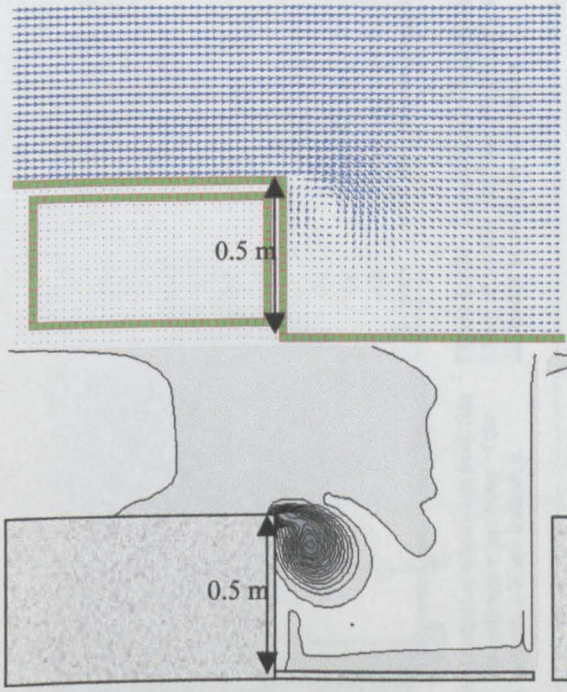

Figure 6.8(c) - (HW) Equivalent peak flood tide conditions (free-slip boundary condition).

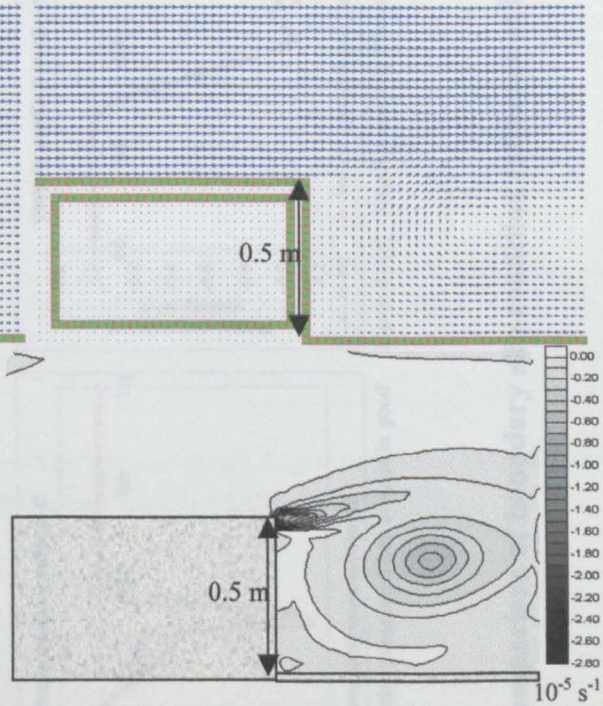

Figure 6.8(d) - Development after steady state maintained for period equivalent to 12 hours at coastal scale (free-slip boundary condition).

Figure 6.8 - Velocity fields and vorticity contours generated at model scale using no-slip and free-slip conditions (boundary layer clearly visible in no-slip case)

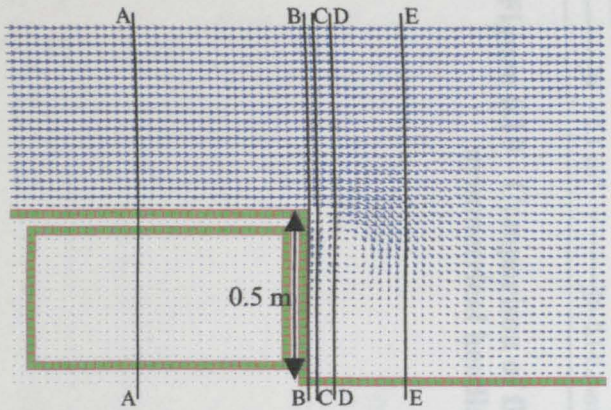

Figure 6.9(a) - Velocity vector plot output at equivalent peak tide for no-slip boundary condition. The respective positions of the comparative cross-sections A-A through E-E are indicated.

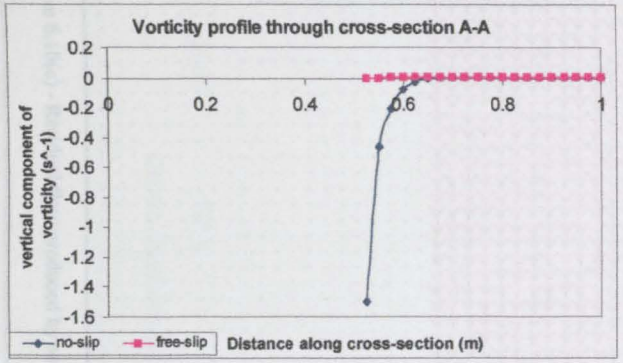

Figure 6.9(b) - Comparison in the upstream flow region (A-A). Effect of no-slip condition on boundary layer creation is the major difference between the two results.

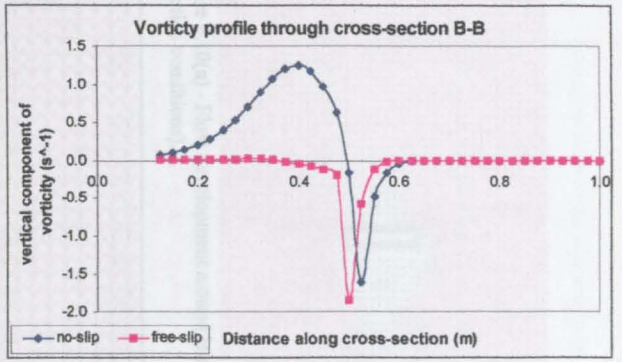

Figure 6.9(c) - Comparison in the cell immediately downstream of the backward facing step. Positive vorticity adjacent to the face not replicated. Negative vorticity transported into domain in good agreement

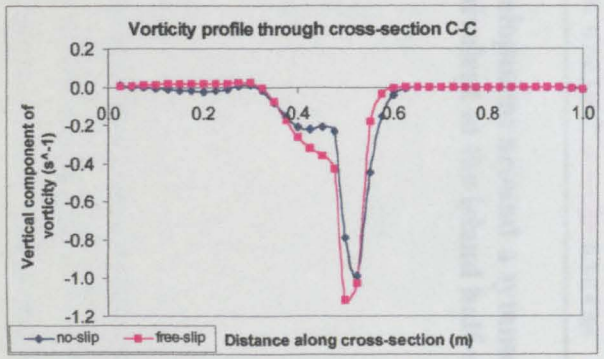

Figure 6.9(d) - Negative vorticity transported into domain in good agreement.

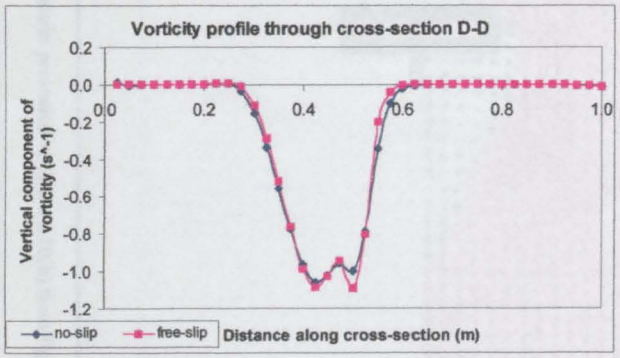

Figure 6.9(e) - Negative vorticity transport in excellent agreement.

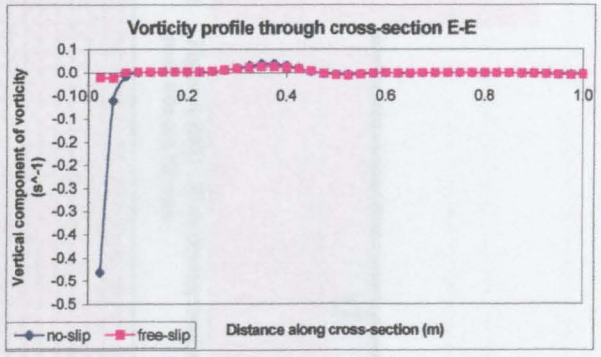

Figure 6.9(f) - Similar vorticity dissipation observed in both cases.

Figure 6.9 - Comparison of boundary slip condition influence at laboratory scale on vorticity profiles at equivalent peak tide.

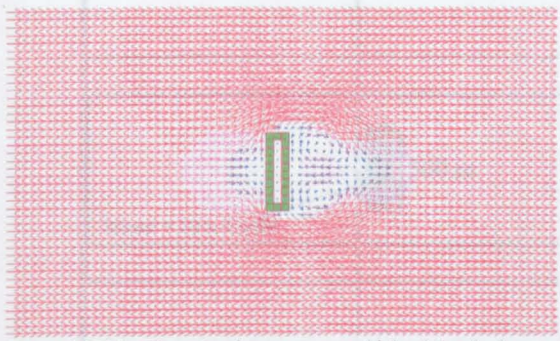

Figure 6.10(a) - Flow development around island (equivalent peak tide conditions).

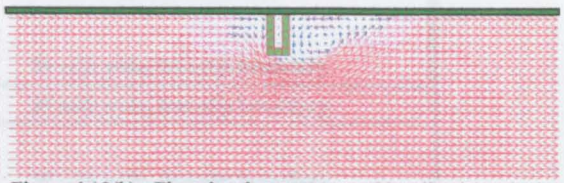

Figure 6.10(b) - Flow development around headland (equivalent peak tide conditions).

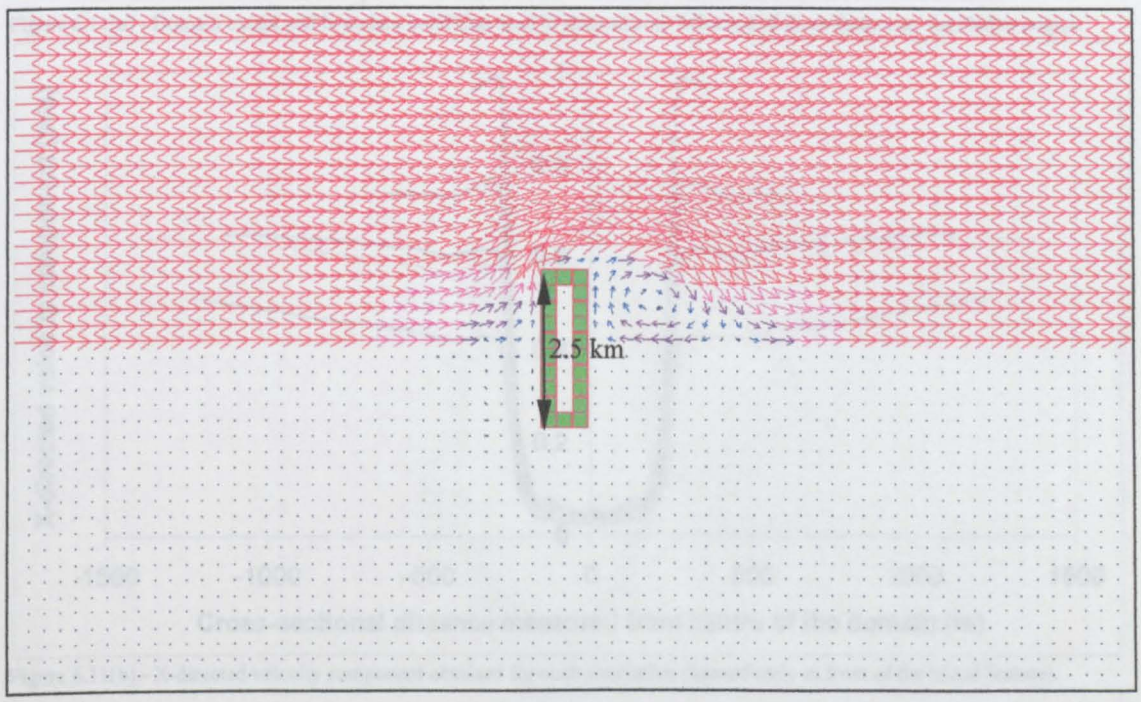

Figure 6.10(c) - Residual flow produced by subtracting the results presented in figure 6.10(b) from figure 6.10(a).

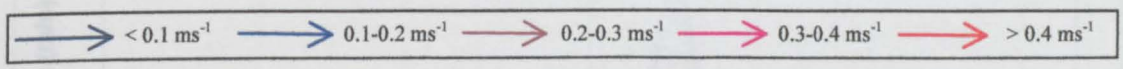

Figure 6.10 - Comparison of flow development around a symmetrical island and symmetrical headland equivalent to the island half-width.

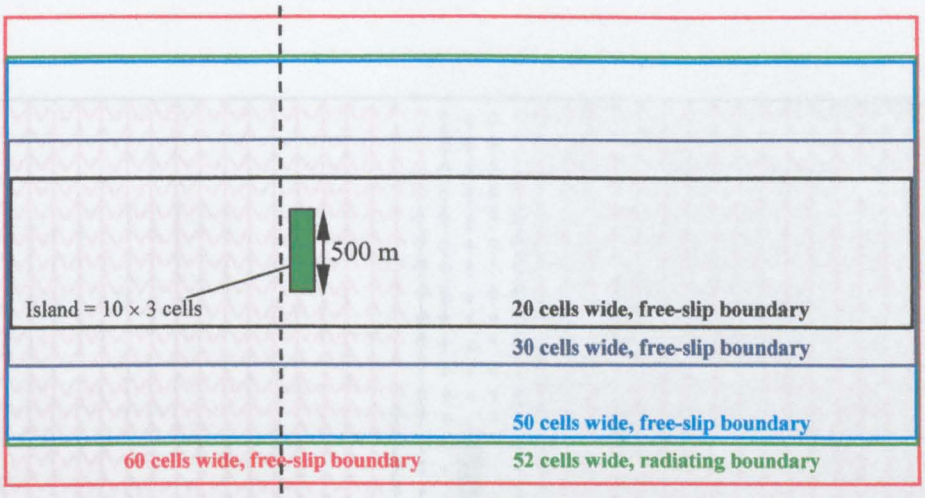

Figure 6.11(a) - Domain extent and boundary condition used to demonstrate influence of these factors on simulation output.

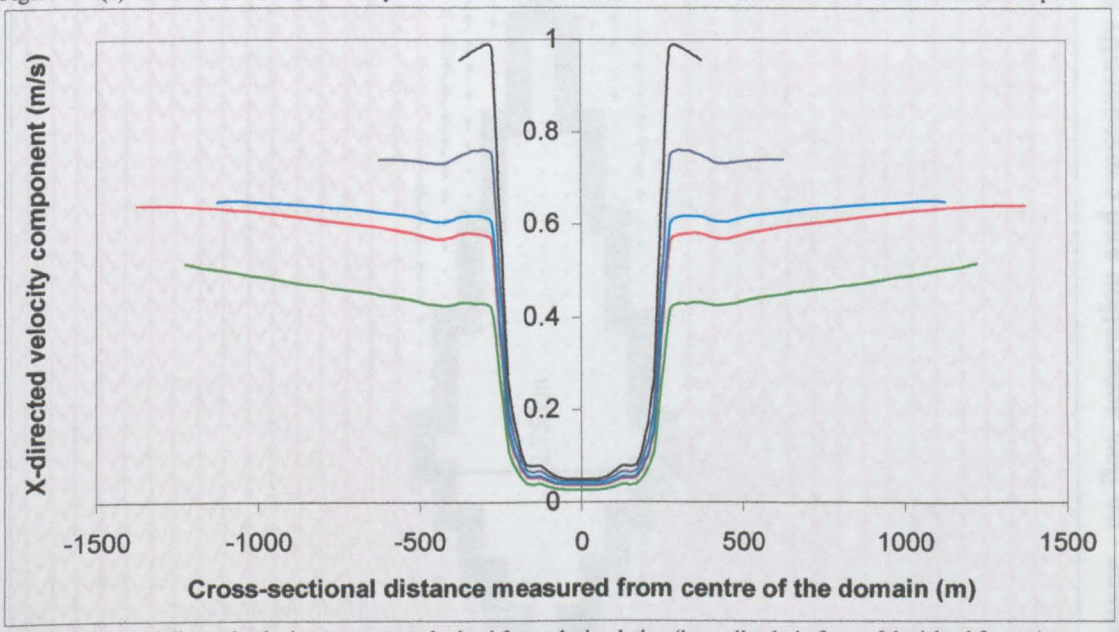

Figure 6.11(b) - X-directed velocity component obtained for each simulation (immediately in front of the island feature).

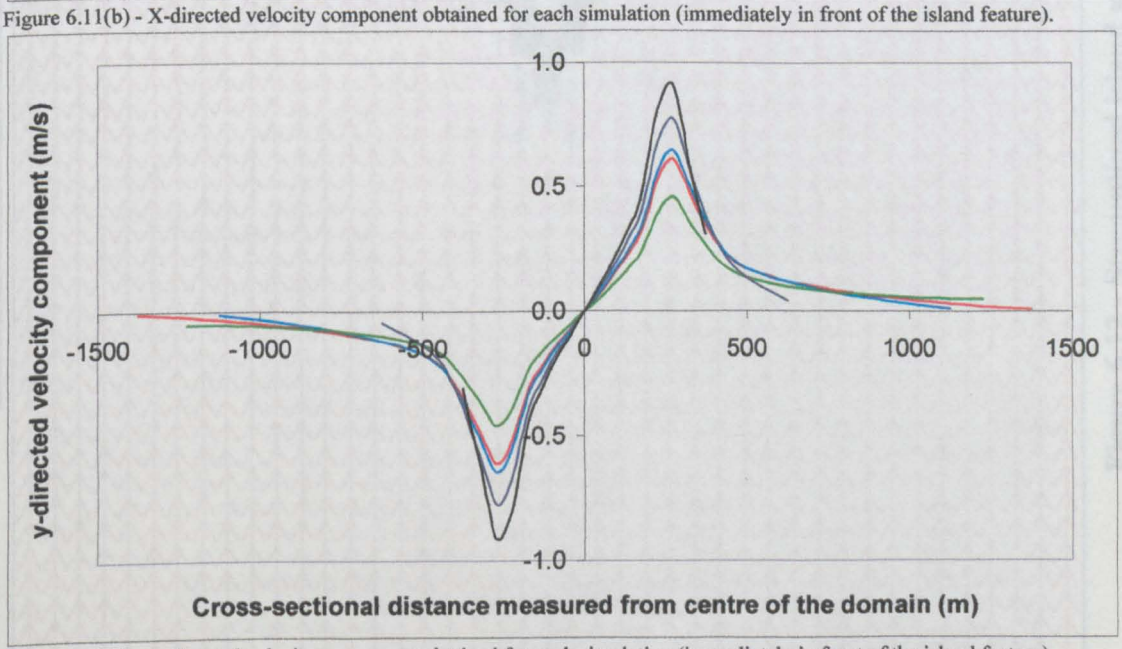

Figure 6.11(c) - Y-directed velocity component obtained for each simulation (immediately in front of the island feature).

Figure 6.11 - Comparison of influence of lateral domain extent and boundary selection.

Figure 6.12 - Streamlined island shape - no flow separation and consequently no eddy generation.

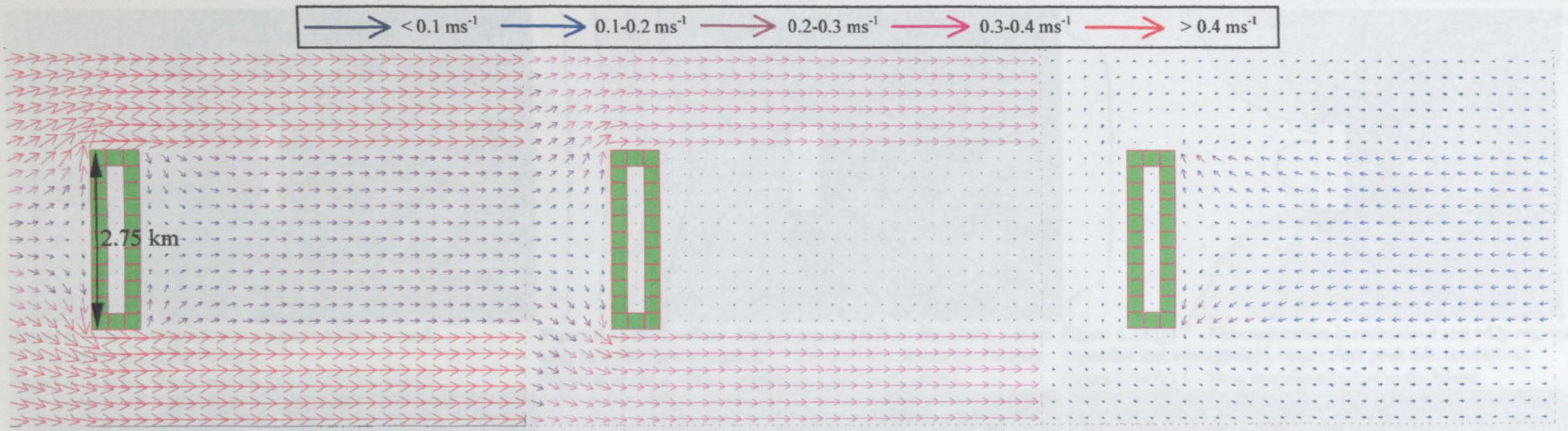

Figure 6.13 (a) - Flow remains attached to the island. Strong shear observed across the shoal break (equivalent peak tide conditions).

Figure 6.13 (b) - Flow remains attached to the island. Strong phase lag observed as the tide reverses. (2 hours after HW).

Figure 6.13 (c) - Flow remains attached to the island. Strong phase lag maintained, and eddy-like features observed (no sign of existence of a closed circulation (3 hours after HW).

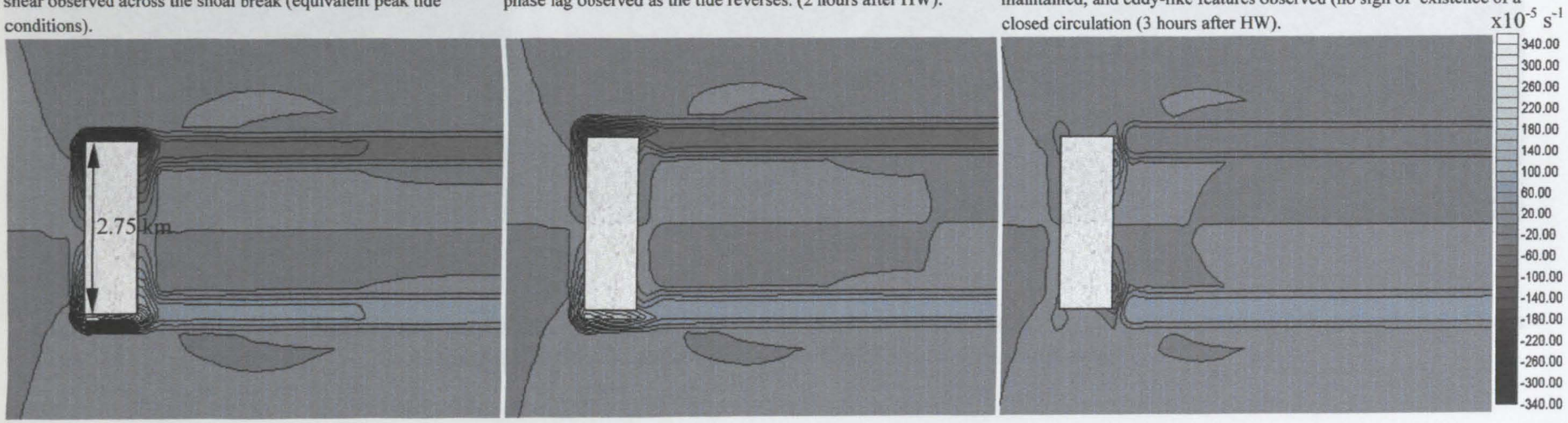

Figure 6.13 - Velocity and vorticity plots demonstrating phase effects (lag).

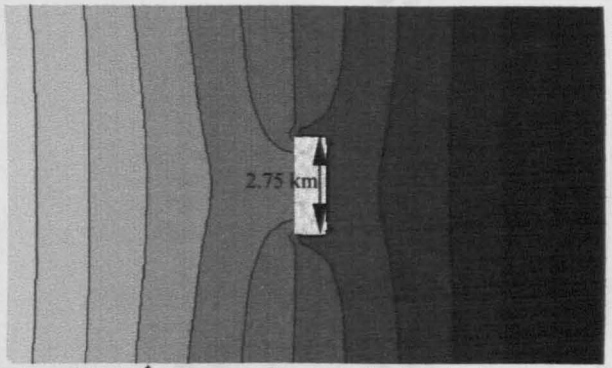

Figure 6.14 (a) ↑ - Flow remains attached to the island. (1 hour after simulation started).

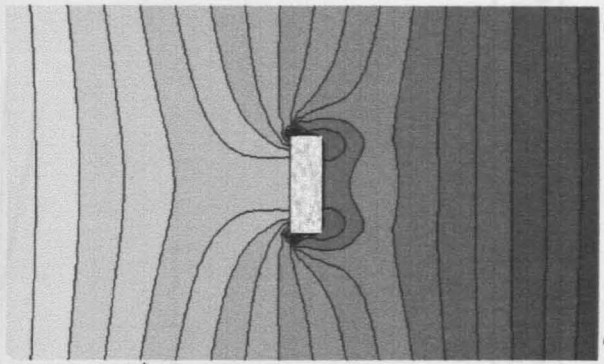

Figure 6.14 (b) ↑ - Flow has just separated from the island, and an eddy pair has been instigated. (2 hours after simulation started).

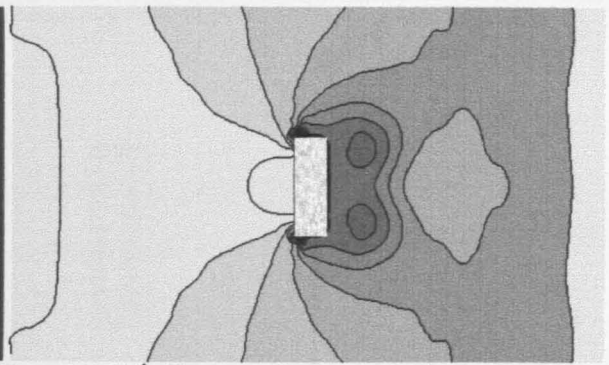

Figure 6.14 (c) ↑ - Flow separation is maintained and eddy regions have expanded and strengthened. (equivalent peak tide conditions).

Figure 6.14 (a) ↓ - Flow remains attached to the island.

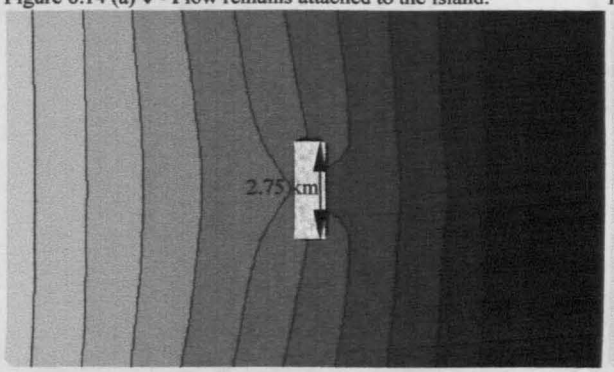

Figure 6.14 (b) ↓ - Flow remains attached to the island.

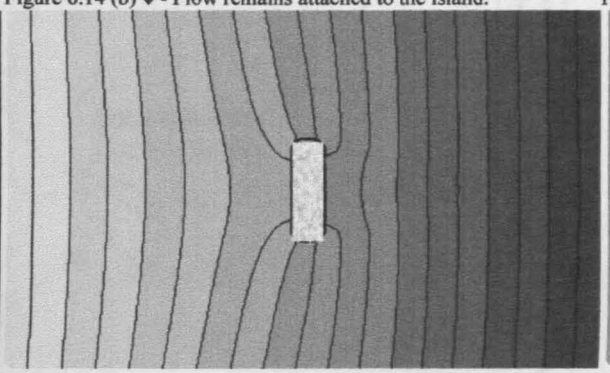

Figure 6.14 (c) ↓ - Flow remains attached to the island.

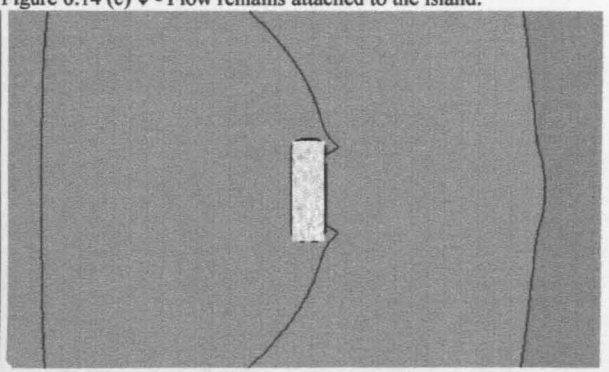

Figure 6.14 - Comparison of flow evolution during the flood tide (elevation contours) for purely topographic and phase effects respectively (contour interval = 0.005 metres in each case).

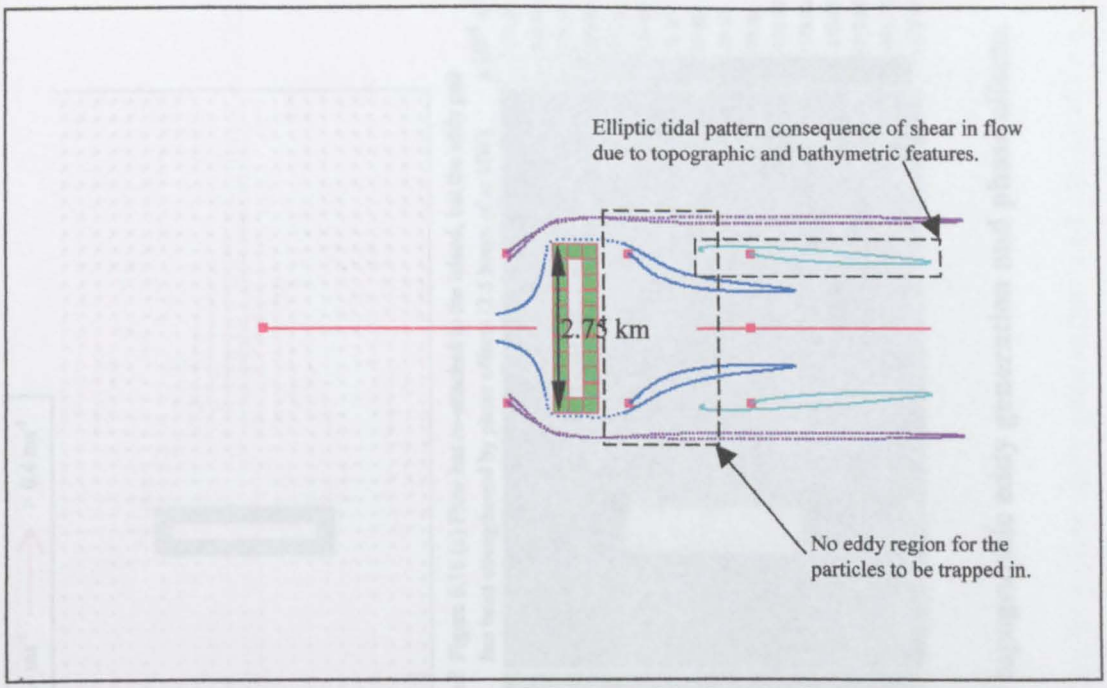

Figure 6.15(a) - Particle tracking output obtained over the initial 12 hours of simulated time for the phase case (section 6.5.3). Velocity and vorticity fields initially presented in figure 6.13.

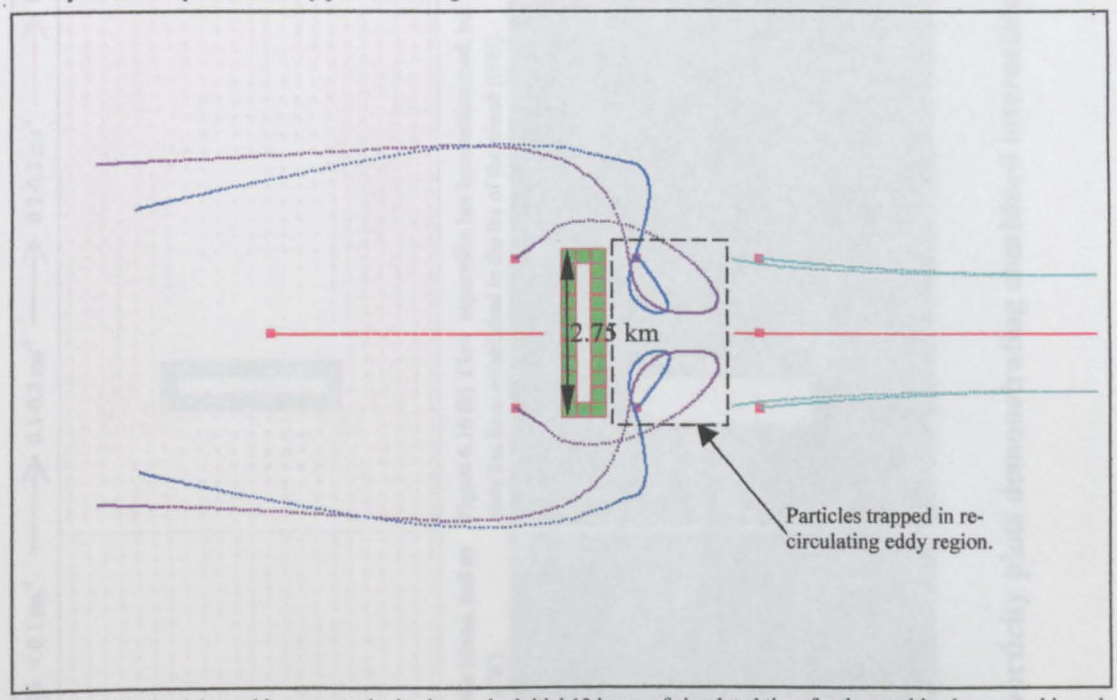

Figure 6.15(b) - Particle tracking output obtained over the initial 12 hours of simulated time for the combined topographic and phase case (section 6.5.4). Velocity and vorticity fields initially presented in figure 6.16

Figure 6.15 - Comparison of particle tracking output for (a) phase and (b) combined topographic and phase cases (Larger squares indicate the particle starting position).

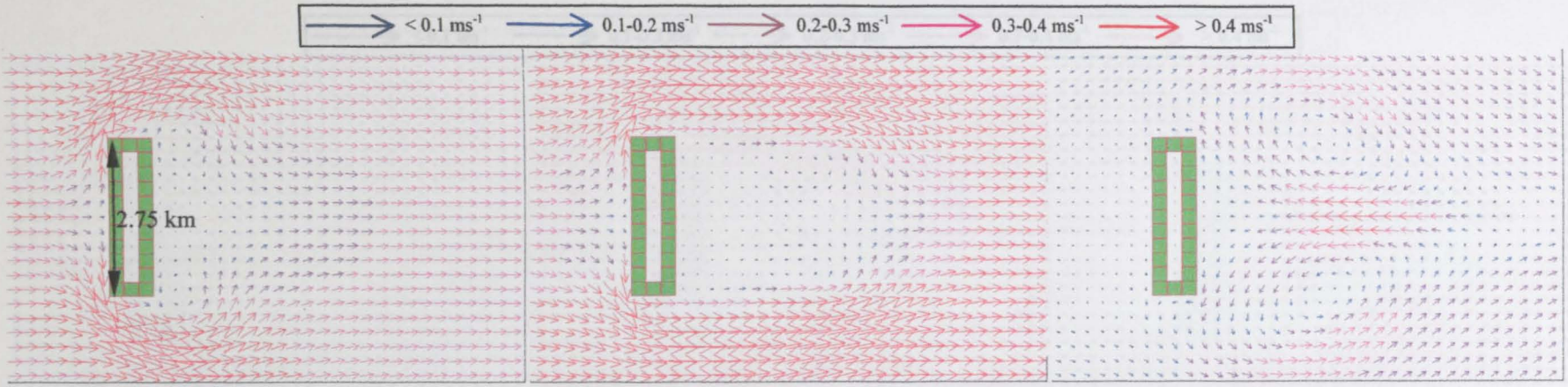

Figure 6.16 (a) - Flow has just separated from the island, and an eddy pair has been instigated (1.5 hours before HW).

Figure 6.16 (b) Flow separation has been maintained, but a 'dead' zone has been established in the lee of the island (HW).

Figure 6.16 (c) Flow has re-attached to the island, but the eddy pair has been strengthened by phase effects (2.5 hours after HW).

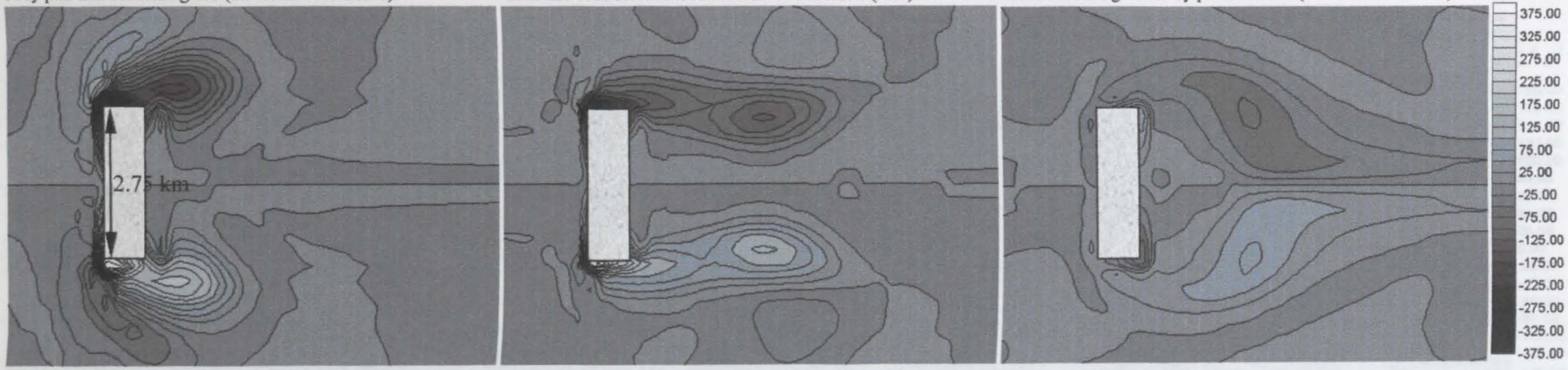

Figure 6.16 - Velocity and vorticity plots demonstrating combined interaction of topographic eddy generation and phase effects.

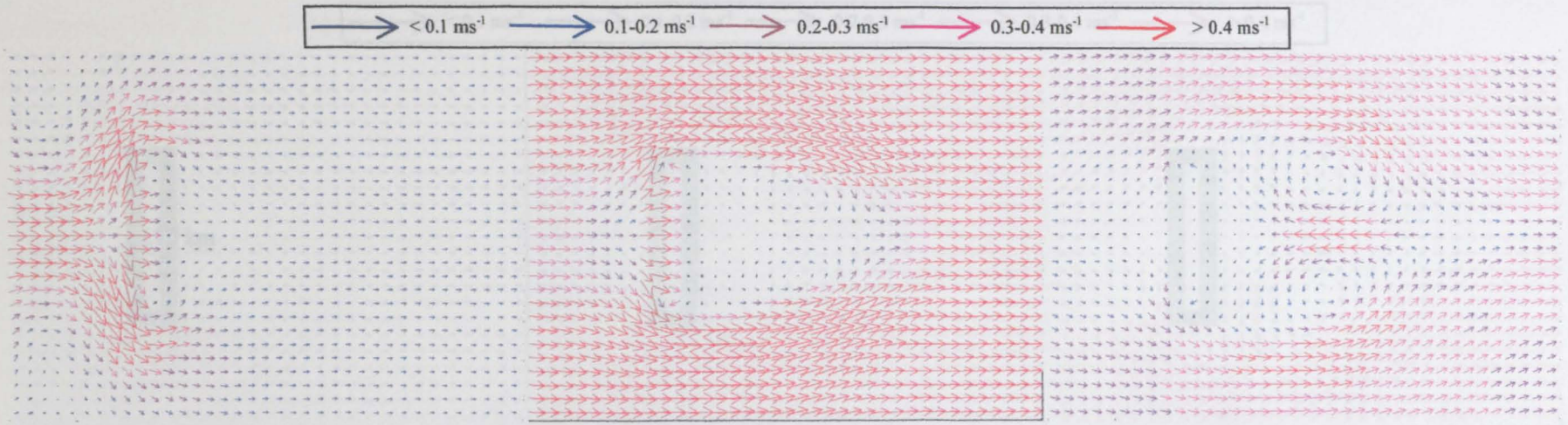

Figure 6.17 (a) - Flow remains attached (2.5 hours before HW).

Figure 6.17 (b) An eddy pair has been established in the low-pressure regions. Flow is being forced around the discontinuity. (HW).

Figure 6.17 (c) The rwin eddies have expanded and strengthened as the free-stream flow is retarded by the tide ebbing (2 hours after HW).

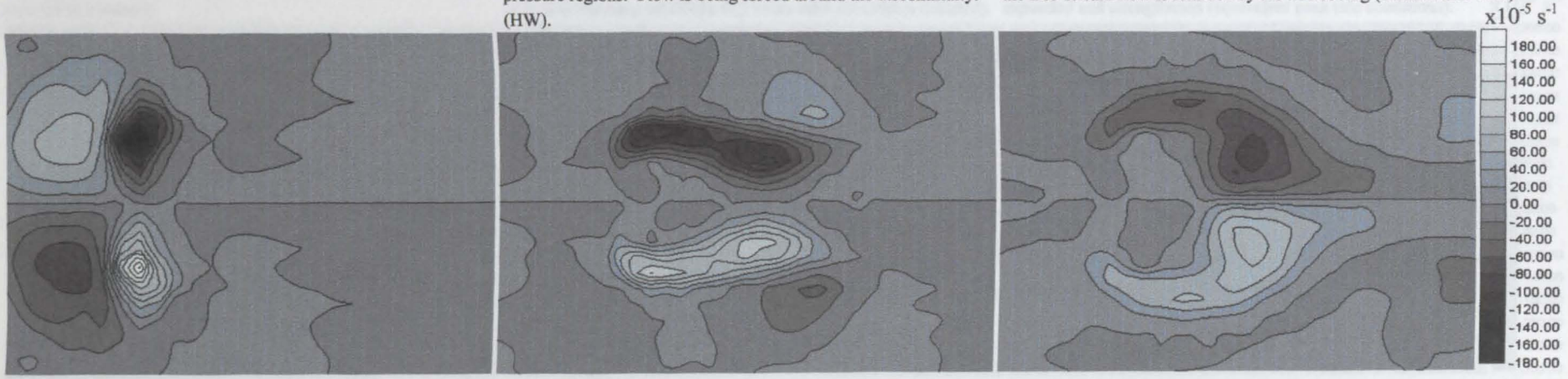

Figure 6.17 - Velocity and vorticity plots demonstrating combined interaction of bathymetric eddy generation and phase effects.

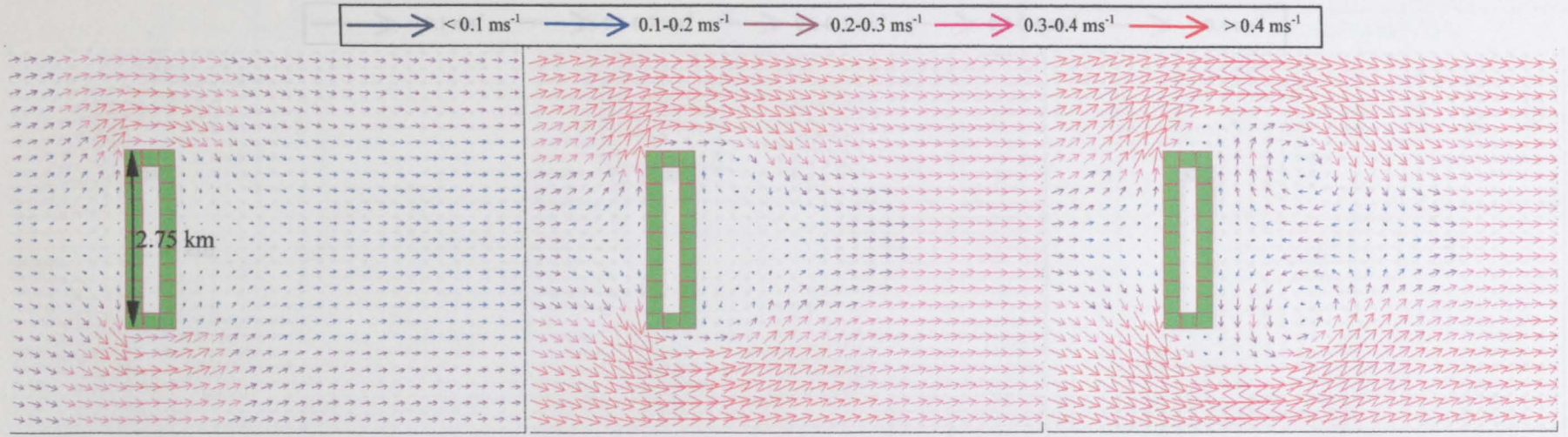

Figure 6.18 (a) - Flow remains attached to the island (1 hour after simulation initiated).

Figure 6.18 (b) Flow has just separated from the island, and an eddy pair has been established (2 hours after simulation initiated).

Figure 6.18 (c) Flow separation is maintained and eddy regions have expanded and strengthened (equivalent peak tide conditions).

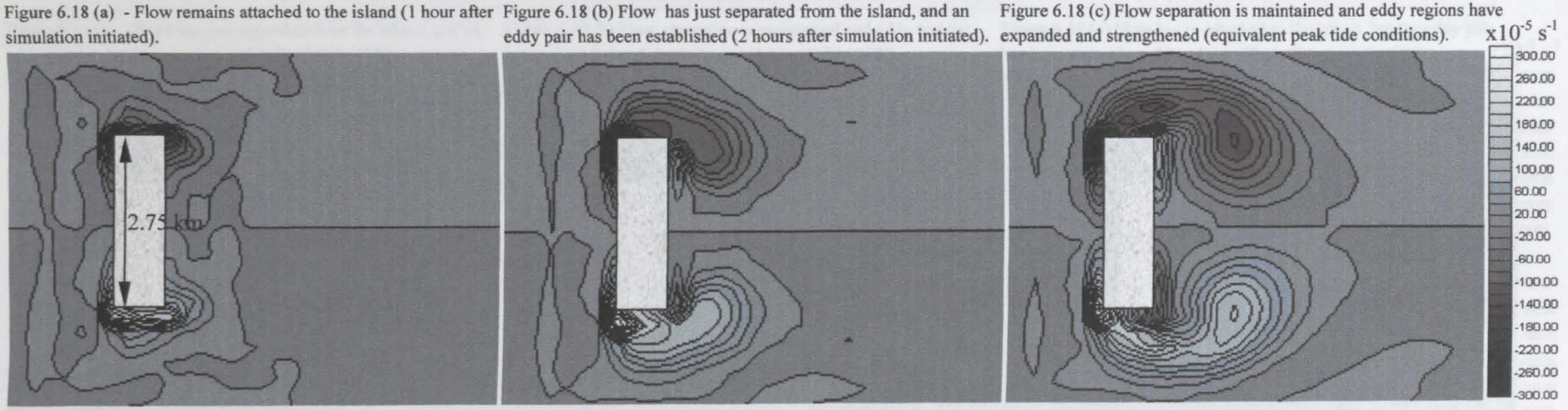

Figure 6.18 - Velocity and vorticity plots demonstrating combined interaction of topographic and bathymetric eddy generation.

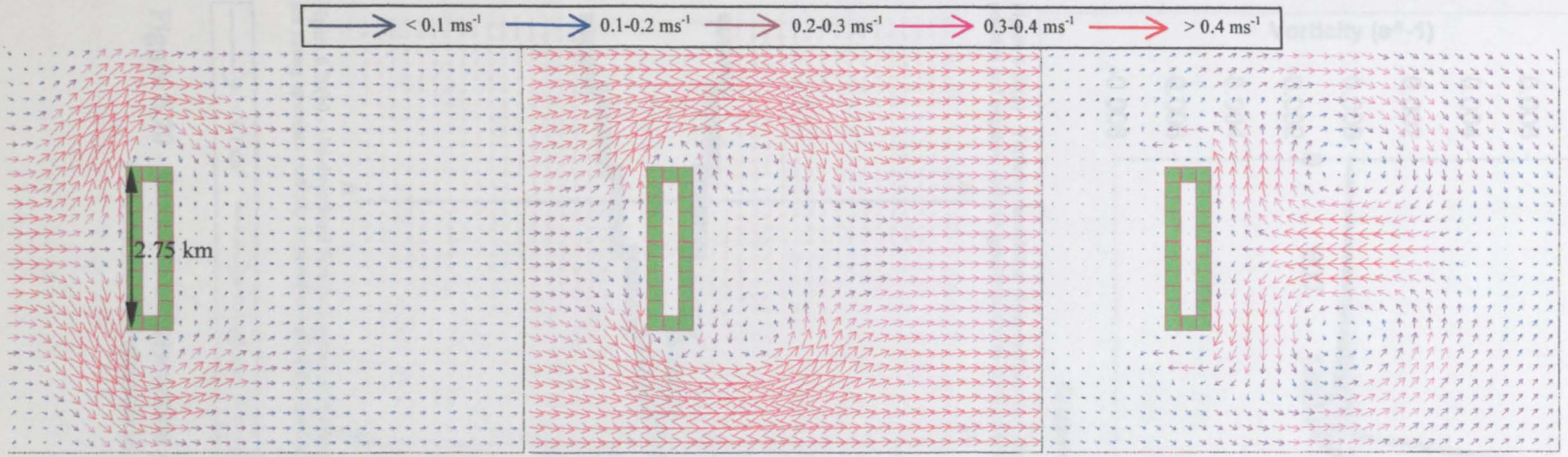

Figure 6.19 (a) - Flow has just separated from the island, and an eddy pair has been instigated (2.5 hours before HW).

Figure 6.19 (b) Flow separation is maintained and eddy regions have expanded and strengthened (1 hour before HW).

Figure 6.19 (c) Flow has re-attached to the island, but the eddy pair has been strengthened by phase effects (3 hours after HW).

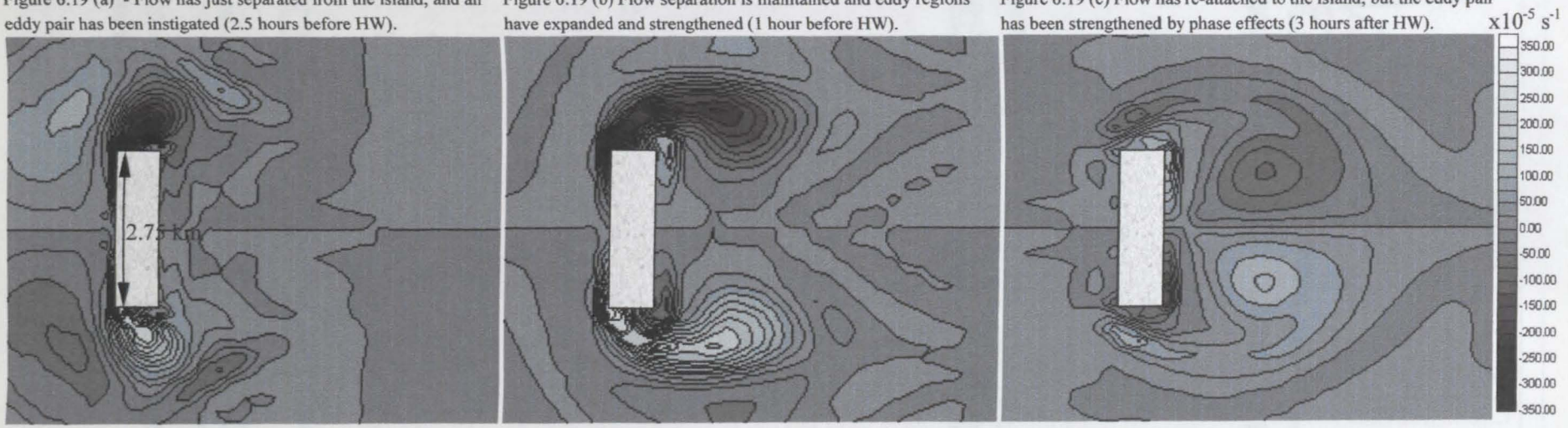

Figure 6.19 - Velocity and vorticity plots demonstrating combined interaction of all three eddy generating mechansims.

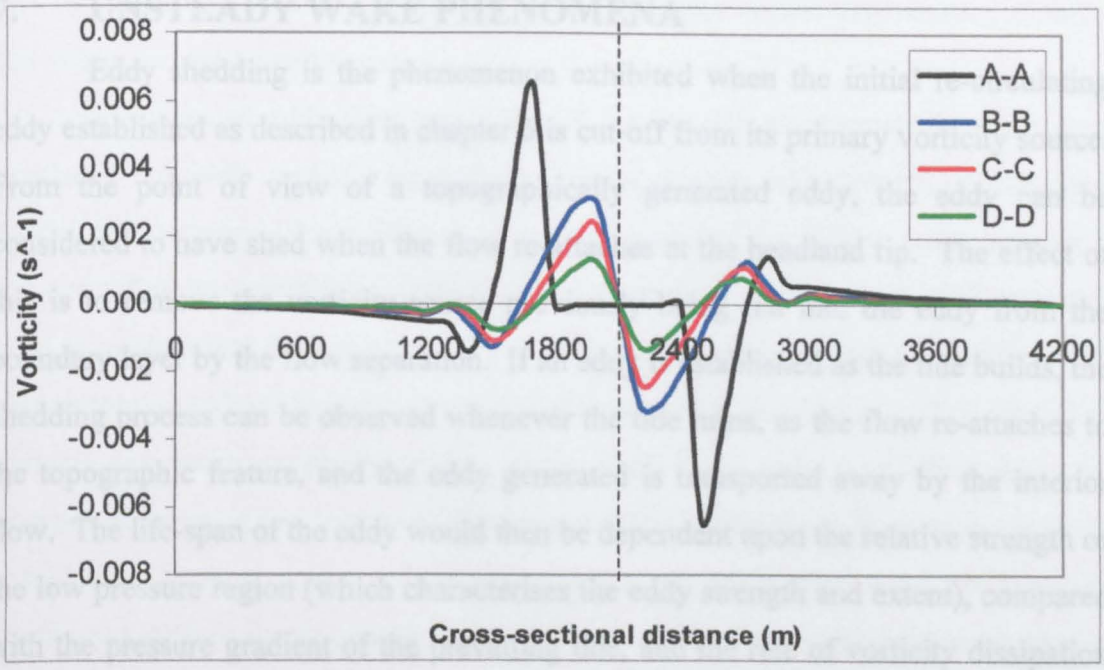

Figure 6.20(a) - Vorticity recorded at cross-sections A-A through D-D. Symmetry (of the absolute value) is observed. The positive and negative vorticity generated across the northern and southern half of the domain cancel along the flow convergence.

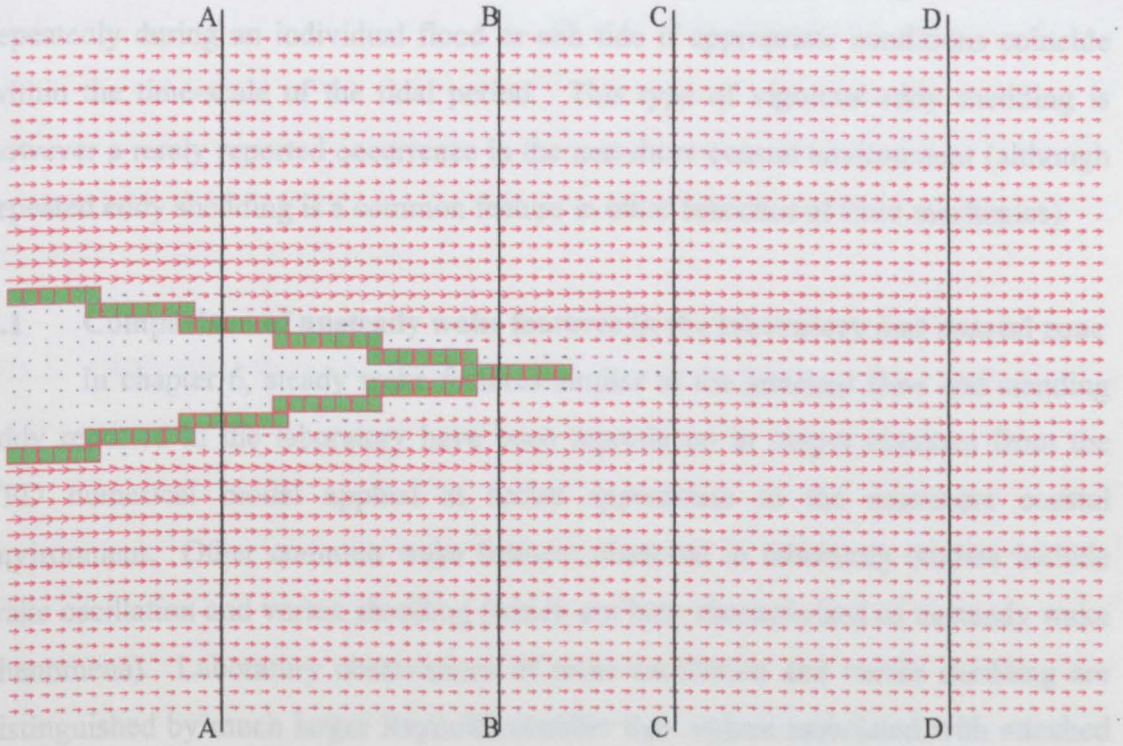

Figure 6.20(b) - Uni-directional flow is observed as the flow converges. No significant separation or wake feature is apparent, as the strong upstream vorticity from either half of the domain is cancelled out.

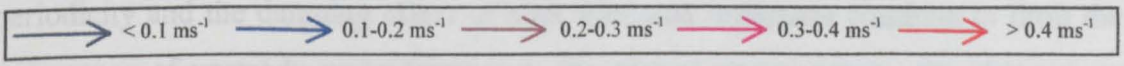

Figure 6.20 - Example of interaction of features associated with eddy generation combining to counteract the eddy generation potential.

7. UNSTEADY WAKE PHENOMENA

Eddy shedding is the phenomenon exhibited when the initial re-circulating eddy established as described in chapter 6 is cut-off from its primary vorticity source. From the point of view of a topographically generated eddy, the eddy can be considered to have shed when the flow re-attaches at the headland tip. The effect of this is to remove the vorticity source previously being fed into the eddy from the boundary layer by the flow separation. If an eddy is established as the tide builds, the shedding process can be observed whenever the tide turns, as the flow re-attaches to the topographic feature, and the eddy generated is transported away by the interior flow. The life-span of the eddy would then be dependent upon the relative strength of the low pressure region (which characterises the eddy strength and extent), compared with the pressure gradient of the prevailing tide, and the rate of vorticity dissipation from the eddy (Imasato, 1983; Signell & Geyer, 1991). Eddy shedding can also occur repeatedly during an individual flood or ebb tide if appropriate conditions coincide within the time-scale of the tidal period. This type of vigorous eddy shedding is however a rarely reported occurrence in the nearshore coastal environment (although repeated eddy shedding is a common feature in other branches of fluid mechanics).

7.1 Comparison of unsteady wake features in the laboratory and coastal zone

In chapter 6, steady wake features similar to the attached flow and standing eddy reported in the laboratory have been reproduced in output obtained from the TFD numerical model applied at scales appropriate to the nearshore coastal environment. Other common wake features observed in laboratory studies include wake oscillation and vortex shedding (which are both characterised as unsteady wake phenomena). Laboratory observations of wake oscillation and vortex shedding are distinguished by much larger Reynolds number than values associated with attached flow and standing eddy regimes. The restricted spin-up time imposed by tidal periodicity and the damping effect of high frictional resistance combine to limit the occurrence of unsteady wake features in the coastal environment. For this reason unsteady wake flows are more closely associate with laboratory (figures 7.1 and 7.2) and atmospheric flow conditions (figure 7.3). Nonetheless, figures 7.4 and 7.23(e) provide evidence of unsteady wake features (eddy shedding) in the coastal

environment. The common feature in these two cases is that the islands generating the wakes are very small in extent.

Evidence of eddy shedding wakes in the coastal environment has only been produced relatively recently through the use of modern remote-sensing techniques (aerial photography). No evidence of the occurrence of oscillatory wake features in the coastal environment is presented in the literature. The laboratory analogy would tend to suggest that the existence of conditions suitable for instigating standing eddy and vortex shedding features at coastal scales would also indicate that conditions suitable for wake oscillation exist. It is likely that wake oscillation is as yet unreported because the density of data necessary to isolate these features is not easily sampled at coastal scales. Indeed, evidence of wake oscillation produced by traditional current meter records is as likely to be interpreted at individual sites as 'noise' in the data, which would subsequently be 'corrected' or 'smoothed' using mathematical analysis techniques. The lack of field data limits understanding of unsteady wake phenomena in the coastal environment. Scaling difficulties to be outlined in the section 7.1.1 restricts physical modelling of these features. Numerical modelling therefore appears to provide the only practical avenue for investigating unsteady wakes at coastal scales.

7.1.1 Difficulties in the application of scaling techniques to physical modelling of the nearshore coastal environment

To highlight the difficulty in reaching a suitable modelling scale while maintaining the correct balance of all the forces involved, a short numerical modelling investigation was performed. A standard test case examined in the oceanographic literature is the two-dimensional flow of a rectilinear current past a shear-sided triangular headland or cape (Mitsuyashu & Hiraki, 1969; Boyer et al. 1987(a); Davies et al. 1991). A similar case appropriate to the nearshore coastal environment will be examined. At prototype scale, a typical set of values will be considered (headland length = 1.04 km, uniform depth = 20m, far field velocity = 1 ms^{-1}, Manning's n = 0.025 and a sinusoidal tidal period = 12.4 hours). It is assumed for the purpose of analysis that the fluid is homogeneous, and that the influence of the Coriolis force can be neglected due to the dominance of the convective terms (as

indicated by the Rossby number). Using appropriate non-dimensional numbers for scaling purposes as outlined in chapter 2 (Fr = 0.0071, Re_f = 8.52 and Re_h = 26000 (model) and 742857142 (prototype) which both fall in the turbulent regime.), model values of headland length = 0.26 m (horizontal scale = 1:4000), depth = 0.2 m (using a vertical exaggeration of 1:40), far field velocity of 0.1 ms^{-1} and Manning's n = 0.0733 are arrived at. The numerical simulations are ramped up to steady state over an equivalent quarter tidal period (calculated at laboratory scale using the Keulegan-Carpenter number (10.73)). Results are examined after the equivalent of a complete tidal cycle. Figures 7.5(a) and 7.5(b) demonstrate the prototype and model scale velocity plots, while figures 7.6(a) and 7.6(b) outline the respective vorticity contours. Within experimental tolerances, the results can be considered to agree favourably. The velocities scale appropriately, and most importantly the effect of the obstacles on the flow development are very similar, both simulations predicting equivalent regions of flow separation both in width and length, with a similar 'dead' flow zone bounded by the separation. Slight differences are apparent upon detailed examination of the results, but these are equally as likely to be numerically derived as opposed to inconsistencies due to scaling (the influence of the boundary layer and eddy viscosity at model scales will far exceed that observed at prototype scales due to the restriction of grid size in the numerical model, as outlined in chapter 5.3 and 6.4.3). Good agreement has therefore been reached between the two systems. This would not quite be the case in the real laboratory environment however, as the value of Manning's n required to provide a realistic representation of the bottom friction effect at model scales as defined using the 'equivalent' Reynolds number (Re_f) is excessively high (n = 0.0733). Table 3.2 demonstrated a realistic range of values of Manning's n that can be achieved using various materials, from n = 0.01 for perspex or planed wood, to an upper limit of 0.035 – 0.04 that would be expected to be achieved by a rocky sea-bed. It is obvious that it would not be possible to generate as strong a frictional effect as indicated by the scaling calculations, at least without completely invalidating the two-dimensional nature of the flow. The test scenario was re-run using the numerical model with more appropriate laboratory scale values of Manning's n of 0.01 (Re_f = 458.56) and 0.025 (Re_f = 73.37). Velocity vector plot results relevant to these tests are shown in figures 7.5(c) and 7.5(d) and vorticity

contour outputs in figures 7.6(c) and 7.6(d) respectively. Comparing these results with the original output, the difference observed is substantial. Although the flow upstream of the obstacle is more or less the same, downstream of the headland, the tests using incorrectly scaled values of Manning's n are significantly more vigorous and energetic than observed in the original cases. In both of the new cases, the flow is no longer bounded by one separation event. Instead eddy shedding can be observed to have occurred, particularly in the low friction case (n = 0.01). The low friction case results bear a remarkable resemblance to laboratory results presented by Mitsuyashu & Hiraki (1969), Boyer et al. (1987(a)) and Davies et al. (1991). Although these analyses were broadly intended to be representative of larger scale features, where a more energetic flow regime may be expected (see Boyer et al., 1987 for example), the results presented here illustrate that laboratory scale modelling of shallow water processes from the nearshore coastal environment is untenable when small scale features are being considered because of the difficulty in achieving the appropriate frictional resistance derived from the scaling calculations. This may be considered in part to be one of the reasons why understanding of flow development and eddy generation at this scale is still in a developing state, as suitable research tools required to properly study such phenomena have only recently become available.

7.2 Coastal Scale Unsteady Wake Phenomena

Analysis of eddy shedding at coastal scales is restricted because of the lack of reported full scale cases that can be used to validate numerical models. Physical modelling of eddy shedding phenomena at coastal scales is restricted because of the difficulty in accurately replicating the geometric and dynamic scaling necessary (see chapters 2.2, 7.1. and 7.1.1), and the consequent over- and under-estimation of various physical parameters of fundamental importance in describing the eddy generation and their continued development (see Falconer & Guoping, 1991). The only reported occurrence of eddy shedding in the literature encountered by the author during this project is that presented by Ingram & Chu (1987), where a series of islands in Rupert Bay, Canada (53°30N, 79°W) were observed to generate eddy shedding and vortex street wake features. These features were recorded using aerial

photography. The numerous islands in Rupert Bay range in extent from 40 metres to 8700 metres in an area of particularly shallow water (< 5 metres). Islands in the bay which exhibited eddy shedding were all of extent 280 metres or less (see figure 7.23(e) for example). The larger islands in the region did not exhibit eddy shedding characteristics. By analogy with similar eddy shedding wake features observed in laboratory studies, and analysis of the relevant physics, Ingram & Chu concluded that eddy shedding was restricted to the smaller islands in Rupert Bay because of (i) the stronger transverse shear exhibited in the lee of the flow obstruction when the obstruction is small (i.e. the velocity gradient is sharper), and (ii) the increased stabilising effect of bottom friction in the case of a larger flow obstruction. Although a numerical modelling aspect was presented in the Ingram & Chu paper, there was no reported attempt to model the shedding phenomenon. Figures 7.4(a, b) also indicates the occurrence of eddy shedding characteristics of very small coastal islands in the Strait of Juan de Fuca. These images were obtained from a large databank of aerial images made available via the Internet by the United States National Ocean Service (http://mapfinder.nos.noaa.gov/default.html).

Taking into consideration the discussion presented so far in this chapter, numerical modelling analysis would appear to provide the most accessible means of analysing unsteady wake features at nearshore coastal scales. The major difficulty that still has to be overcome is the availability of reliable in-situ data that provides coverage of sufficient density spatially and temporally to isolate unsteady wake features in the nearshore coastal environment. Without sufficient data to validate numerical models, it is difficult to have faith in the output produced. However, repeated use and familiarity with the TFD model developed during this research has enabled the author to identify shortcomings of the modelled equations and modelling techniques when applied to cases that would be expected to generate unsteady wake features. The thrust of the remainder of the chapter is therefore to highlight these shortcomings.

7.3 Numerical Modelling of Unsteady Wake Phenomena

Two- and three- dimensional finite-difference models similar to the TFD numerical model developed during this project form the backbone of numerical

analysis tools applied to the coastal and laboratory environment. In general use, these models provide a reliable tool for the practising engineer and for academic investigation. Such models would therefore appear to provide an effective platform for examining or predicting unsteady wake features. Results presented by Denniss & Middleton (1994) and Lloyd & Stansby (1997(a, b)) using 2D finite difference models provide apparently good agreement with expected laboratory type flow regimes indicating unsteady wake features in steady mean flows. However, Furukawa & Wolanski (1998) have stated that 'classical' models (by which they mean two- and three- dimensional finite difference, fixed grid models) are unable to reproduce realistic vortex shedding. These findings were based upon both their own experience and works such as Davies et al. (1995) who reported the results of a numerical modelling exercise across a wide range of the relevant dimensionless parameters without the occurrence of eddy shedding. These conflicting results and viewpoints provide an interesting avenue for investigation.

Previously, the catalyst for the occurrence of an unsteady wake in a symmetrical domain subject to a steady inflow condition (conditions modelled by Denniss & Middleton (1994) and Lloyd & Stansby (1997(a, b))) has been identified as the instability in the flow that is quantified as turbulence. This random instability causes the separation points on a bluff body to oscillate backward and forwards, thereby enabling the downstream eddies to develop at different rates. From the author's own experience of applying the TFD numerical model using a steady input condition across a wide range of scales (extending from the laboratory to the coastal environment), a fully symmetrical flow is always produced when symmetrical input conditions and domain (parallel to the flow direction) are specified. This observation is supported by the output reported throughout chapter 6, and in figures 7.7(a, b), 7.10(a, b) and 7.14. This is an obvious discrepancy between simulated output produced using the numerical model and findings derived from practical experience. From consideration of the shallow water equations applied in the numerical model, the reason for the maintenance of a steady wake structure becomes obvious. In chapter 3 when deriving the model equations it was explained that many flows have a continuously fluctuating velocity. If considered over a long time period, the velocity can be decomposed into a mean and fluctuating velocity component. Calculations are

therefore generally based upon the mean velocity component, and during the derivation, the fluctuating component is introduced (being referred to as 'turbulence') using the eddy viscosity term. From a numerical modelling standpoint, deriving the turbulent contribution of the fluctuating velocity component is very complex due to the inherent chaotic nature of turbulence (this is referred to as the 'closure problem'). In order to obtain closure of the equations, it is necessary to relate the value of the eddy viscosity to existing variables in the simulation. The random fluctuating component of velocity is consequently never introduced into the simulation. This is not a problem that is restricted to zero-equation type eddy viscosity models applied in the TFD model. The reason why no unsteady wake features are observed is therefore related to the mathematical derivation of the shallow water equations. As the derivation applied in this project broadly follows the derivation advocated by the literature (turbulence model derived from Boussinesq's eddy viscosity concept), this is not a case specific problem. It therefore remains unclear as to how Denniss & Middleton (1994) and Lloyd & Stansby (1997(a, b)) managed to generate unsteady wake features under the conditions reported. Examining the original papers and relevant numerical modelling references (Flather & Heaps (1975); Pingree & Maddock (1977); Casulli & Cheng, 1992), there is no report of any divergence from the standard derivation of equations, or from modelling of turbulence via the eddy viscosity term. In fact, the TFD model is based upon much of the same original work. Without direct access to the numerical models applied, the only conclusions that arise are that either (i) there are problems with the coding of these models which have been overlooked (possible causes include, incorrect centring of the equations, or flaws in the boundary conditions), (ii) that the reported symmetrical domain or modelling conditions has been incorrectly set-up (i.e. that it was not actually symmetrical in the model), or (iii) that alterations have been made to the numerical code that have not been reported in the literature.

Using the TFD model, it is the now the intention to demonstrate the effect of various spurious instabilities entered into the simulation, each of which may or may not initiate an unsteady wake feature in an otherwise steady flow. These tests fall into two categories. The first will discuss methods of introducing alterations to the numerical code to produce a very small random fluctuating effect analogous to

turbulence, which should produce a more realistic simulation of turbulent flow regimes. The second category will discuss the introduction of asymmetry to the model domain through modelling 'mistakes' or difficulties. If not fully understood model related problems could adversely impact on the results obtained. In many of the cases discussed in the second category, the results obtained appear at first sight to produce a more realistic simulation than when the model was correctly set-up. This highlights the importance of always questioning the results obtained, rather than settling for what the model produces without enquiring or asking how it is operating.

7.3.1 Effect of introducing small random fluctuations (turbulence) into the simulation on the downstream wake development

The first method to be considered is to introduce small random fluctuations into the simulation. The simplest method of doing so using the TFD models is to add a small varying component to the x- and y- directed velocity at each time-step. Doing so across the entire domain could introduce excessive instability into the solution. As the theory being investigated is the development of small variations introduced upstream into significant flow features downstream, the fluctuating velocity components will be restricted to the area adjacent to the bluff body being examined. The random velocity component is introduced using the RANDOM library function offered by the Salford FORTRAN 77 compiler. The main advantage this offers is that although a random number is introduced at each selected cell for every time-step, the same results is produced each time the simulation is run. This is because the RANDOM value returns to the first number in the library and progresses sequentially through the library whenever the program is re-started (as long as the SEED value remains unchanged). In operation, immediately after calculating the x- and y-velocity components using the standard TFD code, the randomly fluctuating component is introduced as follows,

$$[qu, qv](i, j,3) = [qu, qv](i, j,3) \times (1 + ((var/100) \times (RAN - 0.5))) \quad (7.1)$$

where 'var' is the case specific prescribed maximum value of the fluctuating component expressed as a percentage of the original velocity component, and 'RAN' is a random number between 0 and 1. This produces a randomly fluctuating velocity that varies around the original value of the velocity component within the bounds

specified by the user. The influence of the Coriolis force will be ignored in all the tests considered in section 7.3.

7.3.1.1 *Symmetrical island case*

The symmetrical island domain to be considered in this section is shown in diagram 7.1. In order to ensure the onset of wake oscillation or eddy shedding is not retarded by friction or the size of the bluff body (larger features restrict velocity gradient in the wake of the body), an idealised laboratory scale set-up will be considered in the first instance (Manning's n = 0.000001 $sm^{-1/3}$, Δx = 2 m, island

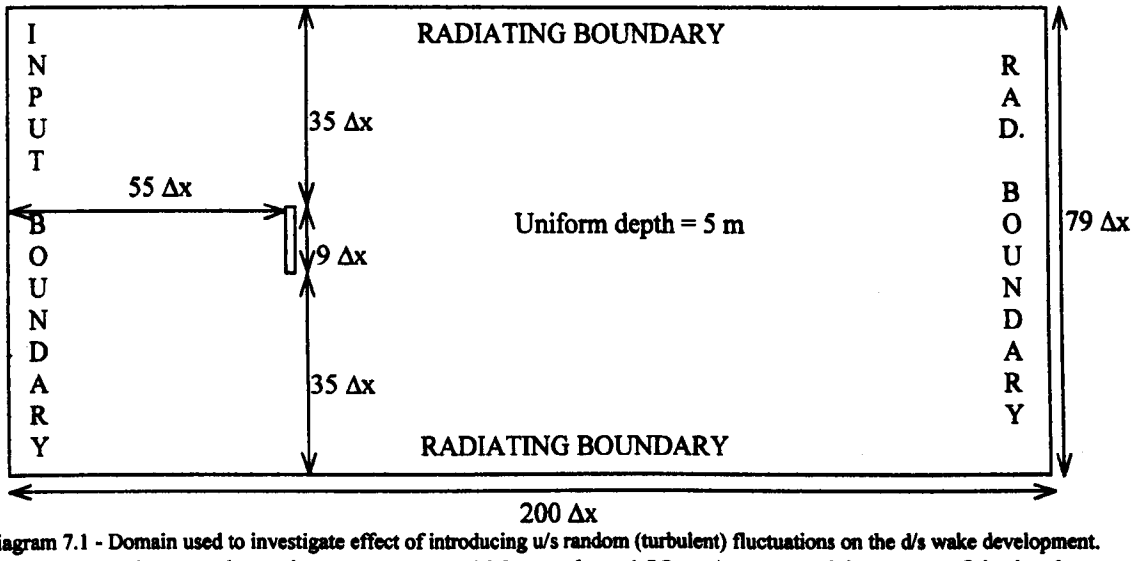

Diagram 7.1 - Domain used to investigate effect of introducing u/s random (turbulent) fluctuations on the d/s wake development.

extent = 18 m, domain extent = 400 m by 158 m). In this near frictionless environment, unsteady wake features would be expected. The elevation input condition is ramped up to 1.00 m from 0.0 m over a period of 250 seconds, and maintained at steady state thereafter. This produces a steady state free-stream velocity of approximately 0.75 ms^{-1}. A datum case was produced with no random component introduced at the island tips in the TFD program. As expected, an eddy pair is formed via the topographic generating mechanism, and expands as the input condition is ramped up. The eddy pair continues to develop after the input condition has reached steady state. It takes around 1000 seconds for the entire domain to reach steady state. Figure 7.7(a) shows the extent of the eddy pair after steady state has become established (the result is obtained after 1900 seconds, at which point the simulation was terminated). Analysis of direct particle tracking output (no random perturbation imposed) demonstrates that particles passing close to the island tips are entrained in the re-circulating eddies while the flow is still developing. After steady

state has been reached, the eddy pair form two separate closed re-circulations. The particles previously rolled-up remain caught in the eddy system, while new particles from upstream stay in the free-stream flow. Figure 7.7(b) shows the particle track output after 1900 seconds of simulated time (equivalent to figure 7.7(a)), which illustrates this point.

The results in figures 7.7(a, b) can be directly compared with 7.7(c, d), which are output at exactly the same time, and derived using the same conditions. The only difference is that the second set of results were generated using a version of the TFD code that incorporated equation 7.1 which introduces the small random velocity component at the tips of the island. The fluctuating component was imposed on the 4 cells directly to the north and south of the island in line with the major axis of the island. The magnitude of the pseudo-turbulent variation was set at ±0.25% of the cell velocity. The effect on the solution generated by the model was significant. Figure 7.8 indicates the flow development from the early near symmetrical flow regime, through the stages of one eddy of the original pair becoming dominant and subsequently shedding. Once the shedding regime is established, the system is self-sustaining while the input condition is maintained at steady state. A vortex street wake reminiscent of a von Karman street is apparent at this stage of the development. The run was terminated after simulating 1900 seconds of flow development (figure 7.6(c, d)). The eddy shedding period (the time taken for two alternate eddies to shed) recorded once the street wake is established is approximately 155 seconds (St = 0.154), with an initial wave-length of 55 metres.

It is well established from laboratory analysis that the rate of eddy shedding in an otherwise steady state flow is directly related to the extent of the bluff body, and the free-stream velocity (via the Strouhal number introduced in chapter 2.1.4). In order to confirm that the wakes being generated by the pseudo-turbulent fluctuating component in the TFD numerical model are also shape dependent (i.e. are only instigated rather than controlled by the random perturbations artificially imposed), a different shape is considered. The domain in diagram 7.1 is maintained, but a 'circular' island replaces the 'flat-plate' island. The diameter of the circular island is set at the same size as the extent of the major axis of the original island (9 cells). Applying the same modelling conditions as for the previous case, the output in figure

7.9 was obtained (compare with figure 7.7). It is important to recall that the RANDOM library function ensures the same perturbation is applied in this simulation in each cell at every time-step as was applied in the previous case. This enables direct comparison between the two cases. The eddy shedding period for the circular island is similar to the flat plate (≈ 160 seconds, St = 0.15), but the initial wave-length is increased to 80 metres. A further significant difference from the 'flat-plate' island, which can only be related to the change in shape of the bluff body feature, is the increased lateral extent of the downstream eddy train. This increase in extent is coupled with a decrease in the concentration of the roll-up of particles into the eddy centre which is being used as an indication of the concentration of vorticity in the core of the developed eddies. Figures 7.9(c-f) demonstrate the rapid growth in the small random fluctuation introduced adjacent to the island into large periodic fluctuations in the downstream domain. The rapid expansion of the initial perturbation is a consequence of non-linear interaction in the wake of the island. In a uniform channel type domain with no island, introducing the same small random fluctuating velocity component would have no discernible effect on the flow development. One point worth raising that is highlighted by figures 7.9(c-f) is that although the eddy shedding is a periodic feature, the length of each shedding period is not constant, there is variation around the figures stated in the two cases discussed above.

The idealised results at laboratory scale discussed have highlight the key role played by turbulence in the generation of asymmetrical and shedding wakes in the lee of symmetrical islands. Will increasing the extent of the cell size, domain and bluff body feature to coastal scales produce a similar set of results? Returning to the 'flat-plate' island shown in diagram 1, Δx is now increased to 200 metres to create an idealised coastal domain. All the other parameters remain unaltered (e.g. Manning's n = 0.000001 $sm^{-1/3}$, input elevation = 1.0 m, no Coriolis). Once more, running a datum case with no pseudo-turbulent effect, a stable eddy pair is simulated at steady state (figure 7.10(a)). Comparing with the respective laboratory scale results (figure 7.7(a)), the downstream extent (in cells) and velocity magnitude of the eddy pair produced at the two different scales are in good agreement. The differences between the two results are related to; (i) numerical diffusion ($0.01U\Delta x \approx 0.02$ m^2s^{-1} at

laboratory scale, and ≈ 2 m^2s^{-1} at the coastal scale applied), and, (ii) the influence of a more defined boundary layer in the laboratory case (because of the small cell size). The main point of interest is however, the impact of introducing small random perturbations to the simulation on downstream wake development. The same technique, area of application (measured in cells) and magnitude of pseudo-turbulence was introduced as in the laboratory cases. Comparing the respective laboratory results (figures 7.10(c, d)) and coastal scale results (figures 7.7(c, d), eddy shedding period = 13100 seconds, St = 0.183), the level of agreement between the two indicates that the small perturbation applied has a similar influence on the downstream wake development irrespective of the scale considered. This statement only holds true when frictional dissipation is negligible. Figure 7.10(e, f) demonstrates the effect of applying a realistic bed friction parameterisation for the coastal zone (Manning's n = 0.025 $sm^{-1/3}$). All other parameters are as for the previous case (figure 7.10(c, d)). No shedding is observed. The wake produced encompasses a very small, almost symmetrical re-circulating eddy pair. This result is not unexpected, as the effect of the small random ±0.25% velocity perturbation applied to the cells adjacent to the island tips would be severely damped by the introduction of frictional resistance. A similar result (not shown) was produced when the simulation was repeated with the random perturbation increased by an order of magnitude (±2.5% of local velocity).

7.3.1.2 *Headland case*

In the previous section, the interaction of two tip eddies subject to small random perturbations was key to the development of eddy shedding in the lee of the modelled island and the subsequent vortex wake observed. As a headland by definition has only one tip, unsteady wakes generated by headlands must be subject to a different mechanism. Headland wakes can therefore no longer be considered equivalent to the half-width of a comparable symmetrical island as was deemed permissible in the steady wake cases considered in chapter 6 (section 6.4.4). This difference is highlighted by the cases shown in figure 7.11. A domain equivalent to the half-width of the island case shown in diagram 7.1 (see diagram 7.2) was considered. The same input and modelling conditions were applied as for the island

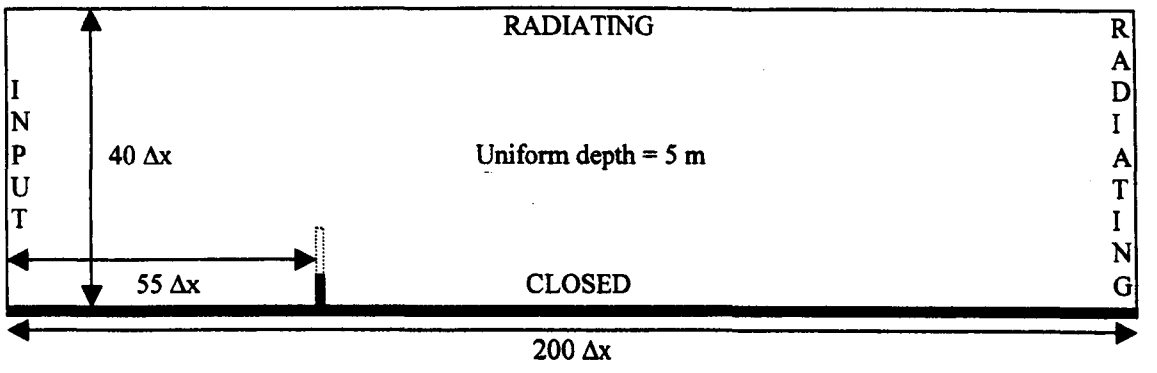

Diagram 7.2 – Headland domain used to compare unsteady wake effects with symmetrical island results (see chapter 7.3.1.1).

case (Manning's n = 0.000001 $sm^{-1/3}$, Δx = 2 m, elevation input ramped up to 1 m from 0 m, steady state free-stream velocity = 0.75ms^{-1}, random perturbation = ±0.25% of the cell velocity for the 4 cells directly north of the headland along the major-axis). With a headland length of 10 m (5Δx = island half-width), a single steady eddy was generated at the headland tip (figure 7.11(b)). The eddy becomes elongated in the downstream region (≈ 12 times the headland extent), but remains attached to the headland. Once steady state has been established in the free-stream region, the downstream wake no longer entrains upstream flow. Consequently, over time the eddy in the lee spins down creating a 'dead-zone' in the lee of the headland (figure 7.11(a, c)). Similar results were observed in the laboratory by the author (see chapter 5.2.1). As shedding is not observed when modelling the island half-width, it seems possible that shedding may occur if the headland is extended. A second headland case (extent = 18 m = 9Δx) was considered using the same modelling conditions. In this instance, the initial eddy generated at the tip is observed to shed from the headland after approximately 800 seconds (see figure 7.11(e)). A second tip eddy is generated as the initial eddy is displaced. The second tip eddy is significantly weaker than the original tip eddy. Both eddies remain entrained in the lee of the headland. No further eddy shedding events are observed (figure 7.11(d, f)). As in the previous case, once the free-stream region reaches a steady state, entrainment of upstream flow into the wake ceases. Over time a 'dead-zone' is observed in the lee of the headland bounded by a strong shear zone. The effect of further increasing the headland extent to 26 m (13Δx) is shown in figures 7.11(g, h, i). Three shedding events are observed. The eddies produced are larger and more vigorous than in the previous case. The first eddy shed from the headland is transported downstream by the free-stream flow and radiated out of the domain. The second and third eddies are

constrained by a strong shear zone, and eventually begin to spin down. A longer period of time is necessary for the wake 'dead-zone' to occur because of the greater energy stored by the more vigorous eddies in this case. The development of the wake 'dead-zone' is shown in figure 7.12.

The question still remains whether or not the small random velocity perturbation input at the headland tip is necessary for eddy shedding to occur in the headland wake. Re-running the shedding event depicted in figures 7.11(g, h, i) without the perturbation produced an almost identical wake and overall flow development (not shown). Differences in the flow velocity between the headland wakes in the two cases were restricted to the 2nd decimal place. This indicates that the TFD model is able to simulate headland eddy shedding using fixed-grid finite-difference techniques without the need to introduce additional terms as was necessary when modelling symmetrical island cases. This is the most significant difference between the headland and island cases. Eddy shedding in the wake of headlands must be instigated by a different mechanism. Key to the occurrence of headland eddy shedding appears to be the start-up of a small secondary counter-rotating eddy in the lee of the headland. This secondary eddy has been noted to occur in every headland eddy shedding case produced using the TFD model (e.g. see figures 7.4, 7.11 and 7.12). If repeated eddy shedding is observed in the lee of a headland, a secondary eddy is required for each shedding event. The effect of the secondary eddy is similar to the eddy generated at the opposing tip in the island shedding cases discussed earlier. However, the secondary counter-rotating eddy is never observed in island cases. The major difference between the two domains is the presence of the closed boundary provided by the coastline in the headland case. This provides the headland case with the ability to support a secondary low pressure region at the point where the headland meets the coastline. The low pressure region is instigated in this area because of boundary layer interaction which acts as a momentum sink. The presence of a no-slip boundary condition is of fundamental importance. Replicating headland eddy shedding conditions using a free-slip boundary condition removes the momentum sink along the boundary region and consequently no shedding is observed. Figure 7.13 provides a comparison of the development of flow in the lee of a headland using no-slip and free-slip boundary conditions respectively. Diagram 7.3

highlights the different pressure fields produced in the lee of a headland (no-slip boundary) and symmetrical island case. Where the headland case can support a low pressure region which can spin-up into an eddy feature (in the corner), the symmetrical island case requires a relatively high pressure region in the equivalent position. The high pressure point in the island case is necessary to provide a 'saddle-point' in the pressure field between the two-counter-rotating tip eddies.

In all the cases of headland eddy shedding events discussed here, a low friction environment and small Δx have been considered. At scales appropriate to the nearshore coastal environment, headland eddy shedding is a rare occurrence because of the significantly greater frictional dissipation encountered. Similarly, applying a fixed-grid finite-difference model at resolutions appropriate for simulation of nearshore flow development would create problems in adequately resolving the boundary layer (see chapter 6.4.3 for further discussion). Such model related problems would probably prevent successful simulation of eddy shedding events occurring in the coastal zone.

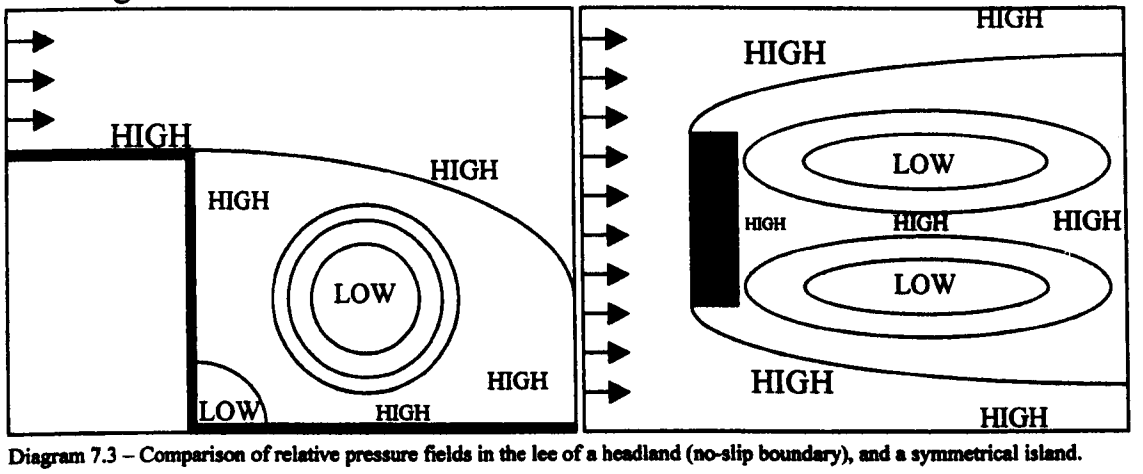

Diagram 7.3 – Comparison of relative pressure fields in the lee of a headland (no-slip boundary), and a symmetrical island.

7.3.2 Effect of introducing model derived asymmetry on the downstream wake development

The second method of generating an unsteady wake feature to be considered is the introduction of asymmetry into the model domain. Asymmetrical islands discussed in the literature such as at Rattray Island (Wolanski et al. 1984) or the islands in Rupert Bay (Ingram & Chu, 1987) produce asymmetrical wakes and eddy shedding respectively. In this section, modelling of significantly asymmetrical island topographies is not the intention. Instead, small model derived or unintentional user generated asymmetries will be the focus. The purpose is to highlight the importance

of accurately describing the model domain, input conditions and boundary conditions. Diagram 7.4 shows the basic domain around which the tests in this section were based. Modelling conditions were specified as, Δx = 100 m (island width = 1 km), uniform depth = 20 m, Manning's n = 0.025 $sm^{-1/3}$ (Re_f = 8.85) and a varying eddy viscosity coefficient is applied (equation 3.3.41). The input condition at the western boundary was ramped up over an equivalent quarter tidal period from cold start conditions to a steady state input elevation of 1 metre. Steady state was maintained for a simulated period equivalent to a lunar day. Use of steady state modelling conditions was necessary to enable unsteady wake features to become fully developed.

The impact on wake development in the lee of the model island in each of the test cases listed in table 7.1 is fairly self-explanatory from examination of the respective figures. In each of the cases where either a domain or model set-up asymmetry is introduced, an unsteady oscillating wake feature is generated, as opposed to the steady eddy pair simulated in the completely symmetric case. Oscillation of the downstream wake, which is best illustrated by the particle tracking results, presents a means of comparing the relative impact of the asymmetry applied in each case. The introduction of a small topographic (figure 7.15) or bathymetric (figure 7.18) asymmetry demonstrates the fundamental importance of accurately representing the model domain. Problems regarding the resolution and accuracy of topographic data used to define the domain, and selection of an appropriate cell size (while balancing computational expense) can prove to be a key source of difference between model results and in-situ data. As expected, when comparing the two results

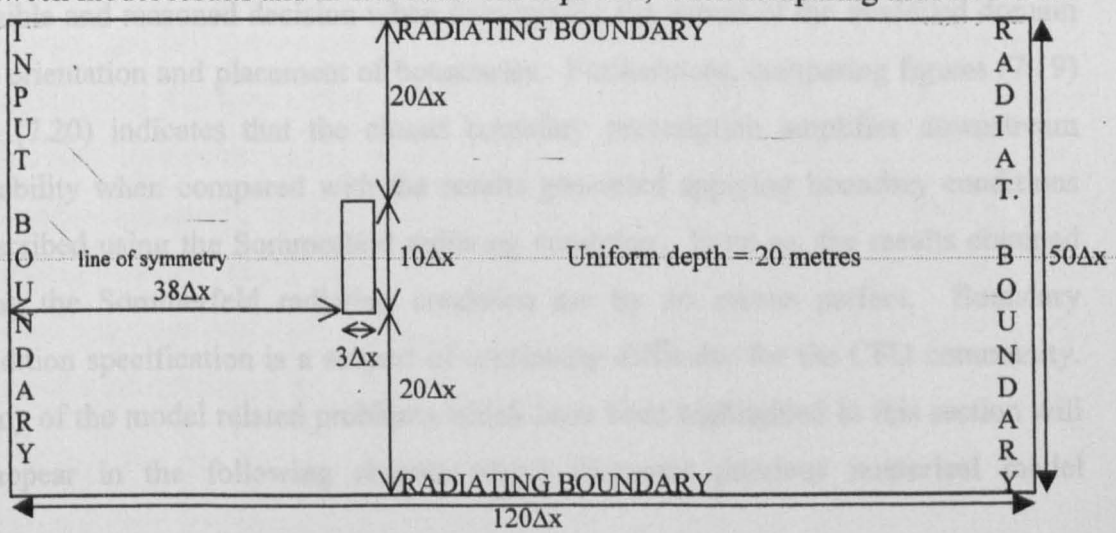

Diagram 7.4 - Basic domain used to investigate effect of introducing model domain asymmetries on d/s wake development.

TEST DECRIPTION	PURPOSE	FIGURE
Fully symmetric domain and modelling conditions	Establish numerically 'correct' result	7.14
Minor topographic domain asymmetry (1 cell), modelling conditions symmetric	Demonstrate importance of topographic shape and definition on d/s flow development	7.15
Fully symmetric domain, Coriolis parameter equivalent to a latitude of 5°N	Demonstrate effect of weak Coriolis force: Unsteady feature requires large spin-up time	7.16
Fully symmetric domain, Coriolis parameter equivalent to a latitude of 60°N	Demonstrate effect of strong Coriolis force: Comparison with previous 'weak' case	7.17
Minor bathymetric domain asymmetry (1 cell × island width = 10 m across north of island), modelling conditions symmetric	Demonstrate importance of accurate bathymetric data, resolution and definition on d/s flow development	7.18
Major domain feature (island) specified off-centre (3 cells) towards northern boundary, modelling conditions symmetric	Demonstrates the effect of asymmetric interaction of flow variables with the lateral **open** boundary condition.	7.19
Major domain feature (island) specified off-centre (3 cells) towards northern boundary, lateral boundaries specified as closed, modelling conditions symmetric	Demonstrates the effect of asymmetric interaction of flow variables with the lateral **closed** boundary condition. Comparison with previous open boundary condition case	7.20

Table 7.1 - Summary of tests used to demonstrate effect of model derived asymmetry on downstream wake development.

that demonstrate the influence of the Coriolis force (figures 7.16 and 7.17), increased latitude produces a larger oscillation. One key factor influencing the accuracy of a simulation that receives little attention in the literature is the positioning and prescription of the lateral boundaries. Figures 7.19 and 7.20 illustrate the effect on the flow development of positioning the key domain feature off-centre in the domain. The asymmetric interaction between the developing a flow and model boundary numerically generates instability as indicated by the downstream wake oscillation. In this particular case, the effect is magnified by the change from a fully symmetric to an asymmetric domain. However this serves to indicate the importance of reaching a sensible and reasoned decision when determining the extent of the modelled domain and orientation and placement of boundaries. Furthermore, comparing figures (7.19) and (7.20) indicates that the closed boundary prescription amplifies downstream instability when compared with the results generated applying boundary conditions prescribed using the Sommerfeld radiating condition. Even so, the results obtained using the Sommerfeld radiating condition are by no means perfect. Boundary condition specification is a subject of continuing difficulty for the CFD community. Many of the model related problems which have been highlighted in this section will re-appear in the following chapter which discusses previous numerical model

simulations of the flow around Rattray Island. An awareness of these problems will hopefully aid in attempts to apply the TFD model to the Rattray Island case.

The existence in nature of a completely symmetrical domain, input condition, and wake flow (as considered in the idealised cases in this chapter), is improbable, if not impossible. The important point that is being raised is the effect of minor adjustments of the model domain and modelling conditions on the model output. The theoretically 'correct' result, which produces a symmetrical flow, as dictated by the modelled equations, is in fact the opposite of what is expected from observational experience from the laboratory and natural environment. Interpreting the model output indicates that the equations used to describe fluid dynamics, in this case the Shallow Water Equations derived from the three-dimensional Equations of Motion are imperfect. The imperfection of the equations is universally accepted. The intuitive response however, is to accept the asymmetric wake results generated by the model, as they appear to the user to provide a closer fit to the expected flow development. The user should not accept model output uncritically because it confirms their own idea of what they *want* the simulated results to indicate. Actually the output may be the response of the model to errors unintentionally introduced by the model user or inherent in the model code.

What the results presented do indicate is that a minor source of flow instability in the domain can have an important influence on the results produced. In the majority of coastal modelling studies, such user or model derived imbalances introduced to the simulation would be masked by; (i) the damping effect of friction in the shallow water environment, (ii) relatively short spin-up time afforded by tidal periodicity, and (iii) the complexity of flow development in real coastal topography. The failings of the user and/or model code would therefore be inseparably inter-twined with 'acceptable' numerical modelling errors derived from the imperfection of the model equations, problems of resolution, variability of bathymetric and calibrating data-sets, etc. It is only when the simplest cases are considered (as in the idealised test-cases discussed in this chapter) that it is possible to identify the effect of such minor alterations on the model output.

7.4 Comparison of significance of friction term versus eddy viscosity term

Previous analysis comparing coastal and laboratory scale flows tends to indicate that frictional dissipation is the dominant controlling mechanism at coastal scales. The representation of friction loss in the Shallow Water Equations would therefore appear to be of major importance. Following the majority of the two-dimensional models outlined in the literature, the friction term in the TFD model is specified using Manning's friction coefficient as outlined in chapter 3.3.2.1. This is a traditional representation of depth-averaged friction loss, which remains unaltered since the early development of numerical models in the 1960's. However, the origins of this and other commonly quoted representations of friction loss are from empirical relationships derived from open channel flow (e.g. Manning, Chezy and Strickler) and pipe flows (Darcy-Weisbach). The related friction coefficients are also normally specified uniformly across the domain. Little attempt has been made to validate or improve on these representations for application to tidally dominated (periodic) flows in the coastal environment. This is in contrast to the level of interest reflected in the literature towards representation of the eddy viscosity coefficient (turbulent closure model). The intention here is to demonstrate that at coastal scales, the friction term has a more significant impact on the flow development than the eddy viscosity (turbulence) term in the Shallow Water Equations. Two cases will be examined to test this theory.

7.4.1 Test case 1

The first case considered compares the effect of the values of the friction and eddy viscosity terms on the life span and magnitude of eddies generated around an idealised symmetrical headland. The domain is represented using a cell size of Δx = 250 m, the headland length is 4 km with a shelf of uniform slope 5 m/cell extending around the headland with a uniform depth of 20 m specified across the rest of the domain. Typical values of the friction and eddy viscosity coefficients are uniformly applied across the domain in the first instance ($n = 0.025\ sm^{-1/3}$, $\overline{\upsilon}_t = 0.5\ m^2s^{-1}$). The output from this case after 2 complete tides at HW-3 (end of the ebb tide) is presented in figure 7.21(a). The dominant eddy feature observed was generated by flow separation around the headland during the ebb tide. Repeating the test with the value

of the friction coefficient halved (n = 0.0125 $sm^{-1/3}$) produces the output shown in figure 7.21(b). The effect of the friction term in the equations is approximately 1/4 of that in the initial case because the friction term is multiplied by the square of the local velocity magnitude in the Shallow Water Equations. Comparing figures 7.21(a & b), two major differences are apparent. The extent and velocity magnitude of the dominant eddy is significantly increased. Of greater significance however is the presence of a secondary oppositely rotating eddy which is paired with the larger eddy. This eddy was generated by flow separation during the previous flood tide. The reduced frictional resistance has extended the life span of this eddy through the ebb tide. Repeating the original case with a similar reduction in the value of the eddy viscosity coefficient, and with the eddy viscosity coefficient disabled had negligible effect on the flow development (not shown). Repeating the exercise but increasing the value of the eddy viscosity coefficient also has limited impact on the flow. The result obtained with the eddy viscosity coefficient increased by an order of magnitude ($\overline{\upsilon}_t$ = 5.0 m^2s^{-1}) is shown in figure 7.21(c). Even with the eddy viscosity coefficient increased to this extent, the effect on the simulation is minimal compared with the results in figure 7.21(a)

7.4.2 Test case 2

The second case compares the effect of the values of the friction and eddy viscosity terms on an unsteady wake generated by a steady flow around a coastal scale island. The domain used in section 7.3.2 (Δx = 100 m) is used with the addition of a slight domain asymmetry to generate an unsteady wake as originally considered in figure 7.15. The results presented were obtained after steady state had been maintained for an equivalent lunar day (25 hours) in order to allow the unsteady wake to fully spin-up. Typical values of the friction and eddy viscosity coefficients are uniformly applied across the domain in the first instance (n = 0.025 $sm^{-1/3}$, $\overline{\upsilon}_t$ = 0.5 m^2s^{-1}) which produces the oscillating wake structure illustrated in figure 7.22(a). As in the previous case, the test is repeated with the value of the friction coefficient halved (n = 0.0125 $sm^{-1/3}$). The effect of reducing friction has enabled a more energetic shedding wake to develop as shown in figure 7.22(b). Reducing the eddy viscosity coefficient by a similar factor (not shown) has no measurable effect on the

simulation. In order to have a significant impact in this case, it is necessary to increase the eddy viscosity coefficient by an order of magnitude ($\overline{\upsilon}_t = 5.0\ m^2s^{-1}$). This dampens the wake oscillation observed in figure 7.22(a) to produce a stable eddy pair in the wake of the island (figure 7.22(c)). Finally, the combined effect of altering both coefficients was considered. Starting with the case presented in figure 7.22(b), where the value of the friction coefficient was halved, the eddy viscosity coefficient was increased in an attempt to counteract the energetic shedding observed. The effect of altering the respective coefficients in this way obviously does not have a linear effect on the solution produced. However, having run a number of cases, progressively increasing the eddy viscosity coefficient each time, a result was produced (figure 7.22(d)) which bears a strong resemblance to the original case presented in figure 7.22(a). This was confirmed by comparing the frequency of wake oscillation in each case (180 minutes). This results was produced using $\overline{\upsilon}_t = 5.0\ m^2s^{-1}$, which effectively implies that the combined effect of the cases shown in figures 7.22(b & c) produces the result in figure 7.22(d).

7.4.3 Discussion

The two test cases outlined in the sections 7.4.1 and 7.4.2 indicate that numerical model simulations of wake development are more sensitive to alterations of the friction coefficient than to alterations of the eddy viscosity coefficient. This suggests that the representation of the friction term in the Shallow Water Equations is of greater importance than the representation of the eddy viscosity (turbulent closure model) term.

7.5 Rupert Bay Island Case Study

The observational study and analysis of island wakes in Rupert Bay by Ingram & Chu (1987) was introduced in section 7.2. This data set provides an interesting resource that can be used to test the ability of numerical models intended for application in the coastal environment to reproduce vigorous eddy shedding and von Karman street wake features. This is of particular interest in light of Furukawa & Wolanski's (1998) assertion that:

"...this [discrete vortex] model also reproduces successfully the observations of a Karman vortex street in the lee of islands in Rupert Bay, Canada. By contrast fixed-grid models predict no such eddy shedding."

While the previous discussion in this chapter would tend to agree with this statement in the specialised case of a symmetrical domain, the islands in Rupert Bay are asymmetric. The author's experience would therefore tend to suggest that fixed grid models would at least be capable of generating eddy shedding given sufficient time for the flow to develop and spin-up. Initial investigation will therefore concentrate on ramping up to and then maintaining a steady state input condition to determine the model's ability to at least instigate eddy shedding.

Analysing the data and results presented by Ingram & Chu, island number 4 presents the most obvious candidate for modelling because it is one of the few islands where an aerial photograph is included in the paper. The island lies in an area of shallow, relatively uniform bathymetry, reported to be 2 metres deep. The bathymetric data is reported to be accurate to ±1 m. The island width is 160 metres, and knowing this, the topographic shape can be determined from the aerial photograph. The peak far-field velocity is listed as 0.3 m/s with a sandy - gravel bottom material (Manning's n = 0.025 $sm^{-1/3}$ is appropriate). The aerial photograph presented was taken between HW+4 and LW (for comparative purposes, will assume HW+5). No random perturbations were applied in any of the results discussed in this section. Initial runs with a uniform bathymetry of 2 metres (not shown) produced a vigorous wake oscillation, but no real signs of eddy shedding (Re_f = 2.57). The obvious damping effect of bottom friction would suggest that an increase in depth would aid the progression from wake oscillation to eddy shedding. Incrementally increasing the depth by 0.25 metres at a time (not shown), limited eddy shedding is observed in the 2.5 metre case (Re_f = 3.49). The results presented were obtained using a uniform depth of 2.75 metres across the domain (Re_f = 3.93). Initial steady state results indicate that an eddy shedding regime reminiscent of a von Karman street wake is established even before the input condition reaches steady state. The eddy shedding follows the classic development of alternate tip eddies becoming established and then shed when the opposing eddy is spun-up. After the eddy shedding has become established, the simulated shedding period is approximately 45 minutes (St =

0.197), which compares favourably with the reported 41 minutes (St = 0.217) quoted by Ingram & Chu (1987). Similarly, the simulated (700 m) and reported (730 m) shedding wave-length are in close agreement. However comparing the downstream wake width with the aerial photograph indicates that the simulated width at steady state is significantly narrower. In order to provide a proper comparison between the simulated output and aerial photograph it is necessary to incorporate the tidal oscillation into the simulation. A sinusoidal input tide is prescribed with a period of 12.5 hours. The simulation is started from cold start conditions, and is therefore allowed to spin-up for one complete tidal cycle before outputting results. Figures 7.23(a, b) indicate the flow development as the tide peaks. This result is very similar to the steady state results discussed earlier. Figures 7.23(c, d) indicate the flow development at HW+5 which is assumed to equate to the aerial photograph shown in figure 7.23(e) (the difference in phase of the shedding events was expected because the aerial photograph is not related to an exact time). Visual comparison of figures 7.23(d) and 7.23(e) indicate that the simulated output is in close agreement. Measuring the wake-widths (and scaling using the known island width in the case of the aerial photograph), the simulation predicts a width of 400 m, which compares favourably with the aerial photograph results of 375 m.

The results presented above indicate that fixed-grid based models are capable of simulating eddy shedding events when the shedding is initiated by topographic asymmetry. This outcome is in direct contrast to the assertions of Furukawa & Wolanski quoted at the beginning of this section.

7.6 Coastal application of the Strouhal and equivalent Reynolds number

The Strouhal number, $St = \frac{\omega L}{U}$, introduced in chapter 2 is a non-dimensional parameter which can be used to quantify the frequency of eddy shedding. The Strouhal number for the eddy shedding regimes modelled in this chapter has been determined in the cases where eddy shedding was instigated by asymmetry in the domain (as opposed to being triggered by small random perturbations). The value of the Strouhal number ranges from a minimum value of 0.150 to a maximum value of 0.197. This is in close agreement with the laboratory derived value for a cylindrical shaped flow obstacle ($St \approx 0.2$) (Liggett, 1994). A suggested application of the

consistency of this relationship in the coastal environment is to determine the spin-up time necessary for an eddy shedding event to occur by rearranging the Strouhal number such that,

$$\omega\left[=\frac{1}{T}\right]=\frac{St_c U}{L} \Rightarrow T=\frac{L}{St_c U}, \qquad (7.2)$$

where T is the elapsed time, and St_c is the 'critical' Strouhal number. The critical Strouhal number is defined by the limits $St_c = 0.15 - 0.20$ based upon output from the previous simulations. This calculation provides an indication of the spin-up time necessary for eddy shedding to occur. This information may be of use for predicting the occurrence of eddy shedding by comparing the time necessary for eddy shedding to develop with the available time within the tidal cycle. A wider data set would be required to confirm the reliability of this relationship.

One of the commonly quoted non-dimensional parameters introduced in chapter 2 and 6 was the 'equivalent' Reynolds number which takes the form $\left(Re_f=\frac{h^{\frac{4}{3}}}{gn^2L}\right)$. It has been suggested in the literature that this parameter can be used to characterise wakes in the coastal environment in a similar way to the classification of laboratory flows using the Reynolds number. Analysing the variation of this parameter using the TFD model output from this chapter will provide an indication of its suitability. Examining the results, standing eddies were observed for Re_f values ranging from 2.57 - 8.52, wake oscillation at $Re_f = 3.49$, and eddy shedding at $Re_f =$ 3.93 - 458.56. There is therefore a general trend of stable wakes occurring at lower values of the 'equivalent' Reynolds number, and eddy shedding at higher values. However, the overlap between the categories suggests that this parameter is unable to provide an accurate prediction of the developing wake.

7.7 Summary and Conclusions

Wake instability in the form of wake oscillation and eddy shedding has been identified as a relatively rare occurrence in the nearshore coastal environment because of the high friction environment and restricted time scale for wake development. For these reasons, wake instabilities are restricted to very small topographic features (< 1000 m in extent). Such small scale features are of limited practical interest to the

practising coastal oceanographer or engineer. Fixed-grid finite-difference based models are commonly used to investigate wake instabilities across a wide range of scales (laboratory to oceanic). The user must be aware of the deficiencies inherent in these techniques (i.e. the inability to simulate shedding instigated by turbulent effects), and of the effects of introducing artificial asymmetry into the model solution (i.e. domain, boundary or coding asymmetry). Overall, great care must be taken when simulating complex flow interactions such as wake development. The degree of complexity inherent in these problems is indicated by the continued reliance of the majority of the computational fluid dynamics community on physical modelling (e.g. wind tunnel testing of cars, buildings and bridges).

Figure 7.1 – Laboratory von Karman street wake flow. *Source:* http://www.eng.vt.edu/fluids/msc/gallery/vortex/k_exp.htm

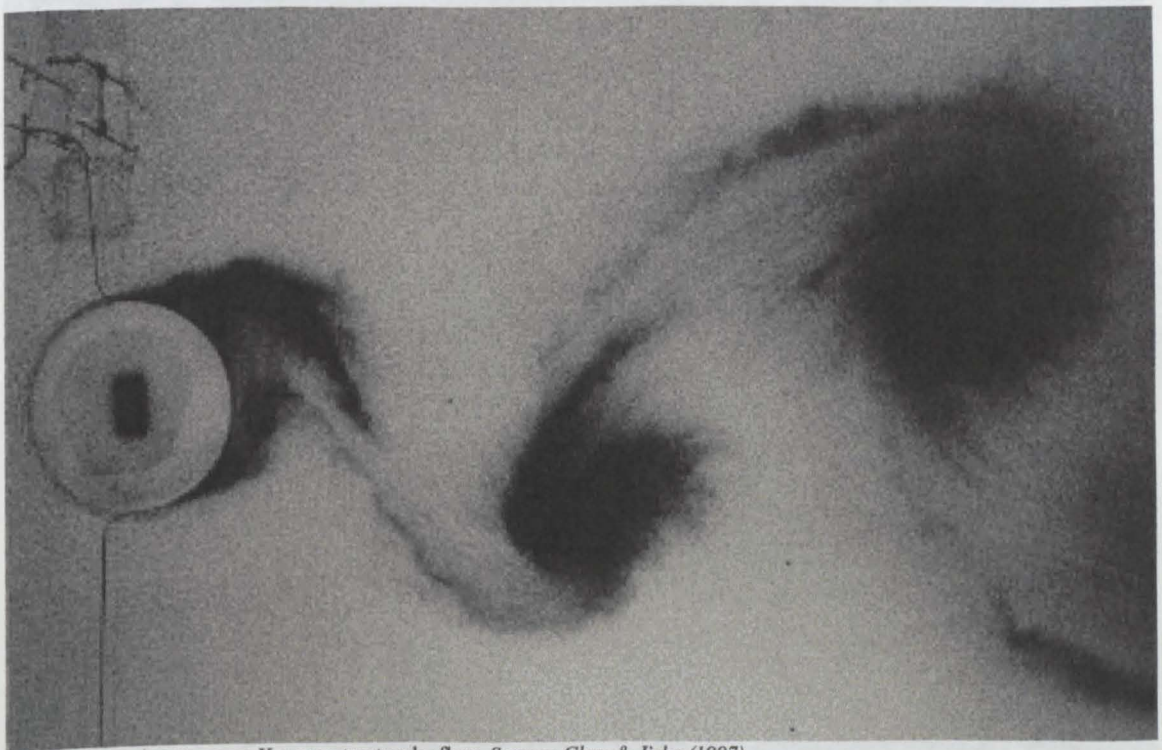

Figure 7.2 – Laboratory von Karman street wake flow. *Source: Chen & Jirka (1997)*

Figure 7.3 – Atmospheric von Karman street wake flow in the lee of Guadalupe Island offshore of Baja, California, USA (20/9/99). *Source:* http://daac.gsfc.nasa.gov/CAMPAIGN_DOCS/OCDST/vonKarman_vortices.html

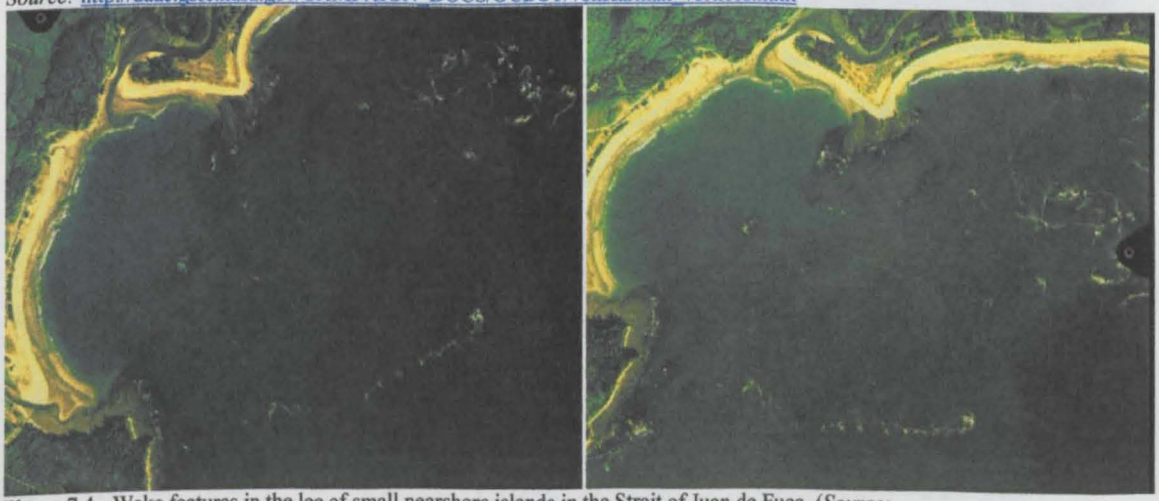

Figure 7.4 - Wake features in the lee of small nearshore islands in the Strait of Juan de Fuca. (*Source: http://mapfinder.nos.noaa.gov/default.html*)

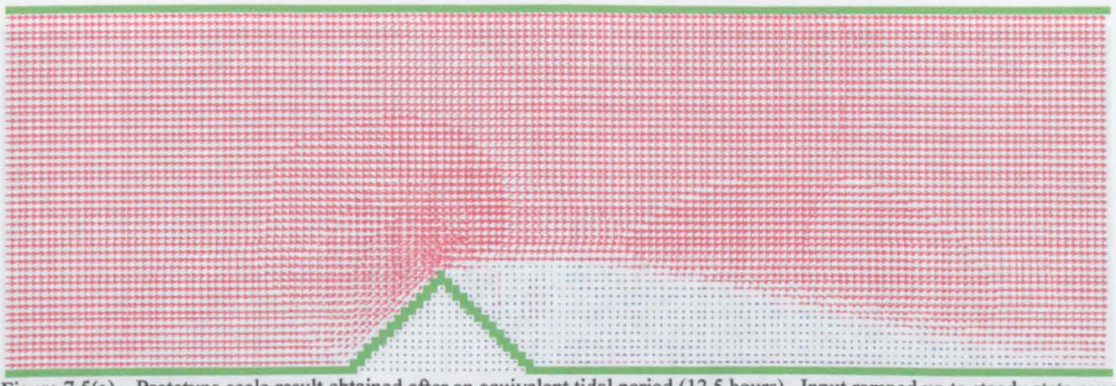

Figure 7.5(a) – Prototype scale result obtained after an equivalent tidal period (12.5 hours). Input ramped up to steady state over ¼ tidal period. Fr = 0.0071, Re_f = 8.52, $Re_h = 7.42\times10^{-8}$.

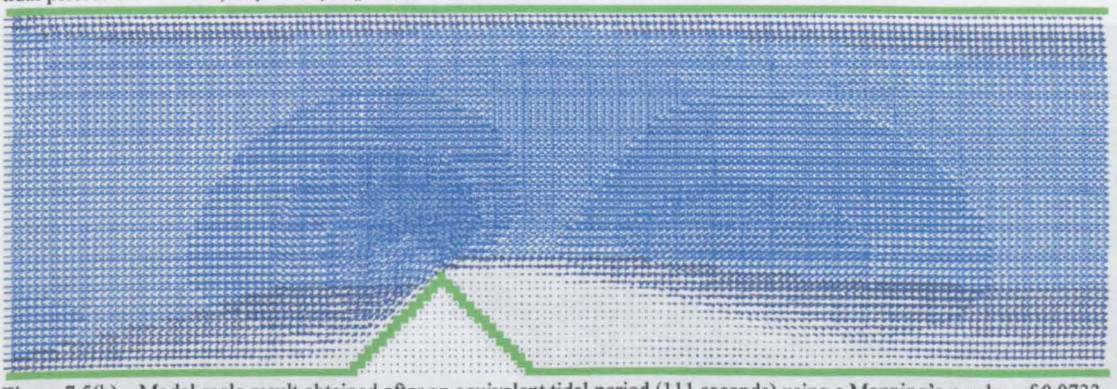

Figure 7.5(b) – Model scale result obtained after an equivalent tidal period (111 seconds) using a Manning's n value of 0.0733. Input ramped up to steady state over ¼ tidal period. Fr = 0.0071, Re_f = 8.52, Re_h = 26000.

Figure 7.5(c) – Model scale result obtained after an equivalent tidal period (111 seconds) using a Manning's n value of 0.01. Input ramped up to steady state over ¼ tidal period. Fr = 0.0071, Re_f = 458.56, Re_h = 26000.

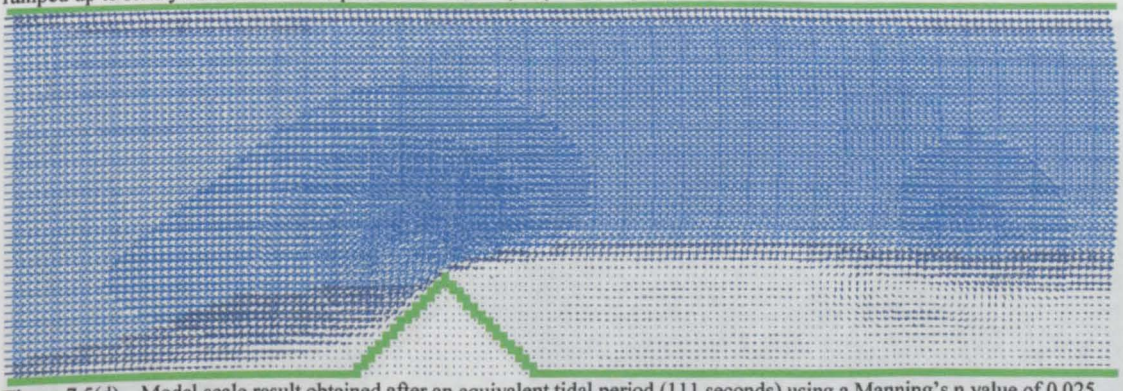

Figure 7.5(d) – Model scale result obtained after an equivalent tidal period (111 seconds) using a Manning's n value of 0.025. Input ramped up to steady state over ¼ tidal period. Fr = 0.0071, Re_f = 73.37, Re_h = 26000.

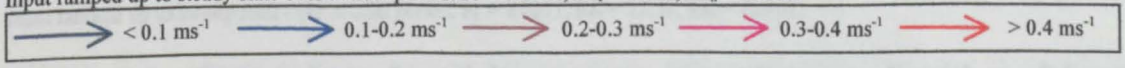

Figure 7.5 – Comparison of velocity plots at prototype scale with model scale results obtained using different values of Manning's number 'n'.

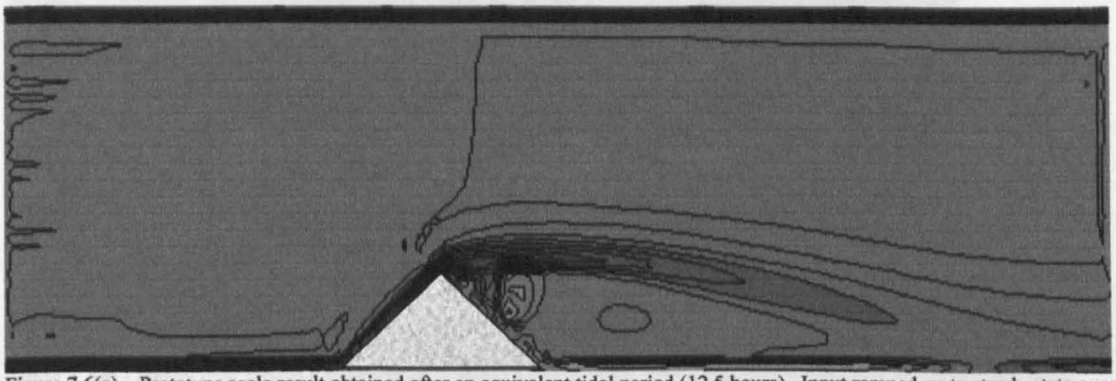

Figure 7.6(a) – Prototype scale result obtained after an equivalent tidal period (12.5 hours). Input ramped up to steady state over ¼ tidal period. $Fr = 0.0071$, $Re_f = 8.52$, $Re_h = 7.42 \times 10^{-8}$.

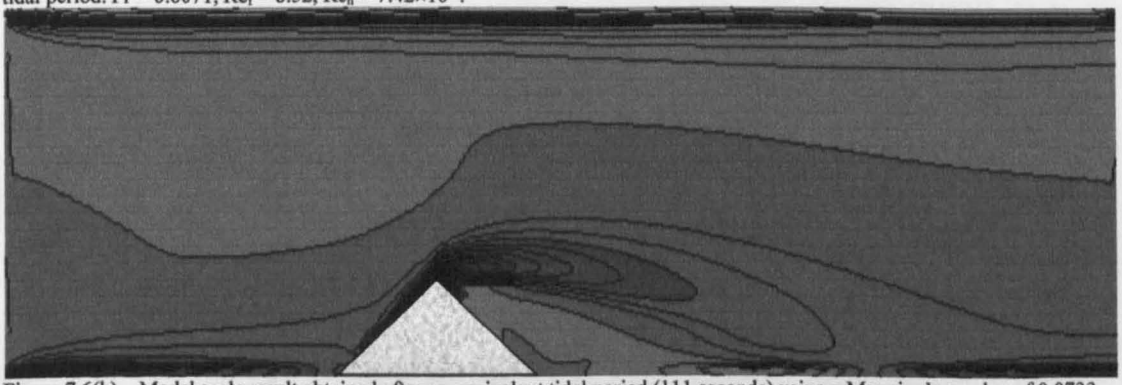

Figure 7.6(b) – Model scale result obtained after an equivalent tidal period (111 seconds) using a Manning's n value of 0.0733. Input ramped up to steady state over ¼ tidal period. $Fr = 0.0071$, $Re_f = 8.52$, $Re_h = 26000$.

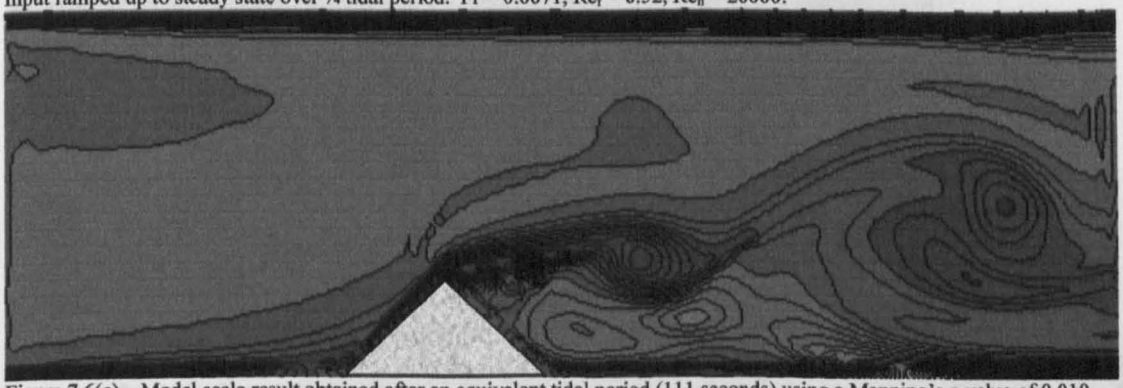

Figure 7.6(c) – Model scale result obtained after an equivalent tidal period (111 seconds) using a Manning's n value of 0.010. Input ramped up to steady state over ¼ tidal period. $Fr = 0.0071$, $Re_f = 458.56$, $Re_h = 26000$.

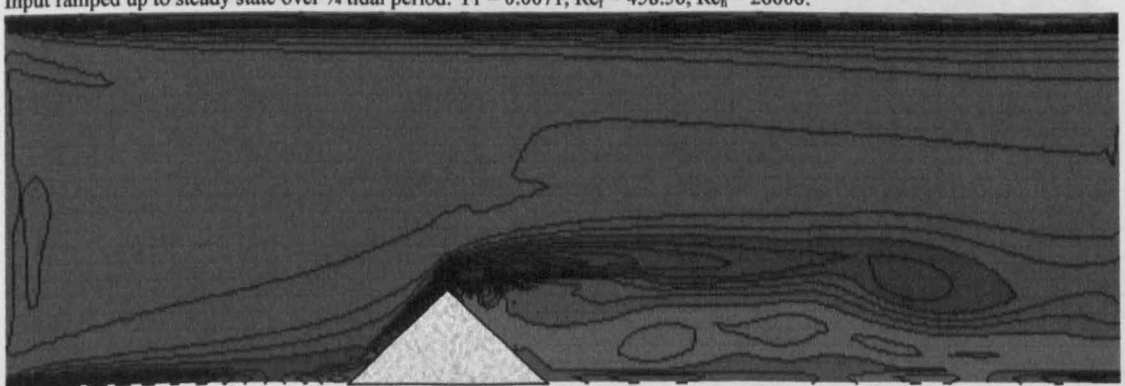

Figure 7.6(d) – Model scale result obtained after an equivalent tidal period (111 seconds) using a Manning's n value of 0.025. Input ramped up to steady state over ¼ tidal period. $Fr = 0.0071$, $Re_f = 73.37$, $Re_h = 26000$.

Figure 7.6 – Comparison of vorticity contours at prototype scale with model scale results obtained using different values of Manning's number 'n'.

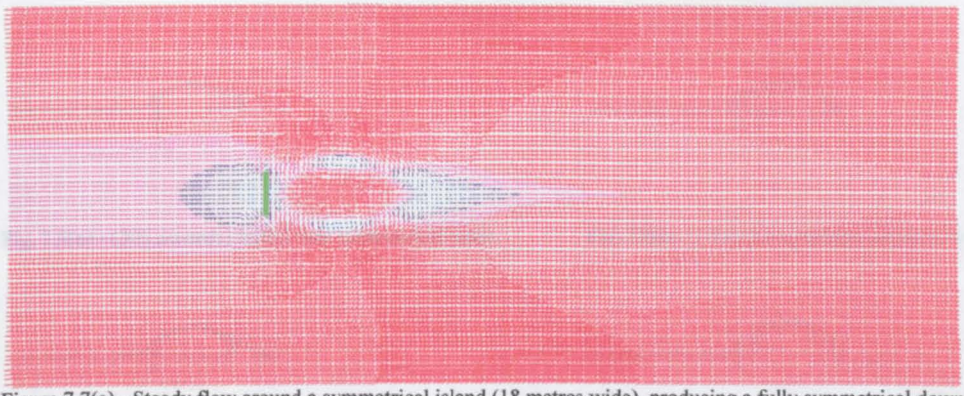

Figure 7.7(a) - Steady flow around a symmetrical island (18 metres wide), producing a fully symmetrical downstream wake.

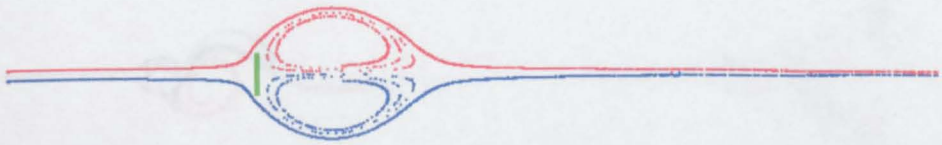

Figure 7.7(b) - Particle tracking output obtained from figure 7.7(a), demonstrating symmetrical flow around modelled island.

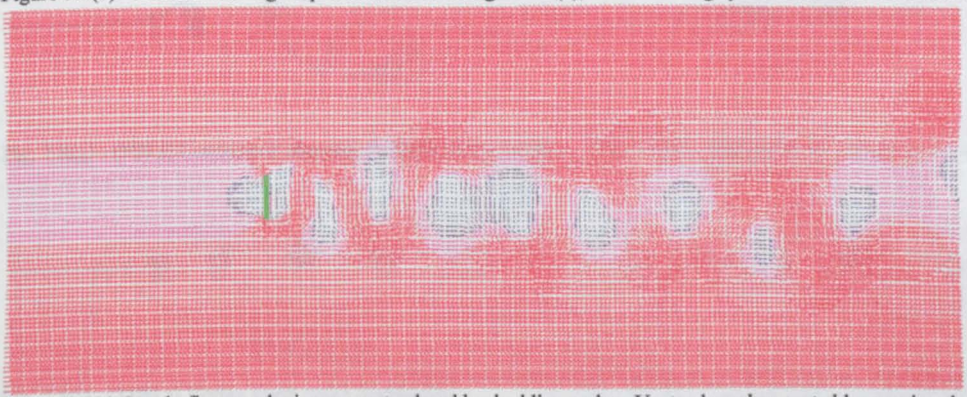

Figure 7.7(c) Steady flow producing an unsteady eddy shedding wake. Unsteady wake created by varying the velocity component randomly in the 4 cells above and below the island tip ±0.25% each time step (small random velocity fluctuations mimic the effect of turbulence). Small fluctuations are amplified by non-linear interaction in the island wake to produce shedding (S_t = 0.154).

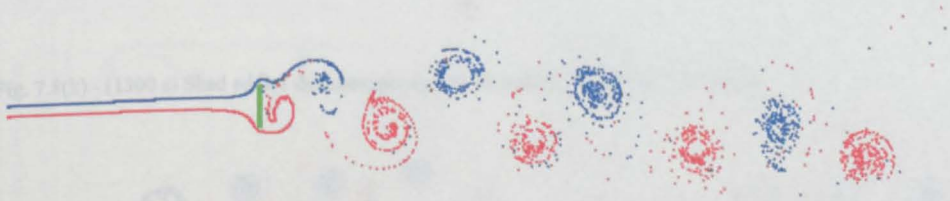

Figure 7.7(d) - Particle tracking output obtained from figure 7.7(c), demonstrating vigorous eddy shedding produced by introducing small random fluctuation into the simulation (S_t = 0.154).

Figure 7.7 - Comparison of downstream wake development around a symmetrical laboratory scale 'flat-plate' island with and without the addition of small (± 0.25%) random velocity perturbation at the island tips.

Fig. 7.8(a) - (300 seconds) Initial near symmetrical wake.

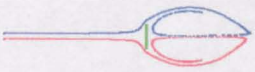

Fig. 7.8(b) - (400 s) Asymmetry apparent in wake.

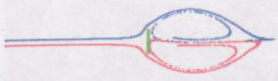

Fig. 7.8(c) - (500 s) Asymmetry develops.

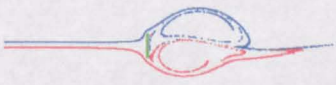

Fig. 7.8(d) - (600 s) Northern eddy starting to shed.

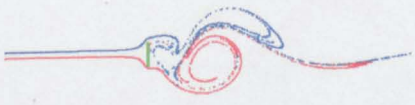

Fig. 7.8(e) - (700 s) Both eddies shed, replacement eddy forming.

Fig. 7.8(f) -(800 s) Initial eddy pair impinging on free-stream

Fig. 7.8(g) - (900 s) Continuous ongoing shedding of tip eddies.

Fig. 7.8(h) - (1000 s) Steady shedding frequency apparent.

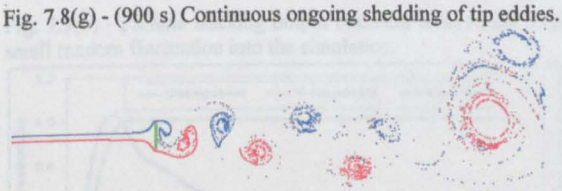

Fig. 7.8(i) - (1100 s) Vortex street wake developing.

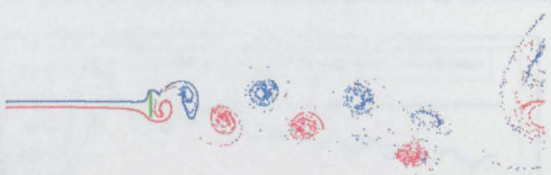

Fig. 7.8(j) - (1200 s) Initial eddy pair advected out of domain.

Fig. 7.8(k) - (1300 s) Shed eddies demonstrate significant roll-up.

Fig. 7.8(l) - (1400 s).

Fig 7.8(m) - (1500 s) Vortex street displaying lateral oscillation.

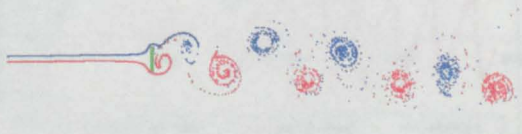

Fig7.8(n) - (1600 s).

Figure 7.8 - Development of vortex street in the wake of a laboratory scale 'flat-plate' island from small (± 0.25%) random velocity perturbations at the island tips (St = 0.154).

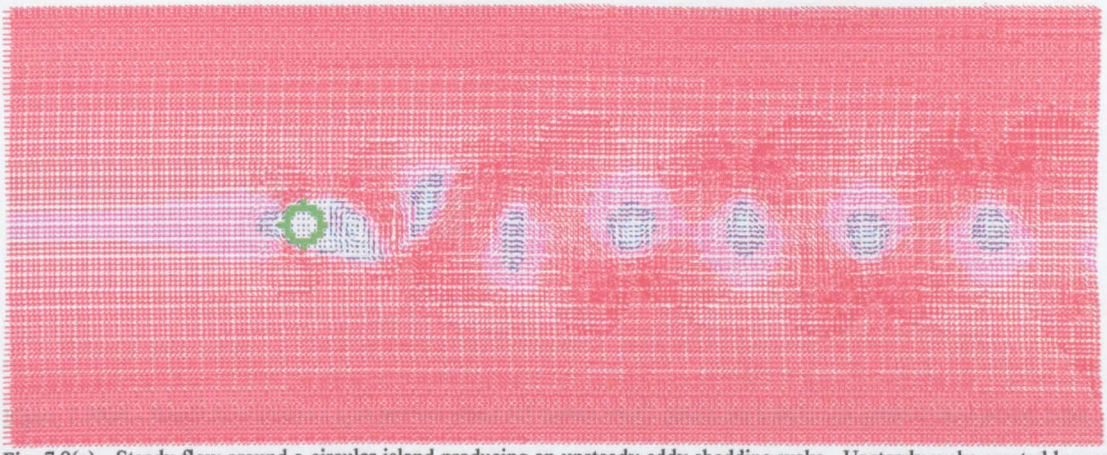

Fig. 7.9(a) - Steady flow around a circular island producing an unsteady eddy shedding wake. Unsteady wake created by varying the velocity component randomly in the 4 cells above and below the island tip ±0.25% each time step (small random velocity fluctuations mimic the effect of turbulence). Small fluctuations are amplified by non-linear interaction in the island wake.

Fig. 7.9(b) - Particle tracking output obtained from figure 7.8(a) demonstrating vigorous eddy shedding produced by introducing small random fluctuation into the simulation.

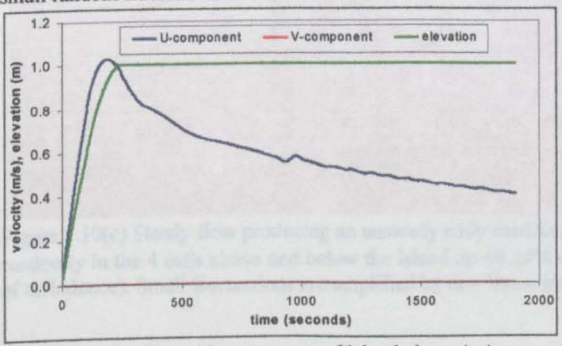

Fig. 7.9(c) - Profiles 100m upstream of island along A-A.

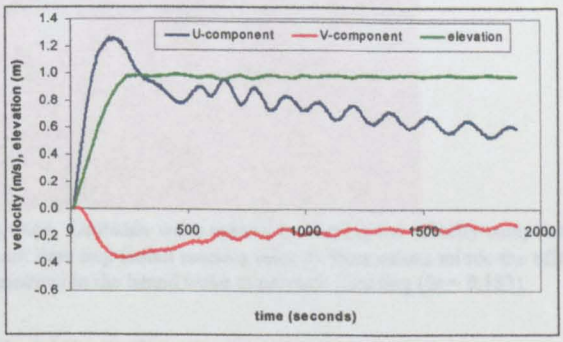

Fig. 7.9(d) - Profiles adjacent to the island along A-A.

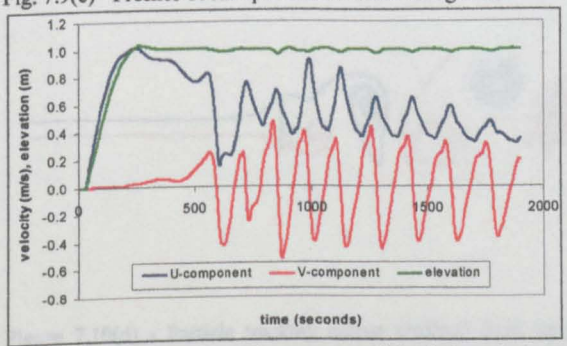

Fig. 7.9(e) - Profiles 100 m downstream of island along A-A.

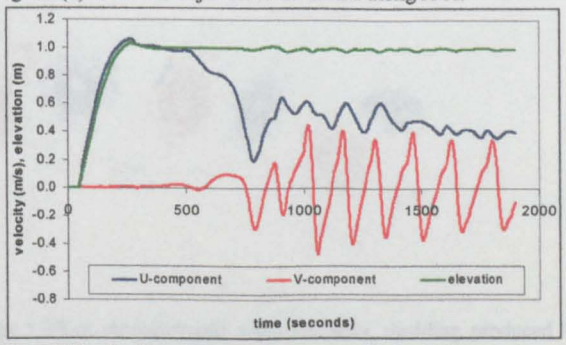

Fig. 7.9(f) - Profiles 200 m downstream of island along A-A.

Figure 7.9 - Development of vortex street in the wake of a laboratory scale 'circular' island from small upstream perturbations (St = 0.15).

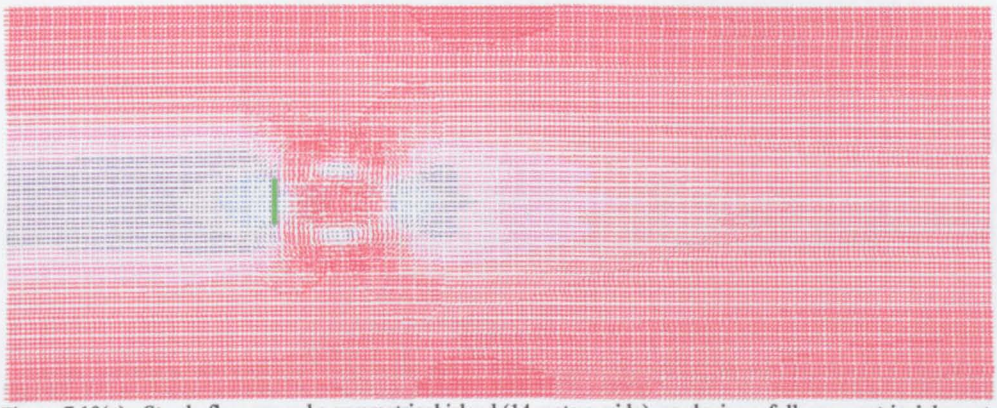

Figure 7.10(a) - Steady flow around a symmetrical island (14 metres wide), producing a fully symmetrical downstream wake.

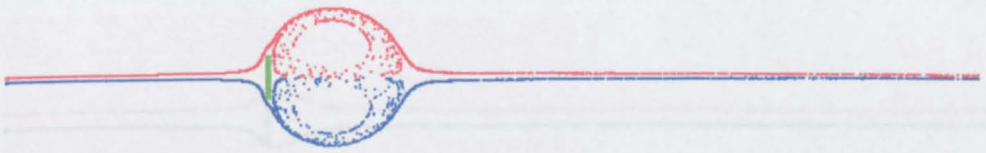

Figure 7.10(b) - Particle tracking output obtained from figure 7.10(a), demonstrating symmetrical flow around modelled island.

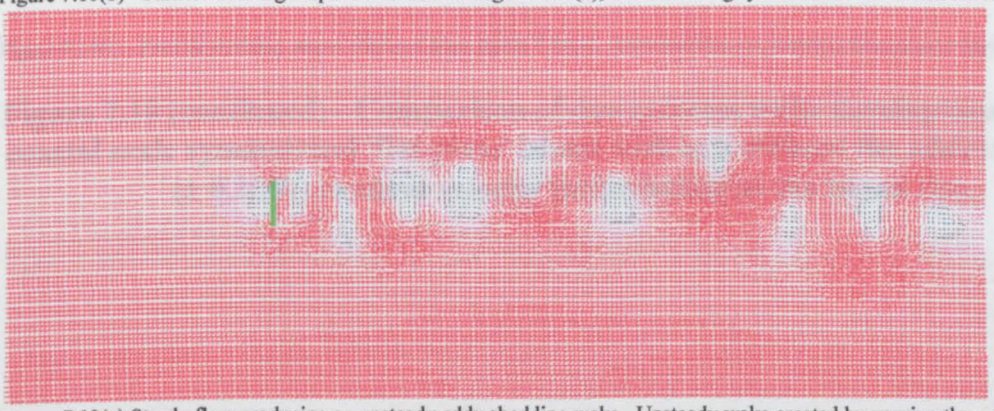

Figure 7.10(c) Steady flow producing an unsteady eddy shedding wake. Unsteady wake created by varying the velocity component randomly in the 4 cells above and below the island tip ±0.25% each time step (small random velocity fluctuations mimic the effect of turbulence). Small fluctuations are amplified by non-linear interaction in the island wake to produce shedding (St = 0.183).

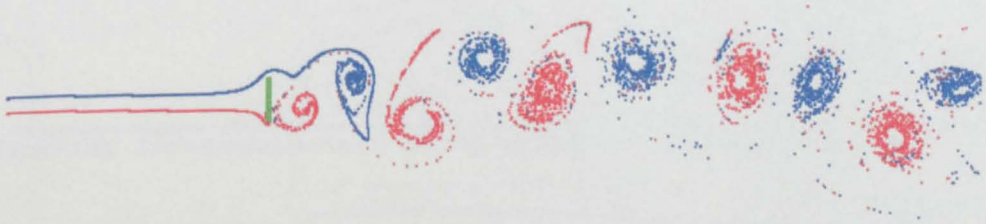

Figure 7.10(d) - Particle tracking output obtained from figure 7.10(c), demonstrating vigorous eddy shedding produced by introducing small random fluctuation into the simulation (St = 0.183).

Figure 7.10 - Comparison of downstream wake development around a coastal scale symmetrical 'flat-plate' island with and without the addition of small (± 0.25%) random velocity perturbation at the island tips.

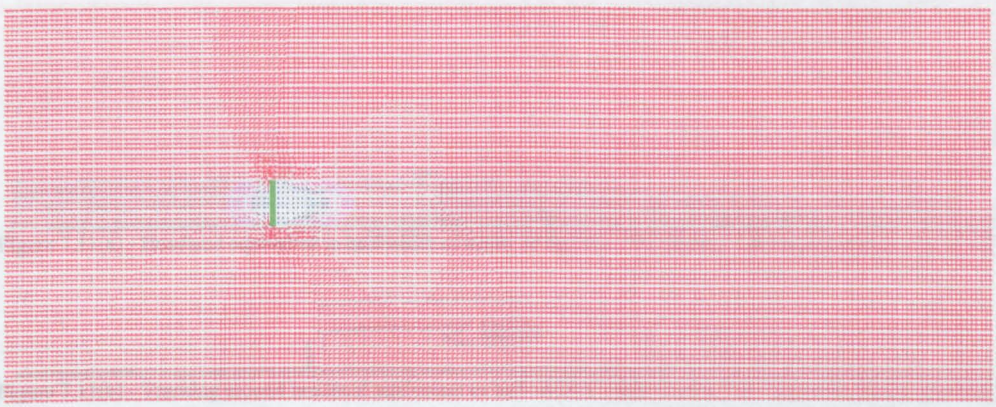

Figure 7.10(e) Steady flow with varying velocity component in the 4 cells above and below the island tip ±0.25% each time step (small random velocity fluctuations mimic the effect of turbulence). Small fluctuations damped by friction ($n = 0.025\ sm^{-1/3}$).

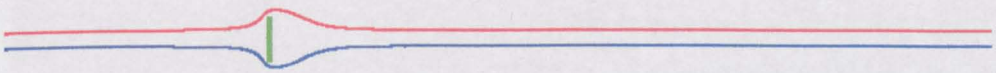

Figure 7.10(f) - Particle tracking output obtained from figure 7.10(e), demonstrating symmetrical flow around modelled island.

Figure 7.10 (continued) - Comparison of downstream wake development around a coastal scale symmetrical 'flat-plate' island with and without the addition of small (± 0.25%) random velocity perturbation at the island tips.

Figure 7.11(a) - Headland equivalent to half-width of island in fig. 7.8. No shedding, one stable eddy observed (1900 s).

Figure 7.11(b) - Tracking around headland equivalent to half-width of island in fig. 7.8. One stable eddy observed (400 s).

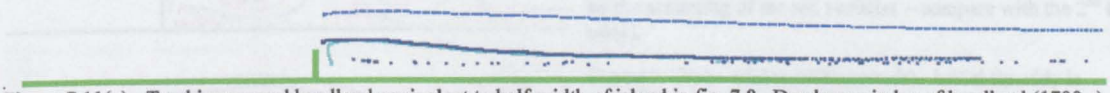

Figure 7.11(c) - Tracking around headland equivalent to half-width of island in fig. 7.8. Dead zone in lee of headland (1700 s).

Figure 7.11(d) - Effect of increasing headland length from case in fig. 7.11(a). One shedding event, two eddied produced (1900 s).

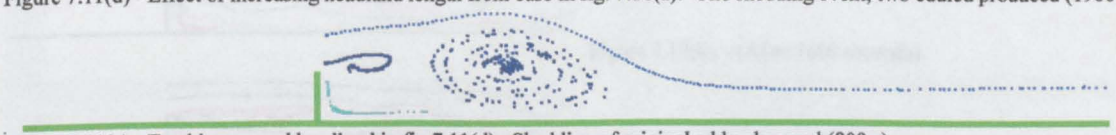

Figure 7.11(e) - Tracking around headland in fig 7.11(d). Shedding of original eddy observed (800 s).

Figure 7.11(f) - Tracking around headland in fig 7.11(d). No further shedding, two eddies shed from tip have merged (1900 s).

Figure 7.11(g) - Effect of increasing headland length from case in fig. 7.11(d). One shedding event, two eddied produced (1900 s).

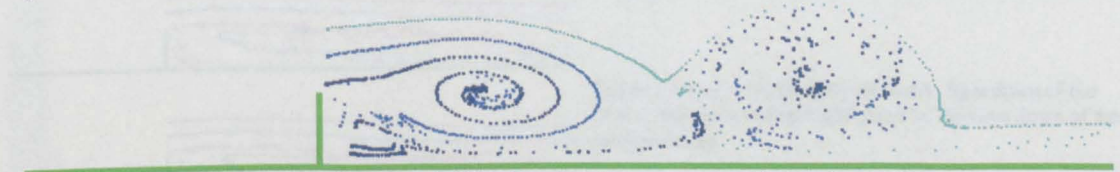

Figure 7.11(h) - Tracking around headland in fig 7.11(g). One shedding event, two eddied produced (400 s).

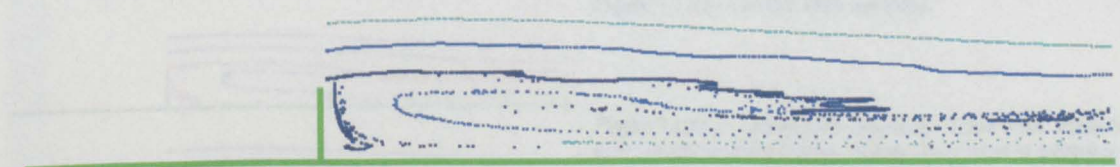

Figure 7.11(i) - Tracking around headland in fig 7.11(g). One further shedding event observed, only third eddy in shot (1900 s).

Figure 7.11 – Comparison of the effect of headland extent on downstream wake development (± 0.25% random velocity perturbation imposed at headland tip).

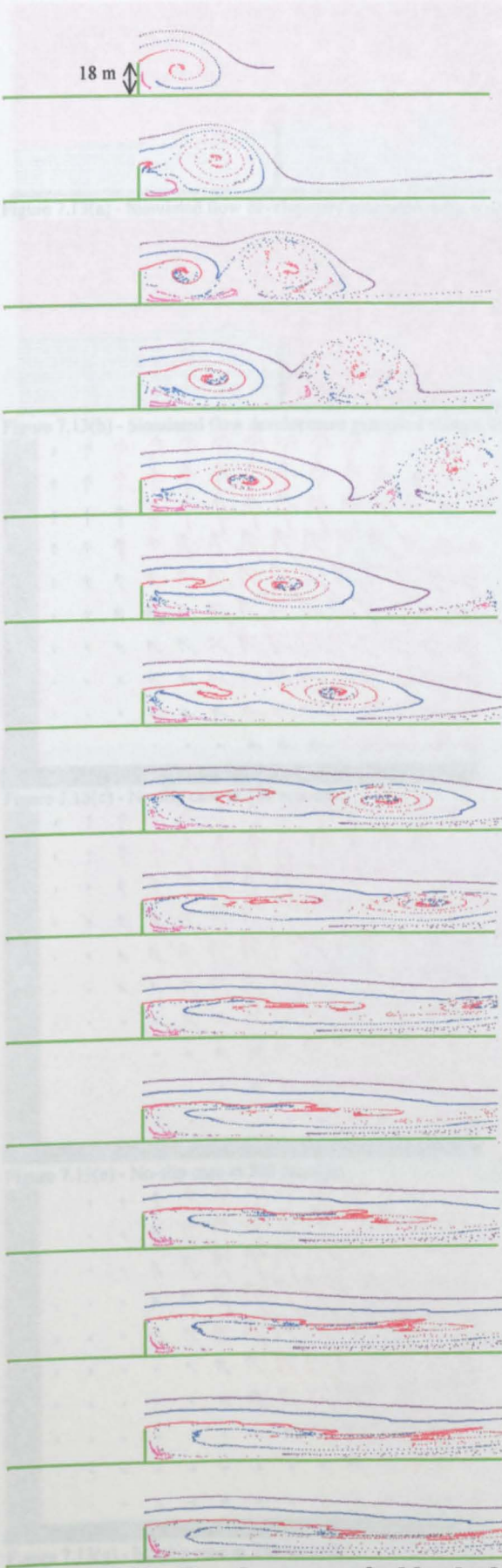

Figure 7.12(a) – (After 200 seconds). As the input elevation is ramped up, an eddy is generated at the headland tip and spins up in the wake of the headland.

Figure 7.12(b) – (After 400 seconds). The initial eddy is shed from the headland, and a new tip eddy is initiated. Note the small secondary eddy in the downstream corner behind the headland indicated by the pink particles.

Figure 7.12(c) – (After 600 seconds). The second tip eddy becomes defined. Note the elongated stream of pink particles indicating a free-stream directed flow region close to the boundary (opposed to the return flow in both eddies)

Figure 7.12(d) – (After 800 seconds). The initial tip eddy which has been shed is beginning to spin-down (note the spread of the previously well-defined roll-up of flow indicated by the scattering of the red particles – compare with the 2nd tip eddy).

Figure 7.12(e) – (After 1000 seconds). Initial tip eddy is transported downstream. The second tip eddy becomes bounded by the free-stream flow. The second tip eddy is shed. A third tip eddy is instigated.

Figure 7.12(f) – (After 1200 seconds). Initial eddy radiated out of the domain. Free-stream flow is still being entrained in the wake (see outer track). Third tip 'eddy' is not supported by a significant enough low pressure region to properly roll-up.

Figure 7.12(g) – (After 1400 seconds). Second eddy still reasonably well defined. Third 'eddy' struggling to roll-up.

Figure 7.12(h) – (After 1600 seconds).

Figure 7.12(i) – (After 1800 seconds). Upstream flow ceases to be entrained in the wake region. 'Dead-zone' (very low velocity, apparently random flow) becoming apparent in the immediate lee of the headland.

Figure 7.12(j) – (After 2000 seconds).

Figure 7.12(k) – (After 2200 seconds). Second eddy is radiating out of downstream boundary.

Figure 7.12(l) – (After 2400 seconds).

Figure 7.12(m) – (After 2600 seconds). Spin down of the flow in the wake region highlighted by the slow down of the particle tracks.

Figure 7.12(n) – (After 2800 seconds).

Figure 7.12(o) – (After 3000 seconds). 'Dead-zone' extends throughout the wake region. Strong shear layer in existence between the red and outer blue particle stream.

Figure 7.12 - Development of eddy shedding and a subsequent 'dead-zone' in the wake of a headland (no random perturbation).

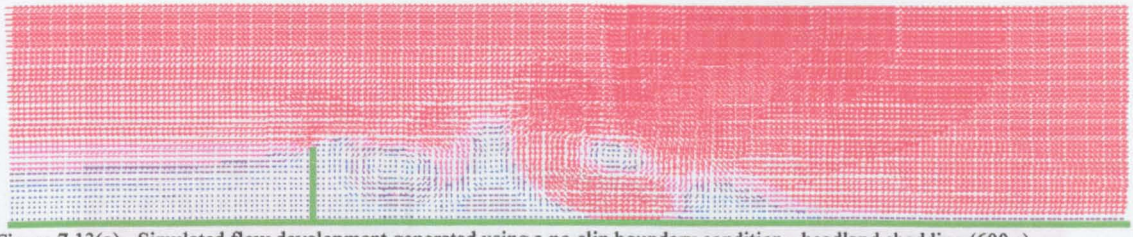

Figure 7.13(a) - Simulated flow development generated using a no-slip boundary condition - headland shedding (600 s).

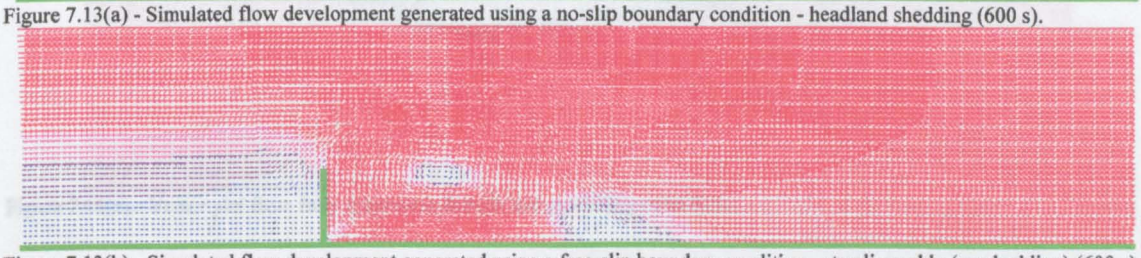

Figure 7.13(b) - Simulated flow development generated using a free-slip boundary condition - standing eddy (no shedding) (600 s).

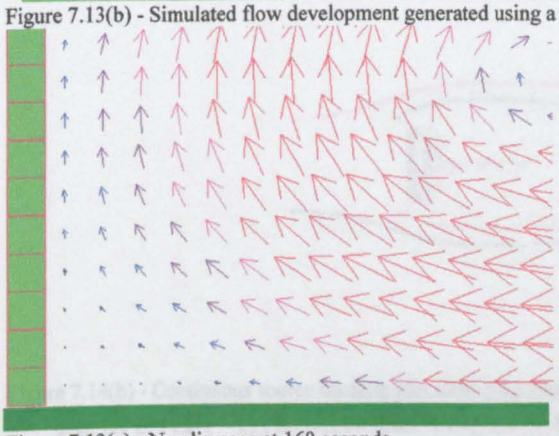

Figure 7.13(c) - No-slip case at 160 seconds.

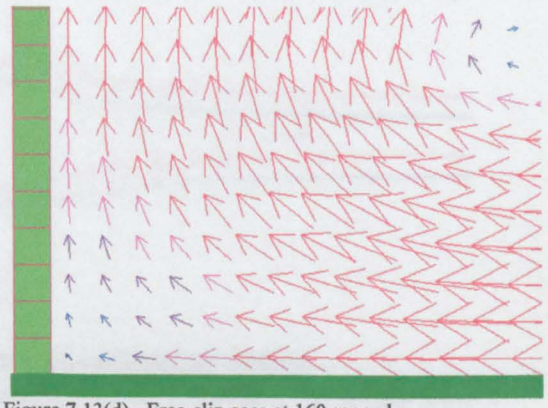

Figure 7.13(d) - Free-slip case at 160 seconds.

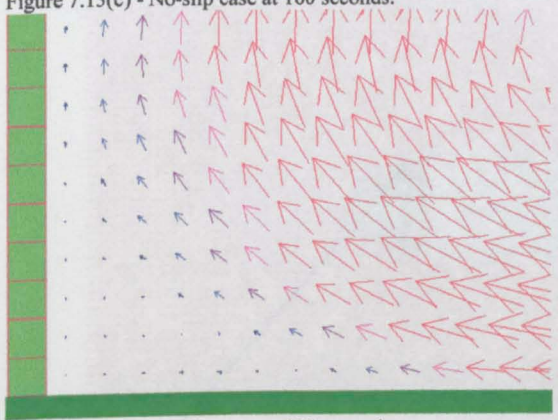

Figure 7.13(e) - No-slip case at 200 seconds.

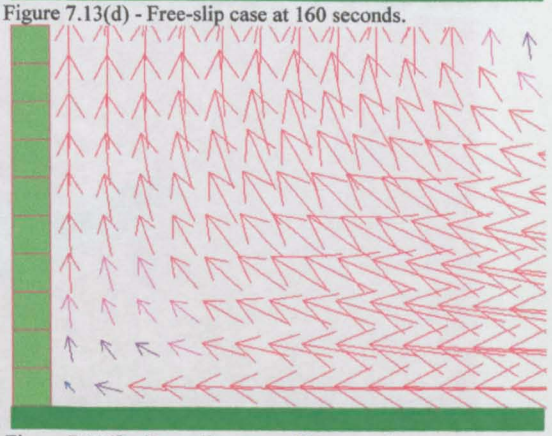

Figure 7.13(f) - Free-slip case at 200 seconds.

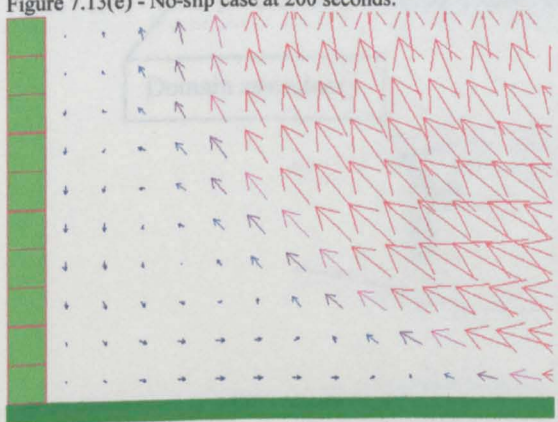

Figure 7.13(g) - No-slip case at 240 seconds.

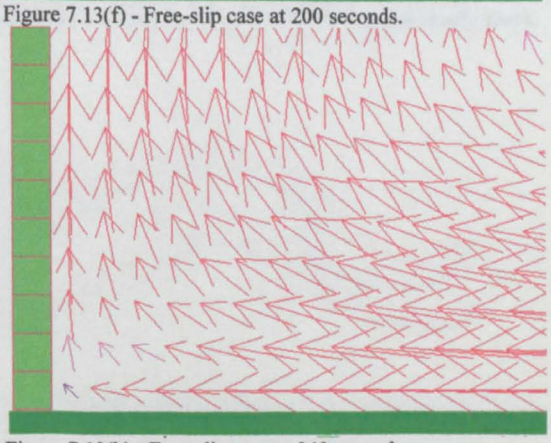

Figure 7.13(h) - Free-slip case at 240 seconds.

Figure 7.13 - Comparison of the development of headland flows using no-slip and free-slip boundary conditions

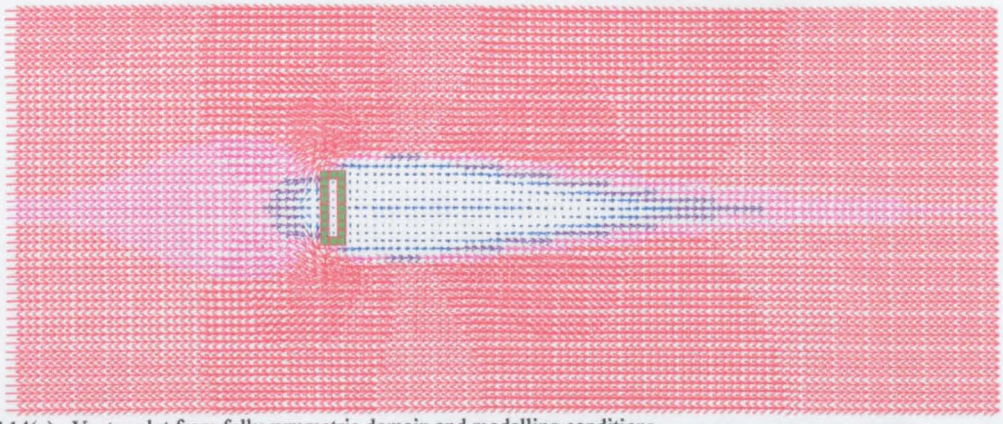

Figure 7.14(a) - Vector plot from fully symmetric domain and modelling conditions.

Figure 7.14(b) - Continuous source tracking plot from fully symmetric domain and modelling conditions.

Figure 7.14 - Symmetrical output after steady state maintained for 25 hours

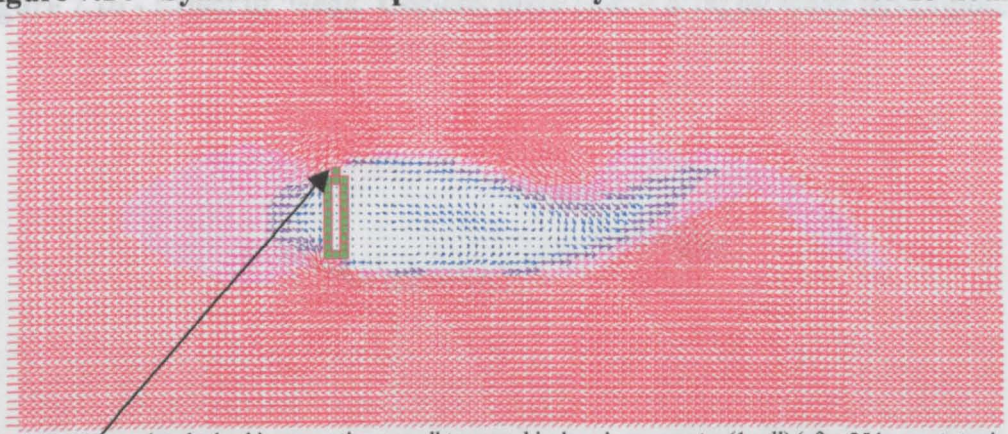

Figure 7.15(a) - Vector plot obtained incorporating a small topographic domain asymmetry (1 cell) (after 25 hours at steady state).

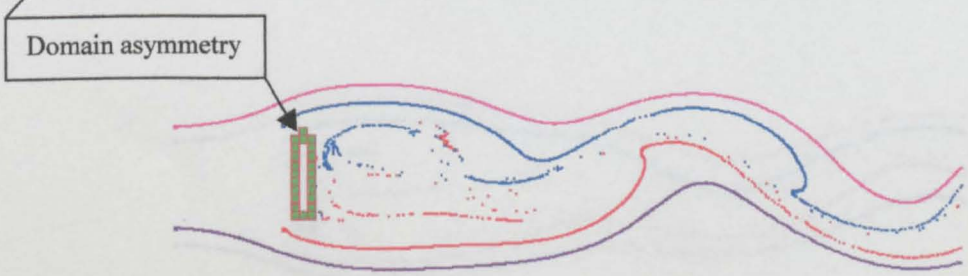

Figure 7.15(b) - Continuous source tracking plot demonstrating oscillating wake created by a small topographic domain asymmetry.

Figure 7.15 - Long-term downstream wake generated by domain asymmetry

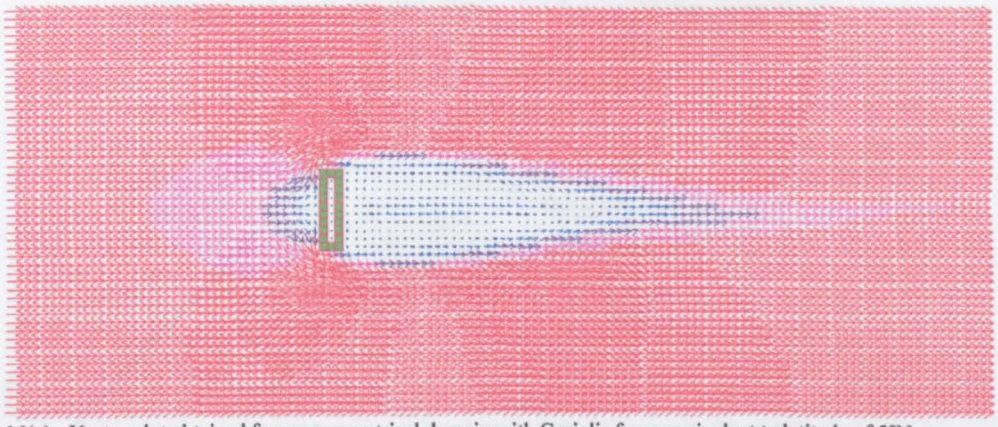

Figure 7.16(a) - Vector plot obtained from a symmetrical domain with Coriolis force equivalent to latitude of 5°N.

Figure 7.16(b) - Continuous source tracking plot indicating very weak downstream wake oscillation (after 25 hours at steady state).

Figure 7.16 - Effect of 'weak' Coriolis force (lat. = 5°N) on wake development

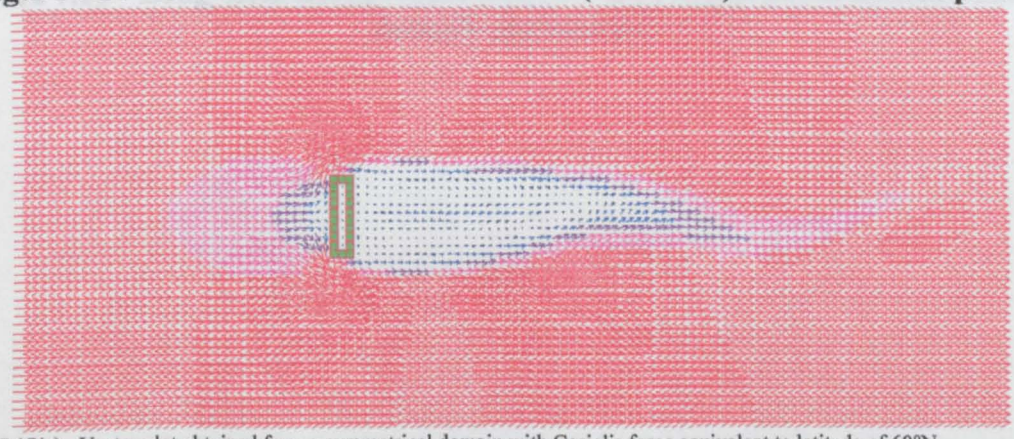

Figure 7.17(a) - Vector plot obtained from a symmetrical domain with Coriolis force equivalent to latitude of 60°N.

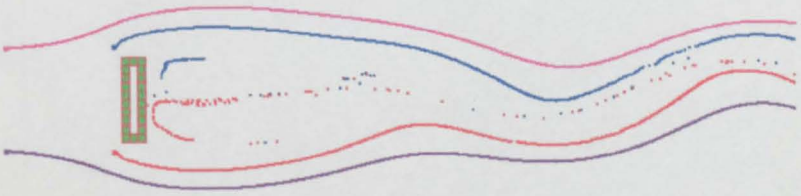

Figure 7.17(b) - Continuous source tracking plot indicating increased downstream wake oscillation (after 25 hours at steady state).

Figure 7.17 - Effect of 'strong' Coriolis force (lat. = 60°N) on wake development

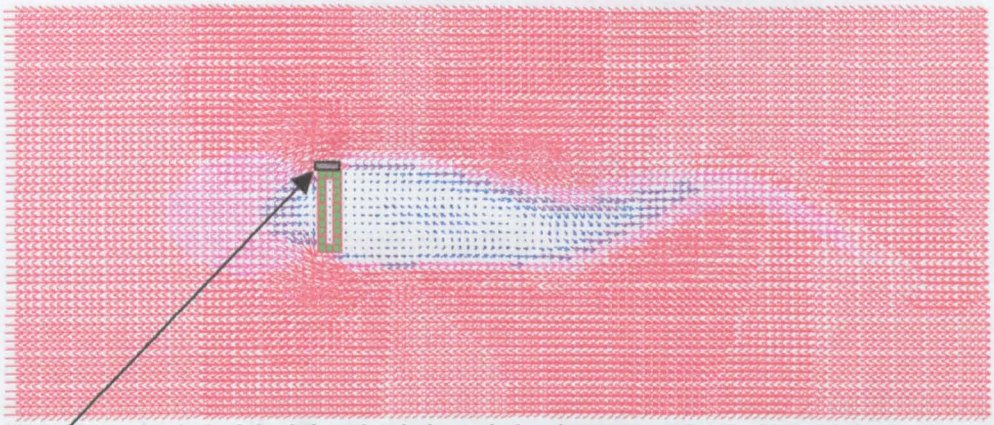

Figure 7.18(a) - Vector plot obtained simulating minor bathymetric domain asymmetry (1 cell × island width = 10 m) at northern tip.

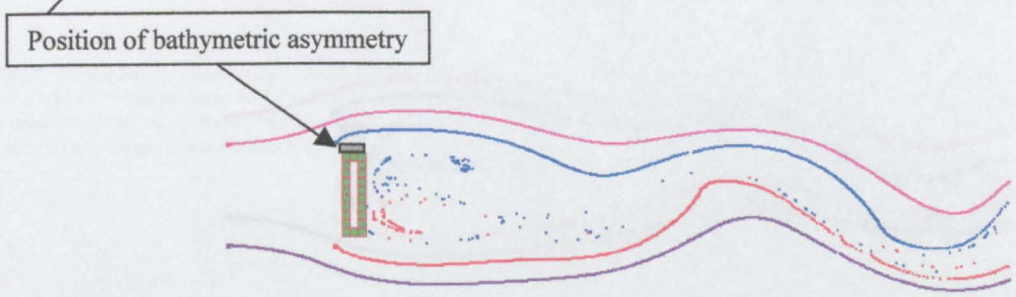

Figure 7.18(b) - Continuous source tracking plot demonstrating oscillating wake created by minor bathymetric domain asymmetry.

Figure 7.18 - Long-term downstream wake oscillation generated by bathymetric domain asymmetry

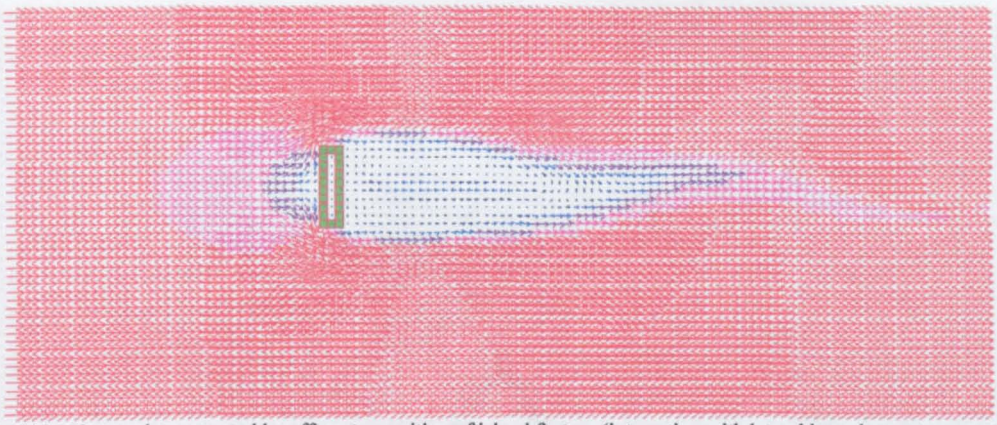

Figure 7.19(a) - Vector plot generated by off-centre position of island feature (interaction with lateral boundary not symmetric).

Figure 7.19(b) - Continuous source tracking plot demonstrating wake oscillation generated by off-centre position of island feature.

Figure 7.19 - Effect of off-centre island feature (open boundary interaction)

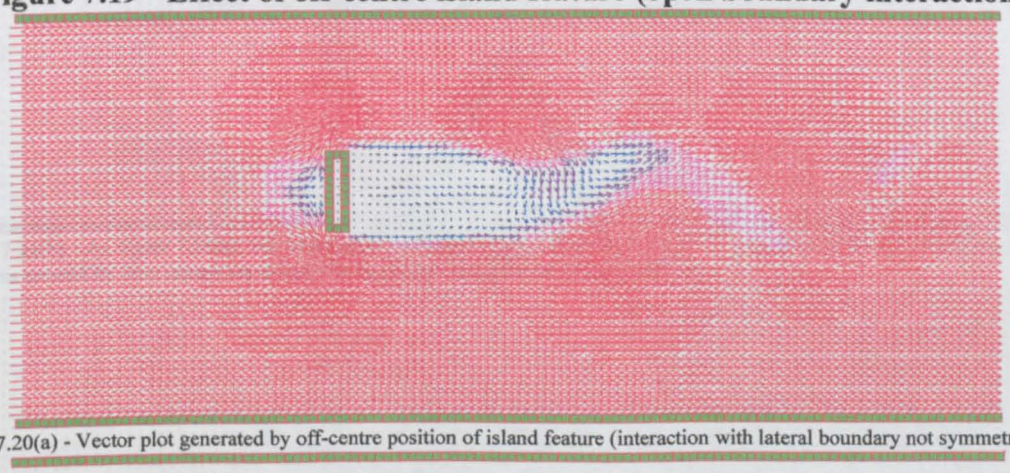

Figure 7.20(a) - Vector plot generated by off-centre position of island feature (interaction with lateral boundary not symmetric).

Figure 7.20(b) - Continuous source tracking plot demonstrating wake oscillation generated by off-centre position of island feature.

Figure 7.20 - Effect of off-centre island feature (closed boundary interaction)

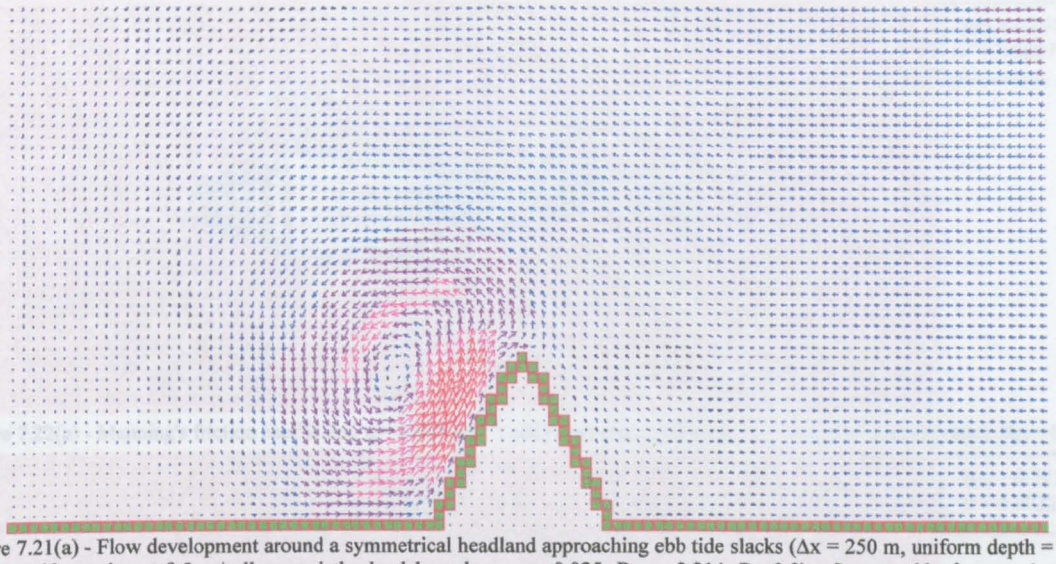

Figure 7.21(a) - Flow development around a symmetrical headland approaching ebb tide slacks (Δx = 250 m, uniform depth = 20m with a uniform slope of 5 m/cell around the land boundary, n = 0.025, Re_f = 2.214, P= 0.2). Strong eddy feature observed generated by flow separation around the headland during the ebb tide.

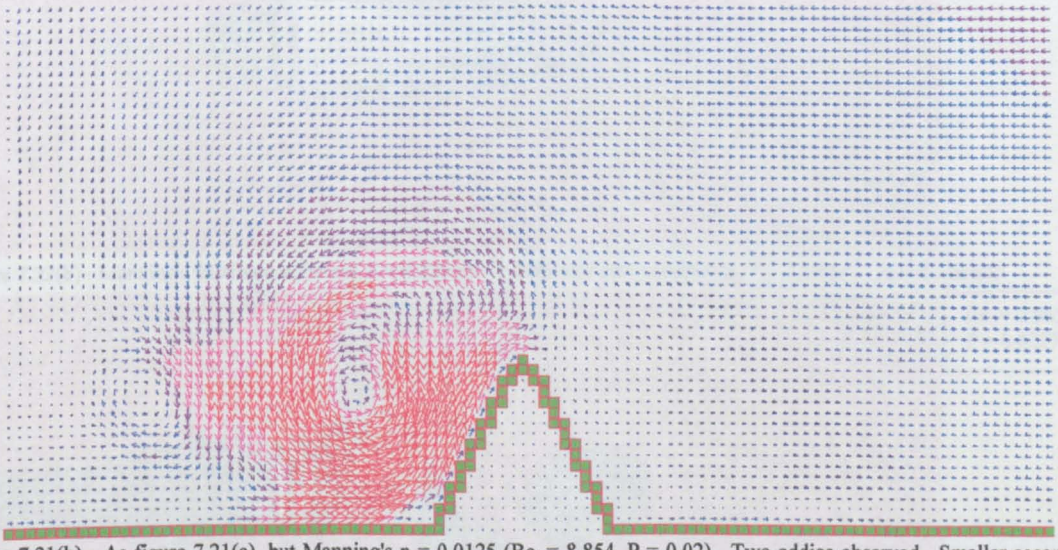

Figure 7.21(b) - As figure 7.21(a), but Manning's n = 0.0125 (Re_f = 8.854, P = 0.02). Two eddies observed. Smaller secondary eddy was created by flow separation around the headland during the previous flood tide.

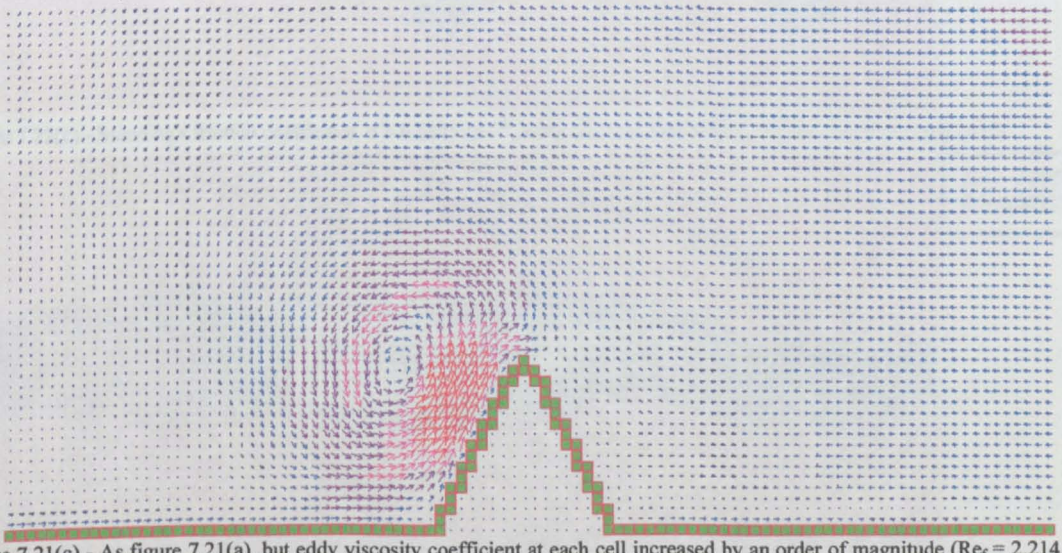

Figure 7.21(c) - As figure 7.21(a), but eddy viscosity coefficient at each cell increased by an order of magnitude (Re_f = 2.214, P = 0.2). Negligible effect on the flow development.

Figure 7.21 - Effect of frictional dissipation and eddy viscosity on eddy life-span.

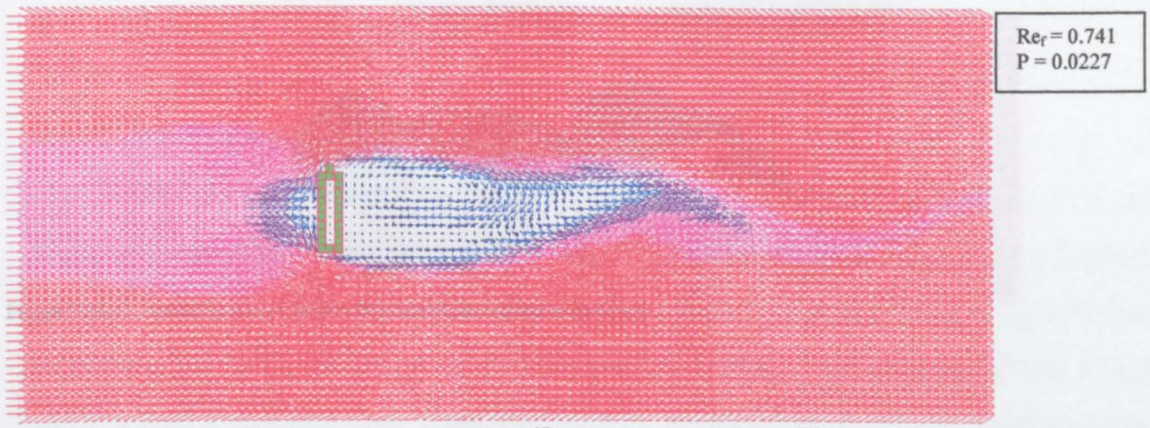

Figure 7.22(a) - Manning's friction coefficient, n = 0.025 $sm^{-1/3}$, eddy viscosity coefficient, $\overline{\upsilon}_t = 0.5\ m^2s^{-1}$ (steady state). $Re_f = 0.74$.

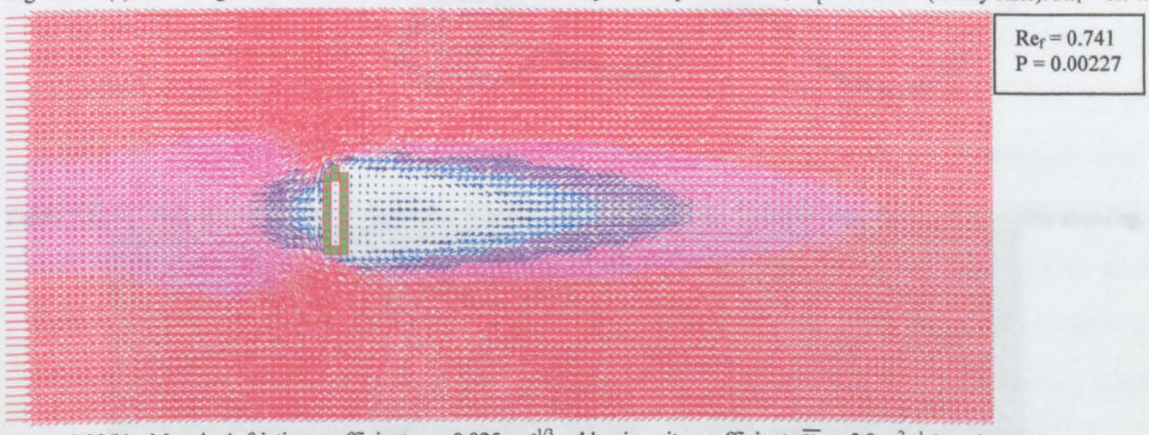

Figure 7.22(b) - Manning's friction coefficient, n = 0.025 $sm^{-1/3}$, eddy viscosity coefficient, $\overline{\upsilon}_t = 5.0\ m^2s^{-1}$ (steady state).

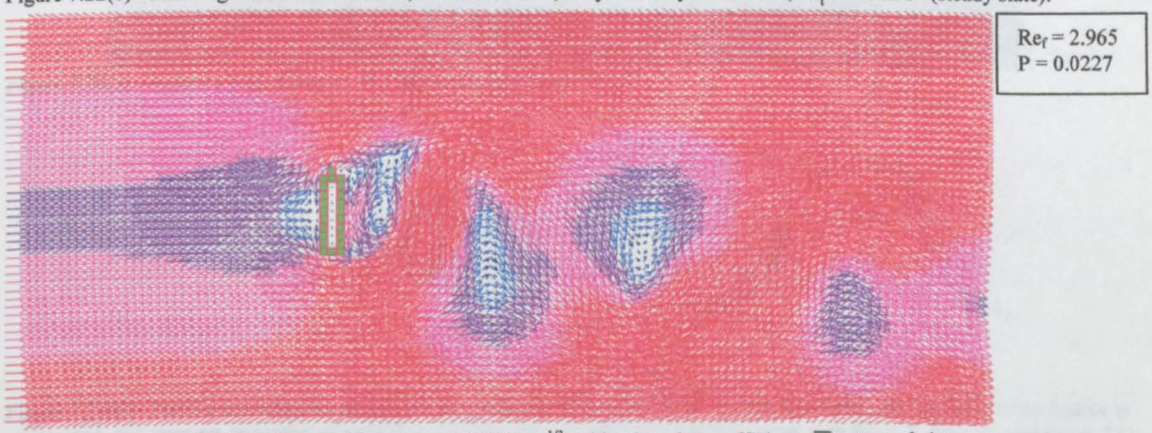

Figure 7.22(c) - Manning's friction coefficient, n = 0.0125 $sm^{-1/3}$, eddy viscosity coefficient, $\overline{\upsilon}_t = 0.5\ m^2s^{-1}$ (steady state).

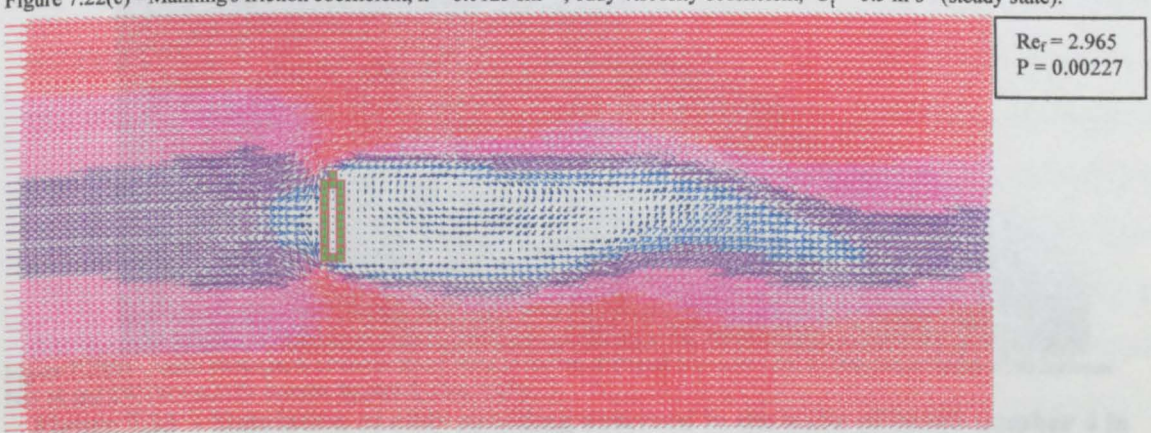

Figure 7.22(a) - Manning's friction coefficient, n = 0.0125 $sm^{-1/3}$, eddy viscosity coefficient, $\overline{\upsilon}_t = 5.0\ m^2s^{-1}$ (steady state).

Figure 7.22 – Effect of frictional dissipation and eddy viscosity on unsteady wake.

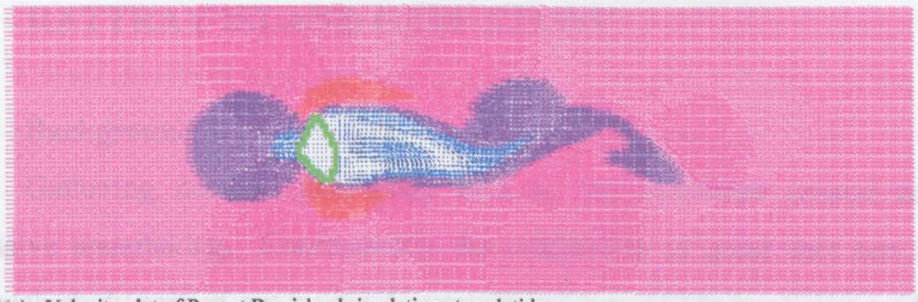

Figure 7.23(a) - Velocity plot of Rupert Bay island simulation at peak tide.

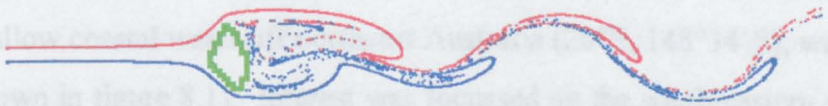

Figure 7.23(b) - Particle tracking plot of Rupert Bay island simulation at peak tide. Unsteady wake feature with possible shedding.

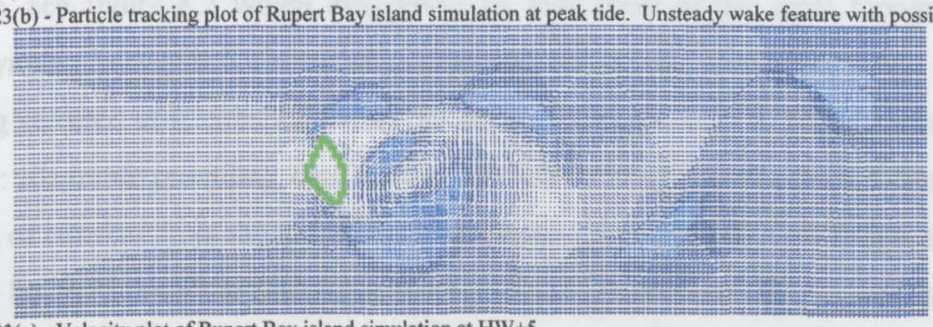

Figure 7.23(c) - Velocity plot of Rupert Bay island simulation at HW+5.

Figure 7.23(d) - Particle tracking plot of Rupert Bay island simulation at HW+5. As the tide slacks, the unsteady wake feature is maintained, and stronger indication of eddy shedding features (St = 0.197) (compare output with figure 7.5(b + e), and figure 7.1).

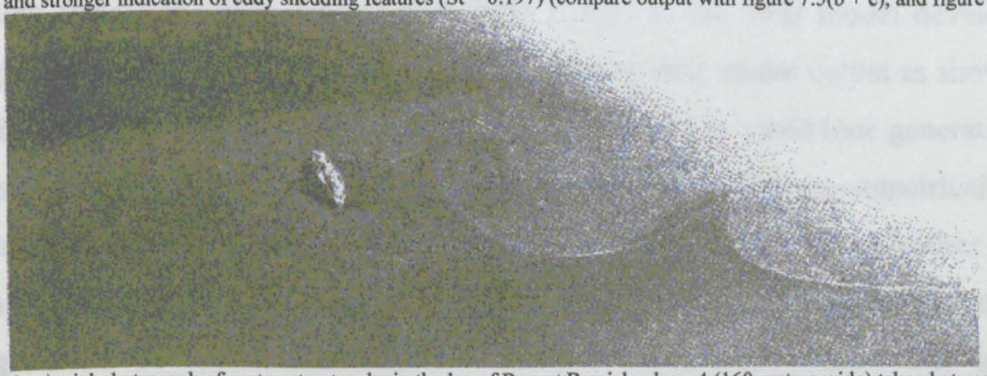

Figure 7.23(e) - Aerial photograph of vortex street wake in the lee of Rupert Bay island no. 4 (160 metres wide) taken between HW+4 and LW (St = 0.217). (source: Ingram & Chu, 1987)

Figure 7.23 - Simulation of eddy shedding observed in the wake of island number 4 in Rupert Bay, Canada (see Ingram & Chu, 1987). Shedding produced by the asymmetry of the island shape, no random perturbation in calculation procedure (Re_f =3.93, St = 0.197).

8. RATTRAY ISLAND CASE STUDY

8.1 Background

Gathering detailed field-study data in the nearshore coastal zone is an expensive undertaking. Consequently the availability of good data sets is limited. One such study carried out by the Australian Institute of Marine Science (AIMS) has been reported in the literature by Wolanski et al. (1984). The purpose of the AIMS study was to investigate flow separation events. Rattray Island, a small (1600m wide) island in shallow coastal water off northeast Australia (20°S, 148°34`E), was selected (location shown in figure 8.1). Interest was focussed on the south-eastern side of the island, where 26 current meters and 3 tide-gauges were deployed for a complete tidal cycle, see figure 8.2 which also gives an indication of the local topography and bathymetry. Detailed output was presented for the 4th December 1982 (this date being selected as it coincided with the aerial photography). Included in the data-set were: diagrams providing data on the sea level throughout the survey period, stick plots of currents from the moored current meters at hourly intervals during the 4th and early hours of the 5th of December 1982 (0800 – 1600 hours, 2000 – 0400 hours), and a number of aerial photographs which coincide with the peak flood tide (1200-1300 hours). The availability of the data provided by Wolanski et al. has encouraged numerous investigators to interpret and analyse the flow development around Rattray Island using numerical models (Falconer et al. 1984, 1986, 1987, 1992; Black & Gay, 1987; Wolanski, 1988; Deleersnijder et al., 1992; Galloway et al., 1996; Wolanski et al. 1996; Furukawa & Wolanski, 1998). The majority of these studies were carried out using fixed-grid, finite-difference models similar to the TFD model developed during this research. Each of these authors interpreted their model output as showing two eddies during the flood tide in the southeastern lee of the island (one generated at each island tip). Each model suggested that the two eddies were asymmetrical (the northern tip eddy being dominant to a greater or lesser extent). Each author then compared their model results with the available current meter data and concluded that the agreement between output from the model and current meters was good. However, as pointed out by Furukawa & Wolanski (1998), this interpretation contradicts the aerial photographic data (figure 8.3 (a, b)), which indicates that only

one eddy is generated during the flood tide. The existence of only one eddy in the wake is supported by the temperature distribution (figure 8.4), and this interpretation is not contradicted by the current meter data. The relatively wide spacing of the current meters provides data too sparse to properly resolve the number and extent of the of eddies in the island wake. Furukawa & Wolanski (1998) presented output from a discrete vortex model (a numerical modelling technique that is not restricted to a fixed uniform grid), which not only compares favourably with the current meter data, but also with the other data, i.e. their results show one eddy of the correct extent in the island wake. Taking all of the above into consideration, Furukawa & Wolanski (1998) surmised:

> "Thus, the 'classical' [i.e. two- and three-dimensional fixed-grid finite-difference] numerical models appear unable to satisfactorily reproduce details of flows around islands in shallow water."

And furthermore:

> "This may be due to the mesh-based models' inability to include details of the shear layer around the separation points, except if the mesh size is smaller than the width of the shear-layer near the separation point. It [the width of the shear layer] is about 20m at Rattray Island...."

The author disagrees that it is necessary to resolve fully the shear layer, although of course in general more resolution will give improved results. Results presented in this chapter demonstrate using the TFD fixed-grid based finite-difference model that the Rattray Island flow can be correctly simulated without resorting to a mesh size of order 20m.

8.2 Methodology

All the previously listed attempts to simulate the wake development in the lee of Rattray island using two- or three-dimensional, uniform grid finite-difference models (i.e. 'classical' numerical models similar to the TFD model being applied here), have employed a cell-size of either 200 m or 300 m. The domain modelled has usually been limited to an area of 12 km × 9 km with the island in the centre of the domain. In the majority of cases reported in the literature, closed (free-slip) lateral boundaries were specified. It is the author's opinion that this combination of

conditions is significantly limiting the accuracy of the simulations produced when applying fixed-grid based finite-difference model techniques. For instance, using a 300 m mesh, the extent of Rattray Island (and of the wake eddy) can only be represented by 5 or 6 cells. The extent of the domain could also limit the solution, particularly as the lateral boundaries are closed (no cross-flow). This may induce artificially strong tidal streaming around the island because of the channelling effect of the boundary specification (see chapter 6.4.5). Finally, as the convective momentum terms play a significant role in determining the flow development around small coastal scale islands, the representation of these terms in the model can have a major impact on the simulation. Many of the previous finite-difference models applied rely on 2^{nd}-order finite-differencing of the convective momentum terms, which as has been discussed in chapter 4, can introduce numerical error into the model solution. This is borne out by the findings of Galloway et al. (1996) who report that the MECCA model developed jointly by two US government agencies was only able to produce a simulation of the Rattray Island case when the convective momentum terms were disabled (which produces an attached, potential flow-like regime). With the convective momentum terms enabled, the MECCA model was found to be unstable. It is shown that by resolving the issues discussed, the TFD numerical model can produce a simulation that is in better agreement with the available data.

An initial run was produced which replicated the most common set-up of the model domain appearing in the literature. This provides a datum with which the other runs can be compared. A series of tests were then carried out, each incorporating a single change which may provide improved results. Table 8.1 lists these alterations and the reasoning behind each change. Minor difficulties had to be overcome to initiate the listed alterations. For instance a uniform flat shelf of depth 27 m was prescribed across the extended domain region because of the lack of bathymetric data. Furthermore, Eshelby Island to the SE of Rattray Island (see figure 8.2) was not included in the extended domain, as its proximity to the boundary generated unrealistic wake features which adversely influenced the flow development. Finally, when re-defining the island, the various aerial photographs presented by Wolanski et al. (1984) of Rattray Island were the best available representation of the island shape.

Run ID	ALTERATIONS FROM DATUM	EXPLANATION OF TEST
Datum	None	Replica of the original Falconer et al. (1984) simulation using the TFD model.
R1	Lateral boundaries radiate.	Investigate the constraining influence of the lateral no-flow boundaries.
R2	Domain extended by 50% in both direction to 18 km × 13.5 km (island remains in centre of domain).	Expand the domain to reduce the influence of boundaries on development of circulation patterns.
R3	Reduce cell size to 200 metres.	Increase resolution (will also enable further refinement of the topography).
R4	Re-define island shape.	More accurately represent the topography.
R5	Prescribe a uniform eddy viscosity across the domain of 1.0 m^2s^{-1}.	Expand downstream eddy width by increasing mixing effect
R6	Reduce cell-size to 150 metres	Further increase resolution.
R7	Re-define island shape	More accurate representation of the island topography

Table 8.1 – List of modelling criteria to be investigated for Rattray Island simulation.

8.3 Modelling conditions and set-up of the TFD model for Rattray Island

As the local tidal velocities and currents are not in phase (see figure 8.5), it is necessary within the confines of the TFD model operation to specify driving conditions on two opposite boundaries. Specifying elevation data at the upstream boundary and velocity data at the downstream boundary will impose the 2 hour time lag between slack water and current reversal. Elevation data is obtained directly from the original survey data presented by Wolanski et al. (1984). As the elevation data obtained during the survey was in the immediate vicinity of the island it is understood that there will be a slight discrepancy between the model and in-situ timing due to the approximation involved. The effect of this will be minimal however, as the velocity of the tidal wave is such that shifting of the data over a comparably short distance upstream will have negligible effect. A degree of model calibration was necessary to accurately fit the downstream velocity boundary data. This is to ensure both that the phase difference across the domain is correctly simulated throughout the tidal cycle, and that the effect of the downstream boundary condition on the free-stream velocity is in good agreement with the survey data. Running simple idealised cases enabled fine-tuning of the velocity boundary data to be carried out by comparing velocity data from current meter sites 1, 8, 22 and 23. These sites lie in the free-stream to the north (1) and south (8) of the island, and six kilometres downstream (22 and 23) respectively (peak free-stream velocity ≈ 0.45 ms^{-1}). Each of the current meter sites

used lies outside the area effected by the flow separation and consequent flow re-circulation. It has become standard practice in general applications to rotate the domain such that the input boundary is perpendicular to the flow direction, thereby simplifying the input boundary condition specification. As the far-field flow is reported to be generally rectilinear, this would appear to be a logical simplification.

All the test cases listed in table 8.1 were allowed to spin-up from a cold start condition for a complete tidal cycle to enable non-linear effects to become established in the vicinity of the island. Bathymetric data for the area around Rattray Island was obtained from a 300 m resolution isometric plot produced by AIMS and presented by Falconer (1984). Rattray Island protrudes almost shear-sided from the surrounding sea floor (see figure 8.6). The island lies in an area of reasonably uniform bathymetry (25 m deep). In the immediate vicinity of the island, two scour holes are apparent, one at either tip. Manning's friction coefficient was set at 0.025 $sm^{-1/3}$, as the bed material is reported to consist of a mixture of silt and fine sand across the majority of the domain (Furukawa & Wolanski, 1998). Coriolis acceleration was uniformly prescribed throughout the domain as being equivalent to a latitude of 20° S, and the elevation slope this generates was factored into the prescribed input condition.

8.4 Interpretation of the in-situ and remote-sensing data

The original results and output generated by the AIMS investigation presented by Wolanski, et al. (1984), and Falconer et al. (1984) are concentrated on the flood tide, in the southern-eastern lee of the island. The far-stream flow is directed from NW to SE, and is therefore roughly aligned perpendicular to the major axis of the island. A semi-diurnal tidal condition prevails in the region, with a strong diurnal inequality giving one high-high water (HHW) and one low-high water (LHW) each day (see figure 8.5). Coriolis acceleration is of limited significance because the Rossby number based on the island length is large (Ro = 5.6). Flow development during the 4th December 1982 is similar for both the first (dominant) and second flood tide. In both cases, shortly after the flood tide becomes established, flow separation occurs at the north-eastern tip of the island, and a small eddy is immediately established in the lee of the island, apparently as a consequence of the flow separation. Through time, the eddy expands, remaining attached to, and 'fed'

vorticity from the separation point. As the eddy expands to the extent of the island width, the flow around the southwestern tip of the island, which had initially remained attached to the island, is forced to separate by the progression of the separated region expanding from the northeast tip. The separated flow from the southwest island tip is constrained by the existing eddy feature on the one hand, and tidal streaming on the other; consequently a wake develops (no vorticity roll-up). At HHW, the maximum eddy extends downstream approximately 3 km and laterally across an area slightly wider than the island. At LHW, the eddy length is approximately half the size, although the width is similar. After the flood tide peaks, the development of flow in the domain is less obvious from the available data. The eddy appears to be maintained, and as the ebb tide becomes established, the eddy generated on the flood tide is carried around the northeastern tip of the island. Flow development during the ebb tide is not detailed in the literature apart from some comment on the occurrence of two eddies occurring to the north of the island, that generated by the north-eastern tip being slightly dominant (Wolanski et al., 1984). Eddies shed as the tide reverses were observed to advect around the island after the tide had turned before fully spinning down. Repeated eddy shedding during a single tide is not apparent in the available in-situ nor in the remote-sensing data. Assuming a critical Strouhal number within the limits 0.15 - 0.2 as suggested in chapter 7.6, an eddy shedding period of between 5.6 and 7.4 hours is predicted. A suitable free-stream velocity to support eddy shedding ($U > 0.4$ ms^{-1}) persists on the flood tide for approximately 4 hours. Therefore the occurrence of even a single shedding event is unlikely.

8.5 Results

Output from the datum case attempting to replicate as closely as possible the model set-up of Falconer et al. (1984) is presented in figure 8.7. Inspection of the TFD output indicates that at least as good or better agreement with the field data is achieved compared with previous fixed-grid finite-difference modelling (Falconer et al. 1984, 1986, 1987, 1992; Black & Gay, 1987; Wolanski, 1988; Deleersnijder et al., 1992; Galloway et al., 1996; Wolanski et al. 1996). The major improvement is in the representation of the wake eddy instigated at the northern tip of the island. The downstream extent of the eddy at HHW (2.9 km) is in excellent agreement with the

in-situ observations (Wolanski et al. (1984): "slightly less than twice that of the island" (= 3.2 km)). Galloway et al. (1996) compared the output of 4 different 3-d finite-difference models presenting depth-averaged results. All of these severely underestimated the downstream extent of the Rattray Island wake (ranging between 20% – 60% at best of the observed extent). However, the TFD simulation significantly under-predicts the lateral extent (1.45 km) of the eddy at HHW compared with the field data (estimated from aerial photographs as 2.3 km). This lack of agreement between the TFD result and field data is replicated in the other fixed-grid finite-difference output reported in the literature. Of greater significance however is the repetition of the occurrence of two asymmetrical eddies. The secondary eddy generated at the southern tip of the island is observed throughout the flood tide. The overall extent of the secondary eddy generated in the TFD solution is no larger than 30% of the size of the larger northern tip eddy. The existence of this eddy is one reason why the lateral extent of the northern eddy is restricted in the simulation. The degree of asymmetry between the two eddies is in line with the best of the fixed-grid based simulations presented in the literature.

The initial interpretation of the survey data by Wolanski et al. (1984) stresses the importance of three-dimensional effects on the flow development as indicated by the upwelling and downwelling inferred from the survey and remote-sensing output. This suggests that a fully three-dimensional model may be necessary to properly model the flow in the vicinity of Rattray Island. Deleersnijder et al. (1992) applied a version of the three-dimensional hydrodynamic model GHER originally developed at the University of Liege to study the three-dimensional features. The results presented demonstrate limited improvement over previous two-dimensional modelling efforts, but did manage to qualitatively corroborate the previously inferred upwelling and downwelling patterns. From this it can be surmised that three-dimensional effects have limited influence of the two-dimensional depth-averaged flow around Rattray Island.

Systematically repeating the TFD model procedure incorporating the various alterations listed in table 8.1, small cumulative improvements occur in each case. These small cumulative gains provided a significant improvement over the datum case by the time the final TFD simulation using a 150 m cell size, an extended

domain (18 km × 13.5 km), specifying a uniform eddy viscosity of 1 m^2s^{-1} and re-defined island shape was analysed. The output from the final case considered is presented in figure 8.8. The most obvious differences from the datum case in figure 8.7 are the enlarged lateral extent of the eddy (1.9 km), and more importantly the occurrence of only one eddy prior to HHW-1. As the tide begins to turn, a small secondary eddy does begin to develop. The development of a secondary eddy this late on in the tide is not apparent in the field data, although the data presented is inconclusive (no aerial photography is presented after HHW-0.7). Previous experience of modelling eddy generation around islands as described in chapter 6 indicates that as the flood tide begins to ebb, a strong phase effect can be observed in the lee of topographic features. This effect causes the tide to turn in areas of reduced flow momentum more rapidly than in the free-stream region. In this case, the increased frictional dissipation of the shallower bathymetry and sheltering of flow in the lee of the island would provide conditions where early flow reversal would be expected. Similar results indicating the pre-dominance of a single eddy throughout the majority of the flood tide were presented by Furukawa & Wolanski (1998) using output from a discrete vortex model (DVM). A comparison of Furukawa & Wolanski's results with the TFD track outputs at 300 m and 150 m resolution is presented in figure 8.9. Both of the TFD model outputs are in excellent agreement with the DVM results when presented as tracking output. However inspection of the velocity fields at 150 m and 300 m resolution indicates that there are significant differences between the two. In particular the cross-stream (v-) component of velocity is in better agreement with the field data in the 150 m simulation, particularly in the immediate wake of the island. The level of agreement is indicated in figure 8.10 where appropriately scaled stick plot data indicating the recording current meter data collected in the field is overlain on the 150 m mesh TFD output at HHW-4, HHW-2 and HHW. Comparing with similar analysis presented by Falconer et al. (1984) the improvement evident in the TFD model output is significant.

To provide a quantitative comparison of the accuracy of the modelling exercise, a simple statistical analysis is presented. Using a scatter plot, the recording current meter data gathered in the field (the 26 sites are shown in figure 8.2) is compared with the simulated results throughout the flood tide at the same locations.

The results generated using (i) TFD model running datum case, (ii) the final TFD simulation, and (iii) the output from the work of Falconer et al. (1984) will be considered. The accuracy of a particular model simulation will be quantified by deriving the gradient of a linear regression analysis. Since the measured data and model data should agree, the gradient of the regression line should be 1. The fit of the scattered data can be quantified using the r-squared value (Moore & McCabe, 1999). As the r-squared value approaches 1, the standard deviation of the data set tends towards 0. The correlation between the field data and the various model simulations in the form of the regression slope and r-squared values are presented in table 8.2. Figure 8.11 presents a graphical representation of each of the three cases correlated with the original field data gathered at HHW on the 4 December 1982 (100% accuracy would be indicated by a 45° line intersecting through the origin with no scattering of the data).

Interpreting the results of Falconer et al. (1984) with the assistance of the correlation data, the stream-wise (U) component of velocity is over-estimated during the early part of the flood tide, and significantly under-estimated at HHW. The early over-estimation of the velocity component is probably related to the boundary condition selected, as a closed boundary artificially increases the effect of tidal streaming around the island. Overall, the magnitude of the simulated stream-wise velocity component ($|(1 - \textit{gradient of the linear regression line}|$) predicted by Falconer et al. (1984) is in error by approximately 33%. The cross-stream (V) component indicates a tendency towards a weakly inverse relationship with the field data as indicate by the negative value of the gradient from the regression analysis. This indicates a substantial under-estimation of the cross-stream velocity in the lee of Rattray Island, and that the cross-stream velocity component considered in isolation is

time	HHW-4				HHW-2				HHW			
Correlation coefficient	Gradient		r^2		Gradient		r^2		Gradient		r^2	
Component	U	V	U	V	U	V	U	V	U	V	U	V
Falconer et al. (1984) output	1.290	-.103	0.678	0.025	0.837	0.326	0.748	0.441	0.453	-.098	0.453	0.041
TFD model (300 m datum case).	0.720	0.188	0.779	0.151	0.709	0.221	0.743	0.279	0.833	0.350	0.856	0.307
TFD model (150 m 'best' case.	0.925	0.139	0.828	0.215	0.851	0.351	0.930	0.481	0.900	0.605	0.894	0.493

Table 8.2 – Accuracy of various model simulations measured as the correlation between the model output and field data (recording current meters).

in general oppositely aligned in the solution compared with the field data. In the free-stream region, the stream-wise flow velocity component is generally an order of magnitude larger than the cross-stream flow velocity, and therefore the difference between the Falconer et al. (1984) solution and field data appears to be small. In the immediate wake of the island, the two velocity components are of comparable magnitude, therefore the difference between the model solution and field data indicated by the weak inverse relationship is significant. This is confirmed when the simulation generates two eddies during in the downstream wake when the data indicates only one occurs.

For the datum simulation produced using the TFD model replicating the experiment of Falconer et al. (1984), the results indicate a general improvement in accuracy. The simulated stream-wise (U) component compares favourably with the trend of the field data, although there is a general overall under-prediction of the velocity magnitude by 20 – 25 %. The under-prediction of the stream-wise velocity component is most apparent in the wake region, whereas the free-stream components are in almost exact agreement. The cross-stream velocity component (V) indicates only a weak correlation between the simulated results and field data. The low r-squared values associated with the 300 m resolution TFD results indicate that there is significant variability in the correlation of individual points. This result indicates an overall improvement compared with the Falconer case, although there is significant room for further improvement.

The stream-wise (U) component of the final 150 m resolution results are in excellent agreement with the field data, on average being within 10% of the magnitude of the corresponding field data. The r-squared values for the stream-wise component are also very high indicating minimal variation from the predicted accuracy throughout the data set. The correlation of the cross-stream (V) velocity data provides a further improvement. Early on in the flood tide the cross-stream results are still only weakly correlated. Significant improvement is observed as the tide approaches HHW. At HHW the correlation between the simulation and field data can be described as moderate to good. The r-squared values however still indicate strong variability when considering one particular data point.

Overall, the 150 m TFD simulation provides a significant improvement in the accuracy of the results when compared with both the 300 m TFD simulation and the results of Falconer et al. (1984). The improvement is most significant as the flood tide approaches HHW. This is a reflection of the better agreement obtained when visually comparing the flow development with the available aerial photographs. A similar quantifiable level of improvement is produced when comparing with the results of 4 different three-dimensional models analysed by Galloway et al. (1996).

8.6 Summary and Conclusions

The flow around Rattray Island has been simulated using the TFD numerical model. These results have been compared with the field data presented by Wolanski et al. (1984), and with various other numerical model simulations of Rattray Island presented in the literature (Falconer et al. 1984, 1986, 1987, 1992; Black & Gay, 1987; Wolanski, 1988; Deleersnijder et al., 1992; Galloway et al., 1996; Wolanski et al. 1996; Furukawa & Wolanski, 1998). The TFD model results at 300 m resolution demonstrated at least as good agreement with the field data as previous attempts using various 2- and 3-dimensional fixed-grid finite-difference models at 200 m or 300 m resolution. The tendency of the fixed-grid, finite-difference models to simulate the occurrence of two significant downstream eddies during the flood tide contradicts the available field data. This outcome has led Furukawa & Wolanski (1998) to question the suitability of fixed-grid finite-difference techniques in situations where the boundary and shear layers are not fully resolved. The results presented here compare favourably with Furukawa & Wolanski's discrete vortex model simulations and with the field data. Significant improvement in the simulated results was obtained using a higher resolution mesh, but the 150 m cell size is still two orders of magnitude greater than the resolution required to adequately resolve the boundary layer or shear layer. This outcome would tend to suggest that at 300 m resolution the model set-up was adversely affecting previous modelling attempts. Increasing the resolution has enabled a more accurate interpretation of the island shape to be specified. Also, the increased resolution provides a more suitable number of cells across which to describe the wake. At the coarser 300 m resolution, the cross-stream wake would be restricted to 6 – 8 cells at most. The influence of numerical error and diffusion across a wake region described by so few cells would

be hard to avoid, particularly as the flow is so strongly non-linear in the lee of the island. The extent of the domain has also been identified as a constraint on the accuracy of the preceding analysis of Rattray Island. Furukawa & Wolanski's (1998) statements regarding the capability of fixed-grid finite-difference models have been shown to be based upon results which are not restricted by the modelling technique, but by the specification of the problem. The inability of the model to provide an accurate solution is therefore a user problem rather than a problem of methodology.

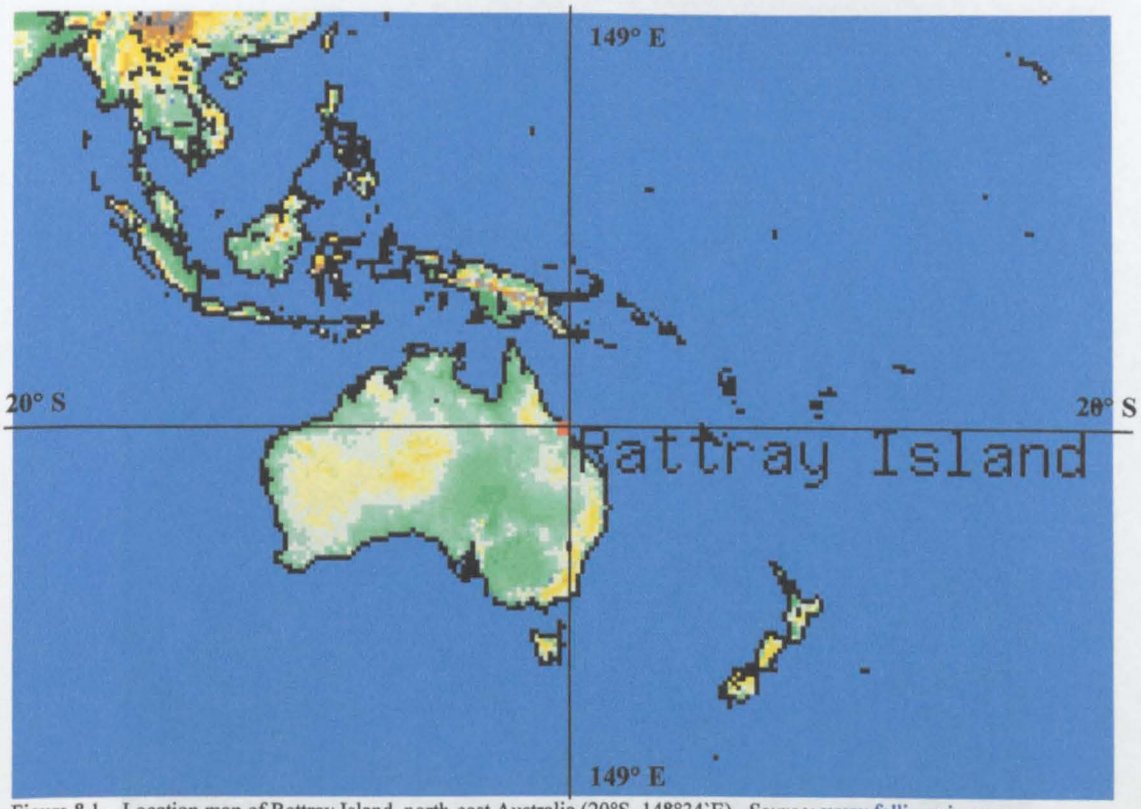

Figure 8.1 – Location map of Rattray Island, north-east Australia (20°S, 148°34`E). *Source:* www.fallingrain.com

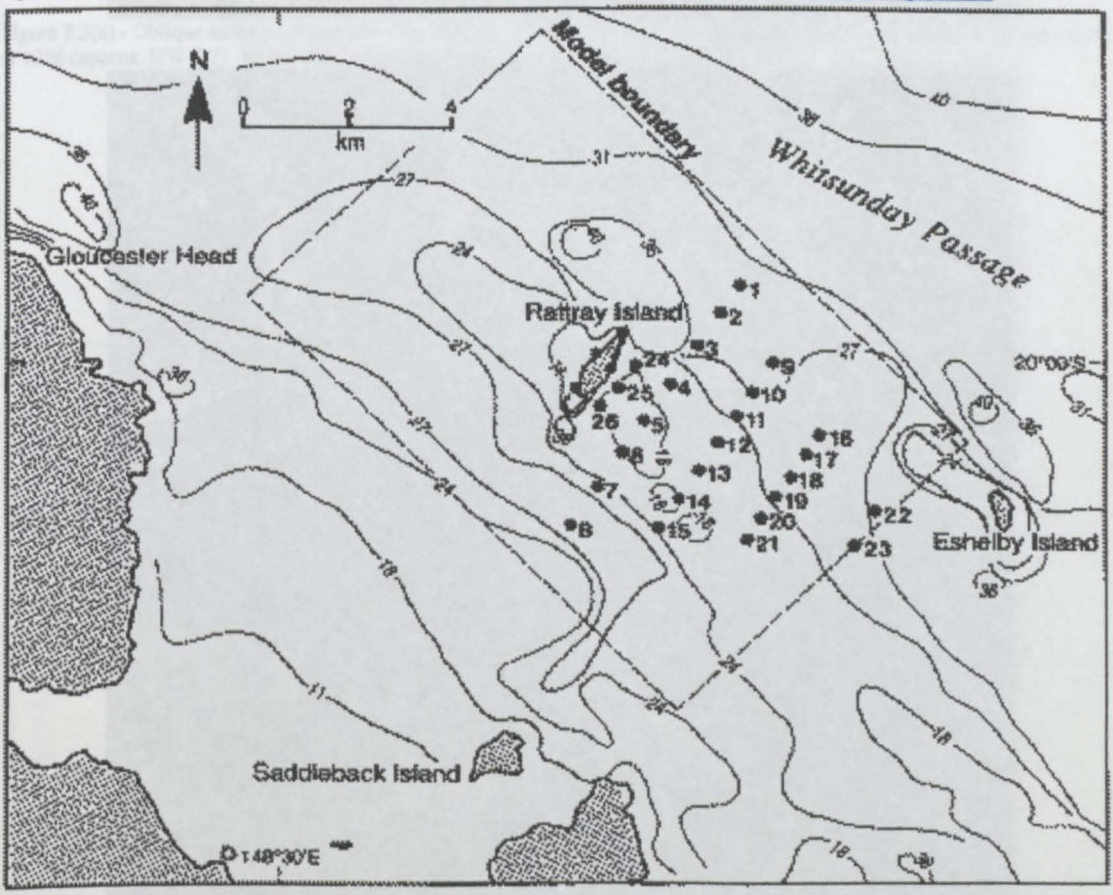

Figure 8.2 – Original Rattray Island model domain, local bathymetry and current meter deployment (filled circles 1-26). *Source: Wolanski et al. 1984.*

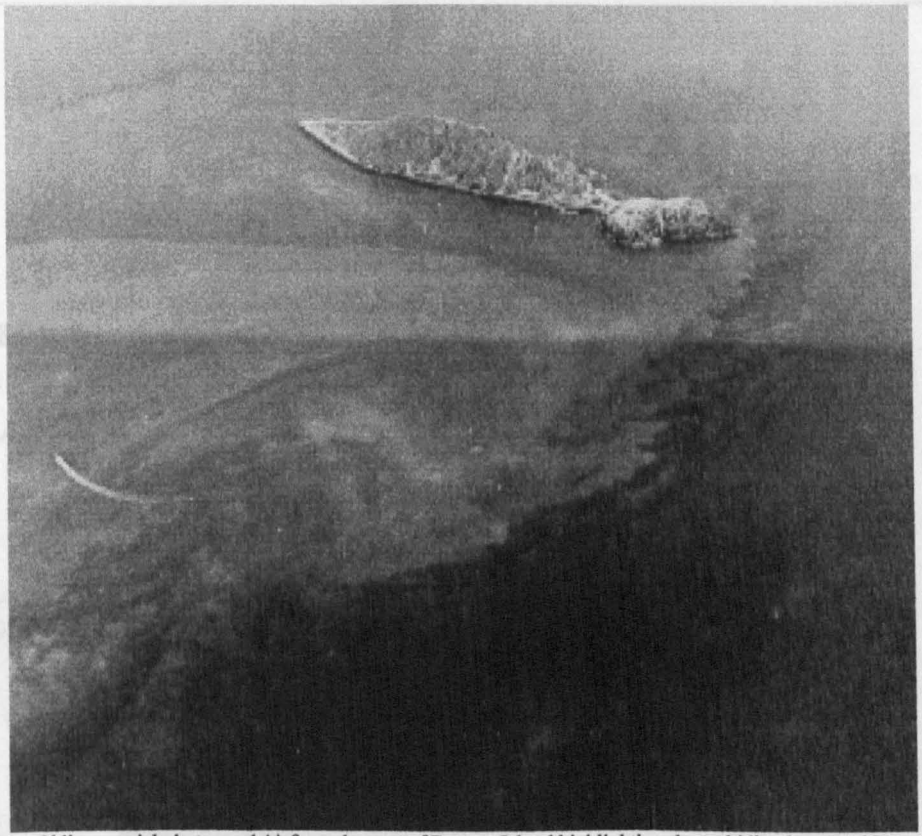

Figure 8.3(a) - Oblique aerial photograph** from the east of Rattray Island highlighting the turbidity front on 4 December, 1982 at 1220 (approx. HW-0.7). NOTE: Only one eddy apparent in the wake of the island

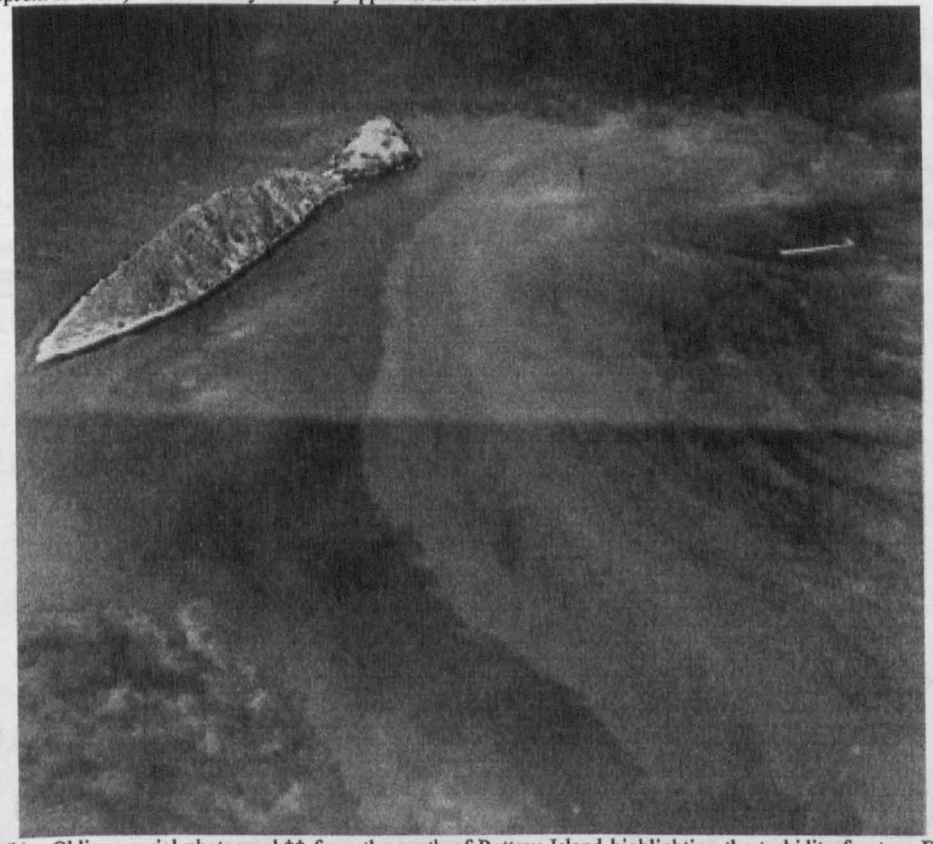

Figure 8.3(b) - Oblique aerial photograph** from the south of Rattray Island highlighting the turbidity front on December 4, 1982 at 1210 (approx. HW-1). NOTE: Only one eddy in wake of the island.

** - **Source: Wolanski et al. 1984.**

Figure 8.3 – Aerial photographs of Rattray Island demonstrating wake development during the flood tide (tracer is surface turbidity)

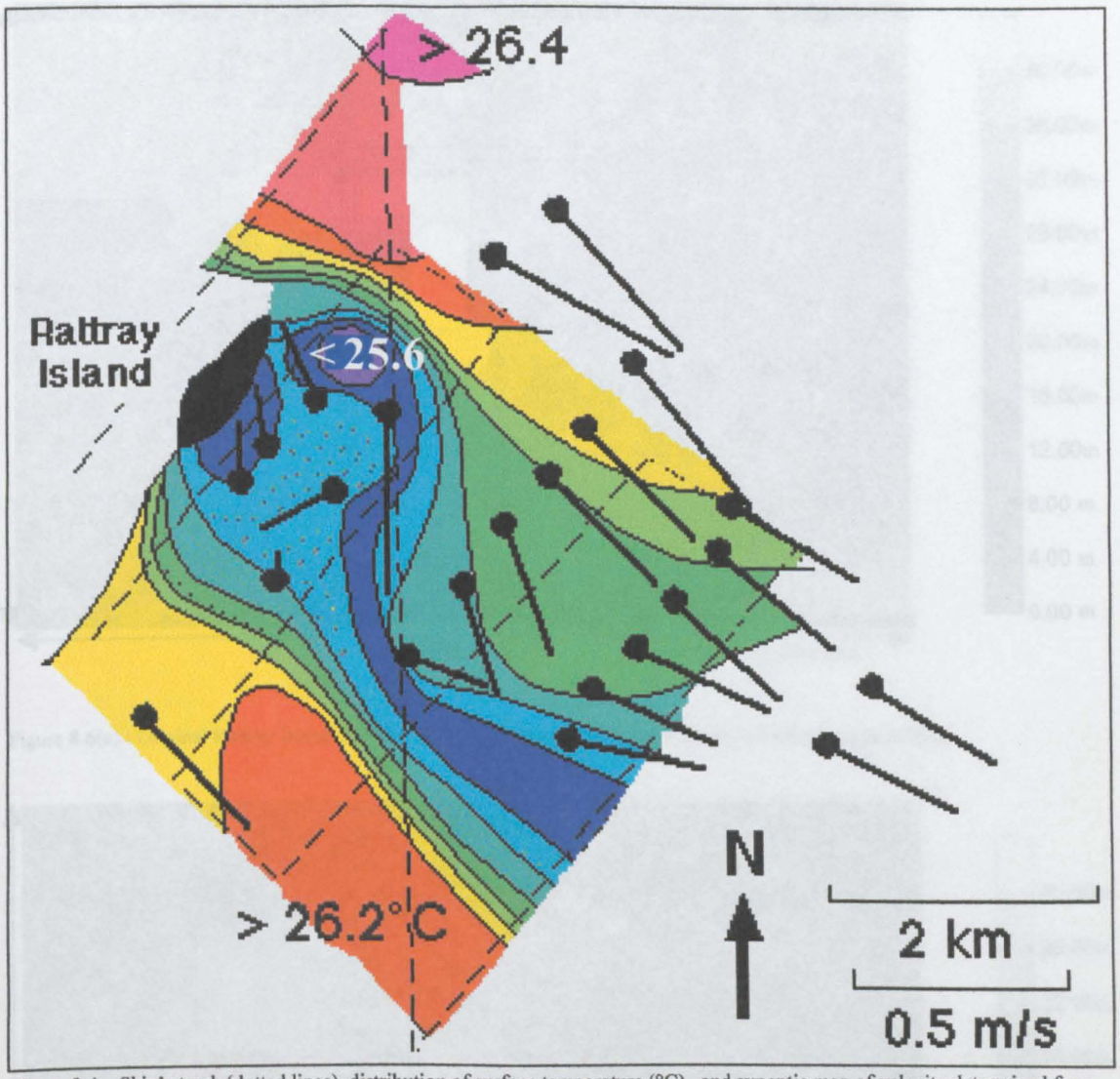

Figure 8.4 – Ship's track (dotted lines), distribution of surface temperature (°C), and synoptic map of velocity determined from current meters. Data collected between HW-2 and HW-1 on 4 December 1982 by AIMS.
Source: http://www.es.flinders.edu.au/~mattom/ShelfCoast/notes/figures/fig7a5.html

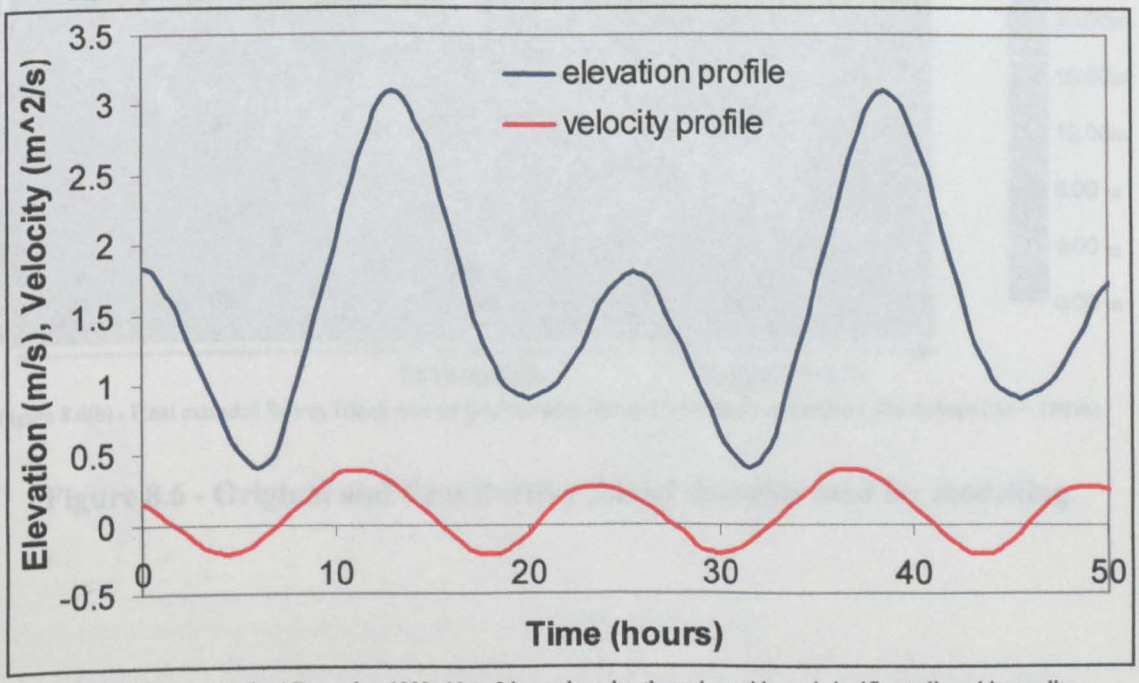

Figure 8.5 - Tidal cuves for the 4 December 1982. Note 2 hour phase lag throughout tide, and significant diurnal inequality.

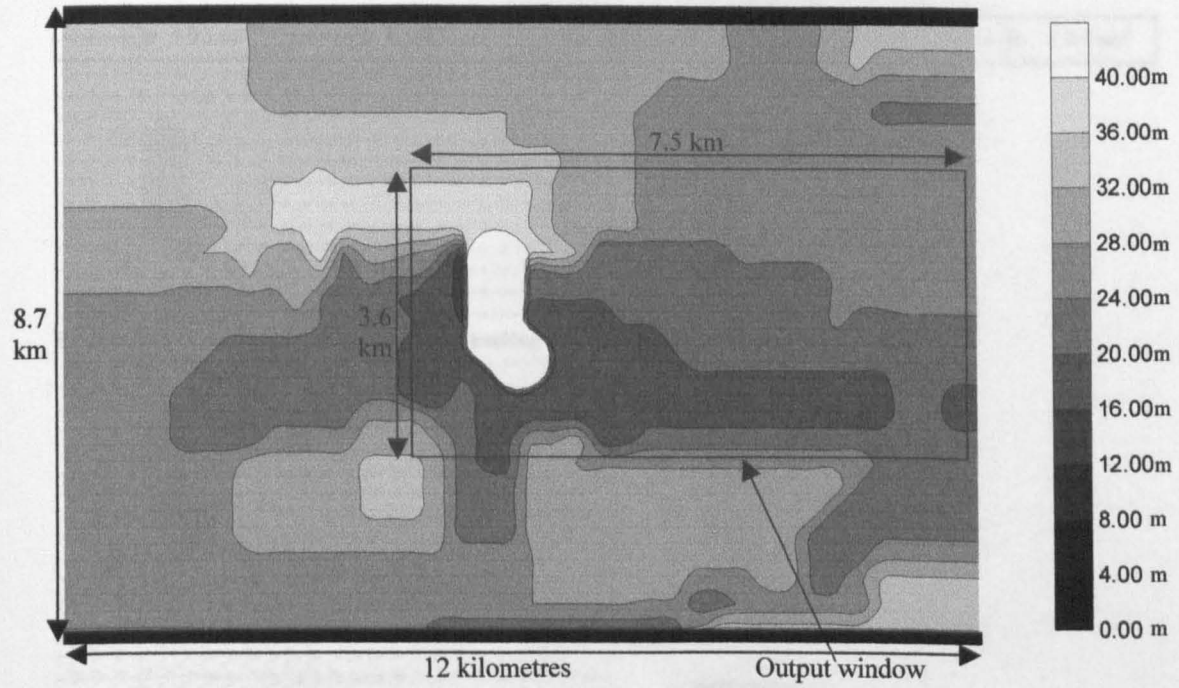

Figure 8.6(a) - Original Rattray Island domain (Δx = 300 m) replicating conditions from Falconer et al. (1984).

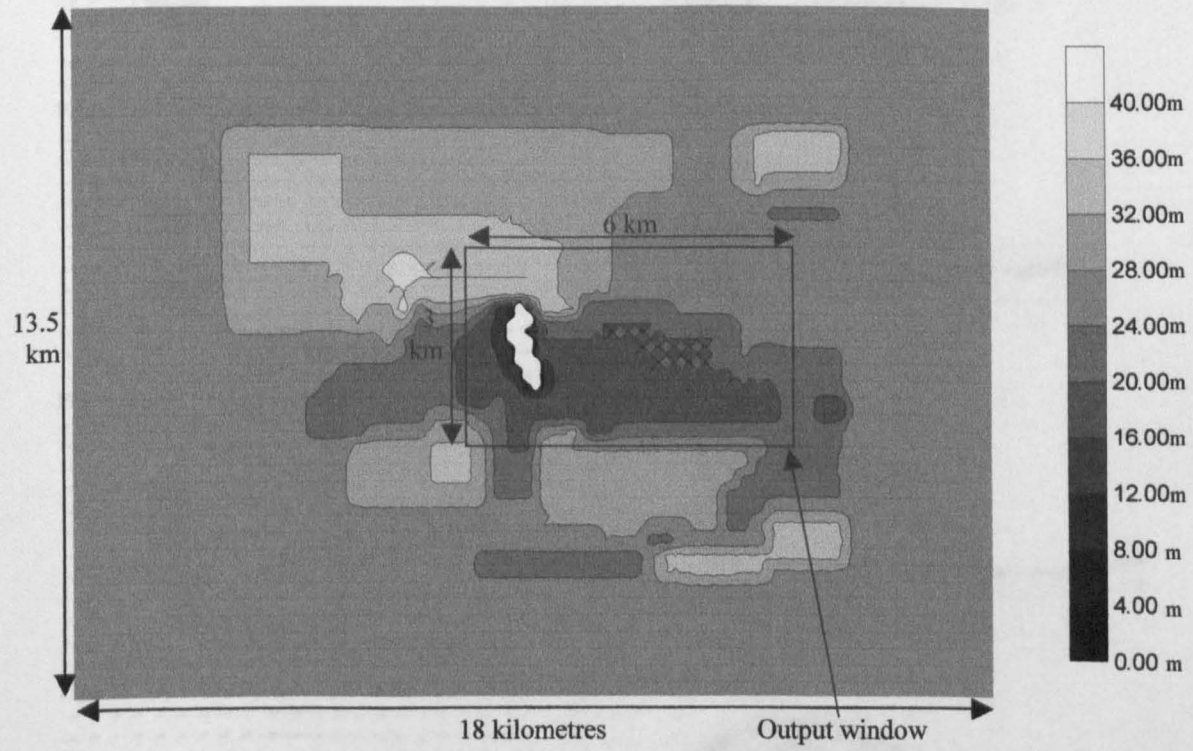

Figure 8.6(b) - Final extended Rattray Island domain incorporating increased resolution and refined island shape (Δx = 150 m).

Figure 8.6 - Original and final Rattray Island domains used for modelling.

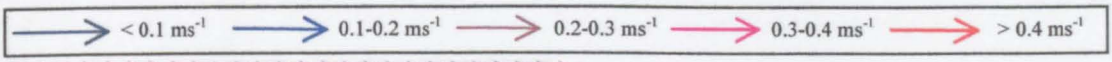

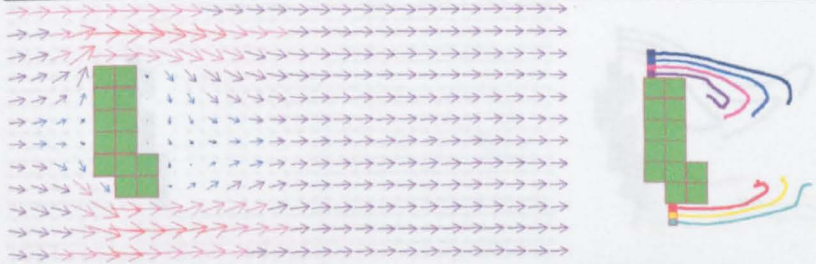

Figure 8.7(a) - Velocity vector plot and particle tracking output at **HW-4** (300m mesh).

Figure 8.7(b) - Velocity vector plot and particle tracking output at **HW-3** (300m mesh).

Figure 8.7(c) - Velocity vector plot and particle tracking output at **HW-2** (300m mesh).

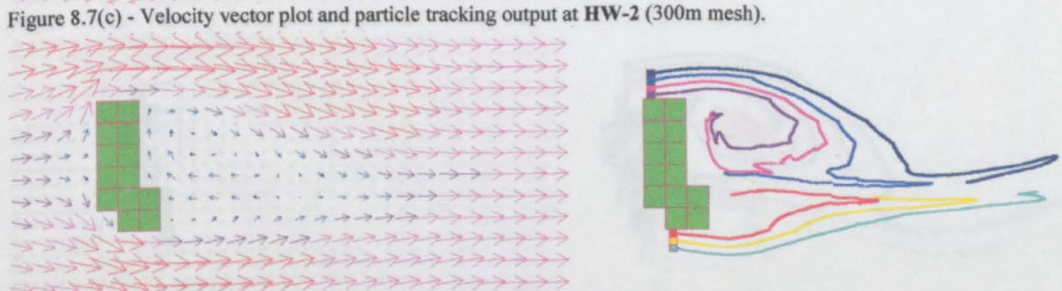

Figure 8.7(d) - Velocity vector plot and particle tracking output at **HW-1** (300m mesh).

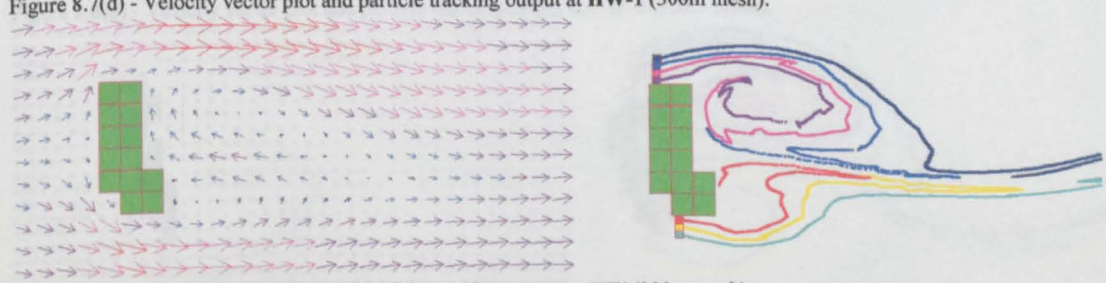

Figure 8.7(e) - Velocity vector plot and particle tracking output at **HW** (300m mesh).

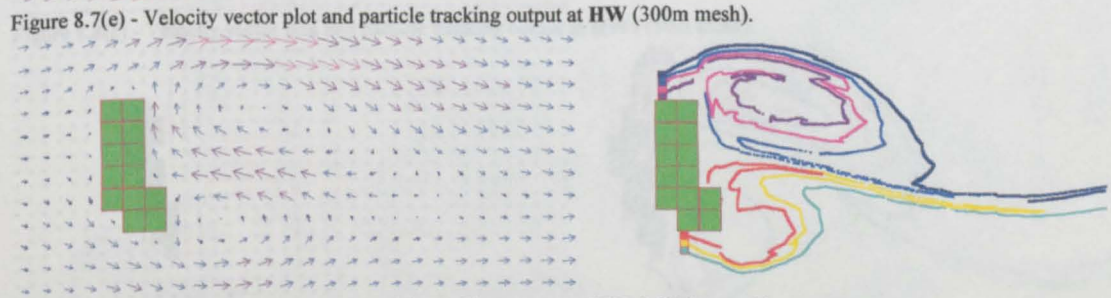

Figure 8.7(f) - Velocity vector plot and particle tracking output at **HW+1** (300m mesh).

Figure 8.7 - TFD model simulation of Rattray Island wake (300 m mesh).

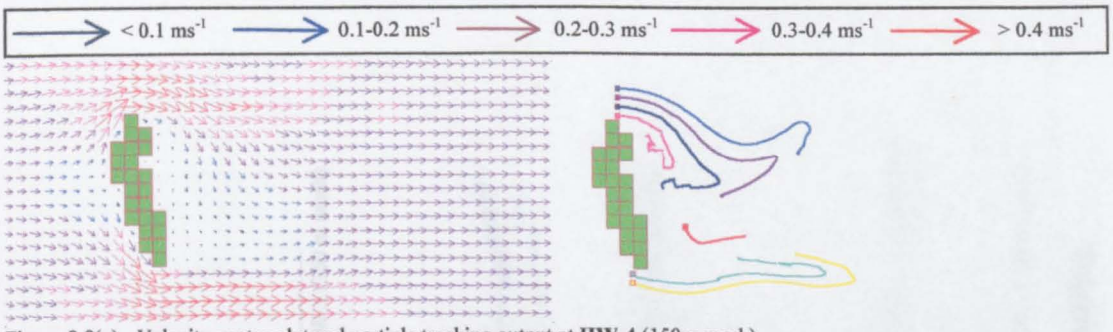

Figure 8.8(a) - Velocity vector plot and particle tracking output at **HW-4** (150m mesh).

Figure 8.8(b) - Velocity vector plot and particle tracking output at **HW-3** (150m mesh).

Figure 8.8(c) - Velocity vector plot and particle tracking output at **HW-2** (150m mesh).

Figure 8.8(d) - Velocity vector plot and particle tracking output at **HW-1** (150m mesh).

Figure 8.8(e) - Velocity vector plot and particle tracking output at **HW** (150m mesh).

Figure 8.8(f) - Velocity vector plot and particle tracking output at **HW+1** (150m mesh).

Figure 8.8 - TFD model simulation of Rattray Island wake (150 m mesh).

Figure 8.9(a) – DVM output at HW-3*

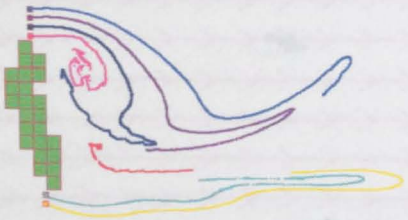

Figure 8.9(b) – TFD model output at HW-3 (150 m mesh).

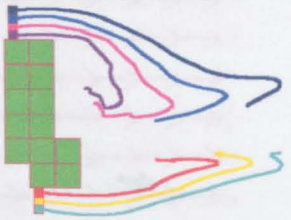

Figure 8.9(c) – TFD model output at HW-3 (300 m mesh).

Figure 8.9(d) – DVM output at HW-1*

Figure 8.9(e) – TFD model output at HW-1 (150 m mesh).

Figure 8.9(f) – TFD model output at HW-1 (300 m mesh).

Figure 8.9(g) – DVM output at HW+1*

Figure 8.9(h) – TFD model output at HW+1 (150 m mesh).

Figure 8.9(i) – TFD model output at HW+1 (300 m mesh).

Figure 8.9 – Comparison of DVM*, TFD (150 m) and TFD (300 m) output using particle tracking.

* - *Source: Furukawa & Wolanski (1998)*

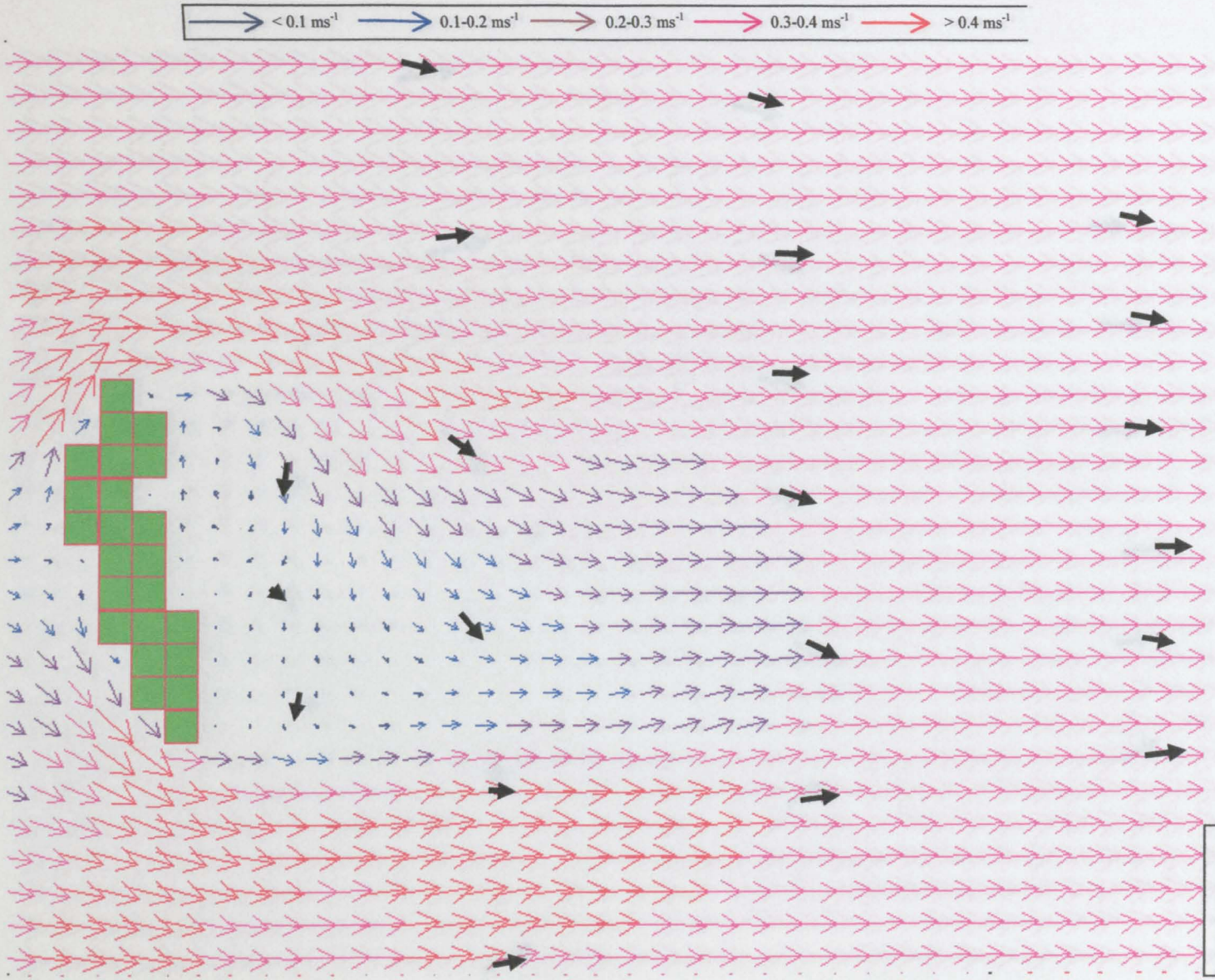

Figure 8.10(a) - TFD model output at HW-4 (150 m mesh) overlain by current meter data.

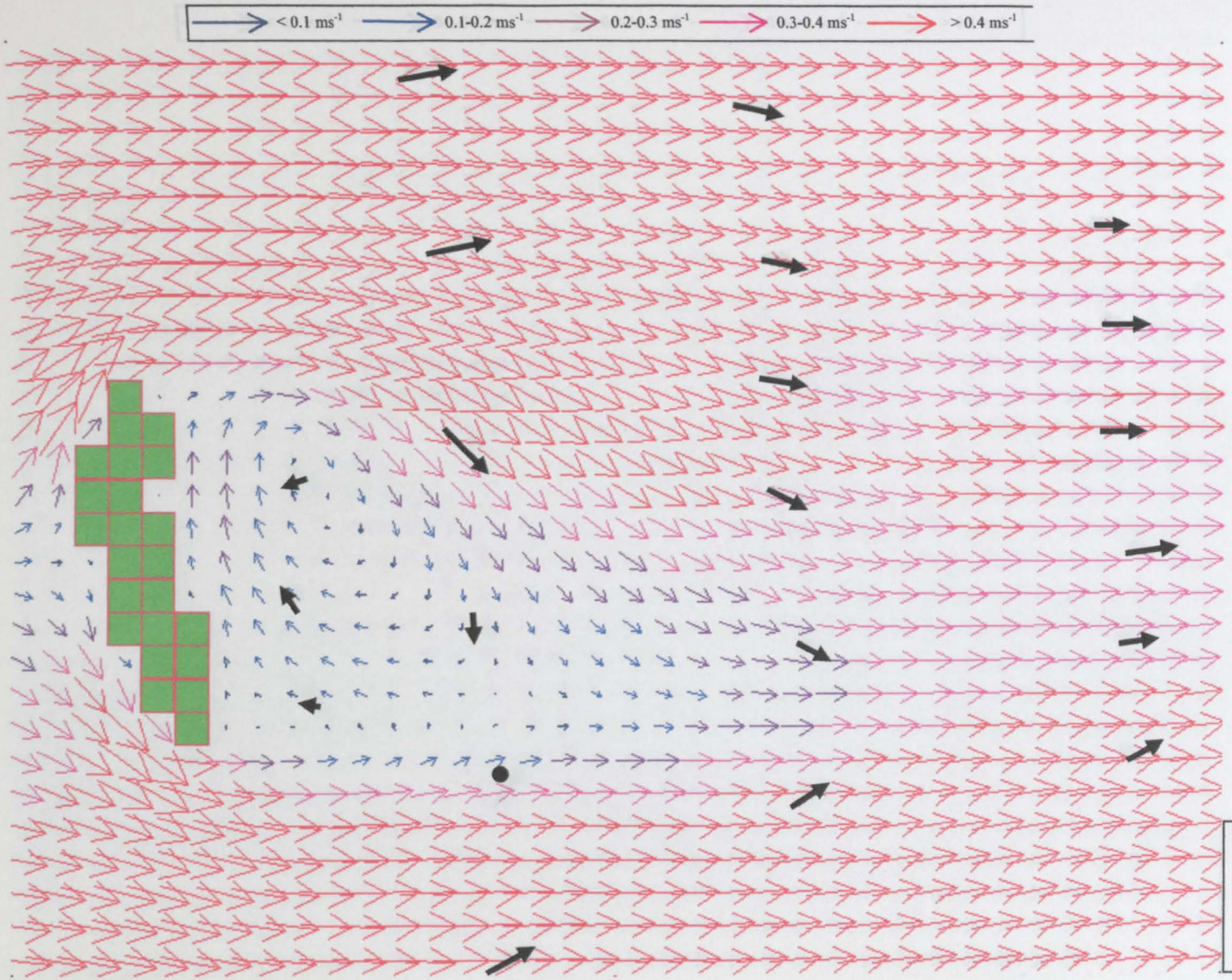

Figure 8.10(b) - TFD model output at HW-2 (150 m mesh) overlain by current meter data.

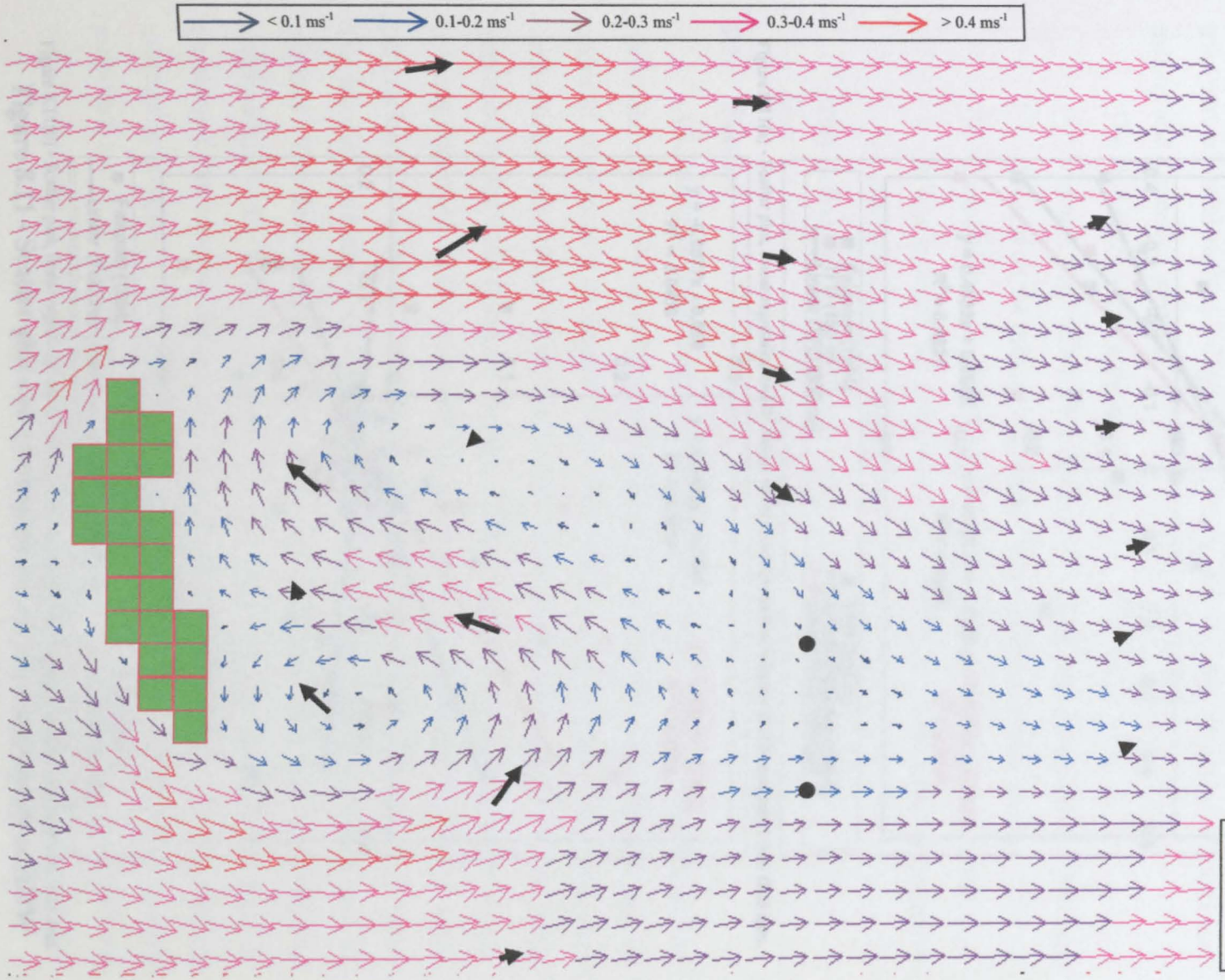

Figure 8.10(c) - TFD model output at HW (150 m mesh) overlain by current meter data

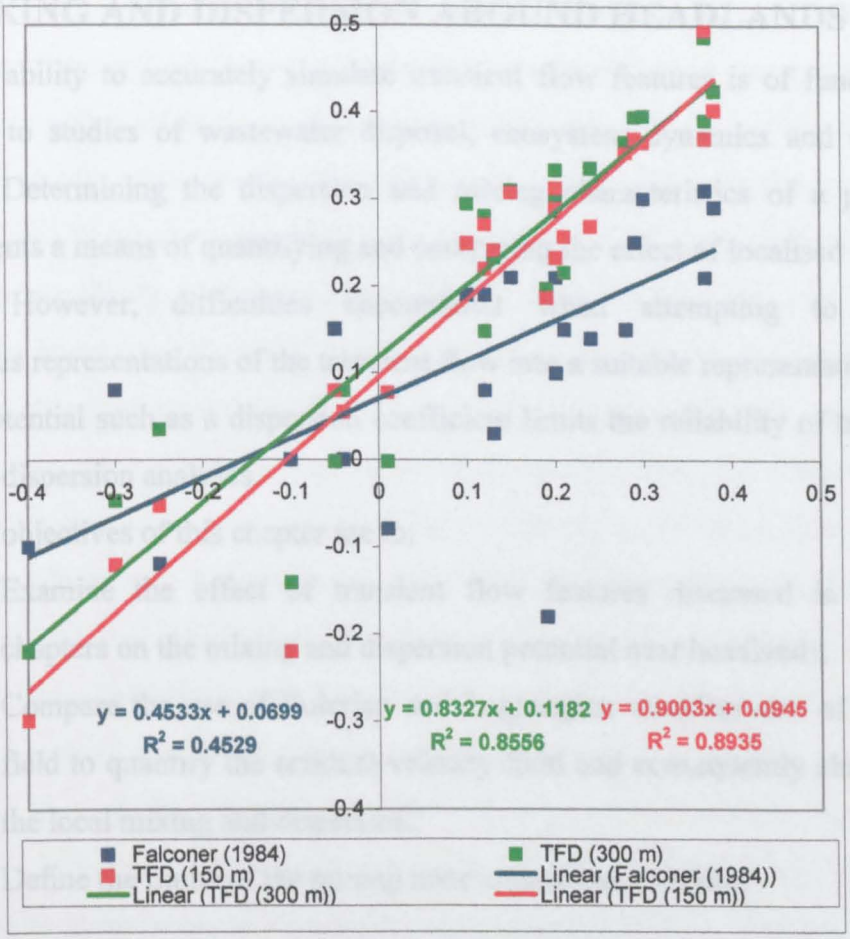

Figure 8.11(a) - Scatter plot, linear regression and R^2 values of the U-component of velocity at HW correlated with field data.

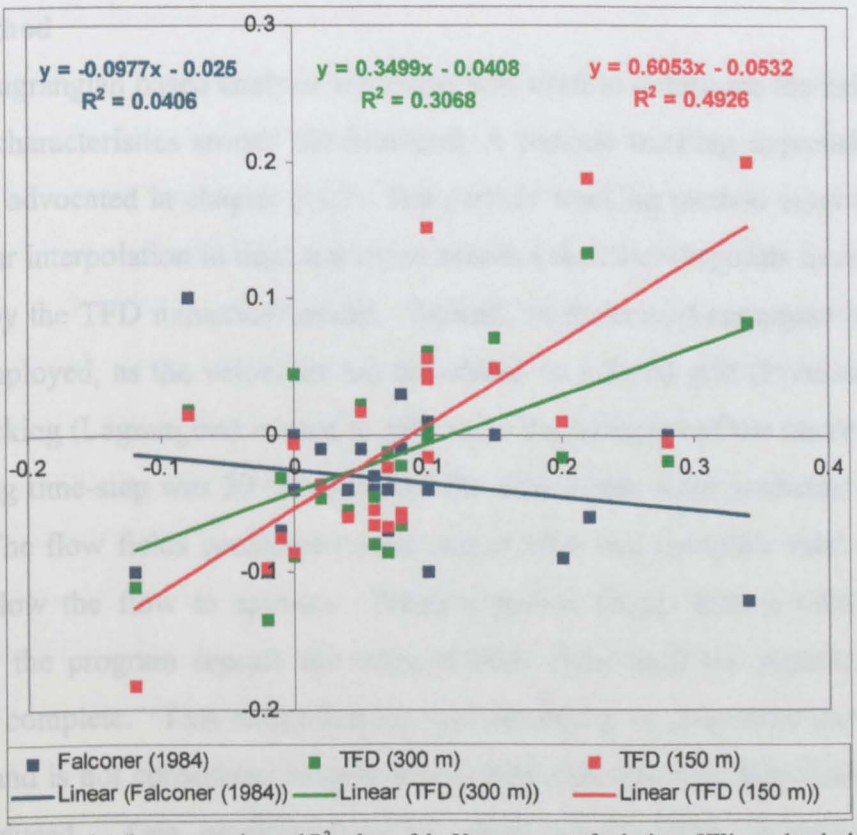

Figure 8.11(b) - Scatter plot, linear regression and R^2 values of the V-component of velocity at HW correlated with field data.

Figure 8.11 - Scatter plot and correlation of velocity components at HHW

9 MIXING AND DISPERSION AROUND HEADLANDS

The ability to accurately simulate transient flow features is of fundamental importance to studies of wastewater disposal, ecosystem dynamics and sediment transport. Determining the dispersion and mixing characteristics of a particular region presents a means of quantifying and comparing the effect of localised transport processes. However, difficulties encountered when attempting to convert instantaneous representations of the transient flow into a suitable representation of the transport potential such as a dispersion coefficient limits the reliability of traditional mixing and dispersion analyses.

The objectives of this chapter are to:

(i) Examine the effect of transient flow features discussed in previous chapters on the mixing and dispersion potential near headlands.

(ii) Compare the use of Eulerian and Lagrangian visualisations of the flow field to quantify the residual velocity field and consequently characterise the local mixing and dispersion.

(iii) Define the limits of the mixing zone around the headland.

9.1 Method

A Lagrangian based analysis technique was used to determine the mixing and dispersion characteristics around the headland. A particle tracking approach will be operated as advocated in chapter 2.4.2. The particle tracking method employed uses simple linear interpolation in time and space between the discrete points in flow fields generated by the TFD numerical model. Overall, an Eulerian-Lagrangian technique is being employed, as the velocities are calculated on a fixed grid (Eulerian), while particle tracking (Lagrangian) is used to determine the transport of the tracer element. The tracking time-step was 30 seconds, and the flow fields were produced every 15 minutes. The flow fields considered were output after two complete tidal cycles in order to allow the flow to spin-up. When a period longer than a tidal cycle is considered, the program repeats the original tidal cycle until the particle tracking exercise is complete. This simplification was necessary to overcome data storage problems, and is not considered to have any detrimental effect on the validity of the results produced. Two predictor-corrector steps were applied to determine the

average velocity of the particle throughout the 30 second time interval. No turbulent diffusion was imposed on the particle tracks, as the investigation was applied only to determine the effect of large scale phenomena that are resolved within the domain (i.e. sub-grid scale processes are ignored). This ensures that only the deterministic mixing effect produced by the action of the current field is modelled (Glasgow, 1993). The simplicity of the particle tracking technique applied is achieved at the cost of some minor imperfections. Most important of these is the occasional trapping of particles along the closed (land) boundary. This is caused by the simple spatial linear interpolation, and has also been reported by Awaji (1982) and Glasgow (1993). Following the procedure of Awaji (1982), the mixing potential will be portrayed using mixing diagrams. A particle was released at the beginning of the simulation at the centre of each cell (16000 particles). Each particle is then considered to represent the water column initially contained within that cell. The particles starting on either side of the headland are identified using different colours. The particles were tracked sequentially through the tidal cycle(s) until the prescribed simulation time elapsed. The position of the various particles can be recorded at any interval specified by the user (normally every hour, or after every complete tidal cycle). The overall mixing effect can then be determined visually.

Residual tidal velocity fields are often used to summarise the transport potential of a particular region. Visual inspection of residual velocity fields can be used to determine areas where strong offshore flow prevails, identify areas where high rates of dispersion would be achieved (indicated by strong shear in the residual flow field), and identify areas where suspended material may accumulate. Two approaches to calculating the residual tidal velocity appear in the literature. The first of these produces the Eulerian tidal residual velocity. This summary visualisation of the flow is simple to determine, and is therefore popular in the literature (Tee, 1976; Pingree & Maddock, 1977; Prandle, 1978; Postma et al. 1989; Falconer & Owens, 1990; Glasgow, 1993; Cheng et al. 1993; Signell & Harris, 2000). Calculation of the Eulerian residual velocity was previously described in chapter 6.4.1, and can be summarised as averaging the model output (velocity or more appropriately the discharge) at each node across the tidal cycle. The Lagrangian residual velocity field presents a more complicated description of the flow. The Lagrangian velocity is

determined by tracking a particle released at the centre of each node throughout a tidal cycle. The end position of the particle is recorded, and Lagrangian velocity is determined as the average velocity required to move from the initial to the final particle position during the specified time period. As the calculation of Lagrangian residual velocity vectors requires significantly more effort than the Eulerian residual representation, its appearance in the literature is restricted (Cheng, 1988; Gadian, 1991). The two residual velocity representations will be compared and contrasted in the following section.

Finally, common techniques used to summarise the dispersion characteristics of a particular area within the domain will be examined. Simple statistical analysis of the spread of a patch of particles is often used to compare the effectiveness of wastewater outfall or dumping sites for example. This information can be presented as the standard deviation (σ), or variance (σ^2) of the particles around the centre of mass, or as the rate of dispersion of the particles (K).

9.2 Results and Discussion

The model domain is shown in figure 1 (Δx = 150 m). A sinusoidal elevation input condition (amplitude = 1 m, period = 12.5 hours) generates a free-stream velocity of 0.5 ms^{-1} with a peak velocity at the headland tip of 1.25 ms^{-1}. A topographic eddy is generated during each half of the tidal cycle which encompasses the region in the lee of the headland. The domain extends far enough upstream and downstream to ensure that rectilinear flow occurs adjacent to the boundaries.

9.2.1 Residual tidal velocity flow fields

When deriving the residual tidal velocity, the intention is to provide a summary diagram which describes the overall transport effect within the domain. While both Eulerian and Lagrangian tidal residual diagrams achieve this objective, interpretation of the information they provide is not immediately obvious. The first obvious comment is that the two velocity fields bear little or no resemblance (compare figures 9.2 and 9.3). The intuitive response is that the Eulerian representation provides a better indication of the overall flow. The near symmetry of the image reflects the symmetry in the transient flow development around the

headland, and also captures the two eddy features. These features of the flow are not captured in the Largangian representation, which provides no discernible pattern. The only area where both images provide superficial agreement is in the far-field where very weak rectilinear velocities predominate. However, the reality of the situation is that the Eulerian representation has very little practical use in cases where there is strong spatial and temporal variability of the flow. This is because the calculation procedure for a particular node takes no account of the surrounding variability. Using Eulerian residual velocities to determine transport potential is therefore an incorrect application as demonstrated in chapter 6.4.1. The Lagrangian representation on the other hand does capture the spatial and temporal variability. However because of this variability, a particular Lagrangian tidal residual flow field is only applicable for a specific starting time during a tidal cycle. If the Lagrangian residual was re-calculated for the same tide, but started at a different phase during the tidal cycle, a different Lagrangian residual flow field would be produced (compare figure 9.3 and 9.4 (initiated 3 hours earlier in the tidal cycle)). This added degree of complexity perhaps explains the reluctance in the literature to take up the Lagrangian representation. Another point peculiar to the Lagrangian residual is that if the simulation is allowed to run for two tidal periods, the residual flow velocity reduces significantly, but the pattern observed after one tidal cycle persists. This process continues through any number of tidal cycles until the residual velocity becomes almost negligible (see figure 9.5). This is of interest for a number of reasons. Primarily, this indicates that a defined mixing zone exists, as none of the particles are managing to escape from the region around the headland. The persistence of the residual flow pattern is also surprising, as during the second and later tides particles will both start and end at positions removed from the original starting positions. The distribution pattern itself is of interest because of the strong almost random variability of the vectors observed in some regions whereas adjacent regions will be smoothly varying. The distribution of the various regions indicates significant 'banding' or 'streakiness' particularly after a number of tides. These observations are taken as an obvious indication of non-linear interaction. Discussion of the source and persistence of pattern will be re-introduced later after discussing mixing and dispersion diagrams.

9.2.2 Mixing diagrams

Mixing diagrams associated with the residual tidal velocity flow fields discussed above are presented in figure 9.6 (over one tidal cycle), and figure 9.7 (over 10 tides). Presenting mixing information in this format is instructive for a number of reasons. Firstly, the short term flow development is elucidated: (i) the first transient eddy feature rolls up (figures 9.6(b, c & d)), (ii) the eddy is shed as the tide reverses (figure 9.6(e)), simultaneously a strong flow jets offshore from the lee of the headland, and (iii) a 'hammerhead' feature is observed as the jetted flow and original eddy interact with the newly generated transient eddy (figure 9.6(f)). The exchange of coloured particles over a number of tides presents a clear demonstration of the significant effect that transient eddy features generally have on the mixing potential. The 'handedness' of the mixing in this case is related to the starting time within the tidal cycle (just as the flood tide is started). The streaky and patchy distribution indicated by the mixing diagrams is also of interest, as this sort of detail is normally lost when sub-grid scale diffusion processes are considered. After 10 tides it is also obvious that there is a defined region of very well mixed fluid, and a strong front between the well mixed and unmixed fluid regions.

9.2.3 Dispersion diagrams

Dispersion is usually considered for a patch of fluid in the domain rather than producing an overall dispersion characteristic. Typically dispersion is of interest when considering the merits of various wastewater outfall sites, higher dispersion rates obviously being desirable. It is common practice to try and position an outfall in a region of flow exhibiting strong shear, and a generally offshore component. Flow around headlands provides a very good combination of the desired conditions. For the purposes of this discussion, three distinct patches of particles were considered (no consideration of decay or a continuous source). The patches were positioned straddling the major axis of the headland shown in figure 1. The three patches were centred 300 m, 1800 m and 3300 m offshore. Each patch initially covered an area equivalent to one cell (150 m × 150 m) with particles released on a 2 metre square matrix within the cell (5625 particles in each of the three cells). The particles in each patch can be identified by their colouring as indicated in the initial set-up (figure

9.8(a)), and are released at LW (i.e. at mid ebb as a running input wave is prescribed). During the first tidal cycle summarised in figure 9.8, the evolution of the individual patches is markedly different. The nearshore patch immediately becomes very elongated reflecting the strain imposed on the patch by the significant shear in the flow at the headland tip associated with tidal streaming. The evolution of the nearshore patch continues to be very rapid. This is not unexpected after the initial stretching, as the patch extends across a number of cells in an area exhibiting strong non-linear flow characteristics. For instance, the interaction of the elongated patch with transient eddy features is indicated by the wrapping of the ends of the elongated streak (see the red patch in figure 9.8). After one complete tidal cycle (figure 9.9(a)) the nearshore patch is already strained across a region equivalent to the tidal extent and is distributed on both sides of the headland. In contrast, the patches released further offshore tend to maintain their integrity, and dispersion is obviously limited throughout the first tidal cycle. This indicates that the offshore patches are initially far enough away from the headland that strong regions of non-linear flow (i.e. the transient features and tidal streaming observed around the headland) are not encountered. However a weak onshore drift experienced by the two offshore patches ensures that they will eventually become entrained in the non-linear flow region which as indicated by the behaviour of the onshore patch encourages rapid dispersion. The intermediate patch becomes entrained after 2 complete tidal cycles, with the furthest offshore patch following suit after 5 tidal cycles (see figures 9.9(b, c)). After 10 tidal cycles all three patches are widely dispersed. Patches released even further offshore (not shown) experience a weak offshore drift, and therefore never interact with the transient eddy features. It is interesting at this stage to note that the Lagrangian tidal residual plot (figure 9.4) correctly shows the same weak onshore drift experienced by the two offshore patches during the early part of the dispersion simulation. In contrast, the Eulerian tidal residual plot (figure 9.2) suggests a strong offshore drift would be experienced. This outcome confirms the conclusions reached in section 9.2.1 regarding the use of Eulerian residuals when studying transport processes.

Another point of interest is the great temporal variability in the amount of straining and dispersion experienced by an individual patch in the short term due to

the dependence upon the phase of the tide when the patch is released. This can be seen by comparing images obtained after one complete tidal cycle for the red patch released at (i) LW (mid ebb) in figure 9.9(a), (ii) HW-3 (start of flood) in figure 9.10(a), and (iii) HW (mid flood) in figure 9.10(c). Here it can be seen that the release at LW produces much more dispersion than in the other two cases. This indicates that discharging from wastewater outfalls and direct dumping of waste at sea should be synchronised with the tidal cycle whenever possible in order to coincide with the best conditions for initial dilution. Considering the short term variability of the straining and dispersive effect it is also worthy of note that the long term distribution (> 5 tidal cycles in this case) is insensitive to the phase of the tide during which the patch was initially released.

After a particle patch becomes well distributed on either side of the headland, the persistence and systematic repetition of the pattern is of great interest. The extent of the outer ring of the streak indicates a front between the well mixed and unmixed regions of the domain. The outer reach of this front defines the limits of an identifiable mixing zone around the headland. A similar frontal region was also observed in the mixing diagrams discussed in the previous section. The rings of the streak form two lobe like structures (figures 9.9(c, d) and 9.10(b, d). The two lobes are squashed and stretched around the headland during the tidal cycle. The overall shape of the mixing zone described by the two lobes is therefore replicated every 12.5 hours in this case (i.e. in phase with the tide). In contrast to the early development of the patch, the overall shape defined by the distribution of particles from any original patch is independent of the initial start time or position of the patch after the patch is strained around the headland. The development of the elongated streak within the mixing zone creates a pattern within each lobe not unlike the annual rings of a tree trunk. The number of 'tree-rings' in the mixing zone matches the number of tides since the patch first became distributed around the headland. A new ring is generated in the centre of each lobe during the tidal cycle, displacing the older rings outwards. This phenomenon is apparent in figure 9.9. The streaking of the original patch also provides an insight into the source of the 'banded' regions apparent in the Lagrangian residual flow fields and mixing diagrams.

A logical continuation of the analysis in chapter 9.2.1 is to determine the Lagrangian residual velocity of each particle within one of the cell-sized patches released at the tip of the headland in figure 9.8 (the red patch is considered). The Lagrangian residual vectors shown in figure 9.11(a, b) are after 1 and 2 tides, and those in figure 9.12(a, b) are after 5 and 10 tides respectively. These show that the pattern developed after 2 tides persists. In each case significant banding of smoothly varying velocity vectors interspersed with regions of apparently random velocity distribution is observed. Similar banding and variation of the velocity vectors was observed in the coarse scale residual results (figure 9.3). Note that the region encompassed by the fine scale patch was represented by one velocity vector in the coarser representation. Furthermore, at both resolutions no sub-grid scale processes are imposed, and the fine scale results are derived from flow fields using the coarse scale velocity resolution. The persistent pattern of smoothly and randomly varying regions at both coarse and fine scale together with the great spatial and temporal variability of the residuals suggests that particle transport may be chaotic. In view of the overall complexity of the system of Lagrangian residuals it is not surprising that existing methods used by practising engineers to determine mixing and dispersion characteristics use combinations of simplified statistical and empirically derived relationships.

9.2.4 Quantifying dispersion

Simple statistical analysis techniques based on a Fickian diffusion model are commonly used to summarise dispersion rates in the coastal environment (Richardson & Stommel, 1948; List et al, 1990; Geyer & Signell, 1992). A Fickian diffusion model assumes a linear growth in variance with time. Therefore the diffusion coefficient can be determined from the relationship

$$K = \frac{\sigma^2}{2t} \ (\mathrm{m^2 s^{-1}}), \qquad (9.1)$$

where t is the elapsed time and σ^2 is the variance of the particles in a patch. The variance is determined as,

$$\sigma^2 = \frac{1}{n}\sum_{1}^{n}(x_i - \bar{x})^2 + (y_i - \bar{y})^2, \qquad (9.2)$$

where $\bar{x} = \frac{1}{n}\sum_{1}^{n}(x_i), \bar{y} = \frac{1}{n}\sum_{1}^{n}(y_i)$ are the co-ordinates of the centre of mass of the particles. Analysing the development of the three particle patches shown in figure 9.8 and 9.9, the variance (figure 9.13(a)) of each patch was derived every 2 hours for 10 consecutive tides (see figure 9.13(a)). A number of points are brought to light by this analysis. Not unexpectedly the dispersion of the patches does not fit the Fickian model. The results show that σ^2 does not increase linearly with time, and so K is not a constant. Therefore K would be better calculated from the gradient of σ^2 in time,

$$K = 0.5\frac{\partial\sigma^2}{\partial t}. \qquad (9.3)$$

However, because of the fluctuations in the curves (figure 9.13(a)), the gradient method would produce rather noisy results with positive and negative values of K. The period of the fluctuation component in this case for all three patches is 12.5 hours (= tidal period). Therefore a 'mean' value of σ^2 (averaged over a tidal cycle) was used to determine the diffusion coefficient K using equation 9.3 (figure 9.13(b, c)), the results of which will be discussed below.

The implication of the negative gradient of the variance of the particles occurring periodically throughout the tidal cycle in figure 9.13(a) is that the particles are becoming 'unmixed'. Examining the development of the red patch in figure 9.8 the source of the negative gradient of σ^2 becomes apparent. During the first three hours of the simulation the patch is strained out into a long elongated streak. After the tide reverses, the two ends of the streak are subject to different velocities. The overall length of the streak continues to expand. However the increased curvature of the streak ensures that the particles become more concentrated around the centre of mass as the streak is 'squashed' around the tip of the headland. The rate of 'squashing' of the streak is greater than the rate of dispersion of particles in the streak at this stage. The variance of the particles is therefore reduced. This pattern is repeated during each half stage of the tide, as the streak is alternately squashed and strained by tidal streaming. The offshore patches experience a similar effect. Examining the offshore patches appears to indicate that the 'squashing' of the overall patch is analogous to a reversible linear straining effect. The only reason the patches don't return to their exact original shape is because of some non-linear straining of the patch.

Analysing the development of the three individual patches using the 'mean' variance, σ^2, and dispersion coefficient, K presented in figure 9.13(b, c) and dispersion diagrams (figures 9.8 and 9.9), 3 distinct stages of dispersion can be identified. During the initial development stage there is minimal dispersion of the particles as indicated by the low values of K and σ^2, and the tendency for the patch to maintain its integrity (see blue patch in figure 9.8). For all intents and purposes the patches remain in the free-stream during this initial stage. The dispersion of a patch released in the free-stream in an area exhibiting a very weak Lagrangian residual flow would never develop beyond this first stage in the absence of sub-grid scale turbulence. During the second stage of development (characterised by the dispersion of the red patch over the first tidal cycle shown in figure 9.8), the patch undergoes rapid straining which disperses the particles along an increasingly extended streak line. This is indicative of the patch being subject to high levels of shear. Non-linear flow development around the headland during each tidal cycle characterised by transient eddy features and tidal streaming is the source of the high shear levels. The Lagrangian tidal residual flow fields (figures 9.3, 9.4, 9.5, 9.11 and 9.12) indicate the potential for strong shear and strain rates in the flow around the headland. The rapid dispersion that the patch undergoes during this second stage is indicated by the diffusion coefficient K which increases substantially. The final stage of the dispersion occurs once the elongated streak reaches the extent of the mixing zone described in section 9.2.3 (which for each of the patches coincides with occurrence of peak diffusion rate in figure 9.13(c)). During this stage, the streak length continues to grow at a similar rate as in the 2nd stage, but is forced to wrap itself up over a constrained region defined by the mixing zone. This phenomenon is illustrated by the distribution of the patches observed in figures 9.9(b-d), and 9.10(b, d). The effect of this is that the rate of increase in variance of the particles from the centre of mass is reduced compared with the growth of the streak length. This is reflected by the steadily decreasing diffusion coefficient from the peak value reached during stage two. Eventually a near steady state situation prevails when the particles in the patch become well distributed throughout the mixing zone. As particles are unable to escape from the mixing zone, the major source of increase in variance of the particles becomes the steadily increasing extent of the mixing zone indicated by the expansion

of the 'tree-rings' in the dispersion diagrams. At this point of the development of the patch, the variance is steadily increasing, and diffusion coefficient is maintained. The value of the diffusion coefficient after steady state has been established for the first two patches settles down to a value of approximately 12 m^2s^{-1}. The patch released furthest offshore does not reach steady state within the duration of the simulation. It would appear that the diffusion coefficient K should be of similar value for each of the patches once stage three has become fully established, as the variance of all three patches is constrained by the extent of the mixing zone.

9.3 Conclusions

The results and subsequent discussion presented in this chapter have demonstrated the key role of non-linear flow structures in providing conditions which enhance the mixing and dispersive potential of the local area. Transient eddy features generated around headlands and islands are commonly occurring non-linear flow structures in the coastal environment. The impact of transient features is indicated in mixing and dispersion diagrams by a distinct mixing zone within which high rates of strain and diffusion are observed. In the free-stream region outside the mixing zone, limited mixing and dispersion occurs. Three distinct stages of development of dispersion in a tidally dominated non-linear flow regime have been identified and elucidated. The dispersion of an individual patch during the first two stages is highly dependent on the starting position and release time of the particles is demonstrated. In contrast, once the third dispersion stage has become established, the distribution of the particles becomes highly predictable and is no longer dependent on these factors.

Attempts to summarise the overall mixing or dispersion potential of a particular region using a single residual flow image or dispersion coefficient are unable to provide an adequate representation of the transport of fluid or suspended particles. The apparently chaotic spatial and rapid temporal variation demonstrated using Lagrangian residual flow fields indicates the complexity of the problem. The reliability of techniques regularly applied in the literature such as determining the Eulerian tidal residual flow and determining the dispersion coefficient using Fickian diffusion have therefore been called into question. Lagrangian analysis techniques appear to provide the only credible approach for studying transport in regions subject

to transient flow phenomena. However, the complexity involved in the Lagrangian analysis indicated by the apparently chaotic spatial variation of the results restricts application of these techniques. Therefore, there is a clear need for continued development of Lagrangian analysis techniques in order to make the output produced more accessible. In the immediate future, mixing and dispersion diagrams of the sort presented in this chapter appear to provide the best overall representation of transport processes occurring in the coastal environment.

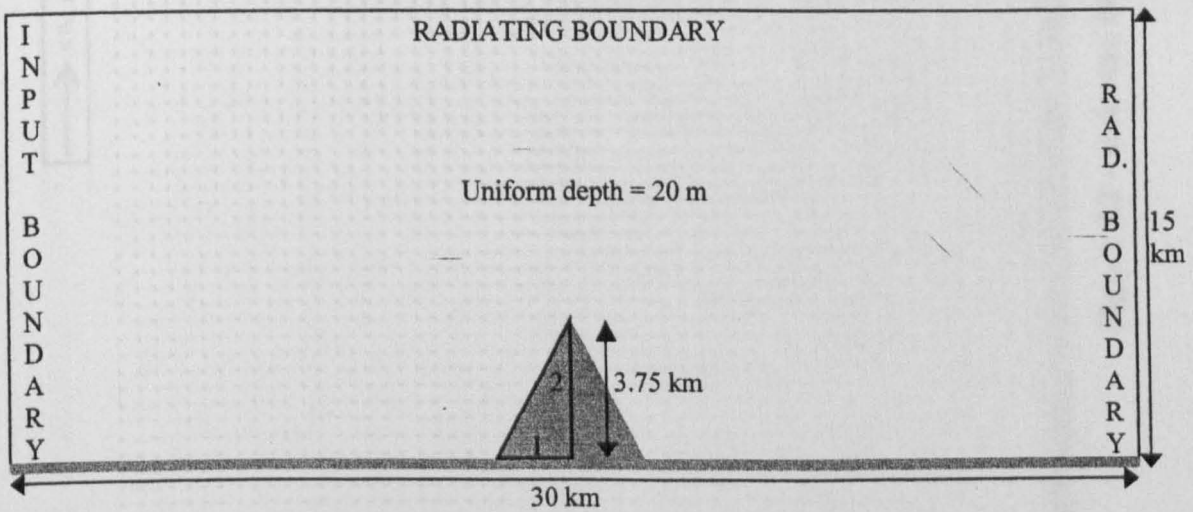

Figure 9.1 - Domain used throughout chapter 9 to investigate the modelling of mixing and dispersion processes.

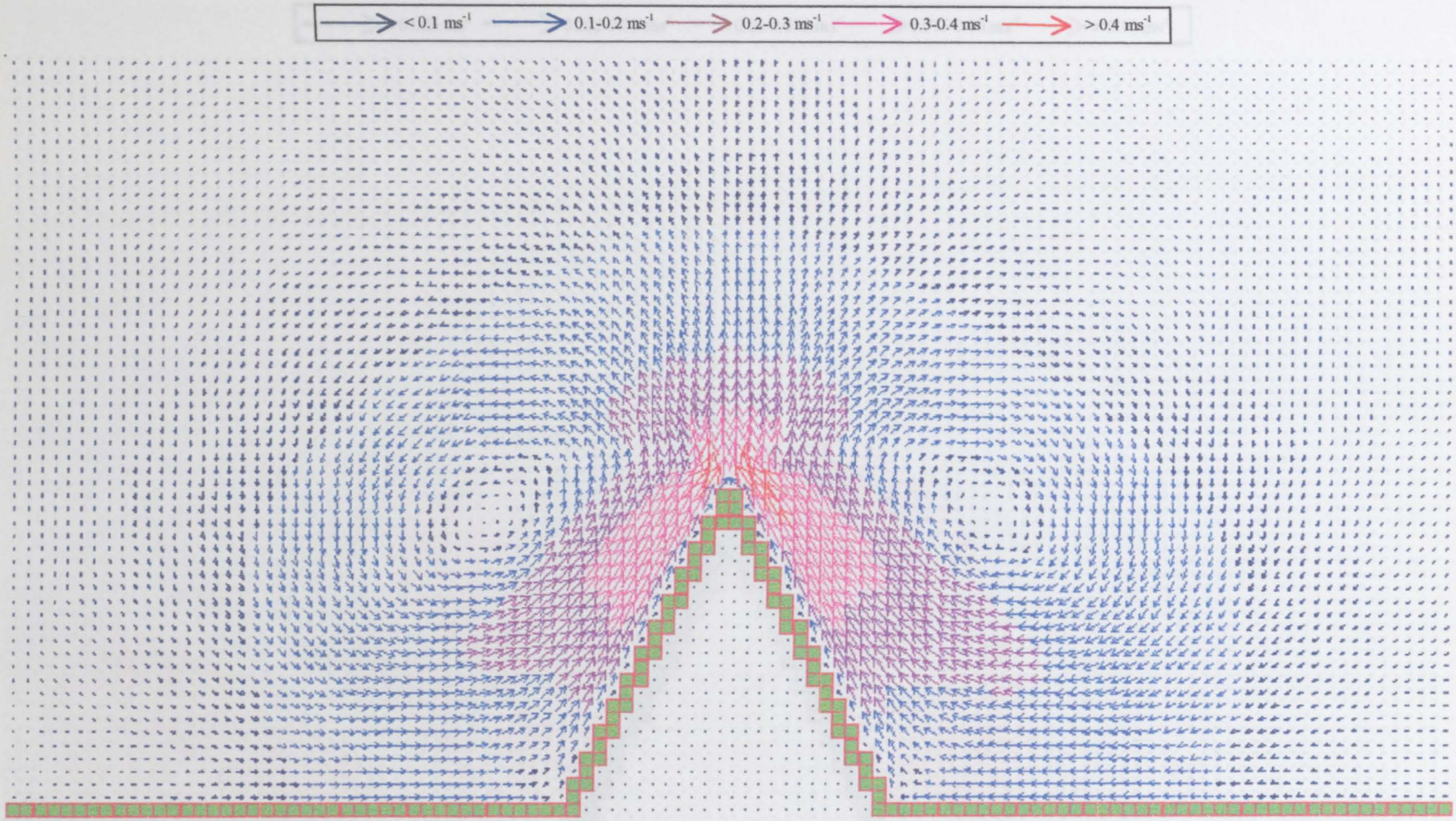

Figure 9.2 – Eulerian tidal residual velocity field after 1 tidal cycle (result independent of tidal phase).

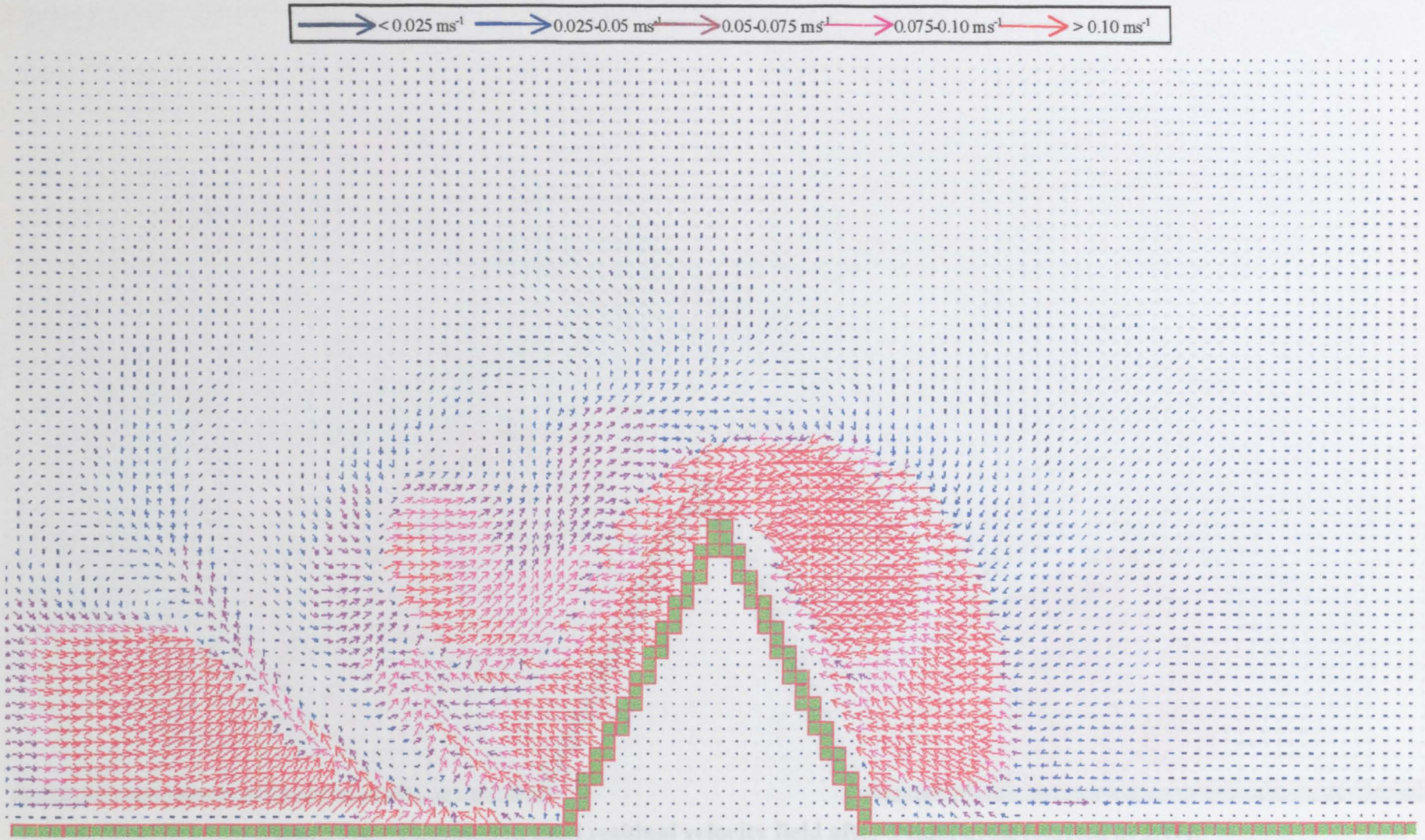

Figure 9.3 – Lagrangian tidal residual velocity field after 1 tidal cycle (started at HW-3).

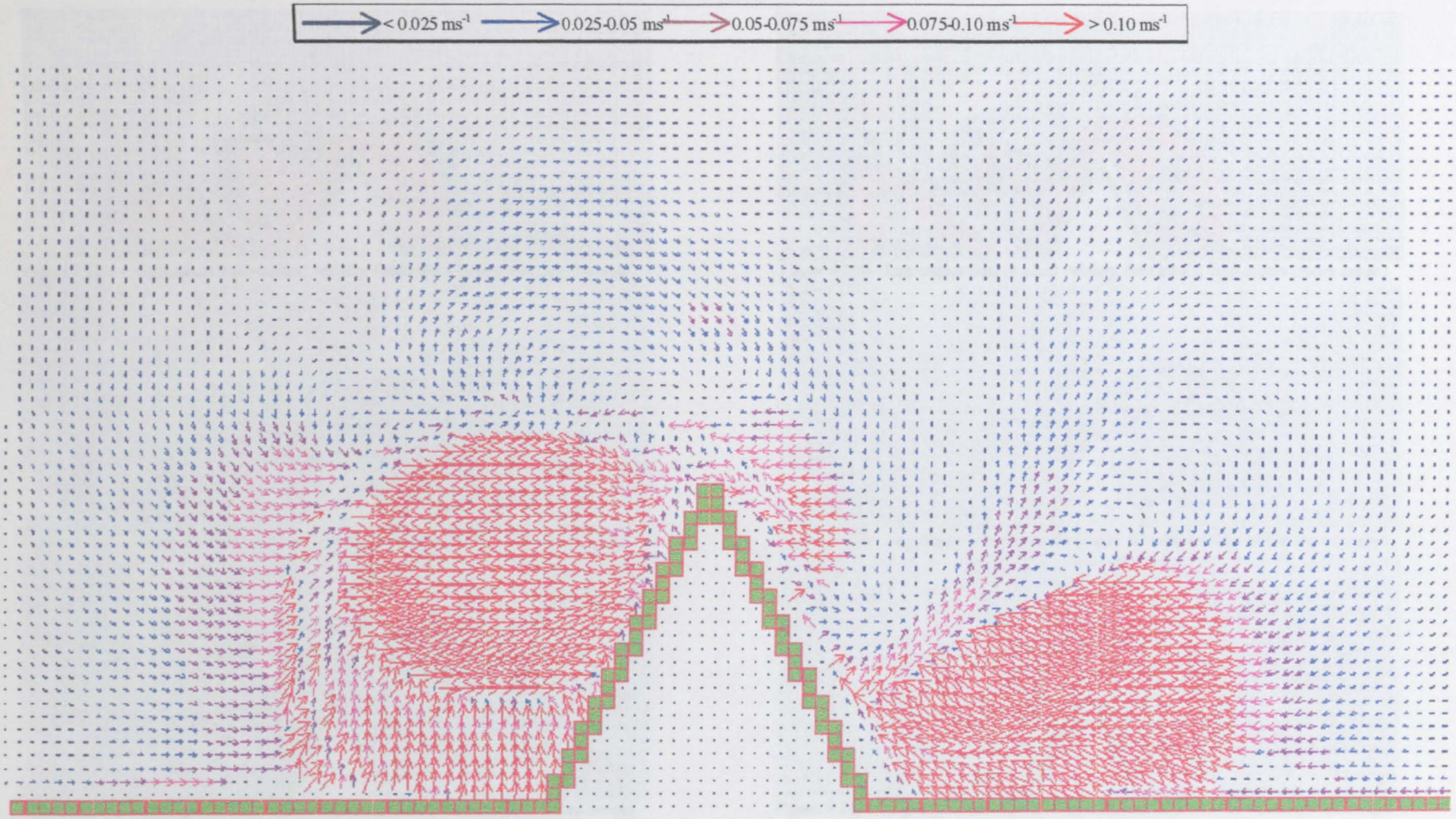

Figure 9.4 – Lagrangian tidal residual velocity field after 1 tidal cycle (started at LW).

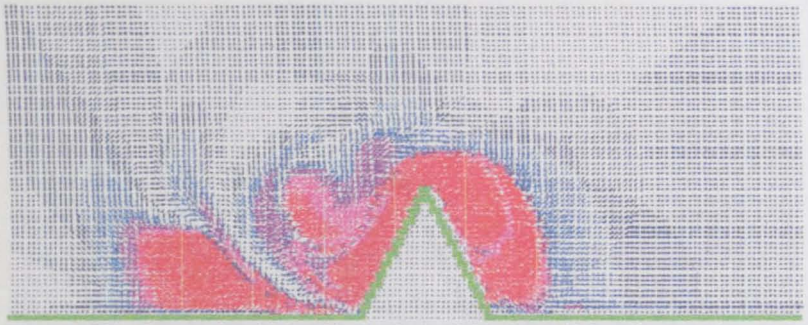

Figure 9.5(a) – Lagrangian tidal residual velocity field after **1** tidal cycle (zoom image).

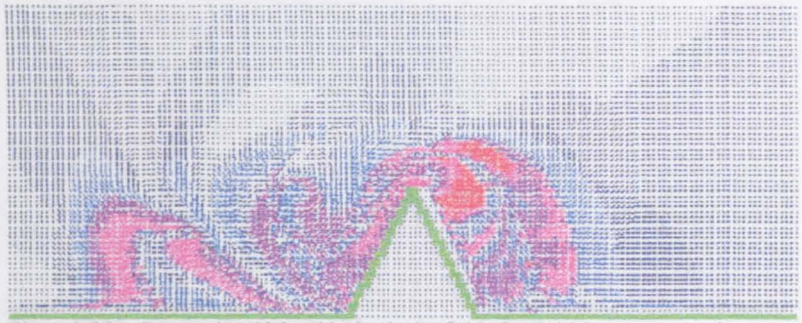

Figure 9.5(b)– Lagrangian tidal residual velocity field after **2** tidal cycles (zoom image).

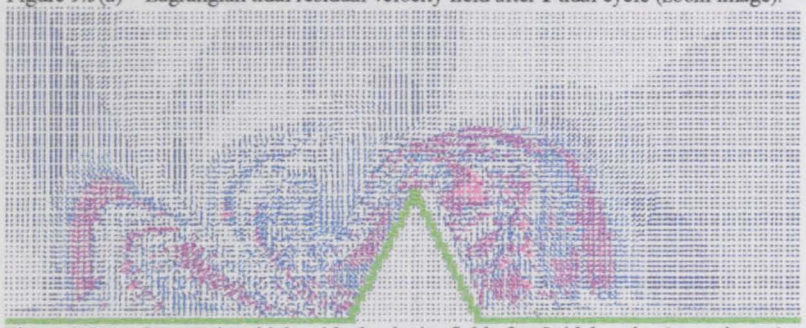

Figure 9.5(c) – Lagrangian tidal residual velocity field after **3** tidal cycles (zoom image).

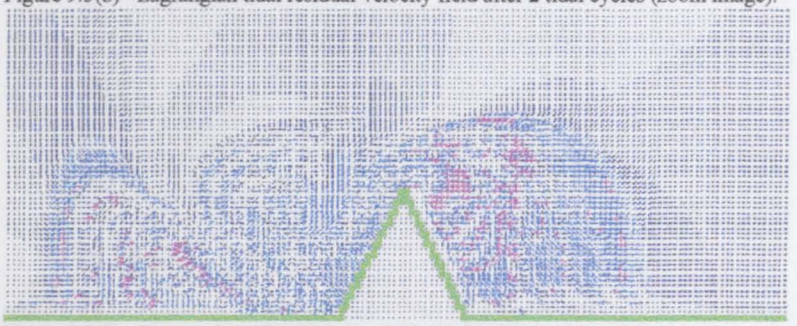

Figure 9.5(d) – Lagrangian tidal residual velocity field after **4** tidal cycles (zoom image).

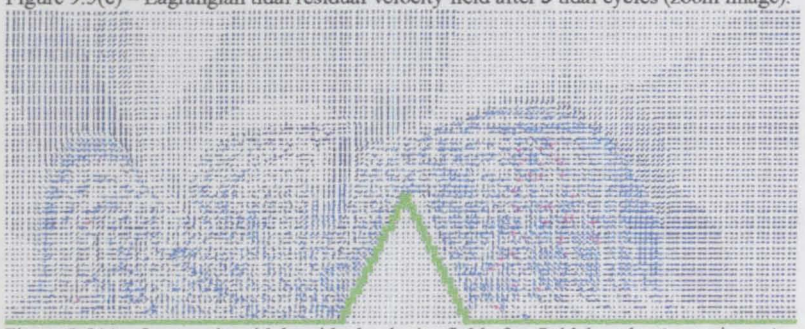

Figure 9.5(e) – Lagrangian tidal residual velocity field after **5** tidal cycles (zoom image).

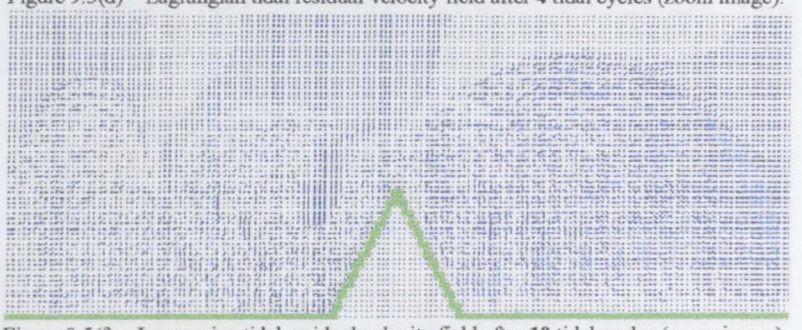

Figure 9.5(f) – Lagrangian tidal residual velocity field after **10** tidal cycles (zoom image).

Figure 9.5 – Evolution of Lagrangian tidal residual velocity over 10 tidal cycles (released at HW-3). Note persistence of pattern.

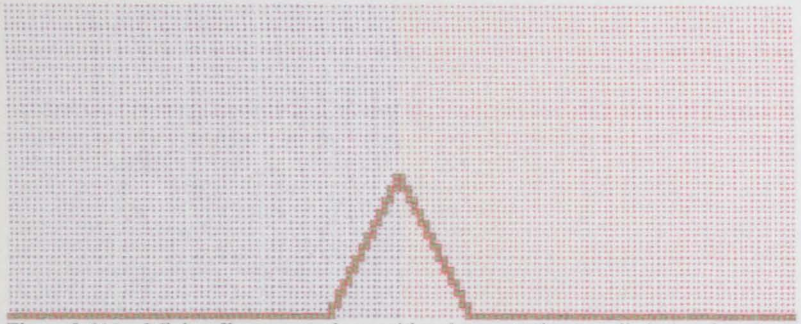

Figure 9.6(a) – Mixing diagram starting position demonstrating two distinct regions (zoom image).

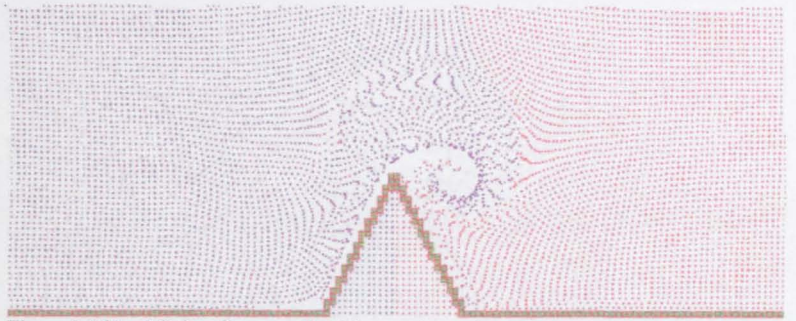

Figure 9.6(b) – Mixing diagram after 2 hours. (zoom image).

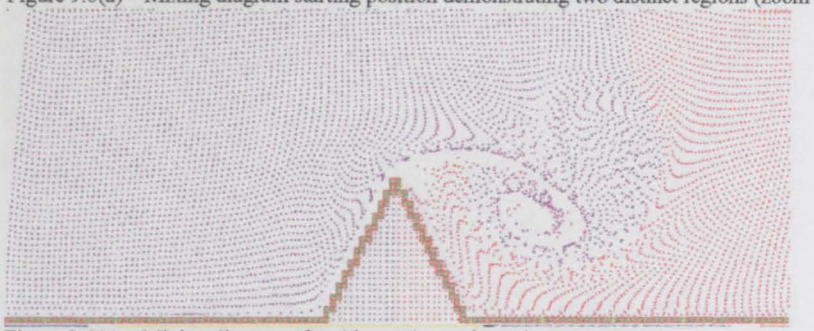

Figure 9.6(c) – Mixing diagram after 4 hours (zoom image).

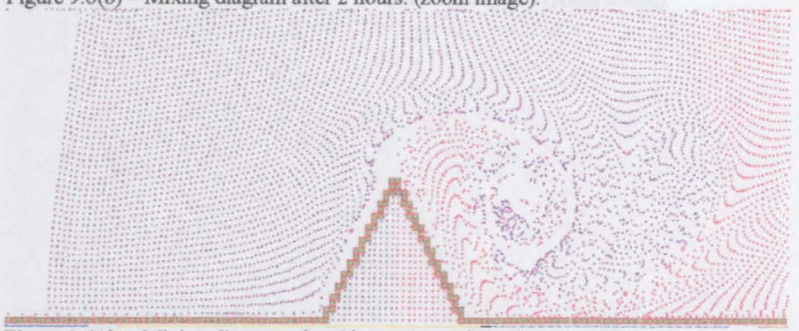

Figure 9.6(d) – Mixing diagram after 6 hours (zoom image).

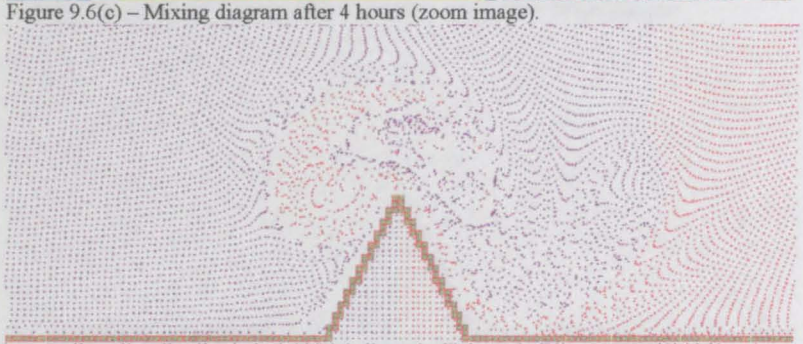

Figure 9.6(e) – Mixing diagram after 8 hours (zoom image).

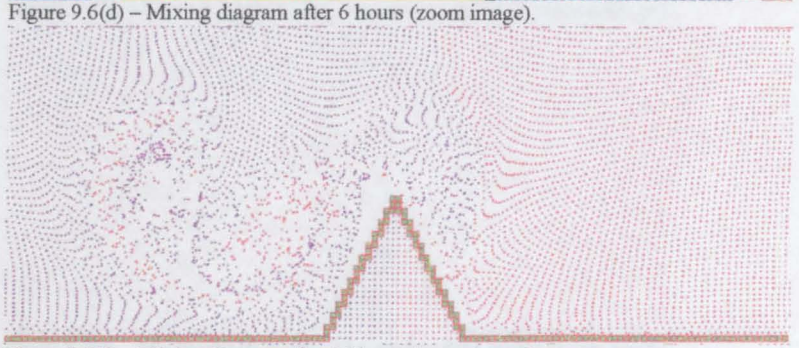

Figure 9.6(f) – Mixing diagram after 10 hours (zoom image).

Figure 9.6 – Evolution of particle tracking diagrams indicating mixing around a 3.75 km headland over the 1st tidal cycle.

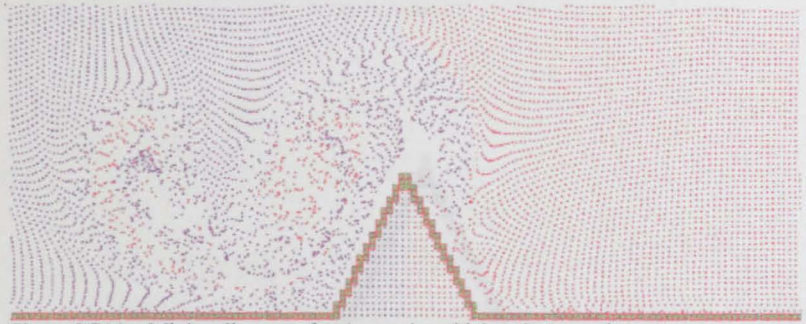

Figure 9.7(a) – Mixing diagram after 1 complete tidal cycle (zoom image)

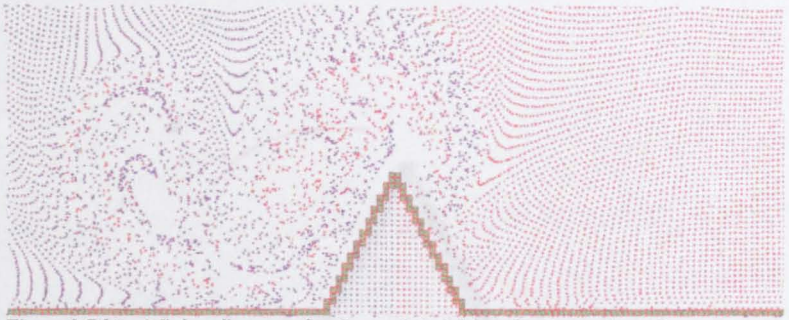

Figure 9.7(b) – Mixing diagram after 2 complete tidal cycles (zoom image).

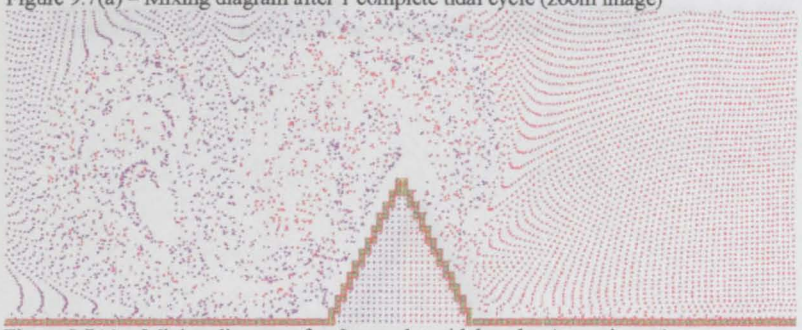

Figure 9.7(c) – Mixing diagram after 3 complete tidal cycles (zoom image).

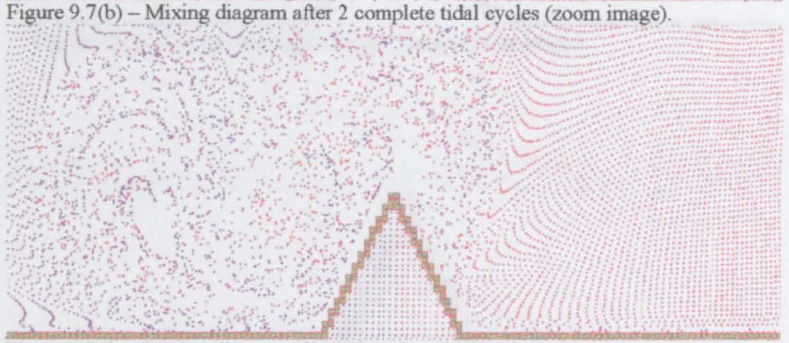

Figure 9.7(d) – Mixing diagram after 4 complete tidal cycles (zoom image).

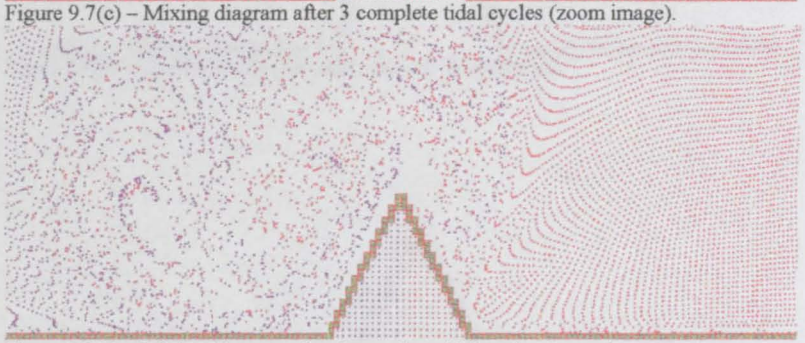

Figure 9.7(e) – Mixing diagram after 5 complete tidal cycles (zoom image).

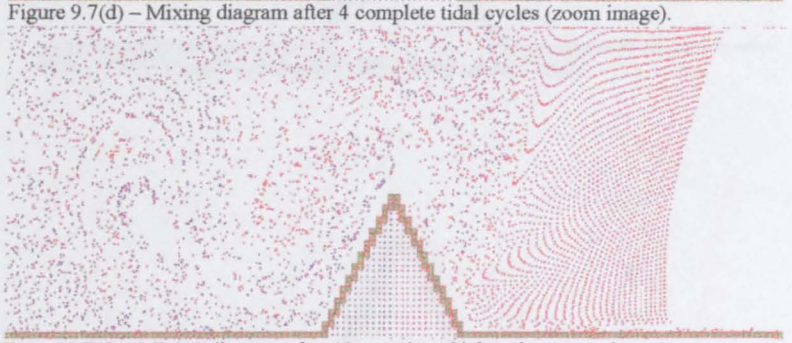

Figure 9.7(f) – Mixing diagram after 10 complete tidal cycles (zoom image).

Figure 9.7 – Evolution of particle tracking diagrams indicating mixing around a 3.75 km headland over 10 tidal cycles.

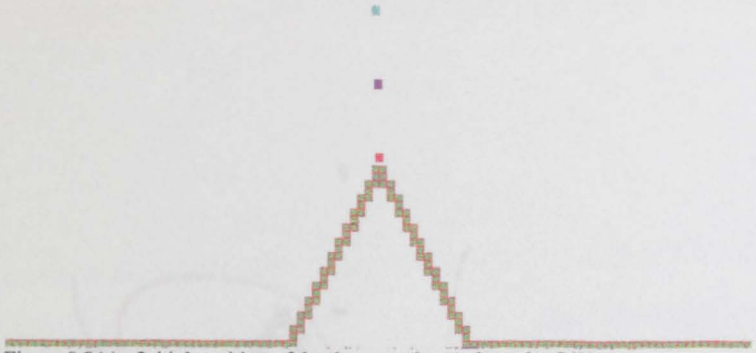

Figure 9.8(a) - Initial position of the three patches (released at LW).

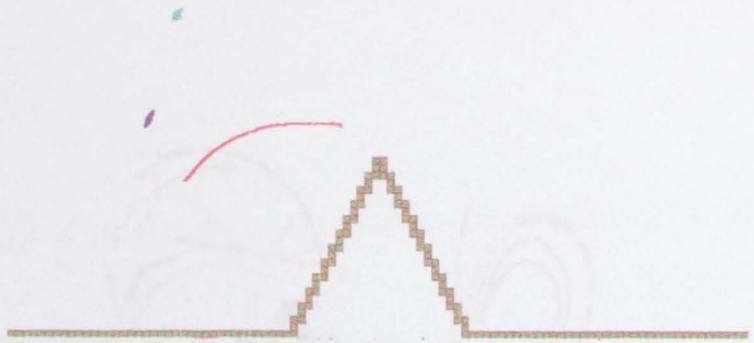

Figure 9.8(b) - Dispersion diagram after 2 hours (zoom image).

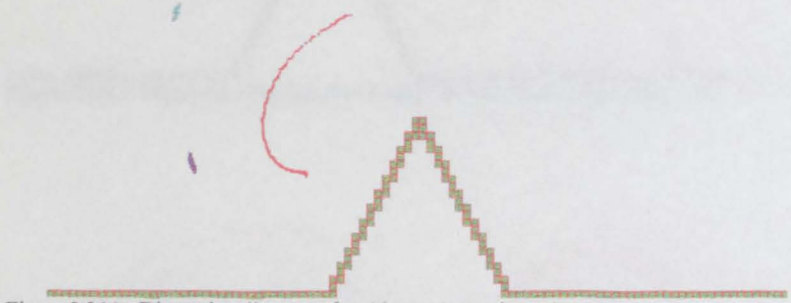

Figure 9.8(c) - Dispersion diagram after 4 hours (zoom image).

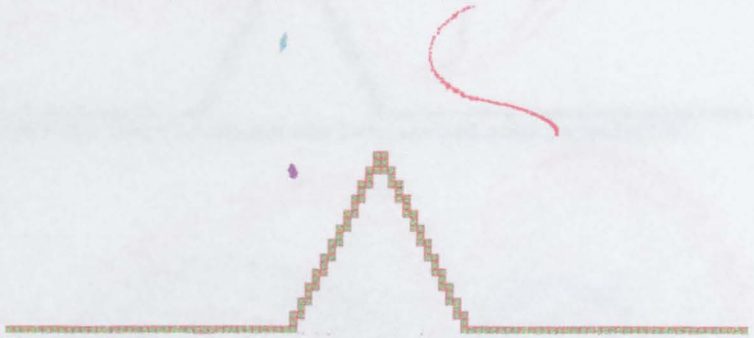

Figure 9.8(d) - Dispersion diagram after 6 hours (zoom image).

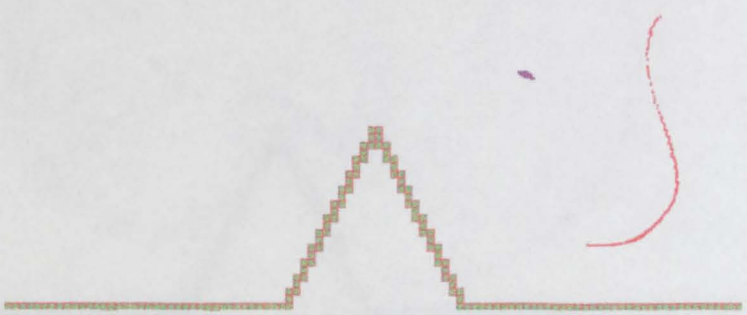

Figure 9.8(e) - Dispersion diagram after 8 hours (zoom image).

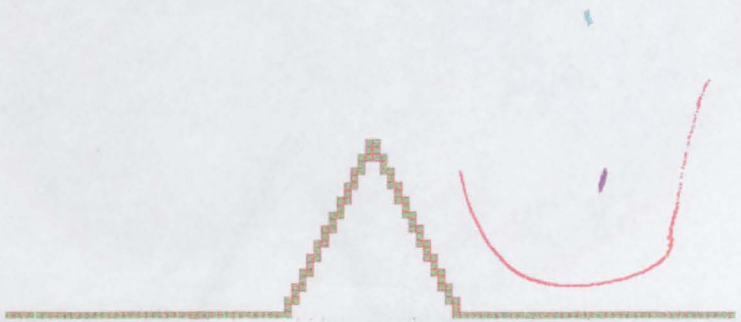

Figure 9.8(f) - Dispersion diagram after 10 hours (zoom image).

Figure 9.8 - Evolution of three patches of fluid (5625 particles each) indicating dispersion around a 3.75 km headland over 1 tide.

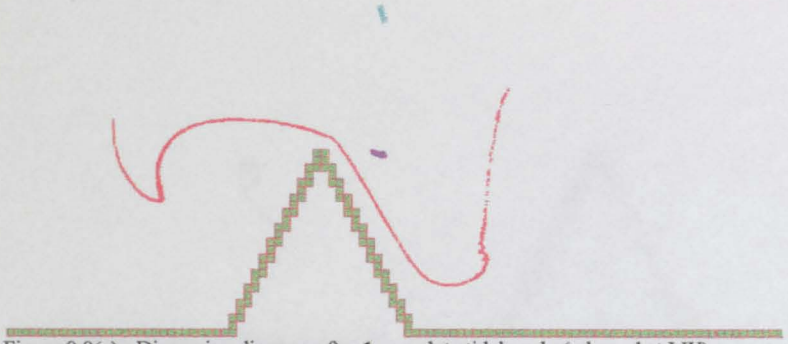

Figure 9.9(a) - Dispersion diagram after **1** complete tidal cycle (released at LW).

Figure 9.9(b) - Dispersion diagram after **2** complete tidal cycles (released at LW).

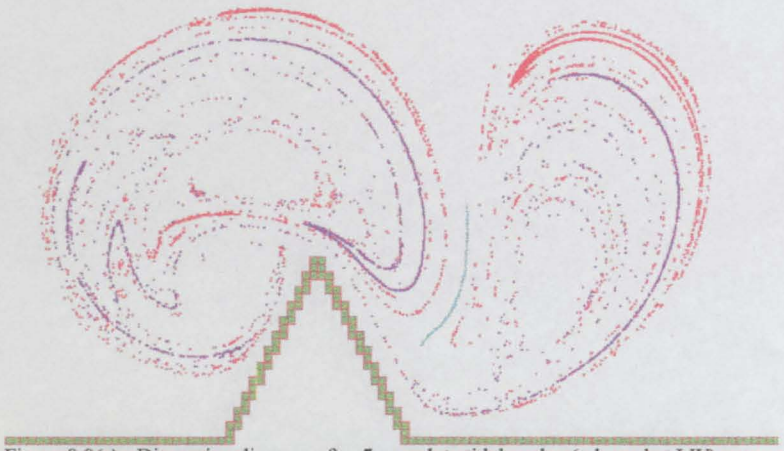

Figure 9.9(c) - Dispersion diagram after **5** complete tidal cycles (released at LW).

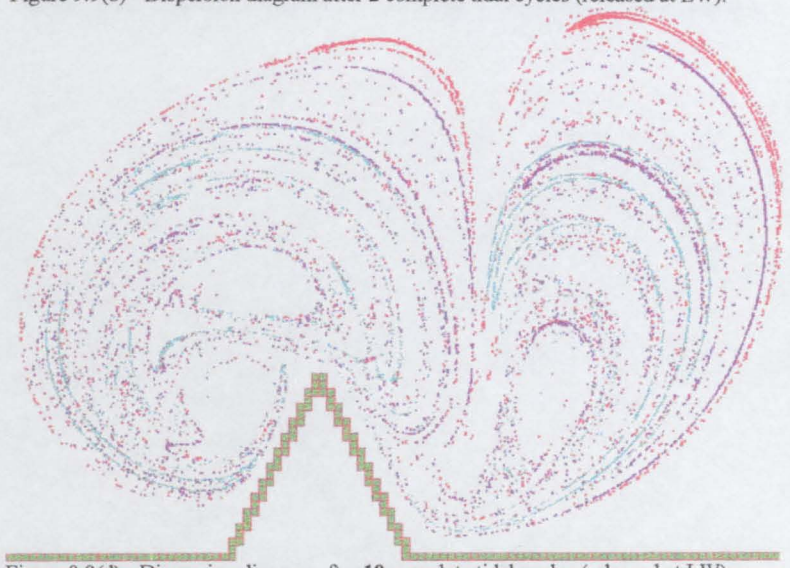

Figure 9.9(d) - Dispersion diagram after **10** complete tidal cycles (released at LW).

Figure 9.9 - Evolution of 3 patches of fluid (5625 particles each) indicating dispersion around a 3.75 km headland over 10 tides.

Figure 9.10(a) - Dispersion diagram after 1 complete tidal cycle (released at HW-3).

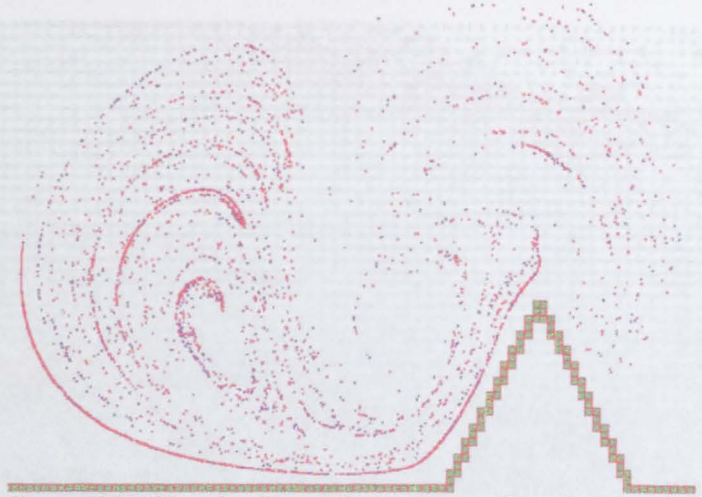

Figure 9.10(b) - Dispersion diagram after 10 complete tidal cycles (released at HW-3).

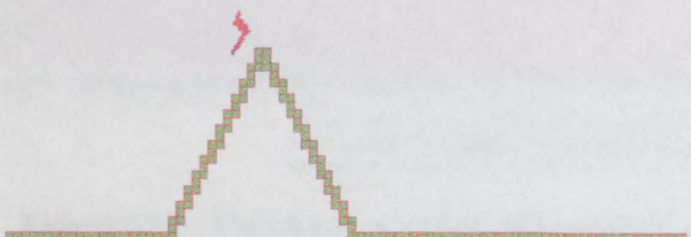

Figure 9.10(c) - Dispersion diagram after 1 complete tidal cycle (released at HW).

Figure 9.10(d) - Dispersion diagram after 10 complete tidal cycles (released at HW).

Figure 9.10 - Differences in short term and long term evolution of dispersion around a headland based upon particle release time.

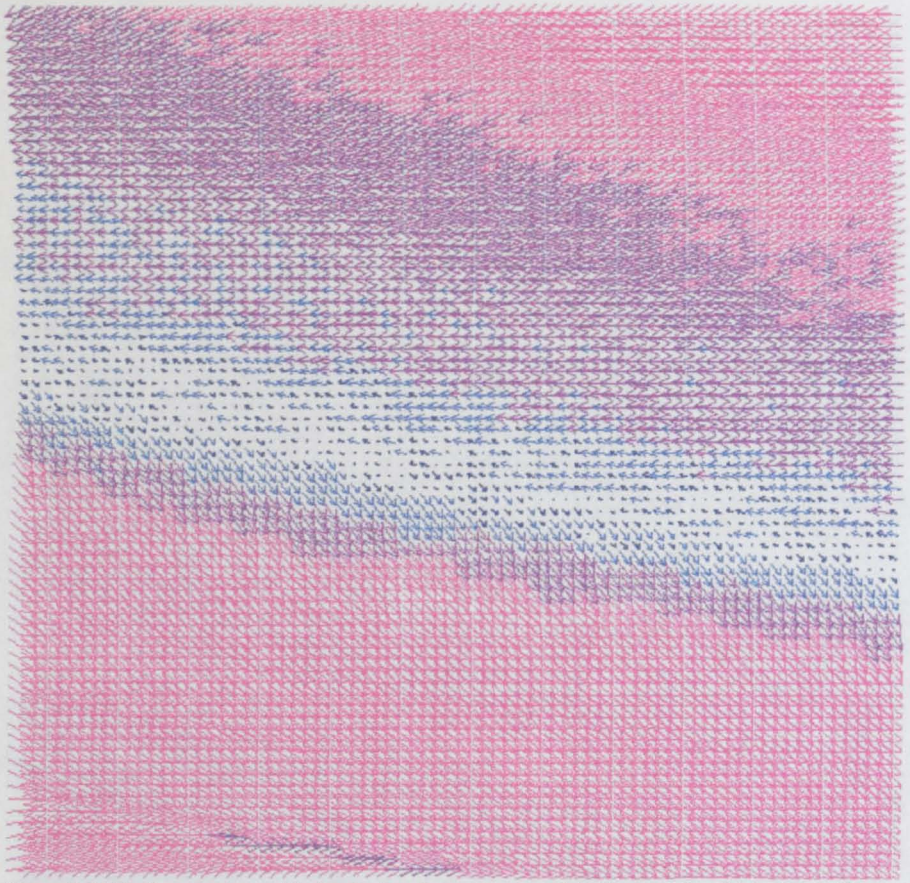

Figure 9.11(a) - Lagrangian residual velocity of nearshore patch in figures 9.8 and 9.9 after 1 tide

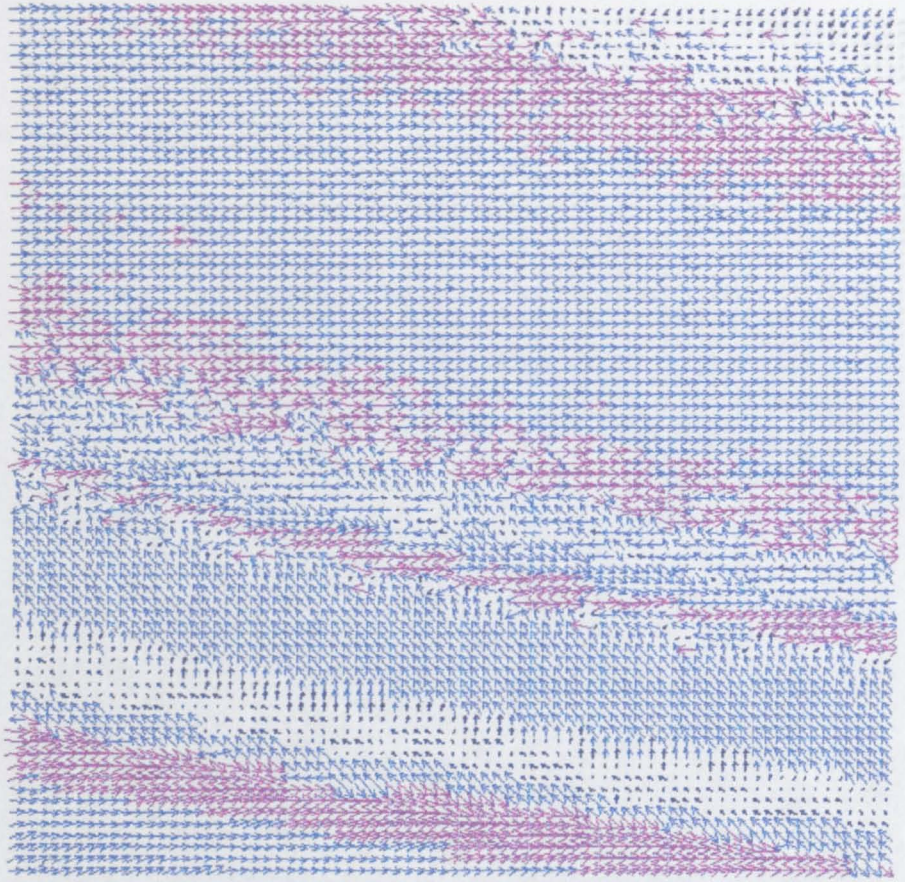

Figure 9.11(b) - Lagrangian residual velocity of nearshore patch in figures 9.8 and 9.9 after 2 tides

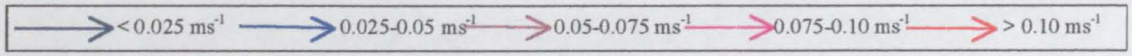

Figure 9.11 – Fine scale evolution of Lagrangian tidal residual velocity in one cell - immediate rapid spatial variability.

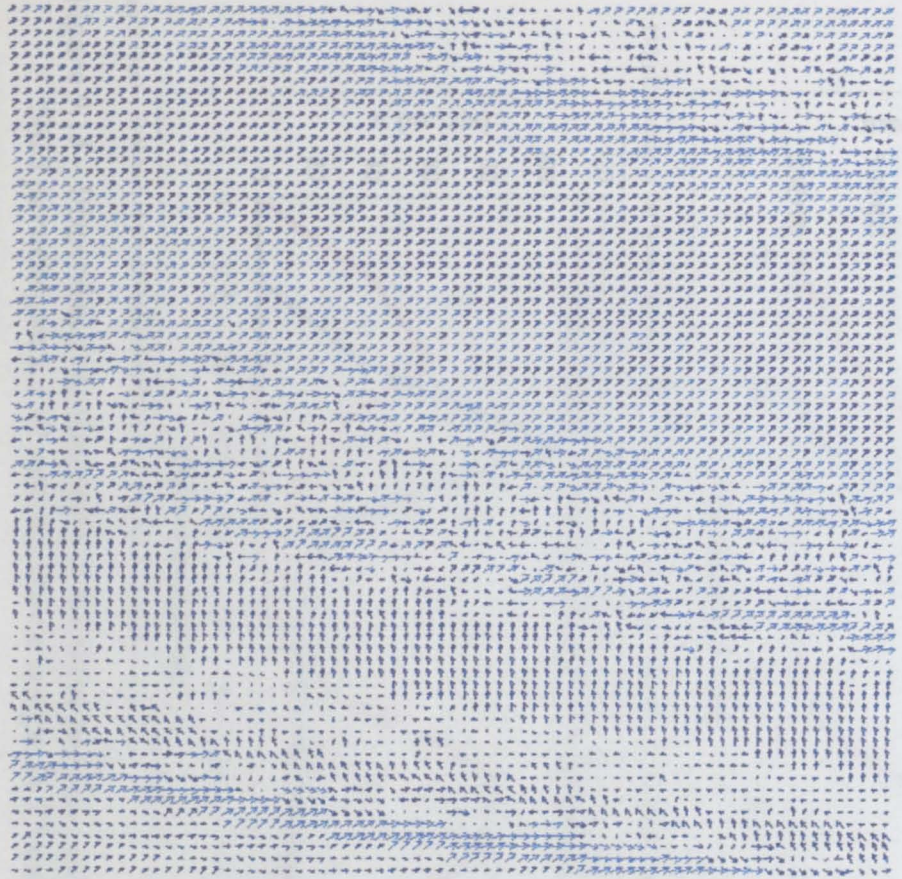

Figure 9.12(a) - Lagrangian residual velocity of nearshore patch in figures 9.8 and 9.9 after 5 tides

Figure 9.12(b) - Lagrangian residual velocity of nearshore patch in figures 9.8 and 9.9 after 10 tides

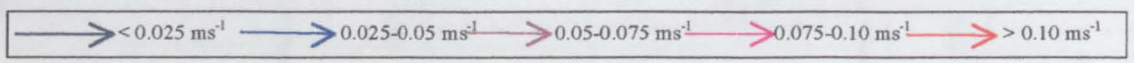

Figure 9.12 - Fine scale evolution of Lagrangian tidal residual velocity in one cell - long term persistence of pattern.

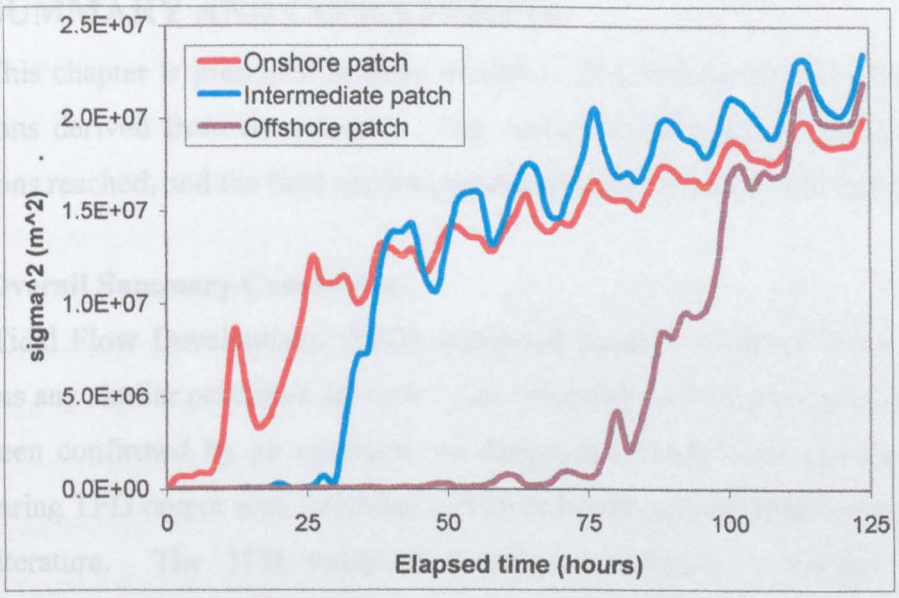

Fig. 9.13(a) - Evolution of the **variance** (σ^2) over 10 tides for the particles in the three patches shown in figures 9.8 and 9.9.

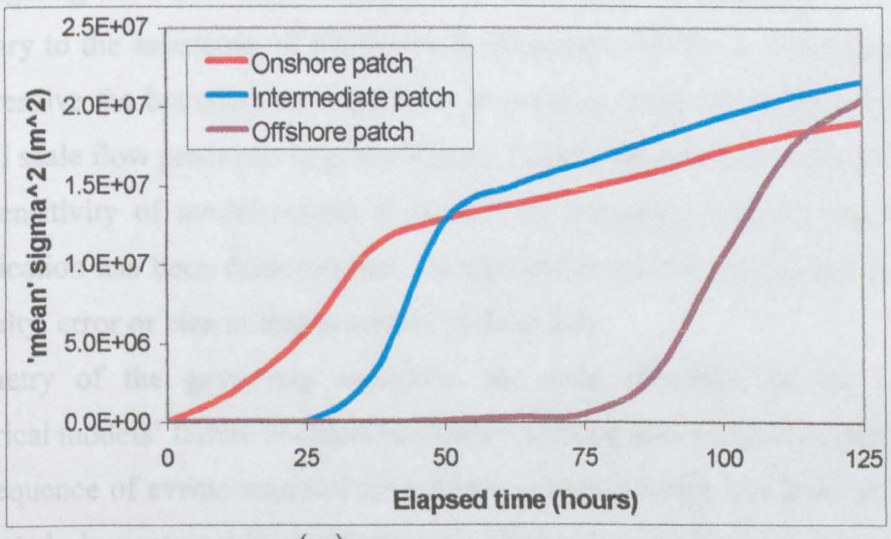

Fig. 9.13(b)-Evolution of the **'mean' variance** $\left(\overline{\sigma^2}\right)$ over 10 tides for the particles in the three patches shown in figs. 9.8 and 9.9

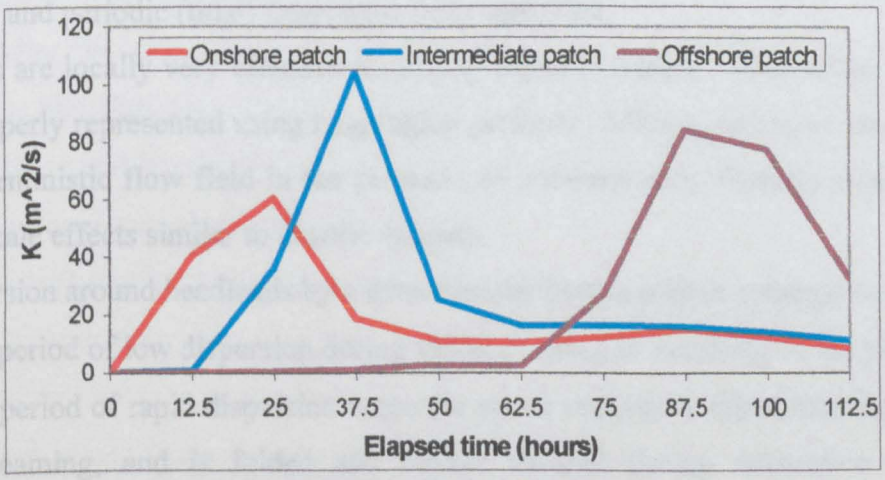

Figure 9.13(c) – Evolution of the **diffusion coefficient** (K) derived from figure 9.13(b).

Figure 9.13 – Dispersion characteristics of the three patches (each comprising 5625 particles, on a 2 ×2 matrix) shown in figures 9.8 and 9.9.

10 SUMMARY AND CONCLUSIONS

This chapter is presented in three sections. The first summarises the overall conclusions derived from the research. The second section presents details of the conclusions reached, and the final section presents recommendations for future work.

10.1 Overall Summary Conclusions

1. The Tidal Flow Development (TFD) numerical model has been shown to be as good as any similar published 2D code. The reliability and robustness of the model has been confirmed by an extensive validation and verification exercise and by comparing TFD output with field data and other numerical simulations presented in the literature. The TFD model is therefore considered a suitable tool for investigating wake and eddy development in the coastal environment.
2. Contrary to the assertions of Furukawa & Wolanski (1998), it is not necessary to fully resolve the boundary or shear layer in order to produce a good simulation of coastal scale flow processes (e.g. see Rattray Island simulation in chapter 8).
3. The sensitivity of model results to resolution, boundary location and boundary specification has been demonstrated. Inappropriate model application can lead to difficulty, error or bias in interpretation of field data.
4. Symmetry of the governing equations has been identified as the source of numerical models' failure to reproduce eddy shedding around symmetrical islands.
5. The sequence of events required for a wake eddy to develop has been successfully elucidated. Important differences between headland and island wakes and between steady and periodic (tidal) flows have been identified.
6. Eddies are locally very effective in mixing adjacent waters. Their effect can only be properly represented using Lagrangian methods. Mixing processes produced by a deterministic flow field in the presence of transient eddy features produce very fine-scale effects similar to chaotic systems.
7. Dispersion around headlands by a deterministic flow is a three stage process:
   - A period of low dispersion during initial shearing or streaking of the patch.
   - A period of rapid dispersion when the streak undergoes rapid straining by tidal streaming, and is folded and further sheared during interaction with the transient eddies.
   - A period of steady (almost Fickian) dispersion after the patch occupies the complete mixing zone.

10.2 Detailed Conclusions

10.2.1 Numerical model development

8. A fixed-grid, finite-difference model incorporating 3rd order upwinding of the convective momentum terms has been developed to solve the two-dimensional shallow water equations (TFD) (chapters 3 and 4).
9. The TFD model has been verified and validated against fifteen analytical, text-book and full-scale test cases (chapters 5, 7.5 and 8).
10. Inherent limitations of the modelling technique (resolution, dissipation, accuracy) have been minimised. The numerical diffusion of the TFD model code has been characterised as being linearly dependent upon the cell size Δx, and quantified as being equal to $0.01U\Delta x$ m^2s^{-1}, where U is the depth mean velocity (chapter 5.2.4).

10.2.2 Headland and Island flow development

11. The sequence of events required for a wake to develop was successfully elucidated and shown to involve the following steps (chapter 6):
    - 11.1 A low pressure region at the tip of the headland grows as a response to tidal streaming around the headland. This can only occur because the no-flow coastline boundary effect supports an adverse pressure gradient.
    - 11.2 The persistence of the adverse pressure gradient associated with the region of low pressure at the headland tip is necessary to instigate flow separation. If the upstream flow does not have enough momentum to overcome the adverse pressure gradient then flow separation occurs.
    - 11.3 After flow separation occurs, flow with high vorticity previously trapped in the boundary layer is injected into the flow interior.
    - 11.4 Island and headlands provide conditions where the three vorticity generating mechanisms (slope torque, speed torque and squashing and stretching of the water column) occur (chapter 6). The three mechanisms can work in tandem or counteract the overall vorticity generating effect by contributing complimentary or oppositely directed vorticity (chapter 6.5.4). A large and important vorticity source occurs just downstream of the tip where accelerated free-stream flow is adjacent to the slower separated flow in the lee (chapter 6.4.3).

11.5 An eddy is formed as highly concentrated vorticity is rolled-up around the separated low pressure region.

12. Unsteady wakes (wake oscillation and eddy shedding) rarely occur around headlands and islands in the coastal environment because of the damping effect of bottom friction in shallow water regions, and restricted spin-up time imposed by the periodicity of the tide and related persistence of the tidal flow. However, a number of eddy shedding mechanisms have been elucidated (chapter 7):

12.1 Eddy shedding occurs when an earlier flow separation point (headland tip) re-attaches. This removes the vorticity source from the eddy and it will begin to spin down over time. The eddy is then transported through the domain by the surrounding flow.

12.2 Repeated eddy shedding in the lee of an island is instigated by interaction of two oppositely rotating eddies in the island wake, one shed from either tip of the island. Vigorous eddy shedding events create a distinctive trail in the wake of the island as the oppositely rotating eddies are carried downstream. This wake structure is known as a von Karman street wake.

12.3 Repeated eddy shedding in the lee of a headland is instigated by interaction of the original headland eddy with flow in the boundary layer. This interaction generates a low pressure region within the separated flow 'bubble' on the downstream face of the headland. A secondary eddy is spun up in the low pressure region which causes the region to expand. Once the secondary eddy has expanded sufficiently, flow re-attaches at the headland tip and the initial and secondary eddies become 'paired' and are transported downstream in a similar way to the pairing of eddies shed from an island.

12.4 TFD model output would suggest that vigorous eddy shedding in the lee of a headland is limited by frictional dissipation. Hence for full scale headlands eddy shedding is very rare. TFD model output also suggests that after a number of headland shedding events, flow in the separated 'bubble' spins down under the action of the boundary layer and bottom friction. A dead zone is then observed in the lee of the headland around which the free-stream flow is maintained. This indicates a significant difference between the action of headland and island shedding events.

13. Strong regions of shear created in the domain by phase effects cannot be characterised as eddies, as no re-circulation is observed. Phase effects in isolation are therefore unable to generate eddy features. Phase effects can however have a significant influence on the development of wake features in tidally dominated flow regimes (chapter 6.3 and 6.5.3).
14. Eddy shedding in the coastal environment occurs when a critical Strouhal number (St_c = 0.15 –0.20) is achieved. The occurrence and frequency of eddy shedding can therefore be predicted for a particular domain by comparing the spin-up time required for eddy shedding to occur with the spin-up time available within the tidal cycle (chapter 7.6).
15. Dimensionless parameters proposed in the literature for prediction of wake characteristics in the coastal environment ('equivalent; Reynolds number, Island wake parameter, wake stability parameter) are unable to accurately predict the occurrence of unsteady wakes in tidally dominated flow regimes. This is because they make no allowances for the restricted time-scale available for the wake to develop imposed by tidal periodicity. These parameters are therefore better suited to analysis of wake development in steady shallow water flows (chapter 2 and 7.6).
16. By analogy with other branches of fluid dynamics and from TFD model results it is expected that oscillatory wakes should occur in the coastal environment. However, no evidence of oscillatory wake structures is presented in the literature (chapter 7).

10.2.3 Numerical model applications

17. Realistic unsteady wake features can be simulated using fixed-grid finite-difference based models as long as there is some asymmetry in the domain, or random perturbations mimicking turbulent fluctuations are introduced in the program code (chapter 7.3 and 7.5).
18. When the boundary layer is not fully resolved, selection of closed boundary condition (i.e. the amount of slip specified) has little or no influence on the flow development. This is because numerical modelling of vorticity generation in a fixed-grid, finite-difference model is only adequately simulated when the boundary layer is properly resolved. In situations where the boundary layer is not

fully resolved, an equivalent amount of vorticity is introduced to the domain in the cell immediately downstream of the headland tip. Accurate representation of the topography and bathymetry at the tip of the headland is consequently of fundamental importance (chapter 6.4.3).

19. The level of resolution provided by traditional marine surveys using fixed current meters or float tracks is not sufficient to prevent ambiguity in the interpretation of the flow development. Remote-sensing techniques provide an effective source of complimentary data which can overcome this problem (chapter 8).
20. Because coastal flow regimes are friction dominated, the representation of the friction term in the governing equations is more important than the eddy viscosity description. However, in the literature it is found that much more emphasis is placed on eddy viscosity models (chapter 7.4).

10.2.4 Mixing and dispersion

21. The impact of transient wake features on the dispersion and mixing potential in the coastal environment has been determined using mixing and dispersion diagrams. These show a distinct mixing zone within which high rates of strain and dispersion occur. In the absence of sub-grid scale diffusion processes, a strong front exists between the well mixed and unmixed regions (chapter 9).
22. Lagrangian analysis techniques appear to provide the only credible approach for studying transport in regions subject to transient flow phenomena. However, the complexity involved in the Lagrangian analysis indicated by the apparently chaotic spatial variation of the results restricts application these techniques (chapter 9).
23. Three distinct stages of development of dispersion in a tidally dominated non-linear flow regime have been identified and elucidated (chapter 9.2.3 and 9.2.4):
    23.1 The first stage is characterised by limited dispersion as the patch is transported around the headland in the body of the free-stream. Dispersion cannot be adequately characterised by linear Fickian diffusion relationships during this stage. The elapsed time before the second stage is initiated is highly dependent upon the position of the patch and the phase of the tide when the patch is released.

23.2 During the second stage of dispersion, the patch interacts with the strong non-linear flow features around the headland. High strain rates are imposed on the patch by shear in the deterministic flow fields which cause rapid elongation of the patch into a long streak. The rate of dispersion increases rapidly during this stage, with peak dispersion coinciding with the start of stage 3. Fickian based diffusion models are again inadequate representation of the dispersion during this stage.

23.3 During the third stage, the development of the dispersed patch becomes very predictable, as the streak expands in a regimented manner dictated by the extent of the transient eddy features observed during each half cycle of the tide. The dispersion rate decelerates during this stage before a steady linear rate becomes established. This is because the patch has become well mixed throughout the mixing zone during stage two, so the rate of dispersion of the patch during stage 3 is largely dictated by the rate of expansion of the mixing zone. Dispersion during this stage is similar to that suggested by Fickian based diffusion models.

10.3 Recommendations for Further Work

10.3.1 Numerical model development

24. The accuracy of the TFD model could be improved by adopting a fifth-order representation of the convective momentum terms. Similarly, improving the resolution of the modelled domain would reduce numerical error. Both of these recommendations would require increased computational power to maintain an acceptable run-time.

25. Use of a three-dimensional model may allow better simulations to be made because these flows do have a three-dimensional structure. However Galloway et al. (1996) presented depth-averaged results from three-dimensional models that were not as good as TFD model results. Therefore the development of three-dimensional models that incorporate the advantageous features of two-dimensional models (e.g. increased spatial resolution, higher-order finite-difference representations of the convective momentum terms, radiating boundary condition) are required.

10.3.2 Headland and Island flow development

26. Increased spatial and temporal resolution of current and bathymetric data is required in order to:
    (i) capture details of oscillatory wake features to confirm TFD model predictions of their existence (see conclusion 16),
    (ii) capture details of headland shedding events including the start-up of the secondary eddy that TFD model predictions suggest is responsible for initiating shedding (see conclusion 12.3), and
    (iii) match the increased resolution of numerical models.

    Recent development of ADCP and other remote-sensing techniques should provide the tools necessary to address these problems.

10.3.3 Numerical model applications

27. In a friction dominated environment, the reliance upon empirical relationships derived from open channel flow (e.g. Manning, Chezy, and Strickler) or pipe flow (Darcy-Weisbach) to describe frictional dissipation in the coastal environment suggests a pressing need for further investigation of the accuracy of these techniques. This would highlight whether or not more appropriate friction models are required.

10.3.4 Mixing and dispersion

28. The persistence of patches of smoothly varying Lagrangian residual flow velocities interspersed with areas of apparently random velocity distribution requires further investigation. The occurrence of superficially similar patterns at reduced scale and persistence of these patterns in time may indicate some degree of self-similarity which may indicate chaotic behaviour.
29. Methods of summarising or quantifying the output from Lagrangian analysis of short-term mixing and dispersion in the coastal environment are necessary in order to persuade practising engineers to move on from traditional outdated techniques (e.g. Eulerian representations of the residual velocity).
30. The continuing growth of the mixing zone in the simulations presented in chapter 9 is not expected to continue indefinitely. Determining the long term growth rate of the mixing zone may show a limit to its extent. Analysis may then indicate a

simple relationship between the extent of the headland or island and the effective long term mixing zone. Whether sub-grid scale diffusion processes would invalidate this relationship would also have to be considered.

REFERENCES

Abbott, M.B. (1997). "Range of Tidal Flow Modeling". *ASCE Journal of Hydraulic Engineering*, **123**, pp. 257-277.

Abbott, M.B. and Basco, D.R. (1989). "Computational fluid dynamics: an introduction for engineers". *Longman Scientific & Technical*, ISBN: 0-582-01365-8.

Abbott, M.B. and Price, W.A. (1994). "Coastal, Estuarial and Harbour Engineers' Reference Book". *E & FN Spon*, ISBN: 0-419-15430-2, 736 pp.

Alcrudo, F. and Garcia_Navarro, P. (1993). "A high-resolution Godumov-type scheme in finite-volumes for the 2D shallow water equations". *International Journal for Numerical Methods in Fluids*, **16**, pp.489-505.

Allen, J.S. and Newberger, P.A. (1996). "Down-welling circulation on the Oregon continental-shelf 1. Response to idealised forcing". *Journal of Physical Oceanography*, **26**, pp. 2011-2035.

Allen, J.S., Newberger, P.A. and Federiuk, J. (1995). "Upwelling circulation on the Oregon continental-shelf 1. Response to idealised forcing". *Journal of Physical Oceanography*, **25**, pp. 1843-1866.

Anatasiou, K. and Chan, C.T. (1997). "Solution of 2D Shallow Water Equations". *International Journal of Numerical Methods (Fluids)*, **24**, pp. 1225-1245.

Aubrey, D.G. (1990). "Interdisciplinary Estuarine Research: A Challenge for the Future". *Residual Currents and Long-term Transport*, Cheng, R.T. (ed). Springer-Verlag, pp.7-14.

Awaji, T. (1982). "Water Mixing in a Tidal Current and the Effect of Turbulence on Tidal Exchange through a Strait". *Journal of Physical Oceanography*, **12**, pp. 501-514.

Batchelor, G.K. (1967). "An Introduction to Fluid Dynamics". *Cambridge University Press*, ISBN: 521-04118-X.

Bayne, G.L.S. (1997). "A Direct Minimisation Model to Determine Tidal Flows in Coastal Waters". *PhD. Thesis, University of Strathclyde.*

Bedford, K.W. (1994) "Diffusion, dispersion and sub-grid parameterisation". *Coastal, Estuarial and Harbour Engineers' Reference Book, edited by M.B. Abbott & W.A. Price, ISBN 0-419-15430-2*, pp. 61-81.

Black, K.P. and Gay, S.L. (1987). " Eddy Formation in Unsteady Flows". *Journal of Geophysical Research*, **92**, No.C9, pp. 9514-9522.

Blumberg, A.F. and Kantha, L.H. (1985). "Open Boundary Conditions for Circulation Models". *Journal of Hydraulic Engineering*, **111**, No.2, pp. 237- 255.

Boris, J.P. and Book, D.L. (1973). "Flux-Corrected Transport. I. SHASTA, A Fluid Transport Algorithim That Works". *Journal of Computational Physics*, **11**, pp. 38-69.

Borthwick, A.G.L. and Barber, R.W. (1992). "Numerical Simulation of Jet-Forced Flow in a Circular Reservoir using Discrete and Random Vortex Methods". *International Journal for Numerical Methods in Fluids*, **14**, pp. 1453-1472.

Borthwick, A.G.L., Chaplin, J.R. and Ali, K.H.M. (1988). "Discrete Vortex Model of Jet-Forced Flow in Circular Reservoir". *ASCE Journal of Hydraulic Engineering*, **114**, No. 3, pp. 283-298.

Borthwick, A.G.L., Marchant, R.D. and Copeland, G.J.M. (2000). "Adaptive hierarchical grid model of water-borne pollutant". *Advances in Water Resources* **23**, pp. 849-865.

Boyer, D.L., Chen, R., D'Hieres, G.C. and Didelle, H. (1987a). "On the Formation and Shedding of Vortices from Side-wall mounted Obstacles in Rotating Systems". *Dynamics of Atmospheres and Oceans*, **11**, pp. 59-86.

Boyer, D.L. and Davies, P.A. (2000). "Laboratory Studies of Orographic Effects in Rotating and Stratified Flows". *Annual Review of Fluid Mechanics*, **32** pp. 165-202.

Boyer, D.L., Davies, P.A., Holland, W.R., Biolley, F. And Honji, H. (1987b). "Stratified Rotating Flow Over and Around Isolated Three-Dimensional Topography". *Philisophical Transactions of the Royal Society of London*, Series A, **213**, pp. 14-240.

Boyer, D.L. and Tao, L. (1987). "On the motion of linearly stratified rotating fluids past capes". *Journal of Fluid Mechanics*, **180**, pp. 429-449.

Breusers, H.N.C. and van Os, A.G. (1981). "Physical modelling of the Rotterdamse Waterweg Estuary". *Delft Hydraulics publication no. 249.*

Casulli, V. and Cheng, R.T. (1992). "Semi-implicit finite difference methods for three-dimensional shallow water flow". *International Journal for Numerical Methods in Fluids*, **15**, pp. 629-648.

Casulli, V. and Stelling, G.S. (1996). "Simulation of Three-dimensional, Non-Hydrostatic Free-Surface Flows for Estuaries and Coastal Seas". *Proceedings of the 4th International Conference on Estuarine and Coastal Modelling*, pp.1-24.

Chen, D. and Jira, G.H. (1997). "Absolute and convective instabilities of plane turbulent wakes in a shallow water layer". *Journal of Fluid Mechanics*, **338**, pp. 157-172.

Cheng, R.T. (1988). "Eulerian and Lagrangian modelling of estuarine hydrodynamics". *Hydrodynamics of Estuaries vol. I, Estuarine Processes, edited by Kjerfve, B.*, ISBN: 0849343704, pp. 149-159.

Cheng, R.T., Casulli, V. and Gartner, J.W. (1993). "Tidal, Residual, Intertidal Mudflat (TRIM) Model and its Applications to San Francisco Bay, California". *Estuarine, Coastal and Shelf Science*, **36**, pp. 235-280.

Clarke, S. and Elliott, A.J. (1998). "Modelling Suspended Sediment Concentrations in the Firth of Forth". *Estuarine Coastal and Shelf Science*, **47**, pp. 235-250.

Cooper, A. (1994). "2 dimensional and 3 dimensional transport modelling". *Computational Hydraulics: A modular course for practising engineers, 1-3 February 1994, HR Wallingford*

Copeland, G.J.M. (1997). "Marine Modelling Study for the Eyemouth Wastewater Treatment Scheme: Final Report". *Unpublished.*

Copeland, G.J.M., Marchant, R.D. and Borthwick, A.G.L. (1999). "Quadtree Grids for Dispersion and Inverse Flow Models". *Proceedings of the 6th International Conference on Estuarine and Coastal Modeling, ASCE, edited by Spaulding, M.L. and Lee Butler, H.*

Couch, S.J. and Copeland, G.J.M. (1999). "Generation of eddies, scour holes and shoals by tidal flow past a headland". *Tidal Meeting of the ABEQUA Congress, Porto Seguro, Brazil, 3-9 October, 1999, Unpublished.*

Coutis, P.F. and Middleton, J.H. (1999). "Flow-topography interaction in the vicinity of an isolated, deep ocean island". *Deep-Sea Research*, **46**, pp. 1633-1652.

Davies, A.G. (1992). "Modelling the vertical distribution of suspended sediment in combined wave-current flow". *Dynamics and Exchanges in Estuaries and the Coastal Zone*, Prandle, D. (ed.), American Geophysical Union,pp. 441-466.

Davies, A.M. and Gerritsen, H. (1994). "An intercomparison of three-dimensional tidal hydrodynamic models of the Irish Sea". *Tellus*, **46A**, pp. 200-221.

Davies, P.A., Boyer, D.L., Tao, L. and Davis, R.G. (1991). "Stratified Rotating Flow Past Isolated Obstacles". *Stratified Flows (ASME), Edited by List, E.J. and Jirka, G.H.* pp.228-237.

Davies, P.A., Dakin, J.M. and Falconer, R.A. (1995). "Eddy Formation Behind a Coastal Headland". *Journal of Coastal Research*, **11**, pp. 154-167.

Davies, P.A. and Mofor, L.A. (1990). "Observations of flow separation by an isolated island". *International Journal of Remote Sensing*, **11**, No. 5, pp. 767-782.

Davis, R.W. (1984). "Finite difference methods for fluid flow". *Computational Techniques & Applications, Edited by Noye, J. and Fletcher, C.* pp. 51- 69.

Deleersnijder, E. Norro, A. and Wolanski, E. (1992). "A three-dimensional model of the water circulation around an island in shallow water". *Continental Shelf Research*, **12**, No. 7/8, pp. 891-906.

Denniss, T. and Middleton, J.H. (1994). "Effects of viscosity and bottom friction on recirculating flows". *Journal of Geophysical Research*, **99**, C5, pp. 10183-10192.

Despard, R.A. and Miller, J.A. (1971). "Separation in oscillating boundary-layer flows". *Journal of Fluid Mechanics*, **47**, part 1, pp. 21-31.

Dronkers, J.J. (1964). "Tidal Computations in Rivers and Coastal Seas". *North Holland Publishing Co.*

Duncan, W.J., Thom, A.S. and Young, A.D. (1970) "Mechanics of Fluids: 2nd edition". *Edward Arnold*, ISBN: 7131-3241-8.

Dyer, K.R. (1988). "Tidally generated estuarine mixing processes". *Hydrodynamics of Estuaries vol. I, Estuarine Processes, edited by Kjerfre, B.*, pp. 41-57.

Eagleson, P.S. and Dean, R.G. (1966). "Small Amplitude Wave Theory". *In Estuary and Coastline Hydrodynamics, edited by Ippen, A.T., McGraw-Hill Book Company.* pp. 1-92.

Elder, J.W. (1959). "The dispersion of marked fluid in turbulent shear flow ". *Journal of Fluid Mechanics*, **5**, pp. 544-560.

Faber, T.E. (1995). "Fluid Dynamics for Physicists". *Cambridge University Press*, ISBN: 0-542-41943-2.

Falconer, R.A. (1980). "Numerical Modelling of Tidal Circulation in Harbours". *ASCE Journal of the Waterway Port, Coastal and Ocean Division*, **106**, No. WW1, pp. 31-48

Falconer, R.A. (1984). "Temperature Distributions in Tidal Flow Field". *ASCE Journal of Environmental Engineering*, **110**, No. 6, pp. 1099-1115

Falconer, R.A. (1985). "Residual currents in Port Talbot Harbour: a mathematical model study". *Proceedings of the ICE*, **79**, Part 2, pp. 33-53.

Falconer R.A. (1986). "Short Course on Mathematical Modelling of Flow and Pollutant Transport in Rivers, Lakes, Estuaries and Coastal Waters: Lecture 5 – Finite Difference Techniques I". *Unpublished.*

Falconer, R.A. (1992). "Flow and water quality modelling in coastal and inland water". *Journal of Hydraulic Research*, **30**, No. 4, pp. 437-452.

Falconer, R.A. (1994) "An introduction to nearly horizontal flows". *Coastal, Estuarial and Harbour Engineers' Reference Book, edited by M.B. Abbott & W.A. Price, ISBN 0-419-15430-2*, pp. 27-36.

Falconer, R.A. and Guiyi, L. (1994). "Numerical Modelling of Tidal Eddies in Coastal Basins with Narrow Entrances Using the κ-ε Turbulence Model". *Mixing and Transport in the Environment, edited by Beven, K.J., Chatwin, P.C. and Millbank, J.H.*, pp. 325-349.

Falconer, R.A. and Guoping, Y. (1991). "Effects of depth, bed slope and scaling on tidal currents and exchange in a laboratory model harbour". *Proceedings of the Institution of Civil Engineers, Past 2: Research and Theory*, 91, 561-576.

Falconer, R.A. and Liu, S.Q. (1988). "Modelling Solute Transport Using QUICK Scheme". *ASCE Journal of Environmental Engineering*, **114**, pp. 3-20.

Falconer, R.A. and Mardapitta-Hadjipandli, L. (1987). "Bathymetric and Shear Stress Effects on an Island's Wake: A Computational Model Study". *Coastal Engineering*, **11**, pp. 57-86.

Falconer, R.A. and Owens, P.H. (1984). "Mathematical modelling of tidal currents in the Humber Estuary". *Journal of the Institution of Water Engineers and Scientists*, **38**, Part 6, pp. 528-542.

Falconer, R.A. and Owens, P.H. (1987). "Numerical simulation of flooding and drying in a depth-averaged tidal flow model". *Proceedings of the Institution of Civil Engineers, Part 2: Research and Theory*, **83**, pp. 161-180

Falconer, R.A. and Owens, P.H. (1990). "Numerical Modelling of Suspended Sediment Fluxes in Estuarine Waters". *Estuarine, Coastal and Shelf Science*, **31**, pp. 745-762.

Falconer, R.A., Wolanski, E. and Mardapitta-Hadjipandeli, L. (1984). "Numerical simulation of secondary circulation in the lee of headlands". *Proceedings of the 19th International Conference of Coastal Engineering*, **3**, pp.2414-2433.

Falconer, R.A., Wolanski, E. and Mardapitta-Hadjipandeli, L. (1986). "Modelling Tidal Circulation in an Island's Wake". *ASCE Journal of the Waterway Port, Coastal and Ocean Division*, **112**, No. 2, pp. 234-254.

Featherstone, R.E. and Nalluri, C. (1988). "Civil Engineering Hydraulics: Essential Theory with Worked Examples: 2nd Edition". *BSP Professional Books*. ISBN: 0-632-02201-9.

Fennema, R.J. and Chaudhry, M.H. (1990). "Explicit methods for 2-D transient free-surface flows". *ASCE Journal of Hydraulic Engineering*, **116**, pp. 1013-1034.

Ferentinos, G. and Collins, M. (1980). "Effects of shoreline irregularities on a rectilinear tidal current and their sedimentation processes". *Journal of Sedimentary Petrology*, **50**, No.4 pp. 1081-1094.

Fischer, H.B., Imberger, J., List, E.J., Koh, R.C.Y. and Brooks, N. (1979). "Mixing in Inland and Coastal Waters". *Academic Press*.

Fischer, E.H. and Rhodes, N. (1994). "Uncertainty in Computational Fluid Dynamics". *EPSRC/I.Mech.E. Expert Meeting, Bournemouth, 27-29th November 1994, Unpublished.*

Flather, R.A. and Heaps, N.S. (1975). "Tidal Computations for Morecambe Bay". *Geophysical Journal of the Royal Astronomical Society*, **42**, pp. 489-517.

Fletcher, C.J. (1991a). "Computational Techniques for Fluid Dynamics 1: Fundamental and General Techniques". *Springer-Verlang.*

Fletcher, C.J. (1991b). "Computational Techniques for Fluid Dynamics 2: Specific Techniques for Different Flow Categories". *Springer-Verlang.*

Flokstra, C. (1977). "The closure Problem for depth-averaged two-dimensional flow". *17th International Association for Hydraulic Research Congress, Baden-Baden Germany.* Paper A106, pp.247-256.

Furukawa. K. and Wolanski, E. (1998). "Shallow-water Frictional Effects in Island Wakes". *Estuarine, Coastal and Shelf Science*, **46**, pp. 599-608.

Gadian, A. (1991). "Lagrangian modelling of an atmospheric convective plume and an analysis of the comparative Lagrangian and Eulerian methods". *Computer Modelling in the Environmental Sciences, Edited by Farmer & Rycroft.* pp. 255-271.

Galloway, D., Wolanski, E. and King, B. (1996). "Modelling Eddy Formation in Coastal Waters: A Comparison Between Model Capabilities". *Proceedings of the 4th International Conference on Estuarine and Coastal Modelling,* pp.13-25.

Garrett, C. MacCready, P. and Rhines, P. (1993). "Boundary mixing and arrested boundary layers: Rotating stratified flow near a sloping boundary". *Annual Review of Fluid Mechanics*, **25**, pp. 291-313.

Gaskell, P.H. and Lau, A.K.C. (1988). "Curvature-Compensated Convective Transport: SMART, a new Boundness-Preserving Transport Algorithim". *International Journal for Numerical Methods in Fluids,* **8**, pp. 617-641.

Gerrard, J.H. (1966). "The mechanics of the formation region of vortices behind bluff bodies". *Journal of Fluid Mechanics*, **25**, pp. 401-413.

Geyer, W.R. and Signell, R. (1990). "Measurements of Tidal Flow Around a Headland With a Shipboard Acoustic Doppler Current Profiler". *Journal of Geophysical Research*". **95**, No. C3, pp. 3189-3197.

Geyer, W.R. and Signell, R.P. (1992). "A Reassessment of the Role of Tidal Dispersion in Estuaries and Bays". *Estuaries*, **15**, No. 2, pp. 97-108.

Glaister, P. (1991). "Solutions of a two-dimensional dam break problem" *International Journal of Engineering Science*, **29**, No.11, pp. 1357-1362.

Glasgow, G.D.E. (1993). "Residual mixing of wastewater effluents in the coastal marine environment". *MSc thesis, University of Strathclyde.*

Griebel, M., Dornseifer, T. and Neunhoeffer, T. (1998). "Numerical Simulations in Fluid Dynamics: A Practical Introduction". *SIAM, Philadelphia.*

Hathhorn, W.E. (1997). "Simplified Approach to Particle Tracking Methods for Contaminant Transport". *Journal of Hyrdaulic Engineering*, **123**, pp. 1157-1160.

Heaps, N.S. (ed.). (1987). "Three-dimensional coastal ocean models". *American Geophysical Union.*

Hearn, C.J., Hunter, J.R., Imberger, J. and van Senden, D. (1985). "Tidally Induced Jet in Koombana Bay, Western Australia". *Australian Journal of Marine and Freshwater Research*, **36**, pp. 453-479.

Hu, S. and Kot, S.C. (1997). "Numerical Model of Tides in Pearl River Estuary with Moving Boundary". *ASCE Journal of Hydraulic Engineering*, **123**, pp. 21- 29.

Hulse, R. and Cain, J. (1991). "Structural Mechanics". *MacMillan Education Ltd.*

Hunter, J.R., Graig, P.D. and Phillips, H.E. (1993). "On the Use of Random Walk Models with Spatially Variable Diffusivity". *Journal of Computational Physics*, **106**, pp. 366-376.

Hyder, P. and Elliott, A.J. (1995). "Observations and model simulations of a near-shore tidal eddy". *Journal of Marine Environmental Engineering*, **1**, pp. 315-333.

Hydrographer of the Navy (1994). "Admiralty Tide Tables Volume 1 1995: (UK & Eire)".

Imasato, N. (1983). "What is Tide-Induced Residual Current?" *Journal of Physical Oceanography*, **13**, pp. 1307-1317.

Ingram, R.G. and Chu, V.H. (1987). "Flow around islands in Rupert Bay: An investigation of the bottom friction effect". *Journal of Geophysical Research*, **92**, pp. 14521-14533.

James, I.D. (1987). "A general three-dimensional eddy-resolving model for stratified seas". *Computer Modelling in the Environmental Sciences, Edited by Farmer & Rycroft.* pp. 591- 608.

Jiang, J.X. and Falconer, R.A. (1983). "On the tidal exchange characteristics of model rectangular harbours". *Proceedings of the ICE*, **75**, Part 2, pp. 475-489.

Keller, H.B. and Niewstadt, F. (1973). "Viscous flow past circular cylinders". *Computers and Fluids*, **1**, pp. 59-71.

Knight, D.W. (1986). "Short Course on Mathematical Modelling of Flow and Pollutant Transport in Rivers, Lakes, Estuaries and Coastal Waters: Lecture 1 – Review of Tidal Phenomena and Governing Equations". *Unpublished.*

Koutitas, C.G. (1988). "Mathematical models in coastal engineering". *Pentech Press Ltd.* ISBN: 0-7273-1313-4.

Kramer, K. (1997). Project Report. *University of Strathclyde, Unpublished.*

Kranenburg, C. (1992). "Wind-driven Chaotic Advection in a Shallow Model Lake", *Journal of Hydraulic Research*, **30**, pp. 29-47.

Lee, H.-J., Chao, S.-Y., Fan, K.-L. and Huo, T.-Y. (1999). "Tide-Induced Eddies and Upwelling in a Semi-enclosed Basin: Nan Wan". *Estuarine, Coastal and Shelf Science*, **49**, pp. 775-787.

Leon, S.C. (1997). "Numerical Solution of the Shallow Water Equations on Quadtree Grids" *PhD. Thesis, University of Oxford.*

Leonard, B.P. (1978). "A consistency check for estimating truncation error due to upstream differencing". *Applied Mathematical Modelling*, **2** pp. 239-244.

Leonard, B.P. (1979). "A stable and accurate convective modelling procedure based on quadratic upstream interpolation". *Computer Methods in Applied Mechanics and Engineering*, **19**, pp. 59-98.

Leonard, B.P. (1981). "A Survey of Finite Differences With Upwinding for Numerical Modelling of the Incompressible Convective Diffusion Equation. *Computational Techniques in Transient and Turbulent Flow. Vol. 2 in series. Recent Advances in Numerical Methods in Fluids, Edited by Taylor, C. and Morgan, K.* Pp.1-35. Pineridge Press Ltd.

Leonard, B.P. (1983). "Third-Order Upwinding as a Rational Basis for Computational Fluid Dynamics". *Computational Techniques & Applications: CTAC-83, Edited by Noye, J. And Fletcher, C.*, Elsevier.

Leonard, B.P. (1988). "Simple high-accuracy resolution program for convective modelling of discontinuities". *International Journal for Numerical Methods in Fluids*, **8**, pp. 1291-1318.

Leonard, B.P. and Drummond, J.E. (1995). "Why you should not use 'hybrid', 'power-law' or related exponential schemes for convective modelling - there are much better alternatives". *International Journal for Numerical Methods in Fluids*, **20**, pp. 421-442.

Liggett, J.A. (1994) "Fluid Mechanics". *McGraw-Hill.* ISBN: 0-07-037805-3.

Lin, B. and Falconer, R.A. (1997). "Three-dimensional Layer-integrated Modelling of Estuarine Flows with Flooding and Drying". *Estuarine, Coastal and Shelf Science*, **44**, pp. 737-751.

List, E.J., Gartell, G. and Winant, C.D. (1990). "Diffusion and Dispersion in Coastal Waters". *ASCE Journal of Hydraulic Engineering*, **116**, No. 10, pp.1158-1177.

Liu, S-K. and Leendertse, J.J. (1978). "Multidimensional numerical modelling of estuaries and coastal seas". *Advances in Hydroscience, Edited by Chow, V.T.*, **11**, pp. 95-160.

Lloyd, P.M. and Stansby, P.K. (1997a). "Shallow-Water Flow around Model Conical Islands of Small Side Slope. I: Surface Piercing". *Journal of Hydraulic Engineering*, **123**, No. 12, pp.1057-1067.

Lloyd, P.M. and Stansby, P.K. (1997b). "Shallow-Water Flow around Model Conical Islands of Small Side Slope. II: Submerged". *Journal of Hydraulic Engineering*, **123**, No. 12, pp.1068-1077.

Macdonald, D.G. and Jirka, G.H. (1997). "Characteristics of Headland Wakes in Shallow Flow". *Proceedings of the 27th Congress of The International Association of Hydraulic Research*, Vol. B1, pp. 88-93.

Maddock, L. and Pingree, R.D. (1978). "Numerical Simulation of the Portland Tidal Eddies". *Estuarine and Coastal Marine Science*, **6**, pp. 353-363.

Milne-Thomson, L. (1968). "Theoretical Hydrodynamics, 5th Edition". *MacMillan & Co. Ltd.*

Mitsuyasu, A. and Hiraki, N. (1969). "Experimental Investigation of the Wake Vortex Behind the Triangular Obstacle Protruding from the Wall". *Proceedings of the 19th Japanese National Congress of Applied Mechanics*, **IV**, Part 2, pp. 171-177.

Monteiro, T.C.N. (1995). "An Inverse Model to Predict Tidal Flows in Coastal Waters". *PhD. Thesis, University of Strathclyde.*

Moore, D.S. and McCabe, G.P. (1999). "Introduction to the Practice of Statistics, 3rd edition". *W.H. Freeman & Co.* ISBN: 0716735024.

Narimousa, S. and Maxworthy, T. (1989). "Application of a Laboratory Model to the Interpretations of Satellite and Field Observations of Coastal Upwelling". *Dynamics of Atmospheres and Oceans*, **13**, pp. 1-46.

Navon, I.M. (1988). "A review of finite-element methods for solving the shallow-water equations". *In Computer modelling in ocean engineering, edited by Schrefler, B.A. and Zienkiwicz, O.C.*, pp. 273-278.

Neill, S.P., Copeland, G.J.M. and Folkard, A.M. (2000a). "Dynamics of tidal fronts in the Tay Estuary, Scotland". *Proceedings of the 10th International Biennial*

Conference on Physics of Estuaries and Coastal Seas, Norfolk, Virginia, USA, 7-11 October 2000.

Neill, S.P., Copeland, G.J.M. and Folkard, A.M. (2000b). "Tidal fronts in the Tay Estuary, Scotland". *Proceedings of the 5th International Symposium on Stratified Flows, University of British Columbia, Vancouver, Canada, 10-13 July 2000,* Vol. II, 909-914.

Neumann, G. and Pierson, W.J. (1966). "Principles of Physical Oceanography". *Prentice-Hall.*

Ng, B., Turner, A., Tyler, A.O., Falconer, R.A. and Millward, G.E. (1996). "Modelling Contaminant Geochemistry in Estuaries". *Water Research,* **30**, pp. 63-74.

Nihoul, J.C.J. and Ronday, F.C. (1975). "The influence of the "tidal stress" on the residual circulation". *Tellus,* **27**, pp. 484-489.

Oey, L-Y. and Mellor, G.L. (1993). "Subtidal Variability of Estuarine Outflow, Plume, and Coastal Current". *Journal of Physical Oceanography,* **23**, pp. 164-171.

Orlanski, I. (1976). "A Simple Boundary Condition for Unbounded Hyperbolic Flows". *Journal of Computational Physics,* **21**, pp. 251-269.

Park, M.-J. and Wang D.-P. (1994). "Tidal vorticity over isolated topographic features". *Continental Shelf Research,* **14**, No. 13/14, pp. 1583-1599.

Patankar, S.V. (1980). "Numerical Heat Transfer and Fluid Flow". *Taylor & Francis.*

Pattiaratchi, C., James, A. and Collins, M. (1986). "Island wakes and headland eddies: A comparison between remotely sensed data and laboratory experiments". *Journal of Geophysical Research,* **92**, No. C1, pp. 783-794.

Peyret, R. and Taylor, T.D. (1983). "Computational Methods for Fluid Flow". *Springer-Verlag.* ISBN: 3-540-11147-6, 358 pp.

Pingree, R.D. (1978). "The formation of the shambles and other banks by tidal stirring of the seas". *Journal of the Marine Biological Association U.K.,* **58**, pp. 211-226.

Pingree. R.D. and Griffiths, D.K. (1980). "Currents driven by a steady uniform wind stress on the shelf seas around the British Isles". *Oceanologica Acta,* **3**, No.2, pp. 227-236.

Pingree, R.D. and Maddock, L. (1977). "Tidal residuals in the English Channel". *Journal of the Marine Biological Association, U.K.,* **57**, pp. 339-354.

Pingree, R.D. and Maddock, L. (1979). "The tidal physics of headland flows and offshore tidal bank formation". *Marine Geology,* **32**, pp. 269-289.

Pingree, R.D. and Maddock, L. (1980). "Tidally induced residual flows around an island due to both frictional and rotational effects". *Geophysical Journal of the Royal Astronomical Society*, **63**, pp. 533-546.

Ponce, V.M. (1981). "Modelling Circulation in Depth-Averaged Flow". *ASCE Journal of the Hydraulic Division*, **107**, pp.1501-1518.

Pond, S. and Pickard, G.L. (1993). "Introductory Dynamical Oceanography, 2nd Edition". *Pergamon Press*. ISBN: 0-08-028727-X.

Postma, L., de Kok, J.M., Markus, A.A. and van Pagee, J.A. (1989). "Long term and seasonal water quality modelling of the North Sea and its coastal waters". *Delft Hydraulics publications*, **407**, 22 pp.

Prandle, D. (1978). "Residual flows and elevations in the southern North Sea". *Proceedings of the Royal Society of London (A)*, **359**, pp. 189-228.

Press, W.H., Teulosky, S.A. and Vetterling, B.P (1992). "Numerical Recipes in Fortran 77 The Art of Scientific Computing Second Edition: Volume 1 of Fortran Numerical Recipes". *Cambridge University Press*, ISBN: 0-521-43064-X.

Price, W.A. and Thorn, M.F.C.. (1994) "Physical models of estuaries". *Coastal, Estuarial and Harbour Engineers' Reference Book, edited by M.B. Abbott & W.A. Price, ISBN 0-419-15430-2*, pp. 275-296.

Rahman, M. (1988). "Topics in Engineering Vol. 4: The Hydrodynamics of Waves and Tides, with Applications". *Computational Mechanics Publications, Great Britain.*

Raudkivi and Callander (1975). "Advanced Fluid Mechanics: An Introduction". *Edward Arnold.* ISBN: 0470709405.

Raymond, W.H. and Kuo, H.L. (1984). "A radiation boundary condition for multi-dimensional flows". *Quarterly Journal of the Royal Meteorological Society*, **110**, pp.535-551.

Richardson, L.F. and Stommel, H. (1948). "Notes on Eddy Diffusion in the Sea". *Journal of Meteorology*, **5**, pp.238-240.

Ridderinkhof, H. and Zimmerman, J.T.F. (1990(a)). "Residual Currents in the Western Dutch Wadden Sea". *Residual Currents and Long-term Transport*, Cheng, R.T. (ed). Springer-Verlag, pp. 93-104.

Robinson, I.S. (1981). "Tidal vorticity and residual circulation". *Deep Sea Research*, **28A**, No. 3, pp. 195-212.

Rodenhuis, G.S. (1994) "Two-dimensional nearly-horizontal flow models". *Coastal, Estuarial and Harbour Engineers' Reference Book, edited by M.B. Abbott & W.A. Price, ISBN 0-419-15430-2*, pp. 129-143.

Rodi, W. (1980). "Turbulence Models and Their Applications in Hydraulics - A State of the Art Review". *IAHR, Holland.*

Rouse, H. (1938). "Fluid Mechanics for Hydraulic Engineers". *McGraw-Hill.*

Runchal, A.K. (1978). "Mathematical Modelling Study of a Large Water Body". *Coastal Zone '78: Proceedings of the Symposium on Technical, Environmental, Socio-economic and Regulatory Aspects of Coastal Zone Management, ASCE.*

Schlichting, H. (1979). "Boundary-Layer Theory". *McGraw-Hill.* ISBN: 0-07-055334-3.

Sharp, J. (1981). "Hydraulic Modelling". *Butterworth & Co. Ltd.* ISBN: 0-408-00482-7.

Signell, R.P. and Geyer, W.R. (1990). "Numerical Simulation of Tidal Dispersion Around a Coastal Headland". *Coastal and Estuarine Studies*, **38**, pp. 210-222.

Signell, R.P. and Geyer, W.R. (1991). "Transient Eddy Formation Around Headlands". *Journal of Geophysical Research*, **96**, No. C2, pp. 2561-2575.

Signell, R.P. and Harris, C.K. (2000). "Modeling sand bank formation around tidal headlands". *Estuarine and Coastal Modelling 6th Int. Conf. ASCE, New Orleans, LA, November 3-5, 1999. Editors, Spaulding, M.L. and Blumberg, A.F.*

Smith, G.D. (1985). "Numerical Solution of Partial Differential Equations: Finite Difference Methods, 3rd Edition". *Oxford University Press*, ISBN: 0-19-859650-2

Tee, K.-T. (1976). "Tide-induced residual current, a 2-D nonlinear numerical tidal model". *Journal of Marine Research*, **34**, pp.603-628.

Tee, K.-T. (1988). "Modeling of tidally induced residual currents". *Hydrodynamics of Estuaries vol. I, Estuarine Processes, edited by Kjerfre, B.*, pp. 134-148.

Tennekes, H. and Lumley, J.L. (1972). "A First Course in Turbulence". *MIT Press.* ISBN: 0-262-20019-8.

The Open University (1984). "Mathematical Methods and Fluid Mechanics: Unit 7 - Vorticity". *The Open University Press, Great Britain.* ISBN: 0-335-14106-4.

The Open University (1989) "Ocean Circulation". *Pergamon Press plc, Great Britain.*

Timoshenko, S.P. and Goodier, J.N. (1970). "Theory of Elasticity, 3rd Edition". *McGraw-Hill.* ISBN: 07-064720-8.

Vallentine, H.R. (1969). "Applied Hydrodynamics, S.I. Edition". *Butterworth & Co.* ISBN: 404-40754-9.

van Dyke, M. (1982). "An Album of Fluid Motion". *The Parabolic Press*. ISBN: 0-915760-03-7.

van Pagee, J.A., Glas, P.C.G., Markus, A.A. and Postma, L. (1989(a)). "Mathematical modelling as a tool for assessment of coastal water pollution". *Delft Hydraulics publications*, **403**, 28 pp.

Vardy, A. (1990). "Fluid Principles". *McGraw-Hill*. ISBN: 0-07-707205-7.

Verboom, G.K., de Vriend, H.J., Akkerman, G.J., Thabet, R.A.H. and Winterwerp, J.C. (1984). "Nested models: Applications to practical problems". *Delft Hydraulics publications*, **329**, 11 pp.

Verron, J., Davies, P.A. and Dakin, J.M. (1991). "Quasigeostrophic flow past a cape in a homogeneous fluid". *Fluid Dynamics Research*, **7**, pp. 1-21.

Vieira, J.R. (1994) "Dispersive processes in two-dimensional modles". *Coastal, Estuarial and Harbour Engineers' Reference Book, edited by M.B. Abbott & W.A. Price, ISBN 0-419-15430-2*, pp. 179-197.

Wang, H. and Falconer, R.A. (1998). "Numerical Modeling of Flow in Chlorine Disinfection Tanks". *Journal of Hydraulic Engineering*, **124**, pp. 918-931.

Wang, P.F., Cheng, R.T., Richter, K., Gross, E.S., Sutton, D. and Gartner, J.W. (1998). "Modeling Tidal Hydrodynamics of San Diego Bay, California". *Journal of the American Water Resources Association*, **34**, No. 5, pp. 1123-1140.

Weare, T.J. (1976). "Instability in Tidal Flow Computational Schemes". *ASCE Journal of the Hydraulics Division*, **102**, HY5, pp. 569-580.

Wolanski, E. (1988). "Island wakes in shallow coastal water". *Journal of Geophysical Research*, **93**, No. C2, pp. 1355-1336.

Wolanski, E., Asaeda, T., Tanaka, A. and Deleersnijder, E. (1996). "Three-dimensional island wakes in the field, laboratory experiments and numerical models". *Continental Shelf Research*, **16**, No. 11, pp. 1437-1452.

Wolanski, E. and Hamner, W.H. (1988). "Topographically Controlled Fronts in the Ocean and Their Biological Influence". *Science*, **241**, pp. 177-181.

Wolanski, E., Imberger, J. and Heron, M.L. (1984). "Island Wakes in Shallow Coastal Waters". *Journal of Geophysical Research*, **89**, No. C6, pp. 10553-10569.

Wu, J. and Tsanis, I.K. (1995). "Numerical study of Wind-Induced Water Currents". *Journal of Hydraulic Engineering*, **121**, pp. 388-395.

Yalin, M.S. (1971). "Theory of Hydraulic Models". *MacMillan Press Ltd*

Yanagi, T. (1976). "Fundamental Study on the Tidal Residual Circulation I". *Journal of the Oceanographical Society of Japan*, **32**, pp. 199-208.

Zimmerman, J.T.F. (1978). "Topographic Generation of Residual Circulation by Oscillatory (Tidal) Currents". *Geophysical and Astrophysical Fluid Dynamics*, **11**, pp.35-47.

Zimmerman, J.T.F. (1980). "Vorticity transfer by tidal currents over an irregular topography". *Journal of Marine Research*, **58**, pp. 601-630.

Zimmerman, J.T.F. (1986). "The tidal whirlpool: A review of horizontal dispersion by tidal and residual currents". *Netherlands Journal of Sea Research*, **20**, (2/3) pp. 133-154.

Zoppou, C. and Roberts, S. (2000) "Numerical solution of the two-dimensional unsteady dam break". *Applied Mathematical Modelling*, **24**, pp. 457-475.

APPENDIX A: MATHEMATICAL METHODS AND IDENTITIES

Sources: Eagleson & Dean (1966), Knight (1986), Raudkivi & Callander (1975), Smith (1985)

A1 The Chain Rule

The Chain Rule tells us that the derivative of f(g(x)), where f and g are both differentiable functions, is the product of their derivatives.

If

$$y = f[g(x)], \tag{A.1.1}$$

then,

$$y' = f'[g(x)] \,.\, g'(x) \tag{A.1.2}$$

In words, to find the derivative of f[g(x)], find the derivative of f(x), replace each x with g(x) and then multiply the result by the derivative of g(x).

A2 Taylor's Theorem

When a function f and its derivatives are single-valued, finite and continuous functions of x, then by Taylor's theorem,

$$f(x+\Delta x) = f(x) + \Delta x \frac{\partial f(x)}{\partial x} + \frac{\Delta x^2}{2}\frac{\partial^2 f(x)}{\partial x^2} + \frac{\Delta x^3}{6}\frac{\partial^3 f(x)}{\partial x^3} + \text{H.O.T.} \tag{A.2.1}$$

and

$$f(x-\Delta x) = f(x) - \Delta x \frac{\partial f(x)}{\partial x} + \frac{\Delta x^2}{2}\frac{\partial^2 f(x)}{\partial x^2} - \frac{\Delta x^3}{6}\frac{\partial^3 f(x)}{\partial x^3} + \text{H.O.T.} \tag{A.2.2}$$

where H.O.T. stands for Higher Order Terms.

Re-arranging equations (A.2.1) and (A.2.2), in terms of the first derivative produces,

$$\frac{\partial f(x)}{\partial x} = \frac{[f(x+\Delta x) - f(x)]}{\Delta x} - \frac{\Delta x}{2}\frac{\partial^2 f(x)}{\partial x^2} - \frac{\Delta x^2}{6}\frac{\partial^3 f(x)}{\partial x^3} - \text{H.O.T.} \tag{A.2.3}$$

and

$$\frac{\partial f(x)}{\partial x} = \frac{[f(x) - f(x-\Delta x)]}{\Delta x} + \frac{\Delta x}{2}\frac{\partial^2 f(x)}{\partial x^2} - \frac{\Delta x^2}{6}\frac{\partial^3 f(x)}{\partial x^3} + \text{H.O.T.} \tag{A.2.4}$$

A3 The Total Derivative

The symbol D/Dt is often referred to as the "total derivative", and represents the total rate of change of some fluid property or quantity experienced by a particular fluid particle as it moves with velocity components u, v and w. Assuming that the fluid particle is very small, the rate of change of any property of the particle as it passes through the point (x,y,z) is determined by the stress, and body force components at that point.

Considering the case of the x-directed component of velocity of a small fluid particle, the velocity can be seen to be a function of the position of the particle and time

$$u = f(x, y, z, t). \tag{A3.1}$$

If the x-directed component of velocity u, alters by Δu in time Δt, and travels a distance with components Δx, Δy, Δz in that time, it is obvious that,

$$\Delta u = \frac{\partial u}{\partial t}\Delta t + \frac{\partial u}{\partial x}\Delta x + \frac{\partial u}{\partial y}\Delta y + \frac{\partial u}{\partial z}\Delta z. \tag{A3.2}$$

Dividing through by Δt produces,

$$\frac{\Delta u}{\Delta t} = \frac{\partial u}{\partial t} + \frac{\partial u}{\partial x}\frac{\Delta x}{\Delta t} + \frac{\partial u}{\partial y}\frac{\Delta y}{\Delta t} + \frac{\partial u}{\partial z}\frac{\Delta z}{\Delta t}. \tag{A3.3}$$

Assuming that Δt is small, Δx, Δy and Δz can also be considered to be small. Therefore, $\frac{\Delta x}{\Delta t}, \frac{\Delta y}{\Delta t}$ and $\frac{\Delta z}{\Delta t}$ can be simplified to u, v and w. Inserting this into equation (A.3.3) produces the rate of change of the x-directed component of velocity of the small fluid particle under consideration (or its acceleration),

$$\frac{Du}{Dt} = \frac{\partial u}{\partial t} + u\frac{\partial u}{\partial x} + v\frac{\partial u}{\partial y} + w\frac{\partial u}{\partial z}. \tag{A3.4}$$

A similar analysis can be carried out for any property of the fluid, and will produce a relationship of the form

$$\frac{D}{Dt} = \frac{\partial}{\partial t} + u\frac{\partial}{\partial x} + v\frac{\partial}{\partial y} + w\frac{\partial}{\partial z}, \tag{A3.5}$$

which is the form of the total derivative. The total derivative can be seen as describing two different effects. The first of these, $\frac{\partial}{\partial t}$, describes the rate of change of a property that a motionless particle would experience at point (x,y,z). This is

often referred to as the 'local' effect as it is a function of position. The second effect, described mathematically as $u\frac{\partial}{\partial x}+v\frac{\partial}{\partial y}+w\frac{\partial}{\partial z}$, describes the rate of change of the property at a given time due to the movement of the particle in a field where gradients of the property exist. This is often referred to as the 'convective' effect.

A4 Depth-averaged Values

Depth-averaged values are denoted by an overbar. The depth-averaged value of a function 'f' is,

$$\bar{f}=\frac{1}{h}\int_{d}^{\eta} f\,dz. \qquad \text{(A4.1)}$$

A5 Leibnitz's Theorem

Leibnitz's theorem provides a procedure for the differentiation of an integral,

$$\int_{a}^{b}\frac{\partial}{\partial x}f(x,y)dz=\frac{\partial}{\partial x}\int_{a}^{b}f(x,y)dz-f(x,b)\frac{\partial b}{\partial x}+f(x,a)\frac{\partial a}{\partial x}. \qquad \text{(A5.1)}$$

APPENDIX B. TFD MODEL PROGRAM LISTING

```
C                              |-------------------------------|
C                              | TFD-MODEL version 1.23        |
C                              |-------------------------------|

C        **********************Tidal Flow Development Model**************************

C Section 1 - Development details.
c 1_____________________________________________________________________________
c Last altered:                        14/05/01
c Version created on:                  15/01/01
c Alterations since last version:      New verification edition (15/01)
c
c Old version name:                    tfd1_22b.for
c Originally developed from:           s80_40.for
c Verified :                           yes
c Validated :                          yes
c
c List of points to be addressed:
1=============================================================================

C Section 2 - Visualisation of the finite-differencing layout.
c 2_____________________________________________________________________________
c
C                              ----------v(i,j+1,k)----------
C                              '                           '
C                          u(i,j,k)                  u(i+1,j,k) '
C                              '                           '
C                      ----------v(i,j,k)----------  '
C                      '       '                   '       '
C                      '       '     n(i,j,k-1)    '       '
C                      '       '     d(i,j)        '       '
C                      '       '     Manvar(i,j)   '       '
C                      '       '                   '       '
C                      '       --------------------'--------
C                      '                           '
C                      ' u(i,j,k-1)                ' u(i+1,j,k-1)
C                      '                           '
C              u/vcor(i,j,k-1)-v(i,j,k-1)----------
C
C 2=============================================================================

C Section 3 - List of variable names, description, and units.
C 3_____________________________________________________________________________
C u(i,j,k) = The x-directed depth-averaged velocity at time k, at point (i,j).        [m/s]
C v(i,j,k) = The y-directed depth-averaged velocity at time k, at point (i,j).        [m/s]
C h(i,j,k) = The total water depth (d+n) at time k, at point (i,j).                   [m]
C n(i,j,k) = The water elevation relative to mean water at time k, at point (i,j).    [m]
C d(i,j) = The depth to mean water level at point (i,j).                              [m]
C ucor(i,j) = X-directed velocity at the l.h. bottom corner of cell (i,j).            [m/s]
C vcor(i,j) = Y-directed velocity at the l.h. bottom corner of cell (i,j).            [m/s]
c slip = Description if boundaries apply (0) no-slip or (1) free slip. Only affects (u/v)cor(i,j)
c qu(i,j,k) = the discharge into cell (i,j) from the x-direction at time (k) per metre.   [m^2/s]
c qv(i,j,k) = the discharge into cell (i,j) form the y-direction at time (k) per metre.   [m^2/s]
C Manvar(i,j) = The value of Manning's number attributed to a cell.
C Manning = The default or uniform input value of the Manning's number
C g = Gravational acceleration (=9.81)                                                [m/s]
C f = Coriolis coefficient.
```

C tidper = Tidal period (default =12 lunar hours = 12.4 hours = 44640 seconds) [s]
C dt = Time step interval [s]
C dx = Grid spacing in the x direction [m]
C dy = Grid spacing in the y direction [m]
C Tamp = Max. amplitude of the input elevation values [m]
C ndx = Number of grid points in the x-direction
C ndy = Number of grid points in the y-direction
C x = Grid reference in the x-direction.
C y = Grid reference in the y-direction.
C mx = The maximum array size in the x-direction. }
C my = The maximum array size in the y-direction. } All read in from *.cmn
C mt = The maximum array size with respect to time. }
C imask(i,j) = Land masking array, related to cell (i,j)
C C = Tidal wave velocity (celerity) [m/s]
C Cour(x/y) = Courant Number in the x and y directions (stability check)
C lamda = Tidal wavelength (=c*tidper)
C nsteps = Number of calculation steps required (=time/dt)
C step = the current time-step
C time = Length of simulation run [s]
C cumdt = cumulative time passed (nsteps past*dt) [s]
C C(x/y) = Wave velocity in a cell adjacent to an open boundary, for use in the radiating boundary
C condition
C vort(i,j) = The value of vorticity at the centre of cell (i,j)
c rt_y_or_n = Residual tide output required? (yes or no)
c simustart = Overall elapsed time before residual tide calculation begins
c simuend = Overall elapsed time before residual tide calculation ends
c (u/v)sum(i,j) = Summated value of (u/v) in cell (i,j) for use in calculating residual values.
c sumdn = sum of the coriolis slope across the input boundary to the n'th grid point.
c theta = phase angle enforced on the input elevation curve. Converted from read in degrees to radians
c within the body of the program.
c tide1 = Inital tidal elevation that is set uniformly across the whole domain.
c ninput = Are driving elevation boundaries (F)ile based or (C)alculated as a sine curve.
c vinput = Are driving velocity boundaries (F)ile based or (C)alculated as a sine curve.
c InTstep = Integer value of the time-step used in a pre-derived driving boundary file.
c ni = The number of steps (to be) read in from a pre-derived driving boundary file.
c InTime = The number of seconds elapsed relating to data read in from a pre-derived boundary file.
c nIn = The elevation value read in from a pre-derived boundary file.
c vIn = The velocity value read in from a pre-derived boundary file.
c iocount = Integer count of time-step number with respect to outputting the selected u,v + n files.
c iscount = Integer count of time-step number with respect to output of tidal curves.
c io_out = Integer count of the next distinct time-step when output will occur. [s]
c io_step = The number of calculation steps between output step for u, v + n.
c io_delay = The delay in calculation steps before outputting for the first time.
c ioseries = The time-step between ouput step for the tidal curves. [s]
c (x/y)max = x- or y- Co-ordinate of the maximum point (i.e. the top R.H. corner).
c (x/y)min = x- or y- Co-ordinate of the minimum point (i.e. the bottom L.H. corner).
c d_(x/y)max = Maximum depth along the input boundary in the x- and y- direction respectively.
c dmax = Maximum depth in the entire domain.
c d_limit = The drying limit s.t. when total depth in cell is < than, it dries.
c hname = Stem of the output file names.
c cname = Name of the file where the land string is saved.
c lname = Derivative name used to store other naming stems during manipulation.
c fname = File name for storing the radiating boundary data (if required).
c oname = Stem of the output file name used for tidal curves.
c tname = File name(s) used for tidal curves.
c cspeed = Maximum tidal wave celerity generated in the domain thro' (gh)^0.5.
c courlim = Input value selected as the maximum acceptable value of the CFL condition.
c try_dt = The maximum permissible time-step derived from dmax and the cell size.
c ibq(x/y) = Boundary value for x/y describing which cells are driving w.r.t. flow.
c ibh(x/y) = Boundary value for x/y describing which cells are used for driving w.r.t. depth.
c query = The boundary alignment to be stored for radiating purposes
c trigger = Description of the boundary in 'query' used to select the file storage name.

```
c dtime = The total time that the pre-derived boundary file lasts for.                    [s]
c dstep = The time-step between the input files in the pre-derived boundary file.         [s]
c dnstep = No. of input steps in the pre-derived boundary file.
c (u/v)_rad(i,j) = The u/v velocity along the boundary cells (i.e. constant i or j).
c licon = The 'real' time-step no. that is in use when imposing 'li' described below.
c li = The time-step no. in the boundary file used to impose a phase shifted radiating boundary.
c Icurves = The number of tidal curves that you want to output.
c Ipx/y(i) = The cell number (in the x and y directions) where the tidal curves are output.
c is = Swith to select or de-select a ramping up to steady state input.
c io_check = Integer value used to trigger on/off ouput sections.
c sinwave = Progressing in time value of the M2 representative input using a sine wave.
c coswave = Progressing in time value of the M2 representative input using a cosine wave.
c mi = Integer count of the input file number read-in to provide driving boundary.
c e_or_w = Is the x-directed input from the (e)ast, (w)est, none(a) or (r)adiating.
c n_or_s = Is the y-directed input from the (n)orth, (s)outh, none(a) or (r)adiating.
c y_e_or_v = Is the x-directed (along y transect) input of (e)levation, (v)elocity or none(a).
c x_e_or_v = Is the y-directed (along x transect) input of (e)levation, (v)elocity or none(a).
c ib(hx/hy/qx/qy) = Prefixes indicate integer boundary coordinates (selection of n/s/w/e boundaries).
c Umax = The input value (if specified as a velocity) describing the amplitude of the x-directed
c          velocity component.
c Vmax = The input value (if specified as a velocity) describing the amplitude of the y-directed
c          velocity component.
c z0 = The datum depth if non-zero.
c isteady = Description of whether an unsteady or steady flow condition is to be used.
c ewderi = Is the east/west radiating boundary values to be used pre-derived (i.e. using a previously
recorded data set ((d)erived or not(a)).
c nsderi = Is the north/south radiating boundary values to be used pre-derived (i.e. using a previously
c          recorded data set) ((d)erived or not(a)).
c pdepth = Centred depth used in the differencing of the pressure gradient term.
c fdepth = Centred depth used in the calculation of the bottom friction term.
c hdepth = Centred depth used for calculation of elevations via the continuity equation.
c (u/v)depth = Centred depth used to calculate u and v respectively from qu and qv.
c uvdepth = Centred depth used to check that the cell values do not fail CFL checks.
c (x/y)frict = The contribution of the bottom friction term in the x/y-direction (momentum eqn.).
c (x/y)conv = The contribution of the convective terms in the x/y-direction (momentum eqn.).
c (x/y)conv1 = The value of the 'direct' momentum term in the x/y-direction (mometum eqn.).
c (x/y)conv2 = The value of the cross-momentum term in the x/y-direction (mometum eqn.).
c (x/y)diff = The contribution of the eddy viscosity term in the x/y-direction (momentum eqn.).
c f(x/y) = The contribution of the coriolis term in the x/y-direction (momentum eqn.).
c (x/y)wind = The contribution of the wind-shear term in the x/y-direction (momentum eqn.).
c Cw = air-water interface resistance coefficient (0.0026 attributed to Munk (Falconer, 1989)).
c Windx = Velocity of the wind in the x-direction at z = -10m.
c Windy = Velocity of the wind in the y-direction at z = -10m.
c (u/v)know = The special differencing value of velocity used in calculating radiating velocities.
c cdepth = The 'centred' (best-fit) depth used in calculating radiating velocity.
c i(x/y) = Prefix used to describe whether x or y directed convective terms to be calcualted.
c drive_in = The type (e/v) and direction(e/w/n/s) of driving boundary used in the simulation.
c i(u/l)limit = Region between which the continuity equation is to be calculated (x-direction).
c j(u/l)limit = Region between which the continuity equation is to be calculated (y-direction).
c (U/V)comp = X- and y- directed components of the R.H.S of the continuity equation.
c bed = The bed level in a cell (=d(i,j)).
c flood = The total depth required to flood a dry cell (=1.25 * drying height(d_limit)).
c speed = The magnitude of the new velocities in a cell used to check for supercritical flow.
c celer = The wave celerity derived from the total depth used to check for supercritical flow.
c cfl = The value of the newly derived cfl condition used to compare with the set limits.
c rad = Is the radiating boundary opposite the input boundary to be recorded, (y or n).
C 3=============================================================

C Section 4 - Set up the arrays, common blocks and variables required by the programme.
C 4_____________________________________________________________
```

```
      implicit real(a-h), real(o-z)
      integer  mx,my,mt
      include 'tfd1_21.cmn'
c-----------------------------------------------------------------
      Double precision qu(mx,my,mt) , qv(mx,my,mt)
      Double precision u(mx,my,2:mt) , v(mx,my,2:mt)
      Double precision ucor(mx,my,2:mt) , vcor(mx,my,2:mt)
      Double precision usum(mx,my) , vsum(mx,my)

      common/flows/ qu,qv,u,v,ucor,vcor,usum,vsum
c-----------------------------------------------------------------

      Double precision n(mx,my,2:mt), h(mx,my,mt)
      Double precision d(mx,my)

      common/elevs/  n, h, d
c-----------------------------------------------------------------

      real Manvar(mx,my), manning

      common/friction/ manvar, manning
c-----------------------------------------------------------------

      integer imask(mx,my)

      common/mask/ imask
c-----------------------------------------------------------------

      Double precision vort(mx,my)
      integer io_out(10000)
      integer ioseries(10000)
      integer scat_out, grd_out

      common/out/ vort, io_out, ioseries, scat_out, grd_out
c-----------------------------------------------------------------

      Double precision nIn(10000)
      Double precision vIn(10000)
      integer InTime(10000)
      double precision z0, tide1, Intstep

      common/input/ nIn,vIn,InTime,z0, tide1, Intstep
c-----------------------------------------------------------------
      Double precision u_out(mx,4,10000)
      Double precision v_out(mx,4,10000)
      Double precision n_out(mx,4,10000)
      Double precision u_rad(1,my,1000)
      Double precision v_rad(mx,1,1000)

      common/storage/u_out, v_out, n_out, u_rad, v_rad
c-----------------------------------------------------------------
      double precision xconv, xconv1,xconv2
      double precision yconv, yconv1,yconv2
      double precision xdiff,ydiff

      common/convdiff/xconv, xconv1,xconv2,yconv, yconv1,yconv2,
     &     xdiff,ydiff
c-----------------------------------------------------------------
      real     x, y,  dx,  dy
      integer ndx, ndy

      common/grid_stuff/ x,y,dx,dy,ndx,ndy
```

```
c-----------------------------------------------------------------------
      integer ipx(15)
      integer ipy(15)

      common/tidecurv/ipx,ipy
c-----------------------------------------------------------------------
      integer i,j,ix,iy,is,slip,phase,
     1  is1,id1,it1,it2,licon,li,Icurves,ni,ibqx,Ibqy,
     1        Ibhx,Ibhy,mi

      integer iulimit,illimit,julimit,jllimit

      real dt,cumdt,g,tamp,simustart,simuend,Latitude,theta,
     1   xmax,ymax,xmin,ymin,d_xmax,d_ymax,dmax,d_limit,courlim,
     1   Umax,Vmax,Cw,Windx,Windy,dstep,dtime,dnstep

      DOUBLE PRECISION uknow,vknow,xgrad,ygrad,ucomp,vcomp,xfrict,
     1                 yfrict,C,cx,cy,fx,fy,pdepth,fdepth,cdepth,
     1                 xwind,ywind,sinwave,coswave,Courx,Coury,lamda,
     1                 sumdn,cspeed,try_dt,hdepth,udepth,
     1                 vdepth,uvdepth,bed,flood,speed,celer,cfl

      double precision vortlim
      double precision f
      integer iocount,iscount,io_step,io_check,io_delay,isteady

      DOUBLE PRECISION xfrict1, xfrict2, xfrict3, xfrict4,
     1                 yfrict1, yfrict2, yfrict3, yfrict4,
     1                 xdiff1, xdiff2, xdiff3, xdiff4,
     1                 ydiff1, ydiff2, ydiff3, ydiff4

c-names---------------------------------------------------------------
      character hname*123
      character*123  dname, cname, tname, oname, vFile, nFile,
     1               fname, drive_in, cumname

      character y_e_or_v*1,x_e_or_v*1,e_or_w*1,n_or_s*1,vinput*1,
     1          nInput*1,hem*1,rt_y_or_n*1,rad*1,ewderi*1,nsderi*1,
     1          trigger,iprogress*1,uvout*1,nout*1,vout*1
c-----------------------------------------------------------------------
C 4=====================================================================
```

C Section 5 - Initialise constants and set default values for read in variables/names.

C 5_____

```
      g = 9.81
      Pie = 4*ATAN(1.0)
      tidper = 44640
      dt = 5
      tamp = 0.5
      time = 44640
      io_step = 200
      io_delay = 0
      manning = 0.03
      courlim = 0.5
      d_limit = 0.5
      y_e_or_v = 'v'
      x_e_or_v = 'v'
      scat_out = 1
      grd_out = 1
      ninput = 'C'
```

```
      vInput = 'C'
      fx = 0
      fy = 0
      Cw = 0.0026
      loop = 1
      xfrict1 = 0
      xfrict2 = 0
      xfrict3 = 0
      xfrict4 = 0
      yfrict1 = 0
      yfrict2 = 0
      yfrict3 = 0
      yfrict4 = 0
      xdiff1  = 0
      xdiff2  = 0
      xdiff3  = 0
      xdiff4  = 0
      ydiff1  = 0
      ydiff2  = 0
      ydiff3  = 0
      ydiff4  = 0

c  default file names
      dname = 'depth.grd'
      hname = 'c:\runa'
      cname = 'land.dat'
      tname = 'tide.dat'
      oname = '1'
      vFile = 'vnone'
      nFile = 'nestnone'
      fname = 'East'
      drive_in = 'aa'
      cumname = 'cumulv8.dat'
C 5=============================================================

C Section 6 - Read in input data from the parameter file.
C 6_____________________________________________________________
      open(unit=10,File='tfd1_23.par',status='old')

      read(10,*)
      read(10,'(a)')      dname
      read(10,*)
      read(10,*)          dt , time
      read(10,*)
      read(10,*)          tidper, isteady
      read(10,*)
      read(10,'(a)')      rt_y_or_n
      read(10,*)
      read(10,*)          simustart, simuend
      read(10,*)
      read(10,'(a)')      y_e_or_v
      read(10,'(a)')      e_or_w
      read(10,*)
      read(10,'(a)')      ewderi
      read(10,*)
      read(10,*)          phase
      read(10,*)
      read(10,*)          Umax, tamp, z0, theta
      read(10,*)
      read(10,'(a)')      x_e_or_v
      read(10,'(a)')      n_or_s
```

```
      read(10,*)
      read(10,'(a)')     nsderi
      read(10,*)
      read(10,*)         phase
      read(10,*)
      read(10,*)         Vmax, tamp, z0, theta
      read(10,*)
      read(10,*)         slip
      read(10,*)
      read(10,*)         manning
      read(10,*)
      read(10,*)         windx, windy
      read(10,*)
      read(10,*)         Latitude
      read(10,'(a)')     hem
      read(10,*)
      read(10,'(a)')     hname
      read(10,*)
      read(10,*)         io_delay, io_step
      read(10,*)
      read(10,*)         scat_out, grd_out
      read(10,*)
      read(10,*)         vortlim
      read(10,*)
      read(10,*)         courlim
      read(10,*)
      read(10,*)         d_limit
      read(10,*)
      read(10,'(a)')     nInput
      read(10,*)
      read(10,'(a)')     nFile
      read(10,*)
      read(10,'(a)')     vInput
      read(10,*)
      read(10,'(a)')     vFile
      read(10,*)
      read(10,'(a)')     rad
      read(10,*)
      read(10,'(a)')     fname
      read(10,*)
      read(10,'(a)')     uvout
      read(10,*)
      read(10,'(a)')     nout
      read(10,*)
      read(10,'(a)')     vout

      close(10)

      If(uvout.eq.'n'.and.nout.eq.'n'.and.vout.eq.'n')then
       Print*,'*********************************************************'
       Print*,'******THIS SIMULATION IS CONFIGURED NOT TO******'
       Print*,'******PRODUCE ANY OUTPUT FILES.                 ******'
       Print*,'*********************************************************'
      Endif
C 6=============================================================

C Section 7 - Read in input boundaries from relevant file (if required).
C 7_____________________________________________________________
      If(ninput.eq.'F')then
c Then read in the elevation input boundary file here.
      mi=1
```

```
        open(unit=11,File=nFile,status='old')
c Read input parameter file
        read(11,*) InTStep, ni
        Do 01    i=1,ni
        read(11,*) InTime(i), nIn(i)
01      Continue
        close(11)
        Endif

        If(vinput.eq.'F')then
c Then read in the velocity input boundary file here.
        mi=1
        open(unit=11,File=vFile,status='old')
c Read input parameter file
        read(11,*) InTStep, ni
        Do 02    i=1,ni
        read(11,*) InTime(i), vIn(i)
02      Continue
        close(11)
        Endif
C 7=============================================================

C Section 8 - Read in the bathymetry and topography from the relevant .grd file, mask
C             land and output coastal string.
C 8_____________________________________________________________
C READ DEPTH DATA from a grid file
        OPEN(20,FILE=dname,STATUS='OLD',err=5750)
        Read(20,*,err=5750)
        read(20,*,err=5750)ndx, ndy
        Read(20,*,err=5750)xmin,xmax
        Read(20,*,err=5750)ymin,ymax
        Read(20,*,err=5750)

        if (ndx .gt. mx .or. ndy .gt. my) goto 5752

        Do 30 j=1,ndy
        READ(20,*,err=5750)(d(i,j),i=1,ndx)
00030   Continue
        CLOSE(20)
c calculate dx and dy cell dimensions
        dx = (xmax-xmin)/(ndx-1)
        dy = (ymax-ymin)/(ndy-1)

        write(*,*)'****** bathymetry read in dx dy', dx, dy, '******'

C Set up output file for coast string
c find end of name string in hname
        lname = index(hname,' ') -1
        cname(1:lname) = hname(1:lname)
        cname(lname+1:lname+6)='-LAND'
        open(unit=15,File=cname,status='unknown')
        write(*,*)cname

c define wet/dry mask
        dland = -100.0
        dmax  = -100.0
        d_xmax = 0.0
        d_ymax = 0.0

        do 31 i = 1, ndx+1
c add extra cells to depth grid at ndy+1
```

```
          d(i,ndy+1) = d(i,ndy)
          if (d(i,1) .gt. d_xmax) d_xmax = d(i,1)
00031     Continue

          do 32 j = 1, ndy+1
c add extra cells to depth grid at ndx+1
          d(ndx+1,j) = d(ndx,j)
          if (d(1,j) .gt. d_ymax) d_ymax = d(1,j)
00032     Continue

          write(*,*)'****** dmax x & y', d_xmax, d_ymax, '******'

          do 33 i = 1, ndx+1
          ip1 = i+1
          if (i.eq.ndx+1) ip1 =ndx+1
          im1 = i-1
          if (i.eq.1) im1 =1

          do 33 j = 1, ndy+1
          jp1 = j+1
          if (j.eq.ndy+1) jp1 =ndy+1
          jm1 = j-1
          if (j.eq.1) jm1 =1
c  find max depth
          If (d(i,j) .gt. dmax) dmax = d(i,j)
       x = xmin + (i-1)*dx
       y = ymin + (j-1)*dy
c  default is wet  => imask() = 1
          imask(i,j) = 1
c  but if depth is negative (but not -100) then could be intertidal
          If (d(i,j)+n(i,j,2) .lt. d_limit) then
           imask(i,j) = -1
           h(i,j,2) = d_limit
           h(i,j,3) = d_limit
          Endif
c  but....
          If (d(i,j) .lt. -99.0) then
c  dry land cell so
           imask(i,j) = 0
c land so check if it is a coastal strip
        If(d(ip1,j).gt.-90 .or. d(im1,j)  .gt.-90. or.
     1    d(i,jp1)  .gt.-90 .or. d(i,jm1)  .gt.-90. or.
     2    d(ip1,jp1).gt.-90 .or. d(ip1,jm1).gt.-90. or.
     3    d(im1,jp1).gt.-90 .or. d(im1,jm1).gt.-90)then
c  coast point, therefore add to coast string file.
                                write(15,*)x,y,dland,dx
           Endif
          Endif

          If (j.gt.ndy) imask(i,j) = imask(i,j-1)
          If (i.gt.ndx) imask(i,j) = imask(i-1,j)

00033     continue
          close(15)

c remove -100 values from depth arrays read in in WOLF format, so that do not upset calculations
          do 34 i = 1, ndx+1
          do 34 j = 1, ndy+1
           if (d(i,j) .lt. -99.0) d(i,j) = 0.0
           do 35 k = 1, mt
C initialise h()
            h(i,j,k) = d(i,j)+ tide1
```

```
00035    Continue
00034   Continue
C 8=============================================================

C Section 9 - Initialise all the variables relevant to this particular simulation.
C 9_____________________________________________________________
        If(nInput.eq.'C')then
c Then initialise relevant variables
         If(x_e_or_v.eq.'v'.or.y_e_or_v.eq.'v')then
          theta = 0.0
          tide1 = z0
         Else
          theta = theta*2*pie/360
          tide1 = z0+tamp*sin(theta)
         Endif
        Else
         tide1 = z0 + nIn(1)
        Endif
C Properties of the tidal wave
        C = (g*dmax)**0.5
        lamda = C * tidper

C Input of Coriolis coefficient
        If(hem.eq.'S')then
         f= 2 * 0.00007292 * sin((latitude*2*pie/360))
        Else
         f= -2 * 0.00007292 * sin((latitude*2*pie/360))
        Endif

C Input of manning coefficient.

        Do 5 i=1,ndx+1
        Do 5 j=1,ndy+1
C  For a constant value use this:
         Manvar(i,j) = manning
C  If a varying value is used (as for Sepetiba) use this:  **(CASE SPECIFIC)**
cc        If(d(i,j).le.0.0)then
cc         Manvar(i,j) = 0.05
cc        ElseIf(d(i,j).gt.0.0.and.d(i,j).le.4.0)then
cc         cosn = 0.0125 * cos(pie*((d(i,j)-0.0)/(4.0-0.0)))
cc         Manvar(i,j) =  0.0375 + cosn
cc        ElseIf(d(i,j).gt.4.0)then
cc         Manvar(i,j) = 0.025
cc        Endif
00005   Continue

C  define  number of iteration steps
        nsteps = time/dt

c  define output steps at intervals of io_step iterations for .grd files and
c  ioseries iterations for output of tidal curves.
        iocount = 1
        iscount = 1
        do 10 i = 1,1500
         io_out(i) = i*io_step + io_delay
         ioseries(i) = i*(io_step/10)
00010   continue

C ***************************************************************************
C The inital start-up condition is that everything = 0 in order to allow the wave propagation
c to set itself up. i.e.cold starting.  (Although certain variables set to a constant
```

```
c value in cases such as elevation boundaries being prescribed not to start at 0).
c ************************************************************************************
        Do 20 i = 1,mx
        Do 20 j = 1,my
         usum(i,j) = 0
         vsum(i,j) = 0
         Do 21 l = 2,mt
          u(i,j,l) = 0
          v(i,j,l) = 0
          n(i,j,l) = tide1
          ucor(i,j,l) = 0
          vcor(i,j,l) = 0
00021     Continue
         do 22 l2 = 1,mt
          qu(i,j,l2) = 0
          qv(i,j,l2) = 0
          h (i,j,l2) = tide1 + d(i,j)
00022     Continue
00020    Continue

        write(*,*)'************** tidal elevation is', tide1,'**************'
        write(*,*)'*************** variables initialised ***************'
C 9=====================================================================

        print*,'************************************************************'

C Section 10 - Warning messages regarding parameter file selections.
C 10____________________________________________________________________
        If(Mod(time,dt).ne.0.0)then
         print*,' '
         Print*,'**********************WARNING**********************'
         print*,'Run duration and time step length do not coincide.'
         print*,'Do you want to continue? (y or n)'
         read(*,'(a)') iprogress
         If(iprogress.eq.'n')then
          stop
         Endif
        Endif

        If(rt_y_or_n.eq.'y')then
         If((simuend+(io_step*dt)).gt.time)then
          print*,' '
          Print*,'**********************WARNING**************************'
          print*,'Run not long enough to properly output residual tide'
          print*,'Do you want to continue? (y or n)'
          read(*,'(a)') iprogress
          If(iprogress.eq.'n')then
           stop
          Endif
         Endif
        Endif

        If(nInput.eq.'F'.or.vInput.eq.'F')then
         If((nsteps*dt).gt.(InTime(ni)+InTStep))then
          Print*,' ****************ERROR*****************'
          Print*,' Input File length exceeded by run time'
          Print*,' ****************ERROR*****************'
          Stop
         Endif
        Endif
C 10====================================================================
```

```
c++++++++++++++++++++++++++++++++++++++++++++++++++++++++++++++++++++++++++++
c++++++++++++++++++++++++ END OF INPUT ++++++++++++++++++++++++++++++++++++++
c++++++++++++++++++++++++++++++++++++++++++++++++++++++++++++++++++++++++++++

c****************************** START CHECKS ***********************************

C Section 11 - Test CFL condition (uses maximum cell depth from entire domain)
C 11_____________________________________________________________________________
      Courx = (dt/dx) * ((g*(dmax+tamp))**0.5)
      Coury = (dt/dy) * ((g*(dmax+tamp))**0.5)
c ************
C CFL condition states that Cour(x/y) < 1, but with a shoaling condition a lesser no., provides
C safety therefore use courlim (I prefer 0.40 from experience to avoid two-cell oscillations).
C ************

      If(Courx.ge.courlim)then
       Print*,' The input values are unstable, reselect either of'
       Print*,' the values dt or dx in an attempt to create a'
       Print*,' valid solution'
      cspeed = (g*(dmax+tamp))**0.5
      try_dt = courlim*dx/cspeed
      write(*,*)'dmax =',dmax,'courant x=',courx
      write(*,*)'try dt=',try_dt
       Stop
      Endif

      If(Coury.ge.courlim)then
       Print*,' The input values are unstable, reselect either
     +  of the values dt or dy in an attempt to create a valid
     +  solution'
      cspeed = (g*(dmax+tamp))**0.5
      try_dt = courlim*dy/cspeed
      write(*,*)'dmax =',dmax,'courant y=',coury ,' try dt=',try_dt
       Stop
      Endif

      write(*,*)'**** cfl checked', courx, coury, '****'
C 11=============================================================================


C Section 12 - EXCESSIVE CREST DISPLACEMENT WARNING
C 12_____________________________________________________________________________
C This is included to prevent the unwitting input of variables that would generate a
C shoaling condition no matter the bathymetry conditions.

C  dC * Tpro  < or = 0.5*(lamda/4)
C  dC = difference between the celerity of the crest and trough.
C  Tpro = Total time available for propogation if wave maintains its initial velocity.
C  (lamda/4) = Quarter wavelength.
C  0.5 is used to prevent the 'dC' created shoaling from causing the wave to start breaking.

      dC = ((g*(dmax+tamp))**0.5)-((g*(dmax-tamp))**0.5)
      If(e_or_w.ne.'a')then
       Tpro = (ndx*dx)/C
      Elseif(n_or_s.ne.'a')then
       Tpro = (ndy*dy)/C
      Endif
      lhs = dC*Tpro
      rhs = 0.5*(lamda/4)
      If(lhs.gt.rhs)then
       Print*,' !!! Excessive shoaling created by dC !!!'
```

```
          Print*,' Do you want to continue ? (1=Y or 2=N)'
          Read*,iabc
          If(iabc.eq.2) Stop
          Endif
C 12=============================================================

c++++++++++++++++++++++++++++++++++++++++++++++++++++++++++++++++++++++++++++
c++++++++++++++++++++++++ END CHECKS ++++++++++++++++++++++++++++++++++++++++
c++++++++++++++++++++++++++++++++++++++++++++++++++++++++++++++++++++++++++++
```

C Section 13 - Establish which directions are input and which are radiating boundaries.

```
C 13_____________________________________________________________________
c ib- prefixes indicate integer boundary coordinates.
          If(e_or_w.eq.'w')then
           ibqx = 1
           ibhx = 1
          Elseif(e_or_w.eq.'e')then
           ibqx = ndx+1
           ibhx = ndx
          Elseif(e_or_w.eq.'r')then
           ibqx = mx
           ibhx = mx
          Endif
          If(n_or_s.eq.'s')then
           ibqy = 1
           ibhy = 1
          Elseif(n_or_s.eq.'n')then
           ibqy = ndy+1
           ibhy = ndy
          Elseif(n_or_s.eq.'r')then
           ibqy = my
           ibhy = my
          Endif
C 13=============================================================
```

C Section 14 - Open and initialise files for storing radiating boundary data (if required),
C OR read in from a radiating boundary files (if required).

```
C 14_____________________________________________________________________
          If(rad.eq.'y')then
           If(e_or_w.eq.'w') then
cc          query = u(ndx+1,j,3)
            trigger = 'E'
           ElseIf(e_or_w.eq.'e') then
cc          query = u(1,j,3)
            trigger = 'W'
           ElseIf(n_or_s.eq.'s') then
cc          query = v(i,ndy+1,3)
            trigger = 'N'
           ElseIf(n_or_s.eq.'n') then
cc          query = v(i,1,3)
            trigger = 'S'
           Endif

           open(26,file=fname,status='unknown')
           close(26,status='delete')
           open(26,File=fname,status='new')
           write(26,10001) time,(io_step*dt/10),((time/(io_step*dt/10))+1)
           If(trigger.eq.'E')then
            write(26,10000) (u(ndx+1,j,3),j=1,ndy+1)
           ElseIf(trigger.eq.'W')then
```

```
          write(26,10000) (u(1,j,3),j=1,ndy+1)
         ElseIf(trigger.eq.'N')then
          write(26,10000) (v(i,ndy+1,3),i=1,ndx+1)
         ElseIf(trigger.eq.'S')then
          write(26,10000) (v(i,1,3),i=1,ndx+1)
         Endif
        Endif

10001   Format(5x,3f8.0)
10000   Format(5x,100f10.5)

C If a pre-derived opposing boundary is used, read-in the data here
C  For an east or west boundary -
        If(ewderi.eq.'d')then
         open(unit=26,File=fname,status='old')
         Read(26,10001)dtime,dstep,dnstep
         Do 40 li = 2,dnstep
          Read(26,*) u_rad(1,1,li)
cc (u_rad(1,j,li),j=1,ndy+1)
00040   Continue
        close(26)
c  Calculate the phase difference between the input and output boundary (i.e., force a phase difference onto
the pre-derived boundary file)
        licon = 2
        li = 2+INT((phase/dstep))
        Do 41 i = 1,ndx+1
        Do 41 j = 1, ndy+1
        Do 41 l = 2,3
         u(i,j,l) = u_rad(1,1,li)
         qu(i,j,l) = u(i,j,l)*h(i,j,l-1)
00041   Continue
        Endif

c  For a north or south boundary -
        If(nsderi.eq.'d')then
         open(unit=26,File=fname,status='old')
         Read(26,10001)dtime,dstep,dnstep
         Do 42 li = 2,dnstep
          Read(26,10000) (v_rad(i,1,li),i=1,ndx+1)
00042   Continue
        close(26)
c  Calculate the phase difference between the input and output boundary
        licon = 2
        li = 2+INT((phase/dstep))
        Do 43 i = 1,ndx+1
        Do 43 j = 1, ndy+1
        Do 43 l = 2,3
         v(i,j,l) = v_rad(i,1,li)
         qv(i,j,l) = v(i,j,l)*h(i,j,l-1)
00043   Continue
        Endif
C 14=============================================================================


C Section 15 - Open files for storing tidal curves
C 15_____________________________________________________________________________
        open(unit=12,File='tidecur.dat',status='unknown')
         Read(12,*)
         Read(12,*)
         Read(12,*)        Icurves
         If(Icurves.ge.1)then
          Do 50 i = 1,Icurves
```

```
          Read(12,*)
          Read(12,*)        Ipx(i),Ipy(i)
          Read(12,'(a)') oname
          lname = index(hname,' ') -1
          tname(1:lname) = hname(1:lname)
          tname(lname+1:lname+10)=oname
          j = 40+i
          open(unit=j,file=tname,status='unknown')
00050     Continue
         Endif
        Close(12)
C 15=============================================================

C++++++++++++++++++++++++++++++++++++++++++++++++++++++++++++++++++++++++++++
C++++++++++++++++++++ TIME-STEPPING CALCULATION ++++++++++++++++++++
C++++++++++++++++++++++++++++++++++++++++++++++++++++++++++++++++++++++++++++

C Section 16 - Initialize time-stepping loop.
C 16_____________________________________________________________________
C 'is' goes to 1 after 0.25 cycle of sine wave.
         is = 0
c Start time-stepping loop.

         Open(51,file=cumname,status='unknown')

         Do 100 step = 1,nsteps
          cumdt = dt*step
C**
cc       Print*,cumdt
C**
c Output progress on screen.
          io_check = (ifix(step)/io_step)*io_step
          If (abs(io_check- step) .lt. 1  )then
           write(*,*)'time elapsed = ', cumdt,'s of ', nsteps*dt, 's'
          Endif
c Set up input waves if input driving is calculated as representative of M2 tide.
          If(nInput.eq.'C'.or.vInput.eq.'C')then
           sinwave = sin(2*Pie*(cumdt/tidper)+theta)
           coswave = cos(2*pie*(cumdt/tidper)+theta)
           if (abs(sinwave) .gt. 0.99) is = 1
          Endif

C         This moves the integer count forward when required by a read-in input file
          If(nInput.eq.'F'.or.vInput.eq.'F')then
           If((cumdt-InTStep).gt.(InTime(mi))) then
                 mi=mi+1
           Endif
          Endif
C 16=============================================================

C         ******************************************************
C         * Calculation of the input variables based upon a sine curve      *
C         * tidal variation of the velocity with a max. value of velmax.    *
C         ******************************************************

C Section 17 - Set-up east/west driving boundary (if required)
C 17_____________________________________________________________________
          If(e_or_w.eq.'w'.or.e_or_w.eq.'e')then
           sumdn = 0.0
           Do 110 j = 1,ndy
            If(imask(ibhx,j).eq.1)then
```

```
            sumdn = sumdn+((f*qu(ibqx,j,2)*dy)/(g*h(ibhx,j,2)))
            If(y_e_or_v.eq.'v') then
             If(vInput.eq.'C')then
c************* to decrease currents in shallow water*****************
c             u(1,j,3) = Umax*sinwave*((d(1,j)/d_ymax)**0.1)*
c*****************************************************************
             If(ibqx.eq.1)   u(ibqx,j,3) =  Umax*sinwave
             If(ibqx.eq.ndx+1)        u(ibqx,j,3) = -Umax*sinwave
            Else
             u(ibqx,j,3) = vIn(mi)+((vIn(mi+1)-vIn(mi))*
     1                        ((cumdt-Intime(mi))/InTstep))
            Endif

           Else

c  elevation boundary
            If(nInput.eq.'C')then
             n(ibhx,j,3) = (z0 + tamp *sinwave) - sumdn
             h(ibhx,j,3) = d(ibhx,j)+n(ibhx,j,3)
            Else
             n(ibhx,j,3) = (z0 + nIn(mi)+((nIn(mi+1)-nIn(mi))*
     1                ((cumdt-InTime(mi))/InTStep))) - sumdn
             h(ibhx,j,3) = d(ibhx,j)+n(ibhx,j,3)
            Endif
           Endif

           If (isteady .eq.1 .and. is .eq. 1) then
c reached steady state
            If(y_e_or_v.eq.'v') then
c velocity boundary
c            u(1,j,3) = Umax *((d(1,j)/d_ymax)**0.1)
             u(ibqx,j,3) = Umax
            Else
c elevation boundary
             n(ibhx,j,3) = (z0 + tamp) - sumdn
             h(ibhx,j,3) = d(ibhx,j)+n(ibhx,j,3)
            Endif

           Endif

c convert to discharge
            If(y_e_or_v.eq.'v') qu(ibqx,j,3) = u(ibqx,j,3)*h(ibhx,j,2)
           Else
c cell is dry
            u(1,j,3)=0.0
            qu(1,j,3)=0.0
           Endif
00110     Continue
          Endif
C 17=============================================================

C Section 18 - Set-up north/south driving boundary (if required).
C 18_____________________________________________________________

          If(n_or_s.ne.'a'.and.n_or_s.ne.'r')then
           sumdn = 0.0
           Do 111 i = 1,ndx
            If(imask(i,ibhy).eq.1)then
             sumdn = sumdn-((f*qv(i,ibqy,2)*dx)/(g*h(i,ibhy,2)))
             If(x_e_or_v.eq.'v') then
              If(vInput.eq.'C')then
```

```
c****************decrease currents in shallow water***************
C ****NOTICE IS TO THE POWER OF 0.2. THINK WOULD HELP EYEMOUTH
c                 v(i,ibqy,3)=Vmax*sinwave*(d(i,ibhy)/d_xmax)**0.2
c************************************************************
             If(ibqy.eq.1)   v(i,ibqy,3) =  Vmax*sinwave
             If(ibqy.eq.ndy+1)        v(i,ibqy,3) = -Vmax*sinwave
            Else
             v(i,ibqy,3) = vIn(mi)+((vIn(mi+1)-vIn(mi))*
   1                          ((cumdt-Intime(mi))/InTstep))
            Endif

           Else
c  elevation boundary
            If(nInput.eq.'C')then
             n(i,ibhy,3) = (z0 + tamp * sinwave) - sumdn
             h(i,ibhy,3) = d(i,ibhy)+n(i,ibhy,3)
            Else
             n(i,ibhy,3) = (z0 + nIn(mi)+((nIn(mi+1)-nIn(mi))*
   1                          ((cumdt-InTime(mi))/InTStep))) - sumdn
             h(i,ibhy,3) = d(i,ibhy)+n(i,ibhy,3)
            Endif
           Endif

           If (isteady .eq.1 .and. is .eq. 1)then
c reached steady state

            If(x_e_or_v.eq.'v') then
c  velocity boundary
c            v(i,1,3)=Vmax*sinwave*(d(i,1)/d_xmax)**0.1
             v(i,ibqy,3)=Vmax
            Else
c elevation boundary
             n(i,ibhy,3) = (z0 + tamp) - sumdn
             h(i,ibhy,3) = d(i,ibhy)+n(i,ibhy,3)
            Endif

           Endif

c  convert to discharge
            If(x_e_or_v.eq.'v') qv(i,ibqy,3) = v(i,ibqy,3)*h(i,ibhy,2)

           Else
c cell is dry
            v(i,1,3) = 0.0
            qv(i,1,3) = 0.0
           Endif

00111     Continue
          Endif
C 18=============================================================

C Section 19 - Calculation of the future step x-directed MOMENTUM using finite-differencing.
C 19_____________________________________________________________
c Derive which is the input and/or radiating boundaries depending upon the input parameters.
          start = 1
          end = ndx+1

          If(y_e_or_v.eq.'v')then
           If(e_or_w.eq.'w') start = 2
           If(e_or_w.eq.'e') end = ndx
          Endif
```

```
          If(ewderi.eq.'d')then
           If(e_or_w.eq.'w')then
            start = 1
            end = ndx
           Else
            start = 2
            end = ndx+1
           Endif
          Endif

          Do 120 i = start,end
           im1 = i-1
           If(im1.lt.1)im1=1
c i = 1 or ndx+1 is already defined as a driving boundary
c i = ndx+1 or 1 is calculated specially as a radiative boundary

          Do 121 j = 1, ndy

C Detemine whether or not the velocity vector is adjacent to land(=> u=0), or not.
           If(imask(i,j).eq.1.and.imask(im1,j).eq.1)then
c not in a cell immediately east of a land cell

C Prevent calculation of the velocity in the final cell in order to apply a radiating
C condition.

           If(i.ge.2.and.i.le.ndx)then

C *PRESSURE GRADIENT TERM*
           pdepth = (h(i,j,2)+h(im1,j,2))/2

           If (pdepth .gt. d_limit*0.99) then
            xgrad = (1/dx)*pdepth*g*(n(i,j,2)-n(im1,j,2))
           Else
            xgrad = 0.0
             write(*,*)'depth too small at', i,j
                write(*,*)'at time step ', step
                write(*,*)'x pdepth =', pdepth
           Endif

C *BOTTOM FRICTION TERM*(Time-lagged by one time-step.)
           If((SQRT(u(i,j,2)**2+(((vcor(i,j,2) +
     +              vcor(i,j+1,2))/2)**2))).gt.1E-20)then
            fdepth =(h(i,j,2)+h(i,j,1)+h(im1,j,2)+h(im1,j,1))/4

            If (fdepth .gt.d_limit*0.99) then
             xfrict = (g*( ((Manvar(i,j)+Manvar(im1,j))/2)**2 )*
     1             u(i,j,2) * SQRT( u(i,j,2)**2+
     1             (((vcor(i,j,2) + vcor(i,j+1,2))/2)**2))) /
     1             fdepth**0.333333
            Else
             xfrict = 0.0
                write(*,*)'depth too small at', i,j
                write(*,*)'at time step ', step
                write(*,*)'x fdepth = ', fdepth
            Endif
           Else
            xfrict = 0.0
           Endif

C *u ADVECTION + DIFFUSION TERM*
           xconv1 = 0.0
```

```
            xconv2 = 0.0
            xdiff = 0.0
            ix = 1
            iy = 0

CC This If statement is key to avoiding crashes early on in simulations caused by Fortran itself.  All it
CC does is disable the convective terms when the value of discharge ABS(qu+qv) is negligibly small.
CC Therefore, when the simulation starts, and the numerical+real diffusion of the input wave spreads
CC across the domain, the convective terms are disabled.

          If(ABS(qu(i,j,2)).gt.0.and.ABS(qu(ip1,j,2)).gt.0.and.
     1          ((SQRT(u(i,j,2)**2+(((vcor(i,j,2) +
     1          vcor(i,j+1,2))/2)**2))).gt.1E-8))then
            call QUICK2(i,j,ix,iy,d_limit,x_e_or_v,y_e_or_v,slip)
          Endif
            xconv = xconv1 + xconv2

C *CORIOLIS FORCE*
            fx=f*((qv(i,j,2)+qv(im1,j,2)+qv(i,j+1,2)+qv(im1,j+1,2))/4)

C *BASIC WIND STRESS TERM*
C 800 is the value for rhoair/rhowater used in MIKE21 (approx. 10 degrees effect).
            xwind = (Cw * Windx *(SQRT(Windx**2+Windy**2))/800)

C *CALCULATION OF THE U VELOCITY AT TIME n+1 (k=3)*
            qu(i,j,3)=qu(i,j,2)-dt*(xgrad+xfrict+xconv-fx-xwind-xdiff)

C *IF RANDOM PERTURBATION REQUIRED: *
cc          If(i.eq.55.and.j.ge.32.and.j.le.48)then
cc          ran = random(1,1)
cc          qu(i,j,3)=qu(i,j,3)+(0.005*((0.5-(1-ran))*qu(i,j,3)))
cc          Endif

            Else
C *RADIATING BOUNDARY CONDITION FOR THE EAST OR WEST OF THE DOMAIN*
C Applies the radiating condition cdu/cdt+(C*(cdu/cdx))=0
            If(i.gt.ndx)then
             id1 = i-1
             is1 = i-1
             it1 = 2
             it2 = 1
            Elseif(i.lt.2)then
             id1 = i
             is1 = i+1
             it1 = 2
             it2 = 1
            Endif

            uknow = qu(is1,j,it1)-qu(is1,j,it2)
            cdepth = d(id1,j)+n(id1,j,2)

            If (cdepth .gt. d_limit*0.99) then
             Cx=(g*cdepth)**0.5
             qu(i,j,3) = qu(is1,j,it1) - (((dx)/(cx*dt))*uknow)
            Else
             qu(i,j,3) = 0.0
                  write(*,*)'depth too small at', i,j
                  write(*,*)'at time step ', step
                  write(*,*)'x cdepth = ', cdepth
             Endif

            Endif
```

```
          Endif

00121     Continue
00120     Continue
C 19=============================================================
```

C Section 20 - If radiating x-directed boundary is pre-derived, then dealt with here.

```
C 20_____________________________________________________________
          If(ewderi.eq.'d')then
           If(cumdt.gt.((licon-1)*(dstep)))then
c Move forward a noutput step in the radiating boundary file record.
        li = li+1
           licon = licon+1
          Endif

          If(e_or_w.eq.'w')then
           Do 520 j = 1,ndy+1
        qu(ndx+1,j,3) = ( u_rad(1,1,li) +
     1                    ( (u_rad(1,1,li+1)-u_rad(1,1,li)) /
     1                      (dstep / (cumdt-( (licon-2) * dstep) ) ))*
     1                      h(ndx,j,2)
00520      Continue
          Elseif(e_or_w.eq.'e')then
           Do 521 j = 1,ndy+1
        qu(1,j,3) = ( u_rad(1,j,li) +
     1                ( (u_rad(1,j,li+1)-u_rad(1,j,li)) /
     1                  (dstep / (cumdt-( (licon-2) * dstep) ) ) ) )*
     1                  h(1,j,2)
00521      Continue
          Endif
         Endif
C 20=============================================================
```

C Section 21 - Calculation of the future step y-directed MOMENTUM using finite-differencing.

```
C 21_____________________________________________________________
c Derive which is the input and/or radiating boundaries depending upon the input parameters.
          start = 1
          end = ndy+1

          If(x_e_or_v.eq.'v')then
           If(n_or_s.eq.'s') start = 2
           If(n_or_s.eq.'n') end = ndy
          Endif

          If(nsderi.eq.'d')then
           If(n_or_s.eq.'s')then
            start = 1
            end = ndy
           Else
            start = 2
            end = ndy+1
           Endif
          Endif

          Do 140 j = start, end
           jm1 = j-1
           If(j.eq.1) jm1 = 1
c j = 1 or ndy+1 is already defined as a driving boundary
c j = ndy+1 or 1 is calculated specially as a radiative boundary
```

```
      Do 141 i = 1, ndx

C Detemine whether or not the velocity vector is adjacent to land(=> u=0), or not.
      If(imask(i,j).eq.1.and.imask(i,jm1).eq.1)then
c not in a cell immediately north of a land cell.


C Prevent calculation of the velocity in the final cell in order to apply a radiating
C condition.

      If(j.ge.2.and.j.le.ndy)then

C *PRESSURE GRADIENT TERM*
      pdepth = (h(i,j,2)+h(i,jm1,2))/2

      If (pdepth .gt. d_limit*0.99) then
       ygrad = (1/dy)*pdepth * g*(n(i,j,2)-n(i,jm1,2))
      Else
       ygrad = 0.0
            write(*,*)'depth too small at', i,j
            write(*,*)'at time step ', step
            write(*,*)'y p depth = ', pdepth
      Endif

C *BOTTOM FRICTION TERM*(Time-lagged by one time-step.)
      If((SQRT(v(i,j,2)**2 +(((ucor(i,j,2) +
     +          ucor(i+1,j,2))/2)**2))).gt.1E-20)then
       fdepth =(h(i,j,2)+h(i,j,1)+h(i,jm1,2)+h(i,jm1,1))/4

       If (fdepth .gt. d_limit*0.99) then
        yfrict = (g *( ((Manvar(i,j)+Manvar(i,jm1))/2)**2 ) *
     1   v(i,j,2) * SQRT(v(i,j,2)**2 +
     1            (((ucor(i,j,2) + ucor(i+1,j,2))/2)**2)))/
     1   fdepth**(0.333333)
       Else
        yfrict = 0.0
            write(*,*)' depth too small at', i,j
            write(*,*)'at time step ', step
            write(*,*)'y fdepth =', fdepth
       Endif
      Else
       yfrict = 0.0
      Endif

C *v ADVECTION + DIFFUSION TERM*
      yconv1 = 0.0
      yconv2 = 0.0
      ydiff  = 0.0
      ix = 0
      iy = 1

CC This If statement is key to avoiding crashes early on in simulations caused by Fortran itself.  All it
CC does is disable the convective terms when the value of discharge ABS(qu+qv) is negligibly small.
      If(ABS(qv(i,j,2)).gt.0.and.ABS(qv(i,jp1,2)).gt.0.and.
     1    ((SQRT(v(i,j,2)**2+ (((ucor(i,j,2) +
     1          ucor(i+1,j,2))/2)**2))).gt.1E-8))then
       call QUICK2(i,j,ix,iy,d_limit,x_e_or_v,y_e_or_v,slip)
      Endif

       yconv = yconv1 + yconv2

C *CORIOLIS FORCE*
```

```
            fy=f*((qu(i,j,2)+qu(i+1,j,2)+qu(i,jm1,2)+qu(i+1,jm1,2))/4)

C *BASIC WIND STRESS TERM*
C 800 is the value for rhoair/rhowater used in MIKE21 (approx. 10 degrees effect).
            ywind = (Cw * Windy *(SQRT(Windx**2+Windy**2))/800)

C *CALCULATION OF THE V VELOCITY AT TIME n+1 (k=3)*

            qv(i,j,3)=qv(i,j,2)-dt*(ygrad+yfrict+yconv+fy-ywind-ydiff)

C *IF RANDOM PERTURBATION REQUIRED: *
cc          If(i.eq.55.and.j.ge.32.and.j.le.48)then
cc          ran = random(1,1)
cc          qv(i,j,3)=qv(i,j,3)+(0.005*((0.5-(1-ran))*qv(i,j,3)))
cc          Endif

            Else
C *RADIATING BOUNDARY CONDITION FOR THE EAST OR WEST OF THE DOMAIN*
C Applies the radiating condition cdu/cdt+(C*(cdu/cdx))=0
            If(j.gt.ndy)then
             jd1 = j-1
             js1 = j-1
             jt1 = 2
             jt2 = 1
            Elseif(j.lt.2)then
             jd1 = j
             js1 = j+1
             jt1 = 2
             jt2 = 1
            Endif

            vknow = qv(i,js1,jt1)-qv(i,js1,jt2)
            cdepth = (d(i,jd1)+n(i,jd1,2))

            If (cdepth .gt. d_limit*0.99) then
             Cy=(g*cdepth)**0.5

          qv(i,j,3) = qv(i,js1,jt1)- ((dy)/(cy*dt))*vknow

            Else
             qv(i,j,3) = 0.0
                  write(*,*)'depth too small at', i,j
                  write(*,*)'at time step ', step
                  write(*,*)'y c depth = ', cdepth
             Endif

            Endif

            Endif

00141       Continue
00140       Continue
C 21=========================================================================

C Section 22 - If radiating y-directed boundary is pre-derived, then dealt with here.
C 22_________________________________________________________________________
            If(nsderi.eq.'d')then
             If(cumdt.gt.((licon-1)*(dstep)))then
              li = li+1
              licon = licon+1
```

```
          Endif

          If(n_or_s.eq.'s')then
           Do 620 i = 1,ndx+1
       qv(i,ndy+1,3) = ( v_rad(i,1,li) +
     1                   ( (v_rad(i,1,li+1)-v_rad(i,1,li)) /
     1                       (dstep / (cumdt-( (licon-2) * dstep) ) )))*
     1                       h(i,ndy,2)
00620      Continue
          Elseif(n_or_s.eq.'n')then
           Do 621 i = 1,ndx+1
                    qv(i,1,3) = ( v_rad(i,1,li) +
     1              ( (v_rad(i,1,li+1)-v_rad(i,1,li)) /
     1              (dstep / (cumdt-( (licon-2) * dstep) ) ) ) )*
     1              h(i,1,2)
00621      Continue
          Endif
         Endif
C 22=============================================================

C Section 23 - For elevation boundaries, the velocity normal to the boundary must = 0 s.t.
C              the boundary velocities do not distort the prescribed elevation set-up. (This
C              has been checked and IS necessary).
C 23_____________________________________________________________
         If (y_e_or_v .eq. 'e') then
c set qv adjacent to driving boundary = 0.
          do 170 j = 1, ndy
           If(e_or_w.eq.'w') qv(1,j,3) = 0.0
           If(e_or_w.eq.'e') qv(ndx,j,3) = 0.0
00170      continue
          Endif

          If (x_e_or_v .eq. 'e') then
c set qu adjacent to driving boundary = 0.
          do 175 i = 1, ndx
           If(n_or_s.eq.'s') qu(i,1,3) = 0.0
           If(n_or_s.eq.'n') qu(i,ndy,3) = 0.0
00175      continue
          Endif
C 23=============================================================

C Section 24 - Calculation of the future step elevation value using finite-differencing.
C 24_____________________________________________________________
          illimit = 1
          iulimit = ndx
          jllimit = 1
          julimit = ndy

          If(y_e_or_v.eq.'e')then
           If(e_or_w.eq.'e')then
            iulimit = ndx-1
           ElseIf(e_or_w.eq.'w')then
            illimit = 2
           Endif
          Endif

          If(x_e_or_v.eq.'e')then
           If(n_or_s.eq.'s')then
            jllimit = 2
           Elseif(n_or_s.eq.'n')then
```

```
            julimit = ndy-1
           Endif
          Endif

C *APPLY CONTINUITY TO UPDATE ELEVATIONS*
          Do 220 i = illimit,iulimit
           Do 221 j = jllimit,julimit

           If(imask(i,j).eq.1)then
c  wet cell
           Ucomp = (1/dx)*(qu(i+1,j,3)-qu(i,j,3))
           Vcomp = (1/dy)*(qv(i,j+1,3)-qv(i,j,3))

           n(i,j,3) = n(i,j,2)-dt*(Ucomp+Vcomp)

C 24=============================================================

C - Continues onto

C Section 25 - Define total depths h() and determine flooding and drying.
C 25_____________________________________________________________
c  now look at total depth for cells which may go dry and define values of total depth h()
           hdepth = d(i,j)+n(i,j,3)

           If (hdepth .gt. d_limit) then
c  enough water in cell
           h(i,j,3) = hdepth
           Else
c  not enough water - cell to shallow
           imask(i,j) = -1
           h(i,j,3) = d_limit
c  therefore dry out the cell
           u(i,j,3) = 0
           v(i,j,3) = 0
           qu(i,j,3) = 0
           qv(i,j,3) = 0

           n(i,j,3) = d_limit - d(i,j)
           Endif

           Else
c  land cell
           n(i,j,3) = 0.0
           Endif

00221      Continue
00220      Continue

C Check for flooding of dry cells.
           flood = 1.25*d_limit

           Do 225 i = 1,ndx+1
           ip1 = i+1
           If (i.eq.ndx+1) ip1 =ndx+1
           im1 = i-1
           If (i.eq.1) im1 =1

           Do 226 j = 1,ndy+1
           jp1 = j+1
           If (j.eq.ndy+1) jp1 =ndy+1
           jm1 = j-1
           If (j.eq.1) jm1 =1
```

```
c-only look at intertidal cells which are dry at this time.
            If(imask(i,j).eq.-1)then
c this is a cell which has been dried.
c bed level is -
            bed = d(i,j)

            If(imask(ip1,j).eq.1)then
c east neighbour is wet
             If(bed+n(ip1,j,3).gt.flood)then
              n(i,j,3) = n(ip1,j,3)
              h(i,j,3) = bed + n(ip1,j,3)
              h(i,j,2) = bed + n(ip1,j,3)
              imask(i,j) = 1
             Endif
            Endif

            If(imask(im1,j).eq.1)then
c west neighbour is wet
             If(bed+n(im1,j,3).gt.flood)then
              n(i,j,3) = n(im1,j,3)
              h(i,j,3) = bed + n(im1,j,3)
              h(i,j,2) = bed + n(im1,j,3)
              imask(i,j) = 1
             Endif
            Endif

            If(imask(i,jp1).eq.1)then
c north neighbour is wet
             If(bed+n(i,jp1,3).gt.flood)then
              n(i,j,3) = n(i,jp1,3)
              h(i,j,3) = bed + n(i,jp1,3)
              h(i,j,2) = bed + n(i,jp1,3)
              imask(i,j) = 1
             Endif
            Endif

            If(imask(i,jm1).eq.1)then
c south neighbour is wet
             If(bed+n(i,jm1,3).gt.flood)then
              n(i,j,3) = n(i,jm1,3)
              h(i,j,3) = bed + n(i,jm1,3)
              h(i,j,2) = bed + n(i,jm1,3)
              imask(i,j) = 1
             Endif
            Endif

            Endif

c  ensure there are no negative total depths
            If (h(i,j,2) .lt. d_limit) h(i,j,2) = d_limit
            If (h(i,j,3) .lt. d_limit) h(i,j,3) = d_limit


00226     Continue
00225     Continue
C 25=============================================================

C Section 26 -Calculate the new u and v values from the derived values of qu, qv and h.
C 26_____________________________________________________________
            Do 230 i = 1,ndx+1
```

```
            im1 = i-1
            If(i.eq.1) im1 = 1
            Do 231 j = 1,ndy+1
             jm1 = j-1
             If(j.eq.1) jm1 = 1

C Detemine whether or not the velocity vector is adjacent to land.
            If(imask(i,j).eq.1.and.imask(im1,j).eq.1)then
c not in a cell immediately east or west of a land cell

             If(i.le.ndx)then
              udepth = ((h(i,j,3)+h(im1,j,3)+h(i,j,2)+h(im1,j,2))/4)
             Else
              udepth = ((h(im1,j,3)+h(im1,j,2))/2)
C ** Necessary for when applying a radiating boundary for symmetry.
             Endif

             If (udepth .gt. d_limit*0.99) then
              u(i,j,3) = qu(i,j,3)/udepth
             Else
              u(i,j,3) = 0.0
             Endif

            Endif

C Detemine whether or not the velocity vector is adjacent to land
            If(imask(i,j).eq.1.and.imask(i,jm1).eq.1)then
c not in a cell immediately north or south of a land cell

             If(j.le.ndy)then
              vdepth = (h(i,j,3)+h(i,jm1,3)+h(i,j,2)+h(i,jm1,2))/4
             Else
              vdepth = (h(i,jm1,3)+h(i,jm1,2))/2
C ** Necessary for when applying a radiating boundary for symmetry.
             Endif

             If (vdepth .gt. d_limit*0.99) then
              v(i,j,3) = qv(i,j,3)/vdepth
             Else
              v(i,j,3) = 0.0
             Endif

C Check for supercritical flow
             speed = SQRT(u(i,j,3)**2 + v(i,j,3)**2)
             uvdepth = (udepth+vdepth)/2
             celer = SQRT(9.81*uvdepth)
             cfl = dt*(celer + speed)/dx

             If (speed .gt. celer .or. cfl .gt. 1.0)then
c Supercritical flow created - dry out cell to avoid stability problems
              imask(i,j) = -1
              h(i,j,3) = d_limit
              u(i,j,3) = 0.0
              v(i,j,3) = 0.0
              qu(i,j,3) = 0.0
              qv(i,j,3) = 0.0
c Cell dried out => re-set elevation.
              n(i,j,3) = d_limit - d(i,j)
             Endif

             Endif
C 26
```

```
C - Continues onto

C Section 27 - Calculation of the residual tidal velocity between defined starting and end points.
C 27_____________________________________________________________
          If(rt_y_or_n.eq.'y')then
C Residual calculations enabled.
          If(cumdt.ge.simustart.and.cumdt.le.simuend)then
           usum(i,j) = usum(i,j) + (u(i,j,3)*dt)
           vsum(i,j) = vsum(i,j) + (v(i,j,3)*dt)

           If(cumdt.eq.simuend)then
           x = xmin + (i-1)*dx
           y = ymin + (j-1)*dy
           usum(i,j) = usum(i,j) / (simuend - simustart)
           vsum(i,j) = vsum(i,j) / (simuend - simustart)
          Endif
         Endif
        Endif
00231   Continue
00230   Continue
C 27=============================================================


C Section 28 - Calculate the corner values in each cell for use in advection s.t. adjacent to
C          land = 0 if no-slip boundary selected, otherwise free-slip is imparted (slip = 0/1).
C 28_____________________________________________________________
        Do 160 i = 1,ndx+1
         im1 = i-1
         If (i .eq. 1) im1 = 1

        Do 161 j = 1,ndy+1
         jm1 = j-1
         If (j .eq. 1) jm1 = 1


c -cell corner values of U-

          If(imask(i,j).eq.1.and.imask(im1,j).eq.1.and.
   +      imask(i,jm1).eq.1.and.imask(im1,jm1).eq.1)then
c no neighbouring land cells, so
          ucor(i,j,3) = (u(i,j,3)+u(i,jm1,3))/2
          Elseif(slip.eq.1)then
          If(imask(i,j).eq.1.and.imask(i,jm1).eq.1.and.
   +      imask(im1,jm1).eq.1)then
c NW cell is land, but free slip, so
          ucor(i,j,3) = u(i,jm1,3)
          Elseif(imask(i,j).eq.1.and.imask(im1,j).eq.1.and.
   +      imask(im1,jm1).eq.1)then
c SE cell is land, but free slip, so
          ucor(i,j,3) = u(i,j,3)
          Elseif(imask(i,j).eq.1.and.imask(i,jm1).eq.1.and.
   +      imask(im1,j).eq.1)then
c SW cell is land, but free slip, so
          ucor(i,j,3) = u(i,j,3)
          Elseif(imask(im1,j).eq.1.and.imask(i,jm1).eq.1.and.
   +      imask(im1,jm1).eq.1)then
c NE cell is land, but free slip, so
          ucor(i,j,3) = u(i,jm1,3)
          Elseif(imask(i,j).eq.1.and.imask(im1,j).eq.1)then
c SE + SW cells are land, but free slip, so
          ucor(i,j,3) = u(i,j,3)
          Elseif(imask(i,jm1).eq.1.and.imask(im1,jm1).eq.1)then
```

```
c NE + NW cells are land, but free slip, so
              ucor(i,j,3) = u(i,jm1,3)
             Endif
            Else
c No-slip condition imposed, as at least one neighbour must be a land cell.
             ucor(i,j,3) = 0.0
            Endif

c -cell corner values of V-

            If(imask(i,j).eq.1.and.imask(im1,j).eq.1.and.
     +      imask(i,jm1).eq.1.and.imask(im1,jm1).eq.1)then
c No neighbouring land cells,so
             vcor(i,j,3) = (v(i,j,3)+v(im1,j,3))/2
            Elseif(slip.eq.1)then
             If(imask(i,j).eq.1.and.imask(i,jm1).eq.1.and.
     +      imask(im1,jm1).eq.1)then
c NW cell is land, but free slip, so
              vcor(i,j,3) = v(i,j,3)
             Elseif(imask(i,j).eq.1.and.imask(im1,j).eq.1.and.
     +      imask(im1,jm1).eq.1)then
c SE cell is land, but free slip, so
              vcor(i,j,3) = v(im1,j,3)
             Elseif(imask(i,j).eq.1.and.imask(i,jm1).eq.1.and.
     +      imask(im1,j).eq.1)then
c SW cell is land, but free-slip, so
              vcor(i,j,3) = v(i,j,3)
             Elseif(imask(im1,j).eq.1.and.imask(i,jm1).eq.1.and.
     +.     imask(im1,jm1).eq.1)then
c NE cell is land, but free slip, so
              vcor(i,j,3) = v(im1,j,3)
             Elseif(imask(i,j).eq.1.and.imask(i,jm1).eq.1)then
c SW + NW cells are land, but free slip, so
              vcor(i,j,3) = v(i,j,3)
             Elseif(imask(im1,j).eq.1.and.imask(im1,jm1).eq.1)then
c NE + SE cells are land, but free slip, so
              vcor(i,j,3) = v(im1,j,3)
             Endif
            Else
c No-slip condition imposed, as at least one neighbour must be a land cell.
             vcor(i,j,3) = 0.0
            Endif
00161      Continue
00160      Continue

C In order to ensure that free slip (open) boundary does not generate vorticity.
           do 162 j = 1, ndy+1
            vcor(1    ,j,3) = vcor(2  ,j,3)
00162       vcor(ndx+1,j,3) = vcor(ndx,j,3)
           do 163 i = 1, ndx+1
            ucor(i,1    ,3) = ucor(i,2  ,3)
00163       ucor(i,ndy+1,3) = ucor(i,ndy,3)
C 28=========================================================================

C Section 29 - Decide if output step is necessary and pass the required information to the
C              relevant output subroutine.  Also output nesting data and tidal curves if required.
C 29_____________________________________________________________________
c output a time string of results at selected cells for plotting as tidal curve profiles.
           If(abs(ioseries(iscount)-step).lt.1)then
            Do 250 i = 1,Icurves
            j = 40+i
```

```
            Write(j,*) u(Ipx(i),Ipy(i),2),v(Ipx(i),Ipy(i),2),
     +                 (h(Ipx(i),Ipy(i),2)-d(Ipx(i),Ipy(i)))
250         Continue

            If(rad.eq.'y')then
C Record output boundary conditions if required for future use as pre-defined radiating data.
            If(trigger.eq.'E')then
             write(26,10000) (u(ndx+1,j,3),j=1,ndy+1)
            ElseIf(trigger.eq.'W')then
             write(26,10000) (u(1,j,3),j=1,ndy+1)
            ElseIf(trigger.eq.'N')then
             write(26,10000) (v(i,ndy+1,3),i=1,ndx+1)
            ElseIf(trigger.eq.'S')then
             write(26,10000) (v(i,1,3),i=1,ndx+1)
            Endif
           Endif

           iscount = iscount + 1
          Endif


          If (abs(io_out(iocount)-step).lt.1)then
C **Then this time-step is an output step**

c output results via the relevant file type, (xyuv), or (xyu - xyv)

          If (scat_out .eq. 1) call output(hname, iocount,
     1   vortlim,xmin,ymin,io_step,dt,cumdt,simustart,simuend,
     1         uvout,nout,vout,rt_y_or_n)

          If (grd_out .eq. 1) call grd_output(hname, iocount,
     1   vortlim, xmin,ymin,io_step,dt,cumdt,simustart,simuend,
     1         uvout,nout,vout)

         Write(51,5200)cumdt,xfrict1,yfrict1,xdiff1,ydiff1
         Write(51,5200)cumdt,xfrict2,yfrict2,xdiff2,ydiff2
         Write(51,5200)cumdt,xfrict3,yfrict3,xdiff3,ydiff3
         Write(51,5200)cumdt,xfrict4,yfrict4,xdiff4,ydiff4

          iocount = iocount +1
         Endif
C 29=============================================================

C Section 30 - Move everything back a full timestep and return to the next time-step.
C 30_____________________________________________________________
         Do 260 i = 1,ndx+1
          Do 261 j = 1,ndy+1

          u(i,j,2) = u(i,j,3)
          u(i,j,3) = 0

          qu(i,j,1) = qu(i,j,2)
          qu(i,j,2) = qu(i,j,3)
          qu(i,j,3) = 0

          v(i,j,2) = v(i,j,3)
          v(i,j,3) = 0

          qv(i,j,1) = qv(i,j,2)
          qv(i,j,2) = qv(i,j,3)
          qv(i,j,3) = 0
```

```
            n(i,j,2) = n(i,j,3)
            n(i,j,3) = tide1

            h(i,j,1) = h(i,j,2)
            h(i,j,2) = h(i,j,3)
            h(i,j,3) = d(i,j)+tide1

            ucor(i,j,2) = ucor(i,j,3)
            ucor(i,j,3) = 0

            vcor(i,j,2) = vcor(i,j,3)
            vcor(i,j,3) = 0

00261       Continue
00260       Continue

00100       Continue
C 30=========================================================================
C                                   NEXT TIME STEP


C Section 31 - Close all the files left open for recording.
C 31_________________________________________________________________________
            Do 300 i = 1,Icurves
            j = 40+i
            close(j)
300         Continue

            If(rad.eq.'y')close(26)
C 31=========================================================================

5200        Format (5F17.10)

C Section 32 - End statement.
C 32_________________________________________________________________________
            Print*,' '
            Print*,' This programme is written by Scott J.Couch. This'
            Print*,' version incorporates the full continuity equation,'
            Print*,' and the following terms in the momentum equation:'
            Print*,'  (i)      Temporal acceleration,'
            Print*,'  (ii)     pressure gradient,'
            Print*,'  (iii)    bottom friction,'
            Print*,'  (iv)     convective momentum,'
            Print*,'  (v)      eddy viscosity,'
            Print*,'  (vi)     coriolis,and'
            Print*,'  (vii)    wind stress.'
            Print*,' '
C 32=========+===============================================================


C Section 33 - Error warnings regarding bathymetry inputs.
C 33_________________________________________________________________________
            Goto 5751
05750       close(20)
             write(*,*)'[Warning]'
             write(*,*)'Error in reading file'
05751       Continue

            Goto 5753
05752       close(20)
             write(*,*)'[Warning]'
```

```
          write(*,*)'arrays not big enough'
05753   Continue
          write(*,*)'end of test'
C 33=============================================================
C END SIMULATION
          END


C+++++++++++++++++++++++++++++++++++++++++++++++++++++++++++++++++++++++
C++++++++++++++++++++++ SUBROUTINES ++++++++++++++++++++++++++++++++++
C+++++++++++++++++++++++++++++++++++++++++++++++++++++++++++++++++++++++

C+++++++++++++++++++++++++++++++++++++++++++++++++++++++++++++++++++++++
C+++++ SUBROUTINE SA - FOUR-POINT UPWIND SCHEME FOR DERIVING THE ++++
C+++++ CONVECTIVE MOMENTUM TERMS AND CALCULATION OF THE          ++++
C+++++ TURBULENT CLOSURE TERMS USING EDDY VISCOSITY              ++++
C+++++++++++++++++++++++++++++++++++++++++++++++++++++++++++++++++++++++


C Section SA1 - Set up the arrays, common blocks and variables required by the sub-routine.
C A1_____________________________________________________________________
c-----------------------------------------------------------------
          subroutine QUICK2(i,j,ix,iy,d_limit,x_e_or_v,y_e_or_v,slip)

c four-point upwind scheme, EQ. 9.53, 10.6  Fletcher Vol 1 - Equivalent to QUICK - see Leonard
c (1981), pp. 22-24 if set q = 0.375  -  See Thesis for description.

C "The very oscillatory behaviour of the three-point centred-difference representation
C  and the very dissipative nature of the two-point upwind scheme suggests that a four-
C  point representation will be necessary to obtain satisfactory results."

C "The equation has been deliberately written as a modification to the three-point centred
C  finite difference represenation [(T(j+1)-T(j-1))/2dx].  the parameter q controls the
C  size of the modification."

C "A Taylor series expansion about node j indicates that
C  T(j-2)-3T(j-1)+3T(j)-T(j+1) = [-dx**3(d^3T/dx^3)+0.5dx**4(d^4T/dx^4)+.....]
C  That is, the modification can be used to counteract specific terms in the Taylor series
C  expansion for the complete equation.  In particular, the choice q=0.5 eliminates the
C  -dx**3(d^3T/dx^3) term and makes the equation of order (dx^3) (i.e. third-order upwinding)."

C "Increasing q is seen to produce a smoother solution but a more diffuse solution,"

C " ... a four-point upwind scheme avoids excessive dispersive-related oscillations (Sects.
C  9.3.2 and 9.4.3) without introducing unacceptable dissipation, as is the case with the
C  two-point upwind scheme."

C Leonard (1984) - "...it is now quite firmly established that third-order upwinding provides
C  a firm foundation for building further refinements in specific applications."

          implicit real(a-h), real(o-z)
c-----------------------------------------------------------------
          integer mx,my,mt
          include 'tfd1_21.cmn'
c-----------------------------------------------------------------
          Double precision qu(mx,my,mt) , qv(mx,my,mt)
          Double precision u(mx,my,2:mt),v(mx,my,2:mt)
          Double precision ucor(mx,my,2:mt),vcor(mx,my,2:mt)
          Double precision usum(mx,my), vsum(mx,my)

          common/flows/ qu,qv,u,v,ucor,vcor,usum,vsum
```

```
c-----------------------------------------------------------------------

      Double precision n(mx,my,2:mt), h(mx,my,mt)
      Double precision d(mx,my)

      common/elevs/  n, h, d
c-----------------------------------------------------------------------
      real Manvar(mx,my), manning

      common/friction/ manvar, manning
c-----------------------------------------------------------------------

      integer imask(mx,my)

      common/mask/ imask
c-----------------------------------------------------------------------
      Double precision vort(mx,my)
      integer io_out(10000)
      integer ioseries(10000)
      integer scat_out, grd_out

      common/out/ vort, io_out, ioseries, scat_out, grd_out
c-----------------------------------------------------------------------
      Double precision nIn(10000)
      Double precision vIn(10000)
      integer InTime(10000)
      double precision z0, tide1, Intstep

      common/input/ nIn,vIn,InTime,z0, tide1, Intstep
c-----------------------------------------------------------------------
      double precision xconv, xconv1,xconv2
      double precision yconv, yconv1,yconv2
      double precision xdiff,ydiff

      common/convdiff/xconv, xconv1,xconv2,yconv, yconv1,yconv2,
     &    xdiff,ydiff
c-----------------------------------------------------------------------
      real    x, y,  dx,  dy, ran
      integer ndx, ndy, slip

      common/grid_stuff/ x,y,dx,dy,ndx,ndy
c-----------------------------------------------------------------------
      integer i,j,ix,iy,k_im1,k_jm1
c-----------------------------------------------------------------------
      DOUBLE PRECISION
     +            hx1a, hy1a,

     +     fip1, fip2, fim1, fim2,fi,

     +     fjp1, fjp2, fjm1, fjm2,fj,

     +            xdiff1, xdiff2, xdiff3,
     +            ydiff1, ydiff2, ydiff3,

     +            edvisc
c-----------------------------------------------------------------------
      Character y_e_or_v*1,x_e_or_v*1
c-----------------------------------------------------------------------
C SA1==========================================================================
```

C Section SA2 - List of variable names, description, and units specific to SA.

```
C SA2_____________________________________________________________
C k_.... = Trigger to prevent calculation of convective momentum on a land cell.
c F(i/j)(p/m)( /1/2/3) = Flux across i/j face off cell (p)lus or (m)inus 0,1,2 or 3.
c (x/y)diff(1/2/3) = The components of turbulent diffusion (explained in program).
c (x/y)conv(1/2) = The components of convective momentum (explained in program).
c (x/y)diff = The summated effect of the turbulent diffusion terms.
c (x/y)conv = the summated effect of the convective momentum terms.
c edvisc = The value of eddy viscosity in a particular cell (bed generated turbulence only represented).
c H(x/y)1a = The depth centred around x/y (time-lapsed by one time-step).
c ui = The u-component of velocity centred around the point being analysed (u or v).
c vj = The v-component of velocity centred around the point being analysed (u or v).
c q = Controls the modification of the fourth-order part of the scheme (0.375 = QUICK, 0.5 =
c    fully third-order).
C SA2=============================================================

C Section SA3 - Initialise constants and set default values.
C SA3_____________________________________________________________

      g = 9.81
c Selecting q = 0.5 becomes fully third order.
c Selecting q = 0.375 is exactly equivalent to QUICK
c Selecting q = 0 gives centred-difference
      q = 0.5

C SA3=============================================================

C Section SA4 - Check for neighbouring dry cells, which must NOT be included in mean depths
C used in this routine. Such values are excluded by making switches (eg k_im1) equal to zero.
C SA4_____________________________________________________________
      im3 = i-3
      jm3 = j-3
      im2 = i-2
      jm2 = j-2
      im1 = i-1
      jm1 = j-1

      ip3 = i+3
      ipc3= i+3
      jp3 = j+3
      jpc3= j+3
      ip2 = i+2
      ipc2= i+2
      jp2 = j+2
      jpc2= j+2
      ip1 = i+1
      ipc1= i+1
      ipx1= i+1
      ipy1= i+1
      jp1 = j+1
      jpc1= j+1
      jpx1= j+1
      jpy1= j+1

      k_im1 = 1
      k_jm1 = 1

      If (im3.lt.1)     im3 = 1
      If (jm3.lt.1)     jm3 = 1
      If (im2.lt.1)     im2 = 1
      If (jm2.lt.1)     jm2 = 1
```

```
      If (im1.lt.1)       im1 = 1
      If (jm1.lt.1)       jm1 = 1
      If (ip1.gt.ndx)     ip1 = ndx
      If (jp1.gt.ndy)     jp1 = ndy
      If (ip2.gt.ndx)     ip2 = ndx
      If (jp2.gt.ndy)     jp2 = ndy
      If (ip3.gt.ndx)     ip3 = ndx
      If (jp3.gt.ndy)     jp3 = ndy
      If (ipc1.gt.ndx+1)ipc1 = ndx+1
      If (jpc1.gt.ndy+1)jpc1 = ndy+1
      If (ipc2.gt.ndx+1)ipc2 = ndx+1
      If (jpc2.gt.ndy+1)jpc2 = ndy+1
      If (ipc3.gt.ndx+1)ipc3 = ndx+1
      If (jpc3.gt.ndy+1)jpc3 = ndy+1

      If(y_e_or_v.ne.'a')then
       If(ipx1.gt.ndx+1)ipx1 = ndx+1
       If(jpx1.gt.ndy) jpx1 = ndy
       If(ipy1.gt.ndx+1)ipy1 = ndx+1
       If(jpy1.gt.ndy) jpy1 = ndy
      Endif
      If(x_e_or_v.ne.'a')then
       If(ipx1.gt.ndx) ipx1 = ndx
       If(jpx1.gt.ndy+1)jpx1 = ndy+1
       If(ipy1.gt.ndx) ipy1 = ndy
       If(jpy1.gt.ndy+1)jpy1 = ndy+1
      Endif


      If (imask(im1,j) .le. 0) k_im1 = 0
      If (imask(i,jm1) .le. 0) k_jm1 = 0
C SA4=============================================================

C Section SA5 - Evaluate convective acceleration for the x-momentum equation -
C                 (du(uh)/dx + dv(uh)/dy  ie flux of (uh))
C SA5_____________________________________________________________
      If (ix.eq.1)then
c Find  x component convective acclns - xconv1 +xconv2

c Default value
       xconv1  = 0

c Hx1a = H centred around u(i,j,2)
       Hx1a = (0.5*(h(i,  j,2)+h(i,  j,1))+
     1   0.5*(h(im1,j,2)+h(im1,j,1))*k_im1)/(1+k_im1)

       If (Hx1a .lt. 0.99*d_limit) Hx1a = d_limit

c---------------------- evaluate  du(uh)/dx----------------

c Find fluxes for upwinding of du(uh)/dx (on land, qu and u = 0, therefore correct gradient
c is applied.  Across boundaries, the boundary value is maintained, so no gradient, prevents
c 'funnies' occuring across boundaries. (At boundaries/land, not calculated, as would not
c enter the sub-routine because of controls in the main program).

       Fip2 = (qu(ipc2,j,2)*u(ipc2,j,2))
       Fip1 = (qu(ipc1,j,2)*u(ipc1,j,2))
       Fi   = qu(i  ,j,2)*u(i  ,j,2)
       Fim1 = (qu(im1,j,2)*u(im1,j,2))
       Fim2 = (qu(im2,j,2)*u(im2,j,2))
```

```
          ui  = u(i,j,2)

          If (ui.gt.0) then
c west is upwind
          xconv1 = (Fip1 - Fim1)/(2*dx)+
     1      (q/(3*dx))*(Fim2 -3*Fim1 +3*Fi -Fip1)

          Elseif (ui.lt.0)then
c east is upwind
          xconv1 = (Fip1 - Fim1)/(2*dx)+
     1      (q/(3*dx))*(Fim1 -3*Fi +3*Fip1 -Fip2)
          Else

          xconv1 = 0

          Endif

c Find xconv2 component of convective acclns
c default value
          xconv2  = 0

c---------------------- evaluate dv(hu)/dy----------------

c Find  fluxes for upwinding of dv(hu)/dy
          Fjp2 = (qu(i,jp2,2)*(vcor(i,jpc2,2) + vcor(i,jpc3,2))/2.0)
          Fjp1 = (qu(i,jp1,2)*(vcor(i,jpc1,2) + vcor(i,jpc2,2))/2.0)
          Fj   = qu(i,j  ,2)*(vcor(i,j  ,2) + vcor(i,jpc1,2))/2.0
          Fjm1 = (qu(i,jm1,2)*(vcor(i,jm1,2) + vcor(i,j  ,2))/2.0)
          Fjm2 = (qu(i,jm2,2)*(vcor(i,jm2,2) + vcor(i,jm1,2))/2.0)

          vj  = (vcor(i,j,2)+ vcor(i,jpc1,2))/2.0

          If (vj.gt.0) then
c south is upwind
          xconv2 = (Fjp1 - Fjm1)/(2*dy)+
     1      (q/(3*dy))*(Fjm2 -3*Fjm1 +3*Fj -Fjp1)

          Elseif(vj.lt.0)then
c north is upwind
          xconv2 = (Fjp1 - Fjm1)/(2*dy) +
     1      (q/(3*dy))*(Fjm1 -3*Fj +3*Fjp1 -Fjp2)

          Else

          xconv2 = 0

          Endif

C SA5==========================================================

C - Continues onto

C Section SA6 - X-directed turbulent closure model ( using eddy viscosity).
C SA6__________________________________________________________
C Set-Up eddy viscosity coeff. - see thesis ch3 ((0.4*g^0.5*n*|U|h^(5/6))/6) (Uh^(5/6) = qu/h^(1/6).
          edvisc = (0.2088*((Manvar(i,j)+Manvar(im1,j))/2)*
     1                (SQRT((qu(i,j,2)**2)+((qv(i,j,2)+qv(im1,j,2)+
     1              qv(i,jpx1,2)+qv(im1,jpx1,2))/4)**2)))/Hx1a**(0.166666)

C Again, following Falconer, edvisc*(2*(cd2uh/cdx2)+(cd2uh/cdy2)+(cd2vh/cdxcdy))

C xdiff1 = 2*(cd2uh/cdx2)
```

```
          xdiff1 = (2/(dx*dx))*
     1              (( qu(ipy1,j ,2))+
     1              ( qu(im1,j ,2))-
     1              (2* qu(i ,j ,2)))
C xdiff2 = cd2uh/cdy2
          If((imask(i,jpy1).eq.1.and.imask(i,jm1).eq.1).or.slip.eq.0)then
          xdiff2 = (1/(dy*dy))*
     1              (( qu(i ,jpy1,2))+
     1              ( qu(i ,jm1,2))-
     1              (2* qu(i ,j ,2)))
          Else
          xdiff2 = 0
          Endif
C xdiff3 = cd2vh/cdxcdy
          xdiff3 = (1/dx)*
     1              (((1/dy)*(qv(i ,jpx1,2)-qv(i ,j ,2)))-
     1         (( 1/dy)*(qv(im1,jpx1,2)-qv(im1,j ,2))))

          xdiff = edvisc*(xdiff1+xdiff2+xdiff3)
C
C SA6=============================================================
          Endif
c - From section SA5 thro' SA6


C Section SA7 - Evaluate convective acceleration for the y-momentum equation -
C                 (dv(vh)/dy + du(vh)/dx  ie flux of (vh))
C SA7_____________________________________________________________
          If (iy.eq.1)then
c Find  x component convective acclns - xconv1 +xconv2

c Default value
          yconv1  = 0

C Hy1a = H centred around v(i,j,2)
          Hy1a = (0.5*(h(i,j,  2)+h(i,j,  1))+
     1       0.5*(h(i,j-1,2)+h(i,j-1,1))*k_jm1)/(1+k_jm1)

          If (Hy1a .lt. 0.99*d_limit) Hy1a=d_limit
c---------------------- evaluate dv(vh)/dy ----------------------

c Find fluxes for upwinding of dv(vh)/dy (on land, qu and u = 0, therefore correct gradient
c is applied. Across boundaries, the boundary value is maintained, so no gradient, prevents
c 'funnies' occuring across boundaries. (On boundaries/land, not calculated, as would not
c enter the sub-routine because of controls in the main program).

          Fjp2 = (qv(i,jpc2,2)*v(i,jpc2,2))
          Fjp1 = (qv(i,jpc1,2)*v(i,jpc1,2))
          Fj  = qv(i ,j,2)*v(i ,j,2)
          Fjm1 = (qv(i,jm1,2)*v(i,jm1,2))
          Fjm2 = (qv(i,jm2,2)*v(i,jm2,2))

          vj  = v(i,j,2)

          If (vj.gt.0) then
c South is upwind
          yconv1 = (Fjp1 - Fjm1)/(2*dy)+
     1       (q/(3*dy))*(Fjm2 -3*Fjm1 +3*Fj -Fjp1)

          Elseif(vj.lt.0)then
c North is upwind
          yconv1 = (Fjp1 - Fjm1)/(2*dy)+
```

```
     1        (q/(3*dy))*(Fjm1 -3*Fj +3*Fjp1 -Fjp2)
          Else

          yconv1 = 0

          Endif

c Find yconv2 component of convective accins
c default value
          yconv2  = 0

c------------------------ evaluate du(hv)/dx ----------------------

c Find  fluxes for upwinding of du(hv)/dx

          Fip2 = (qv(ip2,j,2)*(ucor(ipc2,j,2) + ucor(ipc3,j,2))/2.0)
          Fip1 = (qv(ip1,j,2)*(ucor(ipc1,j,2) + ucor(ipc2,j,2))/2.0)
          Fi   = qv(i  ,j,2)*(ucor(i  ,j,2) + ucor(ipc1,j,2))/2.0
          Fim1 = (qv(im1,j,2)*(ucor(im1,j,2) + ucor(i  ,j,2))/2.0)
          Fim2 = (qv(im2,j,2)*(ucor(im2,j,2) + ucor(im1,j,2))/2.0)

          ui  = (ucor(i,j,2)   + ucor(ipc1,j,2))/2.0

          If (ui.gt.0) then
C West is upwind
          yconv2 = (Fip1 - Fim1)/(2*dx)+
     1      (q/(3*dx))*(Fim2 -3*Fim1 +3*Fi -Fip1)
          Elseif(ui.lt.0)then
C East is upwind
          yconv2 = (Fip1 - Fim1)/(2*dx)+
     1      (q/(3*dx))*(Fim1 -3*Fi +3*Fip1 -Fip2)

          Else

          yconv2 = 0

          Endif

C SA7==========================================================

C - Continues onto

C Section SA8 - Y-directed turbulent closure model (using eddy viscosity).
C SA8__________________________________________________________
C Set-Up eddy viscosity coeff. - see thesis ch3 ((0.4*g^0.5*n*|U|h^(5/6))/6) (Uh^(5/6) = qu/h^(1/6).
          edvisc = (0.2088*((Manvar(i,j)+Manvar(i,jm1))/2)*
     1        (SQRT((qv(i,j,2)**2)+((qu(i,j,2)+qu(ipy1,j,2)+
     1        qu(i,jm1,2)+qu(ipy1,jm1,2))/4)**2)))/Hy1a**(0.166666)


C Again, following Falconer, edvisc*(2*(cd2vh/cdy2)+(cd2vh/cdx2)+(cd2uh/cdxcdy))

C ydiff1 = 2*(cd2vh/cdy2)
          ydiff1 = (2/(dy*dy))*
     1              (( qv(i  ,jpx1,2))+
     1              ( qv(i  ,jm1,2))-
     1              (2* qv(i  ,j  ,2)))
C ydiff2 = cd2vh/cdx2
          If((imask(ipx1,j).eq.1.and.imask(im1,j).eq.1).or.slip.eq.0)then
          ydiff2 = (1/(dx*dx))*
     1              (( qv(ipx1,j  ,2))+
     1              ( qv(im1,j  ,2))-
```

```
     1                (2* qv(i  ,j  ,2)))
          Else
           ydiff2 = 0
          Endif
C ydiff3 = cd2uh/cdxcdy
          ydiff3 = (1/dy)*
     1              (((1/dx)*(qu(ipy1,j  ,2)-qu(i  ,j  ,2)))-
     1              (( 1/dx)*(qu(ipy1,jm1,2)-qu(i  ,jm1,2))))

          ydiff = edvisc*(ydiff1+ydiff2+ydiff3)

C
C SA8=============================================================
          Endif
c - From section SA7 thro' SA8


C Section SA9 - Return to main program.
C SA9_____________________________________________________________
          Return
          END
C ++++++++++++++++++++++++++++++++++++++++++++++++++++++++++++++++++++++++
C ++++++++  SUBROUTINE SB - SCALAR OUTPUT (ie xyuv format in one file). ++++++++
C ++++++++++++++++++++++++++++++++++++++++++++++++++++++++++++++++++++++++

C Section SB1 - Set up the arrays, common blocks and variables required by the sub-routine.
C SB1_____________________________________________________________
c-----------------------------------------------------------------
          subroutine output(hname, iocount,
     1   vortlim,xmin,ymin,io_step,dt,cumdt,simustart,simuend,
     1     uvout,nout,vout,rt_y_or_n)

c-----------------------------------------------------------------
          implicit real(a-h), real(o-z)

          integer mx,my,mt
          include 'tfd1_21.cmn'
c-----------------------------------------------------------------
          Double precision qu(mx,my,mt) , qv(mx,my,mt)
          Double precision u(mx,my,2:mt),v(mx,my,2:mt)
          Double precision ucor(mx,my,2:mt),vcor(mx,my,2:mt)
          Double precision usum(mx,my), vsum(mx,my)

          common/flows/ qu,qv,u,v,ucor,vcor,usum,vsum
c-----------------------------------------------------------------
          Double precision n(mx,my,2:mt), h(mx,my,mt)
          Double precision  d(mx,my)

          common/elevs/  n, h, d
c-----------------------------------------------------------------
          real Manvar(mx,my), manning

          common/friction/ manvar, manning
c-----------------------------------------------------------------
          integer imask(mx,my)

          common/mask/ imask
c-----------------------------------------------------------------
          Double precision vort(mx,my)
          integer io_out(10000)
          integer ioseries(10000)
          integer scat_out, grd_out
```

```
      common/out/ vort, io_out, ioseries, scat_out, grd_out
c-----------------------------------------------------------------
      Double precision nIn(10000)
      Double precision vIn(10000)
      integer InTime(10000)
      double precision z0, tide1, Intstep

      common/input/ nIn,vIn,InTime,z0, tide1, Intstep
c-----------------------------------------------------------------
      double precision xconv, xconv1,xconv2
      double precision yconv, yconv1,yconv2
      double precision xdiff,ydiff

      common/convdiff/xconv, xconv1,xconv2,yconv, yconv1,yconv2,
     &     xdiff,ydiff
c-----------------------------------------------------------------
      real    x, y, dx, dy
      integer ndx, ndy

      common/grid_stuff/ x,y,dx,dy,ndx,ndy
c-----------------------------------------------------------------
      integer i,j
c-----------------------------------------------------------------
      real simustart,simuend,cumdt
      integer iocount,io_step
      DOUBLE PRECISION  vortlim

      character  hname*123

      character  uvout*1, nout*1, vout*1, gname*2, rt_y_or_n*1

      character*123 floname, vortname, elevname, rdname
c-----------------------------------------------------------------
C SB1==========================================================================


C Section SB2 - Initialise constants, set default values and set stem names of output files.
C SB2__________________________________________________________________________
      zilch = 0.0
      one = 1.0
      count = 0

      floname(1:123) = ' '
      vortname(1:123) = ' '
      elevname(1:123) = ' '
      rdname = 'rd1.dat'

c Find end of name string in hname
      lname = index(hname,' ') -1
      floname(1:lname)= hname(1:lname)
      vortname(1:lname)= hname(1:lname)
      elevname(1:lname)= hname(1:lname)
      rdname(1:lname)= hname(1:lname)
      rdname(lname+1:lname+7) = 'rd1.dat'

      If (iocount.lt.10) then
c Set-up stem names with numeric naming between 1 and 9.
       write(gname,102)iocount
       floname(lname+1:lname+7) =  '-'//gname(1:1)//'.vec'
       vortname(lname+1:lname+7) =  '-'//gname(1:1)//'.dat'
       elevname(lname+1:lname+7) =  '-'//gname(1:1)//'.eta'
```

```
        Else
c Set-up stem names with numeric naming between 10 and 99.
         write(gname,103)iocount
         floname(lname+1:lname+8) =  '-'//gname(1:2)//'.vec'
         vortname(lname+1:lname+8) =  '-'//gname(1:2)//'.dat'
         elevname(lname+1:lname+8) =  '-'//gname(1:2)//'.eta'

        Endif
c Trying to use a numeric naming convention of more than 2 values IN THESE CASES takes the
c letter count in the file names to its limit, so the file name comes out incorrectly, and
c will not converse with WOLF.
C SB2=============================================================
C Section SB3 - Clear old output files and then re-establish them with the new names.
C SB3_____________________________________________________________
        open(11,file=floname,status='unknown')
        close(11,status='delete')
        open(11,file=floname,status='new')

        open(12,file=vortname,status='unknown')
        close(12,status='delete')
        open(12,file=vortname,status='new')

        open(13,file=elevname,status='unknown')
        close(13,status='delete')
        open(13,file=elevname,status='new')

        If(rt_y_or_n.eq.'y')then
         open(14,file=rdname,status='unknown')
        Endif
C SB3=============================================================


C Section SB4 - Calculate the vertical component of vorticity w = (cdv/cdx)-(cdu/cdy)
C               centred around the centre of each cell.
C SB4_____________________________________________________________

        If(vout.eq.'y')then
         Do 180 i = 1,ndx
          Do 181 j = 1,ndy
           If(imask(i,j).eq.1)then
            vort(i,j) = ((1/dx)*(((vcor(i+1,j,3)+vcor(i+1,j+1,3))/2)-
     +                  ((vcor(i,j,3)+vcor(i,j+1,3))/2)))-
     +                  ((1/dy)*(((ucor(i,j+1,3)+ucor(i+1,j+1,3))/2)-
     +                  ((ucor(i,j,3)+ucor(i+1,j,3))/2)))
           Else
            vort(i,j) = 0
           Endif
00181     Continue
00180     Continue
         Endif
C SB4=============================================================


C Section SB5 - Ouput the relevant variables.
C SB5_____________________________________________________________
         Do 240 i = 1,ndx
          Do 241 j = 1,ndy
c Calculate the grid cell co-ordinates
           x = xmin + (i-1)*dx
           y = ymin + (j-1)*dy
```

```
            If (imask(i,j).gt.0.and.ABS(n(i,j,3)).gt.0.0000001)then

c Cell is not land, so calculate the cell-centred and time-centred values of u,v and n.
             ux = (u(i+1,j,3)+u(i,j,3))/2
             vy = (v(i,j+1,3)+v(i,j,3))/2
             hcent = ((n(i,j,3)+n(i,j,2))/2)
            Else
c Cell is land, so all variables = 0
             ux = 0.0
             vy = 0.0
             hcent = 0.0
            Endif

c Output velocities, (xyuv file).
            If(uvout.eq.'y') Write(11,*)x,y,ux,vy

c Output elevations, (x,y,z,dx file).
            If(nout.eq.'y') Write(13,*)x,y,hcent,dx


cc          If(vout.eq.'y')then
c Output vorticity, (x,y,z,dx file)
cc          If ( abs(vort(i,j)).gt. vortlim) then
c Vorticity output is triggered - Note abs(vorticity) written out.
cc           Write(12,*)x,y,vort(i,j)*100000.0
cc          Endif
c Put in limits to scatter data for vorticity to establish the correct domain (b.L.H. corner).
cc          If (i.eq.1 .and. j.eq.1)then
cc           Write(12,*)x,y,zilch
cc          Endif
cc          If (i.eq.ndx .and. j.eq.ndy) then
c Put in limits to scatter data for vorticity to establish the correct domain (t.R.H. corner).
cc           Write(12,*)x,y,zilch
cc          Endif
cc         Endif

            If(vout.eq.'y')then
             If ( abs(vort(i,j)).gt. vortlim) then
c Output vorticity, (x,y,z,dx file). - Note abs(vorticity) written out
C**
              Write(12,*)x,y,(vort(i,j)*1000),dx
cc *100000
C**
             Endif

             If (i.eq.1 .and. j.eq.1)then
c Put in limits to scatter data for vorticity to establish the correct domain (b.L.H. corner).
              Write(12,*)x,y,zilch,one
             Endif
             If (i.eq.ndx .and. j.eq.ndy) then
c Put in limits to scatter data for vorticity to establish the correct domain (t.R.H. corner).
              Write(12,*)x,y,zilch,one
             Endif
            Endif

            If(rt_y_or_n.eq.'y'.and.cumdt.ge.simuend.and.
     +       cumdt.lt.(simuend+(io_step*dt)))then
c Residual velocity file is to be output.
             If (imask(i,j).gt.0.and.i.lt.ndx.and.j.lt.ndy)then
c Cell is not land, so calculate the cell-centred values of residual u and v.
              uxsum = (usum(i+1,j)+usum(i,j))/2
              vysum = (vsum(i,j+1)+vsum(i,j))/2
```

```
            Elseif(imask(i,j).gt.0.and.i.ge.ndy)then
c Special case to deal with radiating boundary to the east.
             uxsum = usum(i,j)
             vysum = vsum(i,j)
            Elseif(imask(i,j).gt.0.and.j.ge.ndx)then
c Special case to deal with radiating boundary to the north.
             vysum = vsum(i,j)
             uxsum = usum(i,j)
            Else
c Cell is land, so all variables = 0
             uxsum = 0.0
             vysum = 0.0
            Endif
c Output the residual velocity file, (x,y,u,v file).
            Write(14,*)x,y,uxsum,vysum
           Endif

00241    Continue
00240   Continue

C Write message to confirm output stage successful.
         write(*,'(a)') floname
C SB5=============================================================

C Section SB6 - Tidy up loose ends and return to the main program.
C SB6_____________________________________________________________
C Format statements used in file stem naming procedure.
00102   Format(i1)
00103   Format(i2)
C Close output files.
         close(11)
         close(12)
         close(13)
         close(14)

C Return to the main program
         Return
         END
C SB6=============================================================


C +++++++++++++++++++++++++++++++++++++++++++++++++++++++++++++++++++++++++++++
C ++++ SUBROUTINE SC - GRIDDED OUTPUT (ie xyu, xyv format in two separate files). ++++
C +++++++++++++++++++++++++++++++++++++++++++++++++++++++++++++++++++++++++++++

C Section SC1 - Set up the arrays, common blocks and variables required by the sub-routine.
C SC1_____________________________________________________________
c-------------------------------------------------------------
         subroutine grd_output(hname, iocount, vortlim, xmin,ymin,
     1                         io_step,dt,cumdt,simustart,simuend,
     1                         uvout,nout,vout)
c-------------------------------------------------------------
         implicit real(a-h), real(o-z)

         integer mx,my,mt
         include 'tfd1_21.cmn'
c-------------------------------------------------------------
c-------------------------------------------------------------
         Double precision qu(mx,my,mt) , qv(mx,my,mt)
         Double precision u(mx,my,2:mt),v(mx,my,2:mt)
```

```
      Double precision ucor(mx,my,2:mt),vcor(mx,my,2:mt)
      Double precision usum(mx,my), vsum(mx,my)

      common/flows/ qu,qv,u,v,ucor,vcor,usum,vsum
c-----------------------------------------------------------------
      Double precision n(mx,my,2:mt), h(mx,my,mt)
      Double precision  d(mx,my)

      common/elevs/  n, h, d
c-----------------------------------------------------------------
      real Manvar(mx,my), manning

      common/friction/ manvar, manning
c-----------------------------------------------------------------
      integer imask(mx,my)

      common/mask/ imask
c-----------------------------------------------------------------
      Double precision vort(mx,my)
      integer io_out(10000)
      integer ioseries(10000)
      integer scat_out, grd_out

      common/out/ vort, io_out, ioseries, scat_out, grd_out
c-----------------------------------------------------------------
      Double precision nIn(10000)
      Double precision vIn(10000)
      integer InTime(10000)
      double precision z0, tide1, Intstep

      common/input/ nIn,vIn,InTime,z0, tide1, Intstep
c-----------------------------------------------------------------
      double precision xconv, xconv1,xconv2
      double precision yconv, yconv1,yconv2
      double precision xdiff,ydiff

      common/convdiff/xconv, xconv1,xconv2,yconv, yconv1,yconv2,
     &     xdiff,ydiff
c-----------------------------------------------------------------
      real    x, y,  dx,  dy
      integer ndx, ndy

      common/grid_stuff/ x,y,dx,dy,ndx,ndy
c-----------------------------------------------------------------
      integer i,j
c-----------------------------------------------------------------
      real simustart,simuend,cumdt
      integer iocount,io_step
      real xmin, ymin
      DOUBLE PRECISION  vortlim
      character hname*123

      character  uvout*1, nout*1, vout*1, gname*3,  dsaa*4

      character*123 uname, vname, ename, vortname, pgname, rdname
c-----------------------------------------------------------------
C SC1============================================================

C Section SC2 - Initialise constants, set default values and set stem names of output files.
C SC2____________________________________________________________
      DSAA = 'DSAA'
```

```
      xmax = xmin + dx*(ndx-1)
      ymax = ymin + dy*(ndy-1)

      zilch = 0.0
      one = 1.0
      gname(1:3) = ' '
      uname(1:123) = ' '
      vname(1:123) = ' '
      ename(1:123) = ' '
      vortname(1:123) = ' '
      pgname(1:123) = ' '
      rdname = 'rd.dat'

c Find end of name string in hname
      lname = index(hname,' ') -1
      uname(1:lname)= hname(1:lname)
      vname(1:lname)= hname(1:lname)
      ename(1:lname)= hname(1:lname)
      vortname(1:lname)= hname(1:lname)
      pgname(1:lname)= hname(1:lname)
      rdname(1:lname)= hname(1:lname)
      rdname(lname+1:lname+7) = 'rd1.dat'

      If (iocount.lt.10) then
C Set-up stem names with numeric naming between 1 and 9.
       write(gname,102)iocount
       uname(lname+1:lname+9) =  '-u0'//gname(1:1)//'.grd'
       vname(lname+1:lname+9) =  '-v0'//gname(1:1)//'.grd'
       ename(lname+1:lname+9) =  '-e0'//gname(1:1)//'.grd'
       vortname(lname+1:lname+7) =  '-'//gname(1:1)//'.vrt'
       pgname(lname+1:lname+9) = '-pg'//gname(1:1)//'.grd'

      Elseif(iocount.lt.100) then
C Set-up stem names with numeric naming between 10 and 99.
     write(gname,103)iocount
       uname(lname+1:lname+9) =  '-u'//gname(1:2)//'.grd'
       vname(lname+1:lname+9) =  '-v'//gname(1:2)//'.grd'
       ename(lname+1:lname+9) =  '-e'//gname(1:2)//'.grd'
       vortname(lname+1:lname+8) =  '-'//gname(1:2)//'.vrt'
       pgname(lname+1:lname+9) = '-pg'//gname(1:2)//'.grd'
      Elseif(iocount.lt.1000)then
       write(gname,104)iocount
       uname(lname+1:lname+10) =  '-u'//gname(1:3)//'.grd'
       vname(lname+1:lname+10) =  '-v'//gname(1:3)//'.grd'
       ename(lname+1:lname+10) =  '-e'//gname(1:3)//'.grd'
       vortname(lname+1:lname+10) =  '-'//gname(1:3)//'.vrt'
       pgname(lname+1:lname+11) = '-pg'//gname(1:3)//'.grd'
      Endif
C SC2============================================================

C Section SC3 - Clear old output files and then re-establish them with the new names.
C SC3____________________________________________________________
      open(11,file=ename,status='unknown')
      close(11,status='delete')
      open(11,file=ename,status='new')

      open(12,file=uname,status='unknown')
c     close(12,status='delete')
c     open(12,file=uname,status='new')

      open(13,file=vname,status='unknown')
```

```
c       close(13,status='delete')
c       open(13,file=vname,status='new')

        If(vout.eq.'y')then
         open(15,file=vortname,status='unknown')
         close(15,status='delete')
         open(15,file=vortname,status='new')
        Endif

C This was for when I was looking at outputting the pressure gradient term.
cc      open(17,file=pgname,status='unknown')
cc      close(17,status='delete')
cc      open(17,file=pgname,status='new')
C SC3==========================================================

C Section SC4 - Calculate the vertical component of vorticity w = (cdv/cdx)-(cdu/cdy)
C               centred around the centre of each cell.
C SC4__________________________________________________________
        If(vout.eq.'y')then
         Do 180 i = 1,ndx
          Do 181 j = 1,ndy
           If(imask(i,j).eq.1)then
            vort(i,j) = ((1/dx)*(((vcor(i+1,j,3)+vcor(i+1,j+1,3))/2)-
     +                  ((vcor(i,j,3)+vcor(i,j+1,3))/2)))-
     +                  ((1/dy)*(((ucor(i,j+1,3)+ucor(i+1,j+1,3))/2)-
     +                  ((ucor(i,j,3)+ucor(i+1,j,3))/2)))
           Else
            vort(i,j) = 0
           Endif
00181     Continue
00180     Continue
        Endif
C SC4==========================================================

C Section SC5 - Ouput the relevant variables.
C SC5__________________________________________________________
        If(nout.eq.'y')then
c Establish the maximum and minimum values for the elevation file header.
         etamax = -10000.0
         etamin =  10000.0
         Do 1051 j = 1,ndy
         Do 1051 i = 1,ndx
          If (n(i,j,3).gt. etamax) etamax = n(i,j,3)
          If (n(i,j,3).lt. etamin) etamin = n(i,j,3)
01051     Continue

c Output elevations, (.grd file)
         write(11,'(a)')'DSAA'
         write(11,*)ndx,ndy
         write(11,*)xmin,xmax
         write(11,*)ymin,ymax
         write(11,*)etamin,etamax
         Do 2051 j=1,ndy+1
          write(11,*)(n(i,j,3),i=1,ndx+1)
02051    Continue
         Close(11)
        Endif

        If(uvout.eq.'y')then
c Establish the maximum and minimum values for the u-velocity file header.
```

```
          umax = -10000.0
          umin =  10000.0
          Do 1052 j = 1,ndy
          Do 1052 i = 1,ndx
           If (u(i,j,3).gt. umax) umax = u(i,j,3)
           If (u(i,j,3).lt. umin) umin = u(i,j,3)
01052     Continue


c Output the u-velocity component (.grd file)
          write(12,'(a)')DSAA
          write(12,*)ndx+1,ndy+1
          write(12,*)xmin,xmax
          write(12,*)ymin,ymax
          write(12,*)umin,umax
          Do 2052 j=1,ndy+1
           write(12,*)(u(i,j,3),i=1,ndx+1)
02052     Continue
          Close(12)

c Establish the maximum and minimum values for the v-velocity file header.
          vmax = -10000.0
          vmin =  10000.0
          Do 1053 j=1,ndy
          Do 1053 i = 1,ndx
           If (v(i,j,3).gt. vmax) vmax = v(i,j,3)
           If (v(i,j,3).lt. vmin) vmin = v(i,j,3)
01053     Continue

c Output the v-velocity component (.grd file)
          write(13,'(a)')DSAA
          write(13,*)ndx+1,ndy+1
          write(13,*)xmin,xmax
          write(13,*)ymin,ymax
          write(13,*)vmin,vmax
          Do 2053 j=1,ndy+1
           write(13,*)(v(i,j,3),i=1,ndx+1)
02053   Continue
          Close(13)
         Endif

          If(cumdt.ge.simuend.and.cumdt.lt.(simuend+(io_step*dt)))then
c Residual velocity file is to be output.
          open(14,file=rdname,status='unknown')
          Do 2055 i = 1,ndx
          Do 2055 j = 1,ndy
           x = xmin + (i-1)*dx
           y = ymin + (j-1)*dy
           If (imask(i,j).gt.0.and.i.lt.ndx.and.j.lt.ndy)then
c Cell is not land, so calculate the cell-centred values of residual u and v.
            uxsum = (usum(i+1,j)+usum(i,j))/2
            vysum = (vsum(i,j+1)+vsum(i,j))/2
           Elseif(imask(i,j).gt.0.and.i.ge.ndy)then
c Special case to deal with radiating boundary to the east.
            uxsum = usum(i,j)
            vysum = vsum(i,j)
           Elseif(imask(i,j).gt.0.and.j.ge.ndx)then
c Special case to deal with radiating boundary to the north.
            vysum = vsum(i,j)
            uxsum = usum(i,j)
           Else
c Cell is land, so all variables = 0
```

```
            uxsum = 0.0
            vysum = 0.0
           Endif
c Output the residual velocity file, (x,y,u,v file).
           Write(14,*)x,y,uxsum,vysum
02055     Continue
          Close(14)
          Endif

          If(vout.eq.'y')then
c Output vorticity, (x,y,z,dx file)
           Do 2100 i = 1,ndx
           Do 2100 j = 1,ndy
            x = xmin + (i-1)*dx
            y = ymin + (j-1)*dy
            If ( abs(vort(i,j)).gt. vortlim) then
c Vorticity output is triggered  -  Note abs(vorticity) written out.
             Write(15,*)x,y,abs(vort(i,j))*100000.0,dx
            Endif
c Put in limits to scatter data for vorticity to establish the correct domain (b.L.H. corner).
            If (i.eq.1 .and. j.eq.1)then
             Write(15,*)x,y,zilch,one
            Endif
            If (i.eq.ndx .and. j.eq.ndy) then
c Put in limits to scatter data for vorticity to establish the correct domain (t.R.H. corner).
             Write(15,*)x,y,zilch,one
            Endif
02100     Continue
          Close(15)
         Endif

C This was for when I was looking at outputting the pressure gradient term.
cc          do 2110 i=1,ndx+1
cc           do 2111 j=1,ndy+1
cc            x = xmin + (i-1)*dx
cc            y = ymin + (j-1)*dy
cc            pg = (9.81 * h(i,j,3)* ((n(i,j,3)-n(i,j-1,3))/dy))
cc            If(abs(pg).gt.0.0001.and.H(i,j,3).gt.0.1)then
cc             Write(17,*)x,y,pg,dx
cc            Else
cc             Write(17,*)x,y,0.0,dx
cc            Endif
cc02111    Continue
cc02110   Continue
cc          Close(17)

C Write message to confirm output stage successful.
          write(*,'(a)') uname
C SC5=============================================================

C Section SC6 - Tidy up loose ends and return to the main program.
C SC6_____________________________________________________________
C Format statements used in file stem naming procedure.
00102     Format(i1)
00103     Format(i2)
00104     Format(i3)

C Return to the main program.
          Return
          END
C SC6=============================================================
```

APPENDIX B. TFD MODEL PARAMETER FILE

```
Read in bathymetry file  (dname)
c:\scott\thesis_output\input\expb2.grd
time step (dt). Duration of simulation (time)  seconds
        2.5        111600
tidal period (tidper). (isteady) = 1 for steady flow rampingup over tidper/4
      45000        0
Do you want to output the residual tide (rt_y_or_n)
n
If so, at what stage(secs) during the simulation should recording start, and end at (simustart, simuend)
        45000    90000
define whether velocity 'v' or elevation 'e' driving boundary at x = 1 'w' or x = ndx+1 'e'
e
w
Do you want to use a pre-defined radiating boundary ? (d = yes, a = no)
a
Input phase difference between input and radiating boundary (seconds)
        0
define driving boundary in currents (Umax) and elev (tamp,z0,theta)
        0.0        1.0        0          0
define whether velocity v or elevation driving boundary  at y = 1 (s) or y = ndy+1 (n)
a
r
Do you want to use a pre-defined radiating boundary ? (d = yes, a = no)
a
Input phase difference between input and radiating boundary (seconds)
        0
define driving boundary in currents (Vmax) and elev (tamp,z0, theta)
        0.0        1.0        0          0
define land boundary either no-slip (0) or free slip (1)
        0
manning nr
        0.025
Wind velocity in the x and y direction at z = -10m
        0          0
latitude in decimal form and hemisphere (n or s)
        0
S
stem of output files (hname)
c:\scott\thesis_output\output\shed\frict+edvisc\expv15
nr of iteration steps delay before output and nr steps between output files (io_step)
        0          720
switch on/off (1/0) scatter output and gridded output files
        1          0
limit below which vorticity in a cell will NOT be output (vortlim)
        0.000000001
upper limit of CFL number (<1)
        0.40
minimum total depth (m) before cell omitted from computation
        0.25
Elevation driving boundary is either (F)ile based or completely(C)alculated
F
If file based, input directory and file name
c:\scott\thesis_output\input\ramping_in.dat
Velocity driving boundary is either (F)ile based or completely(C)alculated
C
If file based, input directory and file name
c:\temp\
Record radiating boundary data ?
n
```

Input directory and file name to store radiating boundary data in
c:\scott\thesis_output\output\Rattray\input\drivingu4.dat
Do you want to output u and v data 'y' or 'n' - (uvout)
y
Do you want to output elevation data 'y' or 'n' - (nout)
y
Do you want to output vorticity data 'y' or 'n' - (vout)
y

APPENDIX B. TFD MODEL ARRAY SIZING FILE

```
      PARAMETER(mx=252,my=101,mt=3)
```